ORNL-4446
UC-41 — Health and Safety

HEALTH PHYSICS DIVISION

ANNUAL PROGRESS REPORT

FOR PERIOD ENDING JULY 31, 1969

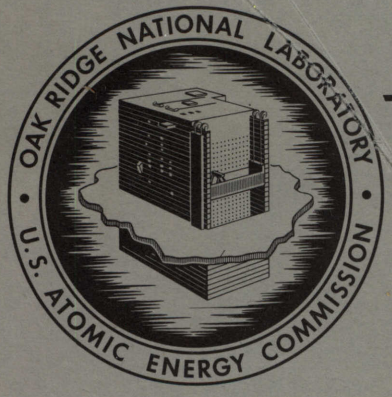

OAK RIDGE NATIONAL LABORATORY
operated by
UNION CARBIDE CORPORATION
for the
U.S. ATOMIC ENERGY COMMISSION

Printed in the United States of America. Available from Clearinghouse for Federal Scientific and Technical Information, National Bureau of Standards, U.S. Department of Commerce, Springfield, Virginia 22151
Price: Printed Copy $3.00; Microfiche $0.65

ORNL-4446
UC-41 — Health and Safety

Contract No. W-7405-eng-26

HEALTH PHYSICS DIVISION ANNUAL PROGRESS REPORT

For Period Ending July 31, 1969

K. Z. Morgan, Director

W. S. Snyder, Assistant Director
E. G. Struxness, Assistant Director

OCTOBER 1969

OAK RIDGE NATIONAL LABORATORY
Oak Ridge, Tennessee
operated by
UNION CARBIDE CORPORATION
for the
U. S. ATOMIC ENERGY COMMISSION

Reports previously issued in this series are as follows:

ORNL-2384	Period Ending July 31, 1957
ORNL-2590	Period Ending July 31, 1958
ORNL-2806	Period Ending July 31, 1959
ORNL-2994	Period Ending July 31, 1960
ORNL-3189	Period Ending July 31, 1961
ORNL-3347	Period Ending July 31, 1962
ORNL-3492	Period Ending July 31, 1963
ORNL-3697	Period Ending July 31, 1964
ORNL-3849	Period Ending July 31, 1965
ORNL-4007	Period Ending July 31, 1966
ORNL-4168	Period Ending July 31, 1967
ORNL-4316	Period Ending July 31, 1968

Contents

PART II. RADIATION ECOLOGY

PART III. RADIATION PHYSICS

PART V. INTERNAL DOSIMETRY

THESES, PAPERS, PUBLICATIONS, AND LECTURES

Summary

PART I. RADIOACTIVE WASTE DISPOSAL

1. Fate of Trace Elements and Radionuclides in Terrestrial Environment

Tests with several organic suspending agents have resulted in maintaining dispersion of clay-size minerals in the density-gradient solution. Mineral segregation has thus been achieved with standard clay minerals as well as with different soils and with calcareous sediment. Results show that the purity of the standard clay minerals is suspect. With soils, minerals heretofore undetected were identified through concentration in the gradient solution. Calcium carbonate was segregated from the clay minerals, and this permitted better characterization of the forms of phosphate existing in the sediment.

2. Disposal by Hydraulic Fracturing

The waste disposal injections are now going well, and a total volume of about 1,500,000 gal of water and slurry, containing nearly a quarter of a million curies, has now been pumped down our disposal well. More observation and rock-cover monitoring wells are being added as funds become available. Drilling into the waste-filled fractures deep underground raises minor problems of contamination. The initial work in New York State suggests that our experiments there can be carried out much as planned, although some minor modifications will be required.

3. Disposal in Natural Salt Formations

Most of the effort in this program is now directed toward the establishment of an actual high-level waste repository capable of accepting all of the power reactor wastes until about the end of the century. This effort is currently along three different lines: (1) the development of a computer program modeling the long-term deformational behavior of mine pillars of different designs under the influence of stress, elevated temperatures, and thermal gradients; (2) the development of a mine management program capable of defining the spacing required between successive cans of waste; and (3) the preparation of a report providing information on where the disposal facility should be located, how big it should be, and when it should be ready for operation.

Other work is continuing, including the preparation of a final comprehensive report on the demonstration experiment, Project Salt Vault, and the examination of rock types other than salt which might be usable for radioactive waste disposal. This latter work has been concerned recently with the determination of the effects of heat, stress, and radiation on the deformation of limestone.

4. Engineering, Economic, and Safety Evaluation

The amount of transuranic nuclides anticipated in the wastes from processing of reactor fuels is such that it must be considered in the management of such wastes. The major potential hazard seems to be associated with inhalation as the exposure mode, and containment times on the order of hundreds of thousands of years would be required. Rehandling of the waste, especially after the container and its contents had lost integrity, would be hazardous to operating personnel.

In view of the extremely long containment times required, consideration of long-term geologic alterations in the earth's crust is under study. Some examples of the rates of these changes are given.

Many exposure pathways must be investigated to estimate the potential internal dose to population groups from radionuclides that may be released by nuclear facilities. This involves consideration of foods consumed by man as well as ingestion of water and inhalation of air. A preliminary version of the computer program PATHWAY has been formulated to trace the movement of ^{131}I, ^{137}Cs, and ^{90}Sr through environmental food chains to man.

5. Earthquakes and Reactor Safety

Laboratory and field tests have been made to determine the usefulness of the photoelastic coating technique on representative samples of the rock column for assessing geotectonic activity. Preliminary investigations have been made to define the mechanisms causing slope instability in portions of the Atlantic and Gulf coastal plains. A description of the recently activated ORNL seismological station is given, along with a report of significant recordings during the past year.

6. Dose Estimation Related to Peaceful Uses of Nuclear Explosives

Estimates have been made of the dose equivalents to various population groups from the hypothetical utilization of natural gas and other products from the Gasbuggy cavity. The major radionuclides of concern, ^{3}H and ^{85}Kr, would be transported through the collection, processing, and distribution system and would be released during combustion of the gas.

Study continues of the radiological safety feasibility of using nuclear explosives to excavate a sea-level canal across the isthmus of Central America. Modifications have been made in the computer code EXREM, which is used to estimate external dose. Complex parent-daughter decay chains can now be handled directly in any external dose calculation. Internal dose calculations will be limited to ingestion of radionuclides in food and beverages. The list of potentially significant radionuclides to be studied in detail has been reduced to 31. Estimates of internal dose will be made for five age groups of indigenous populations, as follows: 0 to 1 year, 1 to 5 years, 5 to 10 years, 10 to 15 years, and over 15 years. Selection of age-dependent parameters required in the dose calculations is discussed.

A hypothetical cratering event is used to illustrate application of internal and external dose estimation codes. Only ^{137}Cs-^{137}Ba is assumed to be vented during two cratering detonations spaced 30 days apart. Cumulative dose equivalents to total body are calculated as a function of time and age since the first detonation for a number of potential exposure modes.

7. Related Cooperative Projects

Representatives of other agencies continued to participate in the Radioactive Waste Disposal Section's studies. One alien guest was in residence during the year. One member served as assistant news editor for the United States for *Health Physics* and as an assistant editor of *Nuclear Safety*. Two members of the Section taught courses at the University of Tennessee. Members of the Section participated part time in the Nuclear Safety Information Center, the Civil Defense Research Project, and the agroindustrial complex study.

PART II. RADIATION ECOLOGY

8. Responses of Animal Populations to Ionizing Radiation

Primary objectives of our growing and diverse research on radiation effects in animals are: (1) comparative measurements and interpretations of consequences of acute and chronic irradiation in wild species of animals and (2) evolution of models for prediction of radiation effects in animal compartments of ecological systems. Implicit in these objectives is the requirement that interactions of biotic and abiotic environmental factors be delineated and quantified. Separation of effects of specific environmental factors in ecosystems is difficult, and current studies are employing laboratory research to complement field experiments. Systems analyses (compartment models) of population responses to radiation stress involve extrapolations of laboratory-derived theories to natural habitats and subsequent comparisons of actual field data for tests of long-term predictive capability. It is already clear that laboratory results, although useful for single-factor analyses and initial design of field experiments, are insufficient for realistic extrapolations and predictions of radiation effects in actual environments.

Current studies include measurement of genetic, cytological, individual, and populational effects in vertebrates and invertebrates receiving acute and/or chronic irradiation. Parameters being tested include tissue damage, changes in radionuclide incorporation rates, radiation profiles, survivorship, fecundity, chromosomal aberrations, metabolism, food consumption, energy flow, competition, temperature, and RBE. Dosimetry for such studies is critical, of course, and refined techniques must be developed for measuring acute and chronic gamma and beta radiation in tissues and environmental sites of interest.

Construction of a field facility and contamination of 100-m^2 enclosures with ^{137}Cs-tagged fallout simulant (88 to 177 μ, 22 mc/m^2), funded by the Office of Civil Defense (OCD), permitted initiation of field studies on dosimetry, movement of fallout particles, ^{137}Cs incorporation into the biota, environmental factors that affect cesium movement, and radiation effects in the animals within the enclosures. Application of the fallout simulant was completed in August 1968. Effects

of physical and chemical factors on ^{137}Cs movement and incorporation into plants are discussed elsewhere in this report. The dominant vegetation in these enclosures is a fescue, *Festuca arundinacea*. Biological and ecological responses of invertebrates and rodents living in the pens and exposed to acute and chronic radiation from external and internal sources are being examined seasonally in replicated experiments under natural or seminatural conditions. The honeybee is one of the most valuable agricultural animals because of crop pollination, and another OCD-funded facility is permitting the first studies on the effects of radiation on colonies under field conditions. This research also is the first study of radiation effects on intact populations of a colonial insect.

9. Responses of Plants to Ionizing Radiation

Small white pine (*Pinus strobus*) and red oak (*Quercus rubra*) trees were contaminated in the field with a fallout simulant consisting of 88- to 175-μ-diam quartz particles containing ^{134}Cs. Whole plants were harvested at intervals up to 33 days after application of the simulant, and the ^{134}Cs retention by each species was determined.

The initial fraction of the simulant retained by foliage was higher in the oaks (0.35) than in the pines (0.24). However, after 1 hr, the broad-leaved oaks had lost 90.5% of the initial ^{134}Cs concentration, while the pines had lost only about 10%. These early retention differences are related to the effects of wind on the two distinct foliage types.

Effective half-lives were calculated for both species at intervals of 0 to 1, 1 to 7, and 7 to 33 days. For pine trees these values were 0.25, 4.53, and 20.66 days, respectively. For oaks they were 0.12, 1.41, and 24.86 days. Loss of particles (^{134}Cs) was due, primarily, to the weathering action of wind and rain during the study. The effects of wind and the first rain following contamination accounted for a large percentage of the total radionuclide loss during the study.

10. Radionuclide Cycling in Terrestrial Ecosystems

Research on processes and components of terrestrial ecosystems emphasizes (1) the structure and mechanisms governing the function and ecological organization of natural landscapes, for example, nutrient cycling, productivity, and energy flow; (2) the relation of these processes to the distribution and flux of radionuclide and other pollutants in the environment; and (3) the application of radioisotope techniques and computer simulation to developing predictive mathematical models of ecosystem performance.

The need for the capacity to understand, describe and develop predictive capabilities about the performance of natural ecosystems follows from recognition that man's impact on his environment should be anticipated before damage is done, not afterward. Such ecological competence is a prerequisite to anticipating the pathways and fluxes of radionuclide contaminants, other environmental pollutants, and vital nutrient resources. The experimental application of radionuclides and tracer techniques continues to be invaluable in extending our knowledge of fundamental ecological processes.

Ecosystem research on radionuclide cycling has concentrated on a long-lived fallout radionuclide, ^{137}Cs, in two contrasting ecosystems: a mesic *Liriodendron* forest and a *Festuca-Andropogon* grassland. In these studies techniques are being developed and tested using radionuclide tracers to identify and quantify ecosystem processes, for example, plant-soil-root relations, productivity, animal food chains, and microbial activity. Plant production and food-chain studies also have examined the pathways and fluxes of important nutrient elements in these ecosystems using ^{47}Ca, ^{22}Na, ^{42}K, and ^{54}Mn. Other research includes the cycling of selected radionuclides (e.g., ^{60}Co and ^{144}Ce) in plant-soil systems based upon nutritional requirements of the species and position of the element in the periodic table. Objectives are to develop predictive capability for chemically related elements, whose radionuclides may be potential environmental contaminants as by-products from nuclear operations. Further investigations using other radionuclides will eventually be required to round out knowledge of radionuclide and stable element dynamics in contrasting terrestrial ecosystems. Emphasis has been placed on synthetic interpretation of trophic level concentrations and transfers of biologically important radionuclides to develop mathematical descriptions of radionuclide behavior in the environment.

11. Radionuclide Cycling in Aquatic Ecosystems

Research in aquatic ecology is providing data on radionuclide movement in surface waters such as rivers and lakes. These data are needed for interpretation and quantitative prediction of the behavior of radionuclides in aquatic habitats. Such research investgations also increase our knowledge of the functioning and organization of aquatic ecosystems and provide data required for application to practical problems of atomic energy

programs such as nuclear power, desalination, radioactive waste disposal, or Plowshare projects.

White Oak Lake continues as the focal point for studies of radionuclides under natural environmental circumstances. Organisms living in the lake are essentially in equilibrium with waste radionuclides such as ^{90}Sr, ^{137}Cs, ^{106}Ru, and ^{60}Co; hence, extrapolations can be made to steady-state conditions. Laboratory studies in conjunction with the field work provide data needed for more sophisticated predictive models of nonsteady-state situations. These data are pathway description, turnover rate, and fractional assimilation coefficients of radionuclides from various foods. These investigations provide a better quantification of radionuclide behavior in aquatic food chains.

12. Watershed Aquatic Habitat Interactions

This project is organized to assess the potential ecological inpact of new technology being applied to the field of natural resource management. These studies coalesce the efforts of aquatic and terrestrial ecologists with those of earth scientists into a unified program directed toward elucidating the interactions between land and water. The project will contribute to the understanding of biogeochemical relationships between aquatic habitats and associated watersheds through the synthesis of an empirical watershed model which will (1) relate the water quality and productivity of the stream to the characteristics of the adjacent terrestrial ecosystem, (2) equate the net loss of chemical elements through streamflow to the rate of mineral cycling, (3) establish the relationship between the hydrologic cycle and the mineral cycle, (4) provide bench-mark information of natural terrestrial-aquatic ecosystems for comparison with those modified by man's cultural practices, and, finally, (5) apply the knowledge gained from this small, controlled drainage basin study to broader landscape units to evaluate the impact of man's activities on the total ecosystem.

Industrial technology is advancing at an accelerated rate. Accompanying this technology is a continual degradation of the environment from the release of by-products, wastes, and misused chemical amendments. Assessment of the impact of new technology on the landscape is imperative if we are to abate the chronic degradation of our natural ecosystems which is now occurring.

Localized problems have developed in water bodies and water courses adjacent to agricultural areas from intrusion of agricultural fertilizers, agricultural chemicals, and animal wastes. When normally innocuous inorganic fertilizers and pesticides flow into streams via groundwater and runoff, a chemical enrichment results which can cause eutrophication of the water, resulting in excessive plant growth and impairment of general water quality.

Presently these problem areas are localized. However, when forest fertilization becomes a widespread practice as a means to increase forest productivity, serious eutrophication problems may result. It appears that forest fertilization will be necessary to compensate for urban encroachment and land-use pressure if the nation's future timber demand is to be satisfied. Average rates of fertilizer application for forestry purposes usually exceed those of normal agriculture several-fold; frequency of forest fertilization, however, is generally less.

A potential problem could develop if large acreages of forest were fertilized, because our water supplies originate in upland forested regions prior to entering the agricultural and industrial regions downstream. Presently, these virgin waters contain only natural chemical enrichment resulting from normal cycling and decomposition. If, however, the watersheds also contribute significant inorganic salts lost from fertilized forests, the problem will compound the effect of present agricultural, industrial, and urban pollution and perhaps exceed a threshold which could result in a costly and serious degradation of water quality.

The Walker Branch Watershed project is presently emphasizing the characterization and modeling of the undisturbed, natural forest ecosystem. Within three years this initial characterization will be completed, and one subwatershed will be fertilized to measure the differential effect of fertilization on the ecosystem. Fertilizer effects will be related to biomass growth, animal and plant species-diversity, enrichment and rate of movement of chemicals through the soil-water system, and stream water quality and aquatic productivity.

Studies have been initiated to evaluate the transfer rates and characteristics of the transfer functions among the principal components of the watershed ecosystem. This year's report summarizes the initial data evolving from some of these subsystem studies.

13. Systems Ecology

The overall purpose of the ORNL ecological systems analysis program is to provide a practical methodology that ecologists can use to make useful predictions about the outcome of environmental interactions, both empirical and theoretical. Progress has been made in evalu-

ating the pertinence of recent ecological literature to the modeling of ecosystems, a biogeochemical ecology information center was established, and several systems analysis computer programs were written and tested on various ecological problems.

PART III. RADIATION PHYSICS

14. Theoretical Radiation Physics

A report of the task group on high-energy radiation for Committee III of the ICRP has been prepared. A new model for calculating the penetration of high-energy neutrons and protons through matter has been described which neglects the effects of binding and grouping of nucleons within nuclei. A Monte Carlo method has been used to determine the distribution of track lengths in cavities of various shapes and to unfold LET spectra from pulse-height measurements made with energy-proportional detectors. This unfolding procedure promises to bring LET spectral determinations within the grasp of health physics surveyors routinely.

A calculation has been made of the spectral and angular distribution of optical radiation from metal surfaces due to radiative decay of tangential surface plasmons excited in the metal by grazing incidence electrons. These theoretical results, together with sufficiently detailed experiments, should allow determination of parameters which can describe the irregularities of metal surfaces.

We have studied the influence of surface plasmons on the reflectivity of a nonuniform, bounded electron gas. This theory should be valuable in the analysis of experimental results on the surface plasmon effect.

The mean free path has been derived for the second-order process of double-plasmon excitation due to the interaction of a fast charged particle with a free-electron gas.

The theory of low-energy electron scattering by atomic systems was considered through new developments in two standard approaches in the quantum-mechanical theory of scattering. The Wigner R-matrix analysis was applied to the atomic scattering problem including long-range interactions, and an expression was obtained relating the elastic scattering phase shifts with the scattering energy. In another study a new variational method was developed for application to problems in atomic scattering theory where long-range forces play a significant part in determining low-energy cross sections.

The ground-state energy eigenfunctions for an electron bound to a finite dipole which were earlier obtained in elliptic-hyperbolic coordinates have been analyzed in spherical polar coordinates. These results serve as a first step in determining the effects of other interactions and of molecular rotation on the binding of an electron to a real physical dipole potential.

The stopping power of matter for extremely relativistic protons and muons has been treated through a relativistic quantum-mechanical calculation. Expressions for the stopping power contain contributions from the spin, anomalous magnetic moment, and form factors for the proton and muon. The stopping power of aluminum has been determined for a wide range of extreme relativistic energies.

15. Interaction of Radiation with Liquids and Solids

Optical constants in the vacuum ultraviolet have been determined for Rb, Na, and K, and for the organic liquids C_6H_6, C_6H_{14}, CH_3OH, C_2H_5OH, and DC704 pump oil. Interpretation is in terms of free electron effects, interband transitions, and collective oscillations. The collective oscillation seen in benzene, presumably involving the π electrons, is the first known reported observation of a collective oscillation in a liquid insulator. The hexane and alcohols are of basic interest because they are used as solvents for other organic compounds, and the pump oil is of interest because it is present as a contaminant in vacuum monochromators using this as a pumping fluid.

Photoemission measurements have been made on Mg and Al as a function of time after film deposition for various incident photon energies. These data can be interpreted in terms of the growth of an oxide layer on the surfaces. Changes in the photoelectron energy distribution curves with time after film deposition have also been correlated with changes in the work function and in the reflectance.

Considerable refinements have been made to the ultrahigh vacuum ellipsometer and to the methods used in the analysis of the data obtained with this apparatus.

The optical emission spectra from Al films bombarded with high-energy electrons have been investigated experimentally, and it is possible that radiative surface plasmons have been detected. Surface plasmon resonance effects in the light diffracted from concave diffraction gratings with various overcoatings have also been observed and interpreted.

16. Atomic and Molecular Radiation Physics

The Atomic and Molecular Radiation Physics Group has obtained new information on the following specific topics: scattering of slow electrons by polar molecules, energy lost by slow electrons in collisions with molecules, electron swarm energy distribution functions, electron attachment to N_2O, azulene, oxygen containing biologically important molecules and other organics, and long-lived polyatomic negative ions formed by electron capture in the field of the ground and excited electronic states of the parent molecule. Also, new information has been obtained on degradation spectra, efficiencies of photosensitized ionization, molecular complexes, transient molecular photoassociation, and lifetimes of excited fluorescing species in organic liquids. Our experimental and analytical techniques have been refined and standardized. Accurate sets of electron swarm energy distribution functions have been well documented. Low-energy electron-polyatomic molecule studies have revealed new physical phenomena not observable in simple molecules. Formation of long-lived negative ions by electron capture in the field of an excited electronic state of a polyatomic molecule has been discovered for the first time. Negative-ion autoionization lifetimes and absolute capture cross sections have been measured as a function of the electron energy and have been related to basic molecular structure, yielding molecular electron affinities and molecular electron accepting capacities. Biologically important molecules containing $n \rightarrow \pi^*$ transitions have been found to attach electrons forming long-lived (lifetimes of the order of 10^{-5} sec) parent negative ions with simultaneous excitation of a "lone-pair" electron. Evidence for electron capture into various vibrational modes of the molecular skeleton has been obtained also, the negative-ion lifetime decreasing with energy. The effect of molecular structure and geometry on electron capture has been investigated; to this end a detailed study of the N_2O molecule has been made. Evidence has been obtained also which suggests that electron capture may be accompanied by a simultaneous excitation of more than one orbiting electron, the parent molecular ion so formed being long-lived. Our experimental data also suggest that the electron affinity of a molecule in an excited electronic state may exceed that of the ground state.

17. Electron and Ion Collision Physics

Electrons with energy barely sufficient to excite an energy level of an atom or molecule can undergo a completely inelastic collision and be reduced to zero energy. Also, when the electron energy is sufficient to ionize the gas, it is found that a fraction of the collisions produce zero-energy electrons. We have employed the SF_6 "scavenger" and "trapped-electron" techniques for studying threshold excitation of the rare gases, ammonia, xenon hexafluoride, xenon tetrafluoride, and a number of organic molecules. For the rare gases the number of slow electrons produced above the ionization potential is fairly constant with increasing incident electron energy. Some evidence is also observed for inner-shell ionization. The most interesting threshold excitation spectra of the rare gases are found in the region of the two-electron excitation states. Here simultaneous excitation of two electrons may cause the incident electron to be "thermalized." Doubly excited states have been detected in the ionization continuum of helium, neon, and argon. Triply excited negative-ion resonances are also evident in the slow-electron spectrum of helium. Negative-ion resonances in helium at 57.2 and 58.3 ev are also seen as strong "dips" in the cross section for production of He^+ ions.

The formation of long-lived ($>10^{-6}$ sec) temporary negative ions has been studied extensively with both electron swarm and electron beam techniques. Slow electrons are known to temporarily attach to sulfur hexafluoride with a cross section approaching the theoretical maximum for *s*-wave capture. A mass spectrometer search for negative ions of hexafluoride molecules formed from atoms directly below sulfur in the periodic chart revealed no detectable SeF_6^- or TeF_6^- ions. Uranium hexafluoride likewise does not directly attach slow electrons. However, molybdenum hexafluoride readily forms MoF_6^-. Surprisingly, SeF_6, TeF_6, and UF_6 negative ions can be easily formed by charge exchange with SF_6. The lifetime for temporary attachment of electrons to complex molecules has also been determined for a number of theoretically important attachment reactions.

A technique for studying charge exchange and ion-molecule reaction cross sections in the energy region from 0 to 2 ev has been applied to a number of interesting collision partners, for example, H^-, H_2O; O^-, NO_2; Cl^-, NO_2; I^-, NO_2; and others. Charge exchange between the halogen negative ions and NO_2 is believed to exhibit a very sharply increasing cross section with decreasing ion energy.

18. Graduate Education and Vocational Training

The Health Physics Training Program included fellowship students from Vanderbilt University, University of Tennessee, Georgia Institute of Technology, University

of California, and the University of Kansas. These reported to ORNL for summer on-the-job instruction in applied and research health physics.

Division personnel visited 20 colleges and universities to give seminars on various research problems of current interest and also to help interest qualified students in the fellowship program.

The Health Physics Division provided research facilities and advisors for 19 Oak Ridge Graduate Fellows, AEC Fellows, and USPHS Fellows who were conducting thesis research. A total of 34 university personnel ranging from undergraduates to professors spent the summer in the Division.

Teaching assistance was given to the University of Tennessee for its program in Radiation Physics and to Vanderbilt University for its course in Radiation Physics. Lectures and tours were given for several university groups visiting ORNL.

Assistance and consultation was given to eight schools that were interested in establishing health physics courses or programs in their science departments.

The Division cooperated with ORAU in the presentation of a ten-week course in applied health physics and in the screening of applicants for AEC Fellowships.

19. Physics of Tissue Damage

A dispersion analysis incorporating an internal field correction has been made of the optical properties of liquid water in the vacuum ultraviolet. This analysis, which uses our previously obtained optical constants, yields energies, line widths, and oscillator strengths for the absorption peaks.

The possibility of observing transition radiation from electron-bombarded liquid water has also been investigated. Calculations have been made of the theoretical transition radiation spectra, and indications are that it should be observable. An apparatus has been constructed to observe such radiation, but so far efforts have been frustrated by intense background light.

Work was continued on the interaction of low-energy electrons with metals. Attenuation lengths and stopping powers in aluminum were measured. The general shape of the electron transmission curve as a function of energy was compared with theory, and semiquantitative agreement was found.

An analytical expression for the electron slowing-down flux was derived using an empirical form for the stopping power. The electron flux from ^{64}Cu beta rays slowing down in lead was measured to determine the influence of bremsstrahlung absorption in generating secondary electrons. Work was initiated on the measurement of the electron flux generated by alpha particles and of the slowing-down spectra in germanium and silicon semiconductors. Work was also begun on developing a slowing-down theory using more accurate cross sections.

PART IV. RADIATION DOSIMETRY RESEARCH

20. Dosimetry for Human Exposures and Radiobiology

The calculations of LET and dose distributions in man-sized phantoms, important in nuclear accident and Ichiban studies, were extended to different neutron spectra and to beams of limited area. Calculations of neutron dose and fluence for geometries used during Operation HENRE were completed. An analysis of the blood sodium activation in swine exposed during HENRE was also completed. Thermal-neutron fluences for distances up to 3500 ft from the HENRE accelerator for several heights were measured.

21. Spectrometry Research and Development

The final analysis of the energy and angular distributions of the radiations from the HENRE accelerator was completed; the most important results are related to the failure of 14-Mev neutrons to come into transitory energy and angular equilibrium and the effect of this on radiation propagation and shielding.

Zone refining techniques have been used to purify organic scintillators, with important improvements in the light output of these detectors as the result. In particular, paraquaterphenyl, after zone refining, shows a light output efficiency comparable with anthracene.

An analysis and compilation of x-ray absorption coefficients for low energies have been made. For several elements the results of calculations and measurements by several groups of researchers were found to agree to within a few percent for x rays down to a few kev of energy.

22. Applied Research

Major advances were made in the development of solid-state detector systems. Important progress was made in understanding the basic mechanisms and in the application of insulating solids as charged-particle track detectors. In particular, the breakdown of electrical insulation in thin plastic foils after irradiation and etching led to the development of ultrasensitive detectors for alpha particles and neutrons; a sensitive

personnel exposure detector for radon progeny for uranium miners was developed.

Thermally stimulated exoelectron emission (TSEE) from many substances was measured, and the characteristics of this phenomenon applicable to dosimetry were studied. A reader device for high temperatures was developed which led to the discovery of emission peaks at higher temperatures than those used previously.

In the field of radiophotoluminescence (RPL), a major improvement in the lithium borate detector resulted from the addition of 7.5% of BeO to the glass. The new glass is far less soluble and subject to weathering than without the BeO.

23. HPRR and Accelerator Operations

The Health Physics Research Reactor was used for an increased variety of both physical and biological research, and it operated almost flawlessly. There has been no change in the physical state of the core materials, and continued improvement in the reproducibility of the pulse yield was made. A low-yield neutron generator was installed to trigger bursts so that the precise time of the burst can be predicted. The sixth intercomparison of dosimetric systems was held July 7–18, 1969, with the emphasis placed on the work of representatives of nuclear materials licensees.

The DOSAR Low-Energy Accelerator was used primarily for calibration of neutron spectrometers and for stopping-power studies at low ion energies. The 3-Mv Van de Graaff was used extensively for spectrometry research and for studies of the LET dependence of solid-state detector systems.

PART V. INTERNAL DOSIMETRY

24. Internal Dose Estimation

The metabolism of iron is not governed by a simple compartment system such that the radionuclide present in the various organs or compartments is exchanged at a constant rate. It is well known that some of the iron deposits in red blood cells and remains there during the life of the cell, which is approximately 120 days. A generalized compartment scheme model has been developed which permits one to calculate the total microcurie-days of residence in the various compartments. In general, this would suffice for an estimate of dose commitment; but the method does not offer much advantage if one wishes to have the time course of the dose instead of merely the dose commitment.

When ^{232}Th or ^{228}Th enters the body, the first daughter produced is an isotope of radium. In ICRP Publication 2, it was assumed that this radium daughter, when produced, would be discharged to blood and recirculated, with only a fraction of the radionuclide returning to bone. The data on ^{228}Th from University of Utah dogs cast some doubt on this hypothesis, but because of the short half-life of the daughter ^{224}Ra, the Utah data do not suffice to determine the fate of the radium daughter of thorium. A four-compartment metabolic model has been defined which allows for a two-component representation for bone as well as a soft tissue compartment and the blood pool, and two cases have been computed: (1) a hypothesis is made that the radium daughter recirculates to blood and is then eliminated or redeposited as would freshly injected radium; (2) an alternative is to allow the radium daughter to remain in bone, where produced, and allow it to be eliminated as would freshly deposited radium. Using the Utah retention data for dogs, the exchange constants for such a system are obtained, and the amount of radium daughter present in bone is computed. The estimates of the two models bracket the Utah data but seem to lie somewhat closer to the results obtained by the first hypothesis, that is, recycling. It may be that the recycling of some fraction of the daughter element would produce better agreement. Estimates of microcurie-days residence for human retention are also obtained.

It is well known that the amounts of plutonium excreted per day fluctuate rather widely, although the trend is well represented by a power function. These fluctuations pose a problem for personnel monitoring. Since samples are not taken routinely with great frequency, when a high level is found the question arises as to whether it represents a high value due to a recent intake of the material or whether it is only a chance fluctuation. The distribution of these chance fluctuations has been studied and an attempt made to set limits such that if a urine sample exceeded these limits, one would be confident a new intake of plutonium had occurred. The results are rather disappointing in that the intake must be of considerable magnitude before the increase it entails would be clearly distinguishable from the chance fluctuations. Thus follow-up studies, which are both time-consuming and extensive, seem to be the only present answer to this problem.

25. Stable Element Metabolism

The program for revising and improving standard man as a model for estimation of absorbed dose of radiation

is represented here by a new composition for the whole body. Inasmuch as data come from a wide variety of subjects and by a variety of techniques, it requires considerable study of the data to obtain a balanced composition for a whole body of 70 kg. The percentages of fat, water, protein, bone, etc., to be included must be carefully considered as well as a considerable mass of poorly specified tissue which, for the most part, has not been analyzed in detail. The composition presented here is based on estimates of elemental composition of tissue samples of grossly normal United States adults and on organ and tissue weights considered as typical of a 70-kg male. This report also includes data on the weight of the GI tract and results of some diet-excretion studies which help complete our definition of the standard man.

Part I. Radioactive Waste Disposal

K. E. Cowser

1. Fate of Trace Elements and Radionuclides in Terrestrial Environment[1]

Tsuneo Tamura
W. P. Bonner F. S. Brinkley
C. W. Francis E. R. Eastwood

ZONAL CENTRIFUGATION STUDIES

Recent developments in the zonal centrifugation technique suggest several applications of this tool in aiding our understanding of environmental systems. This technique involves preparing a continuous-density-gradient solution in a tube, layering the test sample on the gradient solution, and centrifuging the tubes to allow each component to collect at its isodensity, or isopycnic, point. Earlier techniques for separating multicomponent mineral systems utilized a series of solutions of different densities; this procedure is especially time consuming, since the floating and settled fractions must be collected and reintroduced to solutions of higher or lower densities. A modification of the "sink-float" technique consists in carefully introducing a series of solutions of differing densities into a tube; however, the interface of the separate solutions imposes a barrier to particle penetration. Though this problem is in part overcome by centrifugation, particles accumulating at or near interfaces are subject to question regarding their densities. With the continuous-gradient solution, the problem of interface barrier is eliminated, and the stepwise preparation of solutions is avoided. The pump used to form the density gradient in these studies was developed at the Oak Ridge Gaseous Diffusion Plant.[2]

The major problem in separating samples containing clay-size minerals is flocculation. When flocculation occurs, several components can form floccules which prevent individual component banding and prevent other components reaching their isopycnic point. To overcome flocculation, several approaches were taken: different sample preparation techniques, different heavy and light liquid combinations to form the gradient solutions, and different suspending agents. Table 1.1 shows selected combinations of these and the observations regarding flocculation or dispersion.

The use of an appropriate suspending agent proved most fruitful. The search for suspending agents was limited primarily to materials compatible with organic density-gradient solutions. Although there are many agents compatible with water systems, density-gradient solutions in the range of 1.8 to 2.8 g/cc require heavy organic liquids which are generally not miscible with water or require heavy inorganic salts which favor flocculation of clays with high charge density in the diffuse double layer. The suspending agent selected for our studies was a polyvinylpyrrolidone polymer (PVP

[1] Other studies are reported in the Radiation Ecology Section as part of cooperative program in land-water interactions.

[2] S. A. Fox, *An Analysis of a Cam Driven Density Gradient Pump*, K-L-2966 (July 3, 1968).

Table 1.1. Test Trials to Obtain Dispersion of Environmental Samples

Number	Sample	Sample Preparation	Density Gradient Medium	Suspending Medium	Observation
1	Suspended pond sediment, 0.08 to 0.2 μ	Oven dried	Thallium formate + water, ρ = 1.8–2.2	Water	Flocculation
2	Suspended pond sediment, 0.08 to 0.2 μ	Oven dried	Thallium formate + water, ρ = 2.4–2.7	Thallium formate + water, ρ = 2.4	Flocculation
3	Suspended pond sediment, 0.08 to 0.2 μ	Oven dried	Diiodomethane + dimethyl sulfoxide, ρ = 2.2	Same as gradient	Flocculation
4	Suspended pond sediment, 0.08 to 0.2 μ	Oven dried	TBE + benzene, ρ = 1.8	EtOH	Flocculation
5	Suspended pond sediment, 0.08 to 0.2 μ	Wet samples washed with EtOH and then acetone	TBE + EtOH, ρ = 1.8–2.8	TBE + EtOH, ρ = 1.8	Flocculation
6	Suspended pond sediment, 0.08 to 0.2 μ	Saturate with methylene blue and then wash with EtOH and acetone	TBE + EtOH, ρ = 1.8–2.8	TBE + EtOH, ρ = 1.8	Flocculation
7	Suspended pond sediment, 0.08 to 0.2 μ	Saturate with anionic guar polymer and then wash with EtOH	TBE + EtOH, ρ = 1.8–2.8	TBE + EtOH, ρ = 1.8	Flocculation
8	Suspended pond sediment, >2 μ	Oven dried followed by EtOH and acetone wash	TBE + EtOH, ρ = 1.8–2.8	TBE + EtOH, ρ = 1.8	Dispersion
9	Bottom pond sediment	Oven dried	TBE + EtOH, ρ = 1.8	TBE + EtOH, ρ = 1.8	Flocculated; also flocculated with ρ = 2.4
10	Bottom pond sediment	Oven dried	TBE + EtOH, ρ = 1.8	TBE + EtOH, ρ = 1.8, plus 2% Nopcosant K	Flocculation
11	Bottom pond sediment	Oven dried	TBE + EtOH, ρ = 1.8	TBE + EtOH, ρ = 1.8, plus 2% Nopcosant Lomar PWA	Flocculation
12	Standard clays, <2 μ	Sodium saturated and dialyzed	TBE + EtOH, ρ = 1.8–2.8	TBE + EtOH, ρ = 1.8	Flocculation
13	Standard clays, <2 μ	Sodium saturated, dialyzed, and freeze dried	TBE + EtOH, ρ = 1.8–2.8	TBE + EtOH, ρ = 1.8	Flocculation
14	Standard clays, <2 μ	Sodium saturated and dialyzed	TBE + Emsol, ρ = 1.8–2.8	TBE + Emsol, ρ = 1.8	Dispersion
15	Kaolinitic soil, >2 μ	Sodium saturated and dialyzed	TBE + EtOH, ρ = 1.8–2.8	TBE + EtOH, ρ = 1.8	Dispersion
16	Kaolinitic soil, <2 μ	Sodium saturated and dialyzed	TBE + EtOH, ρ = 1.8–2.8	TBE + EtOH, ρ = 1.8	Flocculation
17	Kaolinitic soil, <0.2 μ	Sodium saturated	TBE + EtOH, ρ = 1.8–2.8, plus 10% PVP in EtOH phase	TBE + EtOH, ρ = 1.8, plus 10% PVP in EtOH	Dispersion
18	Standard clays, <2 μ	Sodium saturated	TBE + EtOH, ρ = 1.8–2.8 plus 10% PVP in EtOH phase	TBE + EtOH, ρ = 1.8, plus 10% PVP in EtOH	Dispersion
19	Bottom pond sediment	Acetone washed	TBE + EtOH, ρ = 1.8–2.8, plus 10% PVP in EtOH phase	TBE + EtOH, ρ = 1.8 plus 10% PVP in EtOH	Dispersion

K-30), which is a white crystal soluble in ethyl alcohol (EtOH).

From Table 1.1 it may be noted that if the particles are larger than 2 μ in diameter, dispersion is obtained in a tetrabromoethane (TBE) and EtOH gradient without the aid of a suspending agent (Nos. 8 and 15). Limited tests with Emsol as the suspending agent also suggest that this material may be satisfactory for keeping the system in a dispersed state (No. 14). Figure 1.1 is a photo of the separation achieved with and without PVP K-30 in a mixture containing three standard clays. Note that without the suspending agent, the floccule reached an intermediate isopycnic point.

The procedure adopted for analyzing environmental samples is as follows: The sample is washed in nonpolar organic liquids; the sample is suspended in a TBE and EtOH solution containing 5% by weight of PVP K-30 and subjected to 1 to 3 min of ultrasonic treatment at 20,000 cycles and 100 w (samples cooled in ice bath); the sample is layered on a preformed density-gradient solution of TBE + EtOH whose PVP K-30 concentration varied as the EtOH varied; the sample is centrifuged at 1500 rpm overnight (over 12 hr) in a refrigerated centrifuge; individual bands of minerals are removed with a pipet; density gradient is reconfirmed by removing selected samples of clear solution and measuring the refractive index.

In the following section, results of the studies with clays and bottom sediment from a pond are reported. These studies are primarily concerned with an improved mineral identification technique and increased understanding of environmental systems, with particular reference to phosphate distribution in the pond.

CLAY MINERAL STUDIES

Heavy liquids (tetrabromoethane, bromoform, etc.) have been used for several decades to determine

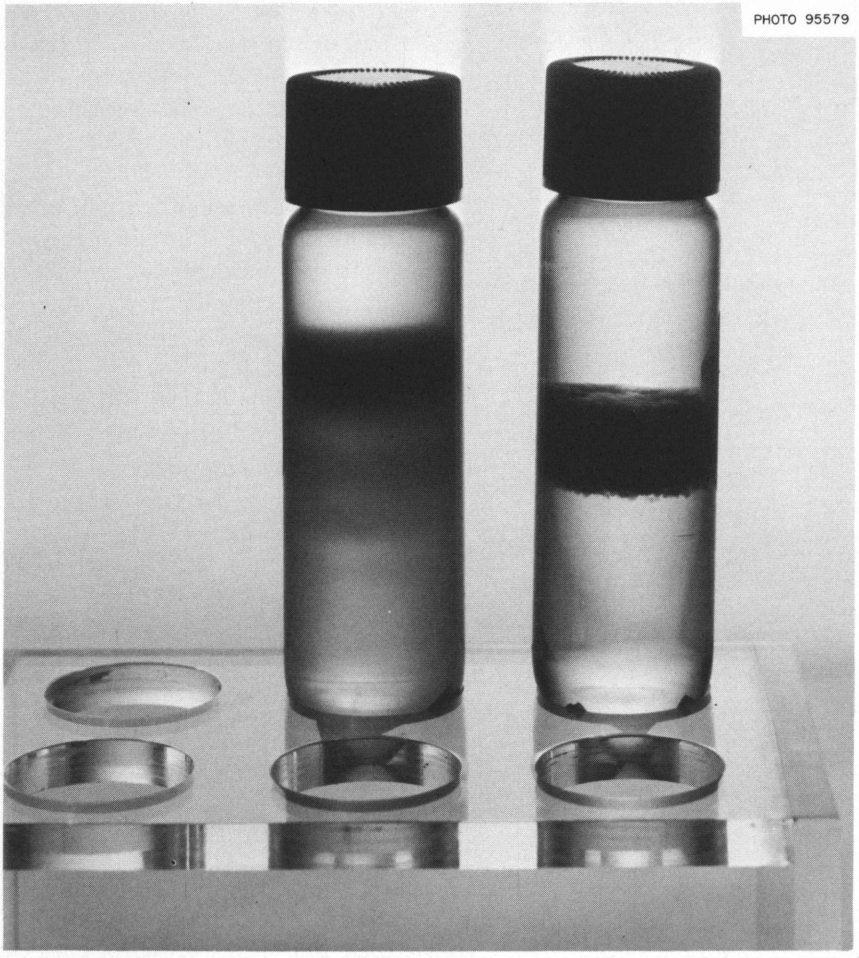

Fig. 1.1. Separation Achieved With and Without PVP K-30 in a Mixture Containing Three Standard Clays.

densities of clays.[3,4] The differences in densities of the clay minerals have led to attempts at using this property for clay mineral identification.[5,6] With a simple, accurate, and reliable density-gradient former available, it seemed desirable to use this tool to isolate mineral fractions and study their properties. However, as noted in the preceding section, most systems containing clay-size particles flocculated in the density-gradient solution. This observation led us to develop a more reliable dispersant system. With the development of the TBE-EtOH plus PVP K-30 dispersant system, the clay system could be evaluated.

The clays selected for study included montmorillonite (API No. 26) from Clay Spur, Wyoming; illite (No. 35) from Fithian, Illinois; and kaolinite (No. 2) from Macon, Georgia. Each of the standard clays was placed (250 mg) on density gradients (1.80 to 2.70 g/cc) of TBE-EtOH plus PVP K-30 and TBE-acetone. In TBE-acetone the observed densities were as follows: montmorillonite, 1.95 to 2.21; illite, 2.38 to 2.54; and kaolinite, 2.46 to 2.58. These densities compare very well with the sodium-saturated clays reported earlier.[6] However, observation of the clays in the centrifuge tubes showed them to be highly flocculated.

The same clays centrifuged through a density gradient of TBE-EtOH plus PVP K-30 not only showed a dispersed state but developed several bands for each clay type. This is shown plotted as "half-blocks" on the upper part of the curve of Fig. 1.2. The recovered bands were x rayed for mineral identification. In band 1 (1.8 to 1.94) of montmorillonite, a strong 17.7-A peak characteristic of glycerol-solvated montmorillonite was noted; in band 2 (2.43 to 2.52) the material was primarily quartz.

Illite separated into four bands whose densities were less than or equal to 1.83, 1.94 to 2.16, 2.29 to 2.37, and 2.49 to 2.54 g/cc. All bands showed the characteristic 10-A maxima of illite; however, with the lighter bands, the peaks showed a much broader character, indicating smaller particles or higher hydration. The bands were distinct and well-separated from each other. This opens the question of the nature of illite. It should be noted that if the clay had flocculated as in the TBE-acetone system, the band would have occurred at 2.38 to 2.54 g/cc. In addition, on potassium saturation and heating, bands 3 and 4 exhibited the presence of appreciable amounts of kaolinite and chlorite.

The kaolinite sample separated into two bands of 2.10 to 2.26 and 2.42 to 2.52 g/cc. Both bands revealed near-ideal kaolinite x-ray diffractograms. Differences of the two bands cannot be explained at this time. Material from the bottom of the centrifuge tube showed a trace amount of kaolinite and a pattern indicative of anatase (3.50 A).

When the clays were mixed in equal weight proportions and separated using the TBE-EtOH plus PVP K-30 gradient, five bands were recovered. The locations of these bands are shown as "half-blocks" on the lower portion of the curve of Fig. 1.2. The smoothed x-ray diffraction tracings of the glycerol-solvated clays from each band are presented in Fig. 1.3. It is evident that each band cannot be associated with one specific mineral; however, the majority of the montmorillonite appears concentrated in the top two bands and the majority of the kaolinite in bands 3 and 4. Illite, which appeared in four bands when separately banded, occurs mostly in bands 3, 4, and 5. Further studies are under way to characterize the different bands and evaluate the role of pretreatment on band position.

[3] Emil Truog *et al.*, "Procedure for Special Type of Mechanical and Mineralogical Soil Analysis," *Soil Sci. Soc. Am. Proc.* 1, 101–12 (1936).

[4] R. W. Pearson and E. Truog, "Further Results of Mineralogical Subdivision of Soil Separates by Means of Heavy Liquid Specific Gravity Separation," *Soil Sci. Soc. Am. Proc.* 3, 20–25 (1938).

[5] J. W. Amburgey, Jr., *A Study of Centrifugal Banding Techniques for Separating Minerals and Clays from Water*, K-L-2386 (December 1966).

[6] E. A. Woolson and J. H. Axley, "Clay Separation and Identification by Density Gradient Procedure," *Soil Sci. Soc. Am. Proc.* 33, 46–48 (1969).

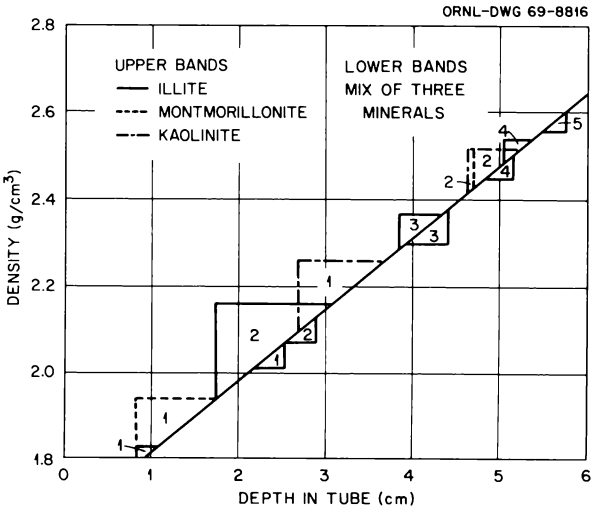

Fig. 1.2. Density of Selected Clay Standards.

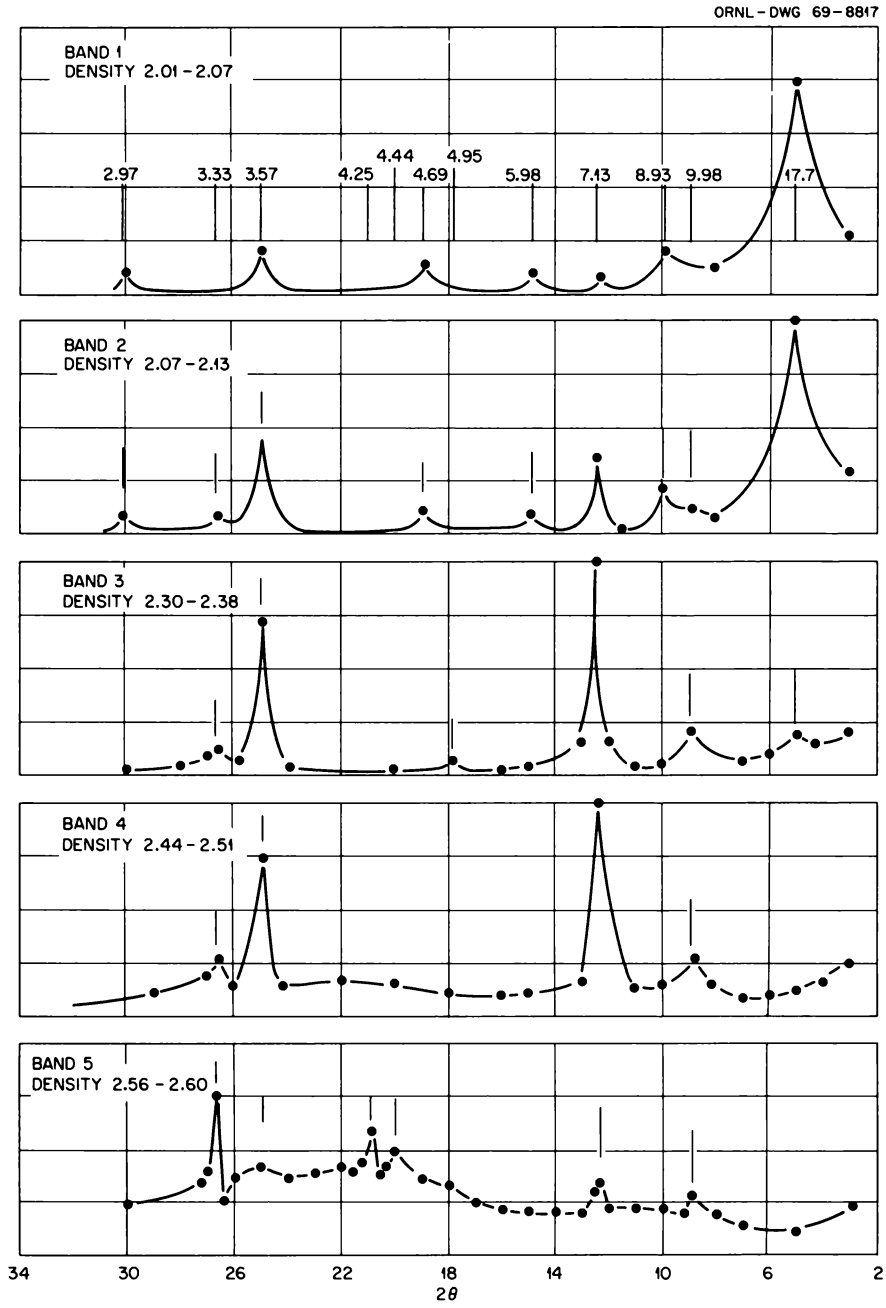

Fig. 1.3. Smoothed X-Ray Diffraction Tracings of Magnesium-Saturated Glycerol-Solvated Clays (Less than 2 μ) from Recovered Bands.

PHOSPHATE DISTRIBUTION IN SOILS AND SEDIMENTS

In our initial studies of the ORIC pond, the distribution of phosphate was determined using the procedure developed by Jackson.[7] Williams *et al.*[8] have shown that the Jackson procedure underestimates the aluminum phosphate and overestimates the iron phosphate, because, during the earlier fractionation procedure for aluminum phosphate dissolution, a portion of the phosphate is resorbed by the iron compounds. To demonstrate this effect, they added known amounts of stable phosphate and calculated the amount transferred during extraction. They also reported that, if calcium carbonate is present, the phosphate released during the extraction of aluminum and iron phosphates could also be sorbed by the calcium carbonate.

To measure the influence of calcium carbonate, to a soil which contained no calcium carbonate was added an equal amount (17%) of calcium carbonate to simulate the sediment. The results are tabulated in Table 1.2. For comparison, the distribution of phosphate in the original soil is also shown. The results show that most of the phosphate originally in the aluminum and iron forms had been resorbed by the calcium carbonate. Thus the reported distribution of phosphate in the sediment sample is suspect.

Table 1.2. Influence of Calcium Carbonate on the Forms of Phosphate in Soil and Sediment

Forms Extracted	^{32}P Distribution (%)		
	Soil 1	Soil 1 + 17% $CaCO_3$	Sediment (17% $CaCO_3$)
Free aluminum phosphate	81.30	11.49	14.19
Free iron phosphate	11.00	1.96	2.78
Occluded phosphate	2.28	5.38	11.84
Calcium phosphate	0.21	76.12	74.93

Consequently, it was believed that better definition of the forms of phosphate might be realized if the calcium carbonate in a sample was segregated from it. This led to the developmental work of zonal centrifugation reported above. The success in developing a gradient solution which did not flocculate the sample made the possibility of mineral segregation most encouraging.

The results of the analysis of the different bands obtained by zonal centrifugation are shown in Table 1.3. In order to avoid using a chemical reagent, which might change the phosphate distribution in the sample, only ultrasonic treatment was given. The analysis shows that approximately 90% of the calcium carbonate was in band 3, and 17% of the phosphate was in this band. At this stage of zonal centrifuge development, the forms of phosphates were not identified; the phosphate analysis represents the total inorganic phosphate as determined by acid-base extraction. More than 50% of the phosphate was in band 2, with a calculated 4.5% calcium carbonate. X-ray diffraction analysis prior to the acid-base treatment did not reveal the presence of this mineral; the assignment is based purely on the chemical analysis of calcium.

Table 1.3. Distribution of Calcium Carbonate and Phosphate in the Bands Recovered from ORIC Sediment (0.150 g)

Band No.	Density (g/cc)	$CaCO_3$ (%)	Phosphate (%)	Residue Weight (g)
1	2.3	0	14.0	0.011
2	2.45	4.51	50.5	0.071
3	2.6	89.5	17.0	0.044
4	2.7	6.01	12.5	0.002
				0.128
Weight of $CaCO_3$				0.014
				0.142

The results should not be interpreted to mean that the phosphate is in the aluminum and iron forms; the ultrasonic treatment could have removed calcium phosphate from the calcium carbonate surface and made it appear in band 2. However, it should be possible to establish the forms of phosphate in band 2, as well as in the other bands, by applying Jackson's technique to the recovered bands. Further work is being pursued along these lines, including direct determination of carbonates in the bands and evaluation of the behavior of known mixtures of different phosphates when subjected to zonal centrifugation.

ORIC POND STUDIES

Starting in the summer of 1966 and continuing through 1968, studies were conducted to establish the nature and extent of eutrophication of the ORIC pond. The findings of the first two summers' work and the

[7] K. Z. Morgan *et al.*, *Health Phys. Div. Ann. Progr. Rept. July 31, 1968*, ORNL-4316, pp. 1–4.

[8] J. D. H. Williams, J. K. Syers, and T. W. Walker, "Fractionation of Soil Inorganic Phosphate by a Modification of Chang and Jackson's Procedure," *Soil Sci. Soc. Am. Proc.* 31, 736–39 (1967).

early history of the pond have been reported earlier.[7] The results for 1968 have been completed and are included in Table 1.4. The data show that the NO_3 concentration remained relatively constant throughout the years, presumably due to the high input of NO_3 from the spring. Phosphate, however, has shown a significant decrease since 1966, and organic nitrogen appears to have increased. The concentrations of other elements show only minor changes.

Table 1.4. Some Chemical Characteristics of Water from the ORIC Pond[a]

	1966	1967	1968
Orthophosphate	0.096	0.017	<0.01
CO_2	7.7	5.1	4.3
D.O.[b]	8.6	6.4	7.8
pH range	7.8–8.4	7.5–8.3	7.8–8.2
NO_3	0.14	0.14	0.12
NO_2	<0.01	0.014	<0.01
Free NH_3	0.07	0.13	0.09
Organic NH_3	0.02	0.04	0.10
Turbidity		60	55

[a]All units are milligrams per liter except for pH and turbidity. All values are the mean of values obtained for the year indicated.

[b]Dissolved oxygen.

Proportional samples and flow measurements are being obtained on both the influent and effluent streams of the pond. Some of these data have been analyzed, and the results are presented in Fig. 1.4. Although insufficient data are available for a quantitative comparison, they confirm that the pond is depleting itself of nutrients and suggest that the minimal algal growths observed during 1968 could have resulted from the decrease in the concentration of PO_4.

Realizing that minimal growth is as undesirable as overgrowth, efforts were made during the summer of 1968 to determine the conditions necessary for the growth of algae and aquatic plants at a desirable level. In order to accomplish this, sediment from the pond was placed in the bottom of glass containers and pond water added to give a 7/1 water to sediment ratio, as is found in the pond. Giant burweed roots and duck potato tubers were placed in the sediment and the containers kept at room temperature with 1500-ft-c (color corrected) lighting supplied 24 hr/day.

This test showed that the rooted aquatic plants grew well when the suspended solids in the pond water settled under the quiescent laboratory conditions. Algae also grew as the suspended solids settled, with growth beginning on the surface of the sediment and then extending upward in the water phase.

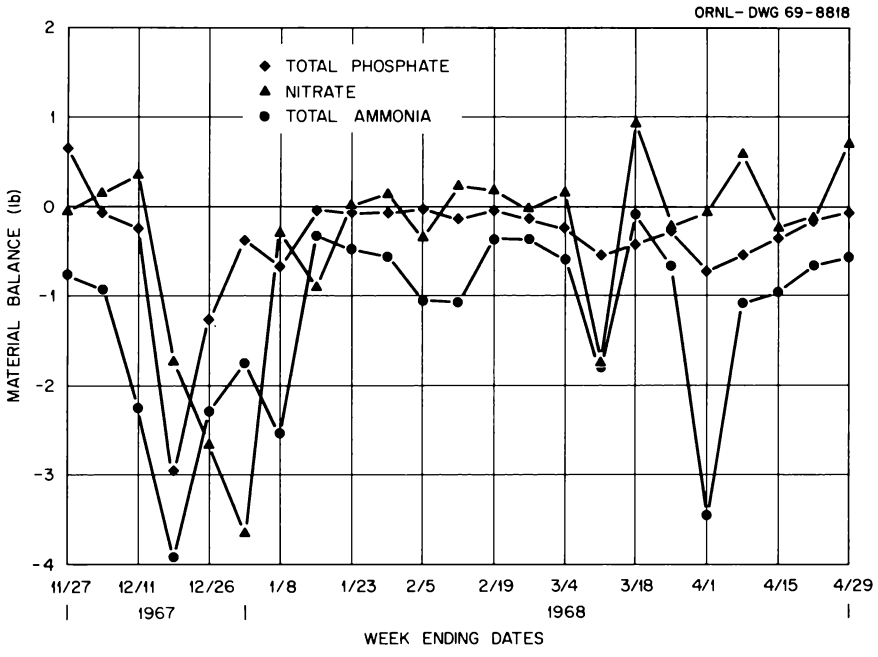

Fig. 1.4. Material Balance for Nutrient Materials in the ORIC Pond.

A portion of the pond has been segregated from the main pond as a study area by means of a wall constructed of fiber glass in order to prevent communication between the study area and the pond. Both the effect of turbidity and fertilization on aquatic weed and algal growth will be evaluated. From these data and a material balance of nutrients in the pond, a fertilization program designed to prevent excessive production in the pond will be developed.

2. Disposal by Hydraulic Fracturing

Wallace de Laguna

Operational injection ILW-5 was made on October 30, 1968, and comprised 85,332 gal of liquid waste and water which made up to 115,174 gal of slurry. As of this date the total volume of liquid and slurry injected underground through the presently operating disposal well was nearly 1,500,000 gal, which contained about 200,000 curies of ^{137}Cs, 16,000 curies of ^{90}Sr, and about 6000 curies of other activity, largely ^{144}Ce (see Table 2.1). Injection ILW-6 was made June 11, 1969, and comprised about 80,000 gal of liquid waste. Further data on this injection are not presently available. Guided by experience, the operational waste disposal injections are now going very satisfactorily. The most important single improvement has been to keep the solids – cement, fly ash, and clay – quite dry as they are blended and stored in the elevated bins. There have been many minor improvements to the plant itself.

A new observation well, S220, for gamma-ray logging to locate the fractures filled with solidified waste was drilled in July of 1968. This well apparently intersected most of the previously formed conformable fractures, although identification of the hardened grout sheets recovered in the cores or located by logging was in many cases uncertain. Unquestionably, logging before and after each injection is the best way to determine

Table 2.1. Test Injections and Waste Disposal Injections at the Shale Fracturing Plant, Oak Ridge

Injection	Date	Depth (ft)	Time Required (hr)	Volume of Liquid Waste and Water (gal)	Total Volume Injected (gal)	Activity (curies)				
						^{137}Cs	^{90}Sr	^{106}Ru	^{60}Co	Other
No. 1	Feb. 13, 1964	945	2.5	40,300	43,383	No activity used				
No. 2	Feb. 20, 1964	924	2.5 ?	33,400	42,891					^{198}Au, 30
No. 3	Apr. 8, 1964	912	3.5	43,090	67,944	74	4.9	0.4	0.1	
No. 4	Apr. 17, 1964	900	3.0	39,070	60,137	50	1.2	0.9	0.1	
No. 5	May 28, 1964	890	4.5	153,683	217,468	193	608	35	4.0	Ce, 4099
No. 6A	May 19, 1965	880	1.0	23,200	24,470	Combined with 6B				
No. 6B	May 22, 1965	872	11.0	68,000	96,800	1,562	330	2.0	1.0	
No. 7	Aug. 16, 1965	872	7.5	86,550	124,961	3,358	492	2.0	14.0	
ILW 1A	Dec. 12, 1966	872	3.0	40,231	57,791	11,500	41	1.0	16	Ce, 20
ILW 1B	Dec. 13, 1966	872	2.5	29,700	40,197	7,600	36	8.0	3	Ce, 13
ILW 2A	Apr. 20, 1967	862	7.5	83,400	121,805	31,329	564	99	236	
ILW 2B	Apr. 24, 1967	862	7.5	79,800	108,600	26,350	474	83	199	
ILW 3A	Nov. 28, 1967	862	2.5	31,000	40,951	Combined with 3B				
ILW 3B	Nov. 29, 1967	862	7.5	68,000	105,800	17,000	9,000	400	200	
Water test	Dec. 13, 1967	852	7.0	44,709	44,709	None				
ILW 4A	Apr. 3, 1968	852	2.5	28,659	34,531	Combined with ILW 4B				
ILW 4B	Apr. 4, 1968	852	6.0	67,396	97,214	51,900	4,300	200		
ILW 5	Oct. 30, 1968	842	9.0	85,332	115,174	69,400	500	300	136	
				965,900	1,444,826	203,271	16,351	1131	809	Ce, 4132

where the individual grout sheets have gone. In this connection it may be noted that the new logging probe, with a miniature G-M tube as detector, is giving excellent logs in the high radiation fields adjacent to the waste-filled fractures.

Well S220 was not cased and cemented in until October 1968, some three to four months after it was drilled. During this interval there was a very slow flow of water out of the well, perhaps 1000 to 1500 gal in all, and the latter part of this flow contained about 3 curies of activity, largely ^{90}Sr, but also a little ^{137}Cs, ^{106}Ru, and ^{60}Co. Apparently this activity came from injection ILW-4, made only three to four months before the well was drilled. Injection ILW-4 had been made into the same slot, at at depth of 852 ft, as the 44,709 gal of water of the test injection of December 1967. The contaminated water that leaked out of well S220 may well have come from the water-injection test rather than directly from the grout sheet formed by ILW-4, although there was a possibility of phase separation of liquid from this injection before it had set solid. The escape of, at most, 3 curies of activity, despite the very favorable conditions for escape provided by well S220, suggests that the cement–clay–fly-ash mix used to solidify the waste is an effective restraint on the movement of the radioactive materials in the waste.

PRELIMINARY INVESTIGATIONS IN NEW YORK STATE

As a part of our continuing research and development program in radioactive waste disposal, we and the AEC (DRDT-Washington) are interested in the application of the fracturing technique to other waste types and in other shale formations. Preliminary evaluation indicated that the shales in western New York State may be amenable to this technique for ultimate disposal of radioactive wastes.

Discussions with AEC and USGS staff members resulted in a proposed test program in New York. Essentially, the work consists in drilling the necessary wells (one 1500-ft exploratory core hole, one 1500-ft injection well, and several monitoring wells) and conducting a series of experimental injections of water and tagged slurry and grout at several depths in the bedded shale.

The principal objectives of this program are: (1) to validate new methods of presite testing and thus avoid some of the costs experienced at Oak Ridge and (2) to demonstrate the applicability of hydraulic fracturing in a different geologic setting. The work is designed to follow an orderly procedure of site investigation, with each subsequent step dependent on the success of the previous step. The proposed program would lead up to, but would not include, the construction of an actual disposal plant.

Discussions with representatives of New York State Atomic and Space Development Authority (NYS-ASDA) and Nuclear Fuel Services, Inc., have resulted in their expressed interest in the program and their wish to cooperate. A site was selected for these tests on land owned by NYS-ASDA which is remote from that of NFS operations.

The first exploratory hole at the fracturing test site near the Nuclear Fuel Services plant in New York State was cored to a depth of 1500 ft in May 1969. Most of the rock was shale, but much of the shale did not break easily or cleanly along the bedding planes, as does the Conasauga shale at Oak Ridge, and may therefore be less apt to fracture parallel to the bedding planes when fractured hydraulically. About 100 ft of the rock penetrated was a sandy siltstone, in part thick-bedded to massive, but even the better bedded siltstone did not tend to break parallel to the bedding. The core samples and the electric log suggest that the siltstone, unlike the shales, has at least some permeability. Some of the dark gray or black shales penetrated, particularly near the bottom of the well, have a distinct odor of petroleum when freshly broken. These oil shales may be the upper part of the Rhinestreet shale of the Java and West Falls groups, and the overlying shales and siltstone probably belong to the Canadaway Group. All these formations are of Upper Devonian age. The log of the well follows. The notation "breaks well" means that the core can be easily broken by hand and that the break is closely guided by the bedding planes, which may be slightly irregular in detail. The notation "breaks medium" means that the core may be broken by hand, but only with some difficulty, and that the break, in general, is guided by the bedding. The notation "breaks poorly" means that the core can only be broken by a sharp blow, as with a hammer, and that the break is but little guided by the bedding.

Log of NX Core Hole, West Valley, New York, Drilled May 1969

0–177	Till; clay, silt, a little sand, and a few cobbles.
177–529	Medium-gray silty shale; thin bedded but bedding is irregular in detail; about 5% is thin beds of light-gray calcareous siltstone showing cross bedding. Breaks well.
529–641	Medium-gray silty shale; thin bedded but bedding irregular in detail; 10% or more is thin beds of light-gray calcareous siltstone. Breaks medium; locally well or poorly.

641–694 Dark-gray shale; few scattered beds of medium- to light-gray calcareous siltstone. Locally faint oily smell. Breaks medium or medium to well.

694–780 Medium-gray and dark-gray shale interbedded; a few scattered thin beds of calcareous siltstone. Locally faint smell of oil. Breaks medium to well.

780–900 Very fine-grained olive-green shale showing very little bedding; interbedded and irregularly intermixed with dark-gray shale which shows some bedding. Breaks poorly.

900–938 Black shale with distinct petroleum smell; interbedded with and irregularly mixed with light-gray sandy siltstone and olive-green shale. Bedding poorly developed. Breaks poorly.

938–1028 Light- to medium-gray sandy siltstone, locally calcareous; bedding generally indistinct, locally easily visible. Does not break on bedding planes. Breaks poorly.

1028–1073 Dark-gray shale, bedding indistinct, interbedded and mixed with light- to medium-gray siltstone, locally calcareous. Breaks poorly to medium.

1073–1194 Medium- and dark-gray shale, interbedded. Bedding shows clearly, but rock does not break easily on bedding. Locally contains beds of light-gray siltstone. Breaks medium.

1194–1254 Medium- to dark-gray shale; bedding thin, regular, and well developed. Faint oily smell, locally. Breaks well.

1254–1293 Dark-gray shale, almost black. Bedding hardly visible. No oily smell. Breaks medium.

1293–1390 Black carbonaceous shale, locally faint smell of oil. Bedding almost invisible, but rock is thin bedded. Breaks fairly well on bedding, but considerable force required. Breaks medium.

1390–1439 Black shale; thin bedding visible when wet; strong oily smell; interbedded with dark-gray shale with more evident bedding, with faint oily smell. Breaks medium.

1439–1500 Black carbonaceous shale; thin bedded, but bedding not easily visible. Bedding is regular and rock breaks fairly cleanly on bedding, but considerable force required. Strong oily smell. Breaks medium.

Present plans are to make four injections by hydraulic fracturing into these rocks.

The first, to consist of about 100,000 gal of water containing 0.1 lb/gal of Grundite (referred to as muddy water) and tagged with about 10 curies of ^{137}Cs, will be made into the black carbonaceous oily shale at a depth of 1450 ft. This shale is probably part of the Rhinestreet formation, and the results of the test can therefore be extrapolated over a fairly wide area. This rock is rated only "medium" for making bedding-plane fractures, and the fracture may be irregular or even vertical.

The second injection, to consist of 60,000 to 80,000 gal of a cement-bentonite grout tagged with about 10 curies of ^{137}Cs, will be made at a depth (as measured in this core well) of 1225 ft. The rock at this depth is a medium- to dark-gray shale with well-developed bedding, which is rated as fracturing well. We have every expectation that this fracture will follow the bedding planes.

The third injection, to consist of 100,000 gal of muddy water tagged with 10 curies of ^{137}Cs, is to be made into the nearly massive siltstone at a depth of 990 ft. This rock is rated as fracturing poorly, and a vertical fracture may well be formed.

The fourth injection will be made into a medium-gray shale at a depth of 500 ft and will also consist of about 100,000 gal of muddy water tagged with 10 curies of ^{137}Cs. This rock is estimated to fracture well, and presumably a bedding-plane fracture will be formed.

3. Disposal in Natural Salt Formations

R. L. Bradshaw
J. O. Blomeke[1]
W. J. Boegly, Jr.
F. M. Empson
T. W. Hodge, Jr.
B. L. Houser
T. F. Lomenick
W. C. McClain
A. M. Starfield[2]
H. J. Wyrick

The long-range objective of this program is to provide for the disposal of high-level solidified radioactive wastes in underground salt formations. In general, the program has been directed toward the solution of various technical problems, including: (1) the effects of heat and radiation on the plastic flow of salt and mine stability, (2) the transfer of heat from the waste containers to the salt, (3) the compatibility of the wastes and their containers with the salt environment, and (4) the investigation of the suitability of other geologic formations in areas where there are no salt deposits. The recently completed successful demonstration experiment, Project Salt Vault,[3] testifies to our progress in the solution of these technical problems. Although some work is continuing along these lines, specifically (1) analysis of the detailed experimental results from the demonstration experiment, (2) preparation of a final comprehensive report on Project Salt Vault, and (3) examination of the geologic and structural properties of formations other than bedded salt (see below), the overall program is now oriented in a different direction. The principal effort during the past year has been toward the establishment of an actual operational waste disposal facility which will accept the waste output from the rapidly expanding nuclear-power industry for several decades.

Three main areas of work toward this objective have been initiated. The first is the development of a computer model of the deformational behavior of the mine pillars,[3] based on laboratory measurements of creep in model salt pillars and data from the demonstration experiment. In a salt mine, the plastic deformation of the support pillars causes the rooms to gradually close. For waste disposal operations the amount of that closure and its rate at any time are functions of:

1. the sizes of the pillars and the widths of the rooms,
2. the general geometry of the mine layout including the depth,
3. the amount and characteristics of the waste materials deposited in it,
4. the characteristics of the crushed salt used to backfill the room.

Since the desired end condition for waste disposal is completely closed rooms with recrystallization of the crushed backfill salt, this computer program will enable a prediction of when that condition has been reached for any set of original conditions.

The second area is the development of a mine management program. In a waste disposal operation, the spacing between adjacent cans of waste will be a function of:

1. the characteristics of the container of waste, especially its size, heat-generation rate, and rate of decay of heat generation (the last two items are a function of the irradiation history of the fuel, time since discharge, and the method of fuel reprocessing used);
2. the characteristics and spacing of the waste already in place;
3. the characteristics of the wastes to be received in the future, with projections of several years being required;

---

[1] Chemical Technology Division.

[2] Consultant, University of Minnesota.

[3] R. L. Bradshaw *et al.*, "Disposal in Natural Salt Formations," *Health Phys. Div. Ann. Progr. Rept. July 31, 1968,* ORNL-4316, p. 21.

4. the applicable design limits (maximum temperature in the waste or in the salt), which may change over the lifetime of the operation.

If all of the waste has identical characteristics, the proper spacing could be determined in advance. In an actual disposal operation, wastes will be received from several fuel-reprocessing plants, probably at a variety of ages, and the characteristics will certainly not be uniform. Therefore this program will provide guidance on the optimum operation of the facility, specifically the spacing required between waste containers, as the waste is received.

Currently, two existing analytic solutions are being reprogrammed to run on the IBM 360 series computers, to enable us to make calculations for guidance in the development of the mine management program. (For example, how far away from a given source will its contribution to the temperature rise be important?) One of these solutions is for an infinite array of line sources, all with the same heat generation. This is a very rough approximate solution to the real situation, since it assumes the entire mine filled at once with identical heat sources. The other solution is for a single isolated line source. By use of superposition theory, the contribution from a number of sources in a given disposal room and from adjacent rooms may be summed up. In this case, each source may have different characteristics and may be located at any point. It is possible that the mine management program may be based on this method, since it is relatively simple in theory. However, a computer program to implement this approach would be quite involved, and some simpler approach may be found.

Another approach which is being pursued is the possible use of existing programs (and modifications thereof) which operate on finite-difference techniques to solve the basic differential equation of heat conduction. These would be used for configurations more closely approximating mine conditions and could take into account such factors as the different thermal properties of the crushed salt used in backfilling disposal holes and rooms.

Most of the effort over the past year has been in the third general area, that is, the preparation of a report to provide the information required to formulate rational decisions concerning the establishment and operation of a high-level waste repository in salt. Specifically, these decisions are related to the questions of: (1) where the facility should be located, (2) when it should be ready for operation, (3) how big the facility should be, and (4) how much it will cost.

The question of "when" is being approached by examining current predictions of the growth of nuclear-reactor-powered generating stations.[4-6] These predictions are in fair agreement and are shown in Fig. 3.1 as the installed electrical generating capacity. The curves representing the installed thermal capacity and the continuous operation (thermal) in Fig. 3.1 were calculated using projected load factors and thermal efficiencies.[4] The amount of fission product waste produced is directly related to the continuous operation curve and is approximately 35 ft^3 of solid high-level waste per year for each 1000 Mw of operation. However, this waste does not become available for disposal for some 6 to 14 years after the power is produced. (This assumes 2 to 4 years for reactor core residence time and 4 to 10 years of interim storage for cooling following fuel reprocessing.)

There is a possibility that other wastes will be available for disposal at a salt mine facility, specifically the pots from the Waste Solidification Engineering

[4] *Forecast of Growth of Nuclear Power,* USAEC, Division of Operations Analysis and Forecasting, WASH-1084 (December 1967).

[5] Phase 2, Case 3, USAEC Systems Analysis Task Force.

[6] *Nuclear Reactors Built, Being Built, or Planned in the United States as of December 15, 1967,* TID-8200 (17th rev.)

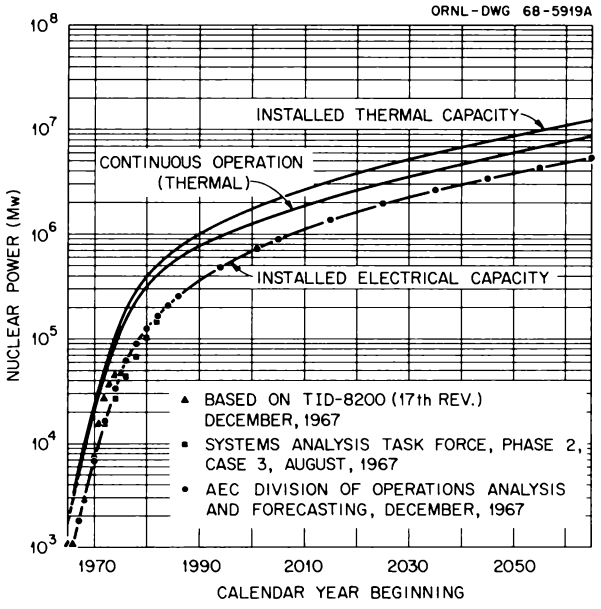

Fig. 3.1. Nuclear Power Projections for the United States.

Prototypes (WSEP) facility at Hanford and packaged calcined wastes from the Idaho Chemical Processing Plant (ICPP). The total volume of wastes from both of these sources is so small that it does not significantly influence the total area of this facility, but it will influence the initial phases of the operation.

Therefore the question of when the facility should be ready for operation depends upon the length of interim storage of the power reactor wastes and the possibility of wastes being available from other sources. A number of cases with various combinations of these variables are being examined.

The question of where the facility should be located is being approached by examining all of the salt deposits in the United States. Although there is no scarcity of salt as a natural resource, there are relatively few areas where mined excavations for the initial high-level waste repository would be desirable. The Gulf Coast area seems undesirable for the initial facility due to insufficient knowledge of the possible behavior of salt domes, coupled with the fact that some domes are known to have contact with circulating groundwater.[7] At least one mine in a dome has flooded, apparently for this reason.

In the other deposits, much of the area may not be suitable for a waste repository because the salt is too deep or the formation is too thin. The minimum depth for a repository is governed, in general, by geohydrological factors. To ensure long-term integrity, a considerable thickness of shale or some other impermeable rock should overlie the salt, and the excavation itself should be located well within a fairly thick salt deposit. The maximum depth is governed by mine stability conditions during the operating period and the increased costs at greater depths (due to shaft length and the increased amount of salt which must be left as support pillars).

A preliminary study[8] indicated that the cost of a facility at 1500 ft depth would be about 15 to 18% more than for a similar facility at 1000 ft. At 2000 ft the cost would be 25 to 33% greater than at 1000 ft. Beyond 2000 ft the stability problems are such that these depths do not seem desirable for the initial facility. This should not be considered as an ultimate limit, however.

Based on these considerations, a maximum depth of about 2000 ft and a minimum thickness of about 200 ft of salt have been selected as desirable for the first waste repository.

In addition to these geologic factors, other considerations are relevant in selecting a site for the facility. Since the quality of the salt excavated during waste disposal operations will probably be too poor to market, that portion not used for backfilling may have to be disposed of as brine as it is mined. This means that the site must have a source of relatively large volumes of water and a suitable porous formation for deep-well disposal of the brine.

Land values and the location of large population centers will also have some bearing on site location. In general, it appears that a waste repository in salt will have considerably less operating-hazard potential than either a reactor or a fuel-reprocessing plant handling equivalent quantities of fuel (or the radioactive by-products of the fuel). However, since the first waste facility will be handling the entire United States output until about 1990 or 2000, large population centers should probably be avoided.

The location of the waste repository could be affected by the cost of shipping the waste from the fuel-reprocessing plants to the repository. This factor is being investigated for various possible sites using shipping distances from those reprocessing plants which are in operation, under construction, or planned.

STORAGE IN NONSALINE ROCKS

T. F. Lomenick H. J. Wyrick

Perhaps the foremost concern in the possible development of storage and/or disposal cavities for high-level radioactive wastes in nonsaline rocks is that of a dry environment. Indeed, dry excavations do exist in limestones and other rocks, several examples having been cited previously.[9,10] Another important consideration is the structural stability of openings excavated in these rocks. Through conventional mining operations, much has been learned of the behavior of mine pillars at ambient temperatures; however, previous experience is not available to predict the effects of

[7] R. B. Hoy, R. M. Foose, and B. J. O'Neill, Jr., "Structure of Winnfield Salt Dome, Winn Parish, Louisiana," *Bull. Amer. Ass. Petrol. Geol.* 46(8), 1444–59 (August 1962).

[8] R. L. Bradshaw *et al.*, *Evaluation of Ultimate Disposal Methods for Liquid and Solid Radioactive Wastes, Part VI: Disposal of Solid Wastes in Salt Formations*, ORNL-3358 (May 1968) and ORNL-3358 (rev.) (March 1969).

[9] T. F. Lomenick *et al.*, *Health Phys. Div. Ann. Progr. Rept. July 31, 1968*, ORNL-4316, pp. 40–41.

[10] T. F. Lomenick, *Health Phys. Div. Ann. Progr. Rept. July 31, 1966*, ORNL-4007, p. 26.

gamma radiation and differential heating on the deformational characteristics of the various rock types of interest.

Gamma radiation is known to cause internal disorder in the crystal lattices of solids; thus it is of interest to determine its effects on the physical properties of rocks that might be utilized for the storage of radioactive wastes. For crystalline materials, such as limestone, radiation disturbs the crystal lattice and forms *F* and *V* color centers. *F* centers, which are the most common, occur when electrons become trapped at negative-ion vacancies, while *V* centers consist of holes trapped at positive-ion vacancies. The mechanisms of color center formation are not fully understood, and even the nature of these centers remains uncertain. Radiation effects would be expected to accumulate with dose; however, there appears to be a finite limit to the *F*- and *V*-center concentrations which can be obtained in a crystal. This is due to the annihilation of positive holes or *V* centers by electrons in the *F* centers.

Even though this knowledge of changes in crystal lattices induced by radiation is helpful in understanding radiation damage in general, it is not directly applicable to a determination of radiation-induced effects to massive limestones that might be subjected to large doses of radiation as a result of waste storage and/or disposal operations. To evaluate this damage, a series of 2.1-in.-diam cylindrical samples, taken from a local limestone mine, were exposed to gamma radiation (up to 3.9×10^9 r) and then deformed using a Baldwin-Tate-Emery universal testing machine. A total force vs total deformation curve was obtained for each sample and then reduced to a stress-strain diagram. The results of these tests for the maximum irradiated samples and the unirradiated ones are shown in Fig. 3.2. It is apparent from this figure that there is little difference in the stress-strain curves up to a stress of about 17,000 psi. Above this the unirradiated specimens appear to be slightly stronger than the irradiated ones. In addition to the normalized stress-strain curves, the compressive strength, yield strength, apparent elastic limit, and modulus of elasticity and their standard deviations were computed for these same samples (Table 3.1). For the compressive strengths and yield strengths, the irradiated samples are slightly weaker than their unirradiated counterparts, while for the moduli of elasticity and apparent elastic limits the values are greatest for the irradiated specimens. However, these differences probably are not significant, since the variation between specimens is rather large, as evidenced by the standard deviations, and thus radiation-induced changes in the physical properties would necessarily have to be rather large to be easily detected. Therefore, within the statistical variation of the experiment, radiation causes only minor changes in the physical properties of limestone.

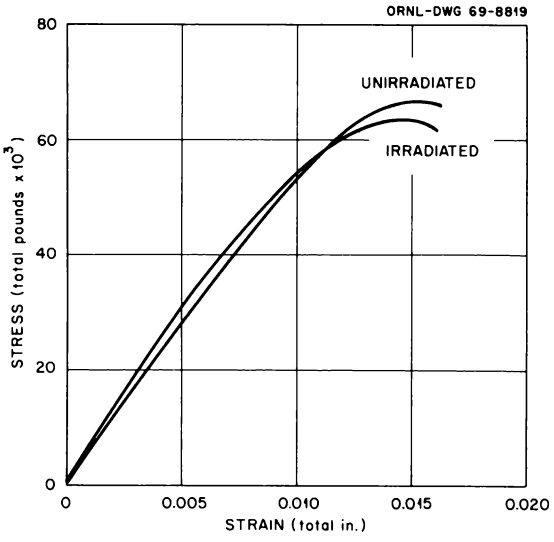

Fig. 3.2. Compression Test of Limestone.

To determine the effects of heat and pressure on the deformation of limestone, a series of model pillars were fabricated and tested at various temperatures and loads.

Table 3.1. Physical Properties of Limestone

Sample Type	Exposure Dose (r)	Compressive Strength (psi)	Yield Strength (psi)	Apparent Elastic Limit (psi)	Modulus of Elasticity (psi)
					$\times 10^6$
Nonirradiated	0	19,000 ± 600	18,700 ± 600	15,500 ± 1400	3.47 ± 0.12
Irradiated	3.86×10^9	18,200 ± 1900	17,900 ± 1800	16,200 ± 3100	3.60 ± 0.26

The model pillar specimens consist of 6-in.-diam cores of limestone that have steel confining rings epoxied to the tops and bottoms of the samples to simulate roof and floor conditions, while the center portion of the specimen is ground out to form the pillar and surrounding rooms. Figure 3.3 shows the deformational curves of limestone samples that have been loaded uniaxially to 10,000 psi at temperatures of 22.5 and 200°C. In both cases it is observed that there is initially a rapid rate of deformation that decreases with time until after a few hours of testing the rate of pillar shortening is so slow as to be barely discernible for the duration of the test period. The difference between the initial deformations of the 22.5 and the 200°C samples is probably due to a lower modulus of elasticity at the higher temperature. Since the slopes of the two curves are essentially parallel, it is concluded that there will be little or no acceleration of creep due to the expected temperature rises; however, fracturing of the limestone may occur as a result of differential heating of the limestone by the waste containers. To determine the effects of differential heating, 4- by 5- by 6-in. blocks of limestone were loaded uniaxially to 2000 psi and then heated by ¼-in.-diam by 4-in.-long heating rods (one emplaced through the center of each block). For samples with peak center-line temperatures of 300°C, no fractures were observed (visually or with x-ray examinations); however, at peak temperatures in excess of 300°C vertically trending fractures (parallel to the axis of greatest stress and through the center line of the sample) appeared in the blocks. It is probable that this fracturing was due to differential thermal expansion that exceeded the tensile strength of the limestone; however, further tests are being made to verify this conclusion.

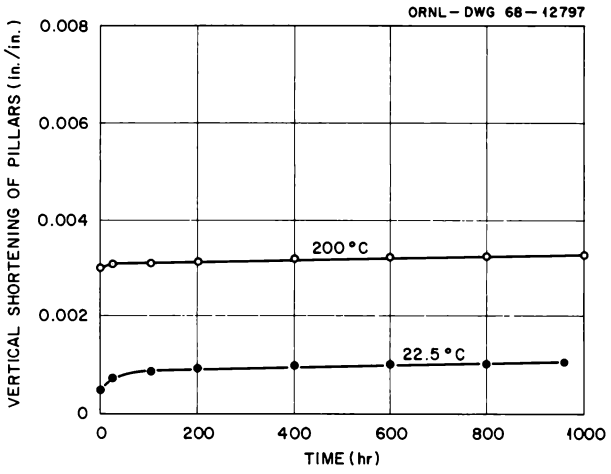

Fig. 3.3. Deformation of Limestone Pillar Models at 10,000 psi.

4. Engineering, Economic, and Safety Evaluation

D. G. Jacobs Ferruccio Gera[1]
K. E. Cowser R. V. O'Neill[2]
O. M. Sealand

DEVELOPMENT OF CRITERIA FOR THE LONG-TERM MANAGEMENT OF HIGH-LEVEL RADIOACTIVE WASTES

D. G. Jacobs Ferruccio Gera[1]

Present considerations of the long-term management of high-level radioactive wastes lead to the conclusion that wastes from reactor fuel reprocessing should be converted to stable solids after their generation. Long-term storage of these wastes as liquids in tanks is deemed to present a greater risk due to the rather high mobility of the wastes in case of an accidental release, even though the probability of such a release can be reduced to a very low number by appropriate engineering safeguards.

Waste Composition

Table 4.1 lists estimated quantities of some of the more critical radionuclides that might be accumulated in the wastes from the processing of fuel from typical light-water reactors (LWR's) and liquid-metal fast breeder reactors (LMFBR's) of the future. The amounts of transuranium isotopes, particularly ^{239}Pu, are such that containment of the wastes would be required for times far exceeding the 1000-year period necessary for the decay of ^{90}Sr and ^{137}Cs. As a first approximation, an indication of the relative importance of these nuclides is given in Table 4.2. The potential hazard indexes given in Table 4.2 were obtained by dividing the quantity of a radionuclide by its annual maximum permissible intake and multiplying by the mean life of the radionuclide. The mean life is used to account for the total time that the potential hazard would persist due to the presence of the waste in the environment. This index of hazard, as we have described it, does not include correction for the environmental behavior of the various nuclides. As a result, the index for ingestion of plutonium is probably grossly overestimated, because plutonium is much less mobile in the environment than cesium or strontium[3-5] and is not readily translocated in plants.[6] Thus the major potential hazard resulting from ingestion of residue from the waste would be due to ^{90}Sr and ^{137}Cs, until these radionuclides had decayed through several half-lives.

The major potential hazard from the transuranics seems to be associated with inhalation as the mode of exposure. In the case of inhalation the potential hazard from the transuranics is greater than that from ^{90}Sr or ^{137}Cs; and, because of the long half-lives of ^{239}Pu and ^{240}Pu, the potential hazard from inhalation may persist for an extremely long period of time. A containment time of a quarter of a million years would be required to reduce the amount of ^{239}Pu by three orders of magnitude. Because the magnitude of the potential hazard due to inhalation of plutonium may be so much greater than that due to its ingestion, it appears that the

[1] Visiting scientist on leave from Italian National Committee for Nuclear Energy.

[2] Radiation Ecology Section.

[3] C. W. Christenson *et al.*, "Soil Adsorption of Radioactive Wastes at Los Alamos," *Sewage Ind. Wastes* **30**, 1478 (December 1958).

[4] W. E. Prout, *Adsorption of Fission Product by Savannah River Plant Soil*, DP-394 (July 1959).

[5] D. W. Rhodes, "The Effect of pH on the Uptake of Radioactive Isotopes from Solution by a Soil," *Soil Sci. Soc. Am. Proc.* **21**, 389 (August 1957).

[6] L. Jacobson and R. Overstreet, "The Uptake by Plants of Plutonium and Some Products of Nuclear Fission Adsorbed on Soil Colloids." *Soil Sci.* **65**, 129 (1948).

Table 4.1. Projected Wastes from United States Nuclear Power Economy[a]

Aqueous processing of all fuels

	Calendar Year				
	1970	1980	1990	2000	2020
Installed capacity, 10^3 Mw (electrical)	14.4	153	368	735	2210
Fuel processed,[b] 10^3 metric tons/year	0.052	2.95	8.16	14.0	41.7
Volume of waste generated, as liquid[c]					
Annually, m^3/year	64	3670	10,180	17,400	51,850
Accumulated, m^3	64	16,654	90,083	227,480	900,830
Volume of waste generated, as solid[d]					
Annually, m^3/year	5	275	760	1300	3880
Accumulated, m^3	5	1250	6740	17,000	67,400
Accumulated radioisotopes[e]					
Total weight, metric tons	1.75	451	2440	6200	24,600
Total activity, megacuries	2.08	18,900	84,500	209,000	666,000
Total heat-generation rate, 10^6 cal/sec	0.22	19.5	82	193	602
^{90}Sr, megacuries	3.98	962	4640	9550	29,400
^{137}Cs, megacuries	5.27	1280	6540	15,600	57,500
^{238}Pu,[f] megacuries	0.002	1.20	8.28	30.7	166
^{239}Pu,[g] megacuries	0.00009	0.022	0.235	1.31	8.45
^{240}Pu,[g] megacuries	0.00013	0.0409	0.395	1.91	11.4
^{241}Pu,[g] megacuries	0.0295	6.63	47.2	191	909
^{241}Am,[h,i] megacuries	0.0089	2.31	27.7	121	763
^{243}Am,[h] megacuries	0.0009	0.232	1.49	5.19	27.0
^{242}Cm,[h] megacuries	0.725	43.2	185	487	1490
^{244}Cm,[h] megacuries	0.128	29.9	137	255	700

[a]Data from Phase 3, Case 42, Systems Analysis Task Force (Apr. 11, 1969), provided by J. O. Blomeke, Chemical Technology Division.

[b]Based on an average exposure of 33,000 Mwd/metric ton, and a delay of two years between power generation and fuel processing.

[c]Assumes 1250 liters of liquid waste per metric ton of fuel.

[d]Assumes 1 m^3 of solid waste per 10.7 metric tons of fuel.

[e]Assumes LWR fuel continuously irradiated at 30 Mw/metric ton to 33,000 Mwd/metric ton and LMFBR fuel (core + blanket) continuously irradiated at 58 Mw/metric ton to 33,000 Mwd/metric ton.

[f]Assumes all ^{242}Cm decayed to ^{238}Pu.

[g]Assumes 0.5% of plutonium in spent fuel is lost to waste.

[h]Assumes no recovery of americium and curium.

[i]Assumes all ^{241}Pu decayed to ^{241}Am.

most prudent scheme of management of these wastes would be one in which the necessity for further handling at a later date is minimized.

Long-Term Geologic Factors to be Considered in Waste Management

When containment times on the order of a few hundreds of thousands of years are needed, the problem of selection of a suitable site and geologic formation requires consideration of long-term changes. In addition to consideration of rather rapid geologic alterations, such as faulting and earthquakes, it will be necessary to consider such factors as changes in climate, erosion, tectonic activity, and volcanism.

We are now living in the Pleistocene Epoch, which is characterized by faster geologic changes than those recorded in earlier time spans of comparable length. During the Pleistocene, which has been estimated to have begun 600,000 to 3,000,000 years ago, wide areas have been uplifted, while others have been covered with hundreds of meters of sediment in proof of rapid subsidence. The climate has been subject to a series of major changes which have resulted in repeated glaciations. The last maximum in the extent of glaciation occurred about 20,000 years ago, during which time

Table 4.2. Hazard Index of Several Significant Radionuclides Accumulated in High-Level Solid Waste by the Year 2020

Nuclide	Quantity (curies)	$(MPI)_{ann}$ in Waste[a]		Hazard Index[b]	
		Ingestion	Inhalation	Ingestion	Inhalation
		At Year 2020			
^{90}Sr	2.9×10^{10}	9.0×10^{15}	1.0×10^{16}	3.6×10^{17}	4.0×10^{17}
^{134}Cs	5.7×10^{10}	4.7×10^{14}	3.6×10^{14}	2.0×10^{16}	1.5×10^{16}
^{238}Pu[c]	1.7×10^{8}	4.2×10^{12}	3.4×10^{16}	5.3×10^{14}	4.3×10^{18}
^{239}Pu	8.4×10^{6}	2.3×10^{11}	2.1×10^{15}	8.1×10^{15}	7.4×10^{19}
^{240}Pu[d]	1.3×10^{7}	3.6×10^{11}	3.2×10^{15}	3.4×10^{15}	3.1×10^{19}
^{241}Am[e]	7.9×10^{8}	2.6×10^{13}	5.3×10^{16}	1.6×10^{16}	3.3×10^{19}
^{243}Am	2.7×10^{7}	7.7×10^{11}	1.9×10^{15}	8.2×10^{15}	2.0×10^{19}
		After 300 Years Decay			
^{90}Sr	1.6×10^{7}	5.0×10^{12}	5.5×10^{12}	2.0×10^{14}	2.2×10^{14}
^{137}Cs	5.7×10^{7}	4.7×10^{11}	3.6×10^{11}	2.0×10^{13}	1.5×10^{13}
^{238}Pu[c]	1.6×10^{7}	4.0×10^{11}	3.2×10^{15}	5.1×10^{13}	4.1×10^{17}
^{239}Pu	8.4×10^{6}	2.3×10^{11}	2.1×10^{15}	8.1×10^{15}	7.4×10^{19}
^{240}Pu[d]	1.3×10^{7}	3.6×10^{11}	3.2×10^{15}	3.4×10^{15}	3.1×10^{19}
^{241}Am[e]	5.0×10^{8}	1.7×10^{13}	3.3×10^{16}	1.1×10^{16}	2.1×10^{19}
^{243}Am	2.7×10^{7}	7.7×10^{11}	1.9×10^{15}	8.2×10^{15}	2.0×10^{19}

[a] $(MPI)_{ann}$ is the annual maximum permissible intake.

[b] The potential hazard index is taken to be the product of the number of annual maximum permissible intakes present in the waste times the mean life of the radionuclide.

[c] Assumes all ^{242}Cm decayed to ^{238}Pu.

[d] Assumes all ^{244}Cm decayed to ^{240}Pu.

[e] Assumes all ^{241}Pu decayed to ^{241}Am.

most of the north-central part of the United States was covered with ice. The mean sea level has fluctuated according to the amount of water bound on land as ice. In the last 20,000 years it is estimated that mean sea level has risen more than 100 m.[7,8] The melting of the ice caps also removed a load from wide areas of the earth's crust, resulting in a rather rapid isostatic uplift. This uplift can be followed by increased rates of erosion.

Rates of erosion are quite variable, both in time and space. The rate of denudation (the rate at which an average thickness of material is removed from an area) is controlled by climate, relief, and lithology. In Table 4.3 are estimates of denudation rates for several geographic regions of the United States. The recent figures are the more reliable. In Table 4.4 the influence of topography is shown quite clearly. It is expected that the denudation rates for plateaus and piedmonts would be intermediate between those of the mountains and the lowlands. Areas of recent orogenesis (mountain formation) would be expected to have the highest relief and the highest rates of denudation.

If the effects of erosion were limited to the average denudation rate for a region, we could reasonably expect no significant stripping of the overburden from a midcontinental area of low relief. However, local rates of erosion can be considerably higher. A notable example is the Grand Canyon, which has been carved to a depth of about a mile by the Colorado River in a time span estimated to range from 1,500,000 to 2,000,000 years. Obviously, not many rivers deepen their valleys at such a high rate, but a cutting depth of a few hundred meters over a similar time span may be possible in some localized areas. These areas should be

[7] R. F. Flint, *Glacial and Pleistocene Geology*, pp. 258–71, Wiley, New York, 1957.

[8] W. L. Donn, W. R. Farrand, and M. Ewing, "Pleistocene Ice Volumes and Sea-Level Lowering," *J. Geol.* 70(2), 206–14 (1962).

Table 4.3. Denudation Rates in the United States

Drainage Region	Rate of Denudation (cm/1000 years)	
	Dole and Stabler[a] (1909)	Judson and Ritter[b] (1964)
Colorado	5.8	16.5
Pacific slopes, California	3.3	9.1
Western Gulf	1.5	5.3
Mississippi	5.1	5.1
South Atlatic and Eastern Gulf	3.6	4.1
North Atlantic	2.3	4.8
Columbia		3.8
United States as a whole	3.3	6.6

[a]R. B. Dole and H. Stabler, "Denudation," *USGS Water Supply Paper 234*, pp. 78–93 (1909).

[b]G. S. Judson and D. F. Ritter, "Rates of Regional Denudation in the United States," *J. Geophys. Res.* **69**, 3395 (1964).

avoided, if identified, in selecting a suitable ultimate waste disposal site.

Glacial denudation is more difficult to evaluate, and available data indicate a wide degree of variability in rates. In the Canadian Shield area, glaciers failed to erase preglacial morphology, and it is believed that the total denudation did not exceed a few meters. On the other extreme, the Sogne Fiord in Norway has been glacially eroded for an apparent depth of 2400 m. Many lakes in North America and Europe occupy valleys and basins excavated and deepened by glaciers for many hundreds of meters.

Areas previously covered by thick layers of ice are subject to isostatic uplift when the load is removed. In the Scandinavian area an uplift of 500 to 600 m has occurred following the latest glaciation. The present rate of uplift is greatly reduced from that in the initial stages of recovery, but it is still nearly 1 cm/year in a small area at the north end of the Gulf of Bothnia. The previously glaciated areas of North America are subject to the same type of uplift, but the available knowledge of postglacial recovery is not so complete as for the Baltic area. Following uplift, the rates of denudation are accelerated.

Interim Storage of Solidified Wastes

Interim storage of solidified wastes will probably be used to allow a drop in the heat-generation rate so that better utilization of space in the ultimate disposal facility will be possible. The problems of heat generation, release of radioactivity to the environment, and geologic stability are quite different for the interim period. Factors relating to the interim storage period are being reviewed.

Table 4.4. Relative Rates of Denudation in Uplands and Lowlands in Different Climates[a]

Physiographic Environment	Estimated Rate of Denudation (cm/1000 years)
Lowlands: slope $\leqslant 0.001$	
Climate with cold winter	2.9
Intermediate maritime climate (Lower Rhine, Seine)	2.7
Hot-dry climate (Mediterranean, New Mexico)	1.2
Hot-moist climate with dry season	3.2
Equatorial climate (dense rain forest)	2.2
Mountains: slope $\geqslant 0.01$	
Semihumid periglacial climate	60
Extreme nival climate (Southeastern Alaska)	80
Climate of Mediterranean high mountain chains	45
Hot-dry climate (Southwestern United States, Tunisia)	18
Hot-moist climate (Usumacinta)	92

[a]Figures are not of uniform quality due to limited sample and variable estimates of contribution of suspended load, bed load, and dissolved load of rivers [after J. Corbel, "Vitesse de l'erosion," *Z. Geomorphol.* **3**, 1–28 (1959), and L. B. Leopold *et al.*, *Fluvial Processes in Geomorphology*, pp. 28–30, W. H. Freeman and Co., San Francisco and London, 1964].

SAFETY CRITERIA FOR NUCLEAR FACILITIES

R. V. O'Neill K. E. Cowser

In siting and operating nuclear facilities, there is concern with the fate of radionuclides that may be released to the environment. This concern is frequently expressed by a request to estimate the potential dose to critical population groups. A general model that may be used to evaluate the sequence of events that result in radiation exposure of man can take the form

Release → Transport → Pathway → Receptor ,

in which each term is intended to identify one significant part of the system. As a computer program, each term can be considered as a subroutine, and in theory feedback from use of this model will permit the development of realistic safety criteria for the siting of nuclear facilities.

INREM and EXREM are used to estimate dose to man due to various modes of exposure and are examples of subroutines of the general model related to the term *Receptor* (see Chap. 6, Dose Estimation Related to Peaceful Uses of Nuclear Explosives).

PATHWAY ANALYSIS: AN APPLICATION OF SYSTEMS ANALYSIS TO NUCLEAR FACILITY SITING EVALUATION

The application of systems analysis techniques to the study of ecosystems has resulted in the development of methods for simulating the dynamic behavior of energy and nutrients in the environment. These methods can be directly applied to the prediction of radionuclide movement through some environmental pathways leading to man following releases from nuclear facilities. To test the feasibility of applying these methods with the present limitations of available data, a compartment model has been developed to predict the concentrations of ^{131}I, ^{90}Sr, and ^{137}Cs in a variety of human foods following a contaminating event. These concentrations are then used to estimate potential dose commitments to man as a consequence of ingesting contaminated foods.

The quantity of an element deposited on a square meter of ground or water surface at various downwind locations can be estimated by a number of available computer programs, such as PLUME. This information is superimposed on a map of the agricultural areas of interest (Fig. 4.1). An average deposition rate on each of these areas is then calculated and serves as input to the PATHWAY program.

The radionuclide is traced through several food chains leading to man by reducing the environmental components to a series of compartments whose temporal behavior can be described by continuous inputs and outputs. A preliminary search of the literature was made to assess the present state of knowledge, and the model largely has been structured by the available information. For example, the lack of data on parameters for a continuous system (i.e., transfer coefficients) has limited the description to a simplified discrete-time simulation. The behavior of the system is described by the system of equations shown in Table 4.5. They are designed to operate on a calculation interval of one day. The pathways that are included in the model are indicated in the last column of the table and include all components for which adequate information could be found. The parameters used to quantify the model are given in Table 4.6. Careful examination of the two tables will indicate that predictions of some compartments will be highly conservative. This is due to the assumption of rapid (24-hr) equilibrium in compartments for which only concentration factors are known.

In its present form the model possesses a rather limited ability to make realistic estimates of radionuclide concentrations in human food. It does attempt, however, to maximize our present predictive ability and can serve to assess the limitations in our present knowledge of the system.

This preliminary version of the PATHWAY model is implemented as a FORTRAN-coded program for the digital computer. An initial test case was formulated using the output from PLUME for a hypothetical release to the atmosphere that involves an exponentially decreasing source of ^{131}I, ^{137}Cs, and ^{90}Sr. A truck farm growing potatoes and leafy vegetables, a reservoir providing drinking water and fish, a farm growing grain products, and a dairy farm producing beef and milk were located at various distances downwind from the source. The time-varying concentration of radionuclides in each food product was calculated. Internal dose estimates will be made for ingestion as the mode of exposure using this information and appropriate dietary characteristics of a hypothetical population group.

The dose estimates from the system analysis approach will be compared with doses computed from the approaches commonly used for siting nuclear facilities which appear in present guidelines. Test cases using environmental monitoring data from existing sites will provide a means to determine which areas and terms are most sensitive and most critical.

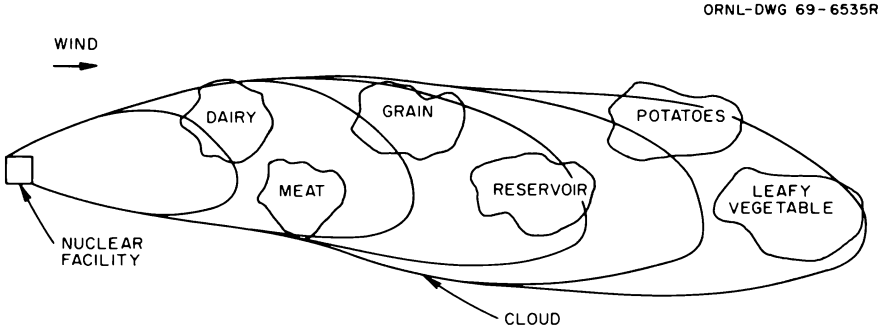

Fig. 4.1 Map of Region Downwind from a Hypothetical Nuclear Facility Showing One Potential Contamination Pattern Superimposed on Six Agricultural Sites.

Table 4.5. Discrete-Time Systems Equations Describe Time Behavior of Radionuclides in Human Food Chains

Compartment No.	Compartment Input-Output[a]	Compartment Description and Units
1	$V_{1i}(t) \rightarrow$ input from cards	Deposition ($\mu c/m^2$)
2	$V_{2i}(t) = V_{2i}(t-1) + \frac{V_{1i}(t-1)}{500} - V_{2i}(t-1)[a_{1i} + a_{2i}]$	Water (μc/liter)
3	$V_{3i}(t) = V_{2i}(t-1)\, a_{3i}$	Fish ($\mu c/g$)
4	$V_{4i}(t) = \frac{V_{4i}(t-1)\, a_{8i} + a_{4i}\, V_{1i}(t-1) - a_{8i} a_{7i}\, V_{4i}(t-1)}{a_{8i}}$	Vegetables ($\mu c/g$)
5	$V_{5i}(t) = \frac{V_{5i}(t-1)\, a_{9i} + a_{5i}\, V_{1i}(t-1) - a_{9i} a_{7i}\, V_{5i}(t-1)}{a_{9i}}$	Potatoes ($\mu c/g$)
6	$V_{6i}(t) = \frac{V_{6i}(t-1)\, a_{10i} + a_{6i}\, V_{1i}(t-1) - a_{10i} a_{7i}\, V_{6i}(t-1)}{a_{10i}}$	Grain ($\mu c/g$)
7	$V_{7i}(t) = V_{7i}(t-1) + a_{11i}\, V_{2i}(t-1) - a_{7i}\, V_{7i}(t-1)$	Grass ($\mu c/m^2$)
8	$V_{8i}(t) = [a_{12i}\, V_{7i}(t-1) + a_{13i}\, V_{2i}(t-1)]\, a_{14i}$	Meat (μc/kg)
9	$V_{9i}(t) = [a_{12i}\, V_{7i}(t-1) + a_{13i}\, V_{2i}(t-1)]\, a(t)_{15i}$	Milk (μc/liter)

[a]The index i varies from 1 to 3 to represent ^{131}I, ^{90}Sr, or ^{137}Cs.

Table 4.6. System Parameters Used to Simulate Radionuclide Movement Through Human Food Chains

System Parameter	Parameter Identification	^{131}I	^{137}Cs	^{90}Sr
Physical decay (day^{-1})	a_{1i}	0.0866	0.00007	0.00006
Water dilution factor	a_{2i}	0.0019	0.0019	0.0019
Equilibrium concentration in fish (ml/g)	a_{3i}	0.0	0.5	0.001
Fractional retention by leafy vegetables	a_{4i}	0.16	0.10	0.05
Fractional retention by potatoes	a_{5i}	0.16	0.10	0.0003
Fractional retention by grain	a_{6i}	0.16	0.05	0.01
Vegetation loss constant (day^{-1})	a_{7i}	0.116	0.0213	0.0233
Yield of vegetables (g/m^2)	a_{8i}	1000	1000	1000
Yield of potatoes (g/m^2)	a_{9i}	1000	1000	1000
Yield of grain (g/m^2)	a_{10i}	140	140	140
Fractional retention by grass	a_{11i}	0.16	0.057	0.10
Grass intake by cow (m^2/day)	a_{12i}	45.0	45.0	45.0
Water intake by cow (liters/day)	a_{13i}	80.0	80.0	80.0
Equilibrium concentration in meat (days/kg)	a_{14i}	0.01	0.04	0.00066
^{131}I concentration[a] in milk	$a_{15,1}$			
$5.6 \times 10^{-3} e^{-0.94t} + 7.5 \times 10^{-5} e^{-0.032t} - 5.7 \times 10^{-3} e^{-6.93t}$				
^{137}Cs concentration[a] in milk	$a_{15,2}$			
$3.6 \times 10^{-3} e^{-0.69t} + 1.5 \times 10^{-3} e^{-0.17t} + 4.0 \times 10^{-5} e^{-0.23t} - 5.1 \times 10^{-3} e^{-1.84t}$				
^{90}Sr concentration[a] in milk	$a_{15,3}$			
$5.5 \times 10^{-4} e^{-0.48t} + 1.0 \times 10^{-6} e^{-0.017t} - 5.5 \times 10^{4} e^{-1.58t}$				

[a]Taken from R. J. Garner, "Mathematical Analysis of the Transfer of Fission Products to Cows' Milk," *Health Phys.* 13, 205–12 (1967).

5. Earthquakes and Reactor Safety

T. F. Lomenick O. H. Myers
H. J. Wyrick W. C. McClain
C. J. Mott[1]

STUDIES OF STRAIN ACCUMULATION IN ROCKS

T. F. Lomenick H. J. Wyrick

Photoelastic measurements of rock fabrics is a simplified, low-cost technique for determining the stress configuration in rock masses. From these measurements the strain accumulation in rocks in highly seismically active areas of the country can be determined through core samples of certain rock types.

To develop the laboratory technique for utilization in evaluating the geotectonic conditions at reactor sites, a series of rock types (limestone, sandstone, and granite) were loaded uniaxially, biaxially, and triaxially and subsequently strained in the laboratory. Upon removal of these loads, measurements of elastic strain recovery, utilizing photoelastic as well as strain gage and micrometer techniques, were made. For these short-term tests it was found that limestone showed the greatest deformation recovery in relaxation, while sandstone and granite were considerably less elastic. For the limestone approximately 50% of the strain recovery occurred within the first 30 min after release of the load, while an additional 30% was released in the next 50 hr. The remaining 20% of strain was only partially recovered after one month. These data indicate that strain release is slow enough to allow measurements of this recovery through photoelastic techniques. Quantitative determinations of the directions of the principal stresses can be determined in this manner, while qualitative determinations of the amounts of strain in the rocks can be made.

To demonstrate the effectiveness of the technique in the field, a series of cores were taken from the exposed faces of a local limestone quarry. Immediately upon their removal from the field, selected portions of the core samples were cut into cubes and oriented with respect to their field positions. Photoelastic patches were then bonded to the faces, and strain directions were subsequently observed and recorded using a polariscope. From these data the directions of the major, minor, and intermediate stresses were revealed. In this case the major stress was oriented parallel to the vertical and approximates the weight of the overburden.

A second field study has been initiated utilizing selected portions of rock cores taken at the Nuclear Fuel Services reprocessing site near Springville, New York. Since the objective of the drilling was to obtain stratigraphic and structural data as part of a study to investigate the applicability of hydraulic fracturing in a different geologic setting, only a cursory examination of the rock core is being made to identify its stress relief patterns. Preliminary analyses of sample specimens of the shale, taken at depths of 1130 ft and between 1140 and 1180 ft, show no unusual stress field existing at that site. In addition, the field measurements verify laboratory tests which show that the strain recovery in shale (essentially the entire rock column at the site down to a depth of 1500 ft is well-indurated shale) is extremely rapid and greatly limits the use of this rock type for photoelastic strain recovery studies.

FIELD STUDIES OF SLOPE STABILITY

T. F. Lomenick C. J. Mott[1]

Geological, hydrological, seismological, and climatological investigations were made to determine parameters of catastrophic downslope movement of soil materials developed on fuller's-earth-bearing strata in northern Florida and southern Georgia. Soil failures of this type may be initiated by earthquake-induced ground motions as well as with favorable lithologic

[1] University of Tennessee graduate student.

factors and above-normal water availability in a short period of time. Since the hydrologic and lithologic features of this area are common in the Southeast Coastal Plain, the results of this study (University of Tennessee dissertation) will be applicable to the determination of stable sites for power reactors throughout the entire region.

Field investigations within Gadsden County, Florida, where mass movement frequently causes major landscape development, have shown that the Hawthorn and Fort Preston formations of Miocene age are the dominant stratigraphic units within the area. The Hawthorn formation consists of beds of clay, carbonates, cherts, and phosphorite with montmorillonite clay forming a significant part of the upper half of the formation. Overlying the Hawthorn formation is the Fort Preston, which is predominantly kaolinitic sand. The nature of the Fort Preston–Hawthorn contact is not apparent. Three possibilities exist:

1. The kaolinitic Fort Preston formation may disconformably overlie the Hawthorn formation, which is high in attapulgite and has considerable amounts of montmorillonite.
2. The Fort Preston–Hawthorn formation contact is conformable, and differences in clay mineralogy are attributable to normal depositional or diagenetic processes.
3. The Fort Preston is developed as a result of intense weathering of Hawthorn sediments and would be mapped as Hawthorn had this degree of weathering not taken place.

Cases 1 and 2 do not adequately explain existence of the apparent gradational sequence of kaolinite-montmorillonite-attapulgite that has been reported.[2] Thus the third possibility appears to be the most plausible. The mechanism of mineral genesis – supergene weathering activity – has been duplicated in the laboratory.[3] One of the contingencies that is being considered in this study is the possibility of the occurrence of mass movement along the montmorillonite zone.

Two major river basins drain the study area. The Ochlockonee Basin, which drains approximately 70% of the area, has an average runoff of 10 to 20 in./year, or roughly 33% of the annual precipitation. The northwest quadrant of the county is located in the Apalachicola Basin, which is formed by the confluence of the Flint and Chattahoochee rivers near the common boundary of Alabama, Florida, and Georgia. Annual runoff in the Apalachicola Basin is estimated at about 20 to 30 in., or approximately 45% of the average annual precipitation.[4] Precipitation has averaged 54.21 in./year for the period 1931 to 1968.

Annual precipitation in the area is variable, from a minimum of 30.02 in. in 1954 to a maximum of 77.44 in. in 1948. Additionally, seasonal fluctuation may vary from 2.31 in. in an average dry month to 6.96 in. for an average rainy month (U.S. Weather Bureau).

Local water tables fluctuate directly as precipitation. These water tables, located within the Hawthorn, generally are nonartesian, shallow aquifers which can be utilized locally for private consumption in areas where water requirements are small. The principal aquifer in the area is the Floridan aquifer – porous limestones of the Ocala, Suwanee, and Tampa formations which underlie all of Florida. In Gadsden County, artesian conditions exist in the Floridan aquifer. The potentiometric surface averages nearly 50 ft above mean sea level.[5]

Water in the Floridan aquifer is replenished by rainfall in northern and central Florida[6] and in Alabama and Georgia where the aquifer crops out or where it is covered by permeable materials.[7]

In general, it has been found that within the area, stratigraphic highs are covered with a porous kaolinitic sand that supports little or no runoff. As a consequence, downward percolating rainfall may lubricate montmorillonitic clays within the Hawthorn, thereby allowing catastrophic landsliding upon the triggering action of earthquake-induced ground motion and/or favorable climatic and hydrologic conditions. One special hydrologic condition that may be associated with the initiation of mass movement in the area is that

[2] Z. S. Altschuler, E. J. Dwornik, and H. Kramer, "Transformation of Montmorillonite to Kaolinite During Weathering," *Science* 5(141), 148–52 (1963).

[3] G. W. Brindley and G. M. Poncelot, "Experimental Formation of Kaolinite from Montmorillonite at Low Temperatures," *Am. Mineralogist* 5(52), 1161–73 (August 1967).

[4] W. E. Kenner, *Runoff in Florida* (map), Florida Geological Survey, Map Series No. 22 (1966).

[5] H. G. Healey, *Piezometric Surface and Areas of Artesian Flow of the Floridan Aquifer – July 6 to 21* (map), Florida Geological Survey, Map Series No. 4 (1961).

[6] C. J. Mott, *The Geology of the Putnam Hall Quadrangle, Putnam County, Florida* (unpublished master's thesis), Department of Geology, The University of Florida, Gainesville, 1967, 54 pp.

[7] L. W. Hyde, *Principal Aquifers in Florida* (map), Florida Geological Survey, Map Series No. 16 (1965).

of the "piston-like" action to the rapid up and down fluctuations of the water table. This phenomenon has been suggested as a triggering mechanism for catastrophic sinkhole development in Florida.[8]

Another possible explanation of translocation of earth materials includes seismic and microseismic excitation, causing a thixotropic effect in the clays of the Hawthorn formation. Campbell[9] cites 15 documented tremors in the state, ranging from slight microseismic shocks to intensities of 6 to 8 on the Rossi-Forel scale. Moneymaker reports 16 additional shocks felt in this part of the Coastal Plain, including tremors in 1948 and 1952 in the proposed study area.[10] Of course the area has also been shaken perceptibly by past great earthquakes that were centered in the eastern part of the United States, such as the New Madrid, Missouri, earthquakes of 1811 and 1812 and the Charleston, South Carolina, earthquake of 1886.

ORNL SEISMOGRAPH STATION

O. H. Myers W. C. McClain

Since the ORNL Seismograph Station (ORT) was established and accepted as a reporting station in the U.S. Coast and Geodetic Survey net, it has reported seismic events twice weekly to the National Earthquake Information Center.[11,12] It is the only station operating in the East Tennessee area and records seismic events that take place locally, as well as most of the major worldwide earthquakes.

The station consists mainly of a vertical short-period seismometer and its amplifying and recording equipment. The seismometer is installed approximately one-fourth mile south of ORNL (ORNL Grid coordinates 20,518 N; 31,812 E) in a select site having low industrial noise. The amplifying and recording equipment is installed within the plant area. Direct recording is accomplished on a revolving drum using special heat-sensitive paper and a galvanometer-driven heated stylus. A maximum amplification of the incoming signal of several million is possible, but because of seismic background noise, the ground motion signal is amplified only about 100,000 times. Other equipment consists of a time-mark generator driven by a synchronous clock and a shortwave receiver tuned to the time service channels operated by the National Bureau of Standards.

During the months of July through December 1968, arrival times of 239 seismic events were supplied to the National Earthquake Information Center and were used and published in their *Summary of Epicenter Determination Data.* Several of these were of local interest, including the Southeastern Illinois earthquake of November 9, 1968. The intensity of this quake was the largest experienced over the southeastern part of the country in recent years.

Several patterns of nuclear detonations have been recorded, including two that took place at the Nevada Test Site that were in the megaton range. The one detonated on December 19, 1968, registered 6.3 on the Richter earthquake scale. It was followed by several aftershocks. Several of these aftershocks registered between 4 and 5 on the Richter scale.

Ground motions were recorded on the vertical component of the ORNL seismograph during the shaking tests at EGCR on August 7 to August 14, 1968. The seismometer detecting these signals is located approximately 2¼ miles N 79½°W (Grid) from the EGCR structure. The times (Eastern Daylight) of the beginning and end of the signal, the recorded frequency of the signal, and the apparent vertical ground amplitude (peak to peak) in millimicrons were recorded.

---

[8] Robert Vernon, Florida State Geologist, personal communication to C. J. Mott, University of Florida, August 1968.

[9] R. B. Campbell, "Earthquakes in Florida," *Proc. Florida Acad. Sci.* 6(1), 1–4 (1943).

[10] B. C. Moneymaker, TVA, personal communication to C. J. Mott, University of Florida, April 1968.

[11] O. H. Myers and W. C. McClain, *The ORNL Seismograph: Installation and Operation from September 1, 1967, to February 29, 1968,* ORNL-CF-68-8-26.

[12] O. H. Myers, *The ORNL Seismograph Station ORT: Operation from March 1, 1968, to August 31, 1968* (in press).

6. Dose Estimation Related to Peaceful Uses of Nuclear Explosives

D. G. Jacobs S. V. Kaye[2]
M. J. Kelly[1] P. S. Rohwer[3]
K. E. Cowser E. G. Struxness
W. S. Snyder

PROJECT GASBUGGY

D. G. Jacobs E. G. Struxness
P. S. Rohwer M. J. Kelly
K. E. Cowser

Project Gasbuggy is a joint undertaking by the U.S. Atomic Energy Commission, the U.S. Bureau of Mines, and the El Paso Natural Gas Company to evaluate the feasibility of the use of nuclear explosives to stimulate low-productivity oil and gas reservoirs.[4] The field test was initiated when a 26-kiloton device was detonated 4200 ft underground on December 10, 1967, near Farmington, New Mexico, at a site located on an El Paso Natural Gas Company oil-and-gas lease in the San Juan Basin, Rio Arriba County, New Mexico. The device was detonated at the base of the Pictured Cliffs formation, which is composed of interbedded sand and shale deposits, constituting a gross interval of 300 ft with about 190 ft of gas-saturated sandstone. Before the detonation the average permeability was 0.14 millidarcy, the average porosity was 11%, and gas occupied an average of about 41% of the pore volume. These sands contain natural gas, predominantly methane, with a calculated amount of in-place gas of 33,000,000 ft^3 per acre.

Description of the Study

We have been asked by the Division of Peaceful Nuclear Explosives (DPNE) to evaluate the dose equivalents to various population groups in the hypothetical utilization of natural gas and other by-products from the Gasbuggy cavity. In order to facilitate our analysis, the study has been divided into three phases.

Phase I will be a consideration of the impact of the hypothetical input of gas from the Gasbuggy well into the gas-collecting network of the San Juan Division of El Paso Natural Gas Company. In this phase of the study, the analysis is restricted to a consideration of the hypothetical population and employee exposures within the San Juan Basin, because it seems likely that in this region the hypothetical dilution of the products will be the lowest and the radiation exposures the highest.

Phase II will extend the problem to include the hypothetical utilization of natural gas and other contaminated by-products by populations outside the San Juan Basin. In the initial stages of this phase we will consider that the gas moves through the Blanco plant into Southern California and is diluted with gas produced from the Permian Basin or that the gas moves northward through the Ignacio plant for Northwest distribution. As additional information is obtained and processed on the demand vs production of the various areas, we will attempt to further refine our estimates of the hypothetical dilution, utilization, and population exposure, as they vary seasonally.

Phase III will be the final extension of the hypothetical problem. During this phase, we will consider the possibility of nuclear stimulation of an entire reservoir. Temporal sequencing of detonations and modifications

---

[1] Reactor Chemistry Division.

[2] Radiation Ecology Section.

[3] Internal Dose Estimation Section.

[4] Fred Holzer (ed.), *Gasbuggy Preshot Summary Report*, U.S. Atomic Energy Commission Report PNE-1001 (November 1967).

in the operation of stimulated wells will be considered. Consideration will also be given to alternative dispositions of the cavity gas if it is necessary to reduce population exposures that would accrue from its use.

Description of the Source

Consistent evidence after some 200 days post shot indicated a chimney volume of 2×10^6 ft^3, containing about 1.3×10^8 ft^3 of gas. Fifty-five million cubic feet of gas was flared at a nominal rate of 5×10^6 ft^3/day. Smith and Momyer,[5] of Lawrence Radiation Laboratory, have reported that one-third of the original cavity gas was removed by this process, with only 17% of the flared gas representing new production from the formation. At this flow rate about 3% of cavity pressure was lost per day. Four days of flaring at 0.75×10^6 ft^3/day followed, and pressure increased in the cavity during this period. It has been estimated that 1.3×10^6 ft^3/day of gas could be withdrawn at steady state.

The radioactivity in gas samples withdrawn from the Gasbuggy well has been analyzed by the Lawrence Radiation Laboratory.[5] Tritium and ^{85}Kr were detected and measured in the gas samples and found to be present in concentrations of 650 and 100 pc/cm^3, respectively, in the samples removed in November 1968. It is of interest to note that ^{131}I was not found post shot in the gas and that gamma scans indicated that gamma emitters other than ^{85}Kr were not present. Argon-37, with a half-life of 35 days, was the only radionuclide besides ^{85}Kr and ^{3}H found in significant concentrations. No report on the activity of hydrocarbons higher than propane has been reported, which leaves in doubt the activity levels of the liquid fraction.

Lawrence Radiation Laboratory has provided a list of radionuclides that were analyzed for and the limits of their detectability with the analytical procedures used.[6] Some additional information, obtained by Isotopes, Inc., was provided by C. R. Bowman, El Paso Natural Gas Company. It is important to keep in mind that the values listed in Table 6.1 are detection limits (i.e., they represent the highest concentration of the radionuclide that could have escaped detection) and that the true concentrations are probably well below these limits.

Table 6.1. Limits of Detection of Radionuclides in Gas from the Gasbuggy Well

Radionuclide	Detection Limit in Undiluted Gas at the Time of Analysis Extrapolated to the Time of Detonation[a] (pc/cc)	Radioactive Half-Life (days)
^{90}Sr	1.4×10^{-3}	1.0×10^4
^{125}Sn	1.8	9.5
^{131}I	0.03	8.05
^{14}C[b]	0.05	2×10^{14}
^{127}Sb	2.25	3.9
^{129m}Te	0.001	3.3
^{125m}Te	7×10^{-4}	58
^{137}Cs	1.4×10^{-5}	1.1×10^4
^{125}Sb	5×10^{-5}	877
^{106}Ru	1.3×10^{-5}	365
^{103}Ru	8×10^{-5}	41

[a]Data from ref. 6 except for ^{14}C.

[b]Data on the detection limit of ^{14}C were supplied by C. R. Bowman, El Paso Natural Gas Co.

If gas is removed from the well at a constant rate, if the bottom-hole pressure is maintained by the influx of an equivalent amount of gas into the cavity, and if the gases within the cavity are well mixed, the concentration of radionuclides in the gas removed from the wellhead would decrease exponentially with time. For radionuclides with half-lives on the order of a few days, the concentration in gas from the wellhead could be significantly reduced by allowing a few months shut-in time for radioactive decay. For long-lived radionuclides, that is, half-lives on the order of a few years, radioactive decay would not significantly reduce the activity levels during a shut-in period of a few months, but the concentrations could be reduced by flaring operations.

Description of Gas Collection and Processing in the San Juan Division of El Paso Natural Gas Company

The gas production from the San Juan Basin can be considered as a closed system, internally complex, having but two outlets. One outlet, to the northwest, typically transmits about 150,000,000 ft^3/day of natural gas, and the second outlet, to the southwest, discharges about 1250 M^2 cf/day.

[5]C. F. Smith and F. F. Momyer, *Gas Quality Investigation Program Status Report for Project Gasbuggy*, UCRL-71314 (Sept. 18, 1968).

[6]C. F. Smith, "Nongaseous Radioisotopes, Project Gasbuggy Chimney Gas, January 15, 1969," an attachment to a letter from G. H. Higgins, Lawrence Radiation Laboratory, to S. V. Kaye, Oak Ridge National Laboratory, Feb. 24, 1969.

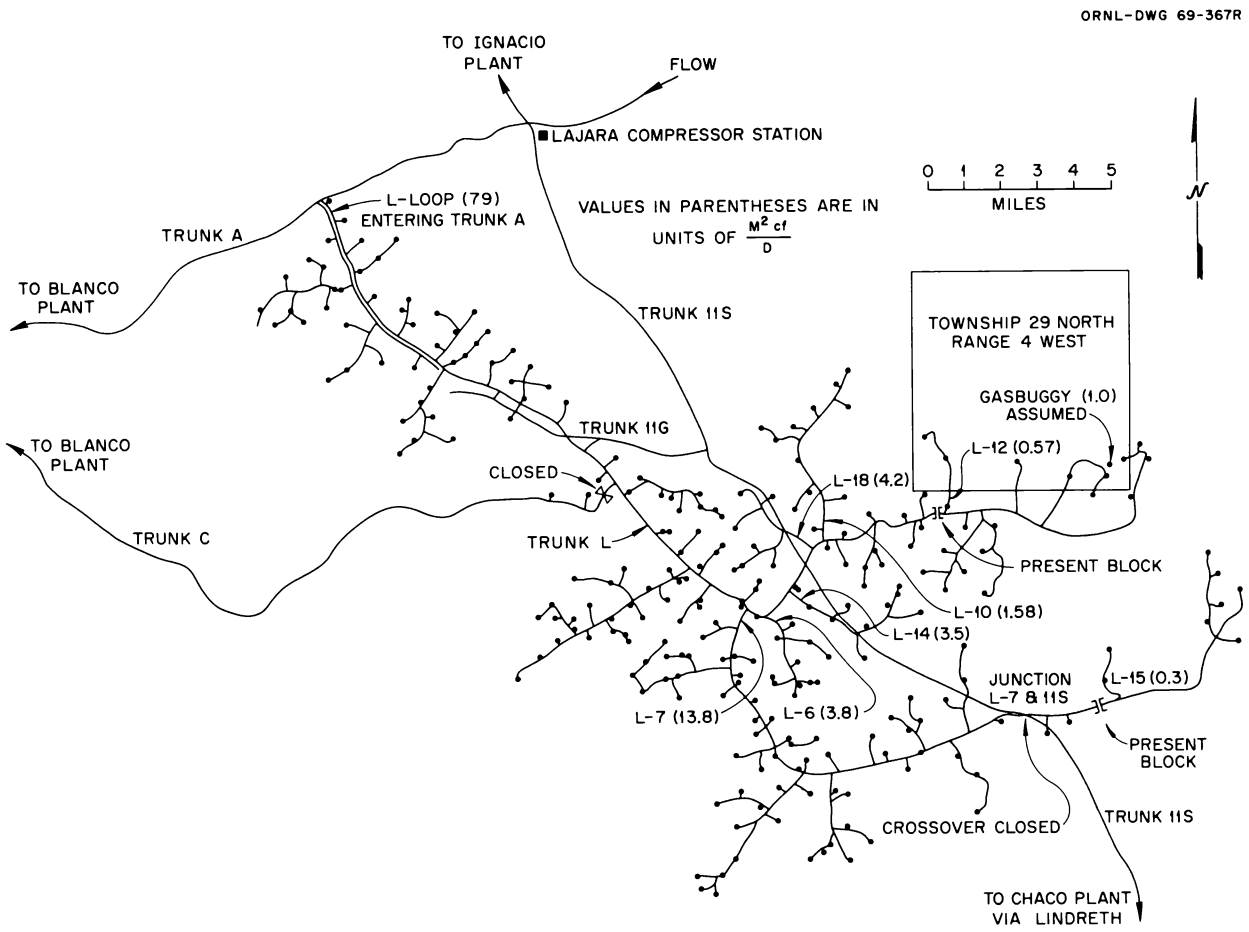

Fig. 6.1 Gas-Gathering System for the Gasbuggy Area. The L loop and trunk are complete; feeders to other loops and trunks are not shown. On the trunk 11S line the only open intersection with trunk 1 or lateral L-7 is at trunk 11G. A physical crossover exists at L-7 and 11S, but it is closed. No physical crossovers exist elsewhere.

The gas from Gasbuggy could be processed at either the Blanco plant, with a capacity of about 600 M^2 cf/day, or at the Ignacio plant, which can handle about 300 M^2 cf/day of wet gas plus 100 M^2 cf/day of dry gas from the drier region of the basin to the northeast.

Figure 6.1 shows the gas-gathering system in the Gasbuggy area. The primary routes are shown in detail, with feeders from other trunks and loops left out for clarity. The gathering line from the Gasbuggy well is physically cut and welded, so that no gas can actually enter the El Paso gathering system from this well.

Ordinarily, gas wells produce liquid hydrocarbons, water, and methane. Some of these liquids, called drip liquids, condense at the wellhead and are collected in tanks for sale to local refineries, where they are fractionated and further refined. Most of the water is removed from these drip liquids at the wellhead, generally by absorption into glycol or sometimes by adsorption on calcium fluoride. After liquid removal at the wellhead, Gasbuggy gas would hypothetically enter trunk *L* and proceed toward one of the processing plants. Dilution with uncontaminated gas from other wells would occur during the transmission. The average daily flow (M^2 cf/day) at various points in the collection system is: 2.1 at lateral L-10, 4.8 at lateral L-10, 22 at lateral L-7, 57 at lateral L-7, 89 at trunk L junction with trunk A, and 576 at the input to the Blanco plant.

During transmission of the gas, further condensation of water vapor and higher hydrocarbons also occurs. The quantity varies seasonally due to temperature changes. These liquids tend to accumulate at low spots in the gathering lines and must be removed periodically so that they do not impede the flow of gas. Removal is

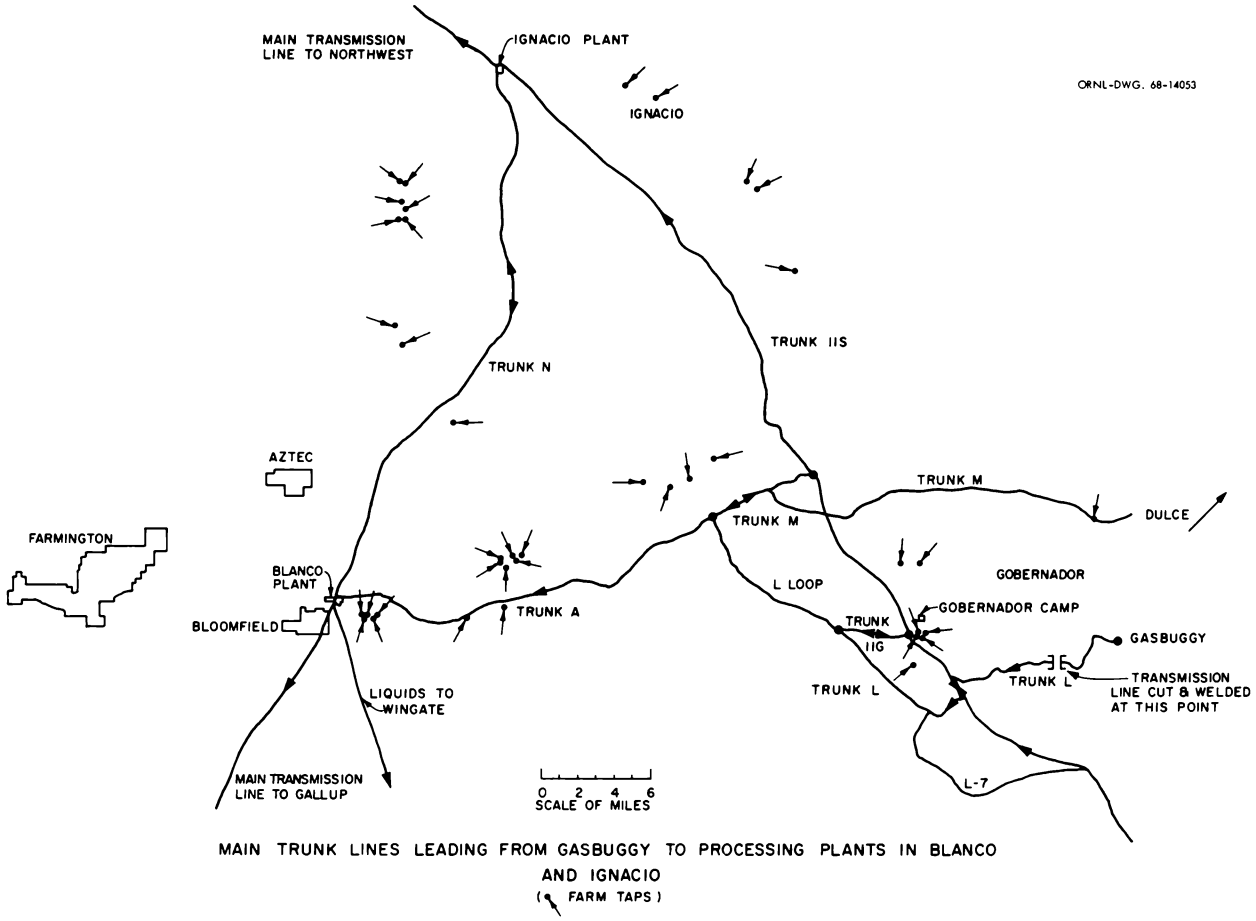

Fig. 6.2 Simplified Schematic of the Gas Collection System in the San Juan Division of El Paso Natural Gas Company.

accomplished by sending rubber balls (pigs) through the lines and removing them and the liquids at pigging stations along the lines. These pigging liquids are stored in tanks and sold to the local refineries along with the drip liquids.

Ranchers in the area have the option of tapping into wellheads or gathering lines to obtain natural gas for domestic use. Several farm taps exist in the San Juan Basin. In Fig. 6.2, various user taps are shown which are hypothecated to be remotely associated with contaminated gas from Gasbuggy. Most of these users lie off main gathering trunks on producing laterals which protect them from contaminated gas by counterflow; protection is also afforded by one-way valves at the wellhead. The community of Dulce also obtains natural gas from the El Paso Natural Gas Co. gathering system. However, the demands of the community are essentially always lower than the production along the spur leading to the town, so that it is not likely that gas from the main trunk would flow toward the community.

Gas entering the system from wells in the vicinity of the Gasbuggy experiment would leave the San Juan Basin through either the processing plant at Ignacio at the northern exit or at Blanco at the southern exit. At the processing plant the gas is dehydrated and absorbed to remove LPG's and liquid hydrocarbons from the product gas. The liquid hydrocarbons and the butanes and propanes are piped to Wingate, where they are fractionated and distributed by rail and truck. At the Ignacio plant the butanes and propanes are separated and marketed locally. The methane product gas enters pipelines leading to Southern California to the south from the Blanco plant or to the Pacific Northwest from the Ignacio plant.

An Approach to Estimating Household Dilution of Natural Gas Combustion Products

Open flame burning of natural gas in a dwelling results in the production of heat, carbon dioxide, and

moisture within a confined space. It is recognized that this nonventilated method of heating is *not representative;* however, for purposes of this report, it is assumed to be a "worst" case. In warm weather we may expect ventilation to be at a maximum to remove the undesirable heat. Dilution of the combustion products with outside air would also be at a maximum. In winter the opposite occurs, and minimum dilution of the combustion products would be expected. Hence, for natural gas containing radionuclides, maximum radiation exposure will probably occur during the heating season. To assess the probable magnitude of this exposure, it is necessary to establish appropriate concentrations of the natural gas reaction products within a variety of inhabited dwelling units.

A consistent approach to the problem is to consider the gas usage required to maintain normal inside temperatures (70°F). Exchange of outside air with that within the dwelling unit must also be evaluated so that we may determine the average dilution of the combustion products within the living space. To accomplish this, a basic framework has been outlined which relates heat transfer, infiltration of air into dwelling units, thermal conductivity, and construction practice.[7]

Conduction losses of heat are assumed to be equal to the rate at which the heat is transferred to the outside surfaces, and this depends on the type of construction materials used. Infiltration of air into dwellings is not so well defined, but values have been obtained from the literature.[8] The numbers were used in conjunction with the minimum recommended design value of one air change per hour. Gas is assumed to supply heat at a rate of 1100 Btu/ft^3.

When different types of construction are considered, the dilution of combustion products in the unit (house or room) can be estimated based on the rate of air change and the rate of gas usage required to maintain an inside temperature of 70°F. For the extreme case in which the outside temperature is assumed to be −10°F, the following dilution factors were estimated, assuming all combustion products released into the heated unit:

Case A: Shack, 10 ft × 10 ft × 8 ft, made of 1-in. wood, with one door and two windows – 110.

Case B: Same as case A with door and windows weather stripped – 58.

Case C: Normal dwelling unit of first-class construction, 100 ft^2 room, 4 in. of rock-wool insulation, doors and windows comprising 15% of outside surface, windows curtained – 110.

Case D: Same as case C but 1000 ft^2 floor area; door and window area 312 ft^2; wall and ceiling area 1768 ft^2 – 191.

Case E: Same construction as cases C and D with floor area 3000 ft^2 – 213.

Case F: Extremely well designed and well constructed, storm doors and windows, floor area 1000 ft^2 – 334.

If infiltration is reduced, the dilution factor may be limited by the stoichiometry of combustion, in which two volumes of water vapor are produced from each volume of burned gas. At 70°F only 2.5% water vapor can exist in equilibrium in air; condensation to liquid occurs above this point. Thus a positive dilution factor of 80 for inhalation exists, assuming equilibrium at 70°F. Local temperature gradients within the shack (higher temperatures would exist near the stove) will decrease this somewhat, but a conservative dilution for inhalation is over 60 even without air infiltration. Asphyxiation can occur at this concentration. The minimum dilution of 60 is dependent only on temperature and on the combustion process and may be considered a fundamental limit; it is not dependent on dwelling size.

The problem still remains for the probable dilution when heating is not required or desirable. A study of nonheating gas usage in Indiana[9] on 30,417 meters gave an average usage of 6870 Btu/hr or 6.2 ft^3/hr of natural gas with a range from 4.0 to 8.6 ft^3/hr. This may be compared with the one-day average usage by:

Kitchen range	27 ft^3/day or 1.13 ft^3/hr
Refrigerator	34 ft^3/day or 1.42 ft^3/hr
Water heater	64 ft^3/day or 2.67 ft^3/hr
	5.22 ft^3/hr

Other appliances, such as clothes dryers, account for the remaining usage shown in the Indiana study. Water heaters and clothes dryers are invariably vented. Ignoring this and using our standard 8000-ft^3 house and the maximum Indiana case of 8.6 ft^3/hr gas usage with

[7] M. J. Kelly *et al., Second Quarterly Progress Report on the Theoretical Evaluation of Consumer Products from Project Gasbuggy,* ORNL-TM-2513 (March 1969).

[8] J. W. Norris, *Warm Air Heating and Winter Air Conditioning,* p. 59, McGraw-Hill, New York, 1950.

[9] C. G. Segeler (ed.), *Gas Engineers Handbook,* sect. 23, pp. 51–58, Industrial Press, New York, 1966.

one air volume change per hour, our dilution is 930. As a cross check we can consider the kitchen only, assuming a volume of 800 ft^3, with the stove and refrigerator using 2.55 ft^3/hr of natural gas. This would give a dilution factor of 314. This would appear the worst credible case under nonheating conditions.

Effect of a Continuously Decreasing Concentration of Radionuclides at the Wellhead on the Dose to Hypothetical Users of Gasbuggy Gas

In the hypothetical utilization of gas from a well that has been stimulated by underground nuclear detonations, there are a number of factors which affect the concentration of radionuclides available for the exposure of domestic consumers. These factors, outlined in a previous progress report,[7] include:

1. concentration of radionuclide at the wellhead,
2. pipeline dilution,
3. quantity of gas consumed,
4. fraction of combustion products vented inside the home,
5. home dilution,
6. occupancy.

These factors can be combined into a general equation to depict the trend of radiation exposures with time.[10] Most of these parameters, of course, are not constant but vary with time. For example, utilization of gas for heating is seasonal and is dependent on weather conditions; also, the rate of air turnover in a given house depends on the ventilation. The equation would give the concentration of a radionuclide in a home for the conditions specified. Intake of radioactivity would be further influenced by the breathing rate and by the occupancy factor.

Dose equivalents calculations have been made for the hypothetical use situations described above as residence A and residence C. These hypothetical situations considered a wellhead production rate of 1 M^2 cf/day for the Gasbuggy well, a pipeline dilution factor of 50, and gas use corresponding to 6000 degree-days of heating per year. Measured values for the initial concentrations of ^3H and ^{85}Kr of 650 and 100 pc/cc were used, as was the estimated initial volume of gas in the cavity, 130 M^2 cf.[5] Further assumptions were that gas would be produced and used continuously, that all combustion products would be vented into the home, and that someone would be present in the home continuously. The exposure modes considered were inhalation and skin absorption of ^3H and submersion in ^{85}Kr. The equation from ref. 8 was used to describe the concentrations of the ^{85}Kr and ^3H with time.

In Table 6.2 are listed the annual dose equivalents for the hypothetical conditions assumed in the calculations. The biological half-life of ^3H is quite short, so that when intake ceases the additional dose due to the ^3H retained in the body ceases shortly thereafter. For ^{85}Kr the dose results from submersion in contaminated air, so that no dose is obtained after the source of radioactivity is depleted.

The limits of detection for other radionuclides were given in Table 6.1. Although the true concentrations are probably well below these limits, it is of interest to estimate the upper limits of the dose that could hypothetically be received. The 50-year dose commitments and the external gamma dose potentials were calculated for the hypothetical use situation described above.

Of the radionuclides listed in Table 6.3, looking ahead to the hypothetical nuclear stimulation of a large producing formation (involving thousands of nuclear stimulated wells), ^{90}Sr might contribute a significant dose commitment (after a shut-in period of a few months) if it were initially present in a concentration approaching its present detection limit. Thus it is suggested that more sensitive analytical techniques should be used to establish a lower detection limit.

Table 6.2. Annual Hypothetical Dose Equivalents to Total Body from the Use of Gas from the Gasbuggy Well

Pipeline dilution factor = 50

Production Year	Annual Hypothetical Dose (millirems)	
	^3H	^{85}Kr
1	15.0	0.93
2	1.1	0.06
3	0.06	

[10] D. G. Jacobs and K. E. Cowser, *Third Quarterly Progress Report on the Theoretical Evaluation of Consumer Products from Project Gasbuggy*, ORNL-TM-2657 (July 1969).

Table 6.3. Limits of Detection of Radionuclides in Gas from the Gasbuggy Well and Their Hypothetical Impact on Dose

The contributions of the daughters are considered in the total
Gas production is assumed to begin immediately following the detonation
Pipeline dilution factor = 50

Radionuclide	Detection Limit in Undiluted Gas at the Time of Analysis Extrapolated to the Time of Detonation[a] (pc/cc)	Critical Organ	Upper Limit of Hypothetical Internal Dose Commitment (50 years) to the Critical Organ (millirems)	Upper Limit of Hypothetical External Gamma Dose Potential (millirems)
^{90}Sr	1.4×10^{-3}	Bone	5	
^{125}Sn	1.8	GI (LLI)[b]	0.9	2×10^{-3}
^{131}I	0.03	Thyroid	0.4	1×10^{-4}
^{14}C[c]	0.05	Fat	0.02	
^{127}Sb	2.25	*d*	*d*	5×10^{-3}
^{129m}Te	0.001	Kidneys	2×10^{-3}	5×10^{-6}
^{125m}Te	7×10^{-4}	GI (LLI)	6×10^{-4}	2×10^{-6}
^{137}Cs	1.4×10^{-5}	Liver	1×10^{-4}	1×10^{-6}
^{125}Sb	5×10^{-5}	Bone	8×10^{-5}	1×10^{-6}
^{106}Ru	1.3×10^{-5}	GI (LLI)	7×10^{-5}	3×10^{-7}
^{103}Ru	8×10^{-5}	GI (LLI)	3×10^{-5}	6×10^{-8}

[a]Data from ref. 6 except for ^{14}C.

[b]Gastrointestinal tract (lower large intestine).

[c]Data on the detection limit of ^{14}C were supplied by C. R. Bowman, El Paso Natural Gas Co.

[d]Not calculated.

ATLANTIC-PACIFIC INTEROCEANIC CANAL STUDY

S. V. Kaye P. S. Rohwer
K. E. Cowser E. G. Struxness
W. S. Snyder

The Health Physics Division, under subcontract to Battelle Memorial Institute (BMI), has been developing procedures to estimate the potential dose to man (and to compare these estimates with appropriate radiological safety standards) as a part of a feasibility study of using nuclear explosives to excavate a sea-level canal across the isthmus of Central America. Battelle Memorial Institute, as a principal AEC contractor, is responsible for the management of studies to determine the radiological safety of such a project. Earlier progress reports provide details on the modes of exposure considered, models for estimating external dose (EXREM) and internal dose (INREM), and suggested radiation safety criteria.[11,12]

The EXREM II Computer Code for External Dose

The EXREM II code has all of the features of the EXREM code,[13] but, in addition, it can handle complex parent-daughter decay chains with any degree of branching. Since some proposed Plowshare projects require multiple detonations, the EXREM II code is able to handle up to 25 consecutive detonations and perform the necessary bookkeeping for buildup and

[11]K. E. Cowser *et al., Health Phys. Div. Ann. Progr. Rept. July 31, 1967,* ORNL-4168, pp. 53–59.

[12]K. Z. Morgan *et al., Health Phys. Div. Ann. Progr. Rept. July 31, 1968,* ORNL-4316, pp. 60–68.

[13]W. D. Turner, S. V. Kaye, and P. S. Rohwer, *EXREM and INREM Computer Codes for Estimating Radiation Doses to Populations from Construction of a Sea-Level Canal with Nuclear Explosives,* Computing Technology Center and Oak Ridge National Laboratory, Oak Ridge, Tennessee, K-1752 (September 1968).

decay of up to 200 parent and daughter nuclides, starting at the time of the first detonation and continuing to any time of interest. The models programmed for submersion in air and water are the adiabatic type; that is, the contaminated medium is assumed to be infinite in extent and of uniform concentration. When this is not the condition, the dose estimates will be proportionately conservative.

The total external dose equivalent (rems) from beta particles ($q = \beta$) or gamma photons ($q = \gamma$) of the ith radionuclide at the lth location accumulated from exposure from t_1 to t_2 for the qth mode of exposure is designated by

$$\mathrm{TD}_{ipql}(t_1, t_2) = D_{ipq} \int_{t_1}^{t_2} C_{ipl}(t)\, dt \,, \tag{6.1}$$

where

i = radionuclide index,

p = exposure mode index (w for water, a for air, s for surface),

q = radiation index (β for beta radiation, γ for gamma radiation),

l = location index,

t_1 = time (hr) for beginning of exposure,

t_2 = time (hr) for ending of exposure,

D_{ipq} = dose-rate factor (rems cm^3 μc^{-1} hr^{-1} for $p = w$ and $p = a$, rems cm^2 μc^{-1} hr^{-1} for $p = s$),

$C_{ipl}(t)$ = concentration (μc/cm^3 for $p = w$ and $p = a$, μc/cm^2 for $p = s$) at time t.

The EXREM II code calculates D_{ipq} separately for both beta and gamma radiation from a model appropriate for the mode of exposure p using input data for radionuclide i. The models used in this code for the various modes of D_{iqp} have been described previously.[13-15]

The concentration, $C_{ipl}(t)$, is derived from the nuclide chain equations for radioactive decay. For a single environmental release, an explicit expression for the concentration at time t of the ith radionuclide in a pathway is denoted by

$$\begin{aligned} C_{ipl}(t) &= C^0_{ipl} \exp(-\lambda_1 T) \,, \; i = 1 \,, \\ &= C^0_{ipl} \exp(-\lambda_i T) + T \sum_{k=1}^{i-1} \left[C^0_{kpl} \right. \\ &\left. \times \sum_{j=k}^{i-1} Y_{ij}(T) \lambda_{j+1} f_j \prod_{\substack{l=k \\ l \neq j}}^{i-1} \left(\frac{\lambda_{l+1} f_l}{\lambda_l - \lambda_j} \right) \right] , \\ & \qquad\qquad i > 1 \,, \end{aligned} \tag{6.2}$$

where

$$T = t - t_0 \,,$$

$$\prod_{\substack{l=k \\ l \neq j}}^{i-1} \left(\frac{\lambda_{l+1} f_l}{\lambda_l - \lambda_j} \right) = 1 \text{ if } k = i - 1 \,,$$

$$Y_{ij}(T) = \left[\frac{\exp(-\lambda_j T) - \exp(-\lambda_i T)}{(\lambda_i - \lambda_j) T} \right] ,$$

λ_i = radiological decay constant (hr^{-1}) of the ith radionuclide,

f_i = fraction of nuclei of the ith radionuclide which decays to the i + 1st nuclide in the pathway,

t_0 = time (hr) of environmental release,

$C^0_{ipl} = g_{ipl} Y_i$,

g_{ipl} = location correction factor for the ith radionuclide, the pth mode of exposure, and the lth location,

Y_i = yield (μc) of the environmental release.

To determine the concentration of a radionuclide in a chain containing more than one pathway, contributions for the nuclide are summed for each pathway that is unique up to that radionuclide.

The concentration, ${}_M C_{ipl}(t)$, at time t of the ith radionuclide resulting from M environmental releases is obtained by evaluating Eq. (6.2), where

$$C^0_{ipl} = {}_{M-1} C_{ipl}(\tau_M) + g_{iplM} Y_{iM} \,, \tag{6.3}$$

[14] K. E. Cowser *et al., Dose Estimation Studies Related to Proposed Construction of an Atlantic-Pacific Interoceanic Canal with Nuclear Explosives: Phase I*, ORNL-4101 (March 1967).

[15] S. V. Kaye and P. S. Rohwer, "Estimating External Dose in Feasibility Evaluations of Plowshare Events," in *Plowshare Research and Development Quarterly Progress Report for April 1, 1968, to June 30, 1968*, ORNL-TM-2249 (1968).

and

τ_M = time (hr) of the Mth environmental release,

$T = t - \tau_M$,

$g_{iplM} = g_{ipl}$ for the Mth environmental release,

$Y_{iM} = Y_i$ for the Mth environmental release,

${}_{M-1}C_{ipl}(\tau_M)$ = the concentration at time τ_M of the ith radionuclide resulting from the first $M - 1$ environmental releases.

Obviously, only digital computer solution is practical for the external dose model, because the complexity of the calculations involves multiple detonations, decay chains with branching, several modes of exposure, and the large number of radionuclides usually considered. The EXREM II code has flexibility in handling problems of varying complexity. Up to 50 dose rates and/or total doses may be computed for each nuclide in each mode of exposure. This code prints out separately the doses and dose rates from the gamma photons and the beta particles of each radionuclide, as well as the total dose and total dose rate, obtained by summing the beta and gamma contributions (for some assessments, dose rate as well as total dose is important). The latest version of this code is described in more detail in a publication by Turner.[16]

Estimation of Radiation Dose Due to Internal Exposure

Constraints placed upon the feasibility study have limited the extent of the dose estimation effort. Ingestion of radionuclides in food and beverages is the only mode of exposure still being considered for internal dose estimation. Efforts to estimate the potential doses which could result due to inhalation of radionuclides are not being continued. The number of radionuclides under consideration for internal exposure has also been reduced. Battelle Memorial Institute (BMI) employed the specific activity concept to eliminate all but 31 radionuclides from more detailed study.[17] Those radionuclides being considered are: ^{3}H, ^{14}C, ^{32}P, ^{89}Sr, ^{90}Sr, ^{95}Zr, ^{95}Nb, ^{103}Ru, ^{106}Ru, ^{124}Sb, ^{125}Sb, ^{127m}Te, ^{129m}Te, ^{132}Te, ^{131}I, ^{141}Ce, ^{144}Ce, ^{143}Pr, ^{151}Sm, ^{155}Eu, ^{181}W, ^{185}W, ^{188}W, ^{195}Au, ^{196}Au, ^{203}Hg, ^{210}Pb, ^{238}Pu, ^{239}Pu, ^{240}Pu, and ^{241}Pu.

An idealized assessment of a population exposure requires radiation dose estimates for each individual in the population. A practical approach is to divide the population into groups, the groups being differentiated by factors influencing dose. Age is a convenient characteristic to use for this purpose, though other differentiating factors may also be operative. The dose models used in the INREM code contain five parameters which may vary as functions of the age of the individual exposed. Dose estimates for the population can be obtained once the age groups have been selected and the age-variant parameters evaluated.

The indigenous populations living along the proposed canal routes are divided into five age groups for internal dose purposes. The age groups chosen are: 0 to 1 year, 1 to 5 years, 5 to 10 years, 10 to 15 years, and over 15 years. These selections were made by ORNL and BMI jointly, on the basis of demographic and dietary data from the canal areas. The paucity of information describing human populations and their age-dependent characteristics leads us to rely heavily upon the tabulated values of "standard man,"[18] even for this coarse age breakdown, recognizing that the populations in the canal areas differ from that which is the basis for standard man.

The dose estimation models in the INREM code can utilize age-dependent information for the following parameters: organ mass (m), effective absorbed energy (ϵ), fraction of radionuclide intake reaching the organ of interest (f), effective half-time of the radionuclide in the organ of interest (T_e), and daily radionuclide intake (I). Evaluation of these age-dependent parameters for the populations indigenous to the canal areas is discussed in the following paragraphs.

The age dependence of organ mass is based on literature describing the Caucasian population from which standard man is drawn. The Caucasian population values for all age groups except the 0 to 1 year olds

[16] W. D. Turner, *The EXREM II Computer Code for Estimating External Doses to Populations from Construction of a Sea-Level Canal with Nuclear Explosives*, CTC-8, Computing Technology Center, Union Carbide Corporation, Nuclear Division, Oak Ridge, Tenn. (in press).

[17] S. G. Bloom and A. A. Levin, Battelle Memorial Institute, Columbus Laboratories, memorandum to K. E. Cowser, Nov. 8, 1969.

[18] *Report of Committee II on Permissible Dose for Internal Radiation*, ICRP Publication 2, Pergamon, London, 1959.

were reduced 20% to allow for the smaller physical size observed for those groups in Central American populations.[19] A notable exception is the thyroid, in which case no mass reduction was made because of the high incidence of goiter which has been noted.[19] Individuals appear to achieve adult physical maturity by the age of 15 years.

The effective absorbed energy values used for the different age groups are adapted from those given for standard man in ICRP Publication 2. Effective absorbed energy contributions of all radiation emissions except gamma and x-ray photons are assumed to be independent of the age of the individual exposed. Preliminary results from energy absorption studies being conducted in the Division suggest that absorbed fractions within organs for gamma and x-ray photons are approximately proportional to the one-third power of the mass of the organ. Therefore the effective absorbed energy contributions of those photons are adjusted in proportion to the one-third power of the ratio of the organ mass for a given age group to the mass of the respective organ for standard man. The data given for the gastrointestinal tract are appropriate for the segments identified in ICRP Publication 2 as critical for the respective radionuclides.

There is little information available on age-dependent variation of the fractional uptake of radionuclides by body organs. Adequate data are not available for specific age-group evaluations for most of the radionuclides remaining under consideration for internal exposure, and, in those cases, standard man values are applied to all age groups. Application of standard man values to all age groups is not conservative necessarily; however, it does not seem prudent to select other age-dependent values without supporting literature. In those cases where uptake fractions for standard man are large (approaching 1.0) the values may be applied to younger age groups with confidence. However, when uptake fractions for standard man are smaller, application of the values to younger age groups must be done with reservation, because there is no guarantee that the body processes controlling uptake are equally discriminating for all age groups, particularly for infants.

Effective half-time is another of the age-dependent parameters in the INREM code for which descriptive data are scarce. Age-dependent values are being used for two radionuclides (^{3}H and ^{131}I);[20,21] standard man values are applied to all age groups for the other radionuclides. Application of standard man values to the younger age groups is probably conservative in most, if not all, cases. At least a slight increase in effective half-time as the individual ages would be anticipated for most radionuclides, because the basal metabolic rate of man decreases with increasing age. Increases in effective half-times accompanying increases in the age of the individual have been observed for several radionuclides (^{3}H and ^{131}I are examples).

Daily radionuclide intake information (microcuries/day) is being supplied by BMI for each population (ethnic group) for which internal dose estimates are desired. The daily intake values for the five age groups are evaluated by BMI with multicompartmental models of the environment in the study areas of Panama and Colombia.

Application of INREM and EXREM to a Hypothetical Cratering Event

Since the feasibility study is in progress, estimates of potential dose to occupational employees and native populations are only partially completed. The application of EXREM and INREM in this study is best illustrated at this time by a simple example. The type of application postulated requires two cratering detonations, 30 days apart, which vent 1 curie of ^{137}Cs-^{137}Ba to the atmosphere. The levels of radioactivity chosen are completely arbitrary and are not related to any real Plowshare applications. However, such a hypothetical problem is useful (1) to identify the type of input data required to assess a real situation and (2) to illustrate the format of the results of the dose computations for a cratering event.

Figure 6.3 is a simple schematic diagram of the modes of exposure considered in the dose assessment. A more detailed outline of the input assumptions may be found elsewhere.[22] The cumulative total-body dose curves generated with the INREM and EXREM computer codes for all modes of exposure are shown in Fig. 6.4. Only estimates applicable to adults are plotted for internal dose. Submersion in the radioactive cloud is unique, because the exposure lasts only a relatively short time (1 hr in the case of the example problem).

---

[19] Interdepartmental Committee on Nutrition for National Defense, *Columbia Nutrition Survey*, U.S. Government Printing Office, Washington, D.C., December 1961.

[20] P. S. Rohwer and S. V. Kaye, *Age-Dependent Models for Estimating Internal Dose in Feasibility Evaluations of Plowshare Events*, ORNL-TM-2229 (April 1968).

[21] M. J. Cook and W. S. Snyder, *Health Phys. Div. Ann. Progr. Rept. July 31, 1965*, ORNL-3849, pp. 190–93.

[22] S. V. Kaye and P. S. Rohwer, "Methods of Estimating Population Exposures from Plowshare Applications," *Proceedings of Symposium on Public Health Aspects of Peaceful Uses of Nuclear Explosives, Las Vegas, Nevada, April 7–11, 1969* (in press).

ORNL-DWG 69-3272A

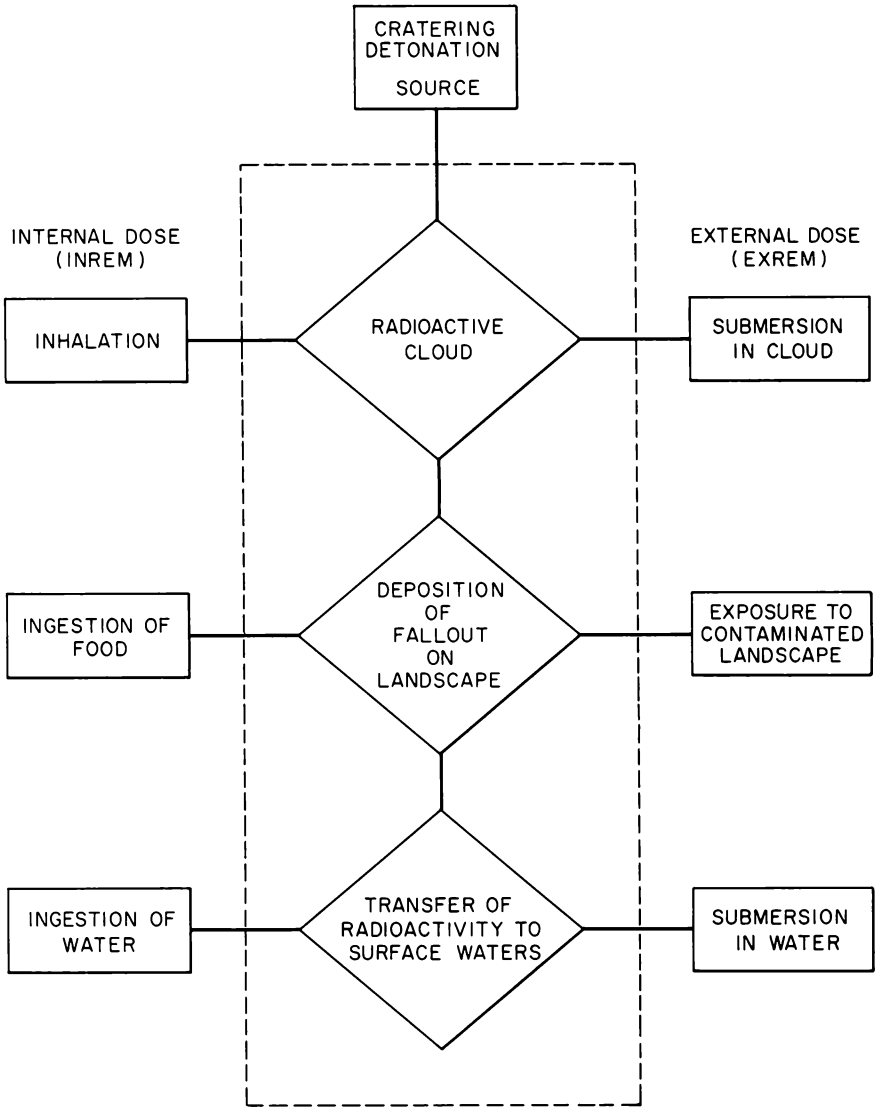

Fig. 6.3. Simplified Block Diagram of Hypothetical Problem.

Consequently, the radioactive half-life is used for this calculation, because the source term represents an average concentration. The expected cumulative dose due to submersion in contaminated water is so low (3.5×10^{-5} millirem) that it does not appear on this graph. On the other hand, Fig. 6.4 shows that drinking the same water results in a dose commitment of 2.2×10^{-3} millirem, almost 100 times as large. Obviously, increasing the use factor from 0.5 hr/day for submersion in water to 2 or 3 hr/day would not result in doses even approaching those from drinking the same water. The magnitude of the differences in doses here is independent of the concentration of radioactivity in water but is dependent on the type and energy of the radiation emitted. A similar comparison can be made of the relative hazard from submersion in a radioactive cloud and simultaneously breathing the same air. From Fig. 6.4 it can be seen that inhalation of radioactivity results in an internal dose almost four times the external dose from submersion in the radioactive cloud. It seems probable that the dose from inhalation will always be higher than the submersion dose, especially for radionuclides having a long biological half-time. The expected doses which are plotted for ingestion of contaminated food and exposure to a contaminated land surface are strictly functions of the arbitrary input

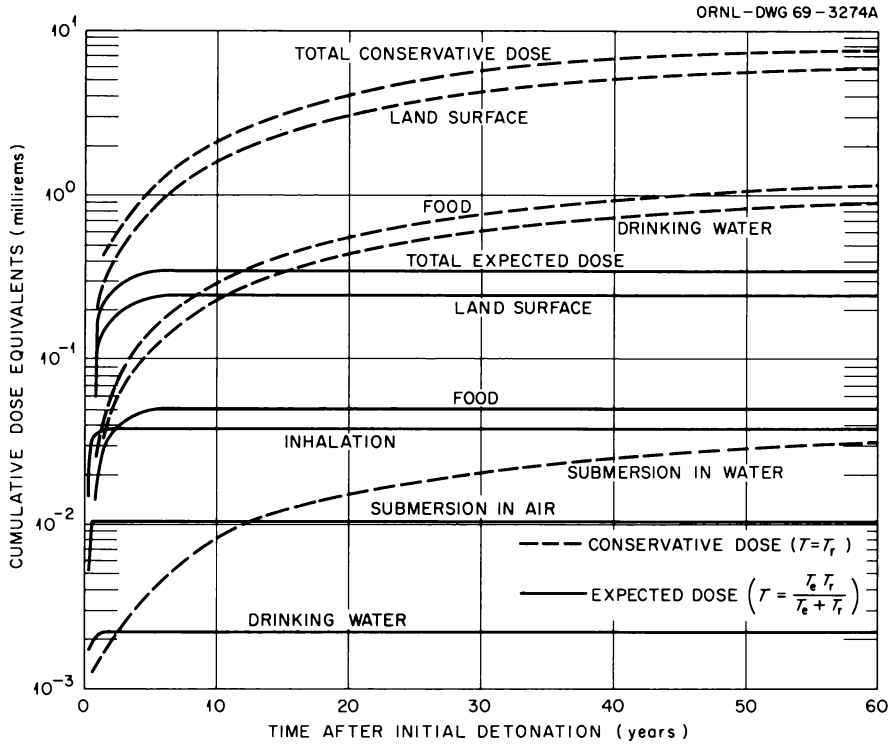

Fig. 6.4. Dose Accumulated in the Period 0–60 Years Following the First Detonation for the Hypothetical Problem.

parameters and are not intrinsically related as are the dose estimates for submersion in water vs drinking water and submersion in air vs inhalation. It is interesting nevertheless to compare the expected dose (effective half-time = 1 year) from the land surface to the conservative dose (effective half-time = radioactive half-life = 30 years). Essentially all the expected dose is accumulated by the fifth year after the initial detonation, whereas the conservative dose is considerably higher and still increasing after 60 years. (The asymptotic condition is not approached until approximately 150 years.) The magnitudes of the expected and conservative doses from the contaminated landscape are entirely dependent upon the arbitrary choice of effective half-times for this hypothetical case, but it raises a question that merits further consideration. For any dose integration period, what is the magnitude of conservatism of dose calculated with $T = T_r$ (conservative dose) vs a dose calculated with $T = T_e T_r/(T_e + T_r)$ (expected dose)? If $F(t)$ represents the magnitude of conservatism for a specified time period due to use of the radioactive half-life only, then

$$F(t) = \frac{D_{T_r}(t)}{D_T(t)}, \tag{6.4}$$

where $D_{T_r}(t)$ is cumulative external dose calculated with radioactivity loss due only to radioactive decay and $D_T(t)$ is cumulative external dose calculated with radioactivity losses due to environmental factors and radioactive decay. Substituting a simple integral expression (assuming no input from parent radionuclides) for $D_{T_r}(t)$ and $D_T(t)$, we get

$$F(t) = \frac{k\int_0^t e^{-\lambda_r t}\,dt}{k\int_0^t e^{-\lambda t}\,dt}, \tag{6.5}$$

where k represents all constant terms necessary to compute dose. Solution of Eq. (6.5) gives

$$F(t) = \frac{T_r(1 - e^{-\lambda_r t})}{T(1 - e^{-\lambda t})}, \tag{6.6}$$

the equation for estimating the magnitude of conservatism due to exclusion of the environmental half-time in dose computations. The utility of Eq. (6.6) is explicit in the family of curves plotted in Fig. 6.5 for ratios of T_r/T as large as 100/1. Figure 6.5 shows that after 5

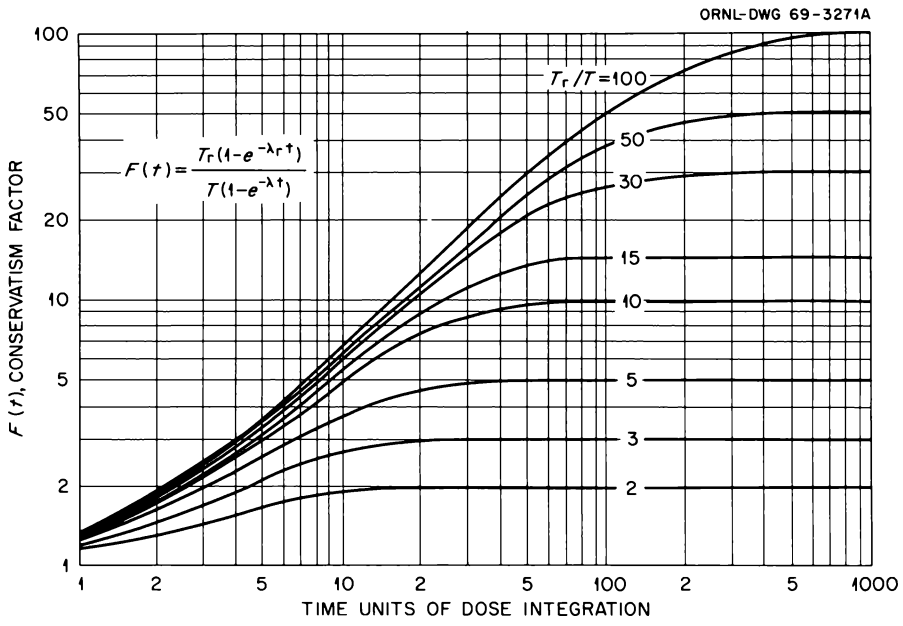

Fig. 6.5. Graph of Conservation Factors for External Dose Estimates Utilizing Radioactive Decay as the Only Process Which Reduces the Radiation Field.

years a cumulative dose calculated with $T = T_r = 30$ years would be conservative by a factor of about 3.3 when compared with a dose calculated with $T = 1$ year. The curves for land surface in Fig. 6.4 verify this conservatism factor. Figure 6.5 can be used for a wide variety of assessments; its use requires no additional calculations of dose, and the time scale can be designated in any convenient time units.

A large portion of the expected dose is accrued during the year following the first detonation, as shown in Fig. 6.6. Even with the greatly expanded time scale of Fig. 6.6 (compared with Fig. 6.4), the dose from submersion in contaminated air appears as a step function, because the total exposure time is only 1 hr in each case. This is in sharp contrast to the steadily increasing dose which results from inhalation during the same 1-hr exposure periods. The cumulative dose from inhalation ceases to increase after a few months, and this is entirely a function of the effective half-time in the body. If ^{137}Cs-^{137}Ba were taken up appreciably by bone, it might take years instead of months for the maximum dose to be attained. The remainder of the curves plotted in Fig. 6.6 reflect the influence of environmental half-times on external exposures or the combined effects of the environmental half-times and effective half-times in the body on internal exposures.

The accumulation of dose from internal exposures is shown in Fig. 6.7 as a function of time and age at the start of intake. With the exception of the first exposure year, the various age groups retain their relative positions throughout the exposure period. If we assume that all age groups have equal biological sensitivity to radiation exposure, those individuals 10.5 years of age at the time of the first detonation comprise the critical population group on the basis of this analysis. While it is of interest to identify the critical population group by age, it is important in population exposure situations to identify the age at a specific point in time. These identifications are necessary, because one age-dependent parameter (daily radionuclide intake) is dependent not only upon the age of the individual but also upon the radionuclide concentrations in the intake media. Radionuclide concentrations in the intake media may vary considerably as functions of time, particularly in transient exposure situations where the concentrations attain peak values for brief periods and then decline steadily.

We assume the genetic dose is equal to the estimated total-body dose due to internal exposure plus the estimated external dose. There is very little difference among these estimated genetic doses, primarily because external exposure constitutes approximately 75% of the total dose and because external dose, as currently estimated with the EXREM code, is not age dependent. The genetically significant dose to the population is estimated to be 0.386 millirem, slightly exceeding the highest individual genetic dose estimate.

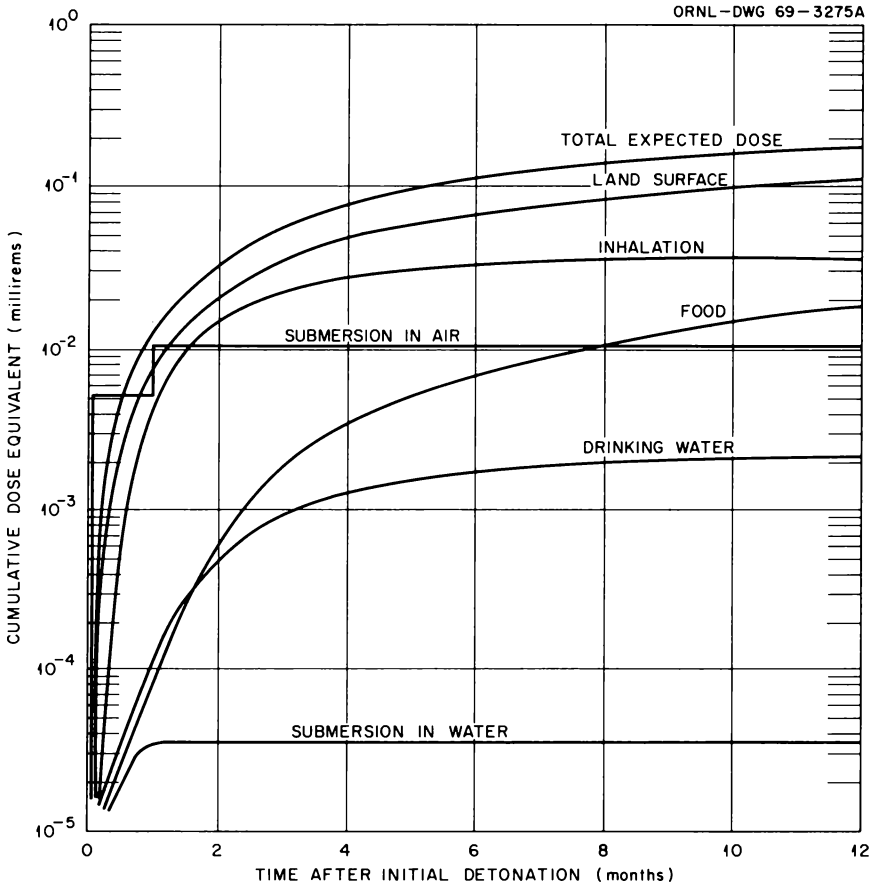

Fig. 6.6. Dose Accumulated in the First Year Following the First Detonation for the Hypothetical Problems.

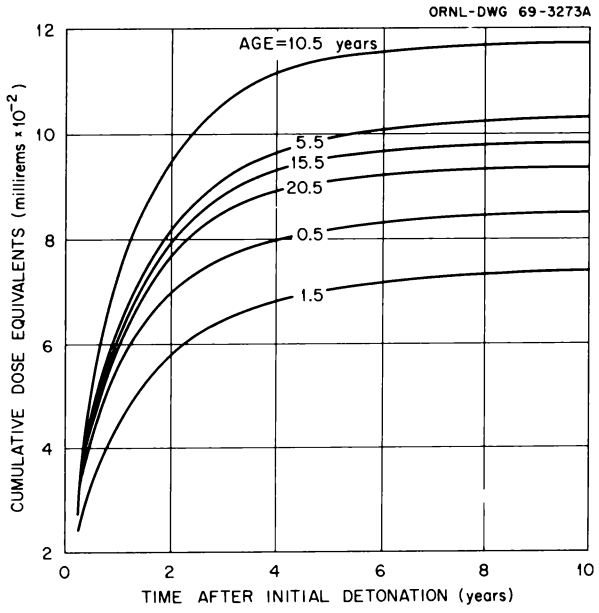

Fig. 6.7. Age-Dependent Variation in Internal Dose During the Period 0–10 Years Following the First Detonation for the Hypothetical Problem.

7. Related Cooperative Projects

COOPERATION OF OTHER AGENCIES IN ORNL STUDIES

The research and development program of the Radioactive Waste Disposal Section is of special interest to various public and private agencies. Several study projects provide an opportunity for others to participate, both to supplement the Laboratory's research effort and to gain information and experience of value to the other agency. The ways in which another agency may cooperate include: assignment of on-loan personnel as temporary additions to the ORNL staff, performance of specific work under cooperative agreements to augment ORNL programs, work authorized under ORNL subcontracts and performed by the contracting agency, and coordination of related work projects with ORNL projects for mutual benefit.

Waste Management Studies

Agencies participating in these programs during the past year have included the Carey Salt Company of Hutchinson, Kansas, and the New York State Atomic and Space Development Authority. Results of the cooperative program with the former agency are included in the section headed "Disposal in Natural Salt Formations" and of the latter agency in the section headed "Disposal by Hydraulic Fracturing."

VISITING INVESTIGATORS FROM ABROAD

During the year, one noncitizen guest participated as a temporary member of the research staff of the Section.

NUCLEAR SAFETY REVIEW

One member of the Section served on the staff of *Nuclear Safety* as assistant editor. During the year, several individuals in the Section contributed review articles which were published under the category "Consequences of Activity Release" or as an AEC Critical Review Series.

PARTICIPATION IN EDUCATIONAL PROGRAMS

Two members of the Section participated in cooperative programs with the University of Tennessee. A course was presented on the Health Physics Aspects of Radionuclides Released to the Environment. A similar series of lectures was presented at a Health Physics Training Course sponsored by ORAU. Another course was presented on Rock Mechanics in the Department of Civil Engineering.

LABORATORY PROJECTS

Several members of the Section served as part-time staff members of the Nuclear Safety Information Center, the Civil Defense Research Project, and the agroindustrial complex study.

Part II. Radiation Ecology

S. I. Auerbach

8. Responses of Animal Populations to Ionizing Radiation

S. I. Auerbach[1]
E. A. Bardill[2]
B. G. Blaylock
Peggy G. Bruno[3]
J. L. Cooley[4]
G. E. Cosgrove[5]
Gladys J. Dodson[1]
P. B. Dunaway[1]
N. A. Griffith[1]
A. M. Jenkins[2]
R. G. Jordan[6]
S. V. Kaye[1]
R. I. Van Hook[4]
J. T. Kitchings III
P. G. Koehler[3]
H. F. Landreth[7]
Margaret F. Miller
M. J. Mitchell[3]
E. Oertel[8]
D. L. Willis[10]
R. V. O'Neill
D. E. Reichle[1]
A. F. Shinn[1]
J. D. Story
C. E. Styron[9]
L. E. Tucker

Primary objectives of our growing and diverse research on radiation effects in animals are: (1) comparative measurements and interpretations of consequences of acute and chronic irradiation in wild species of animals and (2) evolution of models for prediction of radiation effects in animal compartments of ecological systems. Implicit in these objectives is the requirement that interactions of biotic and abiotic environmental factors be delineated and quantified. Separation of effects of specific environmental factors in ecosystems is difficult, and current studies are employing laboratory research to complement field experiments. Systems analyses (compartment models) of population responses to radiation stress involve extrapolations of laboratory-derived theories to natural habitats and subsequent comparisons of actual field data for tests of long-term predictive capability. It is already clear that laboratory results, although useful for single-factor analyses and initial design of field experiments, are insufficient for realistic extrapolations and predictions of radiation effects in actual environments.

Current studies include measurement of genetic, cytological, individual, and populational effects in vertebrates and invertebrates receiving acute and/or chronic irradiation. Parameters being tested include tissue damage, changes in radionuclide incorporation rates, radiation profiles, survivorship, fecundity, chromosomal aberrations, metabolism, food consumption, energy flow, competition, temperature, and RBE. Dosimetry for such studies is critical, of course, and refined techniques must be developed for measuring acute and chronic gamma and beta radiation in tissues and environmental sites of interest.

[1] Dual capacity.
[2] Summer employee.
[3] ORAU-NSF Undergraduate Participant.
[4] ORAU Graduate Fellow.
[5] Biology Division.
[6] ORAU Undergraduate Participant.
[7] ORAU Research Participant.
[8] Consultant.
[9] On loan from U.S. Army.
[10] Sabbatical leave from Oregon State University.

Construction of a field facility and contamination of 100-m^2 enclosures with ^{137}Cs-tagged fallout simulant (88 to 177 μ, 22 mc/m^2), funded by the Office of Civil Defense (OCD), permitted initiation of field studies on dosimetry, movement of fallout particles, ^{137}Cs incorporation into the biota, environmental factors that affect cesium movement, and radiation effects in the animals within the enclosures.[11] Application of the fallout simulant was completed in August 1968. Effects of physical and chemical factors on ^{137}Cs movement and incorporation into plants are discussed elsewhere in this report. The dominant vegetation in these enclosures is a fescue, *Festuca arundinacea.* Biological and ecological responses of invertebrates and rodents living in the pens and exposed to acute and chronic radiation from external and internal sources are being examined seasonally in replicated experiments under natural or seminatural conditions. The honeybee is one of the most valuable agricultural animals because of crop pollination, and another OCD-funded facility is permitting the first studies on the effects of radiation on colonies under field conditions. This research also is the first study of radiation effects on intact populations of a colonial insect.

[11] R. C. Dahlman *et al.*, "Behavior of ^{137}Cs Tagged Particles in a Fescue Meadow," FAO-IAEA Conference, 1969.

OPEN-FIELD DOSIMETRY

S. I. Auerbach S. V. Kaye
J. D. Story

The establishment of pens tagged with ^{137}Cs simulated fallout in the OCD experimental area (ecology area 0800) provides an opportunity to obtain data on the effects of biophysical factors on open-field dose rates. Published empirical data have been lacking from actual situations in which dose rate has been correlated with precipitation, microtopography, vegetation, soil percolation, and related microclimatic factors.

In order to document changes in the radiation fields of the fallout plots, an apparatus (Fig. 8.1) was designed and fabricated prior to the tagging. This

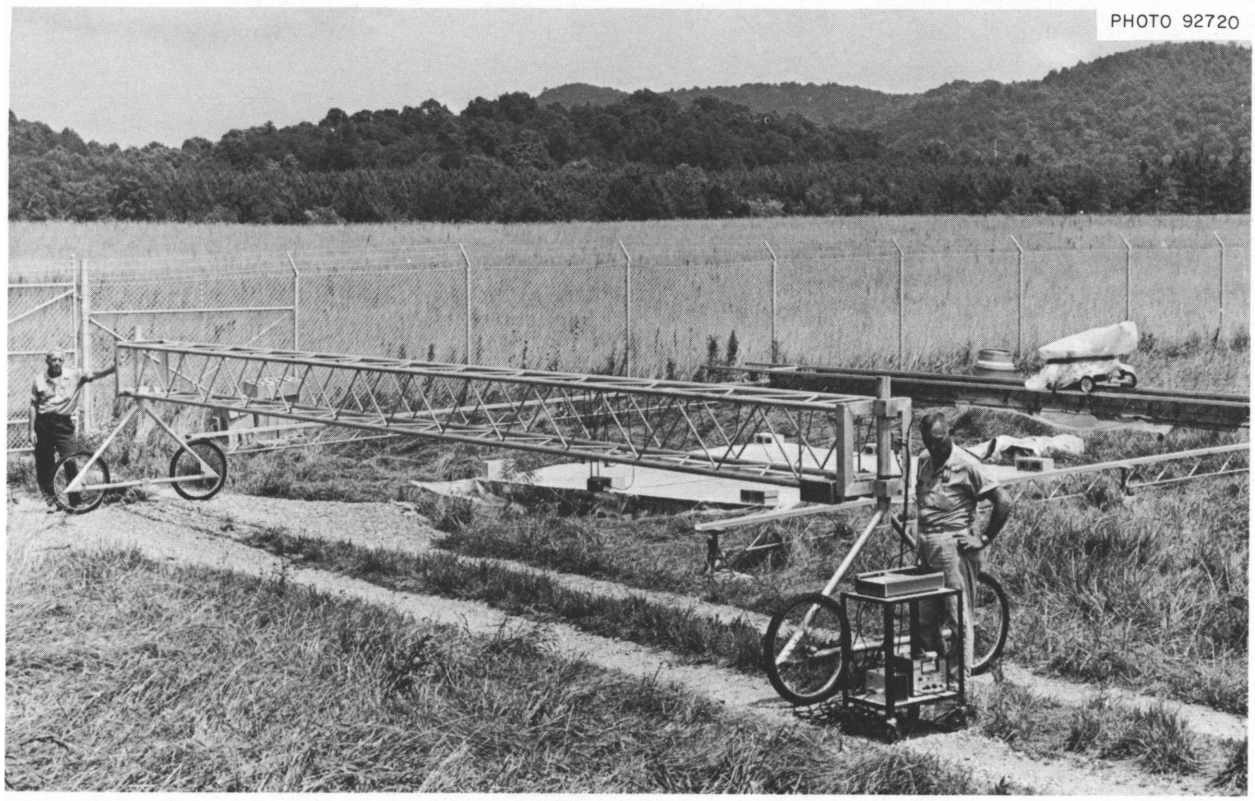

Fig. 8.1. View of OCD Plot Scanning Device. Scanner detector consists of a G-M tube mounted in a collimator so that signals are received from an area 1 m^2 at 1 m height. The G-M tube traverses the pen at a rate of 1 cm/sec, sending its signals to a modified rate meter and X-Y plotter.

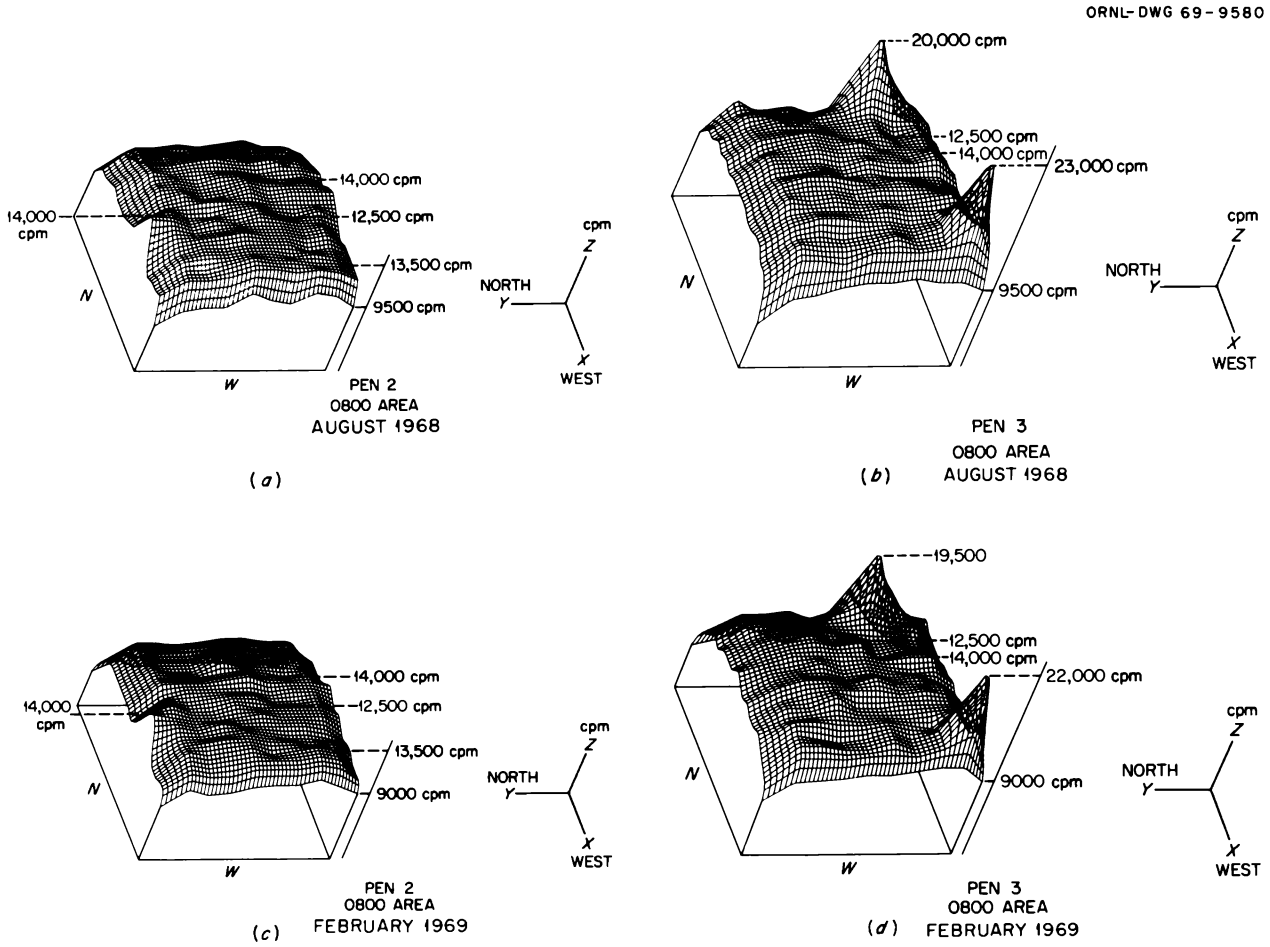

Fig. 8.2. Scans of Two of the Four Pens in the OCD Experimental Area (Ecology Area 0800) Contaminated with ~2 curies Each of ^{137}Cs-Tagged Fallout Simulant in August 1968. Pen 2 (*a,c*) shows the plane dose field typical of three of the four pens. Pen 3 (*b,d*) had two stoppages of the simulant spreader during tagging, resulting in the additional simulant represented by the two peaks shown. Scans made in August 1968 are shown in *a* and *b;* scans of the same pens made during February 1969 are shown in *c* and *d*.

scanning device consists of a wheel-mounted rigid aluminum traversing rig (10 m in length), which spans the pens and serves as the track for a motor-driven collimated G-M tube which traverses the pens at a rate of 1 cm/sec. The collimator was designed so the detector "sees" 1 m^2 at 1 m height, providing thereby a 1-m-wide scan across the pen. Signals from the G-M detector are fed into a modified rate meter, which in turn transmits the signals to an *X-Y* plotter. The plotter graphs the signal as CPM (counts per minute). The apparatus was calibrated to the intensity of the dose field in the pens by using a standard consisting of a 128-ft^2 plywood platform upon which ^{137}Cs-tagged simulant was laid down at a mass loading similar to that used in the pens. The efficiency of the counter, however, has not been determined. Points are taken from the *X-Y* graphs (ten graphs per pen) to generate one *X-Y-Z* (three-dimensional) plot for each pen, using a digital computer program and a Calcomp plotter (Fig. 8.2).

In August 1968, following application of fallout simulant, the four pens were scanned in east to west and north to south directions. Figures 8.2*a* and *b* are scans of two of the four pens in August. The peaks shown in Fig. 8.2*b* resulted from accidental stoppages of the spreader hopper during the tagging operation. Power was interrupted while the hopper was open, causing an extra amount of fallout simulant to be deposited at two points in pen 3. Scans were made on different days in each directional plane, and reproducibility was found to be excellent. Aside from these two peaks, all pens showed that the simulant had been applied evenly, with the radiation intensity varying from 1.25×10^4 to 1.55×10^4 counts/min, neglecting "edge effects." No significant differences were found

between the two directions of scanning; consequently, subsequent scans were made in one directional plane only.

The plots were scanned again six months later (Figs. 8.2*c* and *d*), and no significant changes in the radiation field were noted. A third set of scans will be made one year after tagging (August 1969). The results of all scans will then be subjected to statistical tests and the results evaluated in relation to plot runoff data and precipitation during the first year.

APPLICATION OF LiF CRYSTALS IN ECOLOGICAL RADIATION DOSIMETRY

C. E. Styron Gladys J. Dodson

Radiation levels in contaminated areas are usually determined with ionization chambers, scintillation counters, G-M counters, or silver-activated metaphosphate glass dosimeters. Serious difficulties must be overcome when any of these methods are used in long-term field situations where the radiation levels are low. Expense and inability of electronic equipment to withstand harsh environmental conditions are obvious, and the metal shielding of most sensors obviates their use in measuring beta radiation. Glass rod dosimeters have overcome many of these disadvantages for dosimetry in the field, but they are fragile and light-sensitive, and their response is for all practical purposes limited to a minimum absorbed dose of 1 rad, and for beta radiation it is energy dependent.

At the 0800 ecology research area, simulated radioactive fallout (^{137}Cs on silica sand grains) has been applied to an old field for a study of the effects of the simulant on vegetation, insects, and mammals.[12,13] Measurements of the beta as well as gamma dose rates are needed. Beta radiation may be a primary factor in the survival of organisms ingesting, carrying externally, or living in contact with the fallout. The surface beta dose rate is considered to be 40 times the gamma dose rate,[14] and this is delivered in close proximity to sensitive tissues such as plant meristems and developing insect eggs in the soil. Several mathematical models are available for predicting beta and gamma radiation dose rates from the quantity of fallout present, but these models are rendered inadequate for ecological situations by restrictions on geometry, for example, surface conditions, presence of grass, and movement of fallout. Thermoluminescent dosimeter materials were selected for this study since they are mechanically rugged, available in several geometries and small sizes, and insensitive to light. Cleaved crystals (1 mm^3) and extruded crystals (0.5 X 6.0 mm) of LiF (Harshaw Chemical Company TLD-100) were used, because this material is essentially energy independent for beta and gamma radiation and it can measure doses as low as 5 millirads.

Beta and gamma point dosimetry was begun with the first application; 0.5- by 6.0-mm extruded crystals of LiF were suspended at several heights above the ground. Some dosimeters were unshielded, while others were contained within nylon capsules which absorbed more than 95% of the ^{137}Cs beta radiation. The gamma and

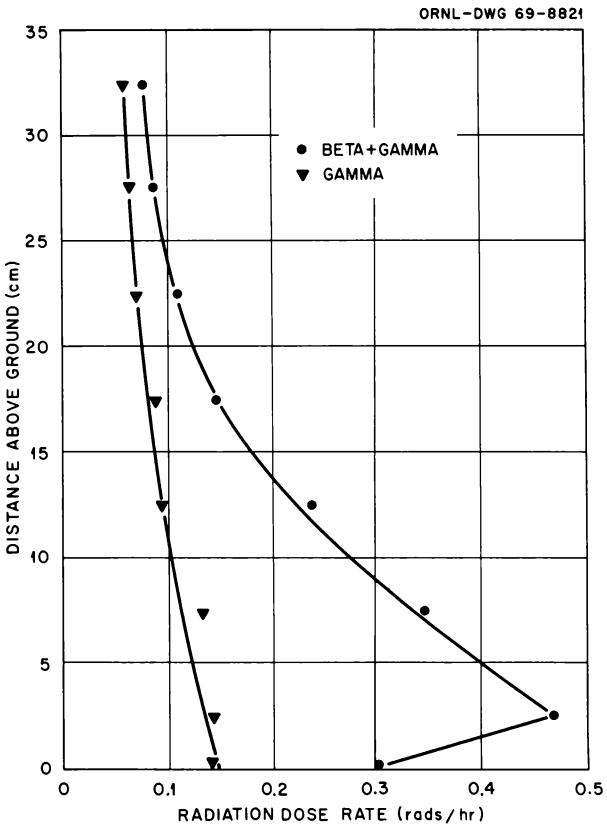

Fig. 8.3. Distance Above Ground Plotted Against Gamma and Beta-Gamma Radiation Dose Rates in the Middle of Site 3 at the 0800 Ecology Research Area During the First Week After Application of Simulated Radioactive Fallout. The distance between the two dose rate lines represents the beta radiation dose rate.

[12] R. C. Dahlman and S. I. Auerbach, *Preliminary Estimation of Erosion and Radiocesium Redistribution in a Fescue Meadow*, ORNL-TM-2343 (1968).

[13] S. I. Auerbach, *Progress Report in Postattack Ecology*, ORNL-TM- 2466 (1969).

[14] S. L. Brown, *Disintegration Rate Multipliers in Beta-Emitter Dose Calculations*, Stanford Research Institute Project MU-5116, 1965.

gamma-plus-beta radiation dose rates integrated over the first week in the middle of site 3 (Fig. 8.3) can be used to estimate the beta radiation dose rate by subtraction. As a consequence of the short range of ^{137}Cs beta particles in air and vegetation, the beta dose rates can be used to estimate the vertical distribution of fallout for the point at which the series of dosimeters was suspended. Beta radiation dose rates during the first week following application indicated that 45 to 50% of the simulant was present in the litter layer and 25 to 30% was on the ground surface. Eleven weeks after the first application and eight weeks after the second dosing of simulant (Fig. 8.4), 50 to 55% of the beta dose appeared on the ground surface, 25 to 30% was delivered in the litter layer, and less than 10% could be accounted for at the height of leaf surfaces (20 to 30 cm).

Microdosimeters have also been placed on and in grass stems and on insects. The attached dosimeters integrate the dose received by an insect as it moves through various dose rate levels and thereby eliminate the disadvantages of estimating total dose from purely physical measurements. Results of a typical emplacement of extruded crystals during the eleventh week after the first application of simulated radioactive fallout (Fig. 8.3) show that most of the intercepted simulant had been washed from the leaf surfaces but that some remained trapped in the leaf axils. The beta-gamma dose rates in the axils ranged from 931 to 1145 millirads/hr, as compared with air dose rates at the same height above ground of 200 to 250 millirads/hr. Grasshoppers (*Melanoplus*) and crickets (*Acheta domesticus*) with cleaved crystals attached to their thorax and abdomen were released in pen 3 during

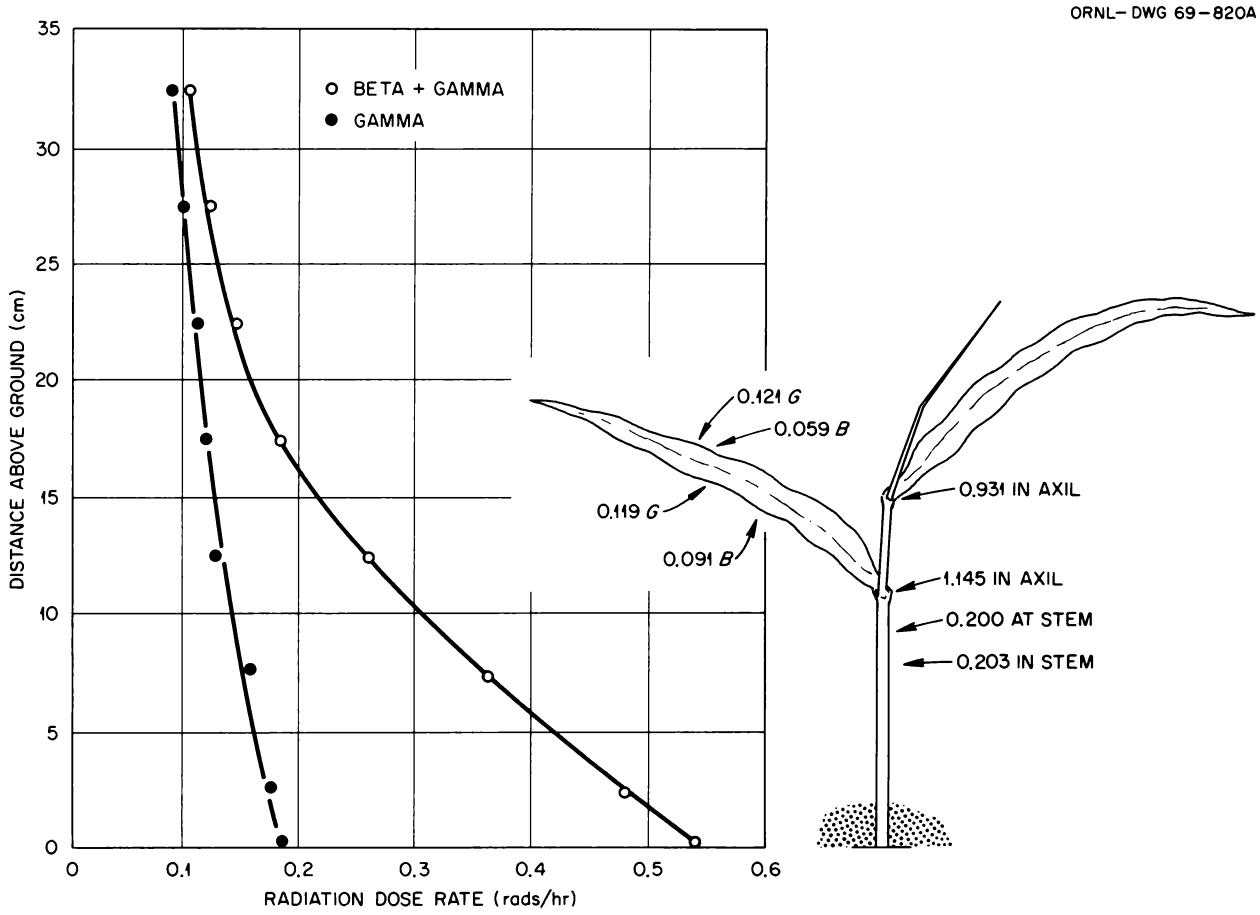

Fig. 8.4. Distance Above Ground Plotted Against Gamma and Beta-Gamma Radiation Dose Rates in the Middle of Site 3 at the 0800 Ecology Research Area During the Eleventh Week After the First Application and the Eighth Week After the Second Application of Simulation Radioactive Fallout. The distance between the two dose rate lines represents the beta radiation dose rate. Beta, gamma, and the combined dose rates observed for a fescue plant are also presented.

Table 8.1. Dose Rate (rads/hr) to Grasshoppers and Crickets from Simulated Radioactive Fallout in Pen 3 of the 0800 Ecological Research Area

Organism	Thorax	Abdomen
Acheta domesticus, living	0.222	0.307
Melanoplus sp., living	0.090	0.095
Melanoplus sp., phantom	0.112	0.203

the same week. Differences between dose rates to the thorax and abdomen of the insects (Table 8.1) were not significant, but there was a significant difference ($P \leqslant 0.01$) between exposure rates of the grasshoppers and crickets. These two insects are closely related taxonomically but occupy different habitats. The crickets dwell primarily on and in litter, where they are exposed to more beta radiation, and the grasshoppers dwell higher on the blades of grass. Thus any attempt to predict ecosystem responses to radioactive fallout based on differential radiation sensitivities must also deal with the problem of differential radiation exposures.

EFFECT OF CHRONIC BETA RADIATION ON *FOLSOMIA* SP. (COLLEMBOLA)

C. E. Styron Gladys J. Dodson

Information on the responses of insect populations to a nuclear attack and to postattack environments is of interest in planning postattack agricultural procedures. Many agricultural situations may be upset by the effects of radioactive fallout on insect populations.[15] In particular, fallout beta radiation may be a hazard to small insects and insects that pass developmental stages in soil and litter. Collembola are among the most numerous microarthropods in the soil fauna, and they are important in soil formation. The objective of this study is to assess the effects of chronic beta radiation on a Collembola population.

Albite sand grains (44 to 88 μ in diameter) coated with ^{90}Sr + ^{90}Y were suspended in glycerol and painted onto charcoal–calcium sulfate substrates. Clean sand grains in glycerol were used to prepare control culture jars. Dose rates of 3.3 to 341.7 rads/hr were determined using 0.5- by 6.0-mm LiF dosimeters (Harshaw Chemical TLD-100 extruded crystals). Groups of 8 to 12 adult *Folsomia* sp. were placed in 10 control and in 19 experimental culture jars. The

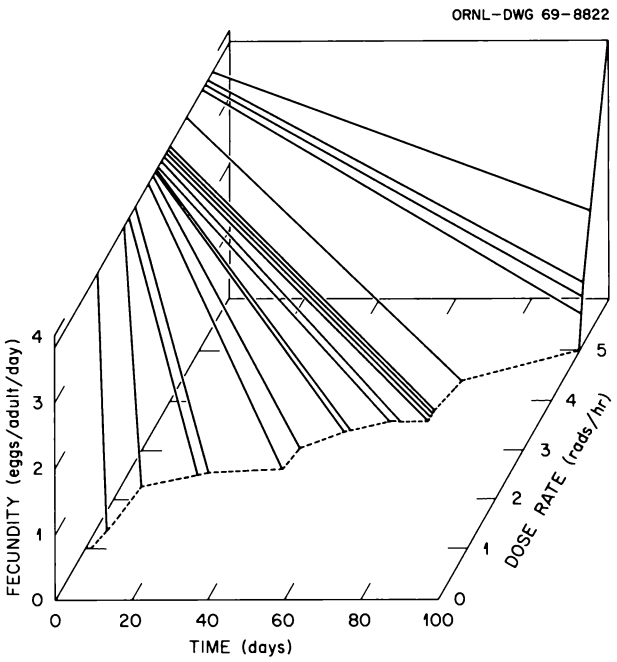

Fig. 8.5. Isometric Projection of Fecundity in Eggs per Adult per Day on Time in Days and $^{90}Sr + ^{90}Y$ Beta Radiation Dose Rate for *Folsomia* sp. The fecundity rates for each dose rate are presented as a regression on time, since the fecundity of each population changed as total doses of radiation accumulated.

cultures were maintained at 20°C, and the substrates were kept saturated with water. The Collembola were fed brewer's yeast, and the numbers of adults, juveniles, and eggs were scored biweekly.

Survival and reproductive ability of the Collembola were reduced by all dose rates. The $LD_{50\text{-}30}$ for adults was estimated by least-squares regression to be 174.5 rads/hr; the $LD_{50\text{-}60}$, 38.1 rads/hr. The LD_{50} for control populations was estimated at 183.7 days. The effects of chronic beta radiation on fecundity rates (Fig. 8.5) could not be anticipated from studies of the effects of acute irradiation on this parameter.[16] Following an acute dose of ionizing radiation, the fecundity rate of each population was reduced to a new rate. Under chronic irradiation conditions, however, all fecundity rates were initially at control levels and were reduced through time as total doses were accumulated. The change in fecundity rates under chronic irradiation conditions must therefore be represented as the slope of a regression line rather than as a point. Fecundity rates approached zero very rapidly at dose rates greater than

[15] P. W. Wong, *Initial Study of Effects of Fallout Radiation on Simple Selected Ecosystems*, NRDL report TR-68-11 (1967).

[16] S. I. Auerbach, *Progress Report in Postattack Ecology*, pp. 40–46, ORNL-TM-2466 (1969).

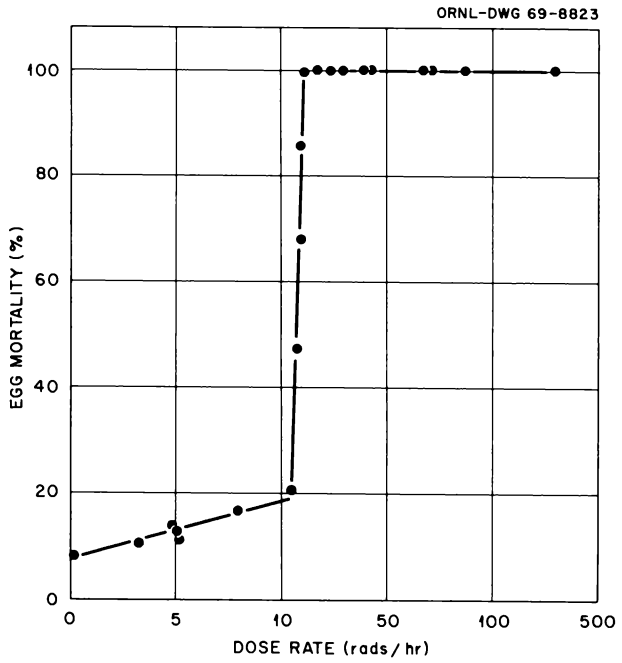

Fig. 8.6. Egg Mortality Plotted Against ^{90}Sr + ^{90}Y Beta Radiation Dose Rate for *Folsomia* sp. The point at 0 rads/hr represents the mean of 10 control populations.

5 rads/hr. Egg mortality (Fig. 8.6) was greatly increased by radiation dose rates above 13.5 rads/hr, and no eggs hatched at dose rates above 17.4 rads/hr. At 14.5 rads/hr, 38% of the eggs grew into adults, but they were sterile.

The data clearly demonstrate that the sensitivity of a population of *Folsomia* to beta radiation is determined primarily by sensitivity of fertility rates (number of eggs surviving) rather than sensitivity of adults. The dose rates estimated to give an $LD_{50\text{-}30}$ or $LD_{50\text{-}60}$ for adults are more than twice as high as the dose rates required to reduce fertility rates to zero. The sensitivity of fertility rates to acute irradiation has been demonstrated for another collembolan (*Sinella*) population.[16] For the acute irradiation regime, however, substantial recovery occurred several weeks following irradiation. If a natural population of these insects were subjected to acute irradiation during a seasonal cycle of low reproductive activity, recovery could occur before the population entered its period of maximum reproductive activity. The ecological significance of the sensitivity of fertility rates could thus be masked by seasonal cycle in reproduction. This situation would not be expected for populations under chronic irradiation conditions, since recovery cannot occur.

SIMULATED FALLOUT RADIATION EFFECTS ON EARTHWORM POPULATIONS

M. J. Mitchell D. E. Reichle C. E. Styron

Earthworms, a major element of the soil fauna, are important in maintaining many natural soil characteristics, for example, aeration, water permeability, and nutrient turnover. Close physical contact of earthworms with soil would expose these animals to some of the highest radiation doses from radioactive fallout. Experiments with ^{60}Co gamma and ^{90}Sr-^{90}Y beta radiosensitivity of adult *Lumbricus terrestris* (the common night crawler) were designed to enable prediction of the effects of simulated fallout radiation on earthworm populations in a grassland ecosystem. Sites of radiation damage for both beta and gamma radiation were the skin epithelium (blistering) and for gamma radiation the intestinal epithelium (necrosis). Average beta ranges of ^{90}Sr and ^{90}Y in soft tissues are 0.33 and 2.1 mm respectively. Since beta irradiations were administered from the ventral surface with a plaque source, many earthworms showed a gradation in histological damage along the dorsoventral axis (Fig. 8.7). Radiation damage to the ventral epithelium (0.5 to 0.7 mm depth) is apparent; dorsal epithelium (1.5 to 1.8 mm depth) does not show necrosis.

The $LD_{50\text{-}30}$ for gamma was 67.8 kilorads; no significant increase in mortality occurred for beta irradiations up to 102.4 kilorads, probably because of muscle shielding of the externally delivered beta radiation. In a natural situation with fallout particles mixed in soil, both intestinal and skin epithelial tissues would receive gamma irradiation and would be shielded substantially from the beta radiation of a surface deposit of fallout. If mixing of fallout particles with soil occurred, beta radiation would be important only for direct contact (due to soil shielding); the gamma component would contribute the major part of total body dose. For example, using a shielding-design dosimetry program[17] 2.4 curies of ^{137}Cs evenly distributed to a depth of 10 cm would give a maximum annual dose of 700 rads – 80% contributed by gamma radiation. The high radioresistance of earthworms to both gamma and beta radiation suggests minimal population mortality due to the radiation from anticipated weapon yields (Table 8.2). Although mortality

[17] E. D. Arnold and B. F. Maskewitz, *SDC, a Shielding-Design Calculation Code for Fuel-Handling Facilities,* ORNL-3041 (1966).

Table 8.2. Approximate Infinity Beta and Gamma Doses at Ground Surface Contact Resulting from a 10-megaton Weapon Burst with 50% Fission Yield

Data recalculated from original source[a]

Exposure rate contour, rads/hr at 1 hr	1	10	50	100	200	500	1000	2000
Area within contour, sq miles	4.6 X4[b]	2.5 X 4	1.4 X 4	1.0 X 4	6.7 X 3	3.8 X 3	2.0 X 3	7.3 X 2
Infinity gamma dose,[c] rads	4.6	4.6 X 1	2.3 X 2	4.6 X 2	9.3 X 2	2.3 X 3	4.6 X 3	9.3 X 3
Infinity beta dose at contact, rads	1.4 X 2	1.6 X 3	8.9 X 3	1.9 X 4	4.1 X 4	1.1 X 5	2.6 X 5	6.0 X 5

[a] P. W. Wong, *Initial Study of Effects of Fallout Radiation on Simple Selected Ecosystems*, USNRDL-TR-68-11 (1967).

[b] x 4 = x 10^4.

[c] Tissue dose.

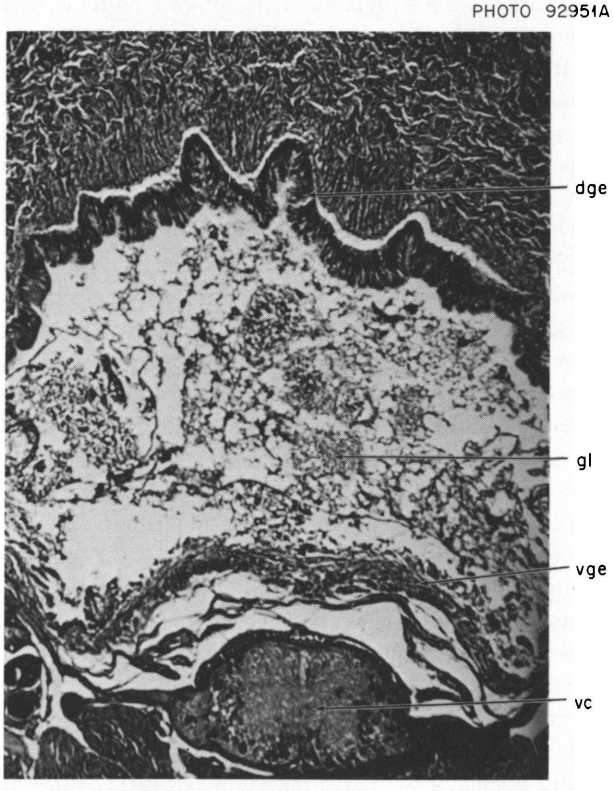

Fig. 8.7. Tissue Necrosis 11 Days Postirradiation in the Earthworm *Lumbricus terrestris* Resulting from Beta Irradiation (51.2 kilorads ventral surface dose). vc is ventral nerve cord; vge, ventral gut epithelium; gl, gut lumen; dge, dorsal gut epithelium. Note necrotic condition of ventral gut epithelium, but normal condition of dorsal epithelium. Photograph is a transverse section (130 X) in the region of the posterior pharynx. Reduced 62%.

will not be expected for the adult earthworm population at these fallout doses, this does not preclude the possibility of effects on other population parameters such as fecundity, fertility, or other genetic responses.

MAMMAL STUDIES IN FIELD ENCLOSURES

P. B. Dunaway J. D. Story
J. T. Kitchings III L. E. Tucker

The first studies with cotton rats (*Sigmodon hispidus*) in ^{137}Cs-contaminated enclosures were measurements of ^{137}Cs uptake into tissues, ingestion of the fallout simulant, and in-vivo dosimetry. Animals were placed in the enclosures on December 2, 1968, three months after the simulant was applied. Whole-body uptake reached a maximum level (3.66 μc) three weeks after the animals were placed in the pens and then began to decrease slightly. The initial increase in whole-body count is explicable by the finding that about three weeks were required to reach near-equilibrium levels in tissues. The decrease was caused by decreased ingestion of the fallout simulant as the particles shifted and washed from the vegetation toward the ground. Whole-body radioactivity due to tagged particles in the gastrointestinal tract was 32.5% on day 1 after introduction of the animals but decreased somewhat linearly to 5.9% by day 28. Gamma-radiation dose received by the rats as they ranged over the area was 3.38 ± 0.15 rads/day.

The first experiment in a series of studies designed to quantify seasonal changes in blood, whole-body uptake

Table 8.3. ^{137}Cs Whole-Body Burdens, Tissue Concentrations, Contributions of Fallout Simulant to Body Burdens, and Radiation Doses to Cotton Rats After 30 and 60 Days in Contaminated Enclosures

	Enclosure[a]	Sex	Time After Introduction into Enclosures					
			30 Days			60 Days		
			Weight (g)	Body Burden (μc)	Concentration (μc/g)	Weight (g)	Body Burden (μc)	Concentration (μc/g)
Tissue								
Whole body	1	F	96.9 (4)[b]	0.001		117.4 (4)	0.003	
	2	F	108.4 (6)	3.592	0.0331	108.7 (4)	1.748	0.0161
	5	M	116.1 (6)	2.707	0.0233	132.8 (5)	1.668	0.0126
	8	M	115.4 (7)	0.001		133.7 (3)	0.003	
Liver	2[c]	F	4.9043 (2)	0.1309	0.0267	4.3419 (2)	0.0448	0.0103
	5	M	5.0597 (2)	0.0687	0.0136	4.8233 (2)	0.0364	0.0075
Spleen	2	F	0.0210 (2)	0.0047	0.2238	0.0167 (2)	0.0022	0.1317
	5	M	0.0246 (2)	0.0023	0.0935	0.0126 (2)	0.0022	0.1746
Muscle (gastrocnemius)	2	F	0.6607 (2)	0.0674	0.0979	0.8686 (2)	0.0287	0.0330
	5	M	0.5757 (2)	0.0320	0.0556	1.0268 (2)	0.0292	0.0284
Other[d]	2	F	86.90 (2)	3.3531	0.0386	92.50 (2)	1.4401	0.0156
	5	M	79.34 (2)	2.2070	0.0278	105.67 (2)	1.660	0.0157
			Contribution of Simulant in GI Tract to Whole-Body Burden (%)					
	2	F		5.00			2.66	
	5	M		5.12			2.11	
			Gamma Radiation Dose					
Daily dose, rads	2 and 5			3.26 ± 0.11			2.65 ± 0.05	
Total dose, rads	2 and 5			97.8			117.3	

[a]Enclosures 1 and 8 are control areas; 2 and 5 are simulant-contaminated areas.

[b]Numbers in parentheses are sample size.

[c]Tissue samples were not taken for control animals due to low ^{137}Cs content.

[d]Includes pelt, heart, kidneys, stomach, large intestine, small intestine, cecum, and residual carcass.

and tissue incorporation of ^{137}Cs, and radiation doses in cotton rats living in ^{137}Cs-contaminated enclosures was completed during the spring period (March 3 to May 2, 1969). Both male and female cotton rats were used in this study to determine if sexual as well as seasonal differences existed in ^{137}Cs uptake, tissue incorporation of ^{137}Cs, and hematological effects caused by chronic low-level gamma radiation. Eight males were placed in a control enclosure, and the same number were placed in an enclosure containing the fallout simulant. The same design was used with the females in two other enclosures. Only the effects of chronic radiation were studied, since a preliminary experiment utilizing a combination of acute (600 rads) and chronic radiation revealed that, under the field environmental conditions, several rats receiving 600 rads died, although higher doses were required to kill *Sigmodon* under laboratory conditions. Thus more understanding of the interactions of chronic radiation and environmental stress is necessary before acute radiation can be introduced as a variable.

Whole-body content, tissue concentrations, and gamma irradiation doses during the spring period are shown in Table 8.3. The average whole-body burden of rats in both enclosures after 30 days (3.15 μc) is close to the 3.66-μc level obtained during the preliminary study in December 1968, and the values for fallout simulant in the GI tract during the 30-day spring period are also not much less than for the 30-day period in December (5.9%). A slow decrease in body burdens is to be expected during the first months because the fallout simulant is moving toward the ground and less simulant is ingested as the rats feed on the vegetation. The relatively high ^{137}Cs levels at 30 days reflect the high ^{137}Cs content of the vegetation left from the preceding season as well as the simulant available above the litter layer. New vegetative growth with less ^{137}Cs content had appeared by day 60, and the lower levels of ^{137}Cs in the rats presumably reflects this decrease, as well as the movement of the simulant toward the soil.

The significantly higher ($P > 0.025$) body burden in the females (Table 8.3) was probably due to greater food consumption by females during this period, since the percentage of whole-body activity contributed by the presence of the simulant in the GI tract was essentially the same in both sexes. Spleen and muscle had the highest ^{137}Cs concentrations, but on an absolute basis the liver contained more than any other organ. The decrease in gamma radiation dose from day 30 to day 60 may be due to gradual changes in radiation-field geometry as the simulant descends. For example, dose rates in October 1968 and February 1969 were 3.45 and 3.38 rads/day respectively.

The hematological values for days 30 and 60 do not indicate any blood alterations caused by chronic gamma irradiation. Even though the percent decreases in white blood cell values on day 30 are greater than the corresponding control values for that same day, the absolute values are not. The results here do not coincide with any results obtained by us using acute doses of a comparable magnitude, and thus the decreases seen in the white cell levels in all groups may be only a reflection of normal environmental levels for this cell type.

Experiments for three more periods – summer, autumn, and winter – will be carried out in the next year, and close cooperation with the plant group working in the same areas will allow comparisons of vegetational content of ^{137}Cs with ^{137}Cs levels in *Sigmodon*. Also, differences in environmental conditions such as temperature, wind velocity, moisture levels, etc. will be analyzed over an entire year.

HONEYBEE IRRADIATION STUDIES

A. F. Shinn E. Oertel A. M. Jenkins

There are no published studies of effects of ionizing radiation on field colonies of honeybees. Ecologically, we are most interested in effects on hive economy and the pollinating activities of bees. Effects of gamma radiation on the daily pollen collection of field colonies and on the longevity of both laboratory-caged bees and field colonies were previously investigated.

For the continuation of honeybee studies, Italian cordovan hybrid bees were used, which were supplied from the Genetic Bee Stock Center of the University of California at Davis. Thirty-two of forty colonies of bees were converted to this type by replacing the queens with the genetically homogeneous cordovan queens. The brightly colored, orange cordovans were easily distinguished from the dark native bees. The cordovans foraged up to 2 miles from the apiary, or over an area of some 8000 acres. No native bees invaded the cordovan colonies.

Laboratory cages of approximately 150 Italian cordovans in each of three replicates were irradiated with 1000, 2000, and 4000 rads of ^{60}Co gamma radiation at ~600 rads/min and maintained at internal hive temperature (34°C) with sugar syrup as food. Only the 4000-rad samples had a mean life-span (8.9 days) statistically different from controls (23 days). These results are similar to those previously obtained for East

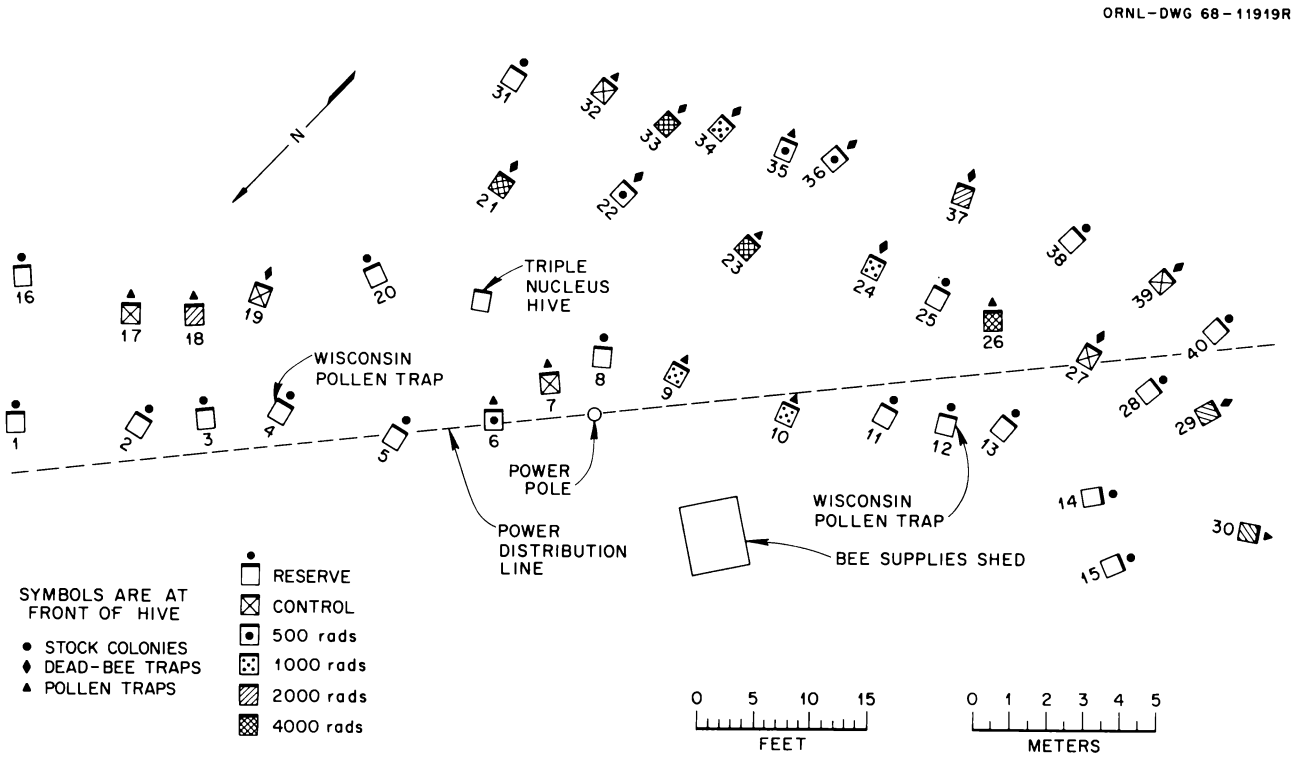

Fig. 8.8. Apiary of the OCD Honeybee Project, 1968.

Tennessee mixed bees (8.5 days) and Illinois Italian bees (7.7 days), which were irradiated with 5000 rads and maintained in the same way a year earlier.

The life-span of laboratory-caged worker bees was determined at three temperatures (24, 34, and 40°C) for starved bees and for bees supplied with 66% sugar syrup, water only, and queen-cage candy. The temperatures had no demonstrable effect on the mean life-spans of unfed bees (1.8 days) or of bees fed 66% sugar syrup (28 days). Bees supplied only with water lived significantly longer at the hive temperature of 34°C than at 24 or 40°C (2.8, 2.0, 2.0 days respectively). Bees fed queen-cage candy had significantly different mean life-spans of 13, 8, and 2 days at 23, 34, and 40°C respectively.

Our field colonies were placed on burial ground 4 and sited so as to discourage the drifting of bees from one hive to another (Fig. 8.8). The colonies of bees were equalized for size and vigor as closely as possible, and those for the several levels of irradiation were chosen at random. Sets of four colonies each received 500, 1000, 2000, and 4000 rads, respectively, of ^{60}Co gamma radiation at ~65 rads/min in the Variable Dose Rate Irradiation Facility of the UT-AEC Agricultural Research Laboratory. They were returned at once to their original position in the apiary along with eight control colonies which had accompanied them (Fig. 8.8).

The criteria for effects of ionizing radiation on the colonies were: (1) the mortality within the hive, (2) the quantity of pollen collected daily by a colony, (3) the flight activity of a colony, and (4) the final status of a colony at the end of the observation period of the experiment. The data were obtained during a 37-day postirradiation period.

Table 8.4 summarizes the data for the first three criteria. The mean daily mortality of the 4000-rad colonies (200 bees) was statistically different from controls (22 bees). The mean daily collections of pollen were not statistically different, but the data suggest that more replicates would yield significance. The mean daily number of flights of the 2000-rad colonies (36 flights per 2-min period) was less ($P > 0.01$) than the 500- and 1000-rad colonies (67 and 61 flights respectively), but we know of no biological basis for the difference.

The final status of the colonies was determined by an inventory of the colonies expressed as square centimeters of honeycomb containing honey, pollen, pupae, larvae, and eggs. The inventories of the 500-, 1000-, and 2000-rad colonies were statistically different from

Table 8.4. Mean Daily Values of Effects of Acute Gamma Radiation on Entire Cordovan Italian Honeybee Colonies

Dose, rads	Controls	500	1000	2000	4000
Mortality, number of dead bees	22.1	18.5	31.1	37.7	200.4[a]
Pollen, g	7.7	17.9	20.9	2.7	0.37
Activity, number of flights per 2-min period	48.2	66.6[b]	61.4	35.6	42.9

[a] $P < 0.01$, compared with each other treatment.

[b] $P < 0.05$, compared with controls, 2000, and 4000.

controls only for pollen ($P > 0.05$); the 1000- and 2000-rad colonies had significantly less pollen per colony (297 and 368 cm^2 respectively) than the controls (768 cm^2). The 4000-rad colonies were obviously moribund, with two dead at inventory time and two more almost dead. More replicates would likely have detected differences between controls and the 2000-rad colonies. Despite as uniform a genetic composition as current knowledge permits, there was still a large amount of variation among colonies within a given dose level.

APPLICATIONS OF CORRELATION MATRICES TO INVESTIGATIONS OF COMMUNITY DYNAMICS

C. E. Styron Gladys J. Dodson

Considerable efforts have been devoted to studies of energy transfers through ecosystems and the associated pathways. The use of radioactive tracers in studies of community dynamics has greatly extended such investigations, but in some experimental situations the use of radioactive tracers may be either undesirable or impracticable. As a case in point, a project has been initiated at the 0800 ecology research area to assess the effects of beta and gamma radiation from simulated fallout (2.44 curies of ^{137}Cs on silica sand grains per 100 m^2)[18,19] on an old-field ecosystem. The objective of this study is to evaluate the technique of cross-correlation[20] as a method for studying predator-prey and competition relationships in an arthropod community.

An old-field arthropod community was sampled bimonthly or monthly, depending on prevailing meteorological conditions. Collections from pitfall traps, soil cores, and biocenometers were sorted for 78 arthropod taxa. The total catch of each species, X, for each sampling period, 1 to N, was used in the analysis. The covariances of $x_1x_2 \ \ldots \ x_1x_n \ \ldots \ x_{n-1}x_n$ were calculated from the equation

$$\operatorname{cov}(x_i x_j) = \sum_{k=1}^{N} (X_{ik} - \bar{X}_i)(X_{jk} - \bar{X}_j) . \qquad (1)$$

The resulting covariance values were strongly biased by the number of each taxa that were caught. It was thus difficult to compare hundreds of aphids with scores of grasshoppers or dozens of crickets. The covariance values, then, were normalized with the partial correlation equation:

$$r_{ij} = \sum_{k=1}^{N} \frac{(X_{ik} - \bar{X}_i)(X_{jk} - \bar{X}_j)}{\sqrt{\Sigma(X_{ik} - \bar{X}_i)^2}\sqrt{\Sigma(X_{jk} - \bar{X}_j)^2}} . \qquad (2)$$

Significant correlations may appear in the arthropod community for two reasons. The populations may vary in response to one common environmental parameter, such as temperature, or in response to several correlated parameters. Populations of Collembola, for instance, achieve their maxima at different seasons. An analysis of this response would yield a large negative value, indicating competition even though the two populations are not active during the same season. Significant correlation values would also be expected for populations varying in response to one another. A high positive value may suggest a predator-prey relationship; a large negative value, competition.

[18] R. C. Dahlman and S. I. Auerbach, *Preliminary Estimation of Erosion and Radiocesium Redistribution in a Fescue Meadow*, ORNL-TM-2343 (1968).

[19] S. I. Auerbach, *Progress Report in Postattack Ecology*, ORNL-TM-2466 (1969).

[20] D. G. Mott, "Determination in Population Systems," pp. 179–94 in *Systems Analysis in Ecology*, K. E. F. Watt (ed.), Academic Press, New York, 1966.

Table 8.5. Cross-Correlation Matrix for Ten Arthropod Taxa

Taxa	Correlation Values									
	Entomobrya	*Pteronemobius*	Carabidae	*Paederus*	Formicidae	Mycetophilidae	Drosophilidae	Aphididae	Lycosidae	Thomicidae
Entomobrya	1.00									
Pteronemobius	0.14	1.00								
Carabidae	0.36	−0.33	1.00							
Paederus	0.29	0.83	0.00	1.00						
Formicidae	0.50	0.00	−0.25	0.50	1.00					
Mycetophilidae	0.07	−0.17	−0.17	0.07	0.07	1.00				
Drosophilidae	0.07	0.00	0.00	0.29	0.36	0.17	1.00			
Aphididae	−0.07	−0.17	−0.17	−0.07	−0.07	0.25	0.07	1.00		
Lycosidae	0.50	0.67	−0.58	0.21	0.29	0.17	−0.07	0.17	1.00	
Thomicidae	−0.07	1.00	0.00	−0.07	0.07	−0.08	0.00	0.17	0.29	1.00

As a means of evaluating this technique, several taxa were selected, based on their documented relationships or responses to environmental conditions. These documented relationships were then compared with relationships predicted from values in a correlation matrix (Table 8.5). The high positive correlation between the cricket *Pteronemobius* and lycosid spiders was expected since these spiders are known to feed on adult crickets. The high correlation between *Pteronemobius* and the thomicid spiders appears to have resulted from predation of young crickets. The low correlation values between Drosophilidae and *Entomobrya, Pteronemobius,* Carabidae, Lycosidae, and Thomicidae would be expected because of their diverse feeding habits. There are also low correlation values between the Mycetophilidae and *Entomobrya, Paederus,* Formicidae, and Thomicidae. The large negative correlation between Lycosidae and Carabidae suggests competition between these two arthropod predators. The high positive correlation between *Paederus* and *Pteronemobius* is less easily explained. Since both the rove beetle and the cricket dwell in the litter, however, it is likely that the populations differ in response to a common environmental parameter.

The agreement of the expected relationships with those suggested by this analysis lends support to its use in investigations of community dynamics. It should be possible, for instance, to establish relationships in an arthropod community before an experimental treatment and then follow changes in these relationships through seasons.

EFFECT OF TEMPERATURE AND RADIATION STRESS ON THE SURVIVORSHIP OF ISOPODS

D. E. Reichle R. I. Van Hook E. A. Bardill

Gamma radiation affects many metabolic processes whose rates are temperature dependent in poikilothermic organisms. Laboratory experiments were designed to test the effects of temperature, acute ^{60}Co radiation, and their interactions on the survivorship of isopods – *Armadillidium vulgare* and *Cylisticus convexus*. A central composite rotatable design in two X variables was used to construct three-dimensional response surfaces described by quadratic polynomial equations of the form

$$\hat{Y} = \hat{b}_0 + \hat{b}_1 X_1 + \hat{b}_2 X_2 + \hat{b}_{11} X_1^2 + \hat{b}_{22} X_2 + \hat{b}_{12} X_1 X_2 .$$

Solutions of the regression coefficients used to evaluate the quadratic functions are given in Table 8.6. Temperature treatments ranged between 12.9 and 27.1°C [$X_1 = (X_i - X_0)/5$, where $X_0 = 20°C$]; radiation doses were between 8.3 and 19.7 kilorads [$X_2 = (X_i - X_0)/4$, where $X_0 = 14$ krads]. The response surfaces (survivorship) varied through time (from 0 to 60 days) both within and between species. For example, both temperature and dose became significant ($P \leqslant 0.05$) at 30 days in the equation for *A. vulgare* survival, but remained nonsignificant for *C. convexus* until day 60. The LD_{50-30} values for *A. vulgare* and *C. convexus* at 20°C were not significantly different at 16.9 kilorads.

Table 8.6. Time-Dependent Values for Regression Coefficients Used in Evaluation of the Quadratic Polynomial Equation for Estimating Survivorship

Regression Coefficient	Time					
	10 Days	20 Days	30 Days	40 Days	50 Days	60 Days
			Cylisticus convexus			
b_0	20.4	15.2	9.0	5.4	3.0	1.2
b_1	0.125	−1.6425	−3.62975	−3.5565	−3.453	−3.453
b_2	−1.125	−1.94875	−2.75875	−2.31925	−2.06925	−1.81925
b_{11}	−1.0125	−1.975	−0.5625	0.675	1.25	2.025
b_{22}	−0.0125	0.275	0.9375	−0.075	0.5	0.775
b_{12}	−1.750	−3.75	−2.75	−2.25	−0.75	−0.25
			Armadillidium vulgare			
b_0	22.8	18.8	14.2	5.4	4.0	3.4
b_1	−0.375	−0.1895	−2.479	−2.634	−1.655	−1.655
b_2	−1.333	−1.384	−2.259	−2.841	−2.893	−1.966
b_{11}	−1.713	−2.338	−3.475	−0.075	−0.75	−1.013
b_{22}	−0.213	−0.088	0.275	1.425	2.00	1.488
b_{12}	0.75	2.00	−1.250	−0.5	−0.75	−0.750

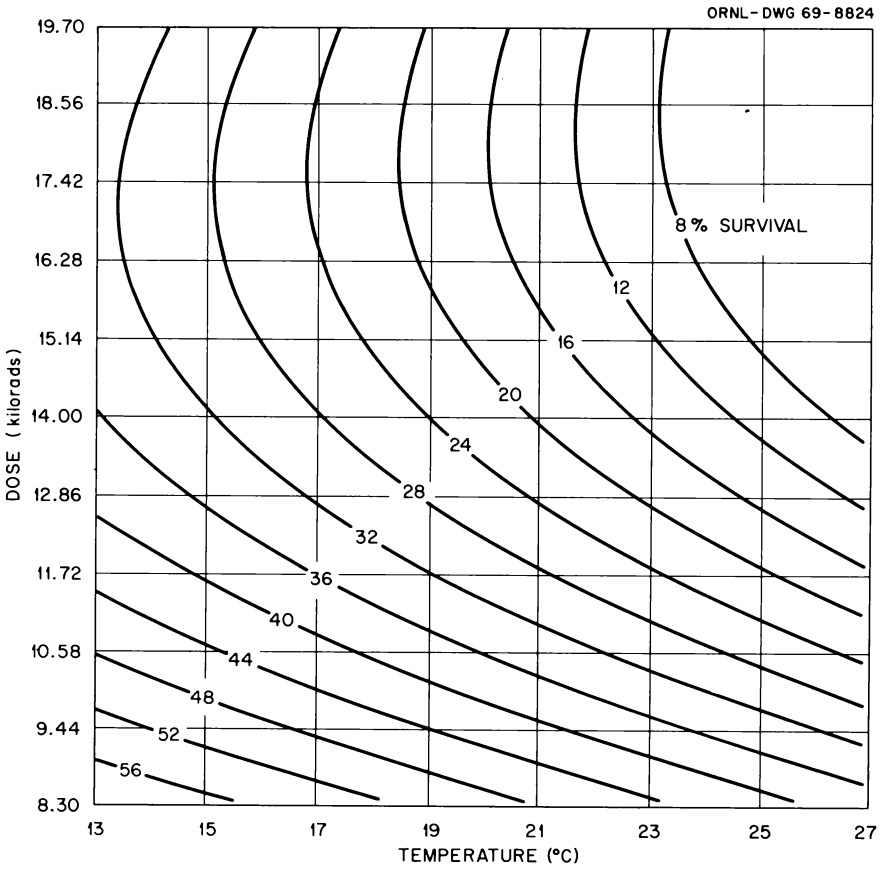

Fig. 8.9. Survivorship of *Armadillidium vulgare* After 40 Days at Various Combinations of Acute ^{60}Co Gamma Radiation and Constant Temperature.

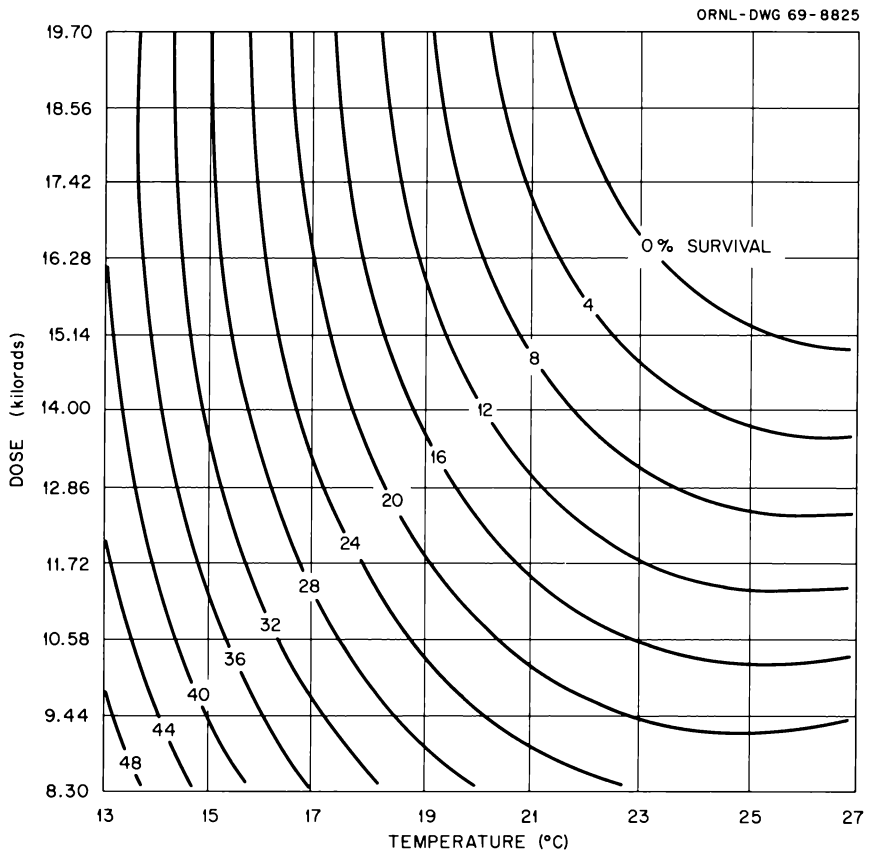

Fig. 8.10. Survivorship of *Cylisticus convexus* After 50 Days at Various Combinations of Acute ^{60}Co Gamma Radiation and Constant Temperatures.

Survivorship responses for both species showed an increase with lower temperatures and lower radiation doses (Figs. 8.9 and 8.10). Since metabolism in these two species follows a temperature Q_{10} of 2, these data suggest increased radioresistance in *A. vulgare* and *C. convexus* at lower metabolic rates. Before precise predictions of the response of irradiated field populations can be made, the effect of temperature and other environmental parameters on metabolism (and radiation sensitivity) will need to be known.

POPULATION GENETICS AND RADIATION EFFECTS STUDIES

B. G. Blaylock Margaret F. Miller P. G. Koehler

The general consensus of most geneticists is that newly induced mutations lower the fitness of an individual. Although this subject has received considerable attention during the past decade, it is still a controversial subject, and conflicting results and conclusions can be found in the literature. In some competition experiments with *Drosophila melanogaster* and *Drosophila simulans*, a radiation-induced increase in fitness was observed.

Laboratory populations were started with equal numbers of highly inbred lines of *D. melanogaster* and its sibling species *D. simulans*. In control populations *D. melanogaster* was the superior species, and the frequency of *D. simulans* decreased rapidly (Fig. 8.11, populations 34 and 21). When the males of *D. simulans* were given a dose of 500 rads of gamma radiation before they were placed in competition with *D. melanogaster* and every 21 days thereafter, the *D. simulans* were better competitors (Fig. 8.11, populations 35 and 33). The frequency of *D. simulans* in the control populations averaged 17% after 21 days of competition, as compared with 50% in the irradiated populations, and the frequency continued to be greater in the irradiated than in the control population for 21 weeks. When the dose to *D. simulans* was increased to

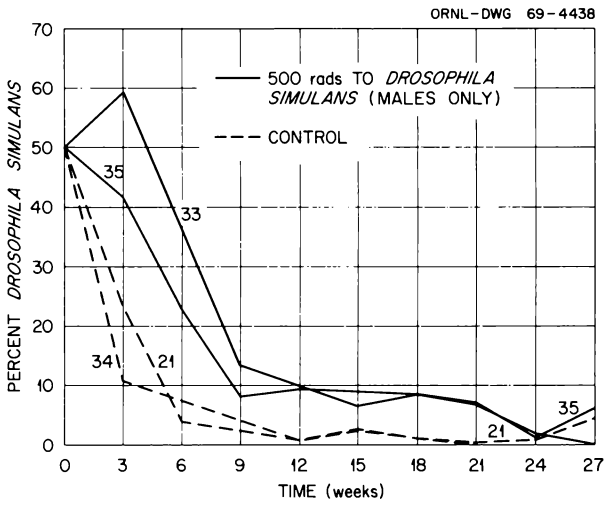

Fig. 8.11. Effect of Radiation-Induced Mutations Introduced into a Homozygous Genetic Background Is Shown by the Frequency of *Drosophila simulans* in Competition with *Drosophila melanogaster*. Populations 21 and 34 were control populations started with equal numbers of inbred lines of *D. simulans* and *D. melanogaster*. In populations 33 and 35 the males of *D. simulans* were given a dose of 500 rads before they were placed in competition with *D. melanogaster* and every three weeks thereafter.

1000 rads, the deleterious effects of radiation were too great a burden on the population, and the *D. simulans* were eliminated in a fashion similar to the controls. These results support the hypothesis that, on the average, newly induced mutations which may be deleterious when homozygous may increase the fitness of an individual when heterozygous, if they are introduced into a homozygous genetic background.

In studies of the sensitivity of germ cells of *Chironomus riparius* to radiation, terminal chromosome aberrations were observed in the salivary gland chromosomes. Although terminal inversions have been reported in several species of *Drosophila* and *Sciara*, the general opinion is that broken ends of chromosomes fuse only with other broken ends.

Newly emerging males and females of *C. riparius* were collected from a laboratory culture and separated. The adult males were given a gamma radiation dose of 2000 rads from a ^{60}Co source and then mass-mated to virgin females. The salivary gland chromosomes of the fourth instar larvae resulting from these matings were examined for chromosome aberrations. In 135 larvae examined, 40 aberrations were observed: 25 inversions, 14 translocations, and 1 deletion. Six of the forty aberrations appeared to be terminal rearrangements; of these, three were inversions and three were translocations. All of the four pairs of chromosomes of *C. riparius* were involved in at least one terminal rearrangement, and five different unbroken ends were included.

The almost universally accepted hypothesis that broken ends of chromosomes fuse only with other broken ends is based primarily on investigations with *D. melanogaster*. However, this study with *Chironomus*, a dipteran taxonomically far removed from *Drosophila*, produced sufficiently disparate data to prompt a questioning of the general acceptance of this hypothesis for all organisms.

EFFECTS OF CHRONIC GAMMA RADIATION ON SNAIL REPRODUCTION

J. L. Cooley

A study evaluating the effects of chronic gamma radiation on snail (*Physa heterostropha*) populations was begun this year. The effects of the radiation on growth, reproduction, and mortality are under study. At present, only the effects on reproduction are complete enough to report.

Twelve containers, each with 23 snails of known age (50 days ± 5 days) were placed in groups of three in front of a 30-curie ^{60}Co source. The groups were exposed to dose rates of approximately 25, 10, 1, or 0 rads/hr. Dose rates were determined using Toshiba Fluoroglass rod dosimeters. The average time of irradiation per week was 166 hr. Figure 8.12 shows the experimental setup.

Once egg laying began (approximately four weeks after the start of irradiation), the following parameters were determined for each container every week: number of capsules laid, total number of eggs laid, average number of eggs per capsule, and percent egg hatchability. Figures 8.13–8.16 summarize the results. The 10- and 25-rad/hr groups are obviously significantly different from the controls for all four parameters studied. However, differences between the 1-rad/hr group and the controls are not obvious. A preliminary statistical analysis employing a two-way nested analysis of variance indicates that, for the ten weeks' data presented here, the 1-rad/hr group is significantly different from the controls in terms of total number of capsules and total number of eggs. There is no difference in average number of eggs per capsule and percent hatchability.

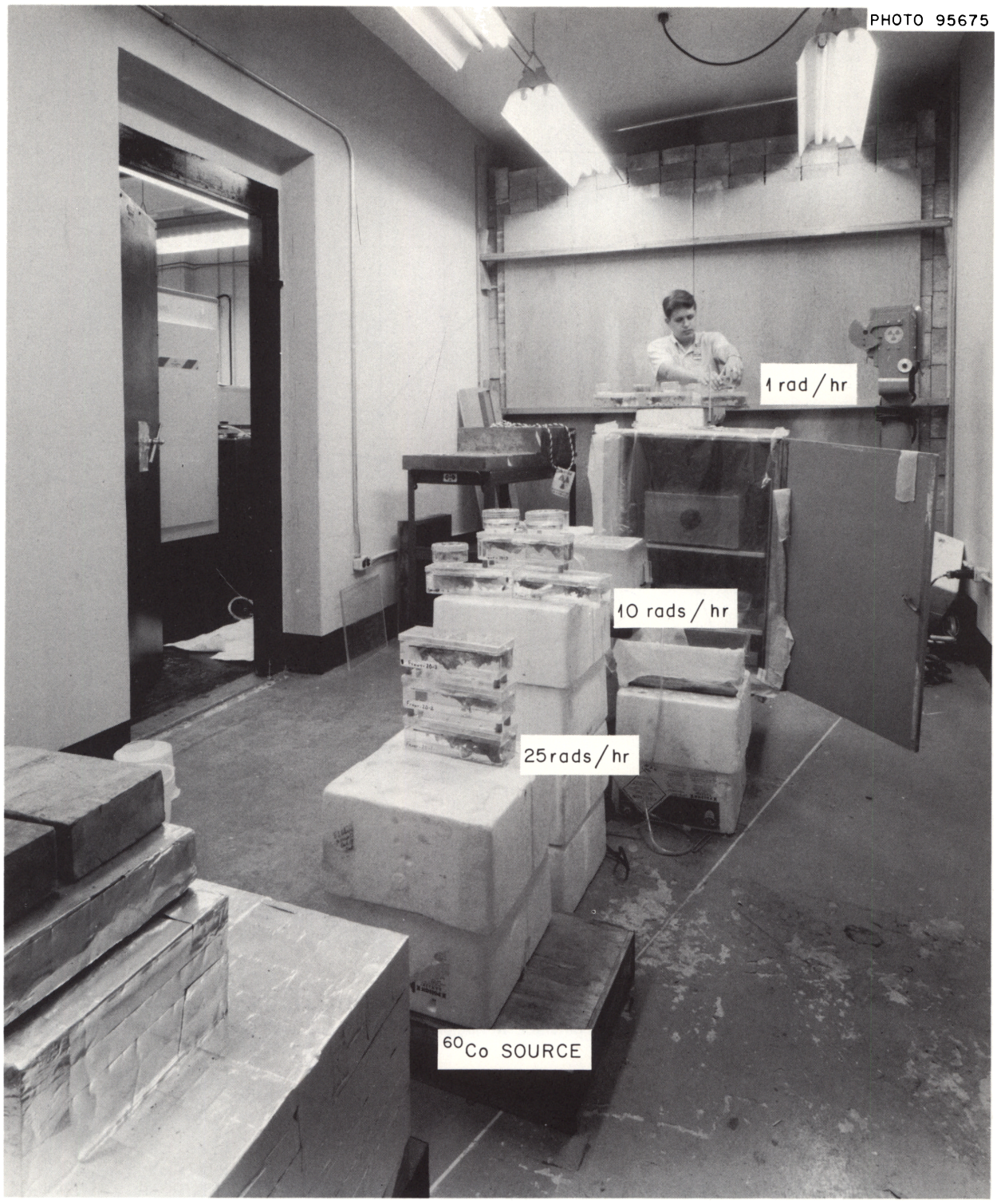

Fig. 8.12. Setup in Source Room for Chronic Exposure of Snails to Three Dose Rates of Gamma Radiation.

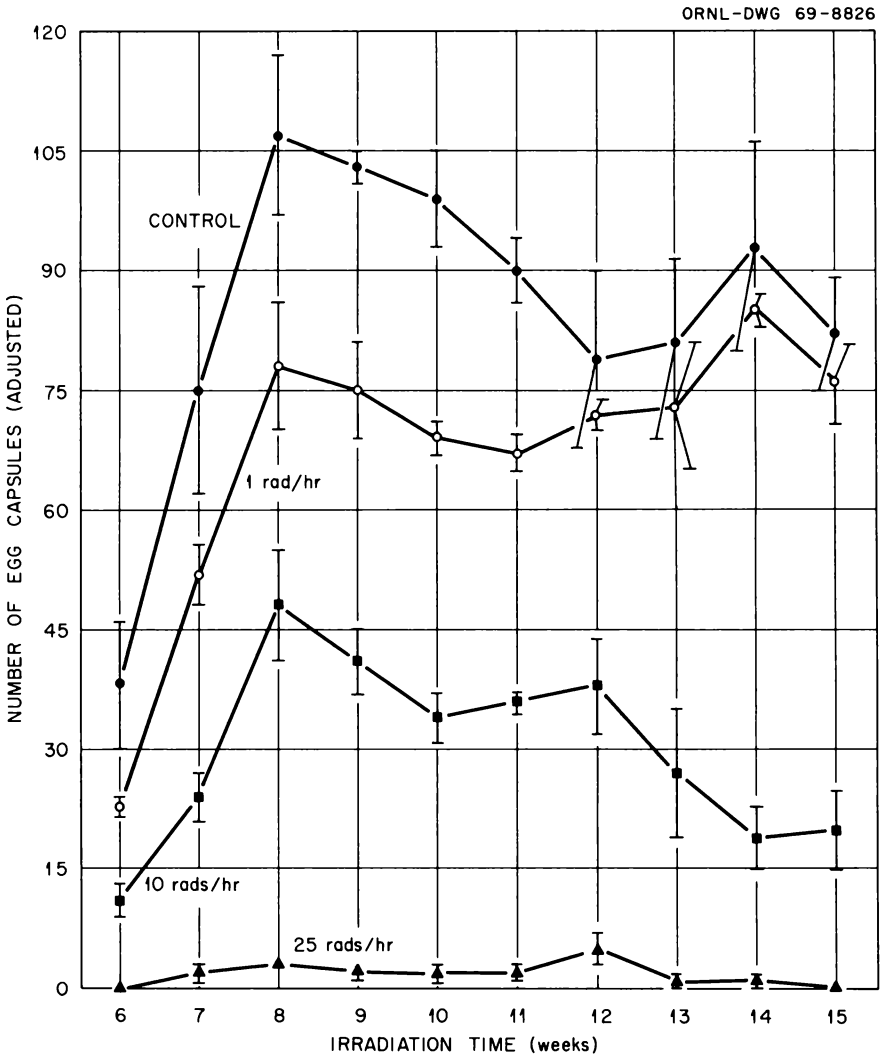

Fig. 8.13. Number of Egg Capsules (± 1 SE) for all Four Dose Groups for Weeks of Irradiation 6 Through 16. In order to account for the differences in number of snails alive in each container, all numbers were adjusted to 23 snails alive [(23/number living) X number of capsules].

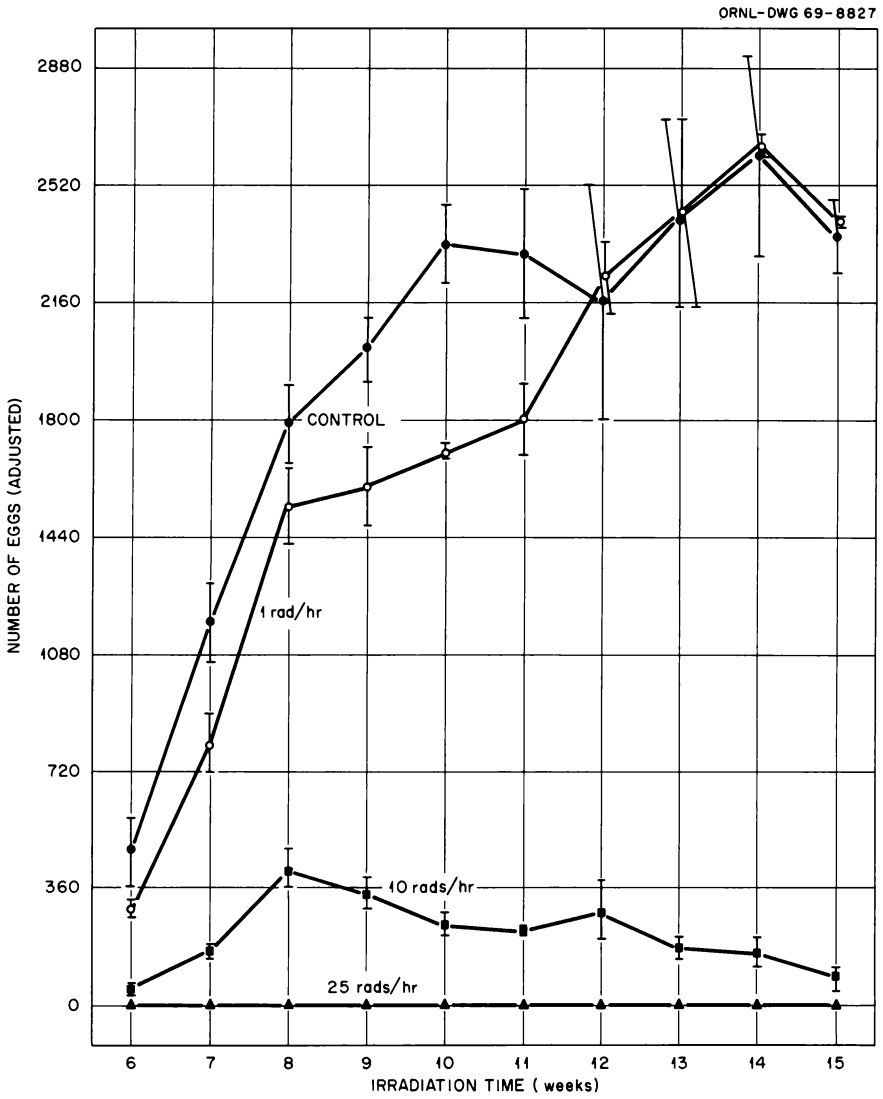

Fig. 8.14. Number of Eggs Laid (±1 SE) for All Four Dose Groups for Weeks of Irradiation 6 Through 15. In order to account for the differences in number of snails alive in each container, all numbers were adjusted to 23 snails alive [(23/number living) X number of eggs].

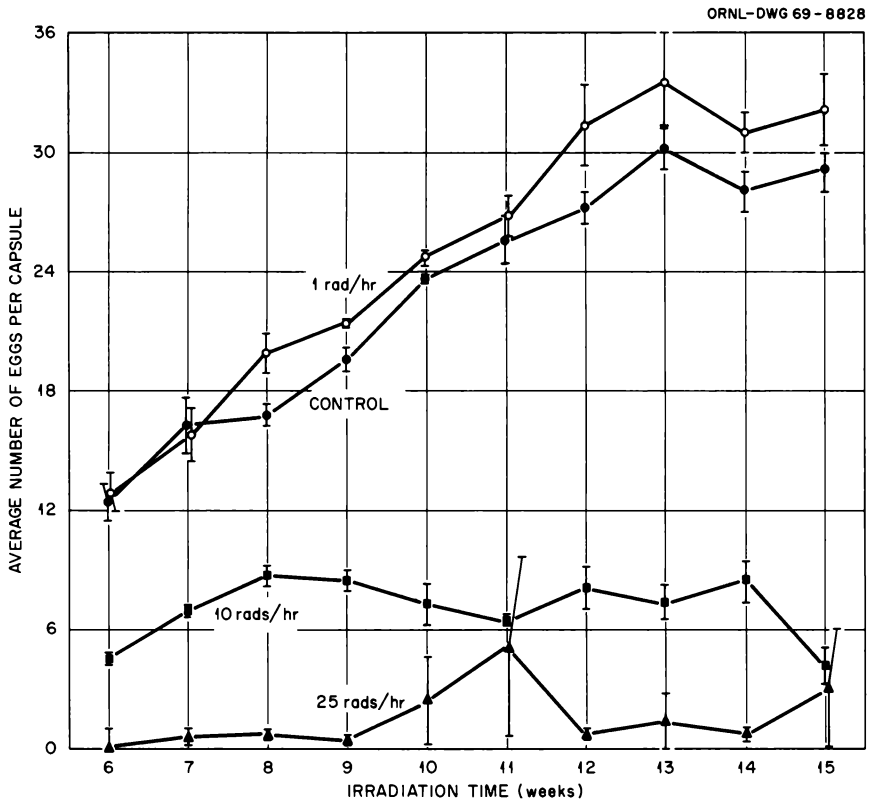

Fig. 8.15. Average Number of Eggs per Capsule (±1 SE) for all Four Dose Groups for Weeks of Irradiation 6 Through 15.

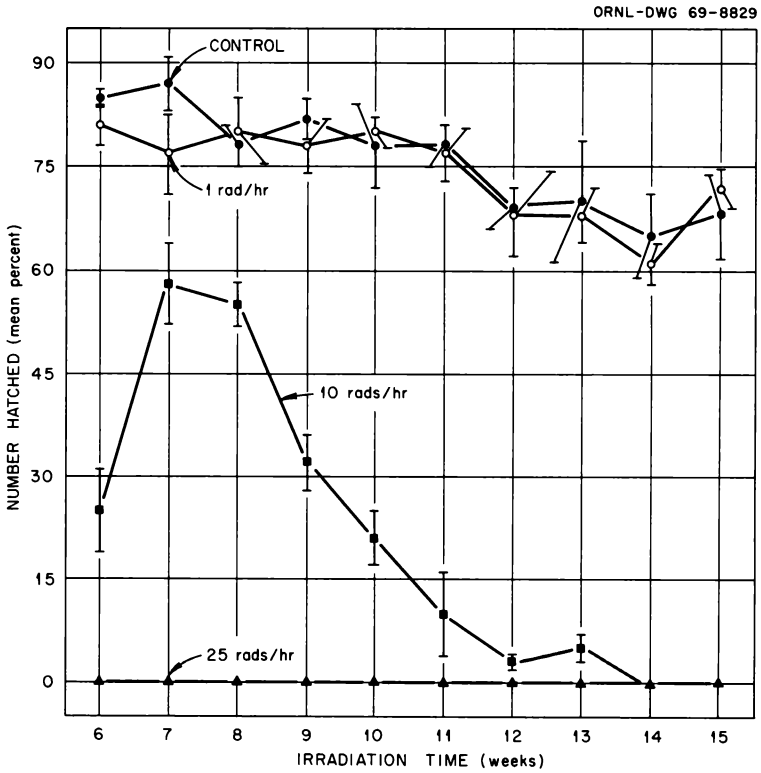

Fig. 8.16. Percent Egg Hatchability (±1 SE) for All Four Dose Groups for Weeks of Irradiation 6 Through 15.

RADIATION SENSITIVITY AND TEMPERATURE EFFECTS IN *GAMBUSIA*

B. G. Blaylock Margaret F. Miller

The radiation resistance of the common mosquito fish, *Gambusia affinis affinis*, from White Oak Lake was compared with a control population. The comparison was made by establishing $LD_{50\text{-}30}$ values for each population at three environmental temperatures. The experiment served two purposes: to confirm our previous results that *Gambusia* from White Oak Lake had not acquired a resistance to acute radiation and to determine the effect of environmental temperature on the $LD_{50\text{-}30}$ of *Gambusia*.

The *Gambusia* population in White Oak Lake has been exposed to chronic environmental radiation of approximately 11 rads/day for over 100 generations, whereas the control population was exposed only to natural background radiation. The fish were irradiated with a ^{60}Co source at doses ranging from 1500 to 9000 rads and maintained at temperatures of 20, 25, and 30°C. An analysis of the data based on a modified form of a "logistic" dose-response model showed no significant difference in radiation response between the fish from the two populations, although the $LD_{50\text{-}30}$ dose at each temperature was less for the White Oak Lake population (Fig. 8.17). However, as temperature increased above 20°C, sensitivity of *Gambusia* to radiation increased. A difference of only 5°C changed the $LD_{50\text{-}30}$ of each population significantly.

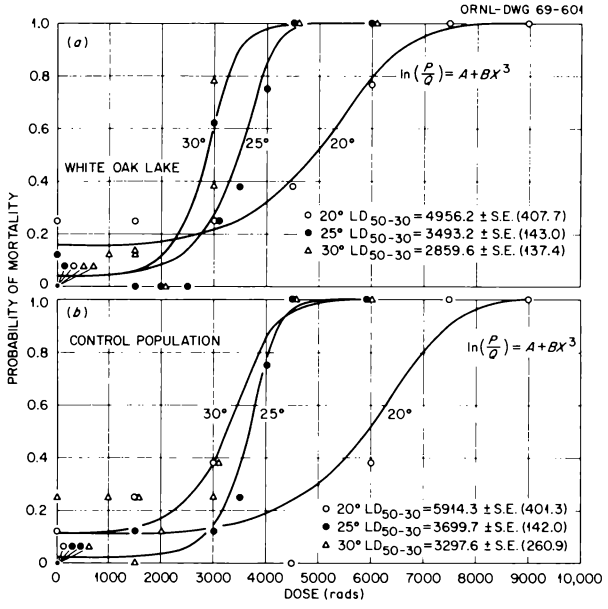

Fig. 8.17. Radiation Response of *Gambusia affinis affinis* from White Oak Lake, a Population That Has Been Exposed to Chronic Environmental Radiation for Over 100 Generations and a Control Population at Three Different Temperatures. The curves fitted to the data were based on the use of a form of the logistic dose response model. No significant difference was detected between the $LD_{50\text{-}30}$'s of the two populations, but a change of only 5°C was sufficient to change the $LD_{50\text{-}30}$ of each population.

Our studies on the radiosensitivity of two natural populations of *Gambusia* showed that a population exposed to chronic environmental radiation for many generations did not develop a detectable resistance to acute gamma radiation. The results also demonstrate that the environmental temperature was very important in the radiation response of *Gambusia* because, as temperature increased, the $LD_{50\text{-}30}$ dose decreased.

RADIATION EFFECTS ON CARP REPRODUCTION

B. G. Blaylock N. A. Griffith Peggy J. Bruno

The small size of fertilized fish eggs makes them susceptible to beta radiation. Since it is plausible that eggs spawned in natural environments could come in contact with beta emitters as a result of fallout or contamination of aquatic environments by nuclear facilities, studies of the effects of radiation on fertilized carp eggs were extended to beta radiation. The technique of artificially spawning carp in the laboratory was employed to obtain fertilized eggs, which were exposed to acute doses of beta radiation 30 min after fertilization. A ^{90}Sr-^{90}Y source having a dose rate of approximately 77 rads/min was used to irradiate the eggs. The effect of the acute beta radiation on the hatchability of the carp eggs is shown in Table 8.7. These results, when compared with our previously reported effects of acute gamma radiation,[21] showed that the effects of acute beta and gamma radiation on the hatchability of carp eggs were similar. The effectiveness of the beta dose in preventing the hatching of carp eggs undoubtedly was due to the great local absorption of energy in a small volume.

The study of the effect of chronic gamma radiation on the hatchability of carp eggs was extended to include dose rates of 4, 10, and 25 rads/hr. The exposure to the chronic doses of gamma radiation was started 30 min after fertilization and continued for 70 hr, when hatching should have occurred. The effects of

[21] S. I. Auerbach *et al.*, *Health Phys. Div. Ann. Progr. Rept. July 31, 1968*, ORNL-4316, p. 79.

Table 8.7. Hatchability of Carp Eggs Irradiated with Acute Beta 30 min After Fertilization

Dose[a] (rads)	Number of Fertilized Eggs	Hatchability of Eggs (%)
	Pair I	
Control	127	89.0
74	101	88.1
185	110	73.6
370	67	73.1
555	46	56.5
1050	140	0.7
1480	67	0.0
	Pair II	
Control	244	90.6
74	221	94.6
185	235	95.7
370	125	74.4
555	73	47.9
740	79	36.7
1050	131	2.3
1480	80	2.5
	Pair III	
Control	227	87.7
74	132	87.9
185	181	85.1
370	264	45.5
555	117	53.0
740	122	40.7
1050	64	1.6
1480	86	2.3

[a] ^{90}Sr-^{90}Y source; dose rate was 77 rads/min.

Table 8.8. Hatchability of Carp Eggs After Chronic Gamma Irradiation for 70 hr

Dose (rads/hr)	Number of Fertilized Eggs	Hatchability of Eggs (%)
	Pair I[a]	
Control	42	85.7
4	64	70.3
10	52	61.5
25	59	40.7
	Pair II	
Control	132	99.2
4	162	91.4
10	243	64.2
25	297	11.1
	Pair III	
Control	242	98.3
4	147	73.5
10	146	82.2
25	239	43.1

[a] Pairs of adult carp.

chronic gamma radiation are shown in Table 8.8. Our previous studies showed that an acute dose of 250 rads given 30 min after fertilization had no detectable effect on hatchability;[21] however, a chronic dose of 4 rads/hr for a total dose of 280 rads reduced the hatchability by an average of 15%. In comparison, an acute dose of 1000 rads was sufficient to prevent all eggs from hatching, but as many as 40% of the eggs hatched when a dose of 1750 rads was administered over a 70-hr period. These data emphasize the different effects that chronic and acute gamma radiation can have on an important stage of the life cycle of an organism.

RADIOSENSITIVITY OF THE NEWT *NOTOPHTHALMUS VIRIDESCENS*

D. L. Willis G. E. Cosgrove

It has been shown repeatedly that amphibians exhibit markedly longer survival times following irradiation than mammals. Most such studies have involved radiation exposures of no more than a few kilorads. The purpose of this study was to determine the response of a representative amphibian, the red-spotted newt (*Notophthalmus viridescens*), to a wide range of radiation doses.

The newts used were field collected from a single local population in Middle Tennessee. Sixty-two newts were used in the initial study. They were maintained unfed throughout the study in small individual containers filled with spring water at 22 ± 1°C. The average weight of the animals was 3.5 g. A ^{60}Co irradiator delivering a gamma dose rate of 453 rads/min was used for a series of radiation doses ranging from 5 to 80 kilorads. Mortalities were recorded daily, and the dead animals were preserved in 10% formalin for subsequent histopathological examination.

The results, plotted as mean survival time vs dose, are shown in Fig. 8.18. A nearly linear dose-dependent relationship was observed over the dosage range. On the basis of previous results in this exposure range using another newt species (*Taricha granulosa*),[22] it is inferred that this range involves a central nervous system response. The mean survival times are considerably longer than for mammalian species at the same radiation doses. Histopathological studies are under way to determine the nature and extent of tissue damage at these doses. No control deaths occurred during the course of the experiment.

[22] D. Willis and J. Price, *Radiation Res.* **31**(3), 600 (1967).

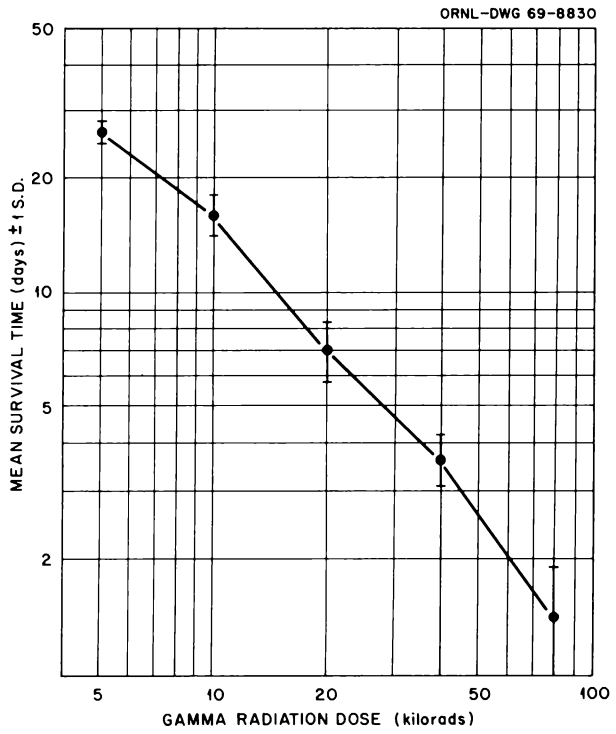

Fig. 8.18. Mean Survival Time of the Newt (*Notophthalmus viridescens*) as a Function of Whole-Body Gamma Radiation Dose. Each point represents the mean of ten animals.

This study is being continued using a series of radiation doses from 200 to 7000 rads in an effort to determine both survival times and tissue responses. It is anticipated that this range will uncover a dose-independent area of response as well as allow determination of the LD_{50} for this species.

COMPARATIVE RADIOSENSITIVITY OF VERTEBRATES

P. B. Dunaway J. T. Kitchings III
J. D. Story L. E. Tucker
H. F. Landreth

Current research in comparative radiosensitivity with mammals has progressed to a point where we are investigating species on the bases of predicted radiation responses, physiological adaptations, or a need to know laboratory responses of selected species for projected field studies. Preliminary analyses of radiation effects in three species in the family Sciuridae showed the nonhibernating, diurnal red squirrel (*Tamiasciurus hudsonicus*), as predicted from hematological parameters, to be radiosensitive ($LD_{50-30} \leqslant 600$ rads), whereas the eastern chipmunk (*Tamias striatus*), a hibernating, diurnal species, is relatively radioresistant ($LD_{50} \cong 950$ rads). Early results ($LD_{50} \sim 500$ rads) for the nonhibernating, nocturnal flying squirrel (*Glaucomys volans*) indicate that this species is even more radiosensitive than the red squirrel and is about the same as the rice rat (LD_{50} 525 rads). Radiation responses were measured in the Mongolian gerbil (*Meriones unguiculatus*), because this species is a typical desert rodent, with physiological adaptations peculiar to such species. This gerbil was radioresistant (LD_{50} 1060 rads).

Red squirrels had relatively short survival times for decedents (6.5–7.3 days from 600–1250 rads), but survival times were long for the chipmunk (12.0–12.6 days at 800–1000 rads) and flying squirrel (11.3–19.0 days at 500–1000 rads). The gerbil was unique in that survival times were much longer at high doses (11.0–12.8 days at 1625–2000 rads) than the times at comparable doses reported earlier[23] for six species of cricetid rodents (5.6–8.1 days), two species of murid rodents (4.4–5.1 days), and two species of soricid shrews (3.5–4.3 days). Also, the flying squirrel is the first species we have examined which is radiosensitive and yet has long survival times.

Radiation responses in amphibians have received little attention, but these vertebrates are important ecologically and are of interest because of the transformations that occur, the changes from an aquatic to terrestrial existence, and the changes from herbivorous-saprovorous feeding to carnivorous feeding. Adults of Fowler's toad (*Bufo woodhousei fowleri*) were more radioresistant than adult mammals; LD_{50} values at 30, 40, 50, and 60 days were 2375, 1925, 1750, and 1675 rads respectively (Fig. 8.19). However, juveniles were extremely radiosensitive. Mortalities in tadpoles increased drastically after 40 days, and at doses of 5000 to 10,000 rads, some tadpoles exhibited symptoms within a few hours post irradiation that indicated equilibrium disorientation and difficulties with respiration. Delays in transformation stages were manifest, and heavy mortality occurred late in the transformations. These findings are provocative and suggest that transforming stages of amphibians may be vulnerable to relatively low doses of ionizing radiation received from a radioactive environment.

[23] P. B. Dunaway *et al.*, pp. 173–84 in *Proceedings of Second National Symposium on Radioecology, Ann Arbor, Michigan, May 15–17, 1967*, CONF-670503 (March 1969).

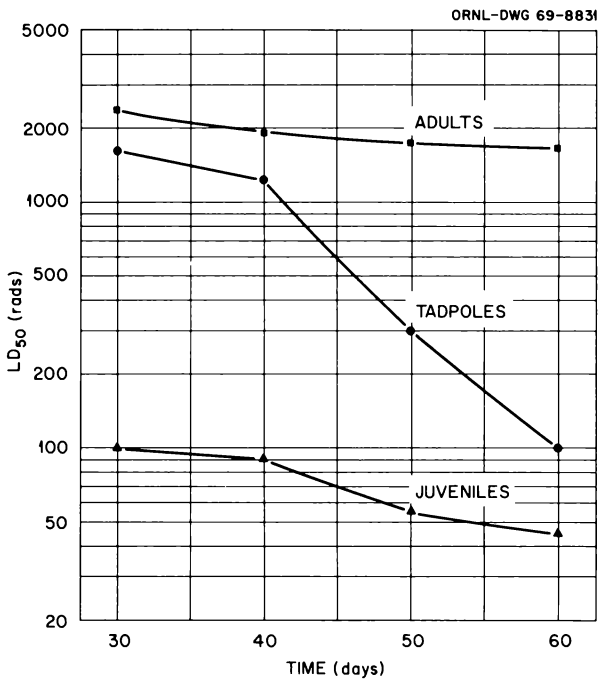

Fig. 8.19. LD_{50}'s at 30, 40, 50, and 60 Days in Tadpoles, Juveniles, and Adults of Fowler's Toad.

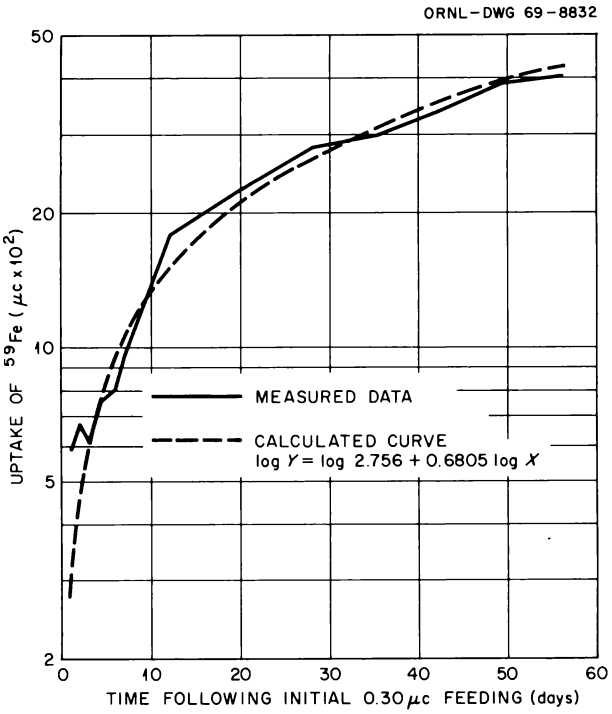

Fig. 8.20. Whole-Body Accumulation of ^{59}Fe in Cotton Rats (*Sigmodon hispidus*) Chronically Fed 0.30 μc/day. Values for whole-body content on days 1 and 2 were deleted for the uptake-equation calculations.

INCORPORATION OF ^{59}Fe IN MAMMALS

P. B. Dunaway J. D. Story
J. T. Kitchings III L. E. Tucker

Despite the long and ever-growing interest in the response of certain hematological elements to radiation, only fragments of the hemopoietic kinetics underlying differential radiosensitivity of mammalian species have been experimentally observed, and much less has been understood and satisfactorily explained. Since the principal cause of death in the LD_{50-30} range is damage to the hemopoietic system, we are continuing to investigate hematological parameters in order to formulate predictive indexes to LD_{50-30} estimates.

Iron is important in erythropoiesis, and recent work indicates that iron turnover rates may provide an index to metabolic rates.[24] Elimination coefficient (λ_b) and biological half-life (T_b) measurements for ^{59}Fe were made in 13 mammalian species (Table 8.9). No correlation could be made between body weight and T_b of ^{59}Fe, which is unusual, because a review paper[25] indicated a relationship between T_b of most radionuclides with body weight of vertebrates and invertebrates. Also, the correlation between interphase chromosome volume, ^{59}Fe λ_b, and LD_{50-30} reported earlier[26] proved unsatisfactory for predicting LD_{50-30} values at the interfamily level. Therefore a detailed analysis into the distribution and transfer of ^{59}Fe in nonirradiated cotton rats was begun, utilizing this species as a representative cricetid rodent.

Twenty cotton rats were fed lettuce tagged with 0.30 μc of ^{59}Fe every day for 56 days. Whole-body radioactivity counts, along with various tissue concentrations of ^{59}Fe, were taken. The whole-body accumulation of ^{59}Fe is shown in Fig. 8.20. Eighty percent of the whole-body radioactivity in the animal on day 1 was found in the nonexcreted material in the gastrointestinal tract, and on the basis of percent of total dose administered only 1.5% had been absorbed by the tissues after 15 hr. The whole-body accumulation appears to be a single-component curve: $\log y = \log 2.756 + 0.6805 \log x$. On a per-gram basis (wet weight) the bone marrow accumulated more ^{59}Fe than any

[24] C. E. Baker and P. B. Dunaway, this report, chap. 10.

[25] D. E. Reichle *et al.*, *Nucl. Safety* (in press).

[26] P. B. Dunaway *et al.*, *Health Phys. Div. Ann. Progr. Rept. July 31, 1968*, ORNL-4316, p. 71.

other tissue up to day 35, when greatest concentration was in the liver.

Measurements are now being made on the excretion of ^{59}Fe in the same cotton rats, which were fed iron to a "near equilibrium" level, in order to arrive at detailed resolution of compartmental transfer rates. Once the normal distribution and intercompartmental transfer of iron have been established it may be possible, by using acute doses of radiation, to pinpoint the areas in the hemopoietic system which are primarily responsible for differences in radiation response of species, that is, $LD_{50\text{-}30}$.

Table 8.9. Elimination Coefficients (λ_b) and Biological Half-Lives (T_b) of ^{59}Fe in 13 Mammalian Species

Taxon	Average Weight (g)	λ_b (%/day)	T_b (days)
Muridae			
House mouse (*Mus musculus*)	14.9	0.47	147
Norway rat (*Rattus norvegicus*)	229.9	0.23	301
Cricetidae			
Eastern harvest mouse (*Reithrodontomys humulis*)	8.1	0.30	231
White-footed mouse (*Peromyscus leucopus*)	20.5	0.43	161
Golden mouse (*Peromyscus nuttalli*)	20.7	0.20	347
Pine vole (*microtus pinetorum*)	26.1	0.47	147
Rice rat (*Oryzomys palustris*)	56.8	0.18	385
Mongolian gerbil (*Meriones unguiculatus*)	58.6	0.18	385
Cotton rat (*Sigmodon hispidus*)	109.2	0.25	277
Soricidae			
Short-tailed shrew (*Blarina brevicauda*)	13.2	0.37	187
Sciuridae			
Eastern chipmunk (*Tamias striatus*)	96.3	0.16	433
Red squirrel (*Tamiasciurus hudsonicus*)	217.0	0.40	173
Caviidae			
Guinea pig (*Cavia porcellus*)	470.0	0.34	204

9. Responses of Plants to Ionizing Radiation

W. F. Harris[1] S. Suzuki[3] J. P. Witherspoon
Carol E. Macklin[2] F. G. Taylor, Jr. W. A. Thomas[4]

RETENTION OF A FALLOUT SIMULANT BY PINE AND OAK TREES

J. P. Witherspoon F. G. Taylor, Jr.

The formulation of realistic predictions of the biological effects of fallout upon vegetation requires information on both the radiosensitivity of plants exposed to radiation in fallout geometries and the interception and retention of fallout particles by foliage under field conditions.

Previous studies on the retention of fallout particles by native plants have been made at the Nevada Test Site following nuclear detonations[5,6] and in Costa Rica following the eruption of the Irazu volcano.[7] The purpose of this study was to determine the retention of a fallout simulant by plant species which have been used in laboratory radiobiological studies at ORNL. Moreover these species (*Pinus strobus*, white pine, and *Quercus rubra*, Southern red oak) represent the most common types of foliage found in the forests of the Eastern United States.

A fallout simulant consisting of quartz particles (88 to 175 μ in diameter) containing ^{134}Cs sorbed at high temperatures was obtained from the Stanford Research Institute for this study. The ^{134}Cs concentration of the simulant was 1.93 μc per gram of particles, and the solubility of the ^{134}Cs was approximately 2% in distilled water (24-hr contact of 1 g of particles with 100 ml of distilled water).

Potted, two-year-old white pine and red oak trees were placed in an open field one week prior to application of the fallout simulant. Thirty trees, 30 to 45 cm in height, of each species were selected for treatment and spaced 1 m apart.

The fallout simulant was applied to each tree by a sieving technique which gave a particle deposition of 4.5 g (8.7 μc) per square foot of ground surface. Three plants of each species were collected for radioactivity determinations: at the time of simulant application, 1 hr afterward, and 1, 4, 7, 14, 18, 26, and 33 days afterward. Samples were collected by placing a plastic bag over the plant, closing the bag around the stem, and cutting the plant stem below the bag closure so that any particles lost from the plant during handling were retained in the bag. Each sample was then placed in a 1-qt cylindrical cardboard container, and the ^{134}Cs activity was measured in a Packard gamma spectrometer with an Armac scintillation detector.

The average concentration of ^{134}Cs in foliage samples and the amount of rainfall during the study are given in Table 9.1.

Table 9.1. Average Concentration of ^{134}Cs in Foliage of Pine and Oak Trees at Different Times After Application of the Fallout Simulant

Time After Application	Picocuries of ^{134}Cs per Gram of Dry Weight of Foliage ±S.E.		Accumulated Rainfall (in.)
	Pines	Oaks	
t_0	47,265 ± 5,340	308,124 ± 26,497	
1 hr	43,061 ± 4,777	29,269 ± 2,518	0
1 day	2,998 ± 360	1,224 ± 195	0.90
4 days	1,515 ± 256	112 ± 19	0.95
7 days	1,198 ± 113	64 ± 9	1.30
14 days	1,015 ± 100	46 ± 4	1.43
18 days	935 ± 158	38 ± 7	1.47
26 days	761 ± 98	31 ± 6	2.88
33 days	566 ± 50	36 ± 7	3.46

[1] ORAU Predoctoral Fellow.
[2] ORAU undergraduate trainee.
[3] Alien guest.
[4] Dual capacity.
[5] E. M. Romney *et al.*, *Ecology* 44, 343 (1963).
[6] W. E. Martin, *Radiation Botany* 4, 275 (1964).
[7] C. F. Miller and H. Lee, SRI-MU-4890 (1967).

Following the notation of Martin[6] and Miller,[7] the initial concentrations of the fallout simulant on foliage may be expressed by a foliage contamination factor, a_i, such that

$$a_i = C_i^0/m_i \,(\mathrm{ft}^2/\mathrm{g}) , \qquad (1)$$

where C_i^0 is the quantity in microcuries of radionuclide initially intercepted per gram of dry weight of foliage and m_i is the quantity of microcuries of radionuclide deposited per square foot of soil surface area.

The fraction of fallout that is initially intercepted by foliage is given by

$$F_i = a_i w_l , \qquad (2)$$

where w_l is the biomass of foliage in grams per square foot of soil surface area.

The initial interception of ^{134}Cs by pine foliage was 0.0472 μc/g from the 8.7 μc/ft^2 deposition. The dry weight of pine foliage in the deposition area was 44.64 grams per square foot of soil surface. For oak foliage the initial interception was 0.3080 μc/g, and the foliage dry weight in the deposition area was 9.88 grams per square foot of soil surface. Calculated a_i values [Eq. (1)] were 0.0054 for pine and 0.0354 for oak trees. The fractions, F_i in Eq. (2), of the simulant which were initially intercepted were 0.242 and 0.349 for pine and oak trees respectively. The broader leaves of the oaks accounted for the greater initial retention by this species.

The early effects of weathering, wind and rain, on particle retention in this study are shown in Fig. 9.1, which illustrates the average percent retention of particles through time. During the first hour following application, the oaks lost 90.5% of the initial ^{134}Cs concentration, while the pines lost only 9.9%. A 0.9-in. rain which fell during the first day accounted for a considerable loss of particles from both species, although the loss rate for oaks was almost twice that for the pine trees. After one week, and three rains totaling 1.3 in., the ^{134}Cs concentrations were reduced to 2.53% of the initial value in pines and to 0.02% in oaks, more than two orders of magnitude difference. After the first week of weathering, the fallout loss rate is quite similar and constant for both species up to 33 days – the length of this study.

In addition to the differential particle retention capacity of these two distinct types of foliage, the pine tree morphology is such that the major retention sites are near the meristematic regions, which are the most radiosensitive parts of the plant. This species not only has a greater fallout retention capability, but also the radioactivity tends to reside where it will do the most biological damage.

The retention curves in Fig. 9.1 cannot be adequately expressed in terms of a single effective half-life. The rapid particle loss rate during the first week and the constant loss rate up to about a month would imply that at least a two-compartment model of these data could be used. Indeed, after a longer period of weathering, particles and absorbed activity on or in the foliage should become essentially nonremovable, so that effective half-life would approach radiological half-life and a three-compartment model would be appropriate.

Table 9.2 gives effective half-lives (T_p) and effective decay constants (λ_p) of ^{134}Cs calculated from the data in Table 9.1. The effective half-lives of ^{134}Cs in both

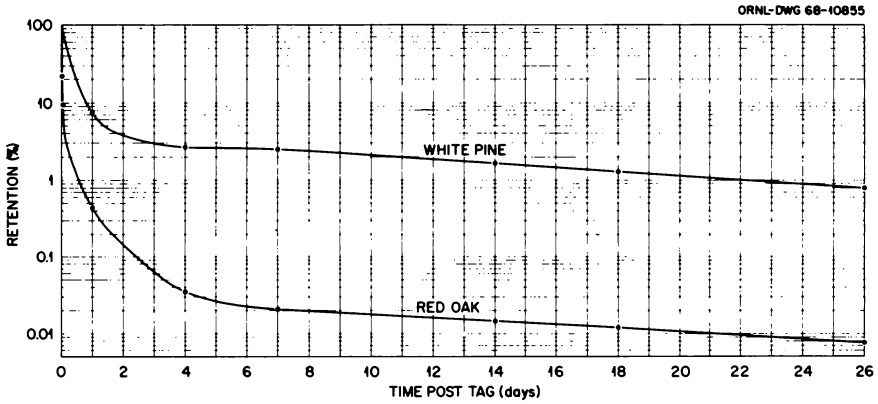

Fig. 9.1. Average Retention of 88-to-175-μ-diam Fallout Particles by White Pine and Red Oak Trees Up to 26 Days Following Application of Particles. t_0 retention = 100%.

Table 9.2. Effective Half-Lives and Effective Decay Constants of ^{134}Cs Fallout Simulant on Pine and Oak Trees

	0–1 Day		1–7 Days		7–33 Days	
	λ_p (day^{-1})	T_p (days)	λ_p (day^{-1})	T_p (days)	λ_p (day^{-1})	T_p (days)
Pines	2.753	0.255	0.153	4.53	0.033	20.66
Oaks	5.570	0.124	0.492	1.41	0.028	24.86

species greatly increased with time after application. Half-life values obtained after 1 week are 81 and 171 times higher than the first day values for pine and oak respectively. Loss of ^{134}Cs due to radioactive decay (λ_r = 0.0009) is negligible compared with the mechanical or weathering loss. During the 7- to 33-day period the loss due to radioactive decay accounts for only 2.7% of the total loss.

The results of this study indicate that concentrations of radionuclides on fallout-contaminated plants can be expected to decrease at rates significantly faster than would be predicted on the basis of radioactive half-lives. While early (e.g., 0 to 7 days) radionuclide concentrations are very important for estimates of radiation dose to plants, the concentrations remaining after a week are more important for determinations involving entry of radionuclides into terrestrial food chains.

BETA DOSIMETRY OF ^{90}Sr-^{90}Y SOURCES

S. Suzuki J. P. Witherspoon

Dosimetric studies employing the LiF dosimetry system (TLD) were initiated this year. Beta radiation doses to various plant parts have been measured in a number of different exposure geometries created with ^{90}Sr-^{90}Y sources. These data are being compared with doses estimated from current dosimetry models prepared by the Stanford Research Institute.

Exposure geometries studies were those that have been used in experiments on the beta radiosensitivity of plants, and they represent geometries commonly produced by particulate fallout.

For exposures in which small portions of a plant (a bud or leaf) were contaminated with small particles (44- to 88-μ-diam albite containing ^{90}Sr-^{90}Y), there was close agreement between measured dose rate values and values calculated with the assumption that the contaminated surface was a point source. Dose rates measured with TLD's placed throughout the crowns of small oak and pine trees with contaminated apical buds were within 4.6% of calculated doses over distances of 5 to 40 cm from the source. The TLD-measured dose was consistently lower, however.

Radiation dose to plants from beta emitters on the soil surface (a plane source) can be readily calculated by using disintegration rate multipliers, such as those furnished by Brown.[8] However, these models for ascertaining beta bath dose postulate an ensemble of point isotropic sources uniformly distributed over an infinite plane. Since our laboratory experiments on beta radiosensitivity of plants utilize ^{90}Sr-^{90}Y plane sources of finite dimensions, it has been necessary to measure beta dose. Dose distributions in plants exposed on fabricated disk sources and to simulated fallout particles on the soil surface have been measured with TLD's.

These measurements with finite plane sources, in addition to furnishing information on attenuation by air and foliage or wood, may be used to extend the use of infinite plane calculations to laboratory botanical studies.

Figure 9.2 gives dose rate measurements at 5 and 10 cm above the centers of ^{90}Sr-^{90}Y disk sources of 5, 10, 20, and 34 cm diameter. Activity per unit area was 826 $\mu c/cm^2$ in all cases. For a source diameter of 25 cm at 5 cm height, the dose rate approached that calculated for an infinite plane source of the same activity per unit area. At 10 cm height the 34-cm-diam source dose rate approximated that from an infinite plane source.

[8] S. L. Brown, SRI-MU-5116 (1965), 173 p.

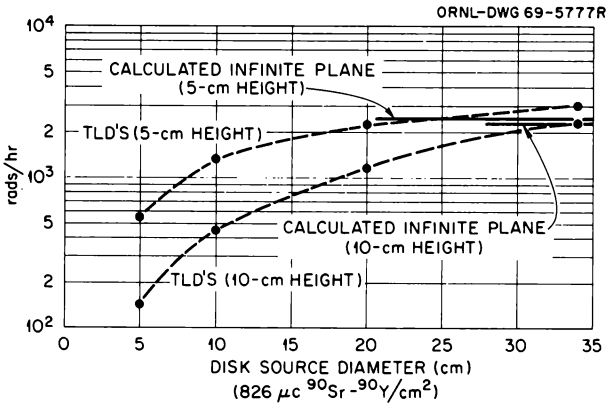

Fig. 9.2. Measured Beta Radiation Dose Rates at 5 and 10 cm Above the Center of ^{90}Sr-^{90}Y Disk Sources of Varying Diameter and Uniform Activity per Unit Area. Solid lines are calculated dose rates from an infinite plane model for 5 and 10 cm above the same activity per unit area (826 $\mu c/cm^2$). Each point is an average of five measurements.

Therefore, where backscatter and attenuation media are similar, dose rates easily calculated for an infinite plane model may be extended to finite planes by applying a reduction factor taken from an appropriate height curve.

Additional comparisons between dose estimates with current dosimetry models and the TLD system are in progress for contact geometries and various tissue depths.

EFFECTS OF EXTERNAL BETA RADIATION ON HIGHER PLANTS

J. P. Witherspoon F. G. Taylor, Jr.

Studies on the radiosensitivity of native and agricultural plants to beta radiation have continued this year. Emphasis has been on experiments designed to assess the hazard of beta-field radiation geometries. Cylindrical and plane sources (^{90}Sr-^{90}Y) have been used to determine thresholds of beta dose necessary to produce biological endpoints ranging from slight growth inhibition to mortality.

Cylindrical sources were prepared by painting glycerol-coated albite particles (44–88 μ diam) containing ^{90}Sr-^{90}Y on filter paper which was rolled into a cylinder (1.5 by 4 cm) and taped shut. These cylinders contained from 6.9 to 12.7 $\mu c/cm^2$ of internal surface area.

Estimates of beta dose to tissues within cylinders were calculated from models furnished by Lane.[9] The beta energy flux density, ϕ_1, in Mev sec^{-1} cm^{-3}, within a cylinder is estimated by

$$\phi_1 = \frac{\beta_0 \bar{E}_\beta}{r},$$

where β_0 is the activity in dis sec^{-1} cm^{-2} of surface area, $\bar{E}_\beta$ is the average beta energy, and r is the inside radius in cm of the cylinder.

If the energy flux density inside the cylinder is assumed to be absorbed by plant tissue of volume v and mass m, then the initial dose rate to tissue inside the cylinder is estimated by

$$D_0 = 5.77 \times 10^{-5} \frac{\phi_1 v}{m} \text{ rads hr}^{-1}.$$

Table 9.3 gives beta bath doses (one- to three-day exposures) which produced LD_{100}'s in apical meristems of several species of native and agricultural plants. The beta radiosensitivity of the most-resistant native plant tested (cocklebur) is about six times that of the white pine. The lethal dose range in crop plants tested varied only by a factor of about 2.

Table 9.3. Lethal Doses ($LD_{100/30\ days}$) of ^{90}Sr-^{90}Y Beta Radiation in Apical Meristems of Some Native and Agricultural Plants

Plant Meristems	Beta Bath Dose (Rads)
White pine	925
Red oak	2315
Eastern cottonwood	3590
Cocklebur	5400
Green bean	3475
Tomato	4715
Wheat	5700
Soybean	6000

Serious shoot growth inhibitions were produced by doses averaging 50 to 60% of lethal meristematic doses. Irradiated flowers of green bean and tomato failed to set seed after doses of 675 and 810 rads (one-day exposure) respectively. Thus, doses in the order of 20% of the lethal dose produced sterility in flowers.

Figure 9.3 illustrates a gradient of growth effects in white pine, a radiosensitive species, following a 12-hr exposure of terminal buds to a cylindrical source placed over the center bud. Dose to buds outside the cylinder averages 30 to 40% of the inside bud dose. Retardation of both shoot and needle growth was produced by acute doses in the order of 100 to 200 rads.

The probable severity of beta radiation effects from fallout can be assessed by comparing these radiosensitivity data with current estimates of beta dose from weapons fallout. Wong[10] estimates a five-day beta contact dose of 7.4×10^3 rads over an area of 2.3×10^3 square miles following a 1-megaton weapon burst with 50% fission. Beta bath doses for this case range from 2.7×10^3 rads at 10 cm in air to 6.3×10^2 rads at 1 m in air. Thus contact doses of beta radiation over this 2.3×10^3 square mile area could be expected to kill species falling in the range of radiosensitivity reported here. The beta bath doses could be expected to produce a range of biological effects from mortality of sensitive species to serious growth inhibitions and sterility of more-resistant species.

[9] W. B. Lane, SRI-MU-6358 (1968).

[10] P. W. Wong, NRDL-TR-68-11 (1967).

Fig. 9.3. Buds of White Pine One Week Following a 12-hr Exposure to a ^{90}Sr-^{90}Y Cylindrical Source. Source was on the center bud, which after 338 rads has failed to grow. Surrounding lateral shoot buds show growth curvature and inhibition of needle elongation on the side which faced the source (122 rads).

MINERAL UPTAKE BY IRRADIATED PLANTS

J. P. Witherspoon Carol E. Macklin

In postattack environments the capacity of irradiated plant populations to absorb and translocate minerals may be important to their survival.

A study on the effects of acute, sublethal beta radiation on potassium and phosphorus uptake in bean plants (*Phaseolus vulgaris*) was completed this year. Young bean plants (shoots only) were exposed to 1125, 2250, and 4500 rads of ^{90}Sr-^{90}Y beta radiation from a 34-cm-diam disk source at a dose rate of 4500 rads/hr. Following irradiation the plants were placed in aerated Hoagland's nutrient solution and maintained in a growth chamber (82°F day, 75°F night, 15-hr day) for the entire experiment. Plant nutrient solutions were sampled through time, and potassium and phosphorus contents were determined. Nutrient solutions were changed at each sampling period. At 45 days postirradiation plants were harvested, and root-shoot biomass and potassium and phosphorus content were determined.

Growth rate was reduced in all radiation treatments, and 4500 rads reduced height growth about 60%, although shoot biomass was similar to controls due to radiation-induced development of lateral branches.

Figure 9.4 shows the uptake rates of potassium and phosphorus in bean plants following the 4500-rad treatment. Uptake rates of potassium in irradiated plants increased over controls up to about 3 weeks postirradiation, while phosphorus uptake rates decreased for about 30 days. Maximum potassium uptake rate in plants receiving 4500 rads was 36% over that of controls. For phosphorus, the maximum decrease was 48% below controls. Increased potassium uptake was probably due to radiation-induced changes in membrane permeability. Analyses of harvested plants showed that most of this potassium was localized in the root system. Decreased uptake of phosphorus was probably due to decreased growth and metabolism of irradiated plants. Phosphorus, unlike potassium, is bound into many organic compounds that are associated with metabolism and energy transfers in plant tissue. The shape of the phosphorus uptake curves approximates that of the growth rate curve.

By 30 to 35 days postirradiation, phosphorus and potassium uptake rates were similar in irradiated and control plants. Vegetative growth was essentially stopped after 1 month due to onset of flowering.

These temporary alterations of nutrient uptake following acute radiation treatment suggest the possibility that under chronic radiation, stress changes in nutrient budgets may affect survival of plants growing on sites of low fertility.

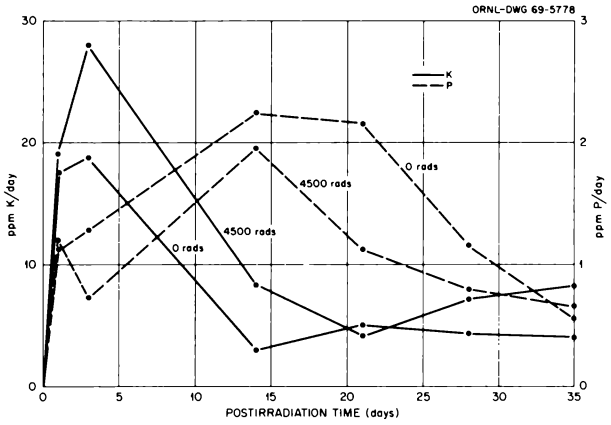

Fig. 9.4. Average Rates of Potassium and Phosphorus Uptake by Bean Plants. Controls are compared with plants treated with an acute exposure of 4500 rads ^{90}Sr-^{90}Y beta radiation. Each point represents an average of five plants.

ECOLOGICAL RESPONSES OF TREES TO FAST-NEUTRON RADIATION AND REDUCED LIGHT INTENSITIES

W. F. Harris

Assessment of the interactions between sublethal ionizing radiation and levels of other environmental factors is a necessary part of evaluating the ecological consequences of indiscriminate or accidental radiation exposure of landscapes. Few studies have experimentally evaluated the interaction of ionizing radiation and environmental stress using measures of treatment effect that relate directly to ecological interpretations. A study was begun this year which will provide some experimental basis for understanding species response to radiation and associated environmental stresses.

This study was designed to evaluate the effects of sublethal radiation stress and reduced postirradiation light environment on trees. Seedlings of shade-intolerant yellow poplar (*Liriodendron tulipifera* L.) and shade-tolerant silver maple (*Acer saccharinum* L.) were given acute fast-neutron doses of 200, 300, and

400 rads as dormancy was breaking. The highest dose was approximately 40% of the $LD_{100/1\ year}$ value. Roots of irradiated seedlings were shielded with 8 in. of barytes concrete to simulate shielding which would occur in the field from soil and microtopographical relief. The seedlings were then grown in 100, 50, and 25% of full sunlight. Plants were watered regularly and were fertilized to remove possible mineral deficiencies which might be interpreted as radiation effects.

At intervals during the growing season, three replicates of each treatment were harvested. Measurements were made on growth of stems, leaves, roots, bud mortality and leaf area. Samples of roots, stems, and leaves were taken for analysis of certain macronutrients (P, K, Fe), chlorophyll and carotenoid content, and carbohydrate accumulation. At 100 days postirradiation net photosynthesis of treated plants was measured, and twice during the season whole plant transpiration was measured.

Analysis of yellow poplar seedling root-shoot ratio (*R/S*) response and net photosynthesis are indicative of the treatment effects. The *R/S* values tend to be constant for a given taxon for a specified age and environment. Any reduction in *R/S* values from the norm implies a decreased amount of root material for a unit amount of shoot material. Ecologically, a reduced *R/S* value implies a decreased competitive ability. Specifically, reduced *R/S* values mean a decrease in water and mineral supplying tissue and a decrease in the amount of stored carbohydrate for subsequent spring growth. Figure 9.5 summarizes *R/S* value response for radiation control yellow poplar seedlings in the three light environments over a 195-day period. The reduction in *R/S* values with reduced light was statistically significant ($P < 0.05$) by 115 days postirradiation.

An additional radiation stress further reduces *R/S* values within a particular postirradiation light environment. Figures 9.5*b* to *d* summarize the response of *R/S* values for radiation treatments within the three postirradiation light environments. The effect of radiation on reducing *R/S* values was statistically significant ($P < 0.05$) 45 days postirradiation. At 195 days postirradiation 400 rads of fast-neutron radiation had an effect on *R/S* values of 100% full sun-grown seedlings (Fig. 9.5*b*) similar to that found in 50% full sun on radiation control plants (Fig. 9.5*a*). The effect of radiation on *R/S* values of seedlings grown in 25% full sun was not as severe as for other light environments (Fig. 9.5*d*). The reductions in *R/S* values following irradiation for 100 and 25% full-sun-grown seedlings were similar when expressed relative to the comparable control plants, but after 195 days the slope of the radiation effect on actual *R/S* values was twice as great for 100% full-sun-grown plants. This differential response to radiation stress between optimum and suboptimum light environments implies that light-suppressed plants respond at a lower rate to an additional radiation stress.

The response of seedlings in 50% full-sun postirradiation light environment (Fig. 9.5*c*) indicates more complete recovery for plants receiving 400 rads compared with other doses. This phenomenon appeared to be related to terminal bud mortality following irradiation, which occurred sooner and to a greater degree with the 400-rad treatment than with the other doses used. Death of the dominant terminal buds initiated lateral shoot development, thus increasing leaf area and photosynthetic potential. Recovery of *R/S* values for the 400-rad treatment occurred in 100% full-sun-grown plants (Fig. 9.5*b*), although recovery after 195 days was not as complete as for the 400-rad treatment in a 50% full-sun environment. Even though 25% full-sun-grown plants produced lateral growth, response was generally poor because of reduced light.

Reduction in *R/S* values implies reduced amounts of photosynthate available for root growth either as a result of altered allocation of available photosynthate, reduced rate of photosynthetic processes, or a combination of altered structure and function. Measurements of net photosynthesis (milligrams of CO_2/100 cm^2/hr) made 90 to 126 days postirradiation indicated that both reduced light environment and sublethal fast-neutron radiation reduced net photosynthesis (Table 9.4). At 100 days postirradiation aberrant foliage, which was produced initially, had been diluted with varying amounts of morphologically normal foliage, so that the pattern of net photosynthesis with treatment was not entirely consistent.

Patterns of net photosynthesis which were evident 100 days postirradiation indicated that light decreases net photosynthesis. Considering the total response of net photosynthesis over the range of light intensities used (0 to 4000 ft-c) 50 and 25% full-sun-grown plants had, respectively, 81 and 47% of the photosynthetic potential as 100% full-sun-grown plants. Such sharp reductions in photosynthesis response to reduced light environment may be a partial reason for the shade intolerance of yellow poplar.

Even though the pattern of net photosynthesis is not entirely consistent at 100 days postirradiation, radiation appears to reduce rates of net photosynthesis within a particular light environment. For example, 200, 300, and 400 rads of fast-neutron radiation

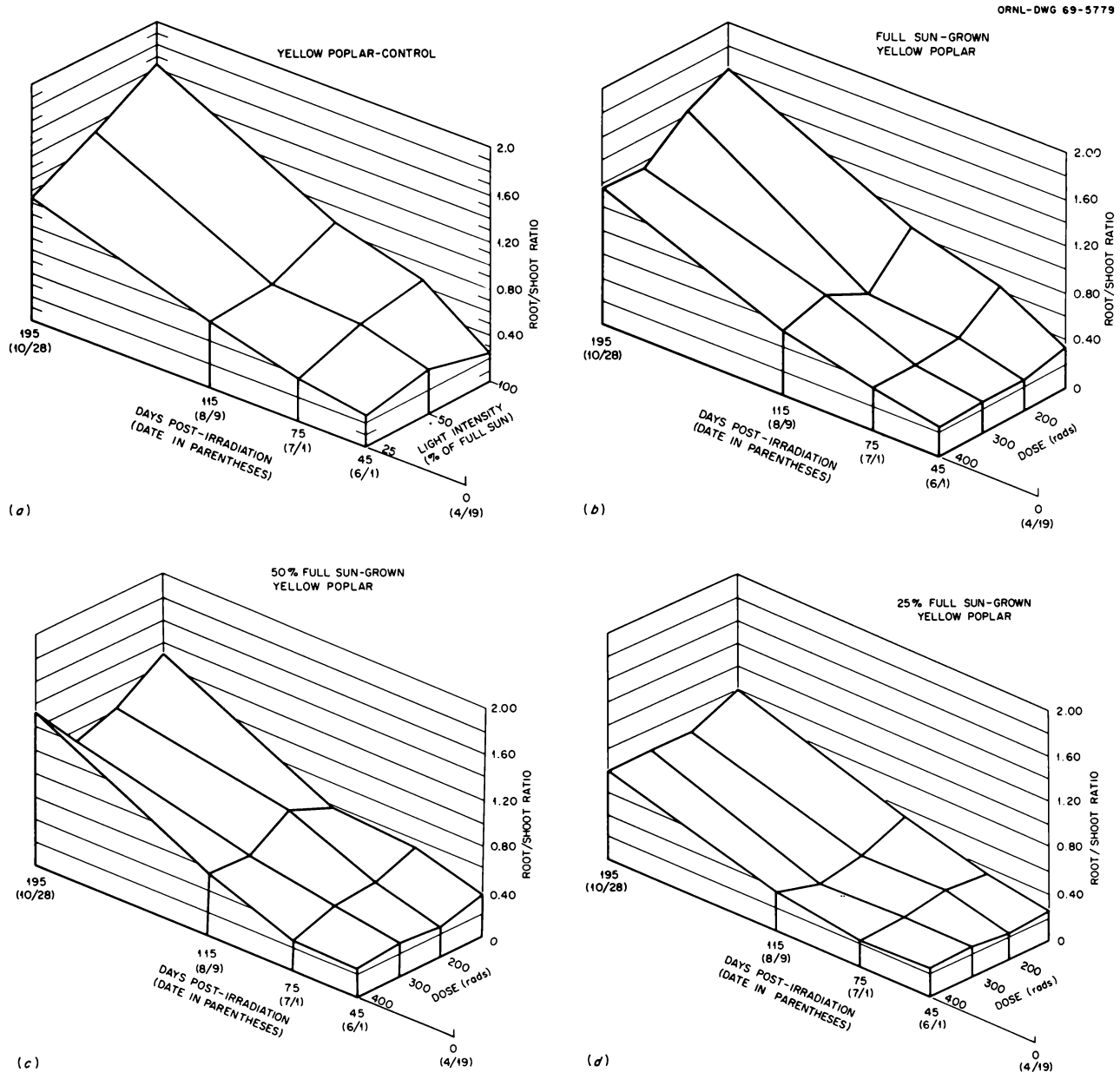

Fig. 9.5. Root-Shoot Ratios of Yellow Poplar Seedlings Exposed to Acute Fast Neutron Radiation and Reduced Postirradiation Light Environment Through One Growing Season. (*a*) Response through time of radiation control plants to reduced light environment, (*b*) response through time of irradiated plants in 100% full sun, (*c*) response of plants in 50% full sun, and (*d*) response of plants in 25% full sun.

Table 9.4. Net Photosynthesis in Yellow Poplar Seedlings Exposed to Fast-Neutron Radiation and Grown Under Varying Sunlight Intensities

Measurements were made in a growth chamber under four constant light intensities at 25°C

Treatments		Light Intensity During Photosynthesis Measurements (ft-c)			
Sunlight Intensity (%)	Dose (rads)	4000	2800	1300	250
100	0	1.96 ± 0.34[a]	1.88 ± 0.15	1.45 ± 0.10	−0.02 ± 0.09[b]
	200	1.10 ± 0.08	0.97 ± 0.07	1.13 ± 0.09	−0.16 ± 0.09
	300	1.69 ± 0.05	1.58 ± 0.05	1.22 ± 0.15	−0.00 ±
	400	1.23 ± 0.12	1.62 ± 0.18	1.04 ± 0.30	0.19 ± 0.21
50	0	1.15 ± 0.11	1.36 ± 0.07	1.25 ± 0.09	0.72 ± 0.09
	200				
	300	0.59 ± 0.06	0.68 ± 0.06	0.74 ±	0.46 ± 0.03
	400	1.35 ± 0.05	1.40 ± 0.06	1.35 ±	0.45 ±
25	0	0.86 ± 0.10	0.87 ± 0.13	0.72 ± 0.10	0.26 ± 0.04
	200	0.81 ± 0.04	1.00 ± 0.03	1.23 ± 0.05	0.35 ± 0.03
	300	0.91 ± 0.14	1.89 ± 0.24	2.51 ± 0.26	0.65 ± 0.06
	400	0.61 ± 0.10	0.76 ± 0.13	1.14 ± 0.09	0.59 ± 0.11

[a]Values are average milligrams of CO_2/100 cm^2 foliage per hour ± 1 standard error where available.

[b]Negative values indicate excess of respiration over photosynthesis.

reduced total net photosynthesis over light intensities measured to 85, 78, and 63% of the 100% full-sun-grown radiation control plants. Inconsistencies in the net photosynthesis pattern following treatment appear to be related to lateral shoot production of morphologically normal foliage. However, at higher light intensities measured (2800 and 4000 ft-c), the reduction in rate of net photosynthesis indicates the possibility of damage at a level not manifested in external morphology. Additional experiments will follow the course of net photosynthesis through the growing season and should show a more consistent pattern.

Analyses of root-shoot ratio and photosynthetic responses tend to support the hypothesis that sublethal radiation stress narrows the ecological amplitude of a taxon, that is, the degree to which the organism can tolerate environmental stress. Subsequent data on second-year plant growth and development, along with certain mineral and organic analyses, should give quantitative support to this hypothesis.

DECOMPOSITION OF IRRADIATED PERSIMMON LEAVES

W. A. Thomas

Ionizing radiation of sufficient dose alters the morphology and physiology of foliage, changes that undoubtedly influence the life of the plant and may influence the decomposition rate of leaves after abscission. The large amounts of organic matter added to the forest floor every autumn in deciduous forests and its subsequent decomposition constitute one of the most important transfers of material in ecosystems.

To study the effects of radiation on decomposition of leaves, 1000 persimmon (*Diospyros virginia*) leaves were collected in mid-September 1967 as they fell from a total of four small persimmon trees growing 15 m from the unshielded Health Physics Research Reactor (HPRR). On the same collection dates, an additional 1000 leaves were obtained from nonirradiated persimmon trees of the same size and growing on the same soil type and same slope azimuth as the irradiated ones. Control trees were about 200 m from the reactor and were shielded from radiation by a hill. About 80% of the irradiated leaves displayed apparent abnormalities, such as thickening, whereas all control leaves had smooth normal leaf blades.

Because the HPRR operates on an irregular schedule, the dose received by irradiated trees cannot be considered to be either acute or continuous. In addition, the trees have been irradiated since 1963, and the leaf buds were irradiated during the dormant season before leaf expansion in the spring. Based on a dose rate/kilowatt-hour ratio and consideration of distance from reactor to the trees, the leaf buds received a dose (tissue dose in air) of 100 rads of gamma plus 430 rads of fast neutron irradiation, and the leaves received an additional 80 rads of gamma and 340 rads of fast-neutron

irradiations. These same trees exhibited foliar abnormalities and retarded branch growth as early as 1964[11].

Two series of litter-bag samples, one with irradiated leaves and the other with control ones, were prepared by putting 20 air-dried leaves with a range in total weight between 3.40 and 3.50 g in each of 39 nylon-net bags (25 X 25 cm; 2 mm mesh). Extra leaves provided conversion factors to the oven-dry-weight basis.

The samples were each placed in as natural a position as possible on the litter layer of an oak-hickory stand on October 19, 1967, during the peak of deciduous leaffall. Collection and oven drying of three samples every four weeks from each of the two series permitted estimation of weight losses during the first year in litter. All irradiated and nonirradiated samples appeared to be well incorporated in the natural litter layer throughout the year.

Loss of weight from the decomposing leaves (Fig. 9.6) occurred at three rather distinct rates in both series of samples: (1) rapid loss for the first 12 weeks due to initial fragmentation and leaching of water-soluble materials, (2) very slow rate during winter (from weeks 12 to 28), and (3) an accelerated rate starting in early May (week 28), corresponding with more favorable conditions for decomposers and extending throughout the year as a result of biological decomposition and physical breakdown and leaching of the smaller fragments.

[11] J. P. Witherspoon, *Health Phys.* 11, 1637–42 (1965).

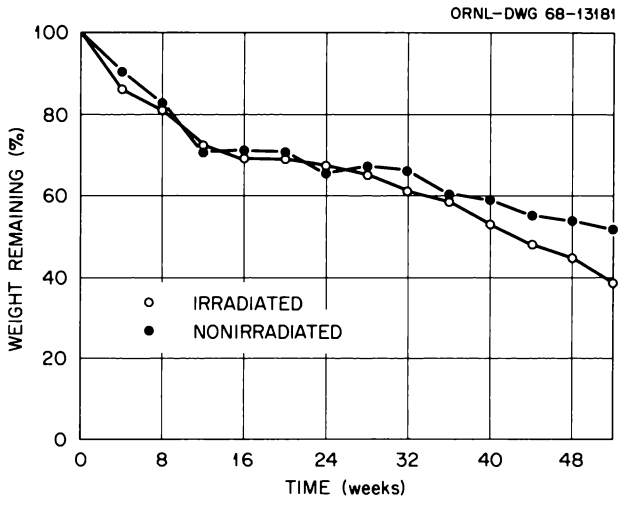

Fig. 9.6. Decomposition of Irradiated and Nonirradiated Persimmon Leaves. Each point represents the mean of three litter-bag samples; variation about the mean values is discussed in the text. Week 0 was 19 October 1967.

Regression analyses of the loss rates yielded the following values, expressed as percentage of weight lost per week.

Week	Loss Rate ($\bar{X}$ ± S.E.)	
	Irradiated	Nonirradiated
0–12	2.20 ± 0.16	2.34 ± 0.18
12–28	0.41 ± 0.08	0.24 ± 0.19
28–52	1.10 ± 0.10	0.75 ± 0.09

No significant differences ($P > 0.05$), as determined by the homogeneity of regression test, occurred between the irradiated and nonirradiated loss rates for either the 0–12 or 12–28 week periods. The loss rate from early May to October (week 28–52) did differ significantly ($P < 0.025$). The mean percentage of weight lost from the three irradiated samples did not significantly differ ($P > 0.05$) from that of the nonirradiated samples at any collection date until weeks 48 (55.4% ± 0.9 vs 46.2% ± 2.1) and 52 (61.5% ± 1.5 vs 48.3% ± 2.9), when the percentage lost from irradiated leaves significantly exceeded that from controls. The coefficients of variation for the three litter-bag samples at each of the 13 collections averaged about 5% for both the irradiated and the control leaves.

The doses required to alter the mineral composition of plant material and the activity of microorganisms using the material as substrate are in the kilorad range, much higher than the doses received by leaves in this study. Woodwell and Marples[12] found that chronic gamma irradiation of scarlet oak (*Quercus coccinea*) trees in the Brookhaven Irradiated Forest did not significantly alter the decomposition rate of foliage. The increased rate of weight loss from irradiated leaves in summer may be due to the favorable habitat afforded decomposers in convolutions of those leaves. The convolutions could provide concealment for decomposers and moderate the fluctuations in moisture and temperature. The coarseness of thickened areas could also affect the samples' palatability for litter-decomposing organisms.

Results of a similar study after a lethal dose to the trees certainly may be different because of concomitant effects of the radiation – specifically, a reduction in tree canopy which would result in markedly altered temperature and moisture regimes, factors which directly, and indirectly through influences on populations of decomposers, affect the decomposition rate of organic material.

[12] G. M. Woodwell and T. G. Marples, *Ecology* 49, 456–65 (1968).

10. Radionuclide Cycling in Terrestrial Ecosystems

Regina M. Anderson
C. E. Baker[1]
F. S. Brinkley[2]
E. E. C. Clebsch[3]
R. C. Dahlman
Gladys J. Dodson[4]
P. B. Dunaway[4]
N. T. Edwards[5]
C. W. Francis[2]
Marilyn L. Frank[4]
Mary P. Hoglund[5]
J. M. Kelly[3]
J. F. McBrayer[6]
C. R. Malone[7]
Virginia Merchant[8]
B. C. Moulder[1]
D. J. Nelson[4]
J. S. Olson[4]
R. V. O'Neill[4]
P. A. Opstrup[3]
L. N. Peters[4]
D. E. Reichle[4]
G. R. Sandberg[5]
M. H. Shanks[4]
Joyce D. Sheedy[9]
Gerald Stanhill[4,10]
Margaret B. Swartout[9]
Tsuneo Tamura[2]
W. A. Thomas[4]
R. I. Van Hook[1,4]
F. W. Wiman[9]
Martin Witkamp[4]

Research on processes and components of terrestrial ecosystems emphasizes (1) the structure and mechanisms governing the function and ecological organization of natural landscapes, for example, nutrient cycling, productivity, and energy flow; (2) the relation of these processes to the distribution and flux of radionuclide and other pollutants in the environment; and (3) the application of radioisotope techniques and computer simulation to developing predictive mathematical models of ecosystem performance.

The need for the capacity to understand, describe, and develop predictive capabilities about the performance of natural ecosystems follows from recognition that man's impact on his environment should be anticipated before damage is done, not afterward. Such ecological competence is a prerequisite to anticipating the pathways and fluxes of radionuclide contaminants, other environmental pollutants, and vital nutrient resources. The experimental application of radionuclides and tracer techniques continues to be invaluable in extending our knowledge of fundamental ecological processes.

Ecosystem research on radionuclide cycling has concentrated on a long-lived fallout radionuclide, ^{137}Cs, in two contrasting ecosystems: a mesic *Liriodendron* forest and a *Festuca-Andropogon* grassland. In these studies techniques are being developed and tested using radionuclide tracers to identify and quantify ecosystem processes, for example, plant-soil-root relations, productivity, animal food chains, and microbial activity (Fig. 10.1). Plant production and food-chain studies also have examined the pathways and fluxes of important nutrient elements in these ecosystems using ^{47}Ca, ^{22}Na, ^{42}K, and ^{54}Mn. Other research includes the cycling of selected radionuclides (e.g., ^{60}Co and ^{144}Ce) in plant-soil systems based upon nutritional requirements of the species and position of the element in the periodic table. Objectives are to develop predictive capability for chemically related elements, whose radionuclides may be potential environmental contaminants as by-products from nuclear operations. Further investigations using other radionuclides will eventually be required to round out knowledge of radionuclide and

[1] ORAU Predoctoral Fellow.
[2] Radioactive Waste Disposal Section.
[3] University of Tennessee.
[4] Dual capacity.
[5] Consultant.
[6] Summer employee.
[7] ORAU Postdoctoral Fellow.
[8] ORAU undergraduate participant.
[9] ORAU-NSF undergraduate participant.
[10] Alien guest.

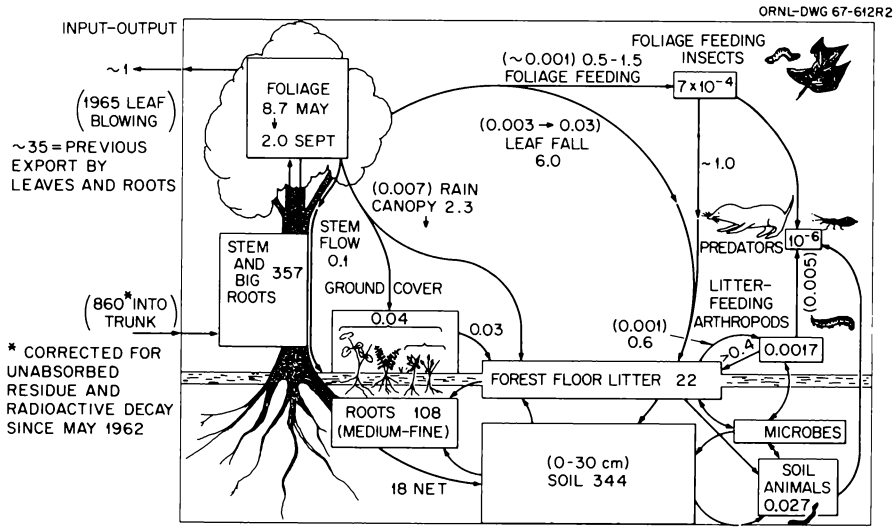

Fig. 10.1 Biogeochemical Cycle of ^{137}Cs in a Forest (*Liriodendron tulipifera*) Ecosystem. Trees of this forest were originally tagged with a total of 467 μc (equivalent to 934 $\mu c/m^2$ ground surface) of ^{137}Cs in May 1962. Continuous inventory has followed the seasonal and annual distributions and fluxes of ^{137}Cs among biotic and abiotic components of the ecosystem. Data presented in this figure are for the 1965 season. Numbers in boxes are microcuries of ^{137}Cs per square meter of ground surface. Arrows indicate the pathways of ^{137}Cs transfer between compartments; numbers by the arrows are estimates of the annual flux, while numbers in parentheses are the averaged transfer coefficients ($days^{-1}$) of ^{137}Cs for the seasons during which the process occurs.

stable element dynamics in contrasting terrestrial ecosystems. Emphasis has been placed on synthetic interpretation of trophic level concentrations and transfers of biologically important radionuclides to develop mathematical descriptions of radionuclide behavior in the environment.

TRENDS IN CANOPY CONTENT OF ^{137}Cs IN TAGGED *LIRIODENDRON TULIPIFERA* TREES

J. S. Olson L. N. Peters Regina M. Anderson

The dominant tulip poplar trees that were tagged in late May 1962 showed a decreasing trend of maximum canopy radioactivity in every year through 1965 (Fig. 10.2) at a rate that would have drastically diminished the main source of ^{137}Cs for animal food chains and other living parts of the ecosystem. Some decrease has continued since 1965, but at a much slower rate. In all years there has been a consistent tendency for a maximum concentration of ^{137}Cs in foliage in spring. Summer is generally a season of decrease in concentration of ^{137}Cs and in total amounts per shoot in spite of some further growth of new leaves after the main period of April-May growth of new shoots. Maximum ^{137}Cs concentration (microcuries per gram) was found around early June in 1962 and through 1964 but in late April or early May in 1965 through 1967.

The yearly reduction is accomplished by three mechanisms: (1) export of ^{137}Cs from foliage to woody tissues during both mature and senescent stages of leaf development, which apparently accounts for the greatest amount of reduction; (2) removal of ^{137}Cs from foliage by rain and dew leaching prior to mid-September; and (3) dilution in ^{137}Cs concentration (microcuries per gram of dry weight) by the formation of new tissue. Some replenishment of leaf ^{137}Cs in summer may be continued by replenishment from ions in the transpiration stream, even after the income rate is exceeded by net loss rate. However, it is not yet known whether replenishment from reserves kept within the tree accounts for either the apparent upward fluctuations in late summer of 1967 or the slower decline since 1965. An alternative hypothesis is that significant recycling from the large reservoir of ^{137}Cs in the soil has become relatively more important than in the early years of the experiment, when the vegetation "pool" was relatively much greater and the soil "pool" was smaller.

Cumulative losses through both rainfall and litterfall (Fig. 10.2) have been much less in the later years than during the first growing season (1962). Yet the total from both sources is still far too small to account for the large reservoir of ^{137}Cs already moved to the soil (see below). These findings and the analyses of root

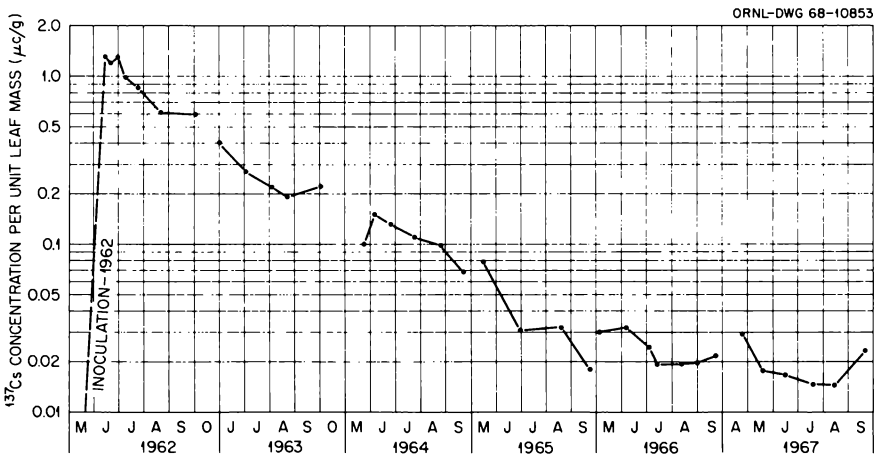

Fig. 10.2. Decline in ^{137}Cs Concentration During Each Growing Season and Between Years (Especially 1962–1966).

distribution and mobility of ^{137}Cs by Waller and Olson[11] and by Olson[12] confirm the interpretation that turnover from the root portions of the tagged trees is relatively more important as the major pathway of transfer out of the dominant vegetation. Unusually high concentrations of ^{137}Cs in the rhizosphere are also confirmed by data of Francis, given later in this chapter.

SEASONAL PATTERN AND COMPONENTS OF LITTERFALL IN *LIRIODENDRON* FOREST TAGGED WITH ^{137}Cs

Regina M. Anderson J. S. Olson L. N. Peters

Income of ^{137}Cs to the forest floor from litterfall since 1962 has been approximately three and one-half times greater than contributions from rainfall (Fig. 10.3). About 47 $\mu c/m^2$ was transferred the first year after inoculation, but rates of transfer decreased in subsequent years, as the ^{137}Cs in the canopy foliage diminished. The amount of ^{137}Cs transferred in 1967 (2 $\mu c/m^2$) nearly equaled that of 1966. One reason for the leveling off in annual litter contribution of ^{137}Cs is the corresponding leveling in canopy concentrations. While the concentration in live leaves was slightly lower in 1967 than in 1966, the cumulative mass of litterfall was greater in 1967 (Fig. 10.4).

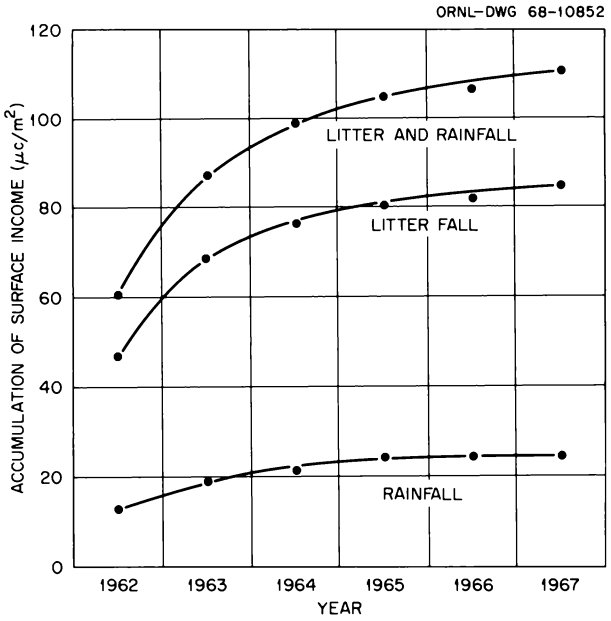

Fig. 10.3. Cumulative Input over Years of ^{137}Cs into Litter and Soil of Tagged *Liriodendron* Forest by Rain Leaching and by Litter Fall.

This increase in litter mass was partly due to higher production of foliage in the rainy summer of 1967. Table 10.1 shows that some of this increase was in *Liriodendron* leaves, even though the mass per growing shoot was slightly less in 1967 than in 1966.[13] Continued infestation of the stand by the weevil

[11] H. D. Waller and J. S. Olson, *Ecology* 48(1), 15–25 (1967).

[12] J. S. Olson, "Distribution of ^{137}Cs Transfers of Roots in a Tagged Mesophytic Appalachian Forest in Tennessee," pp. 133–39 in *Methods of Productivity Studies in Root Systems and Rhizosphere Organisms*, M. S. Ghilarov *et al.*, eds., "Nauka," USSR Acad. Sci., Leningrad.

[13] S. I. Auerbach *et al.*, *Health Phys. Div. Ann. Progr. Rept. July 31, 1968*, ORNL-4316, Fig. 10.1, p. 92.

Table 10.1. Monthly Summary of Litter Fractions (g of dry weight/m^2) for 1965–67 as Input to the Floor of the ^{137}Cs-Tagged *Liriodendron* Forest

	1965						1966						1967					
	Leaves			Others		Total (g)	Leaves			Others		Total (g)	Leaves			Others		Total (g)
	Deciduous		Scales and Needles				Deciduous		Scales and Needles				Deciduous		Scales and Needles			
	Tulip Poplar	Miscellaneous Leaves		Reproductive Parts	Wood		Tulip Poplar	Miscellaneous Leaves		Reproductive Parts	Wood		Tulip Poplar	Miscellaneous Leaves		Reproductive Parts	Wood	
Jan.							7.49	4.51	5.69	12.80	4.20	34.7						
Feb.																		
Mar.																		
Apr.													2.29	5.0	7.5	1.10	11.1	27.0
May	7.9	8.7	3.9	9.6	5.1	35.2	4.51	3.0	1.20	2.70	1.39	12.8	3.30	1.20	2.31	7.5	6.7	21.0
June	14.1	3.9		6.4	1.4	25.8	4.60	1.3	.50	1.49	7.80	15.7	8.20	.60	.90	1.50	4.10	15.3
July	10.4	4.6		4.4	9.0	28.4	9.49	2.41	1.69	1.69	4.60	19.9	14.60	3.39	2.10	1.50	1.80	23.4
Aug.	7.9	1.21	1.30		3.0	13.4	19.69	9.50	2.88	3.78	7.09	43.0						
Sept.	55.6	9.39	5.5		22.5	93.0	34.32	12.1	2.48	6.10		55.0	69.17	26.16	5.17		2.79	103.4
Oct.	104.1	42.6	6.8		7.3	160.8	133.5	46.84	1.87	5.64	0.37	188.1	147.4	70.30	8.3	2.33	4.66	232.8
Nov.	9.8	22.4	4.2		5.6	42.0												
Dec.																		
Total	209.8	92.8	21.7	20.4	53.9	398.6	213.60	79.66	16.31	34.20	25.45	369.2	244.96	106.65	26.28	13.93	31.15	422.9
Percent	53.7	23.3	5.4	5.1	13.5	101	57.9	21.6	4.4	9.3	6.9	100.1	54.7	28.4	6.4	3.2	7.3	
Leaves, percent of total		82						84						90				

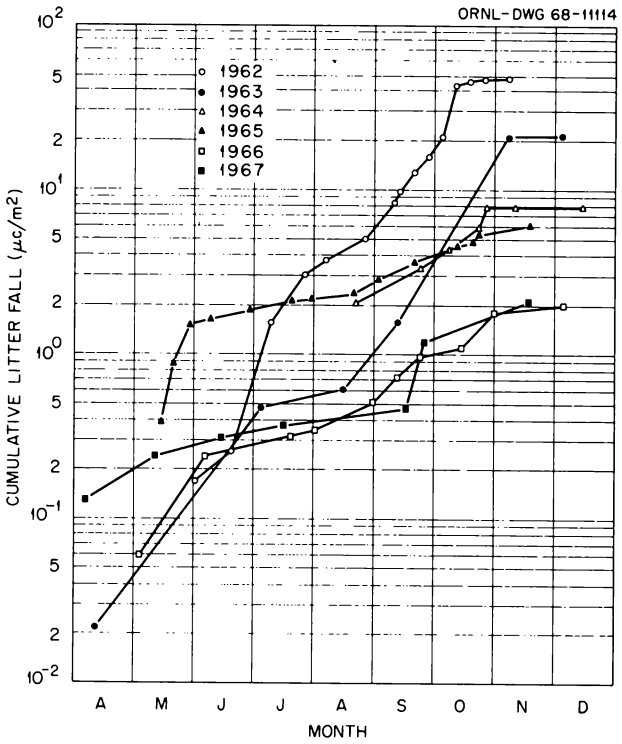

Fig. 10.4. Cumulative Input of ^{137}Cs in Litter.

(*Odontopus calceatus*) led to relatively early and continuing turnover of the new *Liriodendron* leaves as they grew. These leaves became perforated by weevil larvae and adults, and some dropped to the ground prematurely. Perhaps because of the lighter overstory canopy, the fall of non-*Liriodendron* leaves changed from 93 and 80 g/m^2 per year (1965 and 1966); not counting 20 and 16 g/m^2 per year of pine needles (from trees near the edge of the plot) to 132 g/m^2 per year in 1967. Reproductive parts varied from 20 to 34 to 15 g/m^2 in the three years summarized in detail in Table 10.1. The seasonal changes shown in the table indicate that flowering parts and certain seeds that fall early in the season account for more mass than autumn reproductive parts in this kind of forest, unless seed or fruit eaters consume a large fraction before falling. The percentage of leaves in the total litter as collected by 20 plastic baskets (42 cm effective diameter) is relatively high and consistent (82, 84, and 90% in the three years shown here). Coarse branch fall is not adequately sampled by this method, and varies irregularly with natural stand mortality and windstorms.

DISTRIBUTION AND LOSS OF ^{137}Cs FROM ROOTS BY LEACHING OF *LIRIODENDRON TULIPIFERA* L. SEEDLINGS GROWN IN SAND CULTURE

G. R. Sandberg J. S. Olson E. E. C. Clebsch

One-year-old *Liriodendron tulipifera* L. seedlings were inoculated with ^{137}Cs on June 15, 1967. Net increase and initial dry weights were calculated at different time intervals, and the results are given in Table 10.2. Predictive equations were used to calculate the net growth of stems and roots; the total weight of dropped plus harvested leaves was used as a measure of their net increases. Increases in heights of the plants and diameters of the root collars are reported in Table 10.3.

Table 10.2. Initial Estimated and Net Increase in Dry Weight (grams) During the Growing Season[a]

Compartment	June 20 (n = 12)		July 25 (n = 6)		August 24 (n = 7)		October 21 (n = 5)	
	Initial Weight	Net Increase	Initial Weight	Net Increase	Initial Weight	Net Increase	Initial Weight	Net Increase
Leaves	0.00	3.07 ±1.46	0.00	10.97 ±3.86	0.00	23.52 ±10.92	0.00	30.19 ±5.84
Stem	1.45 ±0.84	1.06 ±0.56	1.61 ±0.99	5.06 ±2.70	1.52 ±0.52	11.81 ±3.88	1.88 ±0.96	22.04 ±5.22
Roots[b]	1.70 ±1.03	1.61 ±1.30	1.89 ±1.20	3.32 ±2.47	1.79 ±0.62	11.84 ±3.63	2.21 ±1.12	14.86 ±9.42
Dead roots[c]	0.00	0.00	0.00	0.80 ±0.52	0.00	1.97 ±0.73	0.00	3.66 ±2.10

[a]Mean weight with standard deviation.
[b]Weight of total roots includes weight of dead roots.
[c]Corrected for decay loss.

Table 10.3. Net Increase in Height of Plant and Diameter of Root Collar During Growing Season

	June 20 (n = 12)	July 25 (n = 6)	August 24 (n = 7)	October 21 (n = 5)
Height, cm	10.21 ± 4.68	25.22 ± 8.85	43.18 ± 19.11	61.78 ± 7.94
Diameter, mm	1.55 ± 0.97	3.18 ± 0.89	5.42 ± 1.31	7.80 ± 1.19

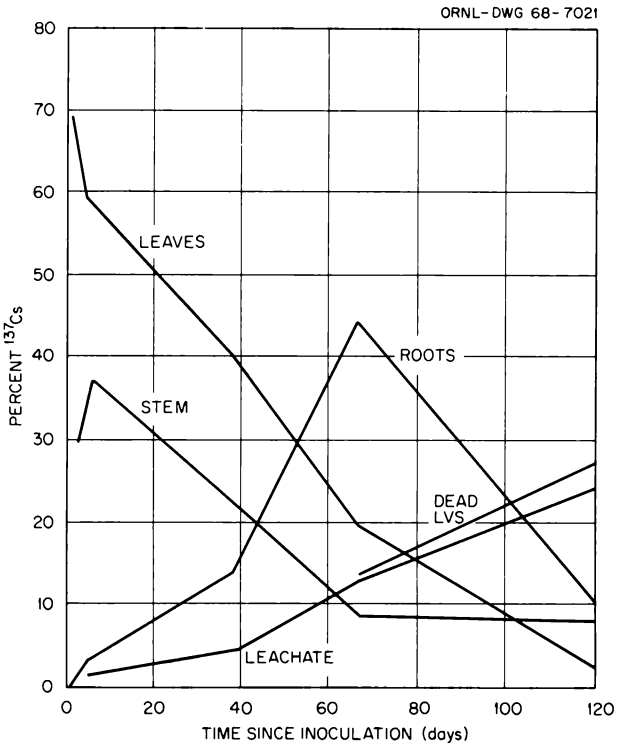

Fig. 10.5. Distribution of ^{137}Cs Expressed as Percent of Total ^{137}Cs Inoculated.

As in the forest experiment[14] the uptake at the beginning of the season was apparently affected by the high transpiration rate. In seedlings almost 70% of the inoculum moved to the leaves on the first day. The roots contained less than 1% of the inoculum on the first day but eventually received almost half of the ^{137}Cs still within the plant by August (Fig. 10.5).

The largest losses from living seedlings during the season were from fallen leaves and leaching. Death of roots and mycorrhizae, exudation, and sloughing off of root cap cells were contributing factors, and were evaluated in sand culture in ways not possible in the field. The ^{137}Cs reported in sand should be considered with leaching loss. Approximately one-third of the original inoculation was lost through the root system. The secondary roots contained two to three times more ^{137}Cs than the primary roots during the entire growing season. A large part of the losses from roots were taken from the secondary root compartment; the amount of ^{137}Cs lost in fallen leaves included some which would have been leached by rainfall in natural conditions because the seedlings were protected from foliage leaching by a plastic canopy. The activity of the roots before death was estimated from the activity per gram of dry weight of the living secondary roots. The activity of the dead roots was subtracted from the estimated value, and a net loss of activity was reported as contribution from dead roots to leachate (plus sand).

THE ACCUMULATION OF ^{137}Cs IN THE SOILS OF A TAGGED *LIRIODENDRON* FOREST

L. N. Peters J. S. Olson Regina M. Anderson

Soil radioactivity (0 to 30 cm depth) has continued to increase since the tagging of trees in 1962 (Fig. 10.6). The 1962 autumn sampling indicated that about 40% of the initial inoculum had already reached the soil (including roots) within the tagged area. Transfer of ^{137}Cs to the soil was less in succeeding years. The amount transferred to the soil by 1967, however, exceeded that for either 1964 or 1965. Approximately 65% (600 $\mu c/m^2$) of the initial inoculation had accumulated in the soil by the October 1967 sampling. A relatively large fraction of soil activity was initially contained in the roots, but this has been continuously released to the soil, so that radioactivity in roots that could be separated manually became a relatively smaller fraction of the total (7% in 1967).

Most of the accumulated ^{137}Cs still has been contained within the litter and organic layer and the surface 10 cm of mineral soil. The activity of litter and organic layer averaged about 32 $\mu c/m^2$ in the late October sampling of 1962 but had decreased to about 19 $\mu c/m^2$ by 1967. Each year there was a net decrease, but at a lesser rate than for foliage. The loss is explained

[14] J. S. Olson, *Health Phys.* 11(12), 1385–92 (1965).

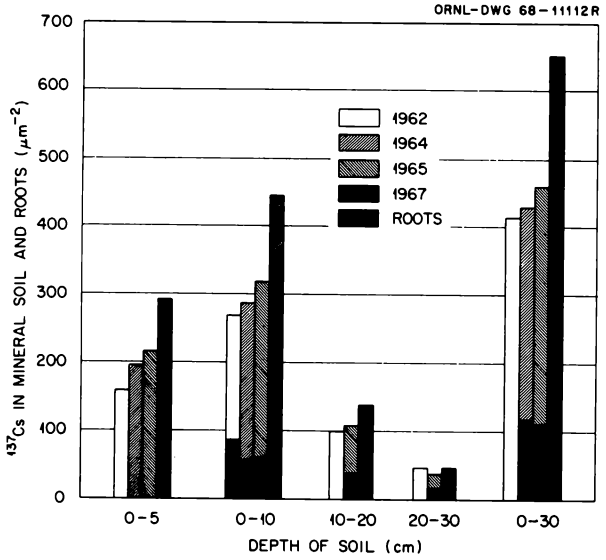

Fig. 10.6. Soil and Root Radiocesium Inside Tagged Plot of Tulip Poplar (*Liriodendron*) Forest from October 1962 to June 1967.

partly by the leaching of ^{137}Cs from litter to the mineral soil (e.g., 50% during the winter months in 1962–63).[15] There is a decreasing amount of surface income to the forest floor each year from leaves. Some upward mixing of soil particles by animals is known to occur, but it is not yet clear whether this is quantitatively important in explaining the difference between rates of foliage and litter changes. Although the ^{137}Cs was gradually leached from organic litter and humus to the mineral soil, it has accumulated mainly in the 0- to 10-cm depth. The leachability of ^{137}Cs from soil minerals is very low. Radiocesium below 10 cm depth has remained relatively constant, and it still seems likely that this contribution could be almost completely from roots.

DISTRIBUTION OF ^{137}Cs IN SOIL OF A TAGGED *LIRIODENDRON* FOREST

C. W. Francis Tsuneo Tamura F. S. Brinkley

Additional information has been obtained concerning the ^{137}Cs distribution in the soil since the 1967 growing season. Early data indicated that the major pathway by which ^{137}Cs is transferred to the soil is through root contribution[16] rather than income from rainfall and litterfall. Roots and root fragments which could be separated from the inorganic soil fraction contributed at least 90% of the total activity on July 16, 1962.[17] However, it has been difficult to obtain data which prove conclusively the transfer (directly or indirectly) of ^{137}Cs in roots to the mineral fraction of the soil. One of the major problems has been inadequate methods to separate very fine roots (<0.5 mm in diameter) from the mineral fraction of soils.

Table 10.4. ^{137}Cs Extracted by *N* Chloride Salts from the A Horizon of an Emory Loam Under a ^{137}Cs-Tagged *Liriodendron* Forest

Extraction Time (hr)	Percent ^{137}Cs Extracted[a] by Solutions of –					
	LiCl	NaCl	KCl	$MgCl_2$	$CaCl_2$	$BaCl_2$
1/4	1.16	2.24	8.46	0.75	2.96	1.19
1	0.71	2.04	9.79	0.84	2.85	0.44
2	0.98	2.24	10.7	0.45	2.50	1.02
4	0.64	2.35	10.3	0.36	2.52	0.76
24	1.10	2.05	12.3	0.84	2.65	1.10
144	1.95	2.28	12.2	0.66	2.63	0.89
312	1.07	2.59	11.9	0.00	2.59	1.00

[a]Five grams air-dried soil (<2mm) – total ^{137}Cs of 9.19 mμc.

Regardless of the pathway involved, the soil has become a major sink for ^{137}Cs, and its distribution within the soil needed to be determined. Methods used to study ^{137}Cs distribution included ^{137}Cs extraction by normal chloride solutions of alkali and alkaline-earth salts; mechanical separations, including sieving; flotation in heavy liquids; and hand removal of roots and barklike material.

Results of the chemical extraction experiment are presented in Table 10.4. Data show that only a small percentage of the ^{137}Cs in the <2.00-mm fraction of soil is extractable by these neutral salts. The highest amount removed was by the K salt (approximately 12% of the total ^{137}Cs) after 24 hr shaking, while the other salts removed only 1 to 2%. Only in the case of the K solution does extraction time appear to be a variable, and its magnitude is very small. (Only 4% more ^{137}Cs was extracted after 312 hr than that extracted in 0.25 hr.) These data conclusively demonstrate that ^{137}Cs in microquantities is not present on cation exchange sites of soils but is rather selectively sorbed to site(s) on or

[15]M. Witkamp and M. L. Frank, *Radiation Botany* 4, 485–95 (1964).

[16]S. I. Auerbach *et al.*, *Health Phys. Div. Ann. Progr. Rept. July 31, 1963*, ORNL-3492, p. 104.

[17]H. D. Waller and J. S. Olson, *Ecology* 48(1), 15–25 (1967).

Table 10.5. Distribution of ^{137}Cs Among Soil Components

Soil Component[a]	Diameter (mm)	Mass Fraction (%)	^{137}Cs per Component (μc)	^{137}Cs/g (μc/g)	^{137}Cs Fraction (%)
Rocks	9.51	12.2	562.0	820.0	1.3
Rocks	3.36–9.51	3.2	295.0	1650.0	0.7
Soil aggregates	2.00–3.36	4.7	1600.0	6050.0	3.6
Soil aggregates	2.00	79.2	4100.0	9190.0	93.3
Bark, woody material		0.1	39.0	6060.0	0.1
Roots		0.6	453.0	14200.0	1.0
Total		100.0	7049.0	7820.0	100.0

[a]Air-dried sample (562 g).

within some soil component. Probably one such site is the edge of minerals showing 10-A basal x-ray spacings. Such minerals (micas, illite, collapsed vermiculite, etc.) are known to have a high affinity for ^{137}Cs in dilute solutions.[18]

Under laboratory conditions 75% of the ^{137}Cs adsorbed by an *Ap* horizon of a Captina soil (microquantities of ^{137}Cs in contact with the soil for 24 hr) was desorbed by a KCl solution in 24 hr, indicating adsorption time and/or laboratory vs natural conditions are parameters that must be considered in understanding more clearly the sorption mechanism. Listed in Table 10.5 are the various soil components and their respective ^{137}Cs contents. Similar to the data one year after tagging, roots (14.2 nc/g) contain higher concentrations of ^{137}Cs than soil <2 mm in diameter (9.19 nc/g), but the ratio (^{137}Cs roots/^{137}Cs soil) of 1.54 in 1969 is considerably lower than the ratio of 36.4 in 1963.[15] Overall inventory indicates that approximately 97% of the total ^{137}Cs is present in the rock and soil aggregates. However, this may be a misrepresentation, because soil passed through 2.00-mm-diam openings will also contain appreciable quantities of small and fragmented roots, and the reverse is true with respect to roots removed manually.

To further separate these components (rock, bark, and roots) from adhering soil particles, samples were dispersed in water with an ultrasonic probe, freeze dried, and sieved. (A sieve with 0.250-mm-diam openings was used in the case of bark and roots and 1-mm diameter for the rocks.) The ^{137}Cs activity of each separate soil component is presented in Table 10.6. Two interesting phenomena occur. First, the concentrations of ^{137}Cs in soil (<2 mm) and that separated from rocks and bark are approximately 9 mμc/g, while the soil separated from the roots contains

Table 10.6. Distribution of ^{137}Cs Among Soil Components After Dispersion in Water by Ultrasonics

Soil Component[a]	Mass Fraction (%)	^{137}Cs/g (nc/g)	^{137}Cs Fraction (%)
Rock (>9.51 mm)			
Rock	96.2	0.45	54.5
Soil	3.8	9.56	45.5
Rock (3.36–9.51 mm)			
Rock	93.2	0.70	53.5
Soil	6.8	8.37	46.5
Bark, woody material			
Bark	58.2	1.31	17.1
Soil	41.8	8.89	82.9
Roots			
Roots	45.6	7.00	24.2
Soil	54.4	18.41	75.8

[a]Soil separated from the individual components by ultrasonics followed by freeze-drying and sieving.

nearly two times this value (18.4 mμc/g). Such data strongly indicate that direct transfer of ^{137}Cs from roots does take place and has occurred for some time, because the concentration of ^{137}Cs in soil (<0.250 mm) is considerably higher (18.4 mμc/g) than that found in roots (7.00 mμc/g).

The rocks contain a surprisingly high relative ^{137}Cs concentration considering the relative surface area. (Theoretical calculations show the soil to have at least five times the surface area as the rocks.) Such a situation may be caused by two conditions: (1) inadequate separation of soil particles from the rock surface or (2) specific primary minerals exposed in the rock surface which have a high affinity for ^{137}Cs adsorption. Further segregation of soil separates (Table 10.7), demonstrating that over 70% of the ^{137}Cs in

[18]Tsuneo Tamura and D. G. Jacobs, "Structural Implication in Cesium Sorption," *Health Phys.* 2, 391–98 (1961).

Table 10.7. Distribution of ^{137}Cs Among Soil Separates

Soil (<2.00 mm)	^{137}Cs Fraction (%)
Sand	5.2
Coarse silt	18.4
Medium silt	38.5
Fine silt	13.2
Clay	13.2
Organo-clay complex[a]	11.5

[a]Separated by "sink-float" method with tetrabromoethane and ethanol (ρ = 1.8 g/cc).

soils (<2 mm) is in the silt size particles, indicates that the latter mentioned condition may prevail.

Future work includes differentiation of the soil separates listed in Table 10.7 by centrifugation through heavy liquid density gradients and x-ray diffraction analyses of the separates so as to elucidate the type of minerals responsible for ^{137}Cs sorption.

POPULATION DENSITY AND BIOMASS OF SOIL MICROINVERTEBRATES IN THE ^{137}Cs-TAGGED *LIRIODENDRON* FOREST

J. F. McBrayer D. E. Reichle M. H. Shanks

The microinvertebrate soil fauna of terrestrial ecosystems are potentially important because of their role

Table 10.8. Estimates of Density and Biomass (Live Weight) of Soil Microinvertebrates in the ^{137}Cs-Tagged *Liriodendron Tulipifera* Forest

Contrasting samples characterize the populations of mineral soil with the total microinvertebrate fauna of soil and litter horizons; values in parentheses are subtotals of preceding major taxonomic categories

	Litter (A_0) plus Mineral Soil (A_1) Populations			Mineral Soil (A_1) Edaphic Populations		
	Mean Weight per Individual (μg)	Mean Number per Square Meter	Mean Weight per Square Meter (mg)	Mean Weight per Individual (μg)	Mean Number per Square Meter	Mean Weight per Square Meter (mg)
Annelida						
Enchytraeidae	18.1	320.8	5.8	47.7	246.5	11.8
Diplopoda	44.5	24.8	1.1	3.6	99.0	0.4
Chilopoda	502.8	370.3	186.2	49.4	197.0	9.7
Pauropoda	0.5	715.8	0.4	0.4	740.6	0.3
Symphyla	14.4	518.8	7.5	25.9	937.5	24.3
Acarina		68,433.1	240.9		34,996.9	180.9
Mesostigmata						
Gamasina	(5.5)	(4,714.6)	(25.9)	(7.7)	(7,552.0)	(58.0)
Rhodocaridae	(2.2)	(2,246.4)	(4.9)	(2.1)	(888.0)	(1.9)
Uropodina	(2.9)	(469.3)	(1.4)	(2.9)	(197.0)	(0.6)
Oribatei	(5.2)	(36,899.0)	(191.1)	(5.6)	(19,745.5)	(110.6)
Trombidiformes (except Scuticaridae)	(0.8)	(15,662.7)	(12.5)	(1.7)	(5,675.9)	(9.4)
Scuticaridae	(0.6)	(8,441.1)	(5.1)	(0.4)	(937.5)	(0.4)
Pseudoscorpionida	145.3	74.3	10.8	0	0	0
Diplura	20.9	419.8	8.8	12.4	987.0	12.2
Protura	*a*	1,258.3	*a*	*a*	839.6	*a*
Collembola	23.6	24,533.2	73.7	33.5	12,292.5	106.5
Entomobryidae	(9.7)	(3,283.0)	(31.8)	(17.4)	(3,998.8)	(69.5)
Isotomidae	(2.9)	(2,764.2)	(8.0)	(5.2)	(4,096.8)	(21.3)
Onychiuridae	(1.5)	(15,524.9)	(23.3)	(3.8)	(3,851.4)	(14.4)
Poduridae	(1.6)	(2,023.6)	(3.2)	(4.1)	(246.5)	(1.0)
Sminthuridae	(7.9)	(937.5)	(7.4)	(3.0)	(99.0)	(0.3)
Coleoptera adults	13.5	197.0	2.7	13.5	49.5	0.7
Coleoptera larvae	26.0	271.2	7.1	25.0	148.5	3.9
Diptera larvae	5.2	2,271.2	11.8	11.6	2,764.2	32.1
Total		99,408.6	556.8		54,290.8	382.8

[a]No estimate of weight available.

in decomposer food chains, which contribute to the recycling of nutrients (as well as pollutants) in the system. The populations of soil microfauna in the ^{137}Cs-tagged *Liriodendron* forest were surveyed in June and October 1968. These data are being used for trophic level interpretations of the bioenergetics of decomposer food chains as well as contributing to the pool size of ^{137}Cs in soil organisms for the ecosystem model (see Fig. 10.1). The density and biomass data in Table 10.8 were obtained from 40 5-cm-diam 18-cm-deep soil cores extracted on modified Tullgren funnels. Samples were designed to enable estimation of the total fauna of both organic and mineral soil horizons (A_0 + A_1) and that portion of the total population (eudaphic animals) associated only with the mineral soil (A_1) horizon. Taxa were measured with an ocular micrometer, and linear dimensions were converted to live weight using appropriate regression equations.[19]

Few thorough studies have been made of the soil fauna of deciduous forests, but our data can be compared with a summary[20] of existing values for other forests. Biomass estimates for Acarina in mull soils range from 200 mg/m^2 in oak forests to 400 mg/m^2 in beech forests, compared with 241 mg/m^2 in the *Liriodendron* forest. Estimates for Collembola averaged about 100 mg/m^2, compared with 74 mg/m^2 in the *Liriodendron* forest. Mull soils are characterized by a smaller biomass of large decomposers compared with mor soils, although the biomass of diplopods (1.1 mg/m^2) includes only immatures. Centipedes (Chilopoda) have the largest biomass (186.2 mg/m^2) of any predaceous group. Our estimates for holometabolous insects, enchytraeid worms, and certain surface-dwelling myriapods are low due to differences in sampling and extraction methods. Previous invertebrate studies in the *Liriodendron* forest have concentrated on macroarthropod populations in litter. Data on microinvertebrate populations (Table 10.8) indicate that at least 70% of the microarthropod biomass of decomposer food chains is eudaphic. Future work on the bioenergetics of decomposer populations will evaluate the role played by the minute but abundant soil fauna in the breakdown of organic detritus (see Characterization of Particulate Organic Matter in Old Field and Forest Soils, later in this chapter).

[19] C. A. Edwards, in *Progress in Soil Biology*, North Holland, Amsterdam, 1967.

[20] A. Macfayden, in *Soil Organisms*, North Holland, Amsterdam, 1963.

SEASONAL DENSITY AND BIOMASS OF FOREST FLOOR INVERTEBRATES

B. C. Moulder Mary Hoglund
D. E. Reichle M. H. Shanks

Soils of the *Liriodendron* forest site are of the mull type, but the faunal composition is intermediate between typical forest mulls, having a greater abundance of large decomposers and mor-type soils, with fewer large decomposers but a greater number of small decomposers. The majority of invertebrates (77.0% by number and 87.7% by weight) collected during the year in ring samples belonged to ten taxonomic groups: Araneae, Chilopoda, Coleoptera, Collembola, Diplopoda, Diptera, Hymenoptera, Lepidoptera (larvae), Orthoptera, and Pulmonata. Of these, Araneae, Chilopoda, and some Coleoptera constitute the primary entomophagous predators on the forest floor. Monthly population biomass for the nine major groups (excluding Araneae) are summarized in Fig. 10.7. Collembola were the most numerous (345.5 individuals/m^2), representing 26.5% of the total annual cryptozoan population. Diplopoda contributed the greatest biomass (249.6 mg dry weight/m^2, or 29.6% of the total annual cryptozoan biomass).

Over 40 spider species, including a few juvenile forms plus the minute linypiids and micryphantids identifiable only to genus or family, were collected from the litter zone during 1966 and 1967 (Fig. 10.8). Total mean density was 126 individuals/m^2 with a mean biomass of 43 mg dry weight/m^2. Mean monthly spider biomass fluctuated differently from that of population density. Lowest spider biomass (15.6 mg/m^2) occurred in August, corresponding with the lowest average density (63.3 individuals/m^2), but biomass peaked during March and April, when numbers were declining sharply. Biomass increased throughout fall and early winter, both as a result of increased numbers (reproduction) and growth. Predatory mortality losses in larger spiders (particularly in adult males searching for mates) caused the sharp reduction in biomass in late spring (from ≅63 mg/m^2 in April to ≅30 mg/m^2 in May). Increased biomass in June (≅47 mg/m^2) was due to late maturation and growth of individuals of the large species *Schizocosa crassipes* (Lycosidae). Decrease in biomass in July (≅26 mg/m^2) was due to death of senescent adults following mating.

Seven major spider families comprised nearly 92% of the total spider populations and over 95% of the total biomass from August 1966 through July 1967. The Dictynidae were the most numerous, with a mean

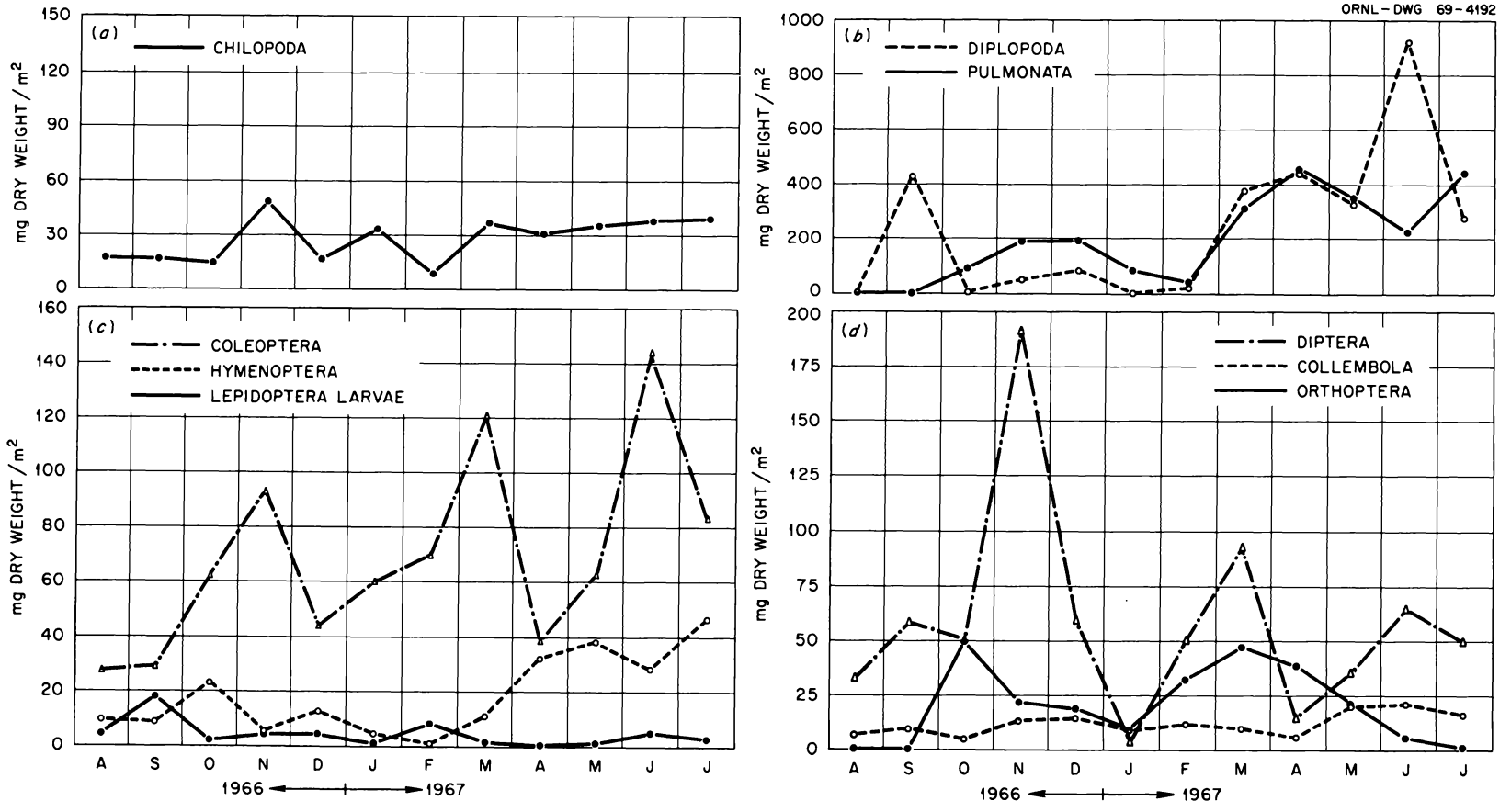

Fig. 10.7. Changes in Mean Monthly Biomass for Nine Major Cryptozoan Groups Collected in Quadrat Samples from August 1966 Through July 1967.

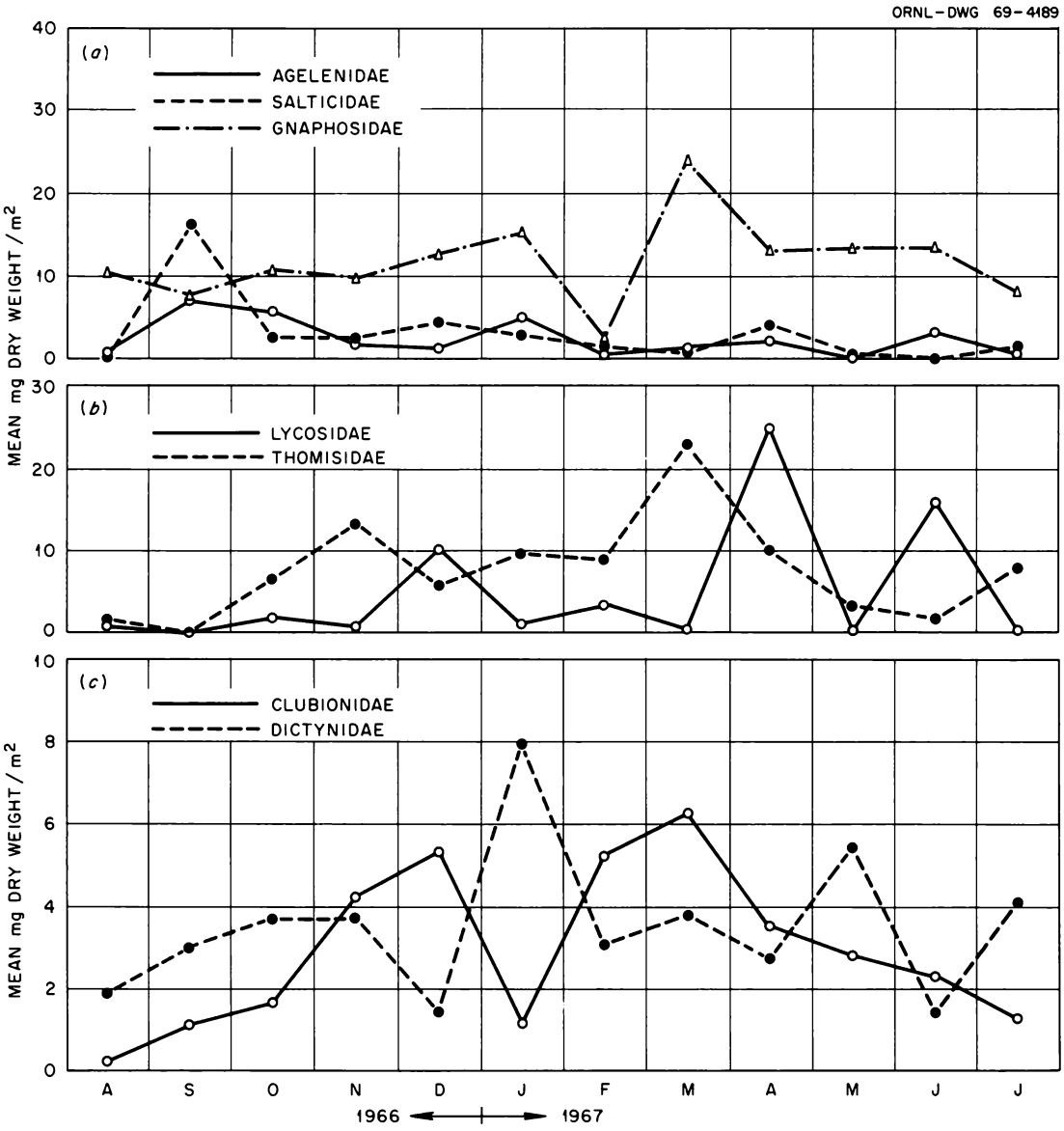

Fig. 10.8. Monthly Fluctuations in Mean Biomass for Seven Major Spider Families Collected in Quadrat Samples (August 1966 Through July 1967).

annual density of over 70 individuals/m^2. Nearly all of these were a single species, *Lathys maculina*. Gnaphosidae contributed the greatest biomass, with an average of 13.3 mg dry weight/m^2. Important spider families and their respective mean annual biomasses were:

Family	Biomass (mg/m^2)
Agelenidae	1.6
Clubionidae	19.5
Gnaphosidae	11.5
Lycosidae	2.1
Dictynidae	70.3
Salticidae	3.7
Thomisidae	6.8

SEASONAL ENERGY BUDGETS FOR FOREST SPIDER POPULATIONS

B. C. Moulder D. E. Reichle Mary Hoglund

Seasonal energy budgets for the predaceous *Liriodendron* forest spider population have been calculated and are depicted as energy flow diagrams in Fig. 10.9. From the estimates of parameters of energy flow (food intake, assimilation, respiratory expenditures, and production), population efficiencies were calculated (Table 10.9).

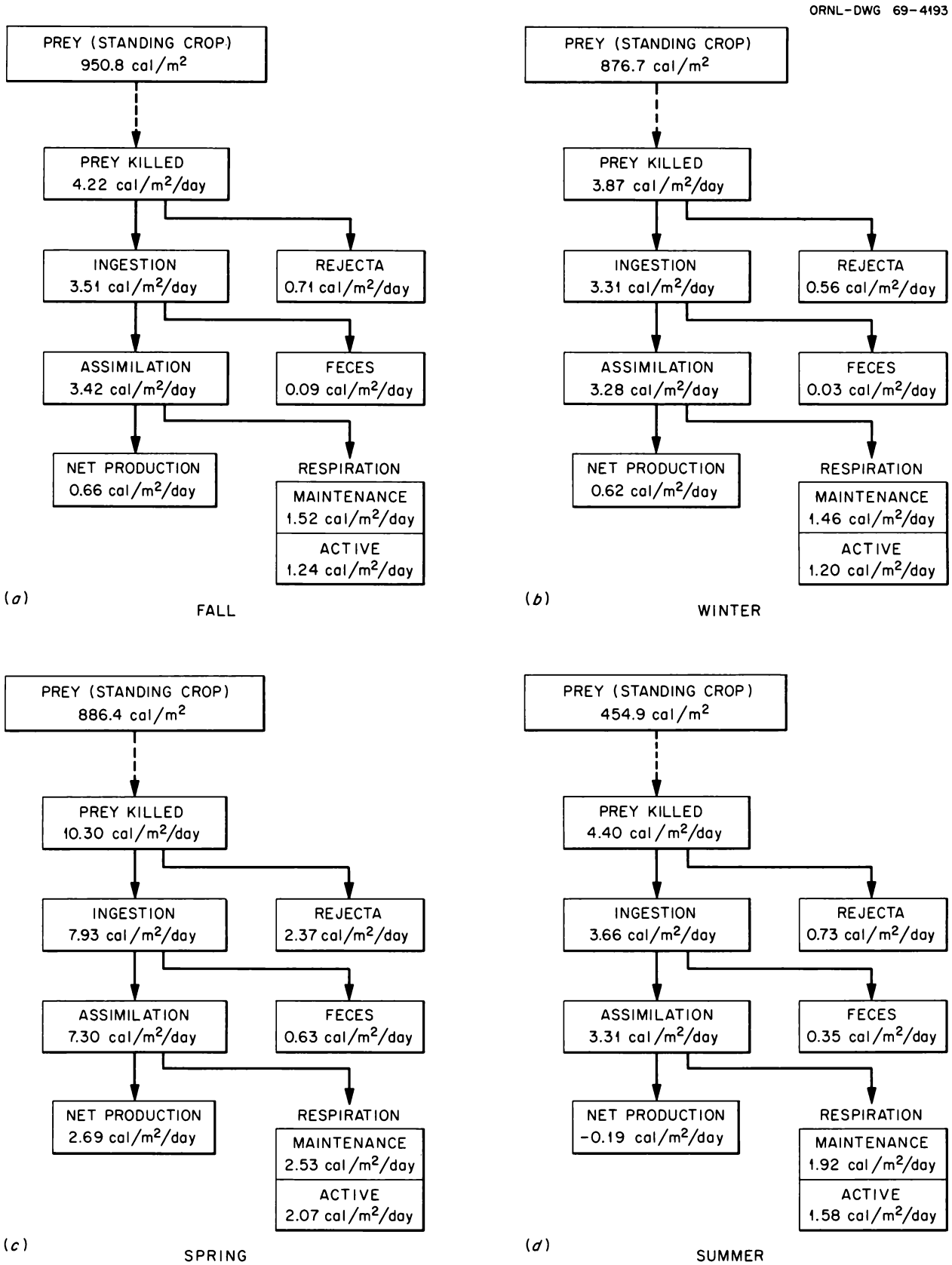

Fig. 10.9. Seasonal Energy Budgets for Forest Floor Spider Populations in a *Liriodendron tulipifera* Forest.

Table 10.9. Comparison of Trophic Efficiency Ratios for Cryptozoan Spider Populations of a Mesic Temperate Deciduous Forest with Predator Trophic Level Efficiencies Summarized for Five Ecosystems by Kozlovsky[a]

	Assimilation / Ingestion	Respiration / Ingestion	Net Production / Ingestion	Respiration / Assimilation	Net Production / Assimilation
Spiders	0.92	0.58	0.34	0.63	0.37
Other Ecosystems[a]	0.90–0.98	0.52–0.67	0.32–0.38	0.62–0.64	0.31–0.37

[a]D. G. Kozlovsky, "A Critical Evaluation of the Trophic Level Concept," *Ecology* 49, 48–60 (1968).

Intake efficiencies (calories of prey ingested/calories killed) for the four seasons were: fall, 0.83; winter, 0.85; spring, 0.73; and summer, 0.83. Spider food utilization is most economical when the greatest proportion of assimilated energy is needed for respiration, that is, during winter and summer (Fig. 10.9). Spiders utilize food less efficiently when more energy is available for growth and more efficiently when energy for growth is at a premium. Assimilation efficiencies (calories assimilated/calories ingested) were: fall, 0.97; winter, 0.99; spring, 0.92; and summer, 0.90. High assimilation efficiency is correlated with advanced trophic level position (secondary or tertiary consumer). Assimilation efficiency of spiders varied seasonally in response to temperature, because at lower temperatures food is retained in the gut for a longer time period. Respiration efficiencies (calories respired/calories ingested) for spiders were calculated to be: fall, 0.78; winter, 0.80; spring, 0.58; and summer, 0.96. These efficiencies were closely related to the ratios of respiration to assimilation, which were: fall, 0.81; winter, 0.81; spring, 0.63; and summer, 1.06. Respiratory losses become greater for higher trophic levels (e.g., spiders) due to the progressive scarcity of food organisms. Predators expend a greater amount of energy in searching and pursuing food than do primary consumers.

Ecological growth efficiency (calories equivalent growth/calories ingested), or the ability to convert ingested calories into biomass (net production), was estimated to be: fall, 0.19; winter, 0.19; spring, 0.34; and summer, −0.05. Ecological growth efficiency declines at trophic levels above primary consumers, decreasing from approximately 50% in herbivores to 35% in top carnivores.[21] Tissue growth efficiency of spiders (calories equivalent growth/calories assimilated), which closely paralleled ecological growth efficiency and which varied inversely with respiration in proportion to assimilation, was calculated to be: fall, 0.19; winter, 0.18; spring, 0.37; and summer, −0.04. Biomass production by spiders was most efficient in spring, a period of rapid growth and maturity for many species. Population efficiencies calculated for spiders during the spring season agree remarkably well with values summarized for predator trophic levels in other ecosystems (Table 10.9). This substantiates the trophic level approach in predicting patterns and rates of energy transfer through natural ecosystems. Recent studies, including the present one, demonstrate that many ecosystems are governed by similar energetic principles.

[21]D. G. Kozlovsky, *Ecology* 49, 48–60 (1968).

SECONDARY PRODUCTION OF BAGWORMS ON DIFFERENT HOST PLANTS

D. E. Reichle Gladys J. Dodson

The evergreen bagworm *Thyridopteryx ephemeraeformis* is a ubiquitous species with a polyphagous habit of larvae including over 100 woody plant species. Although predilection for certain host plants occurs (conifers are favored), the life cycle can be completed on a number of deciduous and coniferous trees. Productivity during the larval stage, however, shows significant differences among host plants. In Table 10.10 are summarized mean body sizes and caloric equivalents for various life history stages of the bagworm reared on seven host plants: eastern red cedar, white pine, arborvitae, blue spruce, redbud, ornamental maple, and honey locust.

Caloric contents of host plant leaves were significantly different ($P \leqslant 0.05$); highest values were found in evergreens, cedar *Juniperus virginiana* (5.41 kcal per gram of ash-free dry weight) and pine *Pinus strobus* (5.32 kcal). Analysis of variance shows that the host tree has a significant effect ($P \leqslant 0.001$) on bagworm performance – for both body weight and caloric content of the different life history stages. Overall,

bagworms on evergreen hosts outperformed their counterparts on deciduous trees, but exceptions were noted. There was also a significant interaction ($P \leqslant 0.05$) between host plant and life stage, implying that not all life history stages perform equally well on the same host tree. Significant differences in body weight and caloric content were demonstrated among life stages. Female stages had highest body weights, correlated with their role in egg production. Males (which are the only active adult sex) had highest caloric values, presumably representing stored energy reserves. Although performance can be evaluated, the mechanism for selection of hosts by bagworms remains unanswered.

Table 10.10. Performance of Bagworm (*Thyridopteryx ephemeraeformis*) Life History Stages on Different Evergreen and Deciduous Tree Hosts

Performance is evaluated as either body weight (mg/individual) or caloric content (cal/g) – mean ± S.E.; numbers in parentheses indicate number of observations. All means followed by the same alphabetic superscript are not statistically different ($P \leqslant 0.05$, Duncan's multiple range test).

	Juniperus virginiana	*Pinus strobus*	*Thuja occidentalis*	*Picea pungens*	*Cercis canadensis*	*Acer palmatum*	*Robinia gleditsia*	Row Mean
Larva								
mg	141.9 ± 10.7 (8)	130.4 ± 6.1 (10)	84.3 (1)	101.6^{a} (1)	110.7 (1)	116.3 ± 9.3 (21)	67.6 ± 10.4 (6)	116.3 ± 5.8 (48)
cal/g	$5405.6^{i\text{-}k}$ ± 18.0 (2)	$5725.6^{f\text{-}k}$ ±85.6 (2)	$5638.3^{g\text{-}k}$ (1)	$6293.4^{a\text{-}g}$ (1)	$5694.6^{f\text{-}k}$ (1)	$5747.8^{e\text{-}k}$ (1)	$5362.0^{i\text{-}k}$ (1)	5666.5 ± 96.3 (9)
Female pupa								
mg	158.5 ± 42.3 (67)	121.1 ± 4.4 (39)	97.0 ± 8.2 (4)	113.1 ± 19.6 (3)	127.4 ± 42.4 (11)	101.6^{a} ± 5.5 (27)	111.8 ± 10.6 (13)	132.1 ± 3.4 (164)
cal/g	$5545.1^{h\text{-}k}$ ± 145.8 (3)	$5813.5^{d\text{-}k}$ (1)	$5854.9^{d\text{-}k}$ ± 132.6 (2)	$6535.2^{a\text{-}d}$ (1)	$5913.4^{c\text{-}k}$ (1)	$5969.4^{b\text{-}j}$ ± 24.1 (2)	$5784.0^{e\text{-}k}$ (1)	5848.2 ± 97.7 (11)
Male pupa								
mg	49.8 ± 1.5 (61)	42.5 ± 1.7 (38)	46.6 ± 2.3 (8)	41.9 ± 1.6 (2)	51.9 ± 8.8 (6)	40.5 ± 1.8 (10)	45.6 ± 3.0 (5)	46.6 ± 1.0 (130)
cal/g	$5924.2^{c\text{-}j}$ ± 9.7 (2)	$6143.0^{b\text{-}g}$ ± 20.6 (3)	$6591.8^{a\text{-}c}$ (1)	$6658.8^{a,b}$ (1)	$6027.6^{b\text{-}j}$ (1)	$6058.7^{b\text{-}i}$ (1)	$6035.8^{b\text{-}j}$ (1)	6165.0 ± 81.3 (10)
Female adult								
mg	116.0 ± 9.9 (32)	113.5 ± 5.8 (36)	128.9 ± 27.3 (5)	43.6 ± 23.2 (2)	155.0 ± 40.6 (2)	81.1 ± 18.5 (2)	122.4 ± 8.2 (11)	115.0 ± 5.0 (90)
cal/g	$5792.9^{e\text{-}k}$ ± 35.5 (3)	$5813.1^{e\text{-}k}$ ± 39.8 (3)	5219.5^{k} (1)	$5758.6^{e\text{-}k}$ (1)	$5486.1^{i\text{-}k}$ ± 14.2 (2)	$5792.8^{e\text{-}k}$ (1)	$5771.4^{e\text{-}k}$ (1)	5694.4 ± 57.1 (12)
Male adult								
mg	42.1 ± 24.9 (19)	32.5 ± 0.8 (27)	30.3 ± 1.2 (7)	28.9 (1)	32.2 ± 6.7 (3)	18.3 ± 1.3 (2)	28.8 ± 4.3 (3)	34.5 ± 2.0 (62)
cal/g	$6203.2^{b\text{-}g}$ ± 116.6 (3)	6707.8^{a} ± 167.5 (2)	$6431.1^{a\text{-}e}$ (1)	$6400.5^{a\text{-}f}$ (1)	$6260.0^{a\text{-}g}$ (1)	$5615.0^{h\text{-}k}$ ± 111.0 (2)	$5698.9^{f\text{-}k}$ (1)	6186.0 ± 129.0 (11)
Egg clutch								
mg	137.1 ± 4.2 (78)	109.9 ± 4.4 (35)	125.7 ± 4.7 (69)	55.8 ± 12.9 (4)	81.3 ± 23.4 (4)	61.0 ± 10.1 (11)	59.0 ± 7.1 (14)	117.5 ± 3.0 (215)
cal/g	$6064.9^{b\text{-}h}$ ± 136.5 (4)	$6043.8^{b\text{-}i}$ ± 80.0 (2)	$6231.5^{a\text{-}g}$ ± 136.1 (2)	$5963.6^{b\text{-}j}$ (1)	$5336.4^{i\text{-}k}$ (1)	$5531.0^{h\text{-}k}$ (1)	$5323.7^{j\text{-}k}$ (1)	5913.7 ± 108.6 (12)
Column mean								
mg	113.2 ± 3.6 (265)	88.9 ± 3.3 (185)	110.3 ± 5.0 (94)	94.7 ± 10.7 (27)	88.5 ± 5.1 (73)	83.6 ± 6.0 (52)	66.5 ± 11.4 (13)	
cal/g	5855.4 ± 83.1 (17)	6048.9 ± 98.4 (13)	6006.7 ± 167.4 (8)	5743.4 ± 127.0 (7)	5787.4 ± 75.4 (5)	5662.6 ± 111.4 (6)	6268.3 ± 140.8 (6)	

BIOLOGICAL TURNOVER OF RADIONUCLIDES

D. E. Reichle P. B. Dunaway
D. J. Nelson

Biological turnover of elements is a basic metabolic process associated with the mineral nutrition of organisms. The rates at which elements and radionuclides are excreted are dependent on such intrinsic biological factors as body size, age, sex, physical activity, physical condition, and deposition in biological sinks. Extrinsic environmental factors affecting radionuclide turnover include chemical composition of the medium and temperature. Many radionuclides can be grouped according to those characterized by either long, intermediate, or short biological half-lives (T_b's) in various animal groups (Table 10.11).[22] Some radionuclides occur in more than one category, because either their biological behavior is too variable to predict accurately or because factors influencing turnover were not sufficiently well-known.

Ordination of biological half-life values for insects yields the following ranking:

$$I > Zn > Fe > Na \geqslant P > K \geqslant Cs \geqslant Co \geqslant Cr > Ru > Ca > Sr .$$

In arthropods with calcified exoskeletons (e.g., millipedes and isopods) both strontium and calcium have much longer T_b's (75 to 125 days), comparable with the overall values reported for zinc and manganese in insects. Iodine has rapid biological turnover by invertebrates, except in those forms with highly pigmented (melanin) cuticula, where significant iodine loss occurs only during molting. Cobalt, manganese, iron, and zinc have slow biological turnover in invertebrate organisms.

[22] D. E. Reichle *et al.*, "Turnover and Concentration of Radionuclides in Food Chains," *Nucl. Safety* (in press).

Table 10.11. Biological Half-Lives of Elements in Major Groups of Organisms

Animal Group	Range of T_b (days)				
	0.1–1.0	1.0–10	10–100	100–1000	>1000
Aquatic Invertebrates[a]	Ca, Sr	P	Co, Zn, Cs (Sr and Mn)[b]	Zn[b]	Mn[b]
Fish		Na, I	Na, K, Cs, I	Ca, Mn, Co, Zn, Sr, Cs	S, Co?, Sr
Terrestrial Invertebrates[c]	Rb, Sr, Y, Cu?	Na, P, K, Ca, Cr, Co, As, Sr, Y, Ru, Cs, I, W, Ir	Na, P, Fe, Co, Zn (Ca and Sr),[b] I	I	
Vertebrates[d]	B, Ge, Tc, Os	H, Li, C, O, Na, P, K, Sc, Mn, Co, Ga, Se, Br, Rb, Mo, Tc, Ru, Rh, Ag, Te, I, Cs, Re, Os, Hg, Tl, Bi	H, B, C, N, O, Na, Mg, Si, P, S, K, Sc, V, Mn, Fe, Co, Cu, Zn, Se, Rb, Ru, Rh, Pd, Ag, In, Sn, Sb, Te, I, Cs, Ba, Eu, W, Ir, Pt, At, Fr, U	F, Mg, Al, P, Ca, Ti, Cr, Mn, Fe, Ni, Zn, As, Sr, Zr, Nb, Cd, I, Cs, La, Ce, Pr, Nd, Pm, Sm, Eu, Gd, Tb, Dy, Ho, Er, Tm, Yb, Lu, Hf, Ta, Au, Pb, U	Ca, Sr, Y, Pb, Ra, Ac, Th, Pa, Np, Pu, Am, Cm, Bk, Cf

[a] Primarily annelids and mollusks.

[b] Invertebrates with calcified exoskeletons.

[c] Primarily adult insects.

[d] Primarily homoiothermic vertebrates.

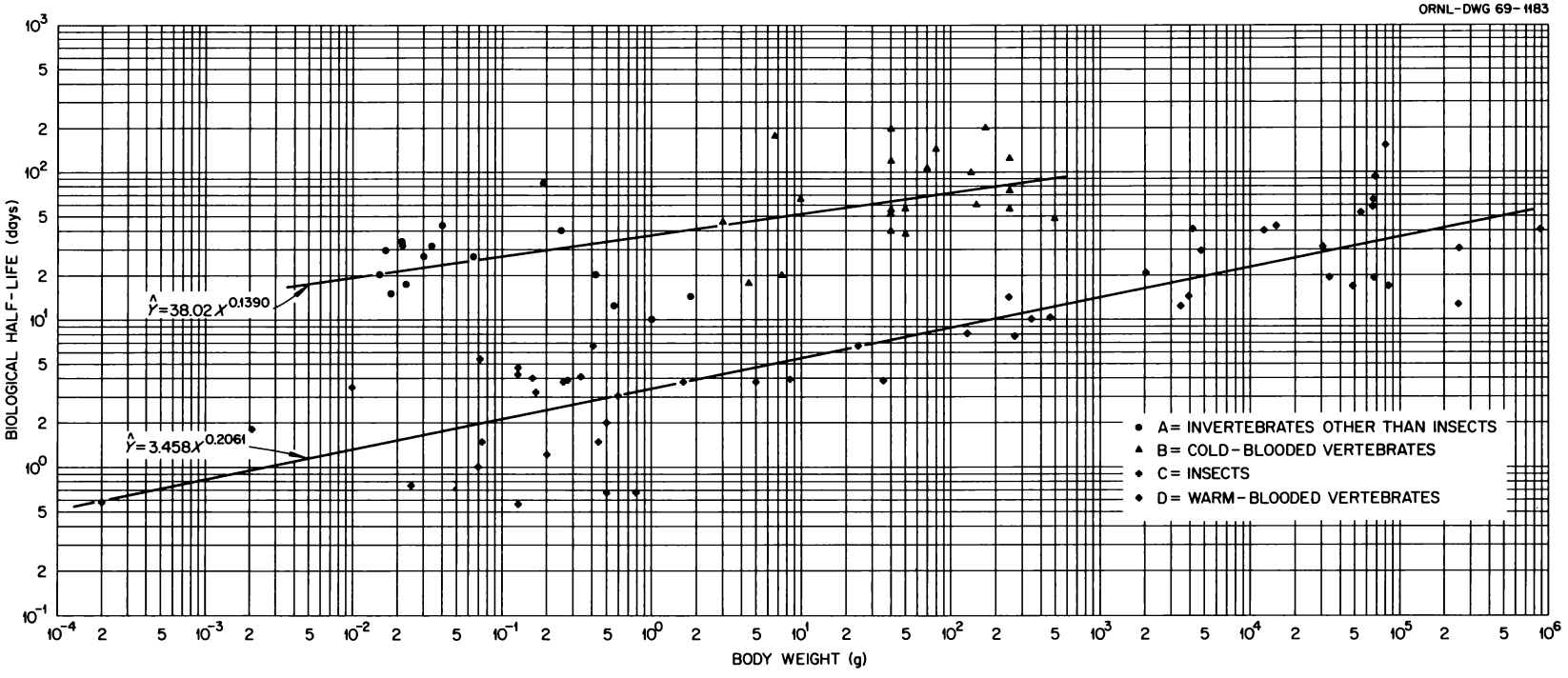

Fig. 10.10. Relationship Between Animal Body Size and Turnover of Radiocesium (T_b's Corrected to 20°C using a Q_{10} of 2). The graph of log Cs biological half-life against the log of live body weight follows a linear power function of the form $Y = aX^b$. Group A, invertebrates other than insects (primarily arthropods); group B, aquatic vertebrates (predominantly fish); group C, insects; group D, mammals and birds.

The alkali metals, Na, K, Rb, and Cs, generally have quite rapid T_b's.

Aquatic invertebrates also illustrate the uniqueness between calcium sink and nonsink organisms. Manganese and strontium values are for clams, where these two elements are accumulated in the shell but also have slow metabolic turnover. Phosphorus, calcium and strontium have rapid turnover in species without well-developed exoskeletons. Fish possess bone sinks for calcium and strontium, as do their terrestrial vertebrate counterparts. The active metabolic pool of elements in soft tissues is divided into those with slow turnover (Co, Zn, and Cs) and those elements with rapid T_b's (Na and K).

Comparative data on T_b's of many elements are not available for a large number of mammalian species; much of the data in Table 10.11 are for man. Most of the elements with short T_b's concentrate in soft tissues, while the remainder with extended T_b's have long residence times in slowly metabolizing or inert tissues such as bone, teeth, and hair. Relatively short T_b's for cesium have been described for domesticated rabbits and species in the families Bovidae, Cervidae, and Suidae in the Artiodactyla. Consistently low values for iodine retention occur in these same groups. Turnover of these elements (and perhaps others) may differ among mammal families. Practically nothing is known about radionuclide metabolism in about 10 of the 13 metazoan phyla, and much more experimental data are needed.

A known variable affecting metabolism is body size, with metabolism a function of approximately the 0.75 power of body weight. Sufficient data were available for ^{134}Cs and ^{137}Cs T_b's (long components) in various organisms to obtain a coherent synthesis of the effect of body size on the turnover of this element. When these data on T_b's are plotted as a function of fresh weight of animals (Fig. 10.10), various groups of organisms form into rather discrete patterns. These groups represent organisms with distinct biological relationships. Group A consists of invertebrates other than insects and includes lower arthropods (millipedes, centipedes, isopods and spiders) and mollusks (snails). Aquatic poikilothermic (cold-blooded) vertebrates in group B include fish (perch, trout, bluegill, and carp) and one amphibian (newt). Group C is composed entirely of insects, ranging from sap-sucking aphids to saprophagous and herbivorous beetles, crickets, and grasshoppers. Warm-blooded (homoiothermic) vertebrates in group D include rodents, lagomorphs (rabbits), artiodactyls (hoofed, even-toed mammals), primates (monkey and man), and chickens.

In fitting a power function model, $Y = aX^b$, to the data in Fig. 10.10, the lower arthropods with calcified exoskeletons (group A) are most closely associated with the cold-blooded vertebrates (group B). Cesium turnover by insects (group C) and warm-blooded vertebrates (group D) are more closely related. The regression equations calculated for these two combinations of organisms, where Y is the biological half-life of cesium in days and X is live body weight in grams, are:

Groups A + B

$$\hat{Y}_{Cs} = 38.02X^{0.1390}, \text{S.E. of } b = 0.03027,$$

Groups C + D

$$\hat{Y}_{Cs} = 3.458X^{0.2061}, \text{S.E. of } b = 0.01499.$$

Such a size-dependency for radionuclide turnover also can be interpreted from comparative data[22] reported for a limited number of species and isotopes, for example ^{110m}Ag, ^{131}I, ^{42}K, ^{22}Na, ^{86}Rb, ^{137}Cs, ^{65}Zn, ^{54}Mn, and ^{59}Fe in mammals; ^{134}Cs and ^{137}Cs in arthropods; and ^{137}Cs in aquatic invertebrates.

Strontium-90 and iodine-131 are additional radionuclides having appreciable radiobiological interest because of their potential bioenvironmental hazard in waste releases. These radionuclides have been the subject of much research, since ^{131}I is accumulated in the thyroid gland of vertebrates and ^{90}Sr is deposited in calcareous skeletal tissues. Research on these two isotopes typifies specific investigations involving biological sinks. The sinks are of contrasting types, since ^{131}I possesses a short radioactive half-life and often is in an actively metabolized pool (thyroid), while ^{90}Sr is a long-lived radionuclide in a slowly exchanged metabolic pool (bone). The whole-body retention data for ^{131}I and ^{90}Sr reflect the dominance of their respective sinks, but also show a body-size relationship across major taxonomic categories.

A MODEL FOR ^{137}Cs MOVEMENT IN A FOREST FLOOR COMMUNITY

R. V. O'Neill D. E. Reichle

The first stages of synthesizing information on the forest floor community in the ^{137}Cs-tagged *Liriodendron* forest have been completed, with the construction and implementation of a compartment model to describe radionuclide movement along food chains. This work has involved several years of research and summarization on the trophic behavior of the forest floor

arthropods. On the basis of these available data, it was possible to realistically divide the cryptozoa into discrete taxonomic categories, each with functional integrity:

0. External source (litter) and external sink (soil)
1. Detritus
2. Formicidae
3. Diplopoda
4. Mollusca
5. Orthoptera
6. Lepidoptera
7. Diptera
8. Isopoda
9. Annelida
10. Collembola
11. Coleoptera
12. Araneida
13. Chilopoda
14. Acarina
15. Predators external to system

These categories were regarded as distinct compartments ecologically, and fluxes between the compartments were designed on the basis of an evaluation of the quantitatively most important trophic transfers that occur within the system. The resulting compartment model in the form of a flow diagram (Fig. 10.11) has enabled reevaluation of important unquantified variables and development of an information retrieval procedure for large bodies of data on biomass and radiocesium concentrations.

A computer program simulates fluxes of ^{137}Cs in the ecosystem from either continuous or pulse inputs. Calculations of temporal behavior of the system are made on the basis of a set of linear differential equations with variable transfer coefficients. The coefficients, describing uptake and elimination of ^{137}Cs from the various compartments, are temperature dependent. Field temperature is simulated with a sine function. Random fluctuations in temperature are introduced by addition of a random variable, N(0,1) to the calculated temperature. Hypothetical data sets have been used to investigate the behavior of the simulation program and to make a preliminary design of the type of simulations that will be performed by the model when the final synthesis of data has been completed.

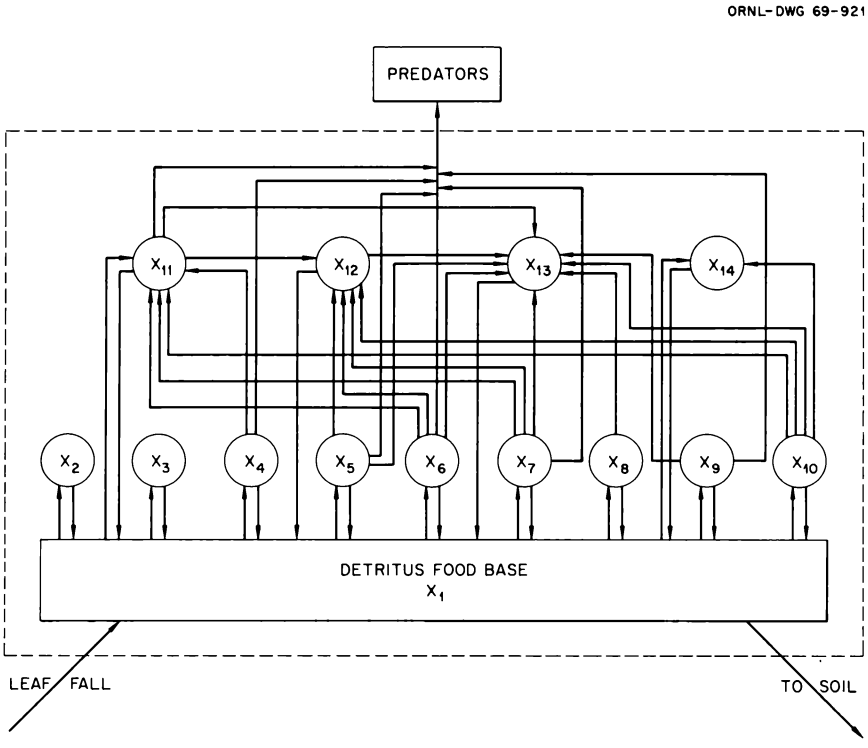

Fig. 10.11. Flow Diagram of Pathways for ^{137}Cs Movement in the Forest Floor Community. Numbers in circles refer to the taxonomic categories in Table 10.12.

RESPIRATION RATES OF *ACHETA DOMESTICUS* ACCLIMATED TO A FLUCTUATING DAILY TEMPERATURE REGIME

R. V. O'Neill

The extrapolation of laboratory studies to field situations is a frequent problem in ecological research. It is ordinarily assumed, for example, that respiration of animals exposed to daily fluctuations in temperature in nature can be approximated by measurements in the laboratory, where the animals are maintained at a constant temperature which represents a mean of the environmental fluctuations. A test of the validity of this hypothesis has been carried out with *Acheta domesticus*.

Populations of crickets were acclimated for two weeks to a daily temperature regime of either 12 hr of 10°C followed by 12 hr of 30°C, or by a constant 20°C. Measurements of respiration rates at 10, 20 and 30°C were made on both groups in a Gilson differential respirometer. A summary of the results is given in Table 10.12. The differences between the two experimental groups at each temperature cannot be shown to be significantly different by a Student's t test ($P = 0.01$). The results indicate that acclimation of experimental animals to a mean temperature is a reasonable approximation in this species and possibly other related terrestrial arthropods.

Although respiration rates at each experimental temperature imply that acclimation of each treatment group is similar, the results do not demonstrate whether respiration under constant and fluctuating temperatures would be comparable. If a Q_{10} (logarithmic) relationship applies over that temperature range, an arithmetic mean temperature is inappropriate. Testing of this hypothesis awaits the development of reliable equipment to measure respiration under fluctuating temperature regimes.

Table 10.12. Respiration Rates of *Acheta domesticus* Acclimated to Either a Fluctuating Daily Temperature or a Constant Mean Temperature

Numbers in parentheses indicate standard errors ($N = 28$)

Acclimation Regime (°C)	Experimental Temperature (°C)	Respiration Rates (microliters of O_2 per gram per hour)
20	10	202.8 (12.9)
10–30	10	193.9 (12.7)
20	20	965.7 (90.6)
10–30	20	1063.4 (87.9)
20	30	1497.2 (82.6)
10–30	30	1719.4 (102.8)

ACCUMULATION OF ^{144}Ce BY HICKORY AND ^{60}Co BY BLACK GUM SEEDLINGS

W. A. Thomas Joyce D. Sheedy

Hickory trees accumulate the rare-earth elements,[23] and black gum trees accumulate cobalt.[24] Selective absorption of elements by accumulator species results in elemental concentrations in their foliage far in excess of those in foliage of other species on the same site. This experiment was designed to compare the differences in uptake of ^{144}Ce and ^{60}Co from tagged nutrient solution and from inoculated soil by seedlings of five species: mockernut hickory (*Carya tomentosa*), black gum (*Nyssa sylvatica*), red maple (*Acer rubrum*), tuliptree (*Liriodendron tulipifera*), and white oak (*Quercus alba*).

Twenty seedlings of each species were collected from the same site and transported to a greenhouse where ten were transplanted into opaque 250-cc bottles containing 150 g of air-dry loam soil; the other ten were placed in similar bottles containing 200 ml of Knop's nutrient solution. Seedlings averaged about 25 cm in height and were probably less than three years old. The nutrient solution contained equal amounts of ^{144}Ce and ^{60}Co (5000 dis min^{-1} ml^{-1}).

Because of differences in both root size and leaf area of seedlings within and among species, the absolute quantity of isotope absorbed by the plants is meaningless in a comparison between treatments or among species because of variation in surface areas available for absorption and for transpiration. Therefore the quantity of each radioisotope in the plant per 100 ml of nutrient solution absorbed was used to compare selective absorption among species. To obtain these data, five bottles of solution and five with soil served as controls to estimate losses of solution by evaporation. Soil in the 50 bottles with seedlings and in the control bottles was maintained at about field capacity with 30 ml of the tagged nutrient solution. Solution in the other bottles was replenished regularly to 200 ml and was aerated for 8 hr/day. Cotton plugs around the stems of

[23] W. O. Robinson, H. Bastron, and K. J. Murata, *Geochim. Cosmochim. Acta* **14**, 55–67 (1958).

[24] V. A. Lazar and K. C. Beeson, *Agr. Food Chem.* **4**, 439–44 (1956).

Table 10.13. Accumulation of ^{144}Ce and ^{60}Co by Tree Seedlings

Species	Number of Seedlings	Index of Selective Absorption[a]	
		^{144}Ce	^{60}Co
Carya tomentosa			
Soil	6	6720 ± 1900	5780 ± 1410
Solution	9	4590 ± 450	4470 ± 890
Acer rubrum			
Soil	8	620 ± 90	1650 ± 580
Solution	7	770 ± 430	990 ± 500
Liriodendron tulipifera			
Soil	6	320 ± 50	750 ± 100
Solution	9	720 ± 350	410 ± 130
Nyssa sylvatica			
Solution	6	650 ± 190	5110 ± 940
Quercus alba			
Solution	4	170 ± 40	780 ± 300

[a]Index of selective absorption ($\bar{X}$ ± S.E.) is the quantity of isotope absorbed by roots and transported to stem and foliage per 100 ml of nutrient solution absorbed (dis/min of isotope/100 ml absorbed).

all 100 plants and in control bottles retarded evaporation. Subtraction of solution volume lost by evaporation from control bottles and that remaining in bottles when the trees were harvested from the total volume placed in the bottles yielded the estimate of solution volume that was absorbed. The difference in weight of soil in bottles before and after oven drying was used with knowledge of moisture content of the soil when the experiment started to obtain the volume of solution still in soil.

Seedlings were harvested after 35 days growth in inoculated media. Due to mortality and the decision not to include in the analysis any seedlings in treatments in which less than four trees survived after 35 days, the analysis includes only 55 plants. When harvested, the plants were separated into leaves, stems plus branches, and roots for oven drying and weighing. Radioassay with a Packard 400-channel gamma analyzer provided data on ^{144}Ce and ^{60}Co contents of leaves and stem plus branches. The near impossibility of distinguishing between absorbed and adsorbed isotope precluded assay of roots. The percentage of total-plant isotope which was in foliage did not significantly differ between treatments for any species or either isotope.

The data for radioisotope uptake by the seedlings are expressed as an "index of selective absorption," defined here as disintegrations per minute of isotope absorbed by roots and transported to aboveground plant parts per 100 ml of tagged solution absorbed. This index for ^{144}Ce by *Carya* significantly ($P < 0.01$) exceeds that of the four other species, both in soil and in solution, in spite of the large variation about the mean values (Table 10.13). The *Nyssa* and *Carya* indices for ^{60}Co in solution are both significantly greater ($P < 0.05$) than the index for other species and are not significantly different from each other. *Carya* seedlings accumulated ^{60}Co almost as efficiently as *Nyssa* seedlings did, but the latter did not selectively absorb ^{144}Ce.

DECOMPOSITION AND LOSS OF ^{137}Cs, ^{144}Ce, AND ^{60}Co FROM LEAVES OF *LIRIODENDRON TULIPIFERA*, *CARYA TOMENTOSA*, AND *NYSSA SYLVATICA*

David E. Reichle Marvin H. Shanks

The breakdown of organic matter is an important step in the biogeochemical cycling of elements in ecosystems. Rates of decomposition and radionuclide loss were determined for leaf litter from three deciduous tree species important in the composition of Appalachian forests: *Liriodendron tulipifera* (tulip tree), *Carya tomentosa* (mockernut hickory), and *Nyssa sylvatica* (black gum). Turnover rates of ^{137}Cs by decomposing tulip tree leaves were a required variable needed for completion of the forest ecosystem model of cesium cycling (see Fig. 10.1). Cerium-144 in *Carya* and cobalt-60 in *Nyssa* were examined because of the potential importance of these species and elements in forest nutrition (see "Accumulation of ^{144}Ce by

Table 10.14. Rates of Decomposition (Weight) and Radionuclide Loss for Leaves of Three Deciduous Trees

Loss rate coefficients k (months) ± one standard error (S.E.)

	Liriodendron tulipifera		*Carya tomentosa*		*Nyssa sylvatica*	
	Weight	^{137}Cs	Weight	^{144}Ce	Weight	^{60}Co
k	−0.045	−0.127	−0.075	−0.090	−0.133	−0.227
S.E.	0.005	0.017	0.013	0.016	0.017	0.029

Hickory and ^{60}Co by Black Gum Seedlings," this section) since hickory accumulates rare-earth elements,[23] and black gum accumulates cobalt.[24]

Leaves were collected in the fall from trees previously tagged with the appropriate radionuclide. Subsamples of 7 g dry weight of leaves were placed in 5-dm^2 area nylon net litter bags with 4- by 6-mm openings. Litter bags were placed in one of three replicated plots on the floor of a *Liriodendron tulipifera* forest with a dense *Cornus florida* understory. The experiment was initiated in mid-November 1967, and bimonthly samples and analyses have continued through May 1969.

Seasonal trends in both organic matter and radionuclide loss were evident in the data; rapid rates of decomposition occurred from September through March but began to diminish during April and May and nearly ceased during the dry summer months. Loss rate coefficients ($month^{-1}$) for the 18-month study period are given in Table 10.14 for each radionuclide and tree species. There was a significant difference ($P \leqslant 0.05$) among species in the rate of dry matter weight loss (decomposition); gum leaves disappeared most rapidly (13.3%/month) followed by hickory (7.5%/month) and tulip tree (4.5%/month). Only in the case of *Liriodendron* tagged with ^{137}Cs was there a significant difference ($P < 0.05$) between the rates of weight and radionuclide loss. This experiment and a previous study[25] using different species support the generalization that cesium (alkali metal) leaches from litter at a rate faster than organic matter breakdown, while the rate of cobalt (transitional element) loss parallels weight loss. There are no other data to further substantiate the correlation between weight and ^{144}Ce (rare-earth element) loss in *Carya* leaves.

[25] J. S. Olson and D. A. Crossley, Jr., pp. 127–32 in *Proceedings of First National Symposium on Radioecology, Ft. Collins, Colorado, 1961*, published 1963.

INTERACTION BETWEEN GRASS COMMUNITIES

Roger C. Dahlman

Invasion of pastured areas by broomstraw (common name synonymy includes broomsedge, sage grass, and poverty grass), *Andropogon virginicus* L., reduces range quality in many parts of southeastern grazing land. This opportunistic species readily succeeds established herbaceous vegetation, even dense stands of tall fescue (*Festuca arundinacea* Shreb.) grass, and the result usually is decreased site valuation. To assess the dynamics of this successional process, broomstraw invasion of a fescue grassland has been documented over a two-year period at an old-field study site in the 0800 ecology area.

Four-year-old stands of broomstraw and fescue were located adjacent to each other on an upper terrace of the Clinch River flood plain. Quantitative measurements of broomstraw frequency, density, and biomass in the fescue field were initiated in 1967, when maximum frequency and density occurred 1 to 30 m from the original stand (Table 10.15) and then decreased between 31 and 50 m. No measurements were made beyond 50 m in 1967 because very few plants were visible in this part of the field. Biomass generally diminished with increasing distance from the stand edge. Broomstraw is a late-season developing and flowering species, and only the intermediate stage of development was recorded in the July observations. Total biomass at maturity would be at least twice that shown in Table 10.15.

Broomstraw occupation of the fescue field increased substantially from 1967 to 1968 according to the three different standards of measure. In the second year, tussock frequency was two to five times greater in the 1- to 50-m zone, and from 51 to 100 m this measure indicated a two- to fourfold increase in broomstraw prevalence than in the closer zone (1 to 50 m) the previous year. Density increased by more than an order of magnitude in the second year. This measure demonstrated most markedly the magnitude of the compositional change which occurred in the span of one year. Biomass increased by two- to threefold, but this parameter was not considered a decisive indicator of invasion because seasonal development is closely related to a regimen of ecological factors (e.g., growing season, climatology, etc.).

Second-year maximum density and frequency was in the 31- to 60-m zone (median = 40 m) compared with 1 to 30 m (median = 20 m) the previous year. This indicates an extension of the broomstraw community

Table 10.15. Abundance of Broomstraw in a Fescue Field

Distance from Original Stand	1967[a]			1968[a]		
	Frequency[b] (line hits/m)	Density[c] (tussocks/m^2)	Biomass[d] (g/m^2)	Frequency[b] (line hits/m)	Density[c] (tussocks/m^2)	Biomass[d] (g/m^2)
0[e]	5.4 ± 0.7	49 ± 7	267 ± 46	5.0 ± 0.6	40 ± 6	226 ± 35
1–10	0.29 ± 0.06	1.7 ± 0.34	66 ± 19	0.35 ± 0.02	2.4 ± 0.4	61 ± 11
11–20	0.41 ± 0.05	1.9 ± 0.20	14 ± 2.8	0.97 ± 0.13	3.0 ± 1.2	46 ± 4.6
21–30	0.38 ± 0.06	1.8 ± 0.33	20 ± 2.7	0.98 ± 0.09	12.5 ± 4.0	36 ± 4.7
31–40	0.21 ± 0.06	1.3 ± 0.38	24 ± 6.9	1.12 ± 0.23	19.6 ± 4.8	49 ± 10.2
41–50	0.25 ± 0.03	1.2 ± 0.12	17 ± 3.2	1.32 ± 0.12	16.4 ± 2.9	50 ± 8.7
51–60				1.15 ± 0.14	13.2 ± 2.5	46 ± 6.4
61–70				0.85 ± 0.07	6.7 ± 0.4	51 ± 5.8
71–80				1.55 ± 0.56	9.6 ± 1.3	55 ± 6.1
81–90				0.93 ± 0.15	9.1 ± 1.4	54 ± 8.3
91–100				0.73 ± 0.15	1.8 ± 0.2	32 ± 4.8

[a]Data collected in late July of both years; 1967 from eight line intercepts, 1968 from six line intercepts.

[b]Defined as the number of line-intercept intersections with the tussock canopy per linear meter in the 10-m increment.

[c]Number of tussocks present per square meter at the point of line-intercept contact with tussock canopy.

[d]Quantity of new growth in sampled area; represents immature plants of the log phase of development.

[e]Measurements made at 1 m inside the four-year-old broomstraw stand.

into the established stand of fescue at the rate of 20 m/year. Once established the broomstraw will gradually replace the fescue by means of new seed introduction or greater competitive vigor.

These observations verify the aggressive tendencies of broomstraw. Future evaluation of the optimal circumstances and mechanisms of invasion will enable a better understanding of complex processes of succession.

CORRELATION OF PREDICTED AND OBSERVED ^{137}Cs IN RUNOFF FROM CONTAMINATED FESCUE MEADOW PLOTS

R. C. Dahlman

A simple compartment model was developed last year[26] for predicting the extent of lateral radionuclide movement in surface water runoff from a fescue meadow. Static terms and transfer coefficients are based on physical characteristics of the fallout material (quantity, nuclide leachability), soil (distribution coefficient), and runoff (relative magnitude of water and soil). New results are consistent with last year's observations, where appreciable runoff from a densely covered grassland system occurs only when soil-water recharge has reached saturation. Usually over 5 in. of precipitation is necessary to saturate dry soil and produce runoff, and this circumstance has occurred only during winter and spring in the past two years.

Table 10.16. Runoff, Erosion, and ^{137}Cs Movement from a Fescue Meadow Contaminated with Fallout Simulant

Event	Runoff		Erosion		Total Activity in Runoff (mc)
	Quantity (liters)	^{137}Cs (μc)	Quantity (g)	^{137}Cs (μc)	
Jan. 20	2	1	0.06	0.2	0.001
Feb. 3	400	117	0.5	1.3	0.118
Feb. 4	2	0.8	0.3	0.1	0.001

There has been only one runoff occurrence of any consequence (Table 10.16, Feb. 3) since last year's report. Four hundred liters of runoff and 0.5 g of eroded soil contained 0.12 mc of ^{137}Cs, nearly all of which was in the water fraction. This observed quantity compared very favorably with the 0.13 mc in 400 liters calculated from the updated revision of the runoff model.[27] Total radionuclide removal was estimated with reasonable accuracy, but there was poor agreement between predicted and observed proportions of ^{137}Cs in eroded soil and in water. That practically all the

[26]S. I. Auerbach, *Health Phys. Div. Ann. Progr. Rept. July 31, 1963*, ORNL-3492, p. 109.

[27]R. C. Dahlman *et al.*, "Behavior of ^{137}Cs Tagged Particles in a Fescue Meadow," in *Proceedings of Seminar Agricultural and Public Health Aspects of Environmental Contamination by Radioactive Materials, Vienna, March 1969* (in press).

activity was present in water was attributed to the unusually small quantity of eroded soil present in runoff and the high mobility of the nuclide during the initial phase of contamination. It was determined from other measurements (see "Behavior of ^{137}Cs Fallout Simulant in a Fescue Meadow," this section) that 15% of the nuclide was leached from simulant particles, temporarily retained by vegetation and then partially removed in surface water runoff. A significant quantity of ^{137}Cs was still in a transient state five months after contamination because it had not yet been immobilized by soil.

According to the available test results one can predict with reasonable accuracy the magnitude of radionuclide redistribution in runoff, based on a working knowledge of the characteristics of fallout material, soil, and runoff. Future observations will provide a measure of variance, and then it will be possible to consider broader application of the model in other situations of environmental contamination.

HYDROLOGIC BALANCE OF A FESCUE FIELD

Roger C. Dahlman Gerald Stanhill

Saturated soil is the most important factor influencing the magnitude of runoff from a heavily vegetated system. Periods of probable runoff would govern the time when lateral redistribution of radioactive contaminant must be measured in the ecology area 0800 postattack radioecology experiment.

The daily status of soil moisture in a fescue field was calculated from a hydrologic balance equation,

$$\sum_{i=1}^{n} \Delta SM = SM_0 + \sum_{i=1}^{n} P - (E + R + I),$$

where SM_0 is the initial soil moisture content, precipitation (P) represents the water input to the system, and evaporation (E), runoff (R), and internal drainage (I) represent sources of water loss. The R and I components of loss occur only during periods of soil saturation when runoff is a measured term, and internal drainage is determined as the difference term in the hydrologic equation. Evaporation from the system is the principal mode of soil water depletion, and daily values for this term were calculated from Penman's combined energy balance and aerodynamics equation

$$E_p = \frac{DQ}{L} + EK(e_a - e_d)(a\mu + b),$$

where E_p is potential evaporation, Q is net radiation, $e_a - e_d$ is average daily vapor pressure deficit, μ is total wind, L is latent heat of evaporation, D and E are temperature-dependent weighting factors, and K, a, and b are empirically derived roughness constants. Only four basic meteorological parameters are required for calculating daily evaporation using Penman's model, and these are net radiation, vapor pressure, air temperature, and wind speed.

The initial soil moisture content was determined gravimetrically and with a neutron probe for a 55-cm depth. This depth was chosen because it contains 95% of the root mass. Then, using appropriate values for P, E, R, and I, the daily soil moisture content was calculated from the hydrologic balance equation. In practice the daily calculated soil moisture values indicate either depletion or recharge, and the rate of recharge serves as an alert for determining surface redistribution of the ^{137}Cs contaminant via runoff.

The soil moisture content was measured at seven different periods between June and December, and measured moisture changes were compared with those calculated from the hydrologic equation (Table 10.17). There was reasonably good agreement between calculated and measured soil water changes for the periods I,

Table 10.17. Measured and Calculated Soil Water Changes in a Fescue Field for Different Periods of the 1968 Growing Season

Period	Soil Water Content[b] (vol %)	Soil Water Change[a]	
		Measured[c] Inches ± S.E.	Calculated Inches
I June 20 to July 5	32.6	−1.58 ± 0.12	−1.20
II July 6 to July 9	23.6	−0.48 ± 0.03	−0.80
III July 10 to July 19	22.3	−0.29 ± 0.03	−0.59
IV July 20 to Aug. 8	20.8	−0.50 ± 0.06	−2.22
V Aug. 9 to Oct. 10	18.3	−0.10 ± 0.01	−3.26
VI Oct. 11 to Dec. 17	17.8	+1.90 ± 0.12	+2.10

[a] Includes allowance for precipitation input and evaporative loss.

[b] Water content for a 55-cm horizon at the beginning of the measurement period.

[c] For 55 cm depth only.

II, and VI. At these times there evidently was no serious limitation in soil moisture, and actual evaporation approached the potential estimate based on Penman's energy balance and aerodynamics equation. During periods III, IV, and V, however, the model predicted considerably more evaporation than was actually observed. Higher moisture tension during midsummer apparently restricted evaporation from the surface horizon (0–55 cm).

Throughout the growing season observed, soil water content was greater than wilting percent (~13% by volume), although reduction below 17.8%, the lowest observed value, probably occurred between sampling dates, but there was no sign of wilted plants in the grass community. The discrepancy between observed and calculated depletion probably was related to other unmeasured factors which regulated the rate of water evaporation from the system (e.g., soil moisture release characteristics, internal water conservation by grass vegetation, or availability of subsurface water). There is a strong possibility that grass roots extended to a water table 1.5 to 3 m below the surface, and this would have provided a source of water during periods of stress. The evapotranspiration quantity from the deeper source would have gone undetected in actual measurements of soil moisture change.

Attempts to use hydrologic balance parameters and Penman's energy balance and aerodynamics equation to assess the daily soil moisture status were only partially successful. During periods of intense evaporative stress, this approach greatly overestimated soil water depletion. Periodic measurement of soil moisture by conventional methods (gravimetric, neutron scatter) should parallel calculation of daily budgets, and then the computational technique can serve as a useful predictor of the state of soil water depletion or recharge.

BEHAVIOR OF ^{137}Cs FALLOUT SIMULANT IN A FESCUE MEADOW

R. C. Dahlman Regina M. Anderson

Surface nuclear detonations produce close-in fallout, and this material represents a dimension of environmental contamination for which there exists limited information and experience. The behavior of this material and the resulting effects on plants, animals, and insects are being investigated in a tall fescue (*Festuca arundinacea* Shreb) meadow. Silica sand particles tagged with 100 μc of ^{137}Cs per gram were applied to a dense stand of fescue vegetation at the rate of 25 g/ft^2, resulting in 2 to 3 rads/day absorbed gamma dose at 1 m. The simulant-sand was 88 to 177 μ in diameter, and ^{137}Cs leachability was 15% ± 0.6 (24 hr in an aqueous system).

Dense fescue foliage intercepted an appreciable quantity of the simulant, and many particles remained in vegetation for three to four days. Particles, which collected in the leaf-sheath axillary crevice, were retained for four to six weeks, until rainstorms washed them to the ground. In the local subhumid climate plants retained the 88- to 177-μ-diam particles more effectively than desert species in the vicinity of nuclear test detonations.[28] There the largest particle class collected from foliage was 44 to 88 μ. Differences in humidity and microclimate probably account for the dissimilarities. Because of the local humid moisture regime, nightly dew deposits develop on plant surfaces, and the resulting water films enhance particle retention and provide the aqueous medium for dissolution and transfer of ^{137}Cs from particles to the vegetation.

Appreciable ^{137}Cs assimilation by vegetation occurred shortly after contamination. Particle-free living and dead vegetation contained 1.32 ± 0.16 and 4.6 ± 0.59 μc/g respectively. Total initial activity on all vegetation was 3.4 mc/m^2, which was 15% of the quantity (22 mc/m^2) applied to the area. The quantity transferred to vegetation agreed remarkably well with the amount removed by simple leaching with water. Apparently the ^{137}Cs, which is loosely bound to particle surfaces, readily dissolves in an aqueous medium and is rapidly taken up by plants. According to laboratory tests[29] the simulant possesses chemical fixation characteristics similar to actual fallout particles. The relationship of comparable leachability and grass assimilation would allow one to predict ^{137}Cs uptake by plants from parameters determined by laboratory analysis of fallout materials.

For living fescue vegetation a two-component loss rate characterized the ^{137}Cs decrease as a function of time. Daily loss rates were derived from two linear regression equations ($r^2 > 0.9$), and the rates were 0.04 μc/day during the first four weeks and 0.002 μc/day for the next seven months (Fig. 10.12). When ^{137}Cs loss rates from living foliage had decreased by an order of magnitude (0.04 to 0.002) in four weeks, the content was approaching equilibrium, and variability was substantially less (S.E. = 10 to 14% of $\bar{X}_{0-4\ \text{weeks}}$; 5 to

---

[28] E. M. Romney *et al.*, *Ecology* 44, 343–48 (1963).

[29] W. B. Lane, *Fallout Simulant Development: the Sorption Reaction of Cerium, Cesium, Ruthenium, Strontium, and Zirconium-Niobium*, SRI Report No. MU-5068, 1965, 19 pp.

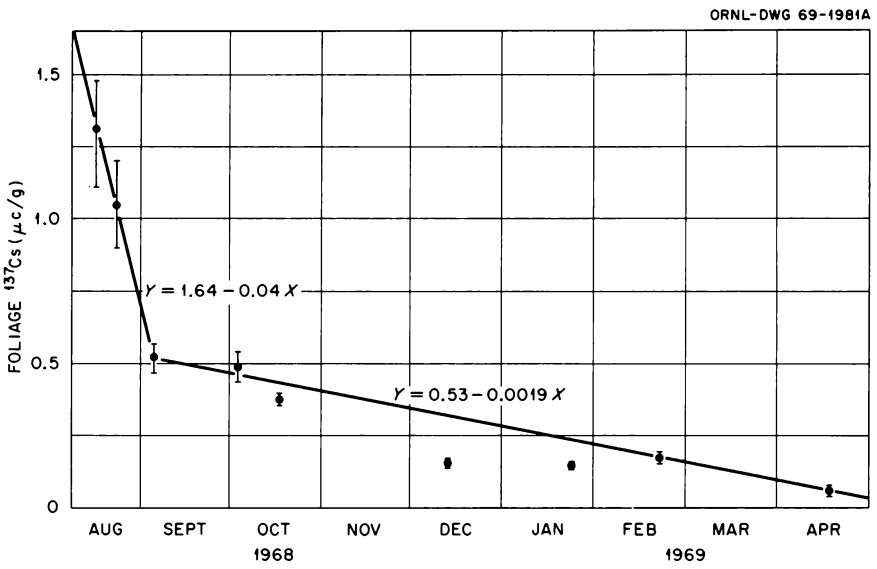

Fig. 10.12. Two-Component Loss Rate of ^{137}Cs by Fescue Foliage. Initial assimilation was by way of particle contact with foliage. Brackets denote 1 SE about the mean.

8% of $\bar{X}_{>4\ \text{weeks}}$). The decrease probably was a manifestation of many processes affecting nuclide distribution, notably particle-retention patterns, new plant growth, and retranslocation to other plant parts. The trend in ^{137}Cs behavior in the second year's fescue growth (spring 1969) follows the established pattern of steady and linear decrease. The quantity of isotope per unit mass was markedly diluted by new growth, but the total quantity present in the plant component deviated very little from the existing equilibrium level (~30 $\mu c/m^2$).

COMPARTMENT MODEL OF SEASONAL CHANGE IN ROOTS, TOPS, AND DEAD BIOMASS OF *ANDROPOGON* AND *FESTUCA* FIELDS

P. A. Opstrup J. M. Kelly
J. S. Olson

Three purposes of this study were: (1) to test various sampling and mathematical techniques in the analysis of grasslands typical of eastern Tennessee, (2) to explore the feasibility of increasing sampling efficiency in future investigations, and (3) to use computer models for theoretical estimation of gross and net production and for mathematical description of transfer coefficients or functions in grasslands of widely planted Kentucky-31 tall fescue (*Festuca arundinacea* Schreb.) and the normal native old-field (or pasture) invader called broomsedge, or sagegrass (*Andropogon virginicus* L.).[30]

The maximum biomass for *Festuca* (408 g/m^2) came in early summer, near time of flowering, while that for *Andropogon* (806 g/m^2) occurred just after frost had killed most of the live tops. Litter on the ground remained low and comparatively constant, near 114 and 181 g/m^2 respectively. Daily mean production rates approximated by biomass changes varied seasonally: 1.21 to 3.29 g m^{-2} day^{-1} for intervals March 1 to April 27 and April 27 to May 15 for the *Festuca* community and 1.05 to 3.34 g m^{-2} day^{-1} for intervals March 10 to June 7 and June 7 to August 7 for the more mixed *Andropogon* community. Declining rate of biomass increase for later dates presumably reflected increased loss rates, as the mass of live and dead compartments increased, although carbon assimilation rates may also have diminished during the same period.

A seven-compartment model was designed as an early approximation, to simulate plausible redistribution of biomass through major live and dead plant parts of the ecosystem. Transfer coefficients of the final model were constant or seasonally varying and were derived from observed rates of change plus several ancillary studies or approximations from the literature.[30] The seasonally varying coefficients were expressed as periodic or

[30] *Health Phys. Div. Ann. Progr. Rept. July 31, 1968,* ORNL-4316, pp. 112–13.

exponential functions of arbitrary input functions that were independent of the system's state variables. Rates were related to seasonal cycles and climatic variables.

From the model, gross production was estimated to be at least 1145 g m^{-2} $year^{-1}$ for the *Andropogon* and 1220 g m^{-2} $year^{-1}$ for the *Festuca* communities. Depending on hypotheses for root turnover coefficients, the net primary production in the *Festuca* community was estimated to range from 921 to 1115 g/m^2, as compared with adjusted clipping estimates of 992 g/m^2. For the *Andropogon* community the range was estimated to be from 853 to 1060 g/m^2, compared with 892 g/m^2 calculated from the clipped data.

These estimates of net production from biomass change in *Festuca* and *Andropogon* old-field communities may seem high but appear to be closer than most estimates found in the literature because (1) frequent samplings were close to peak mass for each significant taxon, (2) subsamples were separated into living and dead tops, (3) the detached (fallen) litter and rates of input and decomposition for it were measured in a supporting study, and (4) root mass changes (ash free) from 20 cores per collection allows estimates of root storage. Estimates of losses due to animal consumption and respiration, translocation of soluble carbohydrates, and better approximations for turnover from roots are still needed. Estimated rates of input to and loss from standing (attached) dead tops for the current year seem realistic but could be refined if separate estimates for the previous year's dead tops could be made. (Many studies neglect or underestimate these transfers for both current and old dead material, and more satisfactory methods of identifying age classes and transfers for such material need further attention.)

Input and decomposition rates for detached litter appear to be balanced, so a steady state was approximated surprisingly well; yet income and loss rates must both vary seasonally and hence seem to be fairly well in phase with one another. For many ecosystems we should not expect such convenient balances and phasing. Total live community biomass is still increasing (mostly as roots) in the young *Festuca* stand, but this total appears more nearly stabilized in the older, more mixed stand, where *Andropogon* contributes only about half the above-ground production.[31] Longer-term measurements are needed to relate slow trends to successional change (in which *Festuca* would normally be replaced by *Andropogon, Rubus,* and more woody communities).

[31] J. M. Kelly *et al., Models of Seasonal Primary Production in Eastern Tennessee Festuca and Andropogon Ecosystems,* ORNL-4310 (June 1969).

SHORT-TERM EFFECTS OF COVER MANAGEMENT ON DECOMPOSITION PROCESSES IN GRASSLAND SOIL

C. R. Malone N. T. Edwards

Research on the ecological effects of vegetation cover management characteristically has concerned changes in species composition, primary production, and microclimate as a function of grazing and mowing intensity or herbicide applications. Little attention has been given to the influence of cover manipulation on decomposition of organic matter, on nutrient cycling, or on the biotic components of ecosystems which influence these processes.

The effects of chemical and mechanical cover control on processes of organic matter decomposition in grassland (*Festuca elatior*) soil were studied in a randomized plot experiment during the 1968 growing season. Treatments consisted of plots mowed and raked biweekly, plots mowed and sprayed with dalapon (2,2-dichloropropionic acid) to kill shoots and roots, and unmowed plots sprayed with dalapon. Dalapon was selected as the chemical treatment, since it is a grass-specific herbicide with minimal direct effects on soil biota. Attributes of the soil system studied in response to cover management were net changes in soil organic matter, decomposition rates of cellulose, soil temperature and moisture, and densities of soil microarthropods and bacteria.

The numbers of herbivorous mites in the soil were not affected by any treatment, but during the latter part of the growing season the densities of soil Apterygota and predaceous-parasitic mites became significantly lower in denuded plots than in covered plots (Fig. 10.13). These differences were associated with high and low extremes of soil temperature and moisture, respectively, which also occurred in denuded plots (Table 10.18). Soil organic matter content perhaps could be thought to have limited saprovores, such as the Apterygota, but such apparently was not the case here, since low organic matter in the plots treated only with dalapon did not correspond to low densities of animals. In fact, these plots had the greatest total number of soil animals, and this was associated with the most favorable microclimatic conditions. This suggests that in grasslands the microclimatic influences of plant cover are more important than its nutritional properties to some microfauna.

Table 10.18. Influence of Fescue Cover Management on Various Attributes of the Soil System

Treatment effects were tested by an analysis of variance; values followed by different enclosed letters are statistically different ($P \leq 0.05$) from all others in that column

Situation	Soil Temperature (°C)	Soil Moisture (%)	Net Change in Percent Organic Matter	Monthly Decomposition Rates of Cellulose (%)	Number of Bacteria (grams dry weight soil)
Control	27 (A)	17 (A)	+0.2 (A)	9.0 (A)	4.5×10^6 (A)
Dalapon treated only	24 (A)	18 (A)	−0.6 (B)	75.0 (B)	6.7×10^6 (B)
Mowed only	34 (B)	14 (B)	−0.3 (C)	9.0 (A)	4.3×10^6 (A)
Mowed and dalapon treated	35 (B)	12 (B)	−0.9 (D)	69.0 (B)	5.8×10^6 (B)

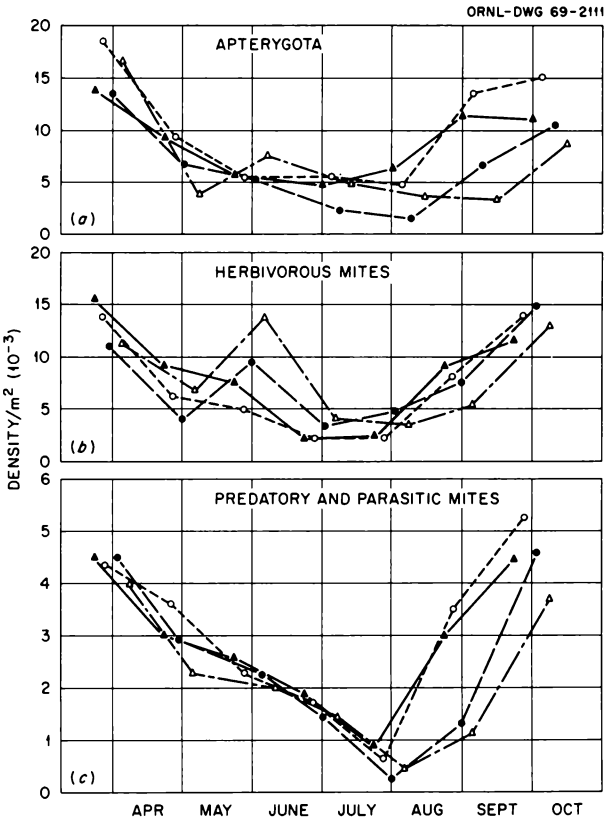

Fig. 10.13. Responses of Soil Microarthropods to Cover Management in a Fescue Grassland. ▲, control; ○, herbicide-treated only; ●, mowed only; △, mowed and herbicide treated.

It is uncertain whether the predaceous-parasitic mites were limited by microclimatic factors or by prey and host availability. Densities of these animals followed high soil temperature, low soil moisture, and low Apterygota densities. Several groups within the Apterygota probably provide the major food source for predaceous-parasitic mites and may have limited their populations in plots where the cover was removed.

In plots upon which fescue had been killed, regardless of whether the dead cover was removed, densities of soil bacteria increased, enhancing rates of cellulose decomposition and losses of soil organic matter (Table 10.18). It subsequently was found, using aqueous fescue extract in inhibition studies, that living fescue produces substances toxic to bacteria. This explained in part the proliferation of bacteria whenever vegetation was killed.

The smaller net loss of soil organic matter in plots covered with dead fescue, compared with plots denuded of dead cover, probably was a consequence of litter breakdown and input to the soil. Reductions of soil organic matter in plots mowed biweekly probably resulted from two factors: (1) less root production compared with controls and (2) reduced input from litter breakdown. It is unlikely that decomposition of preexisting organic detritus in the soil proceeded at a greater rate in the mowed plots than in controls, since cellulose loss rates were similar in the two situations.

A primary consideration in vegetation management is to utilize practices that alter as little as possible such components of the ecosystem as soil biota and organic matter. Of the management techniques studied here, mowing alone probably would best be suited for control of vegetation cover, especially if there are possibilities that the site will in the future be restored to its original status. Mowing would be desirable where long-term control is necessary, since this type of management probably results in less pronounced changes in soil biota and organic matter losses.

If temporary elimination of living vegetation is needed, it would be advisable to leave dead cover intact

or add an organic mulch rather than denude a site. This would result in smaller net change in soil organic matter, since input from litter would partially offset losses by decomposition. Also important would be maintenance of more optimum microclimatic factors for preservation of soil biota. Effective denudation, as achieved here by combining mowing and herbicide treatment, appears to be the least desirable type of vegetation control, since it risks causing the greatest change in soil systems.

This study suggests that one determinant factor in the effects of management techniques on ecosystems is the presence of plant species that inhibit soil bacteria. If such plants dominate an area, any habitat manipulation that eliminates them will alter the soil system. The elimination of plants that produce substances retarding decomposition rates will enhance decay processes and result in rapid changes in the organic matter content of soil. This response undoubtedly changes soil characteristics and hastens mineralization. Such changes over periods longer than one growing season are certain to bring changes in soil biota and ultimately alter the entire nature of an ecosystem in terms of its ability to support a characteristically native biota.

PESTICIDE-INDUCED RESPONSES IN ORGANIC MATTER DECOMPOSITION IN A GRASSLAND

C. R. Malone D. E. Reichle

Through the use of selective pesticides it is possible to remove and exclude specific components of the biota from soil and litter, allowing assessment of the role of those components in ecosystem processes and providing a basis for predicting the impact of environmental perturbations on the functioning of ecosystems. This approach was used in a fescue (*Festuca arundinacea*) grassland to study the role of soil arthropods, earthworms, and microflora in the decomposition of organic matter.

Treatments initiated in July 1968 consisted of a persistent fumigant (phorate at 44.8 kg/hectare) to exclude litter and soil fauna, an earthworm extractant (formalin at 0.13 liter/m^2), and sodium chlorate at 0.57 kg/m^2 to simulate a "biocide." Three randomly allocated enclosures of 2 X 2 m each were used per treatment, and the sheet metal forming each pen was buried 250 cm deep to prevent immigration of soil animals. Data relative to decomposition processes taken at three-month intervals up to nine months posttreatment are given in Table 10.19.

Litter confined in nylon mesh bags disappeared least rapidly in pens treated with sodium chlorate and most rapidly in the two treatments designed to eliminate (1) earthworms only and (2) all invertebrate fauna. Acceleration of litter loss apparently was due to increases in microfloral populations, since litter from these pens characteristically was covered with a heavy growth of fungi. Although arthropods were present in formalin-treated pens, the disappearance rate of litter there was only slightly greater than in fumigated pens, suggesting that neither earthworms nor arthropods are primarily significant in the breakdown of litter. In fact, the data suggest that invertebrate fauna may disturb the microflora sufficiently to interfere with their optimum potential in decomposing grass litter.

Contrary to responses of litter, decomposition rate of confined roots was reduced by removal of earthworms and even more depressed by removal of all invertebrates. Thus the soil fauna probably are very important in the breakdown of dead root material in grasslands. Soil microflora appear to account for less than 50% of the decomposition of roots except under conditions of extreme densities, as occurred in the pens treated with sodium chlorate.

Table 10.19. Pesticide-Induced Responses of Decomposition Processes and Microfloral Populations in a Fescue Grassland

Treatment	Cumulative Percent Litter Loss			Cumulative Percent Root Loss			Monthly Percent Cellulose Loss			Density of Soil Bacteria (10^5)/g Dry Soil			Density of Soil Fungi (10^3)/g Dry Soil		
	Oct.	Jan.	Apr.	Oct.	Jan.	Apr.	Oct.	Jan.	Apr.	Oct.	Jan.	Apr.	Oct.	Jan.	Apr.
Control	42	45	57	6	24	25	17	7	14	30	33	25	24	26	58
Formalin treated	45	50	76	3	18	19	9	6	7	35	48	21	64	79	29
Phorate treated	39	50	72	2	9	10	27	15	29	55	31	17	55	91	62
Sodium chlorate treated	32	42	47	5	13	14	1	0	0	134	86	142	149	25	90

The monthly rate of loss of 5- by 5-cm strips of cellulose inserted into the soil was used as an index of microbial activity in the pens. Cellulose is less readily decomposed than most constituents of organic detritus and is degraded by microorganisms characteristic of climax communities or late successional stages. Reduced rates of cellulose decomposition in formalin-treated and sodium chlorate–treated pens, despite increased densities of soil microflora, suggest that these chemicals constitute disturbances to the soil system sufficient to set back microfloral succession. In the case of formalin, it is more probable that earthworm removal rather than chemical treatment induced this response, since formalin probably is quickly inactivated in soil systems. Formalin sometimes is used as a soil fungicide in agricultural practices, and that inactivation occurred prior to three months is suggested by the almost threefold increase at that time in fungi densities compared with controls.

Soil bacteria were at their lowest densities in control, formalin-treated, and phorate-treated pens in April. This possibly can be explained by the production of bacterial toxins by fescue plants. In October and January, fescue growth largely had ceased, but it was very active in April. In pens treated with sodium chlorate, living fescue was absent; consequently there was no depression of bacteria, and favorable conditions of soil moisture and temperature contributed to peak densities of soil bacteria in April.

Responses within the phorate-treated pens indicate the complexity of association between soil fauna and microflora. Although there was an initial increase in numbers of soil bacteria, their density, compared with controls, decreased after six months. The decrease probably was due to the removal of earthworms, since it is known that the fragmenting of organic detritus by earthworms stimulates bacterial populations. Fungal populations increased in phorate-treated pens, probably due to the removal of microarthropods which graze on hyphae and spores.

This project will be continued until at least 12 months' data are available. By completing analyses of data taken at six-week intervals and by inclusion of information on soil fauna, rates of soil respiration, and changes in nutrient and caloric content of litter and roots, it will be possible to more completely evaluate both the role of soil fauna and the interaction of fauna and microflora in processes of organic matter decomposition.

TOXICITY OF FESCUE EXTRACT TO SOIL BACTERIA

C. R. Malone

Numerous species of plants, including some grasses, are known to produce substances toxic to nitrifying bacteria. Although research largely has been limited to the effects of plant-produced toxins on bacteria important in the nitrogen cycle, it has been suggested that some plants produce broad spectrum inhibitors affecting many kinds of soil decomposers. The advantage given to such plants is through limiting nutrient availability to competing species.

To test the possibility that *Festuca arundinacea* produces broad spectrum bacterial inhibitors, studies were initiated utilizing aqueous fescue extract in inhibition studies. One kilogram of fescue roots and shoots was ground in 500 ml of distilled water, and the resulting solution was filtered with Millipore paper. Disks (2.3 cm in diameter) of No. 3 filter paper were saturated with the filtrate and placed on nutrient agar plates smeared with a soil suspension solution. Two disks were placed on each of 20 agar plates, and a duplicate set of plates using disks soaked in distilled water were used as controls. Responses of bacteria to fescue extract were taken as the radius of the zone of inhibition around each disk, percent area not colonized within the zone, and the percent area not colonized outside the zone.

The effect of the extract on bacterial growth was very pronounced, with a mean inhibited zone of 6.5 mm^2 compared with no inhibition in the controls. Within the inhibited zone, 90% of the surface area was uncolonized, and 40% of the remaining area of the plate was uncolonized due to diffusion of the extract through the agar. These effects, compared with controls, were very highly significant ($P \leqslant 0.001$).

Control and fescue-extract agar plates were treated with gram stain 48 hr after inoculation. Forty percent of control colonies were gram-negative bacteria, whereas in plates having disks soaked in fescue extract, gram-negative bacteria largely were absent. It therefore appears that *Festuca* inhibits the growth of at least some gram-negative bacteria. This fact may explain in part why rates of organic decomposition in soil are drastically accelerated whenever fescue is killed.

The production of broad spectrum bacterial toxins by plants obviously needs further investigation. Little is

known of the amounts and persistence of plant-produced bacteriostatic and bacteriotoxic substances or of the magnitude of depression of organic matter turnover and rates of nutrient cycling induced by toxins. Such an understanding will be helpful in assessing the potential productivity of plant communities and rates of cycling of radionuclides in ecosystems.

CHARACTERIZATION OF PARTICULATE ORGANIC MATTER IN OLD-FIELD AND FOREST SOILS

C. R. Malone Margaret B. Swartout

Particulate organic matter provides the base or growth medium for the bases of many saprovore food webs in soil, making knowledge of the size, quantity, and energy content of organic particles in soil important in understanding the dynamics of soil ecosystems. Most studies of soil organic matter have involved humus and humic acid, with little emphasis on undecomposed particulate matter. The apparent reason for this is the difficulty of separating superhumic organic particles from mineral soil. Use of an aqueous flotation extraction procedure enabled us to overcome this obstacle and characterize soil particulate organic matter by size, quantity, and energy content in two ecosystems, a *Festuca arundinacea* dominated old field (ecology area 0800) and a *Liriodendron tulipifera* dominated forest.

In July 1968, 20 2-cm-diam soil cores were taken randomly to a depth of 30 cm from each site. The 20 cores from one location were composited, and the particulate organic matter was extracted by washing the samples in an aqueous solution of 5% sodium hexametaphosphate and 13% magnesium sulfate. Once the material was floating, the solution was strained through sieves selected to retain particles of 1190, 500, 297, 210, 105, and 44 μ. Particulate organic matter from old-field and forest soils was then characterized by ash-free dry weight (AFDW)/m^2 and caloric content (Table 10.20).

In both soils, greater energy content (cal/g AFDW) of organic particles was associated with larger size classes. There apparently was no relation between particle size and quantity of organic matter, since the biomass of smaller particles often exceeded that of larger ones in both field and forest soils. About 40% of the particulate organic matter was between 44 and 210 μ in size and, under microscopic inspection, appeared to be amorphous detritus. Because of its small size, this material probably is important in the food webs of many soil microarthropods, either directly as food or as growth medium for the bacteria and fungi that these animals graze upon.

Table 10.20. Biomass and Energy Content of Particulate Organic Matter per Square Meter to a Depth of 30 cm in Old-Field and Forest Soils

Particle Size (μ)	Grams Ash-Free Dry Weight		Calories per Gram of Ash-Free Dry Weight		Total Kilocalories per Square Meter	
	Field	Forest	Field	Forest	Field	Forest
>1190	507	956	4198	3366	2129	3217
500–1190	202	337	3707	3247	747	1094
279–500	240	238	2518	2850	604	678
210–297	258	231	2412	2268	622	524
105–210	375	553	2357	2067	884	1143
44–105	559	278	2359	2035	1319	566

The forest soil had larger quantities of particulate organic matter than the field soil; however, the reverse was true of caloric content per gram of AFDW. Thus, although the total biomass of particulate organic matter was 1.21 times greater in the forest soil than in the old field, the energy present was only 1.15 times greater. These data suggest that differences in biomass and total energy content of standing crops between woodland and herbaceous ecosystems are not as great below ground as above, since forests characteristically have 10 to 30 times more plant and litter biomass than fields.

Mathematical models and rate parameters are available for describing litter input, storage, and loss; but the application of such quantitative techniques has been restricted to above-ground systems, with no attempts to describe processes below the soil surface. Data such as those presented here describing the standing crop of particulate organic matter in soil can facilitate studies of decomposition processes and heterotrophic productivity in subterranean systems.

TEMPERATURE DEPENDENCE OF ^{47}Ca, ^{42}K, AND ^{22}Na TURNOVER IN ARTHROPODS

R. I. Van Hook, Jr. M. H. Shanks

The biological turnover of ^{47}Ca, ^{42}K, and ^{22}Na was determined for the following grassland species: *Melanoplus sanguinipes* (grasshopper), *Conocephalus* spp. (grasshopper), *Pteronemobius fasciatus* (cricket), and *Lycosa punctulata* (wolf spider). Adults of these species were collected from the field site (ecology area 0800) and allowed to become acclimated to the experimental

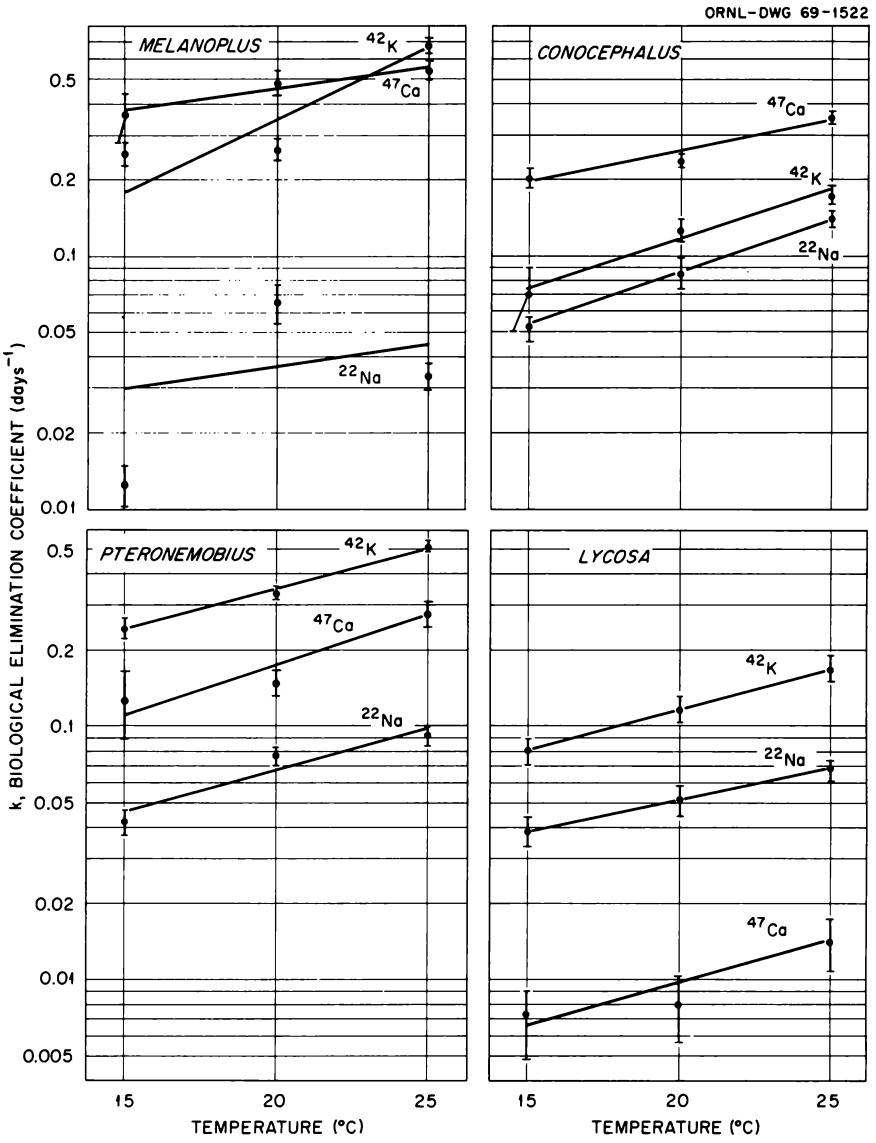

Fig. 10.14. Biological Turnover Rates of ^{47}Ca, ^{42}K, and ^{22}Na in Four Grassland Arthropod Species as a Function of Temperature.

temperatures of 15, 20, and 25°C. Separate experiments were conducted for each arthropod species on each radioisotope at all three experimental temperatures. In each experiment the insects were allowed to feed for 24 hr on fresh fescue shoots which had been placed in radioisotope solution for 24 hr. Spiders were tagged with radioisotope by allowing them to feed on cricket nymphs (*Pteronemobius*) which had been tagged by feeding on fescue shoots. After 24 hr of feeding, the radioactive food was removed from all animals and replaced with nontagged food. Thereafter, food and water were changed daily.

Biological elimination coefficients (k_b) were determined according to a previously described method.[32] The k_b values for each radionuclide in each arthropod species were plotted against temperature on a semilog scale (Fig. 10.14). These data were then regressed in the equation

$$y = ae^{bX}, \tag{1}$$

[32] R. I. Van Hook and D. A. Crossley, Jr., *Health Phys.* 16, 463–68 (1969).

and the slopes of these lines were tested against a slope of 0.0693, which is the slope of a line obeying a Q_{10} = 2 relationship. None of the slopes were significantly different from a Q_{10} = 2 slope ($P \leqslant 0.05$).

The k_b values for a radionuclide in a particular species under field conditions may be calculated from Eq. (1) using a = intercept associated with that particular radionuclide-species combination, e = base of the natural logarithm, b = 0.0693, and X = the field temperature of interest. Turnover rates may be used to describe the movement of stable calcium, potassium, and sodium through each of the arthropod species being studied and will permit a better understanding of the transient behavior of these elements in the secondary and tertiary trophic levels. Data from soil and vegetation studies may be combined with these results to help elucidate mineral cycling in animal components in a grassland community. Turnover rates may also be used to calculate food consumption by arthropods. In this case a knowledge of whole-body concentrations of these elements and their concentration in the food source is necessary.

KINETICS OF ^{137}Cs AND ^{54}Mn IN SAND-GRASS-GRASSHOPPER SYSTEMS

Martin Witkamp Virginia Merchant
Marilyn L. Frank

In previous reports[30] significant effects of temperature and soil fertility on ^{137}Cs and ^{54}Mn kinetics in sand-grass-grasshopper systems were reported. Further analysis of this soil-producer-consumer system, using analog computer simulations of experimentally obtained net transfers of ^{137}Cs and ^{54}Mn, showed that about one-third of the ^{137}Cs and ^{54}Mn content of the standing crop resulted from contact contamination of

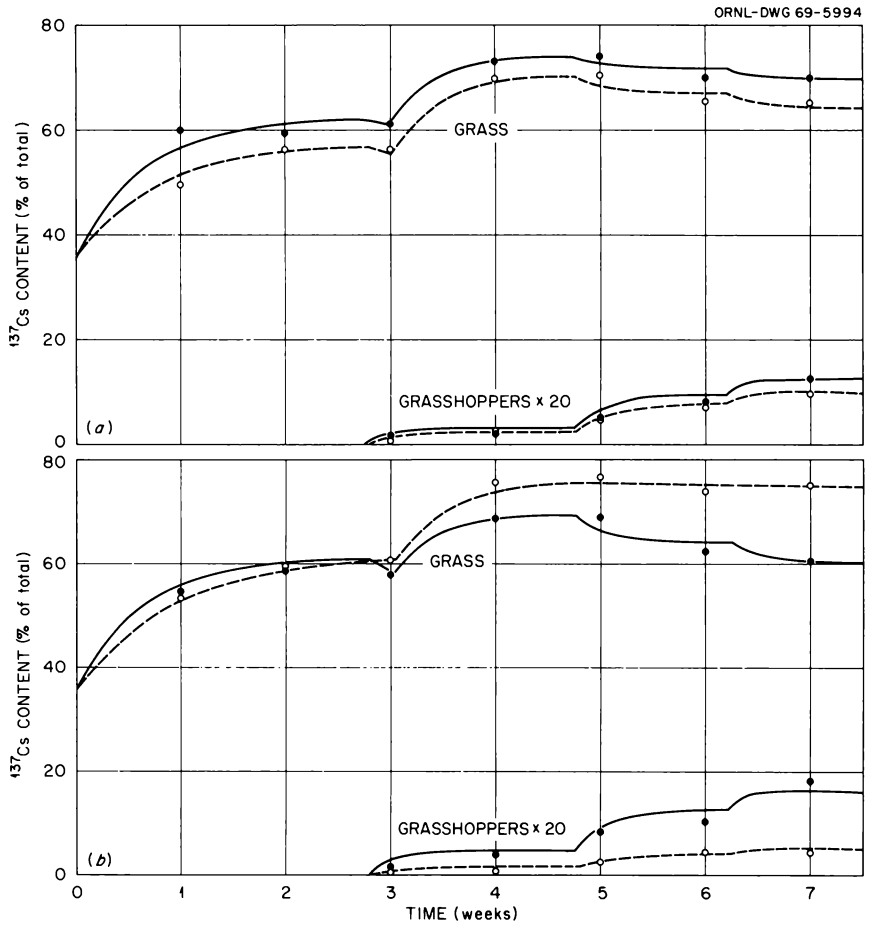

Fig. 10.15. Computer-Simulated Curves Fitted to Experimental ^{137}Cs Distributions in Grass and Grasshoppers (X20) at (*a*) Two Levels of Soil Fertility (● Knop's, ○ Tap Water) and (*b*) Two Temperatures (● 25°C, ○ 16°C).

the grass seeds rather than from root uptake (Fig. 10.15). These simulations also suggested that the introduction of a few grasshoppers in a stand of grass temporarily may increase rates of mineral uptake by grass (Fig. 10.15). The resulting increases in standing crop, however, were not greater than 25% because of increased consumption by the growing grasshopper population (both in biomass and density). A third transfer mechanism suggested by the simulation model was that dropping of cutoff pieces of grass by the grasshoppers contributes as much or more to the isotope return from grass to soil than did the grasshopper excrements. Such computer simulations continue to provide new insight in the ecology of mineral kinetics in producer-consumer systems. Present work concerns measurements on additional transfer rates needed for construction of a more refined and accurate model of nutrient cycling.

AN ENERGY BUDGET FOR WOLF SPIDERS, *LYCOSA RABIDA* WALCKENAER

R. I. Van Hook, Jr. B. C. Moulder

Energy flow is one of the basic functional characteristics of an ecosystem. The herbivore to predator transfer of energy in arthropod food chains constitutes an important aspect of the process of energy flow. To fully describe this transfer of energy, measurements of ingestion, assimilation, and egestion of energy are necessary. These measurements were obtained for the wolf spider, *Lycosa rabida* Walckenaer, to help assess the role of this dominant invertebrate predator in a grassland community.

Adult lycosid spiders were collected in the field (ecology area 0800) and maintained in separate cages under laboratory conditions (20°C and 50% relative humidity) for two days before initiating the study. Spiders were supplied with fresh water and *Acheta domesticus* (L.) nymphs daily. After being discarded by the spider, cricket remains were collected, dried at 105°C for 24 hr, and weighed. Dry weights for spiders and crickets used in this study were determined from log-log regressions of fresh weights against dry weights; for *L. rabida*, log (dry weight) = $-0.4134 + 0.9231 \cdot \log$ (fresh weight) and for *A. domesticus*, log (dry weight) = $-0.8352 + 1.1467 \cdot \log$ (fresh weight). After ten days spider feces were collected and dried at 105°C for 24 hr. Calorific equivalents of cricket body, cricket remains, spider body, and spider feces were determined with a microbomb calorimeter.

The dry-weight measurements of intake and output combined with the calorimetric determinations of these same materials were used in constructing an energy budget for *L. rabida* (Table 10.21). Individual spiders consumed 7.1 mg of cricket dry weight and produced 1.0 mg of feces per day. This is equivalent to an ingestion rate of 9.9% of dry body weight per day and an egestion rate of 1.4%. On an energy basis (cal/day), ingestion was 10.6% of total body energy per day and egestion was 0.9%. Spiders assimilated 70.4% of the killed cricket prey and 85.7% of the dry weight of material actually ingested. In terms of energy flow, these efficiencies are misleading since caloric values of whole prey, prey remains, assimilated portions, and feces differ. Caloric value of ingested food was 1.02 times that of whole prey, and the caloric value of assimilated food was 1.06 times as high as that of ingested food. Of the total energy consumed, 76.3% was assimilated, while 90.8% of the ingested energy was assimilated. Assimilation energy was partitioned into tissue growth (secondary production) and respiration (maintenance and active). Secondary production

Table 10.21. A Food Energy Budget for Lycosid Spiders of Mean Dry Weight 70.94 mg and Caloric Content of 5.45 cal/mg

	Prey	Prey Remains	Ingestion	Spider Feces	Assimilation	Production	Consumption (Percent of Body Value)
Milligrams of dry weight per day	8.61	1.54	7.07	1.02	6.06	2.20	9.9
±S.E.	0.92	0.25	1.05	0.09	1.00	0.60	0.9
Calories/milligram	5.72	5.14	5.85	3.67	6.20	5.45	
±S.E.	0.05	0.14	3.65[a]	0.70	4.29[a]	0.21	
Calories/day	49.25	7.92	41.33	3.74	37.59	11.99	10.6
±S.D.[a]	16.57	4.07	17.06	1.62	17.14	10.38	0.8

[a]Standard deviations calculated indirectly.

accounted for 31.9% of the assimilated energy. The remaining 68.1% was divided between maintenance respiration (30.6%) and respiration due to locomotor activity (37.4%).

ENERGY DYNAMICS OF A TERRESTRIAL SNAIL, *MESODON THYROIDUS* SAY

R. V. O'Neill R. H. Wiman
Gladys J. Dodson

An investigation was made of the summer energy budget of adult snails, *Mesodon thyroidus,* which occur on the 0800 old-field area. Snails were maintained in the laboratory in constant-temperature chambers feeding on leaves of *Plantago* sp. Respiration was measured in Phillipson electrolytic respirometers, and volumes of oxygen were converted to calories by assuming a respiratory quotient of 0.8. The feeding rate for a 24-hr period was measured with weighed disks of *Plantago* soaked overnight in a ^{134}Cs solution and blotted dry. Knowing the concentration of ^{134}Cs in the leaf, it was possible to calculate plant consumption from the radioactivity in the snail after 24 hr. Some snails did not feed during this period and served as controls for external contamination. The rate of ^{134}Cs excretion was measured by collecting feces at 48-hr intervals, drying overnight, and weighing. Weight changes were determined by weighing the snails at intervals during the experiments. To express all data in units of energy, a Phillipson microbomb calorimeter was used to determine the caloric equivalent for a gram of snail flesh, *Plantago* leaf, and excrements.

Table 10.22 shows the estimates for the energy budget of the adult snail during July. The table indicates that respiration losses fai exceeded energy assimilated. Most of the energy deficit was balanced by catabolism of snail tissue. The caloric loss of tissue plus the energy obtained by feeding account for all but 5.6% of the energy losses in respiration; this small difference can be explained by experimental error. During this last season of life, the snails are unable to consume sufficient food to balance metabolic losses. The energy deficit is met by utilizing energy stored in body tissues with associated deterioration and weight loss. There was a clear correlation between the negative energy budget of adult *M. thyroidus* and the stage of the life cycle during which the measurements were taken. Field observations indicated that population density was rapidly decreasing and suggested that few adults would survive until the following season. This population decline is correlated with the large negative energy budget under which adult snails were operating. The snails' feeding rate may be reduced during this time, or age, and the stress of breeding may have produced an abnormally high respiration rate.

Table 10.22. Energy Budget of Adult *Mesodon thyroidus* Say During July

All values are in units of cal cal^{-1} day^{-1} $\times 10^3$; values in parentheses are standard errors

Gross energy intake	7.18 (1.70)
Excretory energy	3.15 (0.35)
Assimilated energy	4.03 (1.27)
Metabolic energy loss	15.39 (1.41)
Body tissue energy loss	10.50 (3.50)

The relationship between population decline and negative energy budget emphasizes the utility of evaluating energy budgets as a means to gain deeper understanding of the mechanisms involved in life cycle events. These findings also point out the need for caution in evaluating population energy dynamics, since the energy balance can change significantly during the life history of an individual.

AVOIDANCE OF DEAD GRASS COVER BY PINE MICE

C. R. Malone

Pine mice (*Pitymys pinetorum*) often become pests in orchards by girdling trees. No physical barriers preventing invasion by these animals have been developed, and the only effective control has been through chemical barriers of endrin, a highly toxic and residual chlorinated hydrocarbon pesticide.

During the course of an experiment on chemical and mechanical management of grass (*Festuca elatior*) cover, it was found that pine mice avoid areas where the vegetation was left intact but killed by dalapon (2,2-dichloropropionic acid). Three such plots (3 X 5 m) were prepared in April 1968, randomly allocated with a comparable number of controls. To demonstrate that pine mice were avoiding the treated plots, counts of the number of active trails were made in late June by establishing three transects across the width of each treated and control plot. As an additional measure of activity, five Sherman live-traps baited with oatmeal and peanut butter were set in randomly selected trails in each plot. The traps were inspected at 24-hr intervals for 14 days, and the number of captures per plot was tabulated.

An average of 14.0 active trails per plot were found in control plots, compared with 0.3 for treated plots.

Capture success during the trapping period was 4.3 animals per control plot; no animals were taken in treated plots. The difference between controls and treated areas for both the number of active trails and the number of animals captured was highly significant ($P \leq 0.001$). The apparent reason for avoidance of the treated areas by pine mice was lack of food and not lack of ample cover, since line-intercept measures of grass cover showed 100% cover in both types of habitat. There is no basis for suspecting that the herbicide contributed to exclusion of pine mice since dalapon presents no toxicity hazard to wildlife.

These findings suggest that construction of ecological barriers in the form of dead grass borders might prove effective in detouring pine mice away from enclosed areas. Such barriers can be constructed by chemicals such as dalapon or by heat-killing grass with polyethylene sheeting and are more desirable than ones provided by residual poisons such as endrin. Avoidance of dead grass cover by pine mice also suggests a possible means of experimentally modifying grassland habitats in attempts to assess the importance of cover in the behavioral patterns and habitat resources of pine mice.

INVESTIGATION OF THE CONCEPT OF USING RADIONUCLIDES FOR METABOLIC MEASUREMENTS IN SMALL MAMMALS

C. E. Baker P. B. Dunaway

The hypothesis that elimination rates of certain radionuclides are proportional to rate of metabolism is being tested in two species of small mammals. This research represents an endeavor to establish a technique for measuring metabolism of free-ranging animals, which, if successful, would generate a better understanding of ecosystem energetics. At the present level of technology, field metabolism of mammals can only be estimated from questionable laboratory measurements, which seldom attempt to account for the influence of normal behavior and activity on metabolic rate.

One experiment has been completed which utilized ^{59}Fe and ^{137}Cs in a simultaneous tagging technique, and another is in progress. The species under study are cotton rats (*Sigmodon hispidus*) and harvest mice (*Reithrodontomys humulis*). The first experiment consisted in a seasonal field study in which cotton rats were maintained in four 10- by 10-m enclosures at McNew Hollow (Ecology 0911 Area). Elimination of ^{59}Fe and ^{137}Cs by one group of these animals was measured in the laboratory (May–June) to provide a third treatment group with which to compare the seasonal data. Results from these three treatment groups are presented in Table 10.23. The basic assumptions in this study were that metabolic rates of cotton rats in the field would be higher in winter than in spring, because of lower temperatures in winter, and higher in the field than in the laboratory, because of greater activity in the field. If these assumptions are correct, ^{59}Fe elimination may be a good indicator of metabolism, while ^{137}Cs elimination does not appear to be metabolically influenced (Table 10.23).

Table 10.23. Biological Half-Times[a] (Mean ±S.E.) of Indicated Isotopes in Three Groups of Cotton Rats

	^{137}Cs	^{59}Fe	N
Winter	7.5 (±0.22)	108.3 (±3.90)	19
Spring	7.3 (±0.35)	147.5 (±8.47)	14
Laboratory	7.9 (±0.38)	200.3 (±30.31)	12

[a]Calculated from the following:
regression equation $Y = ae^{-kt}$
$\frac{-0.6931}{-k} = T_b$ (biological half-time).

The second experiment was designed to allow comparison of laboratory elimination rates of ^{59}Fe and ^{137}Cs and rates of carbon dioxide production in harvest mice and cotton rats. Groups of these animals were given both isotopes intraperitoneally, and 24-hr CO_2 measurements are being taken during the interval of isotope elimination measurement. Carbon dioxide production is monitored with a Beckman IR-215A infrared analyzer, operating in conjunction with an air-supply system designed and constructed by ORNL (Figs. 10.16 and 10.17). The system is capable of continuous automatic operation, and data are recorded by teletype and computer punch tape. Carbon dioxide measurements made thus far indicate good resolution between individuals and reflect definite periods of activity. These measurements are expected to be of great value in determining whether ^{59}Fe and ^{137}Cs elimination is related to metabolism. Only preliminary comparisons of CO_2 production and isotope retention have been made thus far, and a poor correlation between isotope elimination and metabolism has been noted in the few individuals studied. The effects of different environmental temperatures, chemical metabolic regulators, and ionizing radiation are to be determined.

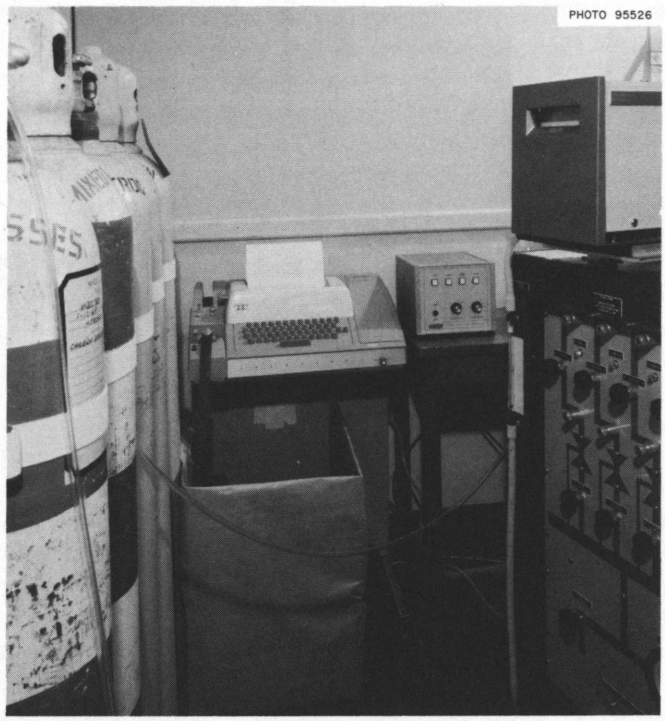

Fig. 10.16. Apparatus for Measuring CO_2 Production of Laboratory Animals. From right to left, CO_2 analyzer resting on specially constructed automatic air-supply system, analog-to-digital converter, teletype.

Fig. 10.17. Metabolism Chambers in Which Animals Are Placed for CO_2 Measurements. The chambers are designed to accommodate the entire animal cage, thus reducing disturbance to the animal being measured.

11. Radionuclide Cycling in Aquatic Ecosystems

Evelyn Brown[1]
J. R. Gammon[2]
N. A. Griffith[3]
S. E. Kolehmainen[4]
Barbara Martinedes[5]
Carolyn Marvin[6]
R. H. Monheimer[7]
D. J. Nelson[3]
J. R. Reed
S. A. Rucker
D. L. Willis[8]

Research in aquatic ecology is providing data on radionuclide movement in surface waters such as rivers and lakes. These data are needed for interpretation and quantitative prediction of the behavior of radionuclides in aquatic habitats. Such research investigations also increase our knowledge of the functioning and organization of aquatic ecosystems and provide data required for application to practical problems of atomic energy programs such as nuclear power, desalination, radioactive waste disposal, or Plowshare projects.

White Oak Lake continues as the focal point for studies of radionuclides under natural environmental circumstances. Organisms living in the lake are essentially in equilibrium with waste radionuclides such as ^{90}Sr, ^{137}Cs, ^{106}Ru, and ^{60}Co; hence, extrapolations can be made to steady-state conditions. Laboratory studies in conjunction with the field work provide data needed for more sophisticated predictive models of nonsteady-state situations. These data are pathway description, turnover rate, and fractional assimilation coefficients of radionuclides from various foods. These investigations provide a better quantification of radionuclide behavior in aquatic food chains.

[1] AEC student trainee.

[2] Visiting investigator – DePauw University.

[3] Dual capacity.

[4] Alien guest.

[5] Health Physics Fellowship student.

[6] NSF-URP Program.

[7] AEC Postdoctoral Fellow.

[8] Visiting investigator – Oregon State University.

[9] S. I. Auerbach *et al. Health Phys. Div. Ann. Progr. Rept. July 31, 1968*, ORNL-4316, p. 122.

RADIOTUNGSTEN STUDIES

J. R. Reed N. A. Griffith
Barbara Martinedes

Studies of radiotungsten uptake and turnover in black bullheads, started last year,[9] were completed. Bullheads accumulated ^{187}W from water, and an apparent equilibrium was reached within four days (Fig. 11.1), and

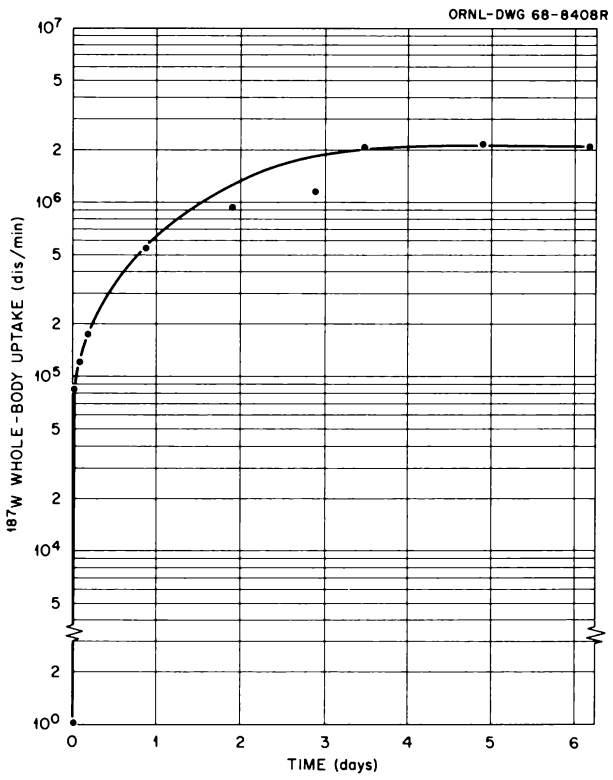

Fig. 11.1. Whole-Body Uptake of ^{187}W from Water by Black Bullheads. Each point represents the mean of four fish. The water contained 2×10^4 dis/min of ^{187}W per milliliter.

76% of ^{187}W fed to bullheads in night crawlers was assimilated. Whole-body elimination of radiotungsten varied with the manner of intake. Fish that had accumulated ^{187}W from water lost activity steadily during a seven-day excretion period with a T_b of 2.75 days (Fig. 11.2*a*). Bullheads receiving ^{187}W in a single feeding lost activity at two rates. The quicker component of elimination had a T_b of 14 hr, while the slower component had a T_b of six days (Fig. 11.2*b*). It was apparent that the different modes of tagging fish with radiotungsten resulted in accumulations of the radiotungsten in pools having slightly different turnovers. These pools were not identified positively in the subsequent experiments where fish were dissected.

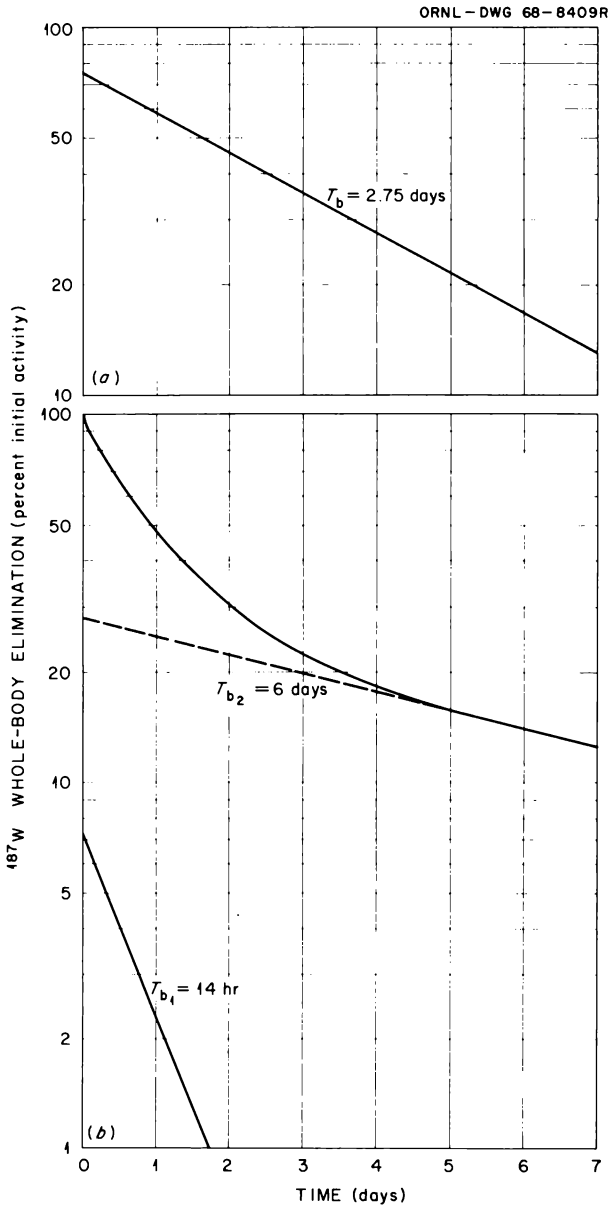

Fig. 11.2. Whole-Body Elimination of ^{187}W by Black Bullheads. (*a*) Fish tagged by holding them in a water solution for four days. The biological half-life of 2.75 days was determined from data on six fish. (*b*) Fish tagged by a single feeding. The T_b's of the two components were determined from data on five fish.

Serial dissections of fish tagged with ^{181}W in water provided information on the localization of ^{181}W in the different tissues during uptake and elimination. Most of the whole-body activity of ^{181}W was found in the bone, flesh, skin, gills, gut, and blood (Fig. 11.3) during the uptake phase of the experiments. Bone, skin, and blood initially accumulated a large proportion of the ^{181}W in the fish. This proportion decreased gradually for eight days, at which time bone still contained 21% of the whole-body activity. Flesh was another tissue where ^{181}W accumulated in a major pool, but activity increased gradually during the eight days. Internal organs contained relatively minor quantities of ^{181}W.

Losses of ^{181}W activity after exposures stopped were followed for 16 days. During this time, all tissues examined decreased rapidly in activity, with T_b's ranging from 2.1 to 8.0 days (Fig. 11.4). Bone had the slowest elimination rate (T_b of 8.0 days), and flesh had a T_b of 3.1 days. These different loss rates affected the percentage retention of ^{181}W among the various tissues during excretion (Fig. 11.5). Thus, ^{181}W in bone became more prominent, and, at the end of the 16-day period, bone contained about 80% of the whole-body burden.

This study showed that black bullheads are capable of accumulating and retaining radiotungsten from both food and water. The distribution of radiotungsten among the various tissues was quite similar to distributions reported for the rat.[10]

Radiotungsten in Crayfish (*Cambarus longulus longerostris*)

In laboratory experiments the whole-body uptake and elimination, as well as tissue distribution, of ^{181}W in crayfish were studied. Crayfish are important links in aquatic food chains and are sometimes eaten by man.

Crayfish were collected locally, and the uptake of ^{181}W by 18 specimens was studied by placing them in a stainless steel kettle containing 50 liters of solution containing 1.3×10^4 dis min^{-1} ml^{-1}. For the

[10] S. V. Kaye, *Health Phys.* 15, 399 (1968).

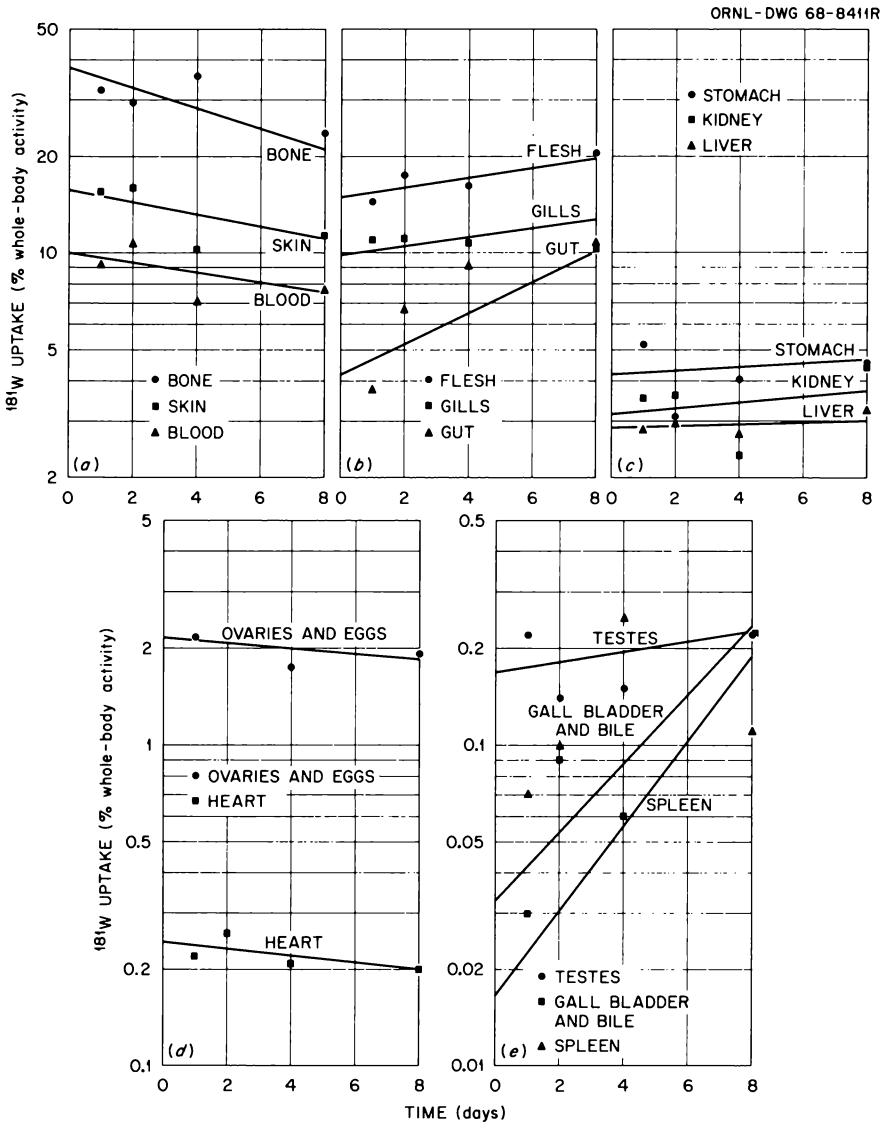

Fig. 11.3. Percent of Whole-Body Activity of ^{181}W Contained in Separate Tissues and Organs of Black Bullheads During Uptake from Water.

elimination study, five crayfish were held in the isotope solution for seven days and then removed to a stainless steel kettle containing 190 liters of flowing spring water (12–16°C). The crayfish in both uptake and elimination studies were rinsed in spring water and counted daily for 16 and 14 days, respectively, in a Packard well-type single-channel analyzer with a 3- by 3-in. NaI(Tl) well crystal. The 58-kev x ray of ^{181}W was counted with 34% efficiency. Data were corrected for decay and efficiency and recorded as disintegrations per minute per gram. The mean values ± 1 standard error were plotted for each day to establish the uptake and elimination curves. The possibility of error in the whole-body counting due to self-absorption was considered in both studies. Material balance data obtained from the dissections indicated that self-absorption was negligible for the majority of animals tested, and slight differences in data between whole-body counts and counts of dissected animals could be accounted for by the statistical variability of the data.

Twenty-four crayfish from 6.1 to 22.1 g were used in the 14-day uptake study. Three were dissected on days 1 through 5, 7, 10, and 14, and heart, hepatopancreas, gastrointestinal tract, gastroliths, gills, exoskeleton,

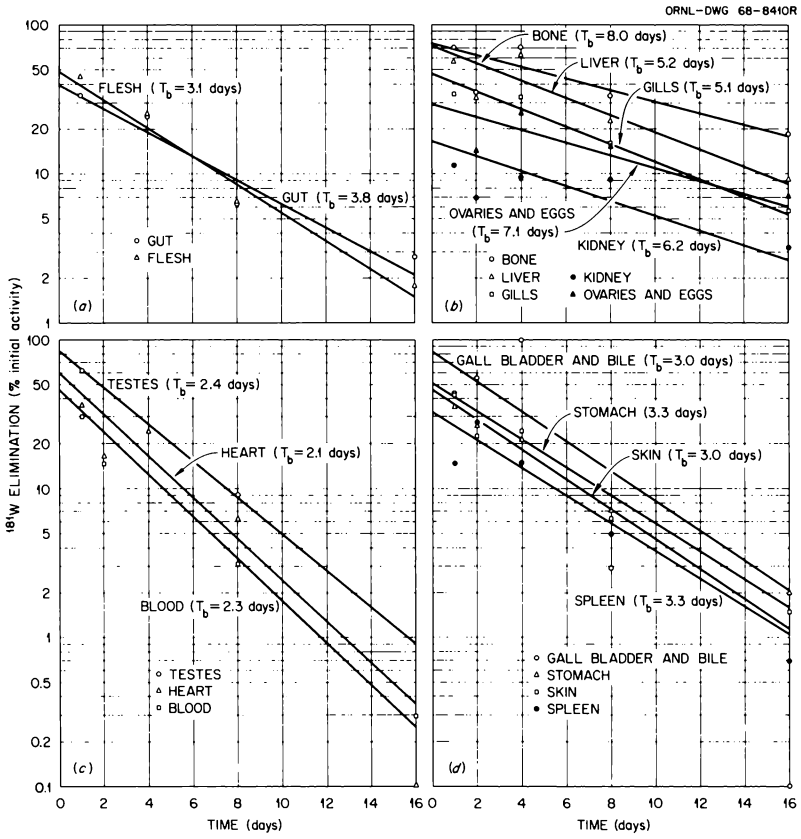

Fig. 11.4. Elimination of ^{181}W Activity by Black Bullhead Tissues After Four Days Uptake from Water. Data are expressed as percent of initial tissue activity. Each point is the mean of three samples, and T_b's are shown in parentheses.

muscle, and gonads were counted for ^{181}W activity as in the whole-body studies. Uptake curves were drawn from linear regression analyses on the mean values.

The whole-body uptake for ^{181}W by crayfish occurred in three stages during a 16-day period (Fig. 11.6). The initial, rapid component accounted for 55.8% of the uptake in the first two days. A second, slower phase existed from the 2d to the 11th day, after which the uptake leveled off through the 16th day. The crayfish concentrated as much as 7.5 times the amount of isotope placed in their environmental water.

In the tissue uptake study, the order of ^{181}W concentration (dis min^{-1} g^{-1}) was exoskeleton > GI tract > hepatopancreas > gills > muscle > gonads. The differences among tissues were not great, however, since the concentrations reached the same order of magnitude, 10^5 dis min^{-1} g^{-1}, in the first four tissues (Fig. 11.7). The heart and gastroliths accumulated negligible amounts of tungsten. If, as suggested by Wase,[11] the tungsten is accumulated in bony structures as calcium tungstate, more activity might have been expected in the gastroliths, which store calcium during the molting cycle. The uptake for all tissues except gills was linear on semilog plots from the 1st to the 14th day. As shown in Fig. 11.7*c*, the uptake by gills leveled off after the 10th day. The rate of uptake was highest for the hepatopancreas and the GI tract, and the slopes for these curves were almost identical (Fig. 11.7*b*). Uptake was slower in the exoskeleton, gonads, and muscle, but these curves also had similar slopes (Fig. 11.7*a*). The fact that two groups of curves appear may indicate the presence of two modes of uptake: (1) simple, rapid adsorption and accumulation of radioactive water in the GI tract, hepatopancreas, and gills and (2) some type of slower incorporation into the gonads, muscle, and exoskeleton.

A whole-body elimination curve for ^{181}W that has a fast initial component probably accounting for elimination from the GI tract is presented in Fig. 11.8. A biological half-life of 12.2 days was calculated from the

[11] A. W. Wase, *Arch. Biochem. Biophys.* **61**, 272 (1956).

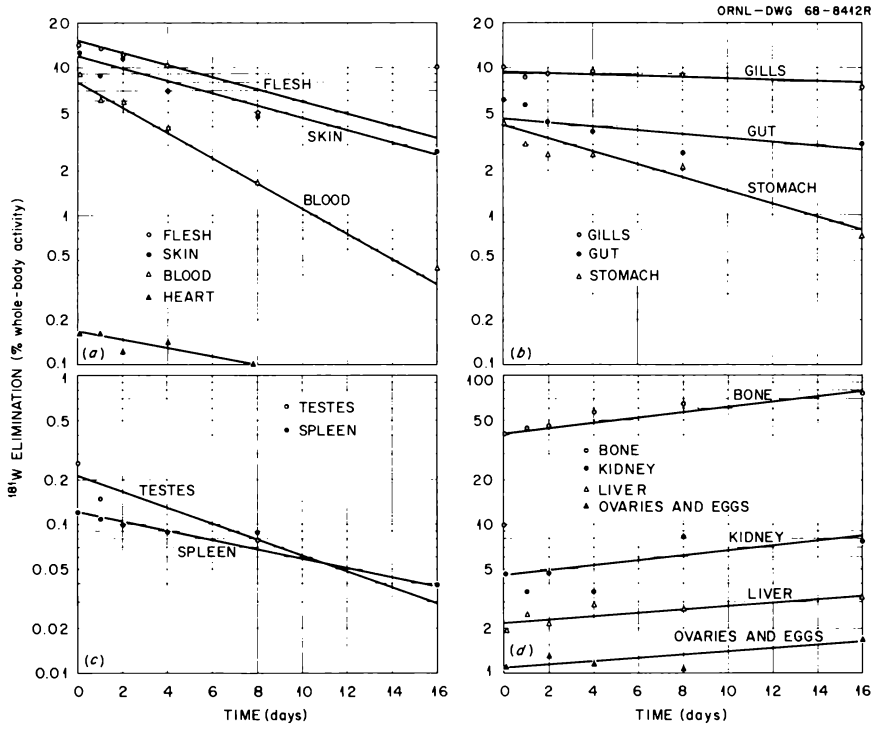

Fig. 11.5. Elimination of ^{181}W Activity by Black Bullhead Tissues After Four Days Uptake from Water. Data are expressed as percent of whole-body activity at the sampling time.

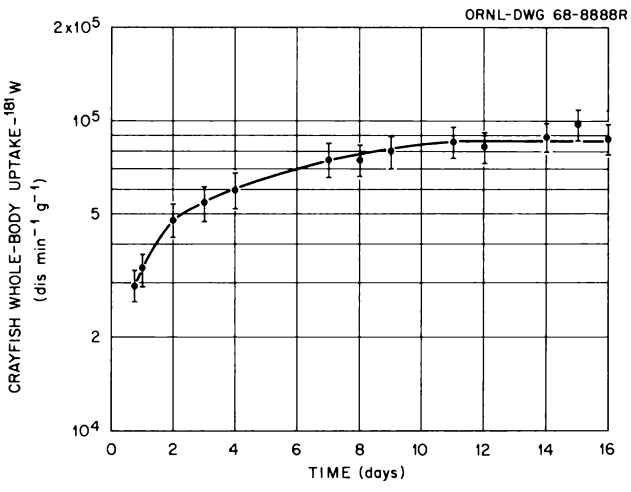

Fig. 11.6. Whole-Body Uptake of ^{181}W from Water by Crayfish. Each point is the mean of 18 animals ±1 SE. The concentration factor at 16 days was 7.5.

second, slower component. The manner in which the individual tissues retained the isotope was not studied. On the basis of studies[12,13] with ^{85}Sr and ^{60}Co, the exoskeleton could be expected to be the major retention site. A correspondingly high concentration of ^{181}W in the exoskeleton during uptake was not found in this study. However, the high retention in the exoskeleton might occur later, due to the recycling of the isotope and the manner in which it is bound in the calcareous structure.

[12] C. W. Wiser and D. J. Nelson, *Am. Midland Naturalist* 72(1), 181 (1964).

[13] J. M. Schurr and M. N. Stamper, *Limnol. Oceanogr.* 7, 474 (1962).

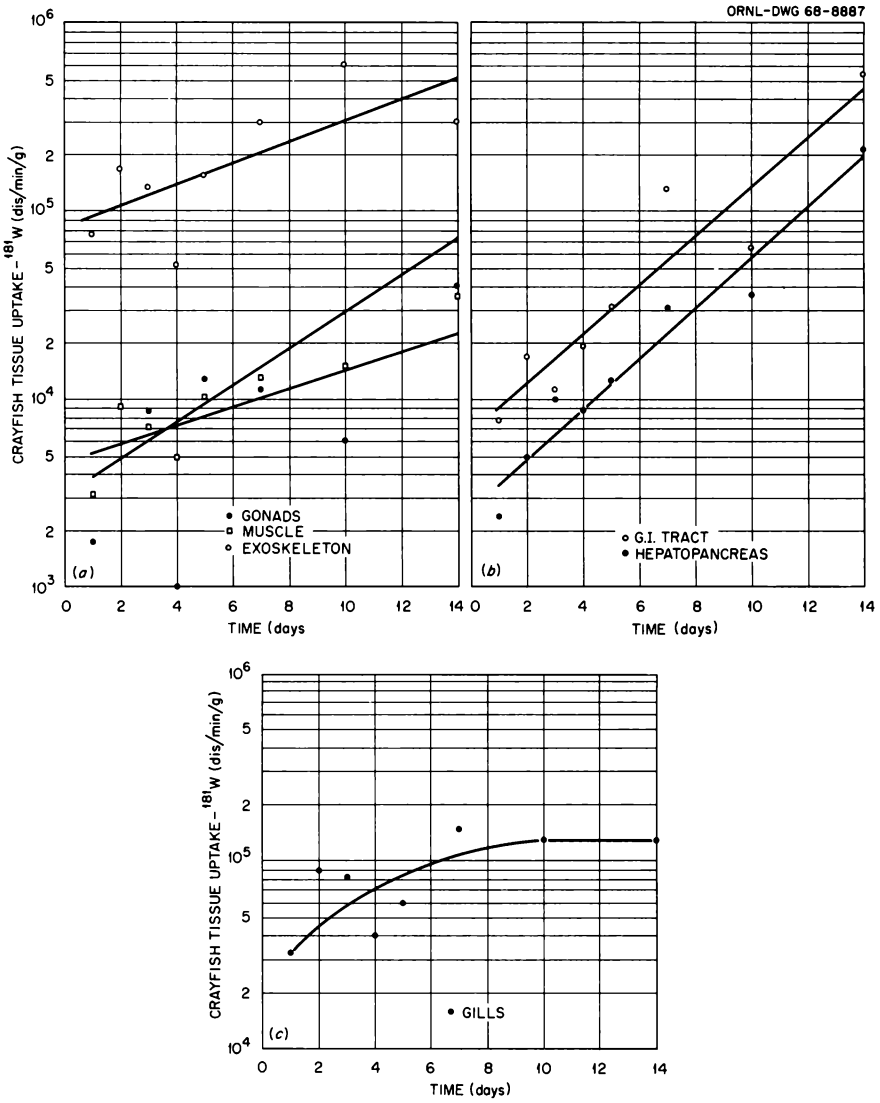

Fig. 11.7. Uptake of ^{181}W Activity in Crayfish Tissues During Whole-Body Uptake from Water. Each point is the mean of three animals.

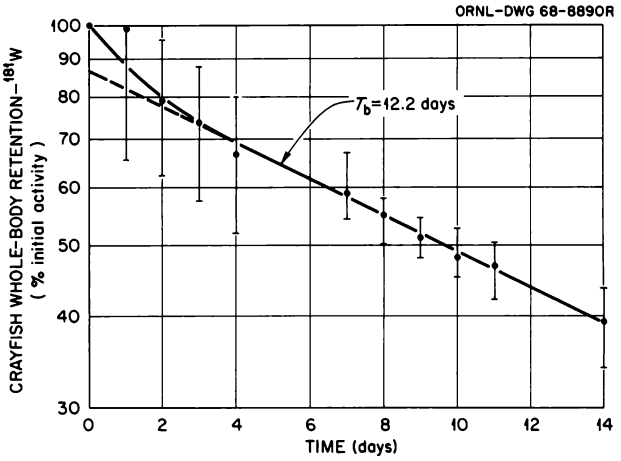

Fig. 11.8. Elimination of ^{181}W Activity by Crayfish After Seven Days of Uptake from Water. The points through day 4 are the means of 5 animals ±1 SE and those from days 7–14 are the means of 2 animals ±1 SE.

RADIONUCLIDE EXCRETION STUDIES

D. J. Nelson N. A. Griffith
Sue A. Rucker

Previous studies of the excretion of radionuclide from chronically tagged snails (*Helisoma* sp.) and newts (*Notophthalmus viridescens*) showed that essentially all of the ^{85}Sr, ^{54}Mn, ^{60}Co, ^{65}Zn, and ^{137}Cs taken up in the bodies of organisms was associated with the long component of the T_b in excretion curves.[14] These studies were completed with an investigation of the turnover time of the same radionuclides by two species of higher aquatic plants, duckweed (*Lemna minor*) and wild celery (*Vallisneria americana*).

Plants were exposed to mixed isotope solutions in 50-gal aquaria so that they would accumulate a combination of either ^{137}Cs, ^{85}Sr, and ^{65}Zn or ^{137}Cs, ^{54}Mn, and ^{60}Co. These combinations of radionuclides were selected to give maximum separations of peak energies to facilitate counting and data reduction. Following the uptake phase, which lasted five months, the plants were removed to tanks through which fresh spring water flowed. The temperature was 16°C, and ambient light was about 50 ft-c with a 12-hr day length. The plants grew under these conditions, and individual *Vallisneria* plants were counted and a weighed aliquot of the *Lemna* population was sampled for counting. The samples were counted on a multichannel analyzer with a dual-detector system utilizing two 3- by 3-in. NaI(Tl) crystals. Count data were reduced by a linear least-squares fit of the counts of unknowns to counts of standards prepared in the same geometry.

The T_b's of the five radionuclides in the two plants were calculated from a linear least-squares regression model. This procedure gave reasonably good fits of the calculated regression line to the observed data points in all cases (Fig. 11.9). The exposed plants excreted the five radionuclides in a single component. An exception was the turnover of ^{85}Sr by *Vallisneria*, which lost about 50% of their activity during the first day. Otherwise, 80% or more of the radionuclides was included in a single pool turning over at a constant rate. These data from the plants are similar to those obtained last year from the snails and newts in two ways. First, initial excretory losses of radionuclides by plants represent a small proportion of the pool of ^{54}Mn, ^{137}Cs, ^{60}Co, ^{85}Sr, and ^{65}Zn in plants. Second, the loss rate is constant in these plants. Thus the single long-term component of excretion is quantitatively the most important in plants as well as animals.

Factors affecting mineral element exchange in aquatic plants are not known. These plants grew throughout the experiments and, in the case of *Vallisneria*, new shoots and roots appeared. With *Lemna*, there were indications

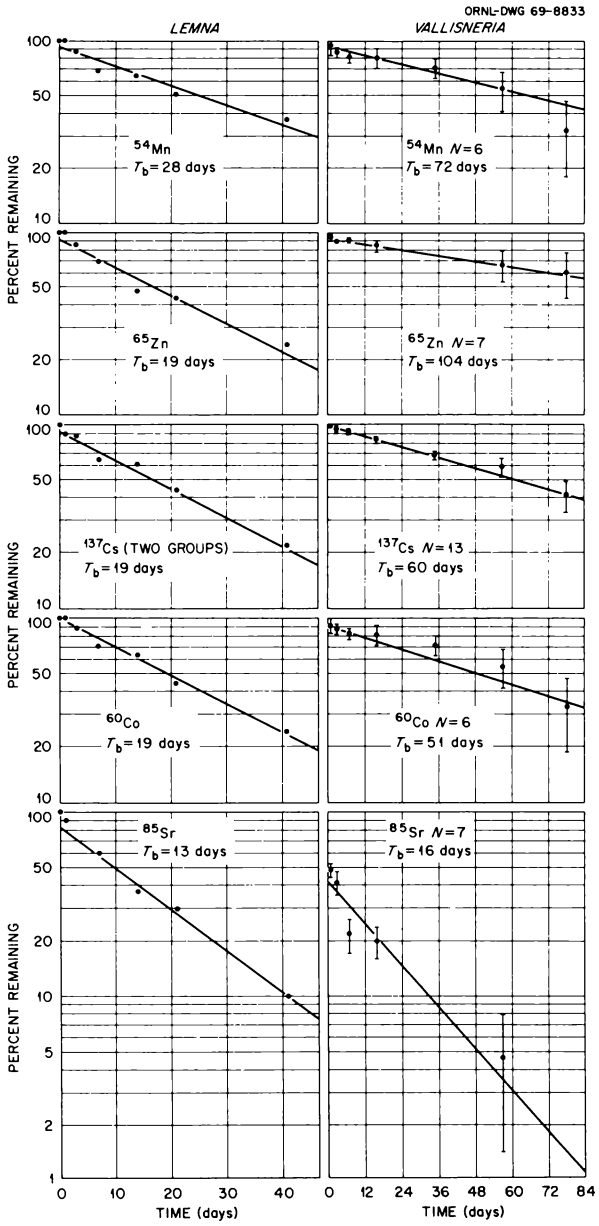

Fig. 11.9. Turnover of Five Radionuclides by *Lemna* and *Vallisneria* After a Chronic Exposure. Mean percent retained ±2 SE are indicated for the *Vallisneria* data from individual plants, but the *Lemna* data are from composite samples of a population maintained in fresh spring water.

[14] S. I. Auerbach *et al., Health Phys. Div. Ann. Progr. Rept. July 31, 1968,* ORNL-4316, pp. 124–25.

of a population turnover, since dead plants accumulated in the bottom of the tank. The extent to which the population turnover affected the T_b is not known. However, the dead *Lemna* accumulated on the bottom of the tank contained insignificant quantities of the five radionuclides.

The data show that the same concepts and principles relating to radionuclide turnover by animals are applicable to aquatic plants. In some heavily vegetated habitats, the submerged aquatic plants may have a significant role in quantitative cycling of radionuclides in aquatic ecosystems.

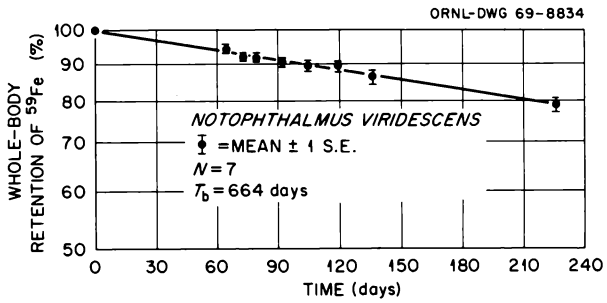

Fig. 11.10. Whole-Body Retention of ^{59}Fe by Newts (*Notophthalmus viridescens*) Following Intraperitoneal Injection. Each point is the mean of seven animals ±1 SE.

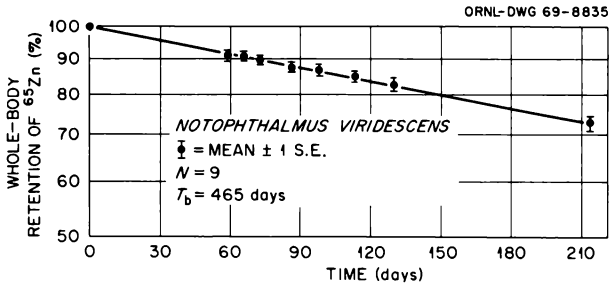

Fig. 11.11. Whole-Body Retention of ^{65}Zn by Newts (*Notophthalmus viridescens*) Following Intraperitoneal Injection. Each point is the mean of nine animals ±1 SE.

RADIONUCLIDE UPTAKE AND RETENTION IN THE NEWT (*NOTOPHTHALMUS VIRIDESCENS*)

D. L. Willis

Few studies of the uptake and retention of radionuclides in amphibians have been made despite the important position of this vertebrate class in freshwater food webs. Although amphibians are seldom utilized directly as human food, they do contribute significantly to the diet of many game fish and birds. Furthermore, their permeable body surface allows them to absorb radionuclide contamination from their aqueous environment more readily than most other aquatic vertebrates.

Red-spotted newts (*Notophthalmus viridescens,* also known as *Diemyctilus viridescens,* or *Triturus viridescens*) were selected as representative amphibians for this study. All animals used were adults weighing 2.5 to 5.0 g. The newts were regularly fed ground meat and chironomid larvae throughout the course of the study. Three radionuclides were used in the study – ^{59}Fe, ^{65}Zn, and ^{181}W. Whole-body radioactivity measurements were made using a Packard Armac system, while individual newts were placed in the counting chamber tightly confined in polyethylene tubes (1.3 cm ID X 11.3 cm). All radioactivity measurements were made to a 1% relative standard deviation, except in the latter stages of the ^{181}W retention studies, where the low counting efficiency (3%) coupled with the low levels of retained activity required the acceptance of larger error values. Standards of approximately the same size and density as the newts were prepared and counted with the animals at each measurement period.

Iron-59

It is well known that iron is strongly bound in vertebrate tissues and, consequently, has a low turnover rate. No information was available, however, regarding its biological half-life (T_b) in amphibians. To determine this value seven newts were injected intraperitoneally with 2 μc each of ferric chloride-^{59}Fe, and whole-body radioactivity measurements were made over a period of 235 days. The newts were maintained together in a 15-gal aquarium at a temperature of 20 ± 2°C. The counting data revealed a single loss component with a T_b of 664 days (Fig. 11.10). Wild rodent species have been shown to exhibit T_b values for ^{59}Fe ranging from 137 to 385 days.[15] The longer T_b for ^{59}Fe found for newts is probably a reflection of their lower metabolic rate and long cellular turnover time.

Zinc-65

Previous work in this laboratory[14] using simple aquaria ecosystems had shown a T_b for ^{65}Zn in this newt of 502 days. This result was based on chronic uptake of the radionuclide and counting data taken

[15] J. T. Kitchings III *et al., J. Tenn. Acad. Sci.* 43(3), 85 (1968).

over only a 45-day span. To compare this finding with retention following acute administration of the activity, nine newts were given intraperitoneal injections of 1 μc each of zinc chloride-^{65}Zn. They were subsequently maintained together as in the previous study, and whole-body counting was carried out over a period of 214 days. Again, the counting data revealed a single loss component with a T_b of 465 days (Fig. 11.11). Thus, it would appear that the T_b of ^{65}Zn in this amphibian is approximately 1⅓ years regardless of the mode of uptake. The implications of such a long-term retention with regard to ^{65}Zn contamination of freshwater ecosystems is clear.

Tungsten-181

Radioisotopes of tungsten are produced in abundance by Plowshare-type nuclear explosions, but few studies have been made of their uptake and turnover in freshwater vertebrates, except in fish.[16] Thus a study was undertaken to measure the uptake of ^{181}W from water and consequent retention by the newt. Twelve newts were maintained unfed in small individual aquaria containing 15 μc of ^{181}W in 500 ml of spring water. Seven of the newts were periodically removed, rinsed, and counted over a 14-day period. A rapid initial uptake rate was observed which declined steadily with time until a near-equilibrium had been reached by the 14th day (Fig. 11.12).

At this point the uptake study was terminated, and the newts were divided into two groups of six each for retention determinations. One group was housed in an indoor aquarium as described in the previous studies. The other was placed in an outdoor concrete basin filled with 600 gal of flowing spring water at 11 ± 2°C. The bottom of the basin was well covered with an algal mat, simulating closely the natural environment of these newts. Whole-body activity measurements were then made periodically for 60 days.

In both groups a very rapid loss of approximately 95% of the initial ^{181}W activity occurred during the first 12 days (Figs. 11.13 and 11.14). The rate of loss

[16] S. I. Auerbach *et al.*, *Health Phys. Div. Ann. Progr. Rept. July 31, 1968*, ORNL-4316, p. 122.

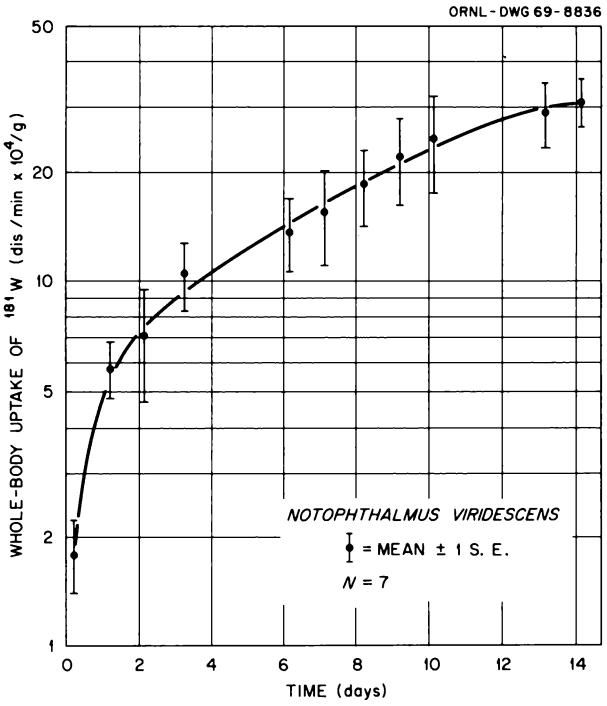

Fig. 11.12. Whole-Body Uptake of ^{181}W from Water by Newts (*Notophthalmus viridescens*). Each point is the mean of seven animals ±1 SE.

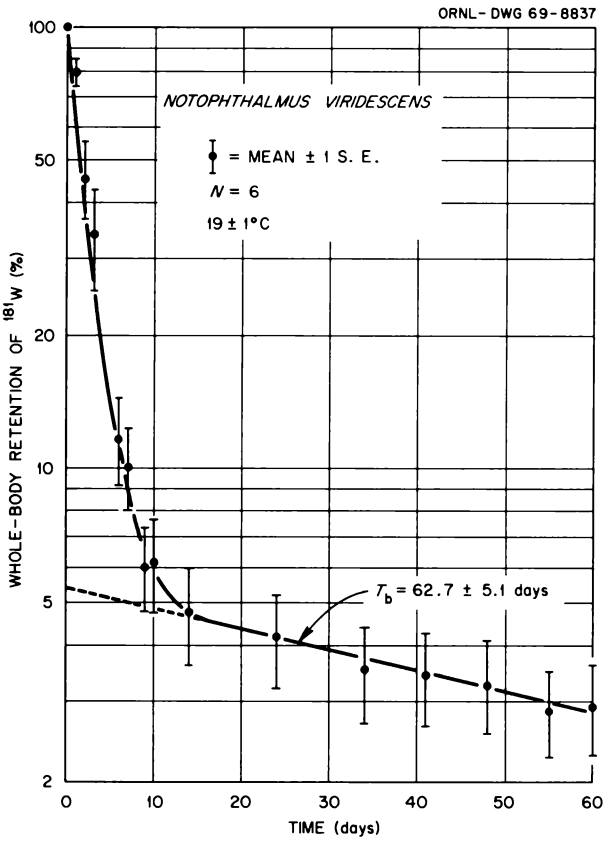

Fig. 11.13. Whole-Body Retention of ^{181}W by Newts (*Notophthalmus viridescens*) Following 14 Days of Uptake from Water. The animals were maintained in an indoor aquarium at 19 ± 1°C. Each point is the mean of six animals ±1 SE.

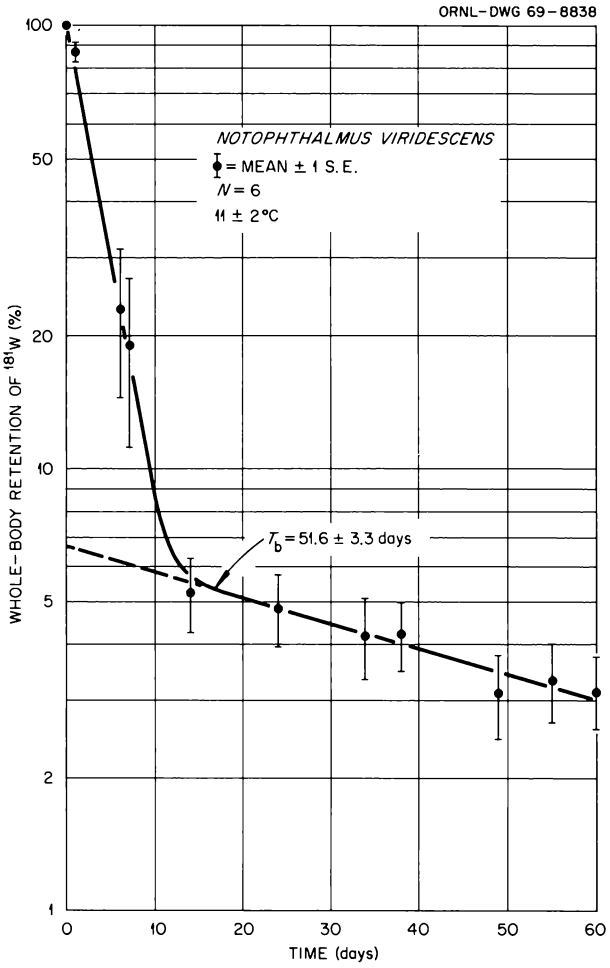

Fig. 11.14. Whole-Body Retention of ^{181}W by Newts (*Notophthalmus viridescens*) Following 14 Days of Uptake from Water. The animals were maintained in an outdoor concrete basin with flowing spring water at 11 ± 2°C. Each point is the mean of six animals ±1 SE.

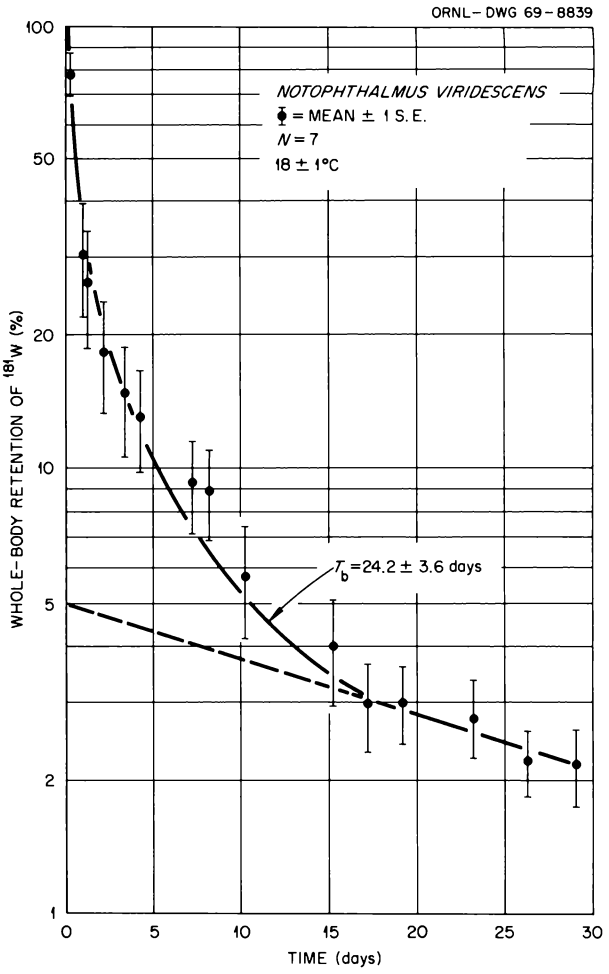

Fig. 11.15. Whole-Body Retention of ^{181}W by Newts (*Notophthalmus viridescens*) Following Intrapertioneal Injection. Each point is the mean of seven animals ±1 SE.

varied widely among animals. Careful examination revealed that the sudden large losses of activity observed for individuals were correlated with the shedding of their skins. That the majority of this initial loss was from this cause was confirmed when the fragments of shed skin were found to contain virtually all the activity lost by the shedding individual since the immediately preceding activity determination. Whether the ^{181}W associated with the skin was metabolically bound or merely adsorbed was not determined.

After the 15th day a single loss component was observed for each group. Linear regression analysis of the counting data yielded T_b values of 51.6 days for the outdoor group and 62.7 days for the newts maintained in the laboratory. Due to the considerable variation within each group, the differences in T_b indicated should not be regarded as highly significant. Thus, in light of the different temperatures (and presumably different metabolic rates) at which the two groups were maintained, it would appear that this longer component is not related to metabolic activity.

An additional study was undertaken to compare the retention pattern following acute administration of ^{181}W. Seven newts were each given intraperitoneal injections of 0.1 μc. They were subsequently maintained and counted as in the previous ^{59}Fe study. The results showed nearly the same pattern as those following chronic uptake (Fig. 11.15), except that the longer component had a T_b of only 24.2 days. It would appear that a different compartment was being turned

over in this case. In all three ^{181}W retention studies the T_b values of the longer components were much greater than those found for freshwater fish (black bullheads).[16] In general, it appears that radiotungsten is not retained by newts to any great extent or for any long period.

From these limited studies it would appear that the turnover of radionuclides (at least ^{59}Fe, ^{65}Zn, and ^{181}W in the newt) in amphibians may be much slower than in other vertebrates. Thus amphibians might serve as important steps in the cycling of radionuclides in freshwater ecosystems.

DETERMINATION OF FEEDING RATES IN TRICHOPTERA USING ^{60}Co

J. R. Gammon

Net building Trichoptera constitute a significant component of the benthos and drift organisms of larger streams and rivers. Because of their importance in lotic food chains, a study to develop techniques for estimating feeding rates was initiated. The uptake of ^{60}Co from solution and its elimination under different environmental conditions were also examined.

Specimens of *Hydropsyche* sp. were collected from Walker Branch downstream from the weirs and maintained in plastic aquaria receiving spring water. Small masonite boxes proved to be acceptable homesites and were quickly colonized. The water temperatures remained fairly constant at 14.5 to 15.7°C throughout the investigations.

Twelve individuals in their makeshift homes were placed in a solution of ^{60}Co and spring water for 65 hr in which a current was maintained by a magnetic stirrer. The initial concentration of ^{60}Co was determined following the removal of individuals from the masonite boxes and a thorough rinsing. Concentration or accumulation factors, defined as the ratio of activity in the *Hydropsyche* (per unit wet weight) to the activity in water, averaged 2533, with a standard deviation of 644.

These organisms were placed in individual polyethylene containers which permitted a slight flowthrough of spring water. Their radioactivity was determined frequently for the next 60 days, during which time no food was provided beyond that entering with the spring water. Excretion was rapid initially, but after approximately 12 hr the loss rate became linear in a semilog plot (Fig. 11.16). Under these experimental conditions about 89.3% of the ^{60}Co was excreted very slowly.

The rate of ^{60}Co excretion could be increased by changing environmental conditions. After 44 days of confinement in still water in the polyethylene container, two individuals were transferred to rapidly

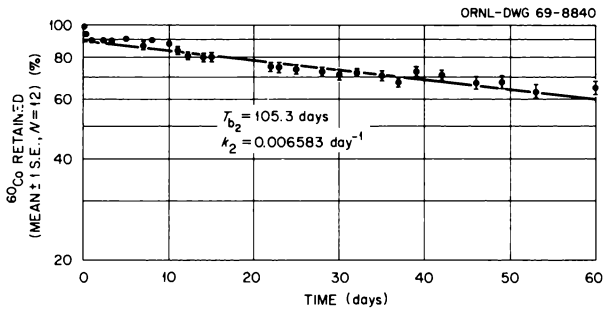

Fig. 11.16. Excretion of ^{60}Co by *Hydropsyche* sp. Following Uptake from Solution.

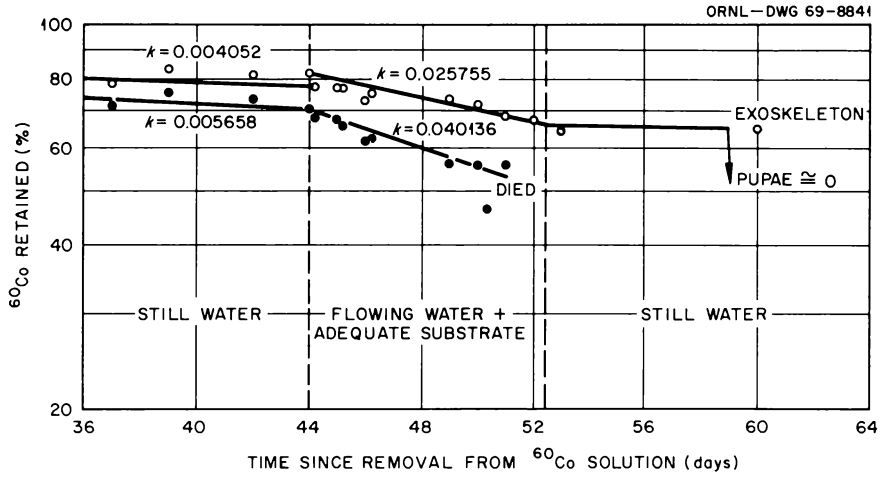

Fig. 11.17. Rates of Excretion of ^{60}Co by Two Hydropsychids as Affected by a Change in Environmental Conditions from Still Water with Inadequate Substrate to Flowing Water with Adequate Substrate.

stirred water and provided with new masonite boxes once or twice daily. Under these conditions, nets were constructed frequently during a one week period, although no nets had been observed under previous conditions. The rate of ^{60}Co excretion increased nearly seven-fold (Fig. 11.17), apparently as the result of net spinning.

In the feeding experiments *Hydropsyche* were placed in a plastic cylinder containing spring water which was stirred continuously. Here they constructed nets on a substrate of spaced stainless steel grids. Once acclimated, they were provided with dried pulverized water cress leaves labeled with ^{60}Co once or twice daily for 8- to 10-day periods, and radioactivity was determined regularly. Corrections were made for uptake of ^{60}Co by direct absorption from water, although the concentration due to leaching from the food was low. Most individuals did not reach equilibrium within this period. For these animals the equilibrium body burden, Q_e, was estimated by drawing a smooth curve through the plotted points of activity vs time (Fig. 11.18) and reading from the curve estimates of activity through time. A plot of daily increments of activity as a function of initial daily activity was essentially linear with the abscissal intercept serving to estimate Q_e (Fig. 11.19).

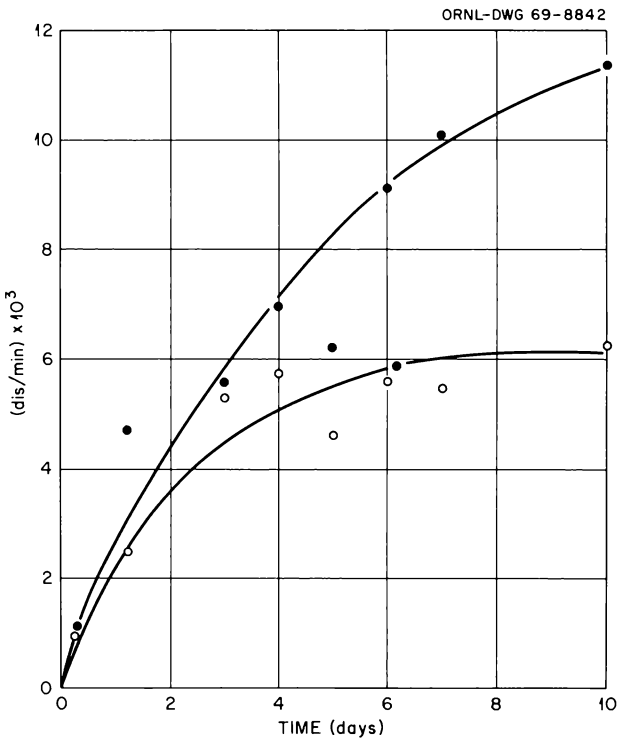

Fig. 11.18. Increase in Radioactivity of Two Hydropsychids Feeding on Pulverized Watercress Leaves Labeled with ^{60}Co and Corrected for Direct Absorption of Radiocobalt from Water.

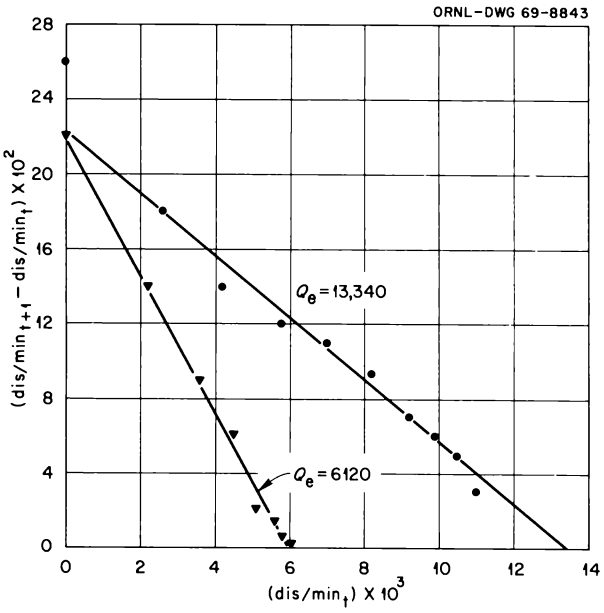

Fig. 11.19. Intercept Method of Estimating the Equilibrium Body Burden, Q_e, Using Data Illustrated in Fig. 11.18.

At the end of the feeding period the organisms were placed without food in polyethylene containers fitted with screening over a chamber which collected feces. The average excretion curve for 11 individuals is shown in Fig. 11.20. The initial rapid loss closely corresponded to, but was only partially the result of, defecation. Weighted elimination coefficients for each experimental animal were determined from the equation

$$k' = \frac{0.693}{p_1 T_{b_1} + p_2 T_{b_2}} ,$$

where p_1 and p_2 are the proportions of each elimination component and T_{b_1} and T_{b_2} are the corresponding biological half-lives.[17] The biological half-life of ^{60}Co was much shorter in the feeding experiments than in the retention experiment following uptake from solution.

The daily intake of food for each individual was then estimated from the equilibrium equation

$$I = k' Q_e ,$$

[17] D. E. Reichle, "Radioisotope Turnover and Energy Flow in Terrestrial Isopod Populations," *Ecol.* 48(3), 351–66 (1967).

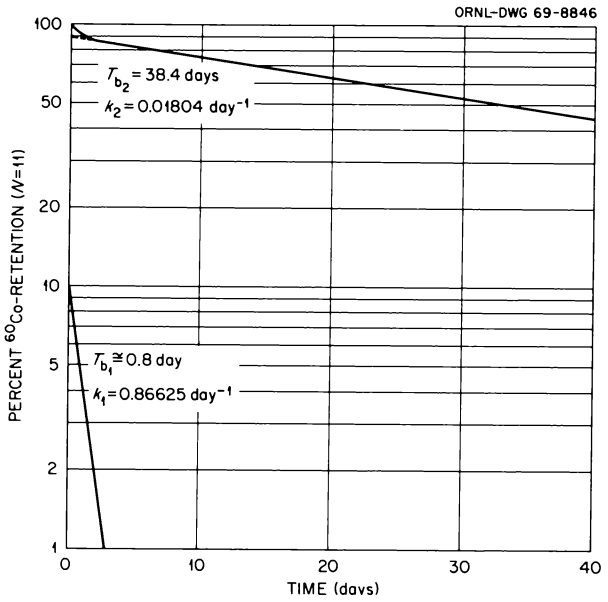

Fig. 11.20. Retention of ^{60}Co by *Hydropsyche* sp. Following Uptake via Pulverized Watercress Leaves, an Average of 11 Individuals.

where I is the intake in disintegrations per minute, k' is the weighted elimination coefficient, and Q_e is the determined or estimated equilibrium body burden. Determinations of the average concentration of ^{60}Co in the food then permitted an estimation of feeding rate in dry weight per day per organism. The mean ingestion rate was only 0.042 mg of dry watercress per day, amounting to only 0.21% of the live body weight per day.

The study suggests that it is feasible to base estimates of feeding rates on experiments which are shorter in duration than would be necessary to reach equilibrium conditions yet longer than single-feeding experiments, which require difficult assumptions in order to extrapolate the results to longer periods of time. Environmental conditions imposed during the retention phase of a food intake experiment must duplicate those present in the feeding phase if accurate estimates of feeding rates are to be obtained.

THE ROLE OF AEROBIC MICROBES IN THE CYCLING OF SULFUR IN AN AQUATIC ECOSYSTEM

R. H. Monheimer

Sulfur is one of the more common elements found in natural waters and is known to have very unique ecological characteristics. Considerable information is available as to the qualitative distribution and movement of sulfur in aquatic environments, but very little is known of the quantitative aspects and related transfer coefficients. This study was initiated to study the movement of sulfur in an aerobic aquatic ecosystem and, in particular, to study the role that microorganisms play in this movement.

Because of the need for biotic-free control groups when studying microorganisms, the work that has been completed to date has been confined primarily to laboratory studies. An attempt has been made to simulate certain compartments of a lake ecosystem in flasks held under controlled environmental conditions. The movement of sulfur within these compartments is being followed by the addition of ^{35}S. Inorganic sulfate, the initial form of the ^{35}S, passes through a 0.45-μ membrane filter, and thus the conversion of SO_4^{2-} to organic (cellular) sulfur can be measured by filtration followed by appropriate isotope detection.

A mixed culture of bacteria and algae (dominant organism *Spongiochloris spp.*) enriched by addition of inorganic nitrate and phosphate, illuminated and held at room temperature, showed that the rate of uptake of sulfur was a function of the physiological state of the organisms present (Fig. 11.21). Prior to the exponential growth phase of the culture, the time to double the amount of organic sulfur (per milligram of plankton) was approximately five days. During the exponential growth phase the culture had a negative rate of uptake on a unit weight basis, but the total organic sulfur continued to increase. When the biomass of the culture stopped increasing, the organic sulfur reached a maximum of approximately 30% of the total sulfur. Initial sulfate concentration in the culture was 7 ppm.

In another experiment, aerobic compartments of the ecosystem being simulated were subdivided into dark and illuminated phases to study the differences between photosynthetic and nonphotosynthetic sulfur utilization. The flasks were incubated at 20°C and mixed continuously using a magnetic stirrer to aerate the system.

The uptake of sulfur was greatest when the microcosms were incubated in the light (Fig. 11.22). This was obvious even though at this writing the lighted cultures had not reached equilibrium. The presence of sediment in the dark increases total sulfur uptake by almost an order of magnitude, the computed equilibrium values being 2.788% for the sediment-water system and 0.395% for the water-only system. The half-time for sulfur uptake for the sediment-water system was computed to be 9.39 days and for the water-only system

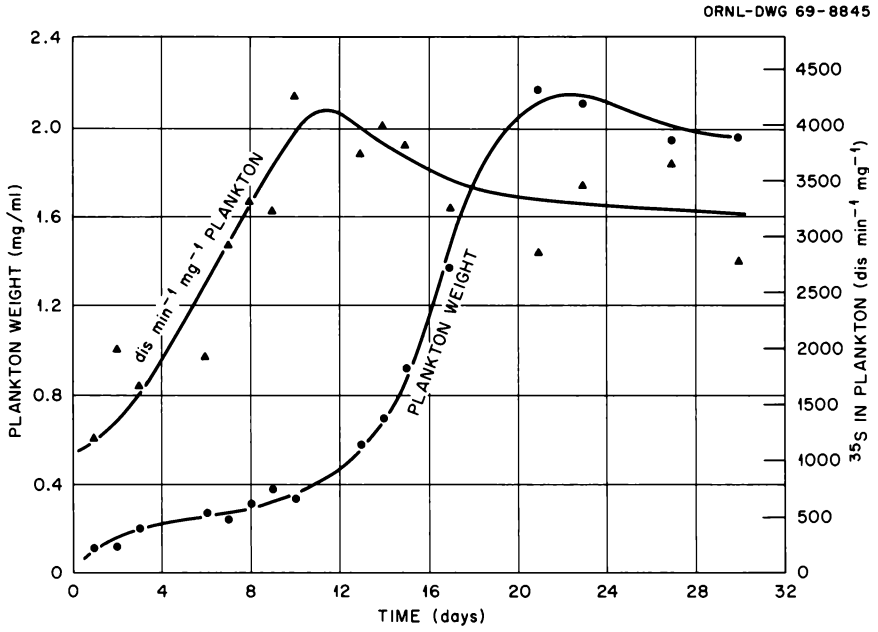

Fig. 11.21. Growth and ^{35}S Uptake by a Culture of Mixed Bacteria and Algae, the Predominant Organism Being *Spongiochloris* spp.

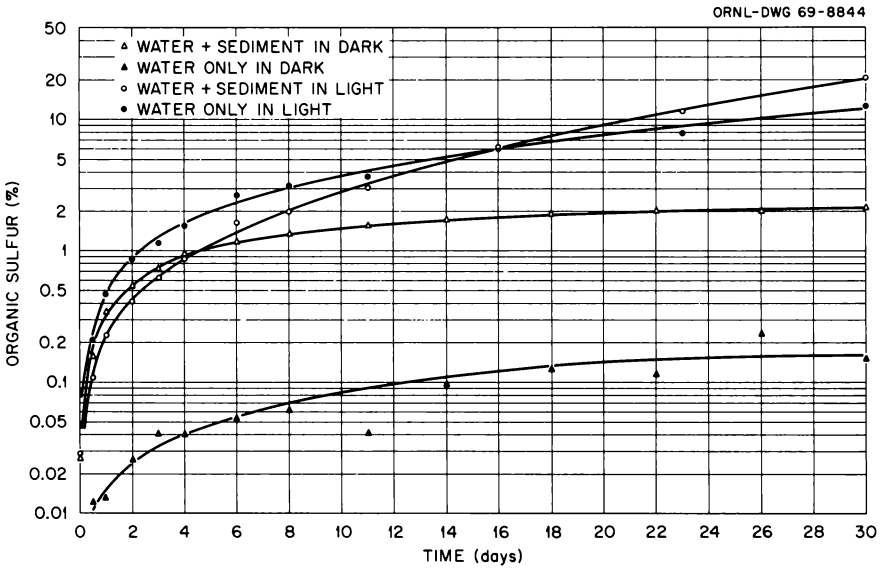

Fig. 11.22. Conversion of $^{35}SO_4$ to Organic ^{35}S by Microorganisms Under Light and Dark Conditions at 20°C.

was 32.40 days. It appears that sediment also increases sulfur uptake in the presence of light, although sufficient data have not been collected to compute specific numbers. However, the role of photosynthetic organisms is obviously most important in the aerobic cycling of sulfur and may play a very important role in the anaerobic phase of the cycle due to sedimentation of the aerobically fixed organic sulfur into the anaerobic zone.

MINERAL KINETICS IN MICROCOSMS

Martin Witkamp Evelyn Brown
Marilyn L. Frank Carolyn Marvin

Even though mineral kinetics have been studied in aquatic and terrestrial environments, rate processes in these two situations have not been related. Knowledge of this relationship would aid in the understanding of mineral kinetics in environments such as tidal marshes, playa lakes, and flood plains where aquatic and terrestrial situations alternate. Since much of the mineral pool in these environments originates from litter and soil, kinetics of biologically important monovalent potassium and bivalent calcium and of the major fallout element cesium were compared in aquatic and terrestrial microcosms. Aquatic systems contained one hundred times more water than their otherwise identical terrestrial counterparts. Mean concentrations of potassium, cesium, and calcium, however, were 42, 31, and 82 (Fig. 11.23*d*) times higher, respectively, in the water of terrestrial than of aquatic systems. The percent of available potassium and cesium going into the water reached maxima within the first one to three days. In contrast calcium continuously entered the water compartment for the entire month (Fig. 11.23*b*).

On the average, twice as much of the system potassium than of the initial cesium and calcium was found in the water. Soil retained more than 95% of the initial cesium (Fig. 11.23*c* and *d*) as opposed to less than 40% of the available calcium (Fig. 11.23*b*). In contrast, leaf litter lost more than 90% of its initial potassium and only 40% of its calcium to the water compartment of litter-water systems. The water in systems with both litter and soil usually contained intermediate mineral concentrations when compared with systems containing litter or soil only.

Differences in mineral contents of water in sterile and nonsterile microcosms were, in general, not significant.

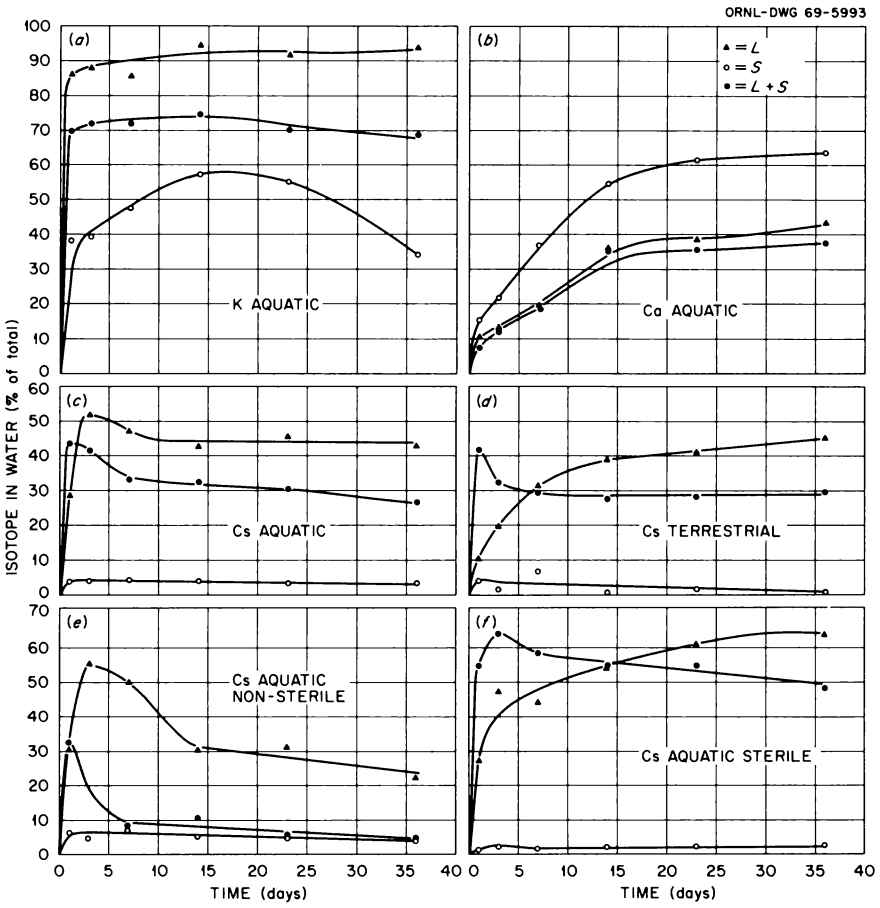

Fig. 11.23. Percent of Total Isotope Input in Water During the First 36 hr of Systems of Water with Litter (▲), Soil (○○○), or Litter on Top of Soil (●). The systems were either aquatic or terrestrial and sterile or nonsterile.

In aquatic systems with leaves, however, there were considerably smaller and declining cesium concentrations in the water of the nonsterile systems than that of their sterile counterparts as a result of microbial immobilization of cesium by the leaf microflora (Fig. 11.23*e* and *f*). These results indicated that in the water of alternately dry and submerged environments, mineral concentrations may change by one to two orders of magnitude, that new equilibria may be established in times varying from days to months, and that the effect of the microflora in these environments is apparently less than in permanently terrestrial environments.

Various pollutants in water tend to affect the community structure of such waters. Aquatic microcosms of increasing complexity were used to investigate the effect of system structure on mineral kinetics. Community structure was varied by varying compartment combinations. All systems included water with either algae, bottom sediments (materials), snails, or a combination of these compartments. In the presence of snails an additional compartment, detritus, was formed. All systems contained ^{60}Co- and ^{137}Cs-tagged water. Accumulation by algae reached equilibrium within three days, whereas snails kept accumulating radionuclides, particularly ^{60}Co, during the three weeks of incubation. In general, ^{137}Cs reached an equilibrium sooner than ^{60}Co, and simple systems reached equilibria sooner than more complex ones. Water remained the main compartment for ^{60}Co in all combinations. Increase in the number of other compartments simply tended to "dilute" the remaining ^{60}Co over the other compartments. For ^{137}Cs, bottom sediments and detritus were the main compartments. These continued to remove ^{137}Cs from the other compartment throughout most of the incubation time. Thus, structural complexity of the systems affects mineral kinetics, and the effects can be quite different for different elements.

The present overfertilization of waters raises many questions as to the changes in mineral movement in such waters. In order to provide some insight into these changes, transfer of the fallout element cesium and the fertilizer element potassium from eutrophic and oligotrophic water onto various combinations of filamentous algae, snails, and microscopic seston was measured in microcosms. In all combinations less of the added ^{137}Cs than of ^{42}K was removed from the water as a result of greater uptake of potassium than of cesium by algae, snails, and seston. Only detritus, mainly the excrement of snails, retained more cesium than of potassium, indicating greater adsorption and less leaching of cesium than of potassium. In particular, in the oligotrophic series, the retention of both cesium and potassium by algae, snails, and seston was much greater when the compartments were single rather than in combination, probably as a result of competition. A much greater percent of the added ^{137}Cs (up to 40%) and ^{42}K (up to 94%) was removed from the oligotrophic creek water than from the eutrophic river water (10 and 12% respectively). Clearly the river water contained a much larger pool of available cesium and potassium than creek water, and less was taken up by the biota. The mineral availability in river water as compared with creek water was also indicated by the earlier equilibrium reached in river water (within 24 hr), as compared with continued accumulation by algae and snails for two days and longer in creek water. Seston reached a maximum ^{137}Cs and ^{42}K content within 10 hr, probably as a result of the small dimensions of the organisms ($<100\ \mu$). These results demonstrate that in aquatic systems, the smaller the mineral pool and the larger the biomass, the larger a portion of fallout and fertilizer added to an aquatic system will be removed from the water by uptake in the biota; the greater the mineral pool and the smaller the biota, the sooner uptake and elimination will be in equilibrium.

WHITE OAK LAKE STUDIES

S. E. Kolehmainen

The Balances of ^{137}Cs, Stable Cesium, and Potassium in the White Oak Lake Bluegill

The balance of a radioisotope in fish can be simulated with a single-compartment system where the rates of uptake (input) and excretion (output) determine the body burden. In practice the body burden and the excretion can be determined and then the uptake can be calculated. Before making the calculations, one has to know whether the fish is in equilibrium with the radioisotope, because this determines the type of the equation that can be used.

The concentrations of ^{137}Cs, stable cesium, and potassium were analyzed in samples of two to ten bluegill collected one to three times a month from White Oak Lake during the period June 1967 to January 1969. Besides the sampling of fish, samples of different food items of bluegill were also collected. The feeding habits of bluegill were determined on the basis of stomach contents.

The concentration of ^{137}Cs in bluegill increased with size of fish up to 70 g, when a steady state was reached (Table 11.1). Bluegill over 70 g showed a seasonal

variation in ^{137}Cs content, with a maximum of 47.4 pc per gram of fresh weight in February and a minimum of 29.0 pc in August (Fig. 11.24). Individual variations of ^{137}Cs in bluegill over 70 g taken on the same day were up to five times. The concentration of dissolved ^{137}Cs in water is also shown in the figure. Dissolved ^{137}Cs was calculated on the basis of the total ^{137}Cs in White Oak Lake water samples analyzed by the Environs Monitoring Section of the Health Physics Division (courtesy W. D. Cottrell) and the proportion of ^{137}Cs in solution in White Oak Lake water, which was 38.5%.[18] No correlation could be seen between the variation of ^{137}Cs in water and in bluegill.

The biological half-life (T_b) of ^{137}Cs increased with the size of bluegill (Table 11.2). There were no significant differences in the long component of the T_b among the fish that received a single feeding of ^{137}Cs and fish from White Oak Lake that had a body burden close to equilibrium (Figs. 11.25 and 11.26). The excretion curve of ^{137}Cs in the White Oak bluegills that were in a steady state with ^{137}Cs did not show any fraction that was excreted by T_{b_1} (Fig. 11.26). However, the calculated proportion of body burden that was excreted by the long component of the T_b in the White Oak Lake bluegill was 2.3%. The standard deviation of the counting was so large that the effect of T_{b_1} on the retention could not be seen (Fig. 11.26).

The concentration of ^{137}Cs in the stomach contents of bluegills was at a maximum in midwinter and a minimum in midsummer. The concentration of ^{137}Cs in bluegills food was calculated on the basis of the percentage of each food item in the stomach samples and the concentration of ^{137}Cs in the food items at that time of the year (Table 11.3). Assimilation of ^{137}Cs from different food items was studied by feeding experiments where the fish were sacrificed after 48 hr, and the body burden, the stomach contents, and the gut contents were counted for ^{137}Cs, or the assimilation was calculated on the basis of the retention curve in the T_b experiment (see Fig. 11.25). The assimilation percentage increased with the size of fish (Table 11.3). Assimilation was low from food containing clay particles (White Oak Lake *Chironomus* larvae and detritus) but was about 70% from organisms not containing clay.

The concentration of stable cesium followed a seasonal cycling similar to that of ^{137}Cs (Fig. 11.27), but the concentration of stable cesium did not increase with the weight of fish (Table 11.1). Potassium concentrations were constant throughout the year (Fig. 11.27) and on the same level in all sizes of bluegill (Table 11.1).

The biological half-life of potassium was determined with ^{42}K by analyzing the daily quantity of ^{42}K that was excreted by fish into water. Potassium had a single-component T_b, 40.1 days, at 15.8°C (Fig. 11.28).

[18] W. T. Lammers, *The Distribution of Cobalt-60, Ruthenium-106, and Cesium-137 Among Suspended and Dissolved Particles in White Oak Lake*, ORGDP report K-1758, 20 pp.

Table 11.1. Concentration of ^{137}Cs in Bluegill of Different Sizes in White Oak Lake

Weight of Fish (g)		Concentration of ^{137}Cs (pc/g)		Number of Fish
Mean	S.D.	Mean	S.D.	
2.1	1.8	10.43	5.59	31
10.5	6.8	13.28	4.32	13
32.0	6.4	21.21	12.69	19
55.1	7.1	30.90	10.52	13
78.0	5.1	39.79	12.69	20
109.6	32.1	40.12	15.21	186

Table 11.2. Combined Results of ^{137}Cs T_b Experiments in Bluegill Calculated for the Temperature 15.8°C

Size of Fish (g)	T_{b_1} (days)	p_1 (%)	T_{b_2} (days)	p_2 (%)
0.5–1.2	6.4	20.6	86.1	79.4
9–10			112.2	
80–120	7.6	36.9	187.1	63.1

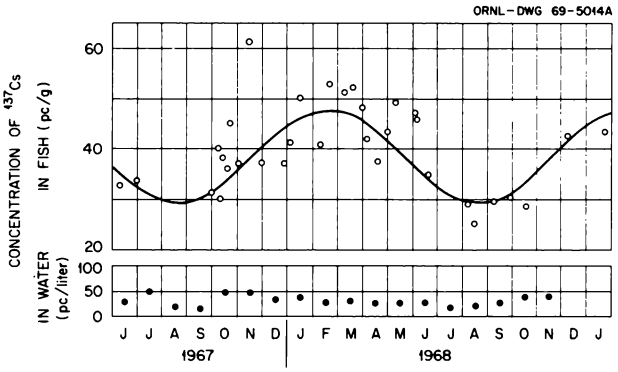

Fig. 11.24. Seasonal Cycling of ^{137}Cs Concentration in Bluegill (70 g) and the Concentration of Dissolved ^{137}Cs in White Oak Lake Water.

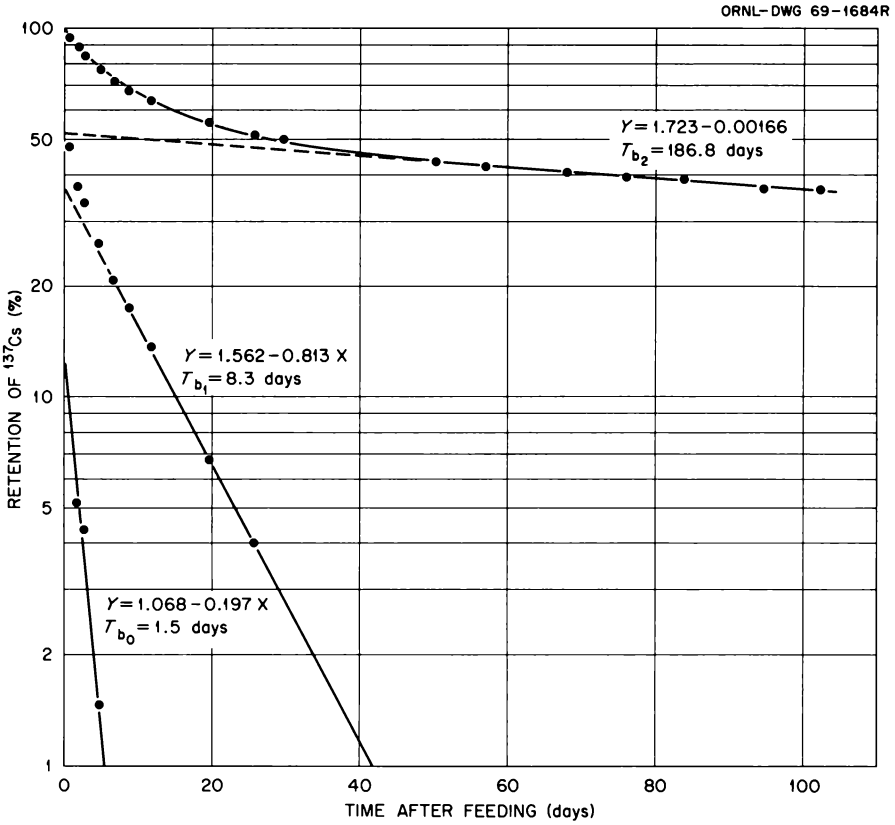

Fig. 11.25. Retention and T_b of ^{137}Cs in a Bluegill (72 g) After a Single Feeding with ^{137}Cs at 15.5°C.

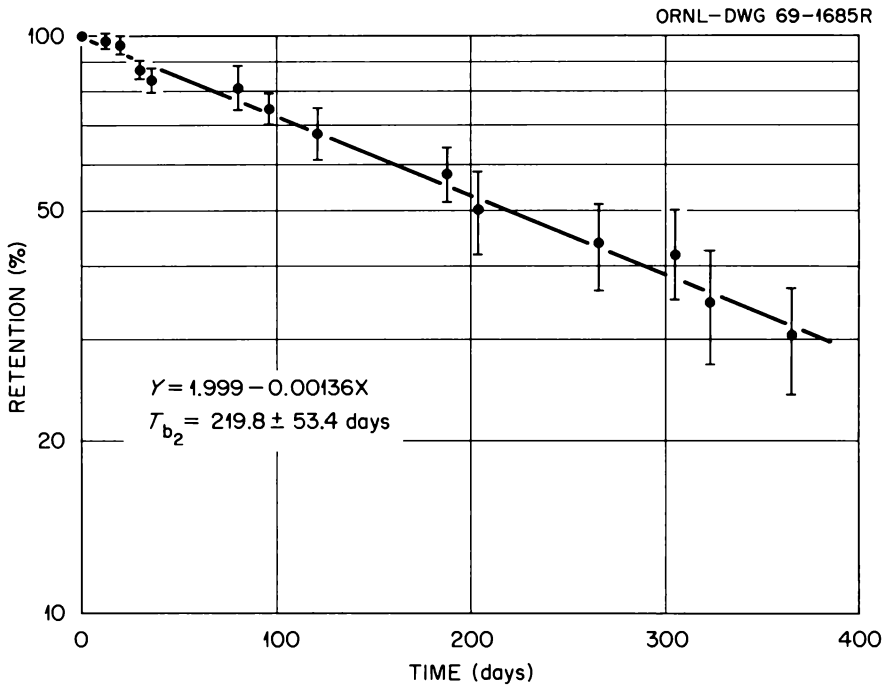

Fig. 11.26. Retention and T_b of ^{137}Cs in the White Oak Lake Bluegill (n = 12) at 14.5°C.

Table 11.3. Percentage Assimilation of ^{137}Cs from Different Types of Food Items in Different Sizes of Bluegill

Food Item	Weight of Bluegill							
	0.5–1.2 g		8–10 g		18–20 g		80–100 g	
	Percent	S.D.	Percent	S.D.	Percent	S.D.	Percent	S.D.
Items similar to those in White Oak Lake								
Chironomus larvae fed on White Oak Lake sediments			7.10	2.08	13.00	2.21	15.98	2.46
Algae							68.72	4.20
Detritus							3.01	0.21
Other types								
Chironomus larvae fed on ^{137}Cs Containing Algae	34.0		68.6	2.2				
^{137}Cs solution in a gelatin capsule							91.3	3.6

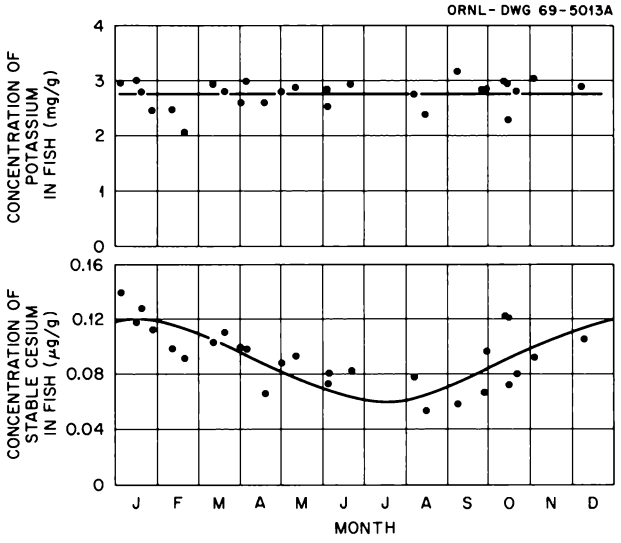

Fig. 11.27. Concentration of Potassium and Stable Cesium in Bluegill over 70 g.

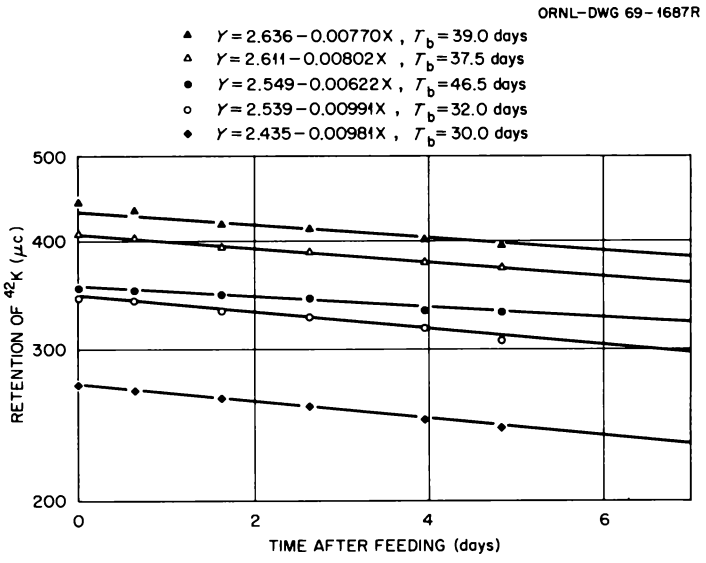

Fig. 11.28. Retention and T_b of Potassium After a Single Feeding with ^{42}K.

Calculation of ^{137}Cs Intake in the White Oak Lake Bluegill

The body burden of ^{137}Cs in bluegill was not in equilibrium because the concentration of ^{137}Cs fluctuated seasonally (Fig. 11.24) and the fish grew yearly. Therefore, calculations of the daily intake of ^{137}Cs were based on a nonequilibrium situation, because all factors, ^{137}Cs, excretion rates of ^{137}Cs, and the weight of fish, were changing daily. The basic equation for the body burden at a nonequilibrium state is:[19]

$$A_t = A_0\, e^{-kt} + \frac{I}{k}(1 - e^{-kt}) , \qquad (1)$$

where

A_t = body burden of the radioisotope at time t,

A_0 = body burden of the radioisotope initially,

k = excretion rate (fraction of body burden excreted per day),

I = assimilated intake of the radioisotope per day.

Since the T_b of ^{137}Cs consisted of two components, the intake was subdivided into two intakes, p_1 and p_2, representing the fractions of each intake that go to the pools of ^{137}Cs in the body excreted by the short component (T_{b_1}) and the long component of the biological half-life (T_{b_2}). By the definition $p_1 + p_2 = 1$, and consequently p_1 and p_2 were the probability values for radioisotope atoms going to either one of the pools.

Equation (1) can now be derived for the intake considering a two-component excretion rate:

$$I = \frac{A_t - (a_1 A_0\, e^{-k_1 t} + a_2 A_0\, e^{-k_2 t}}{(Ip_1/k_1)(1 - e^{-k_1 t}) + (Ip_2/k_2)(1 - e^{-k_2 t})} , \qquad (2)$$

where

a_1 = fraction (pool) of the body burden of the radioisotope excreted by T_{b_1},

a_2 = fraction (pool) of the body burden of the radioisotope excreted by T_{b_2},

k_1 = excretion rate of the radioisotope by T_{b_1},

k_2 = excretion rate of the radioisotope by T_{b_2}.

[19] S. Kolehmainen, E. Häsänen, and J. K. Miettinen, "^{137}Cs in Fish, Plankton and Plants in Finnish Lakes During 1964–65," pp. 913–19 in *Radioecological Concentration Processes* (ed. by B. Åbergand and F. P. Hungate), Pergamon, New York, 1967.

The fraction of the body burden, a_1 and a_2, excreted by T_{b_1} and T_{b_2} can be derived from the equilibrium equation

$$Q_e = \frac{1}{k} , \qquad (3)$$

where Q_e is the equilibrium body burden. For a two-component excretion process, Eq. (3) can be written as

$$Q_e a_1 = \frac{Ip_1}{k_1}$$

and (4)

$$Q_e a_2 = \frac{Ip_2}{k_2} ,$$

and when derived for a_1 and a_2,

$$a_1 = \frac{I}{Q_e}\frac{p_1}{k_1}$$

and (5)

$$a_2 = \frac{I}{Q_e}\frac{p_2}{k_2} .$$

The value of T_{b_1} was 7.6 days, and T_{b_2} equaled 187 days at 15.8°C (bluegill above 70 g). The excretion rate coefficients were

$$k_1 = \frac{0.693}{7.6} = 0.0912$$

and

$$k_2 = \frac{0.693}{187} = 0.00370 .$$

The value of p_1 was 36.9% and p_2 was 63.1%; hence, Eq. (5) gives

$$a_1 = \frac{I}{Q_e}\frac{0.369}{0.0912} = \frac{I}{Q_e}\,4.05$$

and (6)

$$a_2 = \frac{I}{Q_e}\frac{0.631}{0.00371} = \frac{I}{Q_e}\,170.1 .$$

Assuming $I = 1$, Eq. (6) can be rewritten as

$$a_1 = \frac{4.05}{Q_e}$$

and (7)

$$a_2 = \frac{170.1}{Q_e} ;$$

adding both sides of the equation yields

$$\begin{aligned} Q_e \cdot a_1 &= 4.05 \\ Q_e \cdot a_2 &= 170.1 \\ \hline Q_e &= 174.2 \end{aligned} \qquad (8)$$

Now the percentages of a_1 and a_2 can be calculated as

$$a_1 = \frac{4.05}{174.2} 100 = 2.32\%$$

and (9)

$$a_2 = \frac{170.1}{174.2} 100 = 97.7\% .$$

The proportion of the body burden excreted at the rate of T_{b_1} (2.3%) was very small in the equilibrium state compared with that excreted by the rate of T_{b_1} after a single meal (36.9%). The percentage of the body burden excreted by T_{b_1} during continuous feeding of ^{137}Cs is shown in Fig. 11.29.

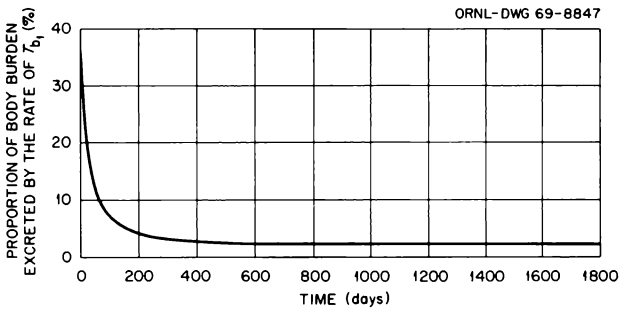

Fig. 11.29. Proportion of Body Burden Excreted by T_{b_1} in Bluegill During Continuous Feeding on ^{137}Cs Contaminated Food. The biological half-lives are T_{b_1} = 7.6 days and T_{b_2} = 187.1 days, with fractional intake of p_1 = 36.9% and p_2 = 63.1%. The proportion of body burden excreted by T_{b_1} in equilibrium, a_1, is 2.3%.

The body burden of ^{137}Cs was not in equilibrium, but the loss term in Eq. (2), $A_0\ e^{-kt}$, was treated as if A_0 was an equilibrium body burden because there is no practical way to calculate the exact values of a_1 and a_2 for a fluctuating body burden. Since the body burden of ^{137}Cs in White Oak Lake bluegill was close to equilibrium, the error in the values of a_1 and a_2 was small (Fig. 11.29). If the proportions of body burden a_1 and a_2 are used in the loss terms in Eq. (2), separate excretion rate coefficients k_1 and k_2 can be used also. However, since the body burden in the loss term, A_0, is treated as an equilibrium body burden, a weighted excretion rate coefficient, k', can be used as well. The weighted excretion rate coefficient can be calculated either on the basis of proportions of the body burden, a_1 and a_2, excreted by k' and k_2 or on the basis of proportions of the intake, p_1 and p_2, excreted by k_1 and k_2. The weighted excretion coefficient was calculated on the basis of a_1 and a_2 in the following way:

$$Q_e = a_1 Q_e + a_2 Q_e . \qquad (10)$$

Substituting $I = Q_e k$ in Eq. (10) gives

$$I = a_1 Q_e k_1 + a_2 Q_e k_2 , \qquad (11)$$

and

$$I = Q(a_1 k_1 + a_2 k_2) . \qquad (12)$$

The weighted excretion coefficient is

$$k' = a_1 k_1 + a_2 k_2 . \qquad (13)$$

Since $k = 0.693/T_b$, Eq. (13) gives

$$k' = a_1 \frac{0.693}{T_{b_1}} + a_2 \frac{0.693}{T_{b_2}}, \qquad (14)$$

and

$$k' = \frac{0.693(a_1 T_{b_2} + a_2 T_{b_1})}{T_{b_1} T_{b_2}} . \qquad (15)$$

The weighted excretion coefficient for the White Oak Lake bluegill was

$$k' = \frac{0.693\ (0.0232 \cdot 187.1 + 0.977 \cdot 7.6)}{7.6 \cdot 187.1} = 0.00573 . \qquad (16)$$

Since intake (I) and excretion rates (k) are considered constants in Eq. (1), short time units must be chosen.

In the calculation of the ^{137}Cs intake by the White Oak Lake bluegill, the time interval for calculations was taken as one day. Equation (1) was then derived for the intake as

$$I = \frac{A_t - A_0 e^{-k'}}{(I_{p_1}/k_1)(1 - e^{-k_1}) + (I_{p_2}/k_2)(1 - e^{-k_2})} . \quad (17)$$

The calculations of intake were based on an average fish in age-group III in January weighing 91.6 g at the beginning of the year and gaining 18.9 g by the end of the year. No correction was made for the losses of ^{137}Cs with the reproductive cells, which were 4.5% in females and <1% in males.

The weight of fish estimated with an empirical fit to a growth curve with maximum growth rate in May, June, and July was

$$M = \arctan [0.02(t - 150)] \cdot 7.19 + 100.7 \text{ g}, \quad (18)$$

where M is the weight of fish in grams, t is the day of the year, and 100.7 is the weight of the fish on the 150th day (May 30). The concentration of ^{137}Cs in bluegill was fitted to a sine function (see Fig. 11.24), and, when multiplied by the weight of fish, it gave a body burden A_t of

$$A_t = \sin\left[\frac{2\pi}{360}(t - 313)\right] 9.2 + 38.2\, M . \quad (19)$$

The value of A_0 was simply the value of A_t on the previous day or A_{t-1}.

The temperature of water in White Oak Lake was simulated with a sine function:

$$\phi = \sin\left[\frac{2\pi}{360}(t - 105)\right] 10.8 + 15.8°\text{C} , \quad (20)$$

with a minimum of 5°C in January and a maximum of 26.6°C in July. The relationship between T_b of ^{137}Cs and the temperature was calculated according to Q_{10} law, $Q_{10} = 2$,

$$k_t = k_{15.8}\, e^{0.0693\,\{\sin[(2\pi/360)(5-105)]\,10.8\}} . \quad (21)$$

Equations of growth (18), body burden (11), excretion rates k_1, k_2, and k' (21), and daily intake of ^{137}Cs (9) were calculated stepwise with a computer program. Values of weight of fish, concentration of ^{137}Cs, body burden of ^{137}Cs, and weighted excretion rates for a whole year are shown in Fig. 11.30. The intake of ^{137}Cs fluctuated from 0.065 pc per gram of fish in late March to 0.334 pc in August, with an annual mean of 0.256 pc.

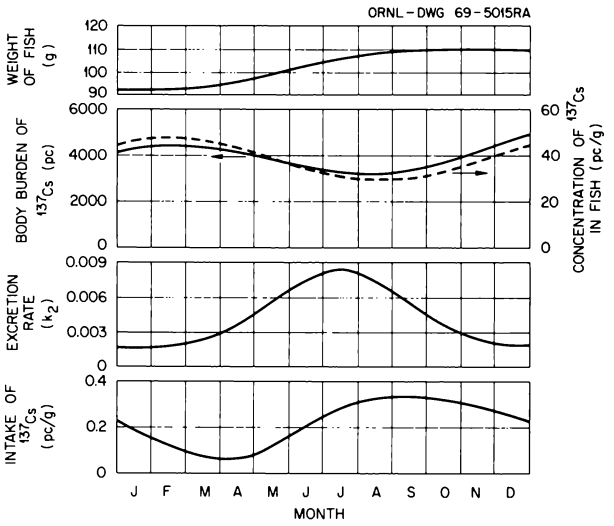

Fig. 11.30. Calculated Values of Weight, Concentration of ^{137}Cs, Body Burden of ^{137}Cs, "Weighted" Excretion Rate (k'), and Daily Intake of ^{137}Cs During a Year for Bluegill in IV Age Group.

The intake of food was calculated with the equation

$$r' = \frac{I}{\Sigma a_i d_i f_i} . \quad (22)$$

The calculations of $\Sigma a_i d_i f_i$ were made as in the following example. On June 4, 1968, the stomach contents of seven bluegill consisted of 50% chironomid larvae, 20% other insect larvae, 11% plants, and 19% detritus. Thus the quantity of ^{137}Cs assimilated from food was as follows:

Food Item	a_i (%)	d_i (pc/g)	f_i (%)	$a_i d_i f_i$ (pc/g)
Chironomid larvae	16	40	50	3.2
Other insect larvae	16	28	20	0.9
Plants	69	14	11	1.0
Detritus	3	22	19	1.3

The intake I of ^{137}Cs on June 4 was 0.168 pc per gram of fish (Fig. 11.29), and the intake of food was 0.168/6.4 = 0.0263 g per gram of fish, or 2.63% of the body weight.

The feeding rate of bluegill was directly related to water temperature (Fig. 11.29) with a linear regression

$Y = 0.32 + 0.081X$ ($r^2 = 0.665$), where Y is the daily meal (percent of body weight) and X is the temperature (°C). The daily meal was at a minimum (0.84% of body weight) in February and increased slowly during March and April. During May the increase in the feeding rate was rapid, reaching a maximum in June (3.24%), after which there was a gradual decrease until February. Feeding rates of the White Oak Lake bluegill did not decrease as rapidly in the fall of 1967 as in the fall of 1968. This might have been caused by differences in the temperature during these two summers; the summer of 1967 was cool, while the summer of 1968 was hot (Fig. 11.29). Weight of the mean daily meal of bluegill for the whole year was 1.75% of body weight. The ecological growth efficiency in the age-group IV was 6.5% during the period from April to October.

^{137}Cs, Stable Cesium, and Potassium Concentrations and Specific Activities of ^{137}Cs in White Oak Lake Fish

Along with bluegill, samples of six other species of fish were collected during 1967 and 1968 for ^{137}Cs, stable cesium, and potassium analyses. Cesium-137 concentrations in all species followed a seasonal trend similar to that in bluegill, with a maximum in winter and a minimum in summer. The highest concentration of ^{137}Cs was in golden shiner, and the lowest was in redear sunfish (Table 11.4). Concentrations of ^{137}Cs did not show the "trophic level effect,"[20] since the concentrations did not increase with the length of the food chain, but high concentrations of ^{137}Cs occurred as well in primary consumers (goldfish) as in piscivorous (largemouth bass). Low concentrations occurred in primary consumers (goldfish), in omnivorous (redear sunfish), and in piscivorous (warmouth).

Interspecific differences in ^{137}Cs concentrations in fish were caused mostly by the differences in the concentration of ^{137}Cs in food and in the percentage assimilated. The concentration of ^{137}Cs in algae was 35 pc per gram of fresh weight, and assimilation of ^{137}Cs from algae was 69% in bluegill (Table 11.3); this indicates that about 25 pc of ^{137}Cs were assimilated per gram of algae consumed. Assimilation of ^{137}Cs from chironomid larvae was only 16%; and, even though the concentration of ^{137}Cs in chironomids was 96 pc per gram of fresh weight, only 15 pc of ^{137}Cs were assimilated per gram of larvae. The concentration of ^{137}Cs in bluegill and redear fingerlings was 10 pc per gram of fresh weight, and, although predaceous fish assimilate about 70% of their ingested ^{137}Cs, only 7 pc per gram of food must have been assimilated by warmouth. Largemouth bass eat larger fish than warmouth, and, since the concentration of ^{137}Cs in larger fish was higher than in fingerlings, this might explain why largemouth bass had higher concentrations of ^{137}Cs than warmouth.

Table 11.4. Concentration of ^{137}Cs in White Oak Lake Fish

Species	^{137}Cs (pc/g fresh weight)	S.D.	Number of Fish
Gizzard shad	47.03	12.16	15
Golden shiner	62.61	22.05	15
Goldfish	34.53	13.86	10
Redear sunfish	26.85	5.86	40
Bluegill	40.12	15.21	186
Warmouth	36.69	15.75	37
Largemouth bass	52.75	13.14	6

The concentration of ^{137}Cs in fish of nonturbid and slightly turbid lakes follows the "trophic level effect,"[21] but in White Oak Lake clay particles change the efficiency of ^{137}Cs assimilation so much that ^{137}Cs is not equally available to fish at different trophic levels.

Stable cesium concentrations did not follow the same order as the concentrations of ^{137}Cs (Table 11.5). Goldfish had the highest concentration of stable cesium, while bluegill had the lowest. The concentration of potassium was lowest in goldfish and highest in largemouth bass. Overall, however, the concentrations were rather uniform in all species.

The specific activity of ^{137}Cs varied greatly among the different species. With goldfish, the specific activity was the same as in water, but in the golden shiner it was 2.5 times higher than in water (Table 11.5). These variations indicate there were differences in the availability of ^{137}Cs and stable cesium to different species of fish. This, in turn, leads to the conclusion that ^{137}Cs and stable cesium must have been in different physicochemical states and that some organisms along the food

[20] R. C. Pendleton *et al.* "A Trophic Level Effect on ^{137}Cs Concentration," *Health Phys.* 11, 1503–10 (1965).

[21] S. Kolehmainen, E. Häsänen, and J. K. Miettinen, "^{137}Cs in Fish, Plankton and Plants in Finnish Lakes During 1964–65," pp. 913–19 in *Radioecological Concentration Processes* (ed. by B. Åbergand and F. P. Hungate), Pergamon, New York, 1967.

Table 11.5. Concentrations of ^{137}Cs, Stable Cesium, and Potassium and Specific Activities of ^{137}Cs in White Oak Lake Fish

Species	^{137}Cs (pc/g)		Stable Cesium		Potassium		Specific Activity (pc $^{137}Cs/\mu g$ Cs)	Number of Fish
	Mean	S.D.	Mean	S.D.	Mean	S.D.		
Gizzard shad	42.49	2.84	0.0115	0.0034	3.00	0.14	3710	5
Golden shiner	76.06		0.0145		2.77		5250	4
Goldfish	38.97	8.41	0.0195	0.0085	2.18	0.37	2000	9
Redear	25.29	5.82	0.0090	0.0022	2.81	0.32	2830	29
Bluegill	40.20	15.23	0.0089	0.0023	2.73	0.24	4550	154
Warmouth bass	28.82	11.03	0.0121	0.0031	2.88	0.10	2380	24
Largemouth bass	58.55	6.54	0.0175	0.0023	3.16	0.65	3340	2
Water[a]	58.2	25.6	0.0284	0.0130	1.77	0.07	2050	3

[a]Values are given per liter.

chain of fish were able to concentrate ^{137}Cs more efficiently than stable cesium.

These differences in specific activity of ^{137}Cs among fish species in White Oak Lake make it impossible to apply the specific activity concept in predicting the concentrations of ^{137}Cs in fish, as was done in the Clinch River studies.[22]

Concentration factors of ^{137}Cs varied by a factor of 2 among different fish species (Table 11.6). The concentration factors of stable cesium were lower than those of ^{137}Cs in all species except goldfish, where it was higher. The concentration factors of potassium were fairly uniform.

Table 11.6. Concentration Factors of ^{137}Cs, Stable Cesium, and Potassium in White Oak Lake Fish

Species	^{137}Cs	Stable Cesium	Potassium
Gizzard shad	810	400	1690
Golden shiner	1080	510	1570
Goldfish	530	690	1230
Redear	460	320	1590
Bluegill	710	310	1540
Warmouth bass	630	430	1640
Largemouth bass	910	620	1770

[22]D. J. Nelson, "Cesium, Cesium-137, and Potassium Concentrations in White Crappie and Other Clinch River Fish," pp. 240–48 in *Symposium on Radioecology* (ed. by D. J. Nelson and F. C. Evans), CONF-670503 (1969).

12. Watershed Aquatic Habitat Interactions

C. H. Abner[1]
W. P. Bonner[2]
J. W. Curlin[3]
E. R. Eastwood[2]
J. W. Elwood[3]
M. L. Frank[3]
N. A. Griffith[3]
D. F. Grigal[4]
T. Grizzard
M. Heath[5]
W. F. Johnson[1]
D. J. Nelson[3]
L. N. Peters[3]
W. M. Snyder[6]
W. J. Selvidge[7]
G. Stanhill[8]
T. Tamura[2]
J. L. Thompson
W. A. Thomas[3]
M. Witkamp[3]

WALKER BRANCH WATERSHED PROJECT

Objectives

This project is organized to assess the potential ecological impact of new technology being applied to the field of natural resource management. These studies coalesce the efforts of aquatic and terrestrial ecologists with those of earth scientists into a unified program directed toward elucidating the interactions between land and water. The project will contribute to the understanding of biogeochemical relationships between aquatic habitats and associated watersheds through the synthesis of an empirical watershed model which will (1) relate the water quality and productivity of the stream to the characteristics of the adjacent terrestrial ecosystem, (2) equate the net loss of chemical elements through streamflow to the rate of mineral cycling, (3) establish the relationship between the hydrologic cycle and the mineral cycle, (4) provide bench-mark information of natural terrestrial-aquatic ecosystems for comparison with those modified by man's cultural practices, and, finally, (5) apply the knowledge gained from this small, controlled drainage basin study to broader landscape units to evaluate the impact of man's activities on the total ecosystem.

Industrial technology is advancing at an accelerated rate. Accompanying this technology is a continual degradation of the environment from the release of by-products, wastes, and misused chemical amendments. Assessment of the impact of new technology on the landscape is imperative if we are to abate the chronic degradation of our natural ecosystems which is now occurring.

Localized problems have developed in water bodies and water courses adjacent to agricultural areas from intrusion of agricultural fertilizers, agricultural chemicals, and animal wastes. When normally innocuous inorganic fertilizers and pesticides flow into streams via groundwater and runoff, a chemical enrichment results which can cause eutrophication of the water, resulting in excessive plant growth and impairment of general water quality.

Presently these problem areas are localized. However, when forest fertilization becomes a widespread practice as a means to increase forest productivity, serious eutrophication problems may result. It appears that forest fertilization will be necessary to compensate for urban encroachment and land-use pressure if the nation's future timber demand is to be satisfied. Average rates of fertilizer application for forestry purposes usually exceed those of normal agriculture several-fold; frequency of forest fertilization, however, is generally less.

A potential problem could develop if large acreages of forest were fertilized, because our water supplies

---

[1] ORNL Engineering.
[2] Radioactive Waste Disposal Section.
[3] Dual capacity.
[4] AEC Postdoctoral Fellow.
[5] Computer Technology Center.
[6] Consultant, Georgia Institute of Technology.
[7] ORNL semitechnical support.
[8] Alien guest.

originate in upland forested regions prior to entering the agricultural and industrial regions downstream. Presently, these virgin waters contain only natural chemical enrichment resulting from normal cycling and decomposition. If, however, the watersheds also contribute significant inorganic salts lost from fertilized forests, the problem will compound the effect of present agricultural, industrial, and urban pollution and perhaps exceed a threshold which could result in a costly and serious degradation of water quality.

The Walker Branch Watershed project is presently emphasizing the characterization and modeling of the undisturbed, natural forest ecosystem. Within three years this initial characterization will be completed, and one subwatershed will be fertilized to measure the differential effect of fertilization on the ecosystem. Fertilizer effects will be related to biomass growth, animal and plant species-diversity, enrichment and rate of movement of chemicals through the soil-water system, and stream water quality and aquatic productivity.

Studies have been initiated to evaluate the transfer rates and characteristics of the transfer functions among the principal components of the watershed ecosystem (Fig. 12.1). This year's report summarizes the initial data evolving from some of these subsystem studies.

Input-Output

The framework of the project is based on the input-output sequence of chemical and water throughput. Subsystem studies are intended to provide hypotheses which will explain the delays, lags, and diversions encountered in the translation of observed meteorological input to observed surface water output.

The meteorological monitoring network and stream gages have been described in an earlier annual report[9] and in a topical report.[10] Beginning January 1969 the facility reached the designed operating level. Records of both chemical content and hydrologic data are being

[9] S. I. Auerbach *et al. Health Phys. Div. Ann. Progr. Rept. July 31, 1968,* ORNL-4316, pp. 127–37.

[10] J. W. Curlin and D. J. Nelson, *Walker Branch Watershed Project: Objectives, Facilities, and Ecological Characteristics,* ORNL-TM-2271 (September 1968).

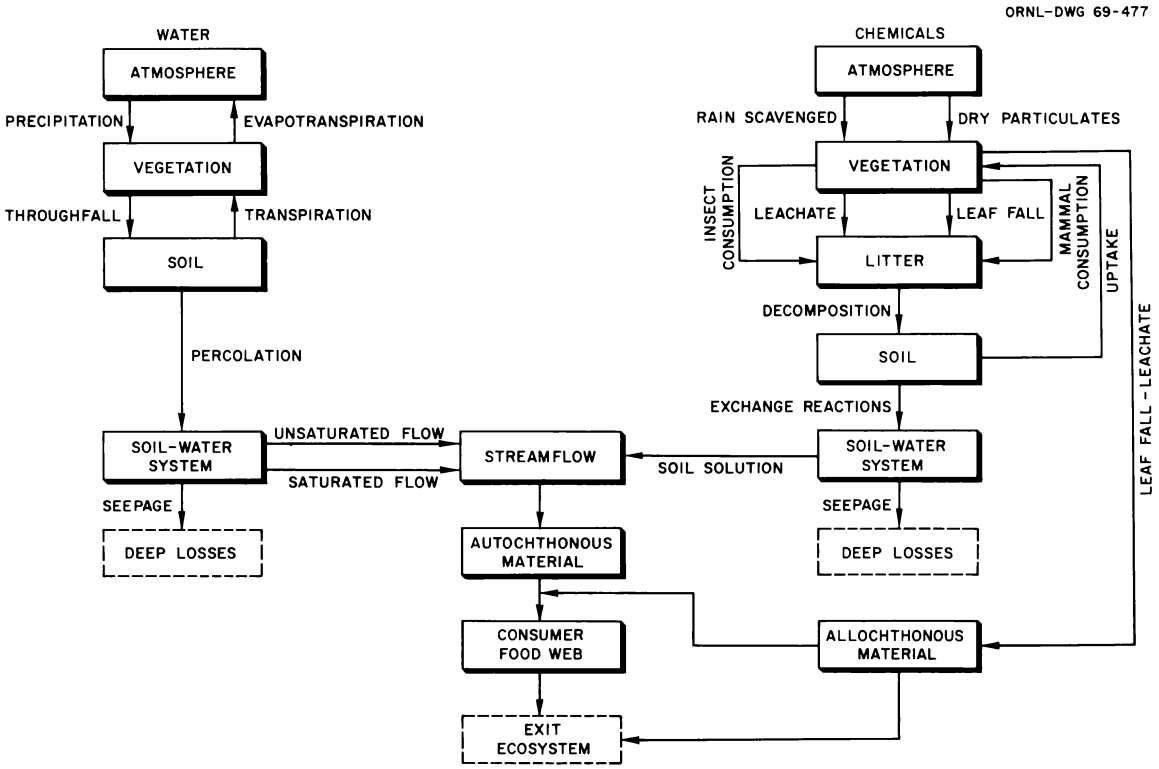

Fig. 12.1. Compartment Model of Walker Branch Watershed. The compartments and transfer paths shown will be the focus of empirical studies for development of a conceptual watershed model.

accumulated routinely. Chemical input and output are estimated weekly for Ca, Mg, Na, K, N, and P from stream water, rainwater, and dry particulate deposition.

Results for the first 16 weeks, through April 21, 1969, are shown in Fig. 12.2. The most striking feature of these data is the comparatively large contribution of chemicals from particulate fallout in contrast to the amounts deposited by rainwater.

In general, the dryfall contribution was an order of magnitude greater than the wetfall for each element. The only exception was that sodium in wetfall exceeded that in dryfall. Chemical concentrations of the dryfall were determined after H_2O_2 treatment to digest the organics, with subsequent extraction in 1 *N* HCl. The expected rate of dissolution of the dryfall component under natural conditions is unknown. Microscopic examination of the particulates indicates that it is fly ash, probably produced by the steam-generating plants of TVA and AEC in the Oak Ridge area. The particulates are highly siliceous, and a large proportion of the volume deposited on the watershed is inert to the extraction procedures used. The rate of deposition of dryfall seems to be seasonal, reaching a maximum in mid-winter, when steam plant activity is greatest (Fig. 12.3). Peak deposition rates of 10 to 12 kg hectare^{-1} week^{-1} were observed for the period January 13 to 27. By March 17 the weekly input of dryfall had receded to a stable 2 to 3 kg/hectare.

The chemical contribution from rainwater seems to parallel similar values reported in the literature. Calcium and sodium input averaged approximately 0.1 kg hectare^{-1} week^{-1} for the 16-week period of record, while magnesium and potassium averaged 0.02 and 0.05 kg respectively. Phosphorus input was extremely low, averaging 0.005 kg hectare^{-1} week^{-1}. The greatest elemental input via wetfall was total nitrogen, 0.2 kg hectare^{-1} week^{-1}, primarily in the NH_4 and organic forms.

Calcium was the most abundant ionic species in the stream water, ranging in concentration between 10 and 30 ppm (Fig. 12.4). Magnesium was found at levels between 2 and 15 ppm, sodium had a stable concentration of about 0.5 ppm, and potassium was the least abundant cation, ranging between 0.3 and 0.9 ppm. Phosphorus was found at extremely low concentrations, ranging widely from 1.3 to 138 ppb. Total nitrogen ranged between 0.1 and 1.0 ppm. Nitrate-nitrogen concentrations were extremely low, mostly in the 0.002- to 0.05-ppm nitrogen range. In general, the ionic contents of waters from the west fork were slightly higher than concentrations in the east fork, with the exception of sodium, which was about the same.

Preliminary analyses of spring water feeding Walker Branch revealed some interesting contrasts. The calcium content of spring water and stream water in the west fork showed little variation during a dry period in September 1967 (Fig. 12.5). The east fork, however, showed greater contrast in calcium content. Spring S4E had extraordinarily low calcium concentrations (5.6 ppm), while water from an adjacent spring, S3E, had the highest calcium content observed in the watershed, 35.2 ppm. This phenomenon leads to a hypothesis that an area occupied by Tarklin soil, with a fragipan which restricts deep percolation, is the source of the low-calcium water from spring S4E, whereas deep percolating water of high calcium content (35.2 ppm) feeds spring S3E. This hypothesis will be tested in subsequent studies.

Terrestrial Studies

The major interface of the biotic and abiotic components of the terrestrial subsystem is at the soil-litter juncture. The circulation of materials within natural terrestrial ecosystems is governed by the rates at which elements are released from leaf litter by decomposition and the velocity with which the ions move through the soil-water system. The decomposition rate of organic matter is a function of the characteristics of both the organic substrate and the environment. Nutrients in solution move through the soil from the uplands under a hydraulic gradient and enter the watercourse as either diffuse riparian seepage or as springs.

An additional route of entry into streams is by direct input of allochthonous organic material, a transfer that can markedly influence water quality and habitat for aquatic organisms.

We have begun studies on both modes of nutrient transfer. Initial emphasis has been placed on movement of calcium in the environment because it is the dominant cation in both the terrestrial and aquatic subsystems. However, other physiologically important elements are also being followed so that comparative loss rates and movements can be evaluated.

Transfer of Ions and Water Through Soil. – Because major input of ions to the soil surface is by litterfall, a small plot study was initiated to gain an understanding of the transfer of ions from litter through the soil-water system. A 3- by 5-m plot was established on an upper slope of the west subwatershed. The plot is on Fullerton soil, which occupies approximately one-half the area of the watershed. A schematic diagram of the experimental area is shown in Fig. 12.6.

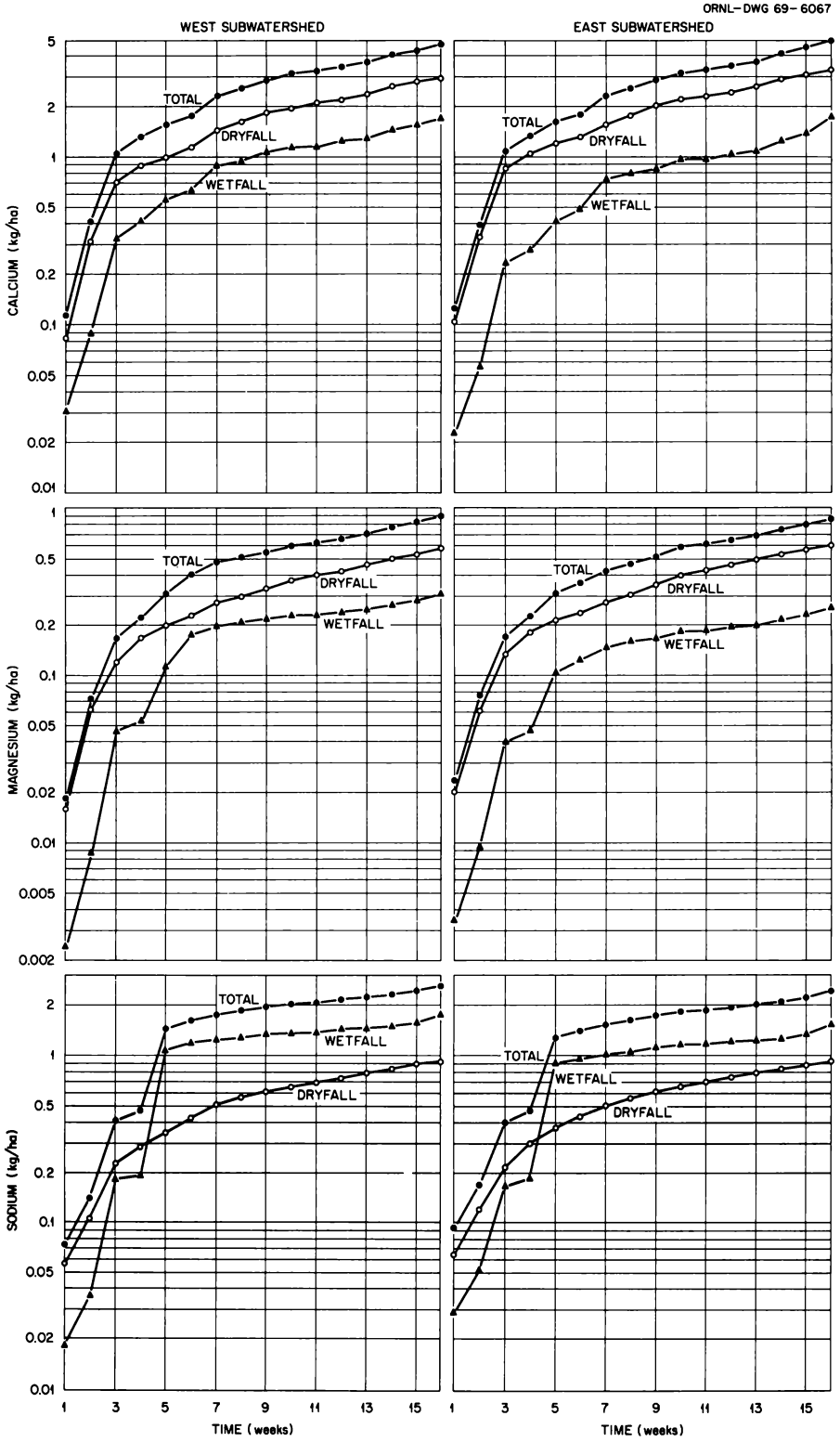

Fig. 12.2. Meteorological Input to Walker Branch Watershed Between January 1, 1969, and April 21, 1969.

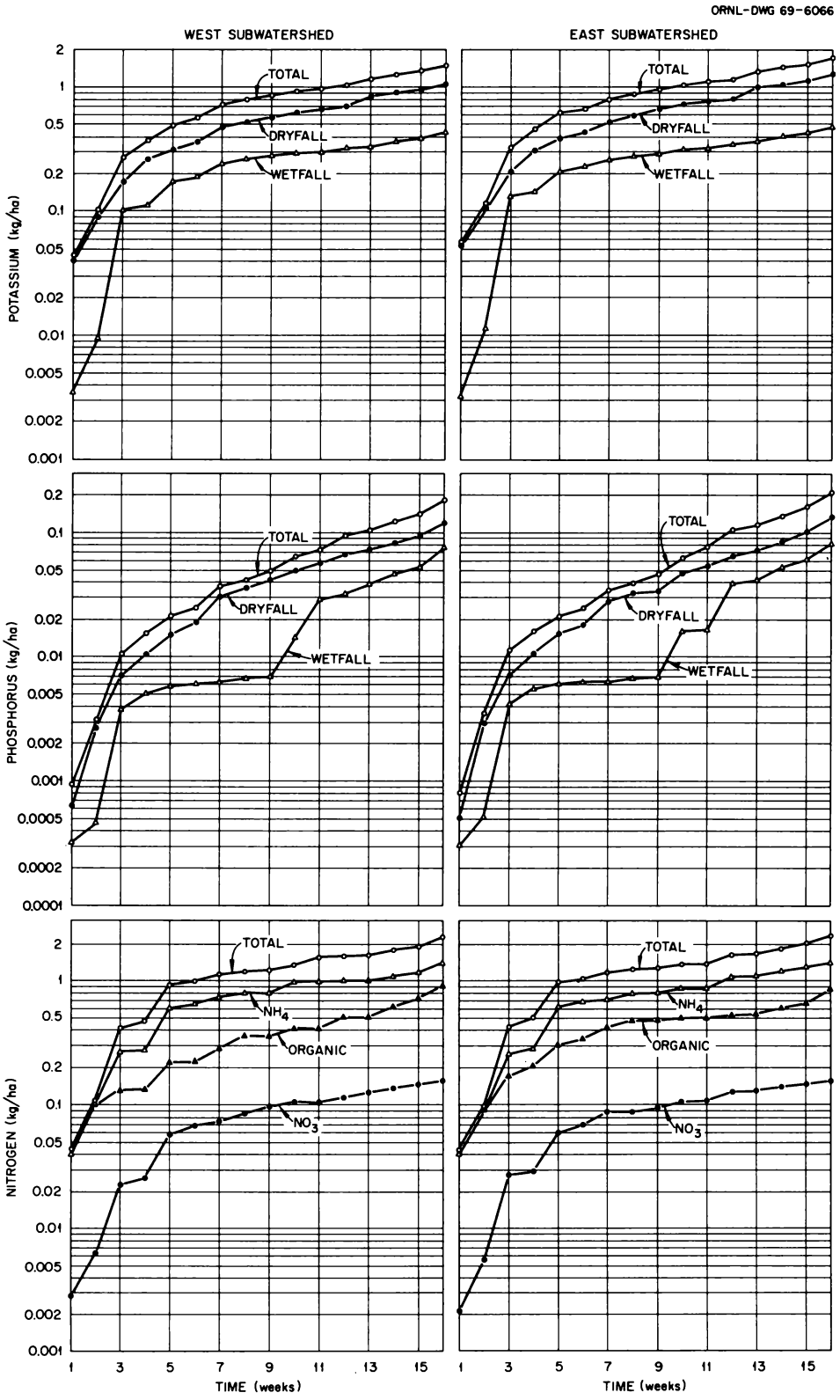

Fig. 2 (continued)

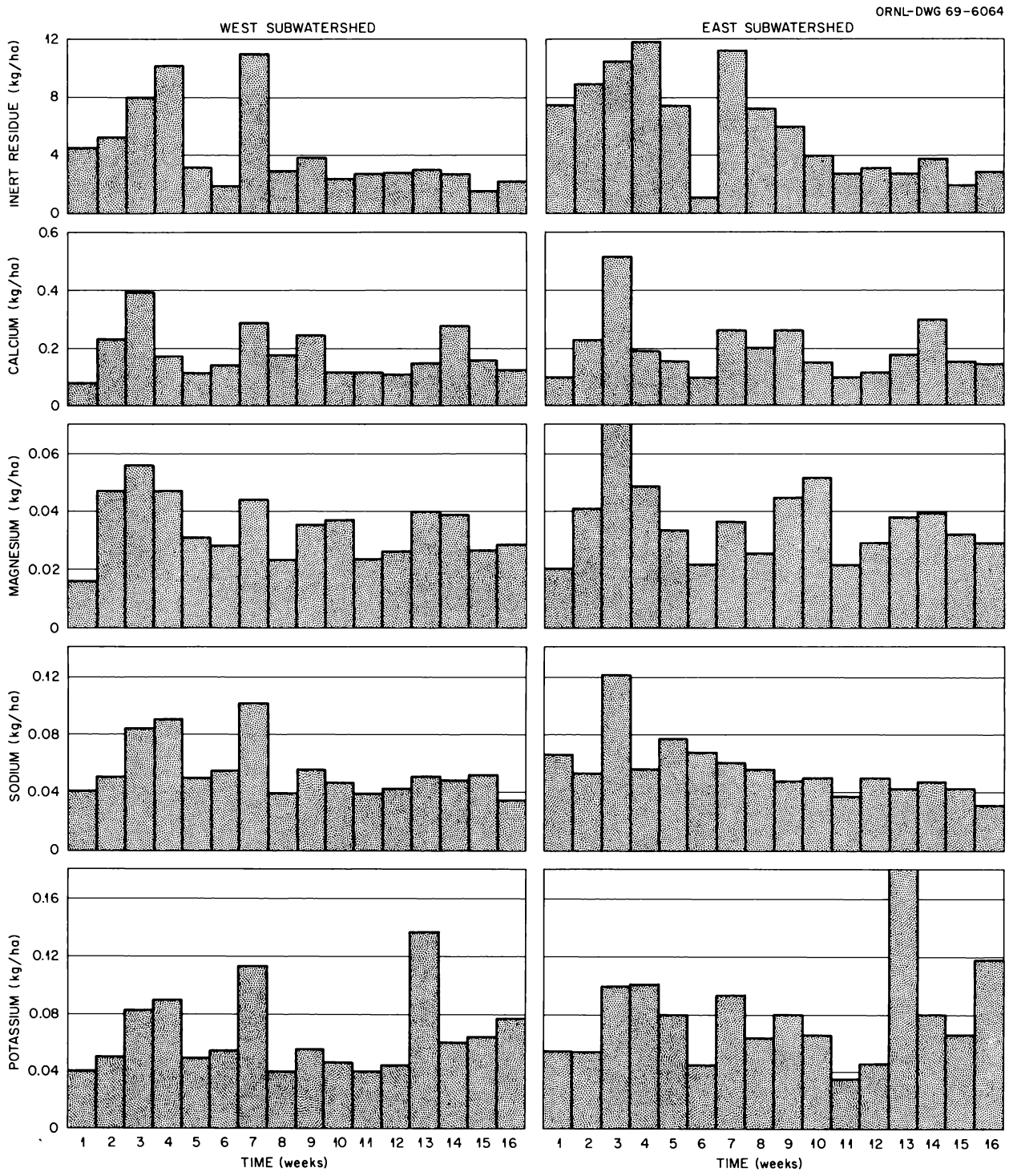

Fig. 12.3. Contribution of Dry Particulate Fallout to the Chemical Income of Walker Branch Watershed.

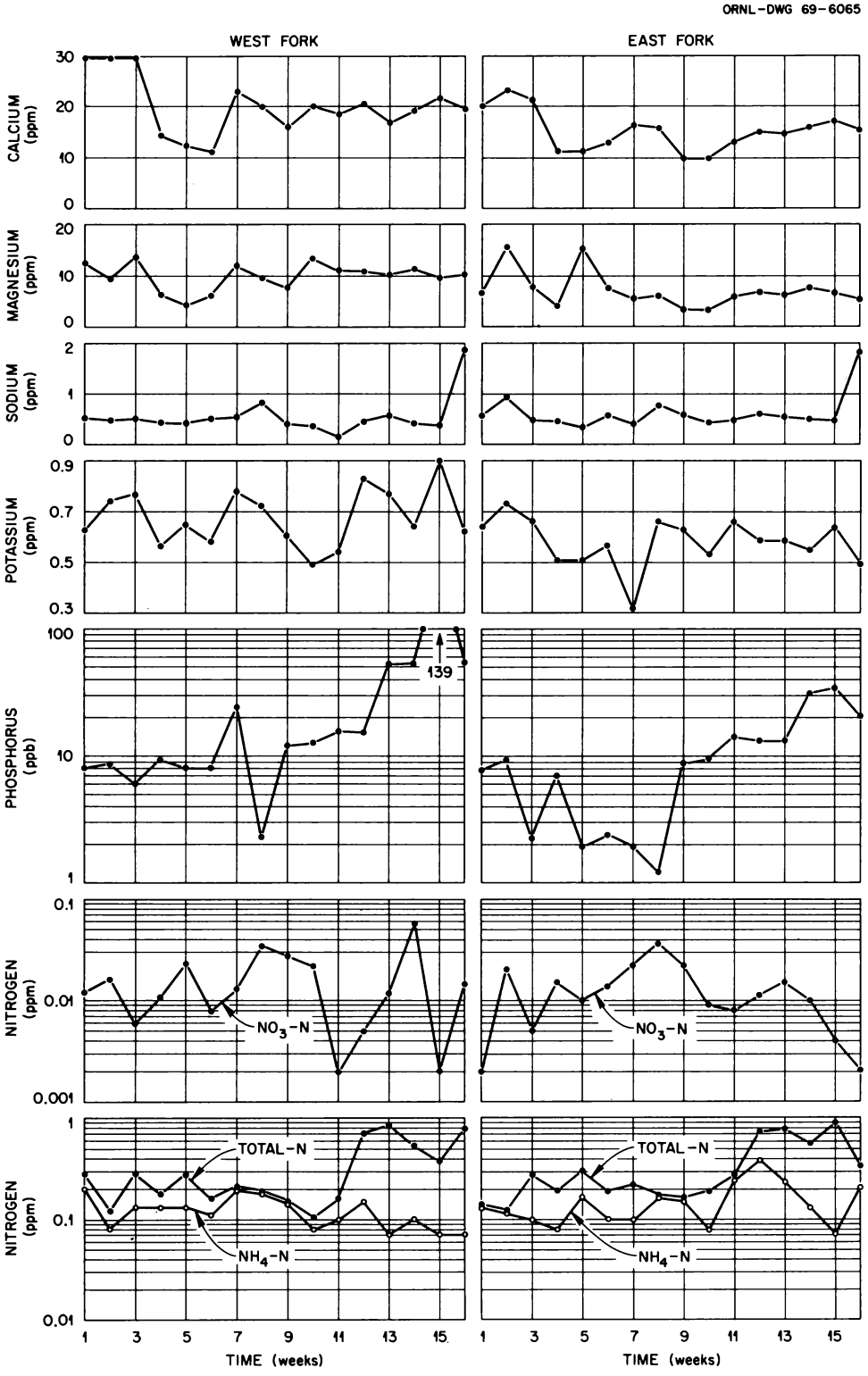

Fig. 12.4. Chemical Concentrations of Stream Water at the Weirs of Walker Branch Between January 1, 1969, and April 21, 1969.

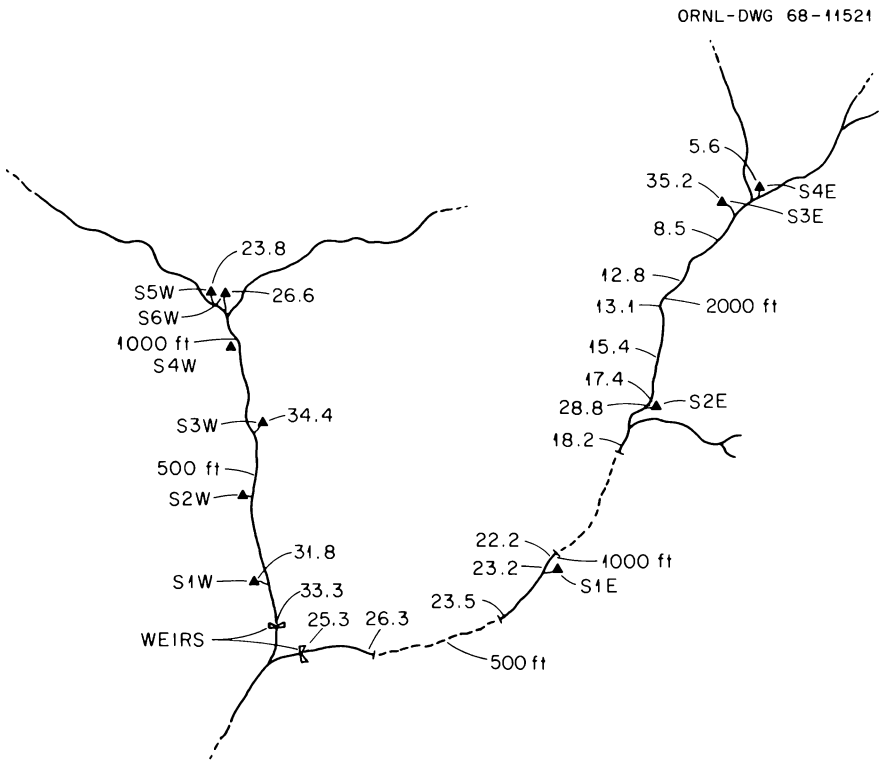

Fig. 12.5. Calcium Content (mg/l) in Spring Water and Stream Water of Walker Branch During a Period of Extremely Low Flow in September 1967. Surface effects were minimum at this time.

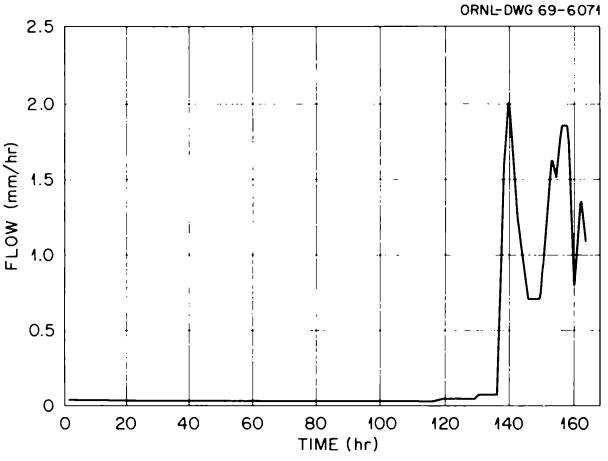

Fig. 12.6. Schematic Drawing of Cross Section of Experimental Area Used to Study ^{45}Ca and Water Movement Through Soil.

The plot is underlain by six tension lysimeters,[11] three placed at the bottom of the A1 horizon (7.5 cm) and three at the bottom of the B1 (50 cm). The lysimeters, 28 cm in diameter, are maintained under 0.1 atm tension in order to extract soil water for subsequent analysis. A sampling face was installed about 5 m downslope from the plot. Both the plot and the face are oriented perpendicularly to the slope. A trough at each of six major soil horizons collects saturated flow from the sampling face. Flow rates into the collectors at the lysimeters and sampling face are electronically monitored. Thirty-five access tubes on a 1-m-square grid have been installed to follow moisture movement.

Red maple (*Acer rubrum*) litter containing about 125 mc of ^{45}Ca was spread on the plot in December 1968. The tagged litter was obtained by inoculating red maple trees with ^{45}Ca the previous May and harvesting the leaves prior to leaffall in October. Table 12.1 compares the composition of natural forest floor (01 and 02 horizons) in the experimental area with the additional quantity supplied by the tagged litter.

Concentrations of the major nutrient ions (Ca, Mg, K, N, and P) and of ^{45}Ca are determined weekly in the soil water collected from the lysimeters and at the sampling

[11] D. W. Cole, "A System for Measuring Conductivity, Acidity, and Rate of Water Flow in a Forest Soil," *Water Resources Research*, pp. 1127–36, 1968.

Table 12.1. Biomass and Elemental Content (kg/hectare) of Forest Floor Under Oak-Hickory Cover Type and Additional Litter Input Added Experimentally

Forest Floor	Biomass	Ca	Mg	K	P	N
01	3,780	67	8	9	2	30
02	12,240	327	18	10	9	163
Total	16,020	394	26	19	11	193
Litter input	45,300	534	100	308	51	621

face. Soil cores are removed at four-week intervals to monitor ^{45}Ca movement in the soil profile. Seventy-five percent of the tagged litter remained on the plot 12 weeks after input. Total amounts of both stable calcium and ^{45}Ca in the litter changed very little from time of application. Sixty-four percent of the original magnesium and only 25% of the original potassium remained after 12 weeks.

Preliminary laboratory and in situ field experiments with short-lived ^{47}Ca indicated that the distribution of water-soluble calcium in the soil is dependent on moisture conditions (Fig. 12.7). Calcium solution applied to a dry soil infiltrates and is absorbed rapidly, and the calcium will adsorb to the soil colloids readily. If, however, the soil matrix is wet when the solution is applied, the calcium diffuses through the soil slowly, resulting in a more uniform distribution.

Initial movement of ^{45}Ca from the litter to the soil was rapid; after four weeks, activity was detected at a depth of 7 cm. This ^{45}Ca was probably a water-soluble fraction which was adsorbed to soil colloids by exchange reaction, since vertical distribution had not changed appreciably after eight weeks (Fig. 12.8). By the 12th week, activity had increased at the surface, and after 16 weeks increases in activity were apparent down to about 4 cm. Calcium-45 was detected at 10 cm after 16 weeks, but most of the activity was confined to the upper 6 cm (Fig. 12.8).

The distribution of ^{45}Ca within the soil is variable. Even after 16 weeks, activity in the surface mineral horizon (0 to 1 cm) ranged from 600 to 3×10^6 dis min^{-1} g^{-1}.

The average concentrations of ions in soil water on a weekly basis during February 1969 are shown in Table 12.2. Soil water near the surface was higher in ionic concentration for all elements except NH_4-N and NO_3-N. These higher concentrations are to be expected

Table 12.2. Average Concentration (ppm) of Ions in Soil Water Collected by Tension Lysimeters During February 1969

Depth (cm)	Ca	Mg	K	Total N	NH_4^+-N	NO_3^--N
7.5	5.94	2.20	2.07	0.54	0.18	0.018
50	2.34	1.56	0.48	0.38	0.28	0.018

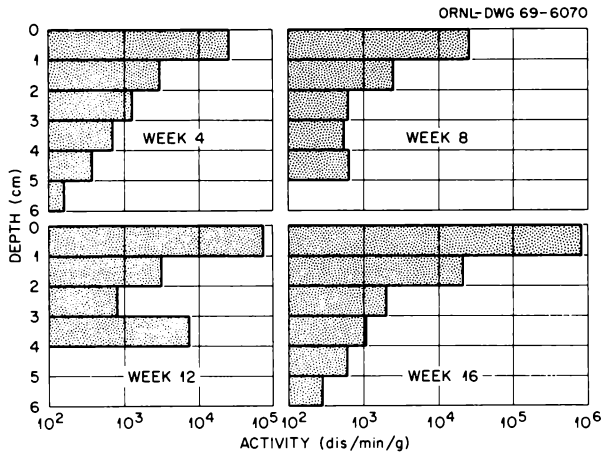

Fig. 12.7. Distribution of ^{47}Ca Applied as a Solution to Soil Cores Moistened to Field Capacity and to Field Soil near Wilting Point.

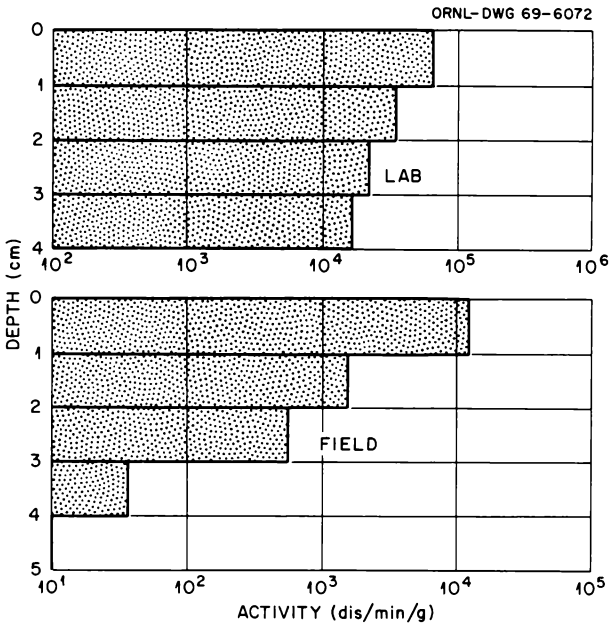

Fig. 12.8. Distribution with Time of ^{45}Ca Released from Decomposing Litter into Fullerton Soil.

because of the ions being released as the litter decomposes. At these concentrations, relatively insignificant quantities of nutrients are being lost to deeper horizons (about 5 kg/hectare of calcium to 0.03 kg/hectare of NO_3-N during the month of February). Most of the ions released from the litter are apparently adsorbed on soil exchange sites and are not rapidly lost from the system. Only traces of ^{45}Ca activity have been found in the water from the lysimeters during the first four months of the study, indicating that most of the ions in the water near the surface are the product of exchange reactions and do not come directly from the litter.

Water flowing from the sampling face is markedly different in concentration from that flowing into the lysimeters. Generally, flow at the sampling face is variable both in time and volume; therefore it is impossible to calculate a reliable average concentration. The concentration of ions in this water is slightly higher but well within the range of concentration of ions in Walker Branch (Fig. 12.4). It is this saturated flow that contributes to stream flow following storm events, and its ionic concentrations would not markedly change those of Walker Branch. The agreement between elemental concentrations in stream water and soil water suggests that perhaps the general chemical character of the water is determined early in the hydrologic process, quite remotely from the watercourse itself. Fourteen weeks after litter application, only very minor amounts of ^{45}Ca have been detected in water collected at the sampling face.

The lysimeters, as expected, respond to major rainfall events by sharp increases in flow rate (Fig. 12.9). The lysimeters vary in response to precipitation volume.

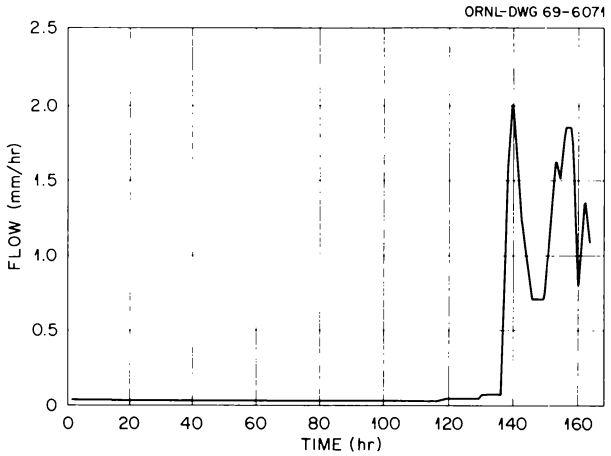

Fig. 12.9. Response of Tension Lysimeter to Rainfall Event.

Three of the six lysimeters, two shallow and one deep, respond similarly to a rainfall impulse. Based on limited data, the volume of incident precipitation and the volume collected are highly correlated ($r = 0.89$).

As part of the original objectives of the experiment, a field test was to be conducted of the use of D_2O as a water tracer and its detection in situ by the gamma-neutron reaction.[12] However, this experiment was postponed until next year due to a malfunction in one of the components of the detection system.

Decomposition and Mineralization of Leaves: Terrestrial vs Aquatic Subsystems. – To compare rates of litter decomposition on land and in water, leaves of each of three species, red maple (*Acer rubrum*), tulip tree (*Liriodendron tulipifera*), and white oak (*Quercus alba*), were collected during leaffall in late October 1967. These species are common on the watershed and make a sizable contribution to the annual transfer of organic matter to the forest floor.

Thirty-nine litter-bag samples of each species were placed in a wire container, which was anchored on the bottom of the west fork of Walker Branch approximately 155 m upstream from the weir, on November 4, 1967, during deciduous leaffall. The stream there is about 1.5 m wide, and decomposing leaves cover part of the stream bottom. On the same date 39 bags of each species were placed in a natural position on the litter layer of an oak-hickory stand approximately 30 m upslope from the stream samples. Three litter-bag samples of each species in both environments were collected every four weeks for determination of oven-dry weight and calcium content. Losses of water-soluble material were estimated by placing three litter-bag samples of each species, prepared in the same manner as the ones put in the field, in an artificial laboratory stream of continuously circulated spring water at 15°C for 24 hr.

The west fork of Walker Branch is a spring-fed perennial stream which drains the 95-acre west subwatershed. Precipitation at the forest floor totaled 97 cm during the year, and water temperature in the stream ranged only 6°C, from 10 to 16°C.

The initial calcium concentrations in these samples of senescent leaves, as percentages of oven-dry weight, averaged 1.48% ± 0.06[13] for *Acer*, 1.78% ± 0.04 for *Liriodendron*, and 1.57% ± 0.03 for *Quercus*. The

[12] C. C. Haskell and R. H. Hawkins, "D_2O-Na^{24} Method for Tracing Soil Moisture Movement in the Field," *Soil Sci. Soc. Amer. Proc.*, pp. 725–28, 1964.

[13] Arithmetic mean ± one standard error $n = 3$.

comparable ash values were: *Acer*, 6.0% ± 0.01; *Liriodendron*, 5.9% ± 0.02; and *Quercus*, 5.1% ± 0.1.

Almost all *Acer* leaves lost their petioles within four weeks in the stream. After eight weeks skeletonization of many *Acer* leaf blades was apparent, and after 16 weeks all leaf structure disappeared, with complete decomposition within 20 weeks. *Liriodendron* and *Quercus* leaves maintained their structure until about week 28, when it became impossible to identify the leaves without reference to tags on the samples. All samples on land retained enough leaf structure to be identified throughout the year. The order of leaf resistance to breakdown on land and in water, *Quercus* > *Liriodendron* > *Acer*, is reflected in Fig. 12.10 for weight loss and in Fig. 12.11 for loss of calcium.

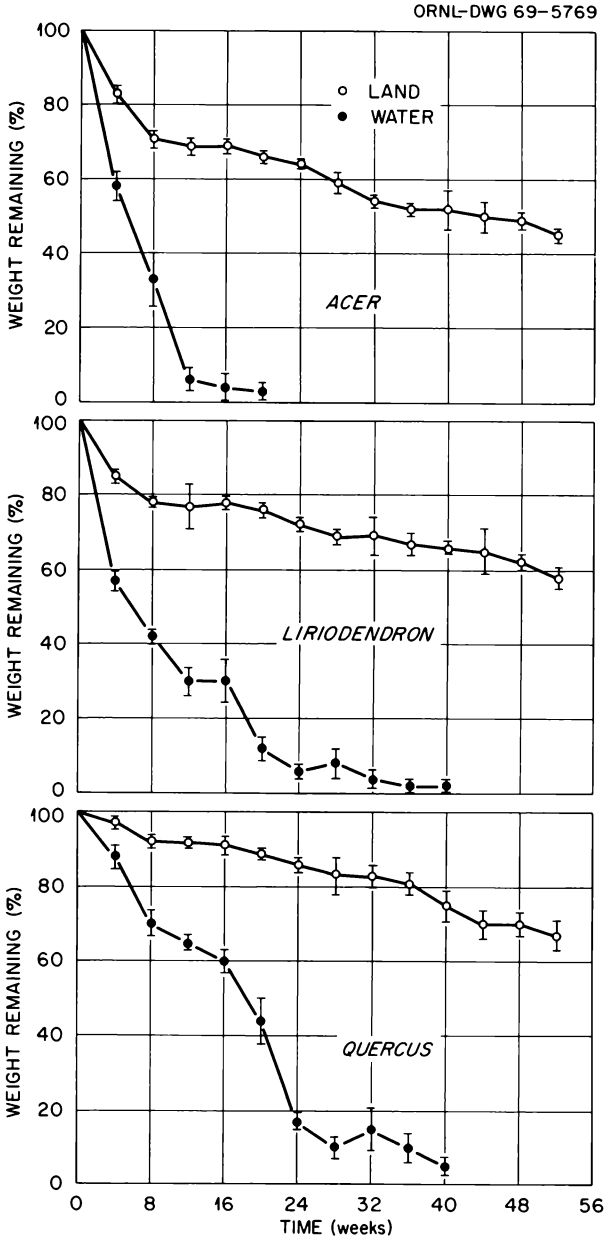

Fig. 12.10. Weight Loss from Tree Leaves on Land and in Walker Branch. Each point represents the mean of three samples; vertical lines show limits of 1 standard deviation about the mean. Week 0 = 4 November 1967.

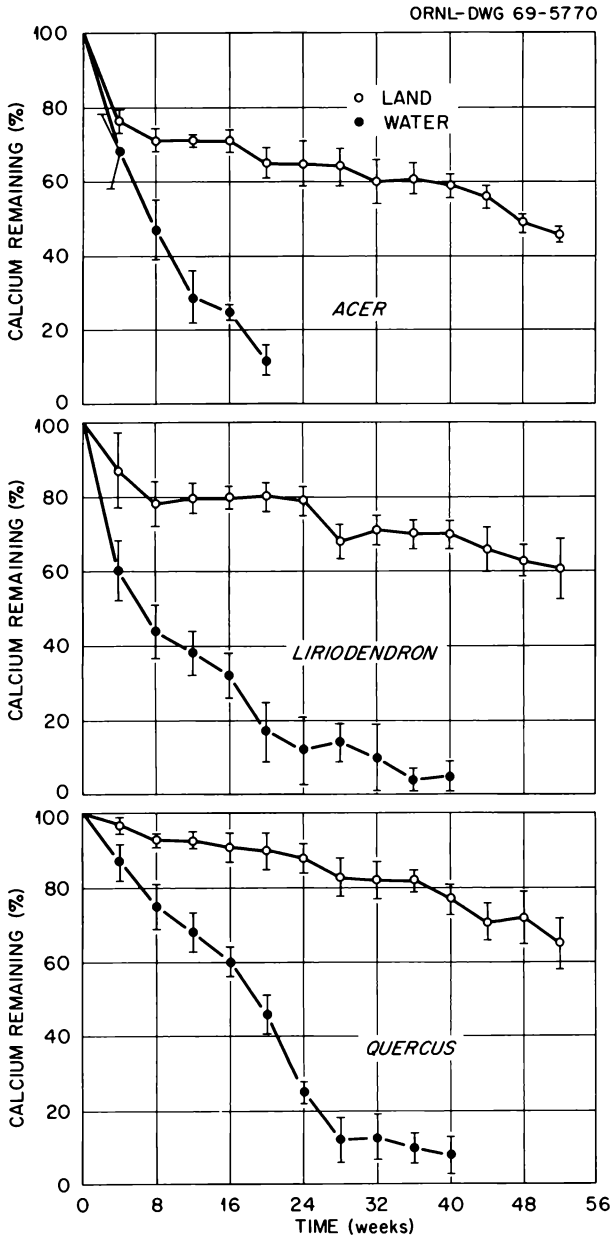

Fig. 12.11. Calcium Loss from Tree Leaves on Land and in Walker Branch. Each point represents the mean of three samples; vertical lines show limit of 1 standard deviation about the mean. Week 0 = 4 November 1967.

The losses from leaves on land during the first eight weeks in litter are largely attributable to leaching of water-soluble material. These values for weight loss, *Acer* 29.3% ± 1.0, *Liriodendron* 22.3% ± 0.4, and *Quercus* 6.8% ± 1.0, approximate those losses from samples in the laboratory stream: *Acer* 25.0% ± 0.6, *Liriodendron* 24.0% ± 0.1, and *Quercus* 3.7% ± 0.3. An additional 24 hr in the laboratory stream removed only 1% of additional weight from all species.

The loss rates from all three species were low from week 8 to about week 16 or 20 before they accelerated in the spring and summer, when environmental conditions for populations of decomposers became more favorable. The calcium loss rates show the same trend.

First-year losses on land for *Acer* average D: weight 55% ± 1, calcium 54% ± 1; for *Liriodendron*, weight 44% ± 2, calcium 38% ± 4; and for *Quercus*, weight 33% ± 2, calcium 35% ± 4.

The more rapid decomposition of litter in the stream can be attributed to constant leaching and to the abrasion of leaves by particles carried in the stream. All sample bags contained bottom sediments, which undoubtedly scoured the leaves.

It is evident that the allochthonous leaf litter in streams functioned as a natural component of the aquatic subsystem because of the organisms found while removing sample litter from the bags. Snails (*Goniobasis clavaeformis*) accounted for 80% of the 79 organisms collected. Other specimens included from one to four larvae each of caddis fly (Trichoptera: Hydropsychidae), mayfly (Ephemeroptera: Heptageniidae), crane fly (Diptera: Tipulidae), dobsonfly (*Sialis* sp.), and stone fly (*Peltoperla* sp.). Three dusky salamanders (*Desmognathus fuscus*) and two crayfish (*Cambarus* sp.) also inhabited the samples. Many of these aquatic organisms exceeded the mesh size of the litter bags, indicating that they had lived in the samples for some time. No attempt was made to extract all of the organisms; therefore the count was biased toward the larger animals. The samples on land also appeared to be naturally incorporated into the litter. Over 60% of all samples collected after May contained easily visible fungal mycelia.

Variation in weight losses among samples was greater in the stream than on land. The greater variance in calcium losses reflects variation in the accuracy of calcium determinations and contamination of plant material by soil. No significant differences ($P > 0.05$) existed between the weight loss and the calcium loss for any collection on land or in water except for *Acer* in water at weeks 12 and 16, when weight loss significantly exceeded calcium loss. The high calcium values for these two collections are unquestionably due to contamination by stream sediments.

Allochthonous material is blown into the stream throughout the year and thus influences the chemical budget. To determine the increase in decomposition rate of partially decomposed leaves when they enter the stream, leaves of each species were collected from the forest floor in late July. The leaves fell from trees the previous autumn and appeared to be about as decomposed as those in litter-bag samples on land. Three bagged samples of each species were placed both on land and in the wire container in the stream on 14 August and were collected for oven drying on 11 September, four weeks later. An additional three bags for each species were placed in the artificial laboratory stream for 24 hr.

The 24-hr water-soluble weight losses averaged 2.9% ± 0.3 for *Acer*, 5.4% ± 0.6 for *Liriodendron*, and 0.5% ± 0.1 for *Quercus*, from 12 to 23% as great as the losses from freshly fallen leaves in the laboratory stream. Weight losses from leaves of all species in the stream greatly exceeded those in the laboratory: *Acer* 32% ± 2, *Liriodendron* 25% ± 1, and *Quercus* 15% ± 2. The fragile condition of partially decomposed litter probably resulted in accelerated losses by physical disintegration, such as scouring. The losses from samples on land, all of which agree with losses from the first series of bags during the same four weeks, averaged 1.8% ± 0.6 for *Acer*, 5.7% ± 0.5 for *Liriodendron*, and 1.1% ± 0.4 for *Quercus*.

The addition of organic matter throughout the year to Walker Branch influences the chemistry of the stream. The similar rates of weight and calcium losses indicate that the weight loss from decomposing litter provides a good estimate of the calcium loss.

Aquatic Studies

The quality of surface waters flowing from the watershed will be reflected by the biotic communities living in the streams. Because of the unidirectional current in flowing waters, populations in streams consist predominantly of benthic communities of organisms living on and in the stream bottom. For an undisturbed watershed such as Walker Branch, the qualitative and quantitative parameters of its benthic communities should provide a base line for measuring changes produced by forest fertilization.

A sampling program was initiated to qualitatively and quantitatively characterize the flora and fauna of Walker Branch. Artifical substrates (3.8- by 7.6-cm glass slides oriented in vertical and horizontal positions in

relation to the stream bottom and parallel with the current) and natural stone substrates were placed in riffles in the east and west forks on July 24, 1968. A random sample of all substrates was removed at biweekly intervals. Standing crops of diatoms reached a maximum on all substrates after 56 days (Fig. 12.12). Biomass was at a maximum after 20 days on some substrates, while others had not reached a maximum even after 70 days in the stream. There were no significant correlations between diatom numbers per unit area and biomass per unit area on any substrates; thus the use of biomass standing crops as a measure of periphyton growth and production on benthic substrates would be misleading. This lack of correlation between numbers and biomass was apparently due to an accumulation of organic detritus on the substrates which added biomass but later sloughed off after large quantities had accumulated. Standing crops of numbers were generally higher in the west fork than in the east fork. A black precipitate, predominantly manganese and manganic oxides known to precipitate under oxidizing conditions, formed on some of the artificial and natural substrates in the east fork at a point where springs seeped into the stream. This phenomenon offers an interesting example of the possible influence of soil and geological characteristics which subsequently affect water quality. Soils in the area contain iron-manganese concretions; the possibility that localized soil conditions are causing this effect will be investigated. Manganese concentrations in the water were less than 1 ppm. Standing crops of numbers on these substrates were very low, which would partially explain the lower standing crops of diatoms in the east fork.

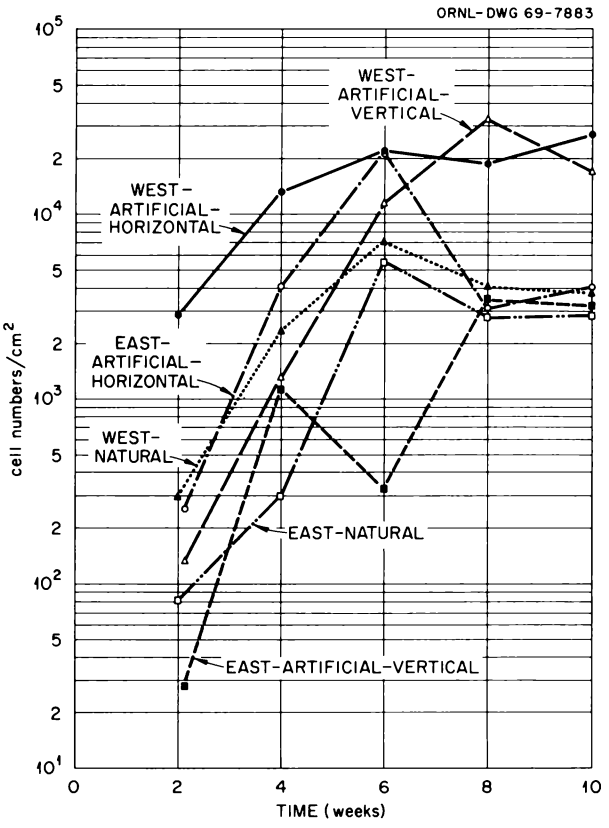

Fig. 12.12. Standing Crops of Periphytic Algae (Predominantly Diatoms) on Artificial Substrates (Glass Slides Oriented in Vertical and Horizontal Positions in Relation to the Stream Bottom and Parallel with the Current) and Natural Substrates 2, 4, 6, 8, and 10 Weeks After Placement in the East and West Fork of Walker Branch Watershed.

In anticipation of making ^{32}P releases into the streams to estimate standing crop of periphyton, a material balance study using ^{32}P and periphytic algae in a closed system in the laboratory was conducted to obtain data on uptake and turnover of phosphorus by stream diatoms. Glass slides were allowed to colonize with stream diatoms from a spring-water source in the laboratory for approximately two months. Slides were held in a plexiglas tray containing approximately 6 liters of water and placed in a temperature bath under a bank of fluorescent lights. The system was spiked with 298 μc of $^{32}PO_4$. Radioactive and stable phosphorus levels were measured in both algae and water for 63 days (Fig. 12.13). A calculated turnover time for phosphorus of algae per unit biomass was approximately 3 days, while the turnover time per unit volume of water was 6.7 days. The biological half-life of ^{32}P in algae was 2.1 days. The standing crop of biomass per unit area remained relatively constant throughout the experiment. The reason for the decrease (Fig. 12.13) in specific activities of both water and algae after equilibrium had been reached is not known. After calculating a material budget, only 33% of the ^{32}P added to the system at the beginning of the experiment was accounted for in removal plus residual in the system at the time the experiment was terminated. The ^{32}P unaccounted for was possibly adsorbed to the surface of the plexiglas tray.

A series of ten random longitudinal bottom samples of stream fauna were collected at approximately monthly intervals from the west fork beginning in December 1968. A cylinder (Fig. 12.14) enclosing an area of 0.1 m^2 was used in the riffle and pool areas, where the substrate was deep enough to press the edge of the cylinder into the stream bottom. A standard Surber sampler was used in shallow areas and on bare bedrock. Mesh opening of netting on both samplers was

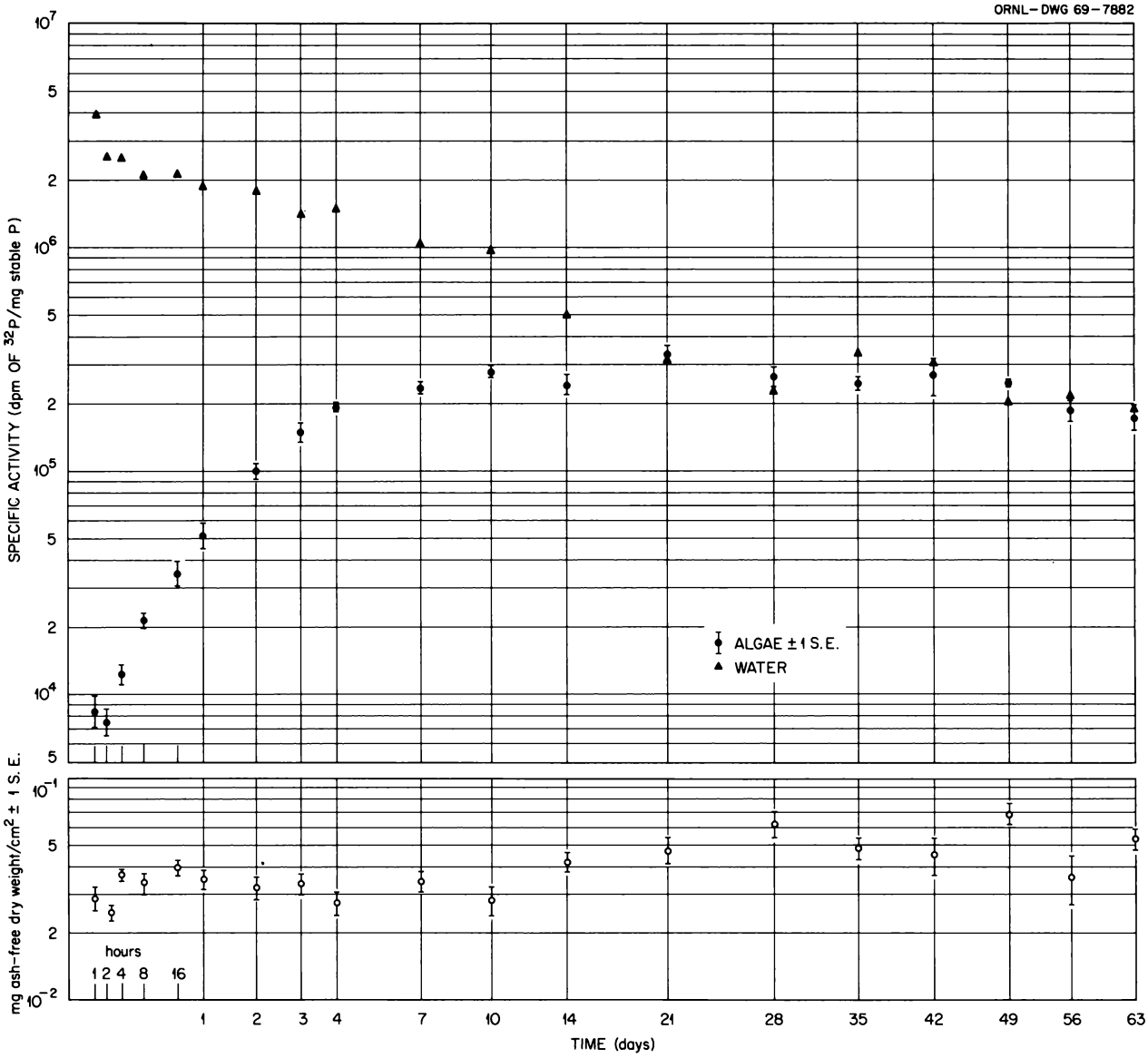

Fig. 12.13. Specific Activities of Phosphorus in Stream Algae (Predominantly Diatoms), Water, and Biomass per Square Centimeter of Algae Measured for 63 Days After Spiking the Closed System with $^{32}PO_4$.

253 μ. Organisms were identified, counted, measured, and weighed. The detritus in each sample was dried, weighed, and ashed. Because of the extreme variation in habitats in the stream, there was variation between bottom samples. Standing crops of macroinvertebrates were minimal in the areas of exposed bedrock and were at a maximum in the pool areas, which had heavy accumulations of organic detritus. The maximum standing crop (numbers) recorded was 8100/m^2. Certain species were collected only from selected habitat types. The stone fly, *Peltoperla* sp., for example, was found only in samples from riffles with a rubble substrate that was relatively free of silt, sand, and fine organic detritus. This species apparently emerges in winter and oviposits in the stream shortly thereafter. The eggs probably hatch in March and April, based on the size of organisms collected in the April bottom samples (Fig. 12.15).

The snail, *Goniobasis clavaeformis*, was one of the most abundant and ubiquitous species present in the west fork. Snails less than 1 mm in shell width were collected in November 1968. These small individuals

Fig. 12.14. Bottom Sampler Used in Sampling Benthic Macroinvertebrates in Walker Branch Watershed Streams. Sampling area of the cylinder is 0.10 m^2.

had recently hatched, because their shells had not yet calcified. Again in April 1969 small individuals that had recently hatched were collected (Fig. 12.16). Two generations per year have not been reported previously for this species. There appeared to be at least three generations of *Goniobasis* in the stream in April. Maximum standing crops of snails were found in the areas of exposed bedrock, where they could graze on the periphyton and detritus. Over 1400 snails/m^2 were found in some areas with exposed bedrock. Riffle areas had the lowest standing crops of snails, ranging from about 10 to 120 per square meter. Quantitative sampling of snails in the riffle areas using the cylindrical sampler was difficult because the organisms would sink to the bottom before the current carried them into the collecting net. A Surber sampler was more efficient in sampling snails.

Drift samples were also collected at four locations in the west fork. Drift nets (253 μ mesh opening) were placed across the stream to filter the entire stream discharge during a 24-hr period. One of the most abundant organisms occurring in the drift samples was a small Baetid mayfly. Drift rates as high as 248 organisms per 24-hr period (excluding the snails) were recorded during conditions of normal discharge. Drift rates were generally higher at the upstream stations, where the habitat was predominantly riffles as compared with the pools, falls, and exposed bedrock characteristic of the downstream sections.

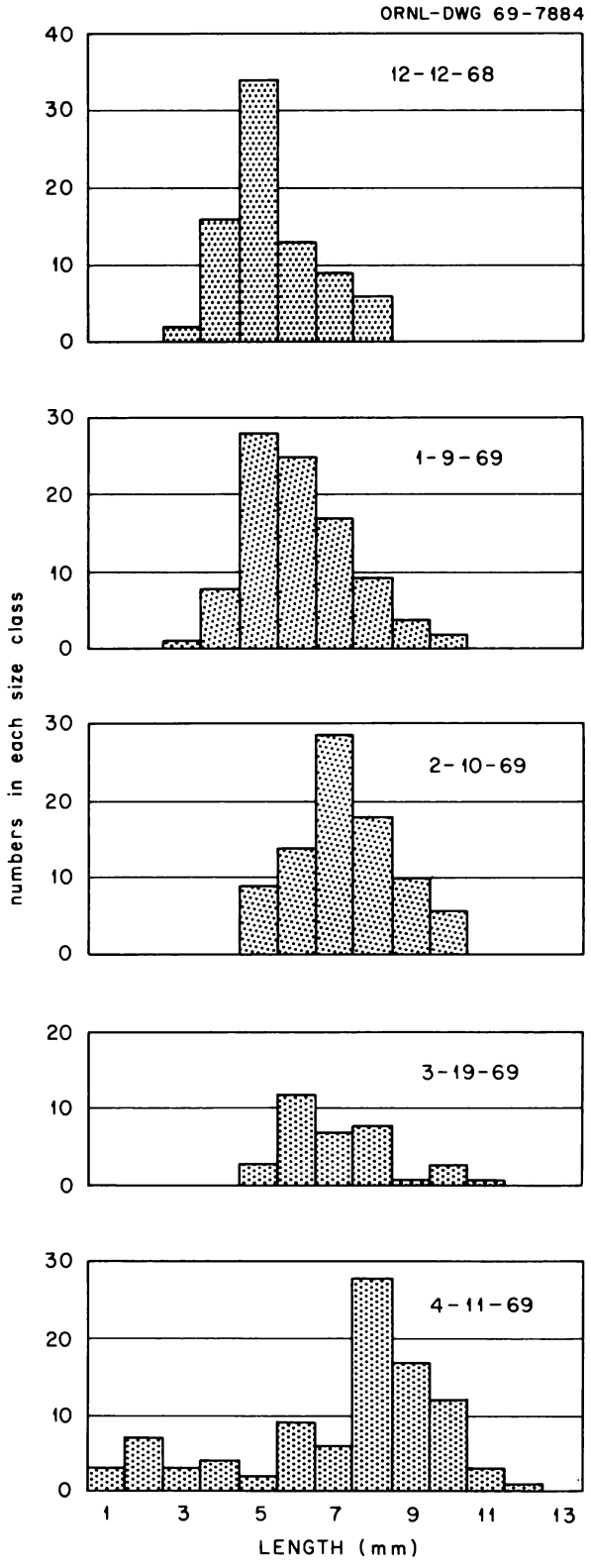

Fig. 12.15. Length-Frequency Distributions of the Stonefly *Peltoperla* sp. in Bottom Samples Collected at Monthly Intervals from the West Fork of Walker Branch Watershed. Numbers are for all bottom samples combined in each month.

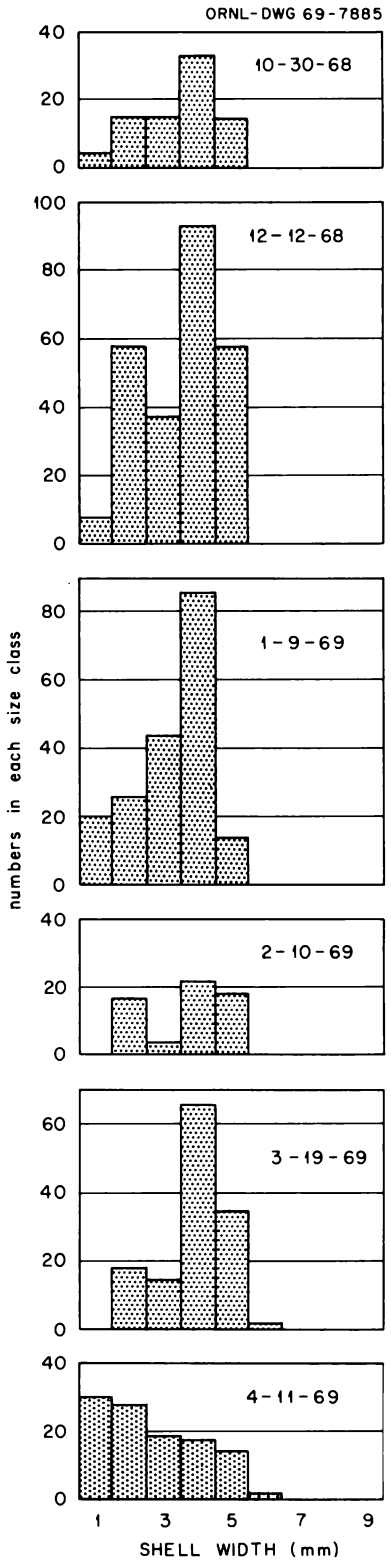

Fig. 12.16. Size (Shell Width)–Frequency Distributions of the Snail *Goniobasis clavaeformis* in Bottom Samples Collected at Monthly Intervals from the West Fork of Walker Branch Watershed. Numbers are for all bottom samples combined in each month.

13. Systems Ecology

G. Baskerville[1]
F. C. Dean[2]
L. J. Bledsoe[3]
N. B. Gove[4]
S. V. Kaye[5]
J. S. Olson[5]
R. V. O'Neill[5]
Nancy F. Sollins[6]
P. Sollins[7]
R. B. Williams[8]

The overall purpose of the ORNL ecological systems analysis program is to provide a practical methodology that ecologists can use to make useful predictions about the outcome of environmental interactions, both empirical and theoretical. Progress has been made in evaluating the pertinence of recent ecological literature to the modeling of ecosystems, a biogeochemical ecology information center was established, and several systems analysis computer programs were written and tested on various ecological problems.

PERTINENCE OF RECENT ECOLOGICAL LITERATURE TO THE MODELING OF ECOSYSTEMS

R. B. Williams J. S. Olson

One of the goals of the Ford Foundation study on the application of compartment models to ecological problems is an attempt to answer the question: "Are the parameters being measured the pertinent ones in terms of at least first-order effects of transfer rates on the stability of an ecosystem?" The question was approached in several ways, including a review of the fraction of recent publications containing information for constructing or testing compartmental models of ecosystems and how this research was distributed in terms of language of publication.

Constructing a compartmental model requires data on the ecosystem's nutritional network. This information permits dividing the groups of taxa into functionally similar organisms. (These groups might be called "pools" rather than compartments, since the materials in their parts may not be "well mixed.") Transfer coefficients – constants or functions defining the flows between compartments – in their simplest form (i.e., for linear differential or difference equations) are fractions of a donor compartment transferred to another compartment per unit time. Since it is usually impractical to measure a transfer coefficient directly, one approach to estimating it is a measurement of (1) the flow regulated by the transfer function, (2) the state variable or standing crop of one (preferably both) of the compartments which the flow joins, and (3) other state variables and inputs or controlling factors which might modify the flows.

The survey of *Biological Abstracts* for almost four years led to the examination of approximately 10,000 titles and abstracts relating to aquatic ecology. The 8918 abstracts in the Oceanography, Limnology, and Aquatic Wildlife Management sections yielded most of the aquatic studies relevant to compartmental modeling. Six hundred and sixty-four studies (including groups of consecutive abstracts by the same authors and on the same subject) were selected as relevant. Others would have been recognized if abstracts were better or if relevant studies published at other times and places could have filled the gaps. Nearly three-fifths of the aquatic studies were in English, and most of the remainder in Russian. French and German, foreign languages commonly studied by American scientists,

[1] Foreign visitor from Canada, Department of Fisheries and Forestry.

[2] NSF visiting investigator from University of Alaska.

[3] Colorado State University.

[4] Mathematics Division.

[5] Dual capacity.

[6] Consultant.

[7] NSF Advanced Science Seminar Project Participant.

[8] Radiobiological Laboratory, Bureau of Commercial Fisheries.

together comprised only 3% of the studies. The remaining languages, Spanish, Italian, Polish, Japanese, Portuguese, and Slovakian, comprised another 3%.

Most of the aquatic research relevant to compartmental modeling consisted of detailed information on one or more compartments, but the majority was on phytoplankton. Nutrient studies were almost exclusively on dissolved nutrients and their relation to phytoplankton nutrition; there was minimal work on nutrients contained in sediment. Organic matter and pigment studies were done chiefly in areas where the bulk of the organic matter was, or at least was considered to be, derived from phytoplankton. Benthic plants received some attention, whereas marsh plants were ignored. The herbivore, decomposer, and carnivore compartments received successively less attention. Zooplankton, benthic animals, marine decomposers, and nonherbivorous fish were much studied, whereas herbivorous fish and freshwater decomposers and carnivores other than fish were largely neglected, as were physical factors affecting the compartments. Little of the research was directed clearly toward the analysis of ecosystems. In approximately four-fifths of the studies, only one compartment was examined, and less than 2% of the studies dealt with three or more compartments.

Over a third of the selected studies contained data on standing crop, and nearly two-thirds had some data on flow. The most frequently measured flow was "photosynthesis," but the precise meaning of this rate would not be the same in all cases. Except in *flowing fresh water* none of the other well-defined input or loss flows (ingestion, respiration, predation, reproduction, etc.) received half as many measurements. However, the flow subcategory "other" (i.e., processes not clearly associated with either input or loss) contained about as many studies as the subcategory "photosynthesis." Studies containing *both* standing crop and flow data comprised only 18% of the total. Only 12% of the 394 studies probably contained data for calculating one or more transfer rates; another 4% possibly contained such data. Most of these transfer rates concerned phytoplankton in terms of photosynthesis, respiration, dissolved nutrients, or organic detritus.

For terrestrial ecosystems many of the foregoing conclusions are also clear, but some differences will be noted, based partly on direct personal contacts or reprint exchange with groups known to be active in the field. Japanese work is relatively more prominent but is increasingly published in English. Work in crop and forest physiology or ecology as well as botany and zoology is developing rapidly, especially in the direction of "subsystem" models for primary productivity (neglecting animal reactions on this in almost all cases). Population models for animals have a large literature in both zoology and terrestrial wildlife management, but additional organized effort seems essential for tying predation models for *consumers* (herbivores, predators, or parasites) to the food base and environmental variables on which they depend. Models involving *decomposers* explicitly are fewer and are understandably tied to laboratory experiments or to microcosms which ideally could provide a "bridge" toward field application of indoor research. Many "energy budget" studies concern the large *abiotic* terms of thermal energy, radiant energy, and water budget on a mathematical basis, but give little attention to the small percentage of solar energy converted to biologically available free energy by photosynthesis and the cycling of nutrient elements.

A symposium held in Gatlinburg, Tennessee,[9] was organized by ORNL to summarize currently available data in the foregoing specialized areas of ecology and approaches that can aid in linking them together.

BIOGEOCHEMICAL ECOLOGY RESEARCH COLLECTION

J. S. Olson Nancy Sollins
N. B. Gove

The newest of ORNL's 21 centers, or collections of specialized information, as of July 1968 has focused on biogeochemical cycles and the parameters of transfer of elements and isotopes through ecosystems. Computerized bibliographic work has been started as a routine aid to compilation of file information, annotations in addition to the basic reference data (for 90% of the references or projects). The prime goal has been toward a system of programs which would retrieve whole tables of desired information. Retrieval can currently be made on the basis of any word, code, or table heading in the total citation. Eventually selected data (such as elements, isotopes, coefficients or functions of transfer, or environmental factors modifying such coefficients) can be restructured into new tables by specialized or general-purpose programs. A general-purpose program already initiated for the Nuclear Data Information Center has been adapted for more versatile use of the 120-character print chain of the ORGDP

[9] D. E. Reichle, ed., *Analysis of an Ecosystem: The Temperate Forest*, Springer Verlag, Heidelberg, in press.

Computing Technology Center. These and other developments are aimed toward aiding and economizing on the senior scientific staff effort in the selection and input of retrievable data that are relevant for models and predictions of biogeochemical changes. Alternative forms of retrieval and output form are aimed toward selective dissemination of information when there is funding for service activities.

PARAMETER IDENTIFICATION IN SYSTEMS ECOLOGY

R. V. O'Neill

Parameter identification refers to techniques which utilize information on the time behavior of a system to obtain "best-fit" estimates for parameters. The parameters represent coefficients in a mathematical model of the system. This is a type of curve-fitting problem, and the solution is approached by an iterative method which attempts to choose new values of the coefficients which will minimize the error between model predictions and data on the system. The procedure is continued until further convergence becomes insignificant.

Preliminary investigations have been completed on the application of these methods to ecological systems[10,11] in order to supplement analog computer techniques that have been used in previous research.[12] Among the methods presently under investigation are hybrid computer techniques, random search, quasilinearization, and steepest descent. These methods represent varying degrees of sophistication, and they are being investigated to identify the contexts in which they would be appropriate. Each step of the procedure is being investigated to determine the appropriate error function, minimization routine, and method for evaluating the model. New methods are being introduced to constrain the parameter values within known bounds and to take advantage of information on the probability distribution about initial estimates.

It is hoped that these studies will lead to the establishment of criteria that would permit an investigator to choose the method which is most appropriate to his problem and to the computer facilities he might have at his disposal.

NUMERICAL METHODS IN SYSTEMS ECOLOGY

R. V. O'Neill

Compartment models of ecosystems are frequently presented as systems of differential equations. In simplest terms, a vector equation can be written as

$$\dot{x} = Ax ,$$

where x is a vector of state variables and A is a matrix of transfer coefficients. If the elements of A are constants, analytical solutions exist in the form of series of exponential functions. The parameters of the series are then eigenvalues and eigenvectors of the original matrices. In the more general case, the system equations will involve forcing functions, time delays, variable coefficients, and nonlinear terms. Since analytical solutions do not exist ordinarily for such equations, numerical methods have frequently been employed.

Investigations are being made on a number of existing numerical solution methods which involve multistep formulas or predictor-corrector combinations. The purpose of these studies is to evaluate the various techniques in the light of particular equation systems useful in ecology. Although useful methods exist, it is possible that their lack of efficiency will be prohibitive with large systems evaluated over long periods of time.

An attempt is being made to solve system equations of varying complexity and to establish criteria which would allow the investigator to select the most efficient method for his problem. In addition, it appears feasible to derive new solution formulas that would be most appropriate to particular classes of models.

CSS: A VERSATILE COMPARTMENT SYSTEM SIMULATION PROGRAM

Phillip Sollins J. S. Olson

While previous programs (COMSYS1: A Stepwise Compartmental Simulation Program, ORNL-TM-2413) permit a variety of nonlinear or stochastic functions in ecological models, each of these requires writing one or more subroutines to modify the model from a set of

---

[10] L. J. Bledsoe and G. M. Van Dyne, *Evaluation of a Digital Computer Method for Analysis of Compartmental Models of Ecological Systems*, ORNL-TM-2414 (1969).

[11] M. R. Buckner, *A Study of the Application of System Identification Techniques in the Analysis of Nuclear Reactor Dynamics*, NEUT-3028-2, Nuclear Engineering Department, University of Tennessee (1968).

[12] B. C. Patten and M. Witkamp, "Systems Analysis of Cesium-134 Kinetics in Terrestrial Microcosms," *Ecology* 48, 813–25 (1967).

linear equations with constant coefficients. The program series CSS was developed to provide for commonly used functions within the program.

As of early 1969 the input functions can be constant or periodic, with adjustable phasing and truncation (clipping) of sinusoidal functions. Flows can be proportional to such functions, to any compartment within the system, to the product of any pair of compartment values, to the product (input function X compartment value), or to another flow rate. Logistic flow is provided through a function of the form (flow = $C_1 Q_i + C_2 Q_j^2$). Michaelis-Menton flow,

$$\text{flow} = C_1 Q_i Q_j / C_2 + Q_i ,$$

allows dependence on one compartment Q_j when another compartment Q_i is large, but on the product of both when Q_i is small.

Applications to a number of recently published models have been made for check-out of technique as well as preliminary attempts to apply the program to a carbon cycle in a boreal New Brunswick forest. Based on accumulating experience a new program is under development that will allow free-format input as well as the flexibility of conventional languages such as FORTRAN in constructing functions and flow equations.

A STOCHASTIC MODEL OF FEEDING IN A FOREST CENTIPEDE

R. V. O'Neill

A Monte Carlo simulation model has been devised to estimate the energy budget of a centipede, *Otocryptops sexspinosus* (Say.). Energy parameters, such as respiration, assimilation, and caloric equivalents, were measured in the laboratory, and observations were made on various aspects of feeding behavior. These data were used to develop a model which can operate with probability distributions as input. The model takes the caloric pool of a randomly chosen individual and allows it to decrease by respiration until a hunger threshold is reached. At this point, behavior parameters, described by probability distributions, are used to decide which of eight potential prey species will be consumed and the hour of consumption. This is accomplished by comparing a computer-generated random variable to a known probability distribution. The assimilated portion of the selected prey is added to the predator compartment, and respiration continues. The process is continued for a simulated period of one month and repeated for a large number of individual predators. Prediction of energy flow is then based on the average behavior shown by the model.

A total of five random variables were used to simulate the feeding behavior of the centipedes (Fig. 13.1).

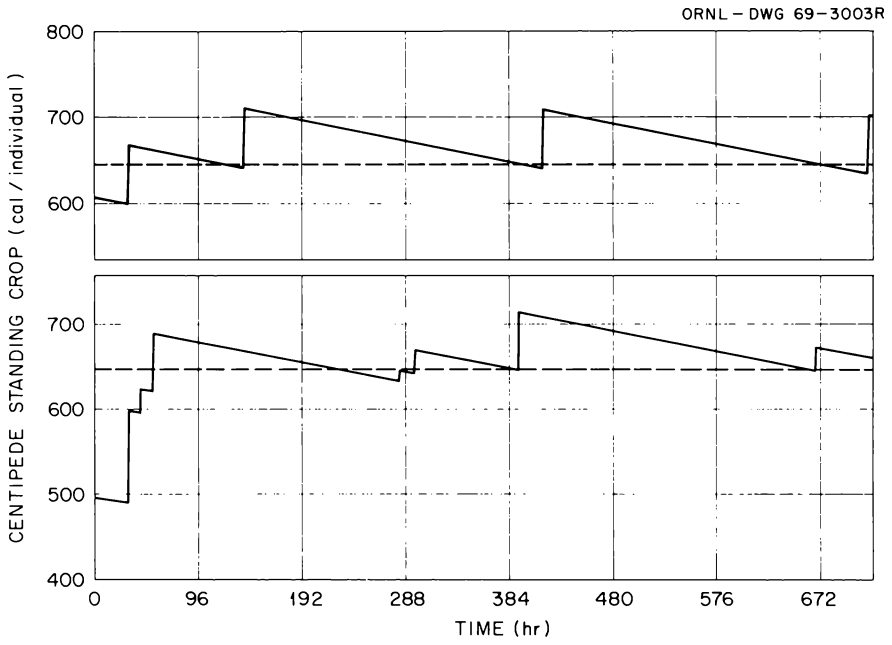

Fig. 13.1. Simulated Energy Content of Two Individual Centipedes. Dashed line indicates hunger threshold (decreases are due to respiration losses and increases to feeding).

Comparison of the two simulation runs shows the effect of initial conditions and size of the prey on the number of individuals consumed during the month. If small prey are encountered and eaten, as in the lower graph, a larger number of individuals must be captured so that the predator can maintain itself above the hunger threshold. Comparison of simulations with the observed feeding of centipede cultures in the laboratory verified the predictive ability of the model. A complete energy budget can be generated by the model (Table 13.1). Along with predictions of expected mean values, it is possible to calculate the expected variability. The standard errors in the table permit an evaluation of the confidence to be placed in each parameter. Additional simulation work has shown that the effects of individual random variables can be investigated by setting them equal to their expected values. In this way the contribution of variance in the input variables to variance in the calculated values can be investigated. A form of sensitivity analysis has been used to assess the effect of changing the values for various system parameters. This permits the investigator to gain insight into the nature of the system he is studying.

The results of this study indicate that energy budgets can be estimated without time-consuming direct measurements of feeding rates. The investigator can utilize his knowledge of predator feeding behavior to arrive at first-order predictions of energy budgets. It is hoped that this approach will be useful in large-scale ecosystem studies where limitations of budget and time make it imperative to arrive at such approximations by an efficient method.

Table 13.1. Predicted Energy Budget for *O. sexspinosus* During May

Values for energy fluxes are in calories individual^{-1} month^{-1}; numbers in parentheses are standard errors, $n = 60$

Initial centipede caloric pool	628.8(46.9)
Final centipede caloric pool	797.7(64.0)
Energy ingested	398.2(100.2)
Energy excreted	20.7(5.2)
Energy assimilated	377.5(95.0)
Energy respired	208.6(13.0)
Energy for reproduction	168.9(87.0)

A MODEL FOR CEDAR BOG LAKE, MINNESOTA

R. B. Williams

The classic data and ideas of Raymond Lindeman[13,14] concerning energy flow and trophic level efficiencies in the ecosystem in Cedar Bog Lake, Minnesota, were fitted into a ten-compartment nonlinear model (Fig. 13.2). Publications by Lindeman and others on Cedar Bog Lake provided only about half the information needed for the model. The remaining information had to be generated by first assuming reasonable but unproven functional relationships among the components of the system and then adjusting details of the functions and coefficients until the behavior of the model approximated that recorded by Lindeman for the natural system's changes through time.

The resulting model may thus have little similarity to the real Cedar Bog Lake ecosystem. Many coefficient estimates are interdependent and could be improved if an attempt were made to gather all the data needed to depict and understand those aspects of an ecosystem which concern flows. But model preparation provided insight into a class of natural systems of shallow waters. This test and the model[15] of the emergent aquatic *Juncus roemerianus* illustrate uses of compartmental modeling as a device for evaluating data. Both studies complement the preliminary trial, by Gore and Olson,[16] for modeling a blanket bog and valley bog as distinct from a bog lake or marsh.

For educational value the model was constructed in a stepwise fashion. First a simple linear model was constructed in which all flows were functions only of the *donor* compartment. This type of model is a mathematically convenient abstraction but is ecologically unsound. It implies that population size (or properties) cannot in any way influence the amount of food available to them. Considering behavior and shortcomings of the linear model, a simple nonlinear model was constructed in which many of the transfers of energy were a function of both food and predator. This model displayed some suggestion of the behavior observed in the natural system but was far more unstable. Finally, stability and the desired behavior were achieved by controlling many of the transfers of

[13] Raymond Lindeman, *Am. Midland Naturalist* 26, 636–73 (1941).

[14] Raymond Lindeman, *Ecology* 23, 399–417 (1942).

[15] S. I. Auerbach *et al. Health Phys. Div. Ann. Progr. Rept. July 31, 1968*, ORNL-4316, pp. 143–45.

[16] A. J. P. Gore and J. S. Olson, "Preliminary Models for Accumulation of Organic Matter in an Eriophorum/Calluna Ecosystem," *Aquilo, Ser. Botanica* 6, 297–313 (1968).

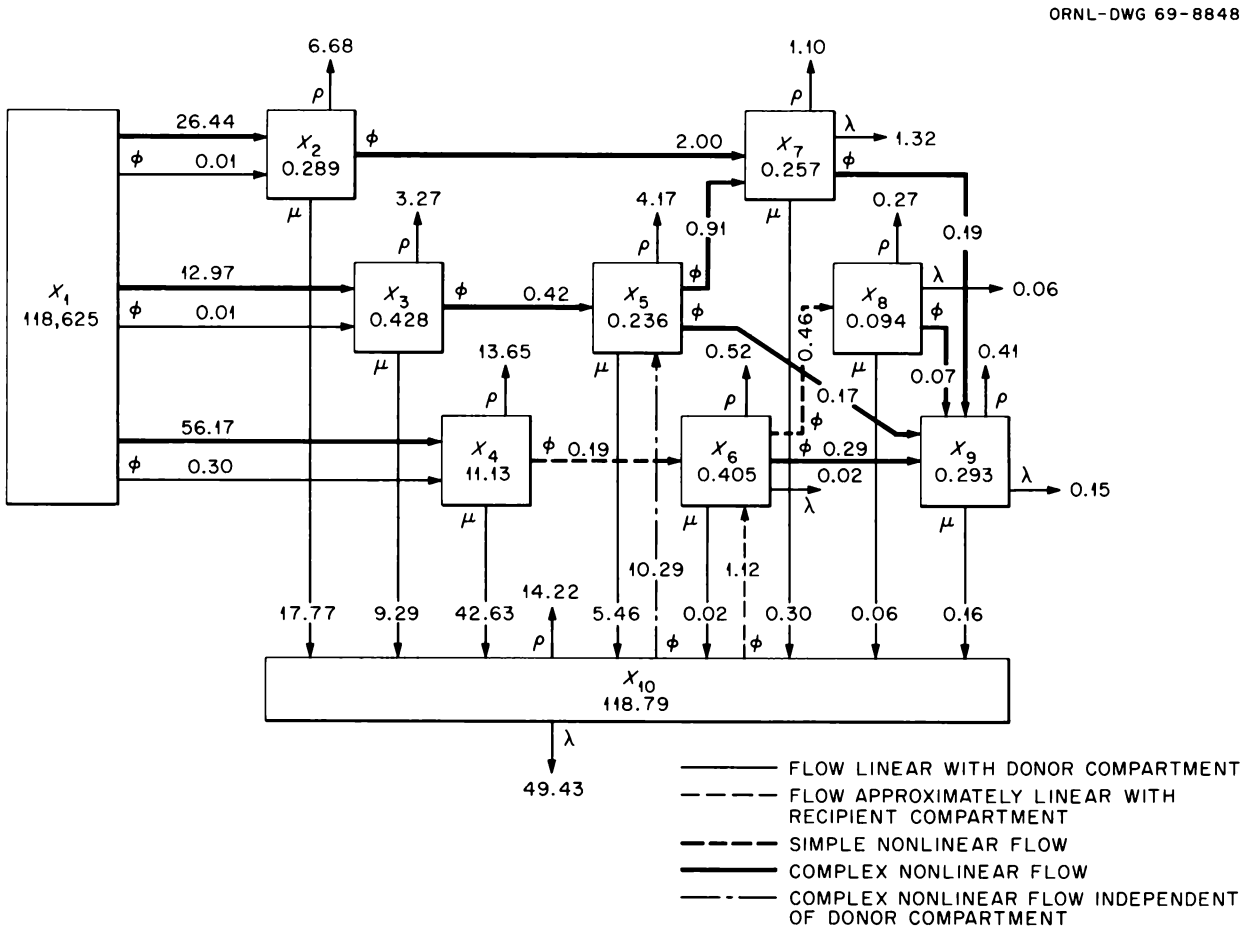

Fig. 13.2. Final Nonlinear Model of Energy Flow in the Cedar Bog Lake Ecosystem. The values near the arrows and the value in compartment 1 (solar input) are flows (cal cm^{-2} $year^{-1}$). Values in the other compartments are average standing crops (cal/cm^2), and their fluctuations are shown in Fig. 13.3.

energy with functions containing terms for cyclic behavior and mutual inhibition (Fig. 13.3). This confirms that the ecosystem was not only an interconnected system rather than an agglomeration; its parts could not be understood except with reference to various kinds of interdependence throughout the whole.

The careful study of Lindeman's data and methods which the modeling required made obvious not only gaps in information but also inconsistencies in the data and in the logic of its previous treatment. Much of Lindeman's picture of energy flow in Cedar Bog Lake may be correct, but its correctness is not completely supported with his own evidence. His widely quoted generalization that the productivity of a body of water is lowest during senescence was derived from an unsupported assumption that phytoplankton had a turnover time of one week during May through September and of two weeks during the remainder of the year. Recent work[17] suggests an average turnover time of one day for lake phytoplankton; such a turnover time in Cedar Bog Lake would destroy Lindeman's argument for low productivity during senescence. The inconsistencies in the data are cases in which a published total is unequal to the sum of its parts. The inconsistencies in logic relate to ascribing multiple sources or destinations to individual flows and in part have been discussed previously.[18] A fuller treatment[19] is based on work supported by the Ford Foundation study in systems ecology.

[17] J. Kristiansen and H. Mathiesen, *Oikos* 15, 1–43 (1964).

[18] Slobodkin, *Advan. Ecol. Res.* 1, 69–191 (1962).

[19] R. B. Williams, *Ecological Systems Research*, B. C. Patten, ed., Academic, in press.

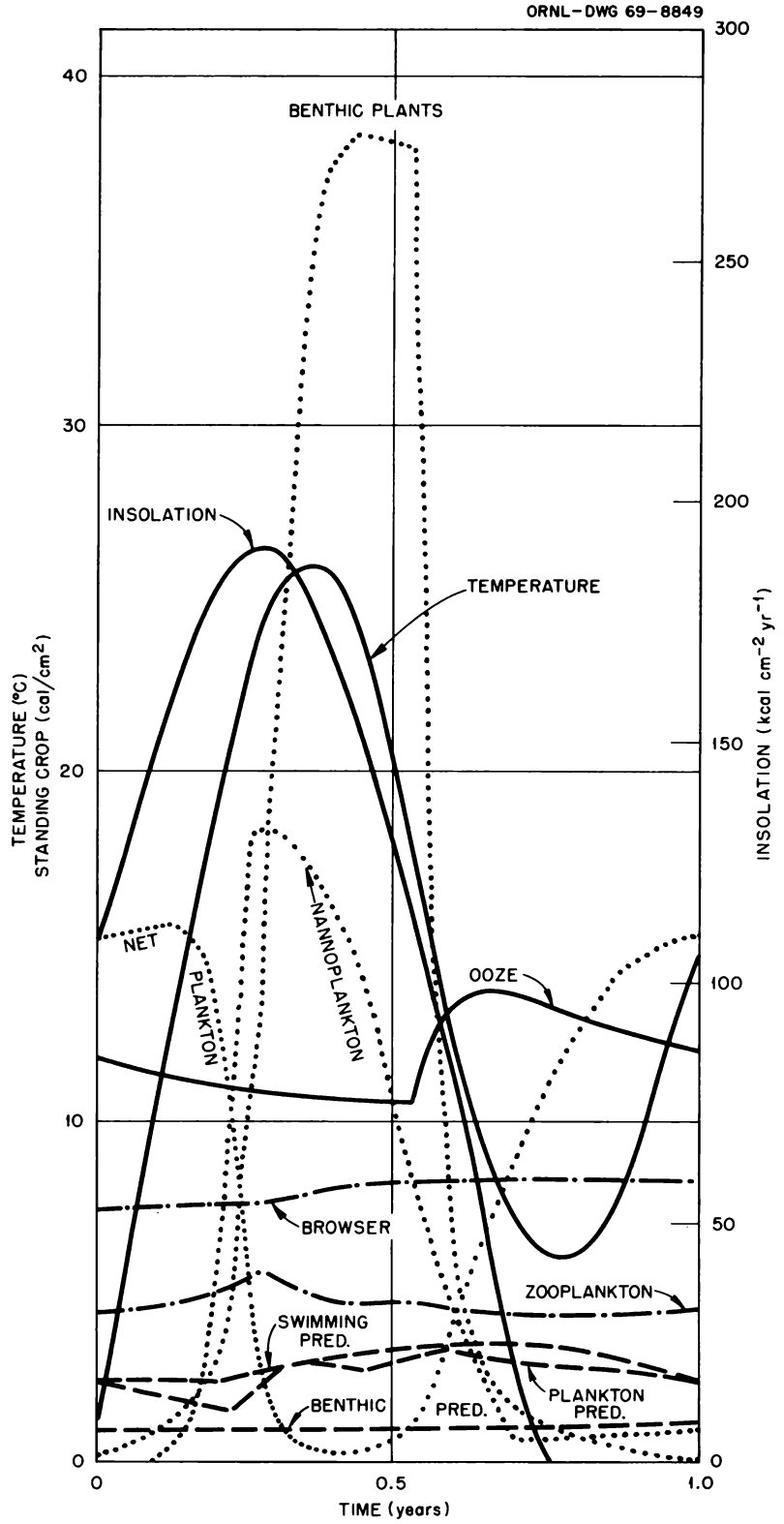

Fig. 13.3. Behavior of the Final Nonlinear Model for Energy Flow in the Cedar Bog Lake Ecosystem. The year starts at the vernal equinox. Values on the ordinate for the ooze are multiplied by 0.1; for insolation, temperature, and benthic plants by 1.0; for the predator compartments by 10.0; and for the remaining compartments by 20.0.

ANALYSIS OF THE CHANGE-IN-RATIO MODEL FOR ESTIMATING POPULATION ABUNDANCE

F. C. Dean

In order to investigate the role of secondary producers in ecosystems, estimates of animal populations are required. One method commonly used by fisheries and wildlife biologists has come to be known as the "change in composition" method. Data gained by this method have been used often enough in the past to make it highly probable that the method would be used as the source of input data for systems models. Since a model is limited by the quality of its input and some questions as to the reliability of the "change of composition" method had arisen, an examination was made of the results of the method when its own input was subjected to error. A FORTRAN program was written that calculated the true and erroneous population values for a wide range of conditions. The equation used as a basis for this study was the general form stated by Rupp[20] as

$$N = \frac{M - p_2 M}{p_2 - p_1},$$

where

N = size of preremoval population,

M = number of animals (of one type) in the removal,

p_1 = preremoval proportion of the total population that is in the subset subjected to removal,

p_2 = postremoval equivalent of p_1.

Varying amounts and signs of absolute error were applied to p_1 and p_2, both separately and in combination. The results were plotted, allowing easy comparison of the effects of the introduced error. The conclusion of this study was clear; the change of composition method is so sensitive to error that it should not be used. There are certain conditions under which it may yield valid results, but these are encountered infrequently and almost require that more be known of the population under study than one is trying to determine. The worst errors in the final population value tend to be associated with the most likely range of error in the required input (Fig. 13.4). The upper

[20] Robert S. Rupp, "Generalized Equation for the Ratio Method of Estimating Population Abundance," *J. Wildlife Management* **30**, 523–26 (1966), Eq. 2.

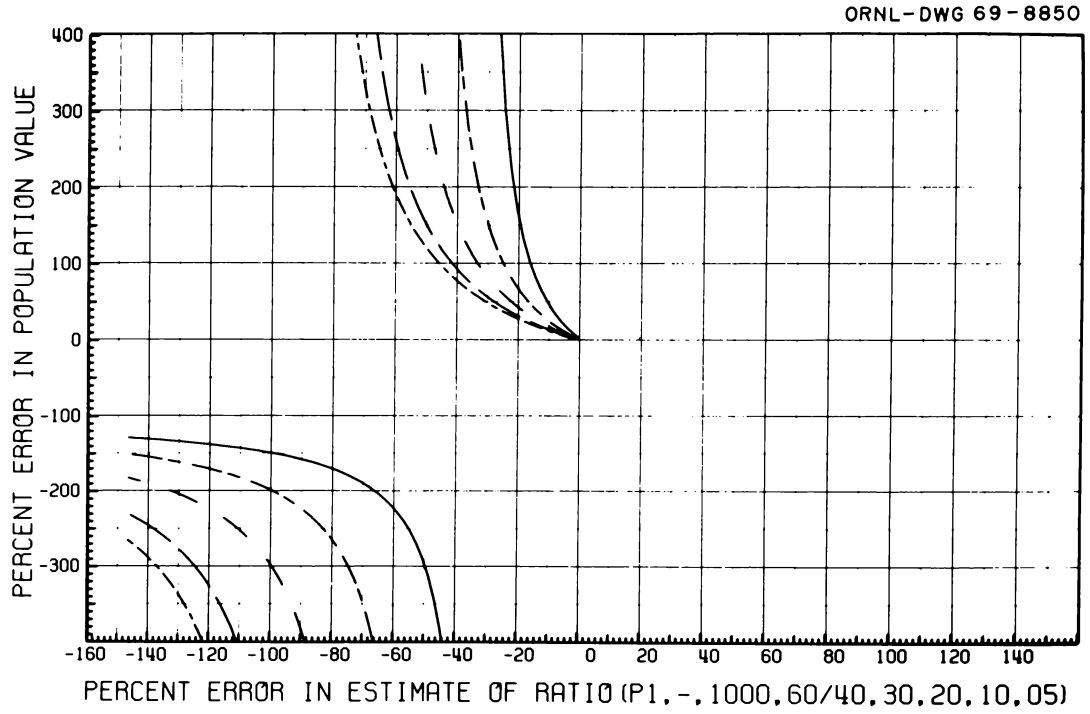

Fig. 13.4. Errors of the Type Associated with Preremoval Population Values Computed by the Change in Composition Method. In each case negative error was applied to P_1, a removal of 1000 males was made, and the shift in the proportion of males was from 0.60 to 0.40, 0.30, 0.20, 0.10, 0.05, respectively, for each of the curves as one moves across the graph from right to left.

and lower groups of lines in Fig. 13.4 are sets of pairs; the error in the population estimate reversed sign and returned from infinity to an asymptote. (Just after a final draft of a paper on this analysis had been completed, the writer learned of Paulik and Robson's 1969 paper on the same subject.[21] Their conclusions generally confirm my own, but some inconsistencies must be resolved before further progress can be made toward publication of my results.)

The results of these analyses of the change in composition method clearly indicate the need for reexamination of some long-standing methods as well as the need for increased use of proven and calibrated population estimation techniques. Modeling of secondary production in terrestrial wildland situations, which accounts for wide dispersal, extensive migrations, etc., will certainly involve enough unknowns and enough complex and eventually stochastic relationships so that accurate population abundance data are mandatory.

SYSTEMS ANALYSIS OF BALSAM FIR FORESTS

G. Baskerville

A considerable body of data has been amassed pertaining to the standing biomass and productivity of balsam fir in the Canadian forests of northern New Brunswick. These data complement, in some respects, the extensive information on the activity of the spruce budworm in these forests. In the past year, considerable effort has been devoted to the organization of these data sets. This effort has proceeded along two lines. First, a rationale has been prepared for the systematic examination of the many allometric relationships used to obtain the biomass and productivity estimates. This procedure provides for testing of the uniformity of variance, the systematic selection of appropriate transforms when the variance is not uniform, and the calculation of unbiased estimates in the original (untransformed) units. The use of such a rationale will ensure that the appropriate regression model is chosen for each allometric relationship.

The second approach to the organization of the data has been through examination of a number of compartment models, the simplest of which is shown in Fig. 13.5. Growth of the fir forest over time periods of 40 to 90 years (usual life cycle) has been simulated using this model and the CSS3 computer code. Data were available on standing crop in each compartment for several ages, and in a few instances there was some direct knowledge of the flows between compartments.

[21] G. J. Paulik and D. S. Robson, *J. Wildlife Management* 33, 1–27 (1969).

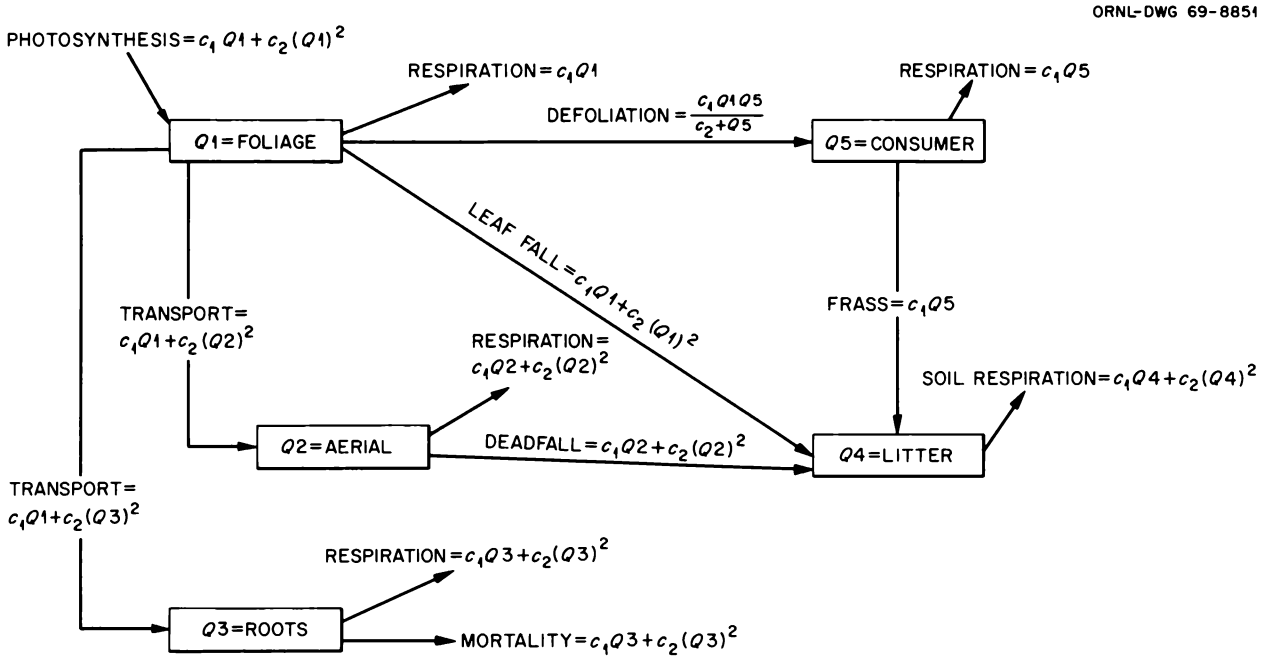

Fig. 13.5. Compartment Model for a Balsam Fir Forest Showing the Form of the Transfer Expressions. The principal consumer is the spruce budworm. The parameters C_i vary, depending on the growth period simulated.

This information has been used to calculate the parameters so that the simulator stays "in bounds" throughout a growth period. The parameters thus depend on the growth period and starting point (initial conditions), but the form of the transfer expression is essentially the same for each period. These forms were chosen presumptively, based on the literature and knowledge of the behavior of the forest in nature.

The model has been run for a number of growth periods with various initial conditions and yielded compartment values that are of realistic magnitude and form (through time). This model, and several other more complex ones developed from it, are being used as guides to the further study of the forest-budworm complex both with respect to data acquisition and analysis.

Part III. Radiation Physics

R. D. Birkhoff R. H. Ritchie

14. Theoretical Radiation Physics

Jacob Neufeld
R. H. Ritchie

V. E. Anderson[1]
J. C. Ashley
W. Brandt[2]
Julian Crowell[2]
Kenneth Fox[2]
W. R. Garrett
J. H. Grossen[3]
R. N. Hamm
Betty McGill
H. C. Schweinler
W. S. Snyder
J. E. Turner
R. B. Vora[4]
H. A. Wright

HIGH-ENERGY DOSIMETRY

A report of the task group on high-energy radiation has been prepared for Committee III of the International Commission on Radiological Protection (ICRP).[5] This report, covering the energy range from 400 Mev to 2 Gev, has utilized the calculations reported in the 1968 annual report[6] to estimate the fluence rate (flux density) of neutrons and protons that deliver dose equivalent at the rate of 2.5 millirems/hr as a function of energy (Fig. 14.1). The variation of quality factor $(QF)_L$ for normally and isotropically incident neutrons and protons has also been estimated (Fig. 14.2). This factor is defined as $(QF)_L = DE_{max}/D_m$, where DE_{max} is the maximum value of the dose equivalent and D_m is the absorbed dose per unit fluence at the position where DE_{max} occurs.

A review of high-energy dosimetry calculations and measurements with a view toward practical problems of radiation protection has been published.[7] This study finds that an estimate of dose equivalent of 2×10^{-7} rem/fluence will be conservative and will not overestimate DE by more than about a factor of 2, whether the particles are protons or neutrons and whatever their energies, within the range 400 to 2000 Mev. A discussion of how the calculated data on high-energy radiation might be used in estimating dose or dose equivalent for an actual or a supposed exposure situation is contained in this paper.[7]

[1] On loan from Computing Technology Center (ORGDP).

[2] Consultant.

[3] USAEC Health Physics Fellow.

[4] World Health Organization Fellow from Bhabha Atomic Research Centre, Bombay-74, India.

[5] Jacob Neufeld *et al.*, "Radiation Dose from Neutrons and Protons in the Energy Range from 400 MeV to 2 GeV," *Health Phys.* (in press).

[6] *Health Phys. Div. Ann. Progr. Rept. July 31, 1968,* ORNL-4316, pp. 162–63.

[7] W. S. Snyder *et al.*, *Nucl. Appl.* **6**, 336 (1969).

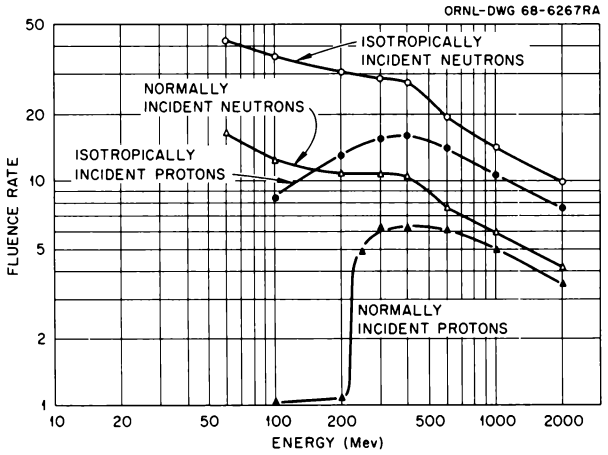

Fig. 14.1. Fluence Rate (Flux Density) of Neutrons and Protons (cm^2/sec) that Deliver a Dose Equivalent Rate of 2.5 millirems/hr as a Function of Energy.

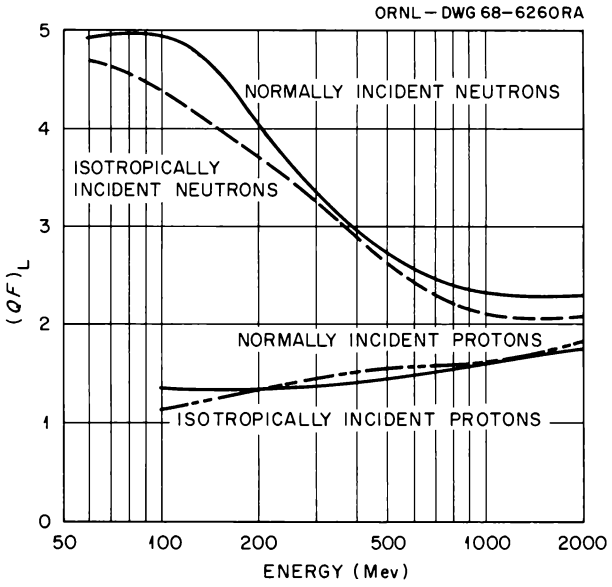

Fig. 14.2. Values of $(QF)_L$ for Normally and Isotropically Incident Neutrons and Protons of Various Energies.

A NEW MODEL FOR CALCULATING HIGH-ENERGY NUCLEON PENETRATION THROUGH MATTER

Calculation of the penetration and accompanying energy losses of a high-energy proton or neutron as it passes through matter is basic to the dosimetry of high-energy radiation and to the design of appropriate shielding. At present, dose calculations have been made for incident energies up to 400 Mev[8] and from 400 Mev to 2 Gev.[9] Both of these calculations used nuclear models that employed experimentally known free nucleon-nucleon differential scattering cross sections for the generation of a cascade when an incident nucleon strikes a nucleus. Such calculations are complicated greatly by the grouping and binding of the target nucleons in atomic nuclei. At energies of several Gev and greater, extensive studies of particle penetration based on detailed knowledge of the free nucleon-nucleon cross sections in calculating nuclear cascades have not been made and, indeed, may prove to be prohibitively difficult. As a practical matter the details of nuclear binding and nuclear structure would appear to be of secondary importance in some dose and shielding calculations, which determine quantities averaged over a large number and variety of nuclear collisions.

With these factors in mind, a program has been undertaken to calculate nuclear cascades as though the target nucleons were free and distributed uniformly at rest in the target. In principle, the new "free-nucleon" model, which also uses experimental differential scattering cross sections, can be used over the entire energy range (up to ~30 Gev) in which data exist. As an initial test of this model, it has been used to calculate, for 400-Mev protons incident normally on a 30-cm soft-tissue slab, the depth-dose curve and the number and energies of particles that leave the slab.[10] The results have been compared with those obtained with the detailed model used earlier. The same nucleon-nucleon cross sections as a function of energy were used with both models.

The circles in Fig. 14.3 show the dose values calculated by the free-nucleon model, and the triangles show those obtained by the detailed model, including nuclear evaporation. In both calculations 5000 incident protons were used. The agreement between the two calculated dose curves is good.

The two calculations give essentially the same total energy absorbed in the slab and a similar depth distribution. They also give about the same number of

[8] J. E. Turner *et al., Health Phys.* **10**, 783 (1964).

[9] H. A. Wright *et al., Health Phys.* **16**, 13 (1969).

[10] J. E. Turner, H. A. Wright, and J. H. Grossen, "A New Model for Calculation of High-Energy Nucleon Penetration Through Matter," *Health Phys.* (in press).

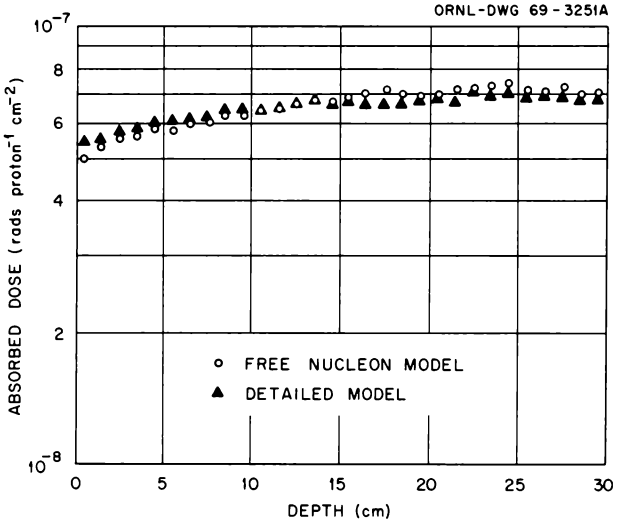

Fig. 14.3. Absorbed Dose as a Function of Depth from 400-Mev Protons Normally Incident on a 30-cm Thick Soft-Tissue Slab.

protons escaping the slab. In the free-nucleon model fewer primary particles escape the back of the slab without having had a nuclear collision, but more high-energy secondary nucleons escape. The agreement of the two models in this initial calculation indicates that details of nuclear binding and nuclear structure may indeed be of secondary importance in some dose and shielding calculations. Additional studies are needed to ascertain the range of conditions over which the free-nucleon model might be expected to give realistic results.

TRACK-LENGTH DISTRIBUTIONS IN CAVITIES

In order to obtain LET spectra from pulse-height measurements made with an energy-proportional device, as described in the following section, it is necessary to be able to calculate the track-length distribution in a cavity having the desired geometry. Analytical solutions have been obtained for spherical and infinite-slab geometries, but the cylinder is of greatest interest, since this is the usual shape of the sensitive volume of a proportional counter. We have performed a Monte Carlo calculation of the chord-length distributions in finite cylinders.[11] The results for

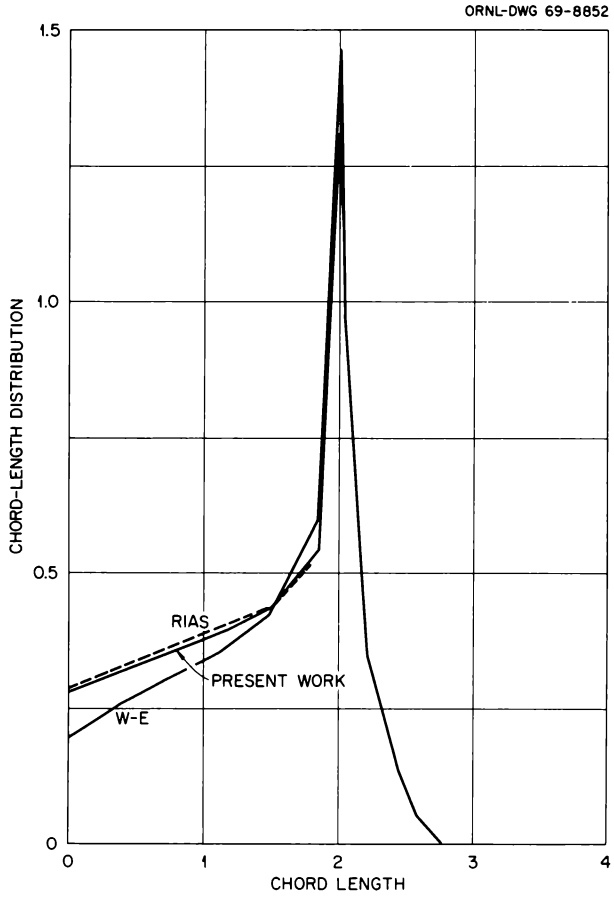

Fig. 14.4. Comparison of Chord-Length Distributions Obtained by Schwed and Ray (RIAS) and Wilson and Emery (W-E) with Present Work.

a cylinder of equal height and diameter are shown in Fig. 14.4. The present results are compared with the published results of Schwed and Ray[12] and of Wilson and Emery.[13] Our distribution is in substantial agreement with that obtained by Schwed and Ray, but differs significantly, for short chord-lengths, from that calculated by Wilson and Emery.

The Monte Carlo method employed here can be used to calculate track-length distributions in cavities of arbitrary shapes bombarded by particles having any

[11] R. D. Birkhoff *et al.*, "The Determination of LET Spectra from Energy Proportional Pulse-Height Measurements. I. Track-Length Distributions in Cavities," *Health Phys.* (in press).

[12] P. Schwed and W. A. Ray, *Distribution of Path Lengths in a Cylindrical Ionization Chamber for a Homogeneous Isotropic Flux*, Research Institute for Advanced Studies, Baltimore, Md., 1960.

[13] K. S. J. Wilson and E. W. Emery, p. 79 in *Proc. Symposium on Microdosimetry*, ed. by H. G. Ebert, European Communities, Brussels, 1968.

specified spatial distribution of track directions. The particle tracks need not span the cavity. The distributions are used, as shown in the following section, in the unfolding of LET spectra from pulse-height measurements.

A MONTE CARLO METHOD OF UNFOLDING LET SPECTRA FROM ENERGY-PROPORTIONAL PULSE-HEIGHT MEASUREMENTS

The problem of obtaining LET spectra from pulse-height measurements can be described simply. Given an observed spectrum $H(h)$ of pulse heights h from an energy-proportional device and the spectrum $P(x)$ of charged-particle track lengths x in the sensitive volume of the device, we wish to find the relative number $L(\epsilon)d\epsilon$ of particles that have an LET between ϵ and $\epsilon + d\epsilon$. Alternatively, we may wish to know the relative dose $D(\epsilon)d\epsilon$ delivered by particles having an LET in the range $d\epsilon$. We treat all of these distributions as normalized to unit area when integrated over the entire range of values of the argument. We also assume that a charged particle travels in a straight line through the sensitive volume, that the energy it loses in the volume is absorbed there, and that its LET ϵ remains constant over the track length x; so that the pulse height from a given particle is given by $h = \epsilon x$.

The problem of unfolding L from H and P is equivalent mathematically to solving a convolution integral equation. In Fig. 14.5 the contribution dH made to the pulse-height spectrum from an interval $d\epsilon$ of LET is given by

$$dH = P(x)\, L(\epsilon) d\epsilon\, 1/\epsilon\ . \tag{1}$$

The shape of dH is the same as that of the first factor $P(x)$, since with constant LET the pulse-height spectrum is proportional to the path-length spectrum. The relative contribution to the total pulse-height spectrum is proportional to $L(\epsilon)d\epsilon$, the relative number of particles in $d\epsilon$, which is the second factor in Eq. (1). Since $P(x)$ has the dimensions of inverse length and $L(\epsilon)d\epsilon$ is a pure number, we multiply the third factor $1/\epsilon$, having the dimensions of length/energy, thus giving dH the dimensions of inverse energy. Keeping $x = h/\epsilon$ and integrating Eq. (1) over LET, we obtain the pulse-height spectrum

$$H(h) = \int P(h/\epsilon)\, L(\epsilon)\, \frac{d\epsilon}{\epsilon}\ . \tag{2}$$

With the substitutions $\epsilon = e^u$ and $h = e^v$, we have $d\epsilon/\epsilon = du$ and $P(h/\epsilon) = P(e^{v-u})$. Therefore

$$H(e^v) = \int P(e^{v-u})\, L(e^u)\, du\ , \tag{3}$$

or

$$H^*(v) = \int P^*(v-u)\, L^*(u)\, du\ , \tag{4}$$

where the asterisks are used to denote the functions of the arguments rather than their exponentials. It follows that finding $L(\epsilon)$ from a knowledge of $H(h)$ and $P(x)$ is formally equivalent to solving a convolution integral equation.

Analytic solutions to the unfolding problem have been found only for the simplest cases in which the track-length distributions $P(x)$ are known analytically in the sensitive volume of counter – namely, for the sphere and for the infinite slab. A Monte Carlo method has been developed to handle the general case.[14] By using an iterative procedure for $L(\epsilon)$ that utilizes the

[14] J. E. Turner *et al.*, "The Determination of LET Spectra from Energy-Proportional Pulse-Height Measurements. II. A Monte Carlo Unfolding Procedure," *Health Phys.* (in press).

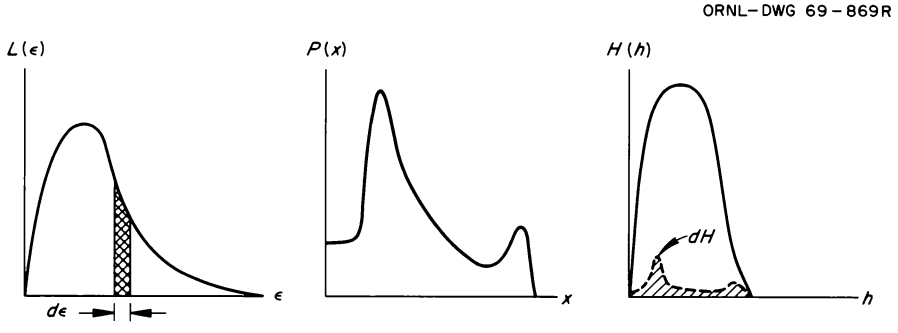

Fig. 14.5. Contribution of dH from Each Interval $d\epsilon$ of LET Spectrum Has the Shape of the Track-Length Distribution $P(x)$.

track-length distributions $P(x)$ described under the preceding heading, it has been found that the integral (4) can be solved for $L(\epsilon)$ in a wide variety of cases of practical interest. Figure 14.6, for example, shows a pulse-height spectrum calculated from a given, known LET spectrum of protons incident isotropically on a cylinder of equal height and diameter. Figure 14.7 shows the results of applying the unfolding procedure with two ways of starting the iterative process. The solid line shows the given distribution. The filled circles give the $L(\epsilon)$ found when it is assumed at the start that the LET spectrum is flat between 0 and 250 Mev/cm. The open circles result when it is assumed, initially, that the LET spectrum is that obtained from Fig. 14.6 by dividing $H(\epsilon x)$ at every point by ϵ.

The unfolding procedure requires 1 or 2 min on machines having a fast core capacity of the order of 100,000 32-bit words. It appears to work over a wide range of LET spectra.[14]

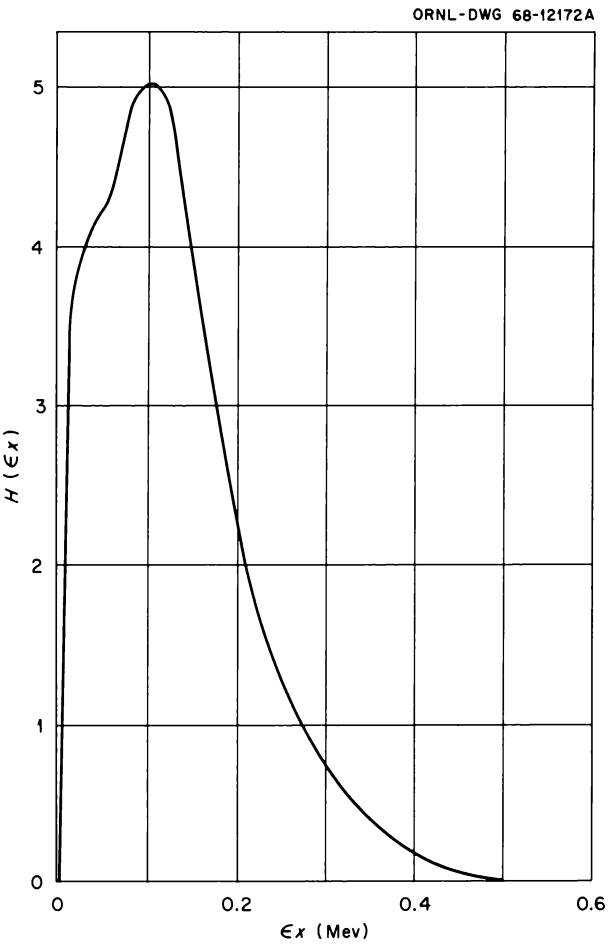

Fig. 14.6. Pulse-Height Spectrum from Cylindrical Cavity Traversed by Protons of Known Spectrum.

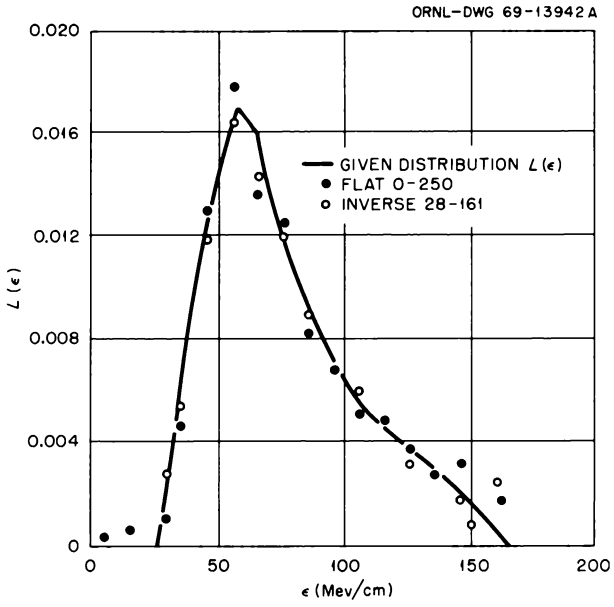

Fig. 14.7. Known Proton LET Spectrum (Solid Line) (Proton Energies 2 to 18 Mev). Unfolded spectra described in text (open and closed circles). The abscissa gives ϵ in units of Mev/cm in a material of unit density (10 Mev/cm = 1 kev/μ).

OPTICAL RADIATION FROM METAL SURFACES BOMBARDED BY GRAZING INCIDENCE FAST ELECTRONS

The first clear evidence that the tangential surface plasmon can undergo appreciable radiative decay was obtained by Boersch *et al.*[15] Using fast electrons incident at grazing angles on thick silver targets and measuring the dependence of the emitted photons on wavelength and condition of the surface, they concluded that these photons originated from the decay of surface plasmons. Jones *et al.*[16] repeated certain of these experiments with similar results.

A theory of this process has been constructed, based upon the notion that a tangential surface plasmon created by a fast electron may undergo radiative decay by colliding with irregularities at a metal surface and is a generalization of earlier work[17] based on a free-electron model for the metal.

It is found that the differential probability for emission of a photon per unit solid angle in a direction

[15] H. Boersch *et al.*, *Z. Physik* 187, 97 (1965).

[16] G. E. Jones, L. S. Cram, and E. T. Arakawa, *Phys. Rev.* 147, 515 (1966).

[17] R. H. Ritchie, *Phys. Letters* 27A, 660 (1968).

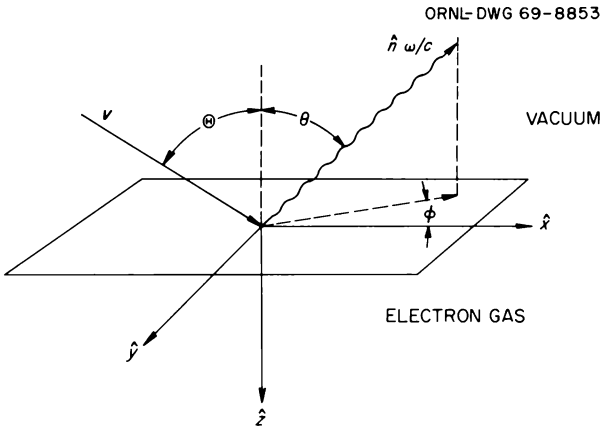

Fig. 14.8. Geometry of the BDFS Experiment. The velocity of the incident electron is v, and the propagation vector of the emitted photon is $\hat{n}\omega/c$, where $\hat{n}$ is a unit vector and ω is the angular frequency of the photon. The photon may be polarized either in the $\hat{n}$-$\hat{z}$ plane (p polarization) or perpendicular to the $\hat{n}$-$\hat{z}$ plane (s polarization). The region $z > 0$ is occupied by an electron gas, and the region $z < 0$ is a vacuum. The velocity v lies in the $\hat{x}$-$\hat{z}$ plane.

specified in Fig. 14.8 per unit frequency and for polarization perpendicular to the plane of emission (s polarization) is

$$\frac{d^2P^{(s)}}{d\Omega\, d\omega} = \frac{\alpha}{2\omega_s} \frac{\overline{\zeta^2} \cos^2\theta}{\lambda_s^2 \cos\Theta} \frac{\omega_s^2}{(\omega - \omega_s)^2 + (\gamma_s/2)^2}$$

$$\times \{\cos^2\phi\, C_i(\mu) + (\sin^2\phi - \cos^2\phi)\, D_i(\mu)\}, \quad (5)$$

where $\alpha = e^2/hc$ is the fine structure constant, θ and ϕ are angles specifying the direction of photon emission (see Fig. 14.8), ω_s is the surface plasmon eigenfrequency, $\lambda_s = 2\pi c/\omega_s$, γ_s is the total decay rate of the surface plasmon, $\overline{\zeta^2}$ is the mean square variation of the height about its average value, Θ specifies the angle of electron incidence, and the parameter $\mu = \beta\lambda_s/2\pi\sigma$, where βc is the electron speed and σ is the correlation distance for surface height variations. The functions $C_i(\mu)$ and $D_i(\mu)$ depend upon the form chosen for the autocorrelation function for variations in the surface height.

The corresponding differential probability for p-polarized photon emission is

$$\frac{d^2P^{(p)}}{d\omega\, d\Omega} = \frac{\alpha}{\omega_s} \frac{\overline{\zeta^2} \cos^2\theta\,(1 + \sin^2\theta)}{\lambda_s^2 \cos\Theta} \frac{\omega_s^2}{(\omega - \omega_s)^2 + (\gamma_s/2)^2}$$

$$\times \left[\cos^2\phi\, C_i(\mu) + \frac{2\sin\theta\cos\phi}{\sqrt{1 + \sin^2\theta}} L_i(\mu) + \frac{\sin^2\theta}{1 + \sin^2\theta} D_i(\mu) + \sin^2\phi\, M_i(\mu)\right], \quad (6)$$

where the functions $L_i(\mu)$ and $M_i(\mu)$ also depend upon the autocorrelation function.

A preliminary analysis of data taken by Dobberstein *et al.*[18] in light of the above analytical results indicates that an exponential autocorrelation function is more appropriate than a Gaussian form for the foils used in their experiments.

The present theory, together with sufficiently detailed experimental information on the process, should allow one to infer the parameters $\overline{\zeta^2}$ and σ for a given metal surface.

SURFACE PLASMON EFFECT IN THE REFLECTIVITY OF A NONUNIFORM BOUNDED ELECTRON GAS

Recent experimental[19,20] and theoretical[21,22] studies have emphasized the importance of surface plasmon creation in the interaction of photons with slightly imperfect metallic surfaces. The effect is manifested in a fairly narrow dip in reflectivity of the surface at the surface plasmon frequency. The theory of this effect has been extended to account for the dispersion in the plasma energy with wave number, using the free-electron gas model to describe the bounded metal. It is assumed that the height of the bounding surface varies in a random way about its mean value and that the autocorrelation function may be adequately described by a Gaussian with correlation distance σ. Figure 14.9 shows a plot of $(1/h)/(d\Delta R/d\omega)$ vs ω, where $d[\Delta R(\omega)]/d\omega$ is the decrease in reflectivity of the surface due to the surface plasmon effect at photon frequency ω, for normally incident photons, and for surfaces described by different correlation distances. The dimensionless parameters employed are defined in the caption of Fig. 14.9. This theory should be valuable in the analysis of experimental results on the surface plasmon effect.

[18] P. Dobberstein, A. Hampe, and G. Sauerbrey, *Bull. Am. Phys. Soc.* **13**, 988 (1968).

[19] S. N. Jaspersen and S. E. Schnatterly, *Bull. Am. Phys. Soc.* **12**, 399 (1967); **13**, 989 (1968).

[20] J. L. Stanford *et al.*, *Bull. Am. Phys. Soc.* **13**, 989 (1968).

[21] P. A. Fedders, *Phys. Rev.* **165**, 580 (1968).

[22] R. H. Ritchie and R. E. Wilems, *Phys. Rev.* **178**, 372 (1969).

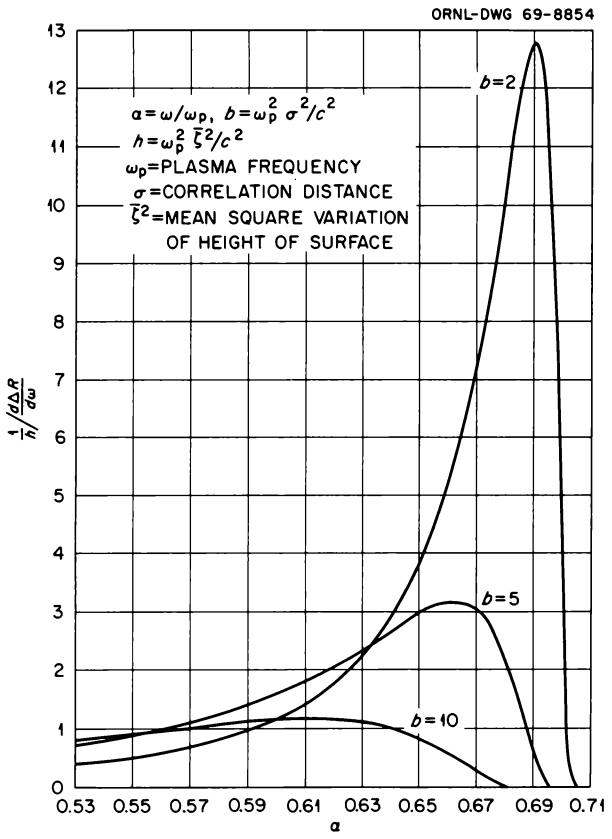

Fig. 14.9. Decrease in Reflectivity at the Surface of a Thick Foil as a Function of Frequency of Incident Light.

DOUBLE-PLASMON EXCITATION IN A FREE-ELECTRON GAS

The interaction of a fast charged particle with a free-electron gas has been described in the random-phase approximation, and the mean free path for the second-order process of double-plasmon excitation has been calculated. We find for the inverse mean free path for double-plasmon excitation, λ_{2p}^{-1}, the result

$$\lambda_{2p}^{-1} = \frac{9k_c^5\hbar}{2^7\pi^2 nm\omega_p}\lambda_p^{-1} , \tag{7}$$

where the inverse mean free path for the single-plasmon excitation process is given by

$$\lambda_p^{-1} = \frac{e^2\omega_p}{\hbar v_0^2}\ln\left(\frac{v_0 k_c}{\omega_p}\right) . \tag{8}$$

In these equations,

k_c = cutoff wave vector,

n = density of the electron gas,

m = electron mass,

ω_p = plasma frequency for the electron gas,

e = charge of the incident particle,

v_0 = speed of the incident particle.

If we take $k_c = \omega_p/v_F$, where v_F is the Fermi velocity for the electron gas, we find

$$\lambda_{2p}^{-1} = 0.0103 r_s^2\,\lambda_p^{-1} . \tag{9}$$

Here r_s is the radius, measured in units of Bohr radii, of the sphere containing on the average one electron in the electron gas. Since r_s varies from about 1.5 to 6 for the conduction electrons in real metals, this may lead to a measurable effect in certain experimental work, for example, characteristic energy loss measurements.

ELASTIC SCATTERING OF ELECTRONS BY HELIUM

For elastic scattering the scattering matrix for waves of angular momentum l and energy E, $S^l(E)$, reduces to a complex number, $\exp[i2\delta_l(E)]$; here $\delta_l(E)$ is the phase shift of the lth partial wave. The Wigner R-matrix analysis also reduces to an R-function analysis, in which S^l is related to $R^l(E)$ and the form of R^l is known:

$$R^l(E) = \sum_\lambda (\gamma_\lambda^l)^2/(E_\lambda^l - E) . \tag{10}$$

A single term of this expansion describes accurately the scattering of electrons by helium for the elastic scattering range ($E < 20$ ev), except for the lowest energies, at which a certain asymptotic expansion is not valid. The polarization potential is included. The relationship is

$$\frac{E_0^0 - E}{(\gamma^0)^2/a_H} = \frac{0.00375}{(ka_H)^2} + \left[ka_H + \frac{0.0061}{ka_H}\right] \times \operatorname{ctn}\left[\delta_0 + 3.25\,ka_H - \frac{0.0066}{ka_H}\right] . \tag{11}$$

Here k is the wave vector ($E = \hbar^2k^2/2m$, with $\hbar$ and m equal to Dirac's constant and the mass of the electron) and a_H is the radius of the first Bohr orbit. The sphere on which incoming and emerging wave functions were adjusted has radius $r_s = 3.25a_H$; this is approximately half the distance between neighboring helium atoms in

solid helium. The other numerical constants in the above expression involve, in addition to r_s and a_H, only the polarizability of helium. The "transition strength" γ^0 is found to satisfy $(\gamma^0)^2/a_H = 1.03(\hbar^2/2ma_H^2)$ ($\hbar^2/2ma_H^2$ = 1 Rydberg = 13.6 ev), and the resonant energy E_0^0 is 0.66 Ry = 9.0 ev. (The constants γ^0 and E_0^0 have no direct physical significance; they depend on the radius r_s.) Similar expressions for higher partial waves involve elliptic integrals.

ANALYSIS OF GROUND-STATE ENERGY EIGENFUNCTIONS FOR A FINITE DIPOLE IN SPHERICAL COORDINATE SYSTEMS

Normalized ground-state energy eigenfunctions for an electron in the field of a stationary, finite electric dipole have been calculated previously by means of a variational technique.[23] Since the Schroedinger equation for the finite dipole is separable in elliptic-hyperbolic coordinates, this system was the most appropriate choice for the calculation. Though the variational calculation was greatly facilitated by use of elliptic coordinates, these are not the most useful in many other contexts. There are, in fact, a number of reasons for having solutions expressed in the more familiar spherical polar coordinates. For example, the dipole bound-state eigenfunctions may serve in a zeroth order approximation to the wave functions for negative ions of polar molecules. The evaluation of matrix elements in perturbation calculations involving dipole functions would be more conveniently expressed in spherical coordinates. Analysis of the ground-state energy eigenfunctions in terms of spherical harmonics (Legendre polynomials) gives the number and relative importance of orbital angular momentum states in the electron wave functions as a function of dipole moment. This information serves as an indicator of the number of partial waves required in a study of low-energy electron scattering from polar molecules. Direct solution of the dipole problem in spherical coordinates serves as a model problem to indicate the feasibility of studying the effects of other interactions (e.g., quadrupole and induced dipole) on the molecular dipole. Finally, a study of the important question of the effect of molecular rotation on the minimum dipole moment required for electron binding can obviously be handled more easily with solutions which are angular momentum eigenfunctions.

The normalized ground-state eigenfunctions of ref. 23 for the electron-dipole problem have been determined in spherical polar coordinates for dipole moments D in the range $0.64 \leqslant D \leqslant 100$. ($D$ is in atomic units, ea_0, where e is the electron charge and a_0 the Bohr radius.) With reference to Fig. 14.10, two sets of spherical coordinates, (r_1, θ_1) and (r, θ), were used in the analysis, the first having the origin at the location of the charge + q and the second at the center of the dipole. The coordinates (r, θ) are convenient in a number of problems, particularly if other potentials are treated in addition to the dipole or if rotational excitation of the dipole about its center is considered. For large dipole moments and for comparisons with properties of the hydrogen atom, (r_1, θ_1) are more convenient. The

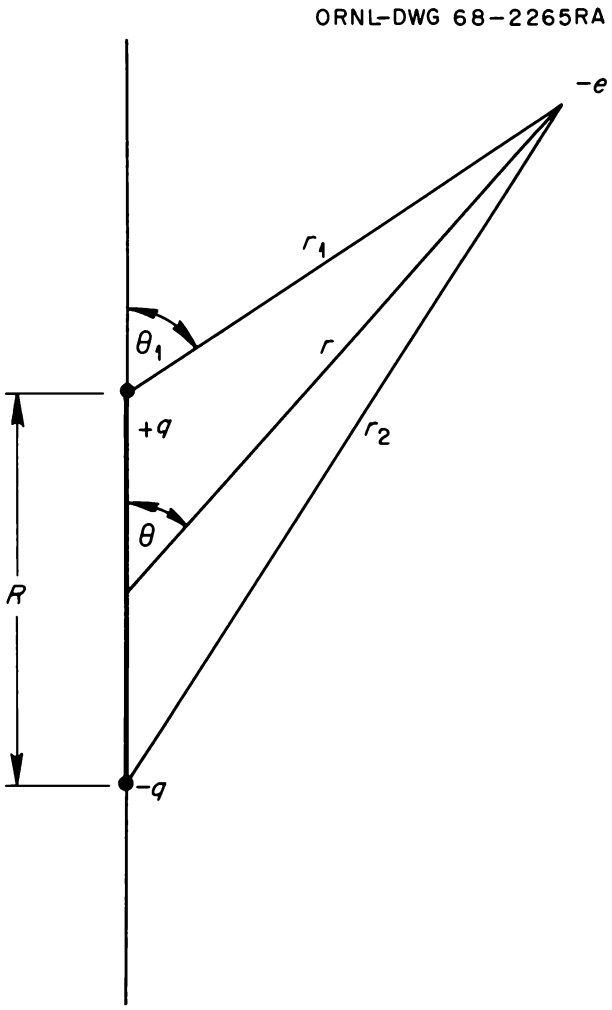

Fig. 14.10. Coordinate System for Electron and Finite Dipole.

[23] J. E. Turner, V. E. Anderson, and K. Fox, *Phys. Rev.* 174, 81 (1968).

normalized wave function for a given value of D can be expressed in these systems in the form

$$\psi(r_1, \theta_1) = \sum_{l=0}^{\infty} F_l(r_1) P_l(\cos\theta_1) , \qquad (12)$$

or, alternatively,

$$\psi(r, \theta) = \sum_{l=0}^{\infty} G_l(r) P_l(\cos\theta) . \qquad (13)$$

The radial functions $F_l(r_1)$ and $G_l(r)$ were determined by transforming the solutions of ref. 23 into spherical coordinates. The summation on l was carried through $l = 9$.

As a first step in a study on the effects of other interaction terms on dipole wave functions, the Schroedinger equation for the finite dipole was written in spherical coordinates and reduced to a set of coupled differential equations for the radial functions. Direct solutions of these equations were obtained by numerical integration. The solutions were identical to four significant figures with those obtained by coordinate transformation as described above.

Figure 14.11 shows the functions $F_l(r_1)$ and $G_l(r)$ for D = 0.67465, a value near the minimum, D_{min} = 0.639315, required for electronic binding. Both $F_0(r_1)$ and $G_0(r)$ are largest at their origins and decrease monotonically with distance. Some slight structure was noted in F_0 and G_0 in the vicinity of the negative dipole charge ($r_1 = D = 0.67$ and $r = D/2 = 0.34$). When $l > 0$, both the $F_l(r_1)$ and the $G_l(r)$ are zero at their origins. In magnitude both $|F_l(r_1)|$ and $|G_l(r)|$ reach maxima in the regions $r_1 = D$ (radial distance of negative dipole charge) and $r = D/2$ (radial distance of both dipole charges). In general, the functions $G_l(r)$ and $F_l(r_1)$ show an oscillatory behavior for higher l values, but no predictable node structure is apparent.

The composition of the wave function when D = 1.00002 is shown in Figs. 14.12 and 14.13. The behavior of $F_l(r_1)$ and $G_l(r)$ is similar to that in Fig. 14.11. For larger dipole moments, the representation of the ground-state energy eigenfunctions about the dipole center in terms of $G_l(r)$ converges poorly, many values of l being needed. When D = 2, for example, representation of the wave function with only ten values of l is wholly inadequate. On the other hand, expansion in terms of $F_l(r_1)$ becomes progressively better with larger values of D. As seen from Fig. 14.14, the wave function outside the vicinity of the dipole charges consists mostly of S and P waves. As D increases further the system approaches the hydrogen atom perturbed by a charge $q = -e$ located at $r_1 = D$ and $w_1 = -1$, and the ground-state energy eigenfunction approaches a pure S state.

Further details of this work are available in ORNL-4431.[24]

[24] W. R. Garrett, J. E. Turner, and V. E. Anderson, *Analysis of Ground-State Energy Eigenfunctions for Finite Dipole*, ORNL-4431 (in preparation).

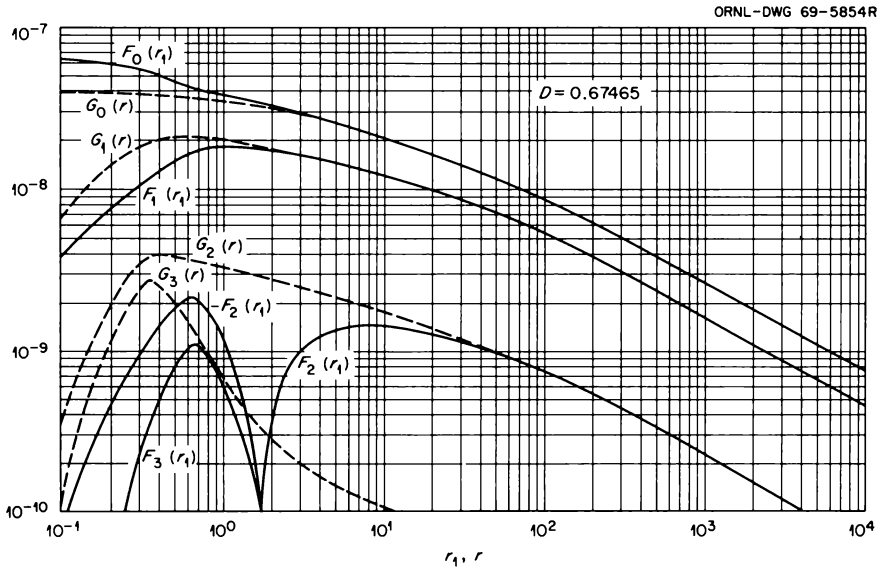

Fig. 14.11. Radial Functions $F_l(r_1)$ and $G_l(r)$ for D = 0.67465.

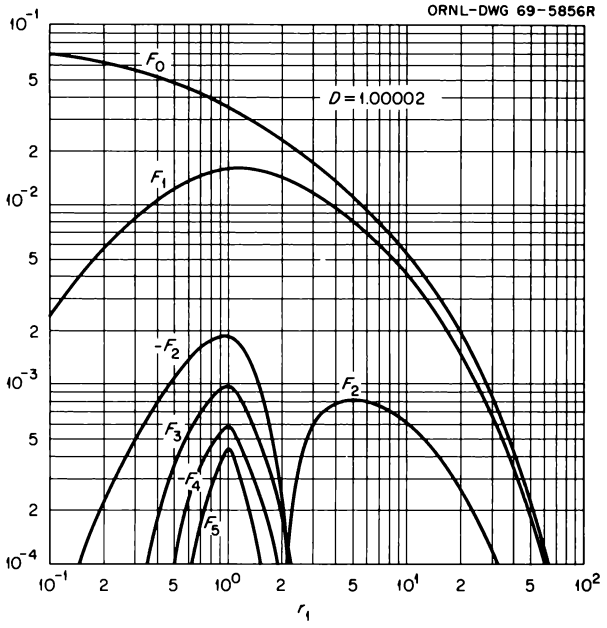

Fig. 14.12. Radial Functions $F_l(r_1)$ for $D = 1.00002$.

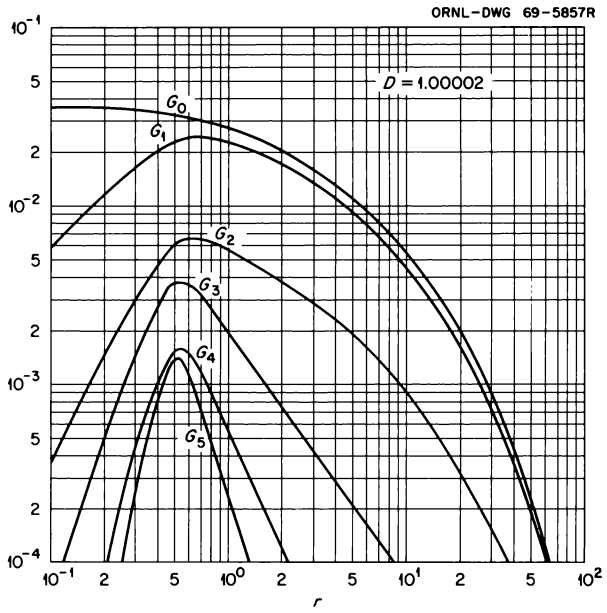

Fig. 14.13. Radial Functions $G_l(r)$ for $D = 1.00002$.

VARIATIONAL METHOD FOR LONG-RANGE SCATTERING INTERACTIONS

In the Hulthen-Kohn type of variational methods an approximate solution to the lth partial wave component

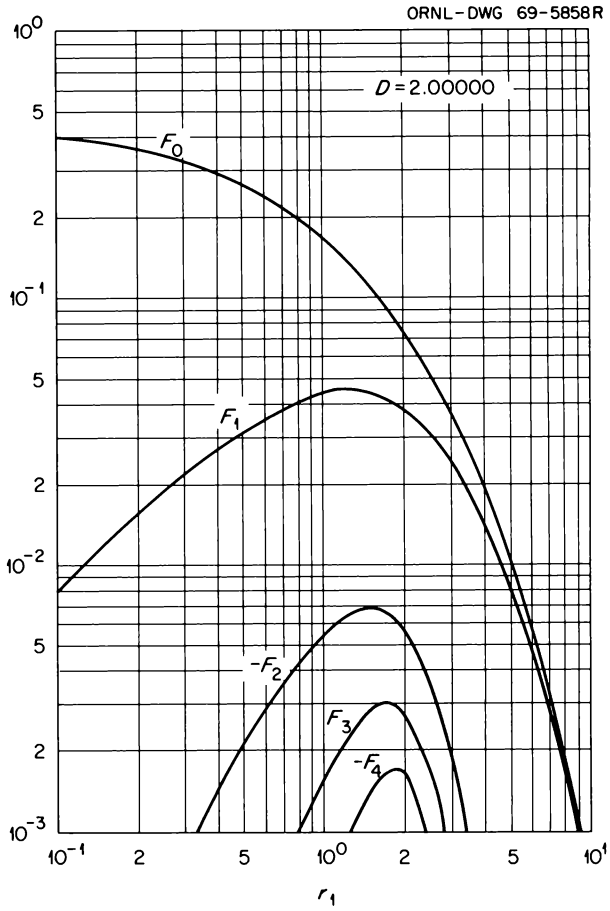

Fig. 14.14. Radial Functions $F_l(r_1)$ for $D = 2$.

of the total continuum solution to the Schroedinger equation for scattering is obtained through the variational integral[25]

$$I_l^t = \int \phi_l^t \, (H - E) \, \phi_l^t \, d\tau \, . \tag{14}$$

The trial function ϕ_l^t is chosen to approximate the component ϕ_l of the solution to the equation $(H - E)\phi_l = 0$ with asymptotic boundary condition

$$\phi_l \sim \psi_\nu(\rho) \, Y_l(\theta) A \sin\left(kr - \frac{l\pi}{2} + \eta_l\right). \tag{15}$$

Here θ and r are the coordinates of the scattered particle, $\psi_\nu(\rho)$ is the wave function of the target,[26] A is

[25] For a general summary of variational methods, see Y. N. Demkov, *Variational Principles in the Theory of Collisions*, chap. VI, Macmillan, New York, 1963.

[26] For electron scattering the asymptotic form of Eq. (15) must be antisymmetrized. This does not affect any of the present arguments.

the normalization factor, and η_l is the phase shift for the scattered wave. The choice of ϕ_l^t in Eq. (14) with asymptotic form (15) leads to the variational statement

$$\delta I_l = kA^2\, \delta\eta_l \,. \tag{16}$$

The Hulthen-Kohn type variational methods have been summarized and extended in a recent paper by John.[27]

In low-energy atomic and molecular scattering the phase shifts are strongly dependent on the long-range polarization forces between target and projectile. Since the success or failure of the variational method rests largely on the judicious choice of the trial function, that function should be appropriate to this type of scattering interaction. A method which satisfies this criterion is proposed. The method leads to a new type of variational procedure with nonlinear trial phases η_l^t.

For convenience we choose the normalization $A = 1$ in Eq. (14). Then

$$\delta(I - k\eta_l) = 0 \,. \tag{17}$$

We now choose a trial function which satisfies the boundary condition (15) (with η_l^t replacing η_l) in a way which is more nearly suited to the scattering problem. This can be done by first considering the problem from the standpoint of potential scattering, where the many-body problem is reduced to a one-body equation with an appropriate interaction potential. Suppose that the scattering equation is solved with a trial potential $V_t(r)$ representing the scattering interaction. We now choose a trial function which contains the solution to the approximate one-body scattering equation. Specifically we write

$$\phi_l^t = \psi_\nu(\rho)\, Y_l(\hat{r})\frac{g_l(r, \eta_l^t)}{r} + Q_l(\rho, \mathbf{r}) \,. \tag{18}$$

Here the term $Q_l(\rho, \mathbf{r})$ is a correlation or close-in function which goes to zero exponentially for large distances from the origin located inside the target. Typically this function contains n-variational parameters $c_1, c_2, \ldots, c_n$. The function g_l is not a simple analytic expression but rather a function which goes asymptotically into the solution to the radial equation

$$\left[-\frac{d^2}{dr^2} + \frac{l(l+1)}{r^2} + V_t(r) - k^2\right] U_l(r) = 0 \,. \tag{19}$$

Thus,

$$\lim_{r\to\infty} g_l(r, \eta_l^t) \to U_l(r) \to \sin(kr - l\pi/2 + \eta_l^t) \,.$$

The phase shift η_l^t is determined from the solution to Eq. (19) by matching to a linear combination of spherical Bessel functions at large r. Thus the trial phase η_l^t is not treated as a parameter in the usual way but is obtained from the solution of a "trial scattering equation." In this equation the potential $V_t(r)$ is partially or totally parameterized and is "varied" in order to yield a set of functions g_l and phases η_l which go into the stationary expression (17). The variation of the potential V_t is repeated, and new solutions g_l and phases η_l along with the linear parameters c_n are determined until (17) is satisfied. Alternatively, Hulthen's procedure[27] may be followed. That is, the integral (14) is made stationary with respect to the c_s and the trial phase determined by finding that solution $g_l(r, \eta_l^t)$ which yields $I_l^t = 0$.

The advantage to be gained from this variational method lies in the fact that full utilization of any prior knowledge of the nature of the interaction potential in a particular scattering problem may be incorporated into the choice of a trial function, thus reducing the requirement for a large number of variational parameters. In fact, if one has sufficient information on the interaction potential the number of variational terms required in (17) shrinks to zero.

POSITRON-HYDROGEN SCATTERING

The scattering of low-energy positrons from atomic hydrogen has been used as a sample problem in the investigation of the new variational method described above. The problem is notorious for the sensitivity of the cross sections to the long-range terms in the interactions and should provide a severe test of the procedure. With reference to the previous section, we chose a trial function for s-wave scattering in the form

$$\phi_0^t(\rho, r) = \frac{1}{4\pi}\frac{P_{1s}(\rho)}{\rho}(1 + A_{n+1}\, e^{-\nu r})\frac{U_0(r)}{r} + \sum_{l,m} C^{l0}_{m,\,-m,\,0}\, Y_l^m(\hat{\rho})\, Y_l^{-m}(\hat{r}) \times \sum_{p,\,q} A_{pql}\, \rho^{p+l} r^{q+l} e^{-\gamma(r+p)} \,. \tag{20}$$

In this expression the coefficients A_i are variational parameters, P_{1s} is the reduced ground-state radial

[27] T. L. John, *Proc. Phys. Soc.* 92, 62 (1967).

function for hydrogen, and the factors $C^{l l 0}_{m,\,-m,\,0}$ are Clebsch-Gordon coefficients. The function $U_0(r)$ which appears in this trial function is itself an approximate solution to the scattering problem at hand, when formulated from the standpoint of potential scattering. That is, $U_0(r)$ is the solution to the radial equation

$$\left[-\frac{d^2}{dr^2} + V_t(r) - k^2\right] U_0(r) = 0 \tag{21}$$

for a particle of energy k^2 moving in a potential $V_t(r)$ and having an asymptotic boundary condition

$$U_0(r) \underset{r\to\infty}{\sim} \sin(kr + \eta^t). \tag{22}$$

The phase shift η^t is obtained and utilized in the variational procedure as described in the previous section. The "trial potential" $V_t(r)$ in Eq. (21) is chosen to represent the true interaction potential as closely as possible. This term is written in the form

$$V_t(r) = V_a(r) + V_p(r)\,, \tag{23}$$

where $V_a(r)$ is the static electrostatic potential and $V_p(r)$ is the polarization potential[28] for positrons incident on hydrogen. The magnitude of the polarization term is varied between successive determinations of $U_0(r)$ and η_l^t by scaling the potential function of ref. 28. The procedure is repeated until values of $U_0(r)$ and η_l^t are found which satisfy the Kohn or Hulthen conditions on the stationary integral.

[28] W. R. Garrett, *Phys. Rev.* **178**, 218 (1969). The polarization potential used in the present calculation is that of this reference multiplied by a scaling factor to either increase or decrease the effective interaction until stationary phases are obtained.

Results obtained from the new variational method and from other techniques are presented in Table 14.1. The values in columns 2, 3, and 4 are the result of including only terms with $l = 0$ in the trial function (20). In columns 5, 6, and 7 results obtained with the inclusion of $l = 0$ and 1 terms are reported. The variational bound results of Hahn and Spruch[29] give the correct limit to the phase shift which results from the inclusion of each angular momentum state in the trial function. The present method, which is much less involved than that of Hahn and Spruch, yields the same correct limit. In the sum over p and q in Eq. (20) the s-wave results required three values (0, 1, 2) for both p and q, and the results with $s + p$ components required four additional values of p and q for the $l = 1$ terms in (20).

The present results indicate that the new variational technique is capable of yielding more reliable results with fewer variational parameters in scattering problems involving long-range interactions as compared with the usual formulation of variational methods.

CONTRIBUTIONS OF SPIN, ANOMALOUS MAGNETIC MOMENT, AND FORM FACTORS TO THE STOPPING POWER OF MATTER FOR PROTONS AND MUONS AT EXTREME RELATIVISTIC ENERGIES

The stopping power of matter for protons and muons is calculated quantum mechanically without the usual restriction that $\gamma m \ll M$, where M is the rest mass of the proton or muon, m is that of the electron, $\gamma = (1 - \beta^2)^{-1/2}$, and β is the ratio of the speed of the proton or muon to the speed of light. The contribution to the stopping power $-dE/ds$ from the so-called "distant" or

[29] Y. Hahn and L. Spruch, *Phys. Rev.* **140**, A18 (1965).

Table 14.1. Positron-Hydrogen $l = 0$ Phase Shifts

$k^2 = E$ rydbergs

k	Close Coupling[a] 1s, 2s, 3s	Variational[b] Bound s Term	Present Variational s Term	Close Coupling[c] 1s, 2s, 2p	Present Variational s + p Terms	Variational[b] Bound s + p Terms
0.2	−0.110	−0.106	−0.106	−0.0426	0.0612	0.0612
0.4	−0.209	−0.200	−0.200	−0.147	−0.0161	−0.0160
0.6	−0.291	−0.275	−0.276			

[a] K. Smith and P. G. Burke, *Phys. Rev.* **123**, 174 (1961).
[b] Y. Hahn and L. Spruch, *Phys. Rev.* **140**, A18 (1965).
[c] W. J. Cody *et al.*, *Proc. Roy. Soc. (London)* **A278**, 479 (1964).

"low momentum transfer" collisions[30] in a medium is the same for different kinds of particles:

$$\left(-\frac{dE}{ds}\right)_{Q<\eta} = \frac{1}{2}\kappa\left(\ln\frac{2\gamma^2 mv^2\eta}{I^2} - \beta^2\right). \quad (24)$$

Here $\kappa = 4\pi z^2 e^4 NZ/mv^2$, where ze is the charge of the particle ($-e$ is the electronic charge), NZ is the number of electrons per unit volume in the medium, v is the particle speed, I is the mean excitation energy of the medium, and η is an "intermediate" value of energy loss Q.[30] Equation (24) is valid for very large values of γ. When $\gamma m << M$, the contribution of the "close" collisions is given by[30]

$$\left(-\frac{dE}{ds}\right)_{Q>\eta} = \frac{1}{2}\kappa\left(\ln\frac{2\gamma^2 mv^2}{\eta} - \beta^2\right) \quad (\gamma m << M), \quad (25)$$

and the total stopping power by the sum of (24) and (25):

$$-\frac{dE}{ds} = \kappa\left(\ln\frac{2\gamma^2 mv^2}{I} - \beta^2\right) \quad (\gamma m << M). \quad (26)$$

At extreme relativistic energies (e.g., tens of Gev for muons and hundreds of Gev for protons) the condition $\gamma m << M$ does not hold, and so Eqs. (25) and (26) must be modified.

The modifying calculations have been carried out for protons and muons[31] and are nearing completion for particles having other spin. The details are being reported in the literature.[31] One can transform the Rosenbluth formula,[32] giving the differential scattering cross section for scattering of a very high-energy electron from a charged spin ½ particle, from the rest system of the particle to that of the electron, the latter being the laboratory system for particle slowing down. The transformed cross section includes explicitly the effect of the particle's spin, anomalous magnetic moment, and form factors for the distribution of charge and magnetic moment. A rather complicated expression is obtained in closed form for proton stopping power. Expanded to lowest order in the electric form factor, $G_E(Q) = 1 - \nu Q$, and with the magnetic form factor $G_M = \mu G_E$, where μ is the proton's magnetic moment, the stopping power is given by

$$\begin{aligned}-\frac{dE}{ds} = \kappa\Bigg[&\ln\frac{2\gamma^2 mv^2}{I} + \frac{1}{2}\ln\frac{M}{M+2\gamma m} \\ &- \frac{1}{2}\beta^2(1+\mu^2) + \frac{\gamma^2\mu^2 m^2\beta^4}{2(M+2\gamma m)^2} \\ &+ \frac{\nu\mu^2\gamma^2 Mmv^2(\beta^2-2)}{M+2\gamma m} \\ &- \frac{4\nu\mu^2\gamma^4 Mm^3\beta^4 v^2}{3(M+2\gamma m)^3} - \frac{2\nu M^2 v^2}{m}(\mu^2-1) \\ &+ \frac{1}{2}(\mu^2-1)\left(1+\frac{M(M+2\gamma m)}{\gamma^2 m^2}\right) \\ &\times\left(1+\frac{4\nu M^2 c^2}{m}\right)\ln\left(1+\frac{\gamma^2 m^2\beta^2}{M(M+2\gamma M)}\right)\Bigg]. \quad (27)\end{aligned}$$

The first term in the square bracket is present in the ordinary relativistic theory. The second term, which is negligible when $\gamma m << M$, arises from the factor $M/(M + 2\gamma m)$ in Q_m in the ultrarelativistic theory with $\gamma >> 1$. The third term gives the factor $-\beta^2$ in the relativistic formula when $\mu = 1$ (no anomalous magnetic moment). The fourth term arises from the spin (½) of the incident particle. The fifth, sixth, and seventh terms vanish for a point Dirac particle ($\nu = 0$), and the seventh and eighth terms vanish when there is no anomalous moment. Equation (27) can be applied to the muon, considered as a point Dirac particle, at all energies by setting $\mu = 1$ and $\nu = 0$. For protons ($\mu = 2.793$) the expansion (27) is valid up to several hundred Gev. At higher proton energies the full closed-form expression can be used.[31] Table 14.2 shows a numerical analysis for muons and protons in aluminum as obtained with the extreme relativistic stopping-power formula. The terms E_μ and E_p are the muon and proton energies as a function of γ. The dimensionless quantities ϵ_0, ϵ_μ, and ϵ_p represent $(-dE/ds)/\kappa$ when calculated by the ordinary relativistic formula and by the extreme relativistic formula for muons and protons. Columns 7 and 8 show that the extreme relativistic effects of particle spin, anomalous magnetic moment, and form factors reduce the stopping power by about 10% at the highest energies given. Column 9 shows the effect of spin and

[30] E. A. Uehling, *Ann. Rev. Nucl. Sci.* 4, 315 (1954).

[31] J. E. Turner *et al.*, "Contributions of Spin, Anomalous Magnetic Moment, and Form Factors to the Stopping Power of Matter for Protons and Muons at Extreme Relativistic Energies," *Phys. Rev.* (in press).

[32] M. N. Rosenbluth, *Phys. Rev.* 79, 615 (1950).

Table 14.2. Analysis of Various Contributions to Stopping Power of Aluminum (I = 163 ev, ρ = 2.71 g/cm^3) at Extreme Relativistic Energies

γ	E_μ (Gev)	E_p (Gev)	ϵ_0	ϵ_μ	ϵ_p	$\frac{100(\epsilon_0 - \epsilon_\mu)}{\epsilon_\mu}$	$\frac{100(\epsilon_0 - \epsilon_p)}{\epsilon_p}$	ϵ_a	δ	$(-dE/ds)_\mu/\rho$ (Mev cm^{-2} g^{-1})	$(-dE/ds)_p/\rho$ (Mev cm^{-2} g^{-1})
10	1.057	9.382	12.35	12.30	12.34	0.37	0.044	12.34	−0.72	1.840	1.846
50	5.285	46.91	15.57	15.39	15.55	1.2	0.088	15.54	−1.9	2.278	2.302
100	10.57	93.82	16.95	16.64	16.90	1.8	0.30	16.92	−2.5	2.464	2.502
250	26.42	234.5	18.79	18.23	18.66	3.0	0.69	18.74	−3.4	2.699	2.762
500	52.85	469.1	20.17	19.38	19.89	4.1	1.5	20.16	−4.1	2.868	2.944
750	79.26	703.5	20.98	20.02	20.52	4.8	2.3	21.03	−4.5	2.964	3.037
1000	105.7	938.2	21.56	20.48	20.92	5.3	3.1	21.68	−4.8	3.031	3.096
2000	211.4	1876	22.94	21.55	21.75	6.5	5.5	23.39	−5.5	3.190	3.220
5000	528.5	4691	24.78	22.95	22.73	8.0	9.0	26.00	−6.4	3.397	3.364

anomalous magnetic moment alone. The column labeled δ gives the estimated density correction based on the work of Sternheimer.[33] This is seen to make a much greater contribution than the extreme relativistic effects to stopping power. The last two columns give the mass stopping power of aluminum as calculated with the complete extreme relativistic formula, the density correction not being included.

[33] R. M. Sternheimer, *Phys. Rev.* **103**, 511 (1956).

15. Interaction of Radiation with Liquids and Solids

E. T. Arakawa

R. D. Birkhoff

A. J. Braundmeier, Jr.[1]
J. J. Cowan[2]
L. C. Emerson
T. F. Gesell[1]
R. N. Hamm
J. A. Harter
A. G. Kenerly[3]
R. A. MacRae[4]
Linda R. Painter[4]
H. C. Schweinler
B. L. Sowers[4]
Uoo Sung Whang[4]
Mary W. Williams[4]

OPTICAL PROPERTIES OF SOME METALLIC FILMS ABOVE THEIR PLASMA ENERGIES

Refractive Index of Rubidium

The refractive index of rubidium has been measured in the vacuum ultraviolet from 1300 to 3600 A by the critical-angle method. Films of rubidium of approximately 10,000 A thickness were deposited in a vacuum of 5×10^{-7} torr onto the flat surface of a quartz or CaF_2 semicylinder. A thin layer of oxide covered the exposed surface of the rubidium within seconds of the evaporation, but measurements were made through the semicylinder so that the uncontaminated film surface was viewed.[5]

In the spectral region of transparency, with the extinction coefficient k being small, the critical-angle method can be used to determine n, the index of refraction. Hunter[6] has shown that for sufficiently small values of k, the critical angle is the angle, θ_m, where the slope of the reflectance vs angle of incidence curve is a maximum. Knowing the refractive index of the quartz or CaF_2 semicylinder the refractive index of rubidium was obtained from

$$n_{Rb} = n_{\text{semicylinder}} \sin \theta_m$$

over the wavelength region of 1600 to 3600 A with the quartz semicylinder and from 1300 to 3600 A with the CaF_2 semicylinder.

Since the extinction coefficient of rubidium is very small in the transparent region of the metal and $n \gg k$, the nearly-free-electron model[5] for metals gives

$$n^2 = 1 + 4\pi N\alpha_1 - \frac{\lambda^2}{\lambda_p^2}.$$

The nearly-free-electron plasma wavelength, λ_p, is equal to $(\pi m_{opt} c^2/Ne^2)^{1/2}$, where m_{opt} is the average optical effective mass of a conduction-band electron and N is the density of free electrons. The polarizability of a single ion modified slightly by interband transitions is denoted by α_1. A plot of n^2 vs λ^2 is shown in Fig. 15.1, both for the present data and those available in the literature.[7,8] The solid line was obtained by a

[1] USAEC Health Physics Fellow.

[2] Radiological Health Physics Fellow.

[3] On loan from Instrumentation and Controls Division.

[4] Consultant.

[5] J. C. Sutherland, E. T. Arakawa, and R. N. Hamm, *J. Opt. Soc. Am.* 57, 645 (1967).

[6] W. R. Hunter, *J. Opt. Soc. Am.* 54, 15 (1964).

[7] H. E. Ives and H. B. Briggs, *J. Opt. Soc. Am.* 27, 395 (1937).

[8] H. Mayer and B. Hietel, in *Optical Properties and Electronic Structure of Metals and Alloys*, F. Abelès, ed., North-Holland, Amsterdam, 1966; S. von Aufschnaiter, Ph.D. dissertation, Clausthal, Germany, 1966; St. v. Aufschnaiter and H. Mayer, *Kurznachr. Akad. Wiss. Goettingen* 23, 109 (1966); H. Mayer, private communication, July 1968.

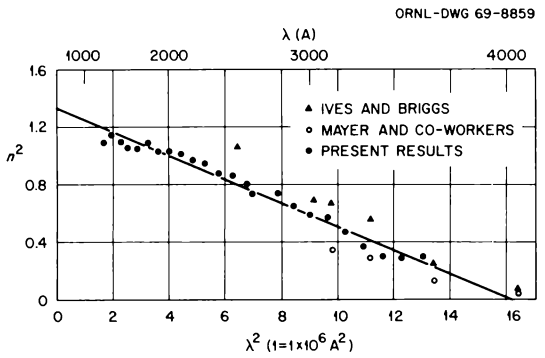

Fig. 15.1. n^2 vs λ^2 for Rb. The line represents a least-squares fit to the present data. Also shown are data from refs. 7 and 8.

least-squares fit to the present data. Since the data points lie almost on a straight line the simple nearly-free-electron model is satisfactory for rubidium, yielding a volume plasma wavelength of λ_p = 4017 A and hence a volume plasma energy of 3.09 ev, an optical effective mass of $1.182m_e$, and an ion-core polarization of 0.3237.

The Imaginary Part of the Dielectric Constants for Sodium and Potassium

The extinction coefficients k of sodium and potassium have been found by measuring the transmittance of vacuum-evaporated films 4000 to 9000 A in thickness deposited on quartz or LiF substrates. Measurements were made at a pressure of less than 3×10^{-7} torr, and the sodium and potassium exceeded 99.5 and 99.9% purity respectively. The quartz plates used as substrates were 3 mm thick, while the cleaved LiF plates were 0.5 mm thick. In calculating the transmittance of the sodium or potassium, corrections were made for losses due to surface reflections, substrate absorption, and contamination of the exposed surface of the metal. The thickness of the metal films was found both by an interference method[5,9] and by measuring the mass of metal deposited by spectrochemical analysis.

The refractive indices of sodium and potassium have previously been determined.[5,10] Thus measurement of k yielded the imaginary part of the dielectric constant, $\epsilon_2 = 2nk$. For those wavelengths at which no value of the refractive index had been reported, n was calculated by interpolation.

Figures 15.2 and 15.3 show our values of ϵ_2 of sodium and potassium as a function of photon energy. We also show the data of Ives and Briggs,[11,12] Smith,[13] Hietel[14] (sodium), and El Naby[15] (potassium). Previously[9] we found ϵ_2 for sodium by a reflectance technique which utilized a quartz semicylinder. These data are included in Fig. 15.2.

For sodium, all of the data of Ives and Briggs and Smith are for photon energies below the plasma energy, $\hbar\omega_p$, while all of our data are above $\hbar\omega_p$. Above the plasma energy, our data show a plateau in ϵ_2 with perhaps a slight decrease with increasing energy. There is very good agreement between the transmission and the reflection data. From 6.2 to 7.7 ev, the region in which the sodium films were deposited on quartz substrates, the scatter in the data is about ±0.005. Above 7.7 ev the films were deposited on lithium fluoride. Here the scatter is less than ±0.01. Thus the accuracy of our technique is comparable with that of the transmission method used by Hunter[16] to measure the extinction coefficient of free-standing aluminum foils.

The plasma energy of potassium is lower than that of sodium, so there is a region in which our data can be compared with those of Smith and Ives and Briggs. Figure 15.3 shows that our values are slightly higher than Smith's and in excellent agreement with Ives and Briggs in the region of overlap. The general shape of ϵ_2 for potassium is similar to that for sodium.

The ability of sodium films to produce strong interference fringes while potassium films give only weak fringes in a limited spectral region is explained by the data in Figs. 15.2 and 15.3. Above the plasma energy, ϵ_2 for sodium never exceeds 0.04 and may drop to 0.02 or below, while for potassium ϵ_2 never goes below 0.06 and appears to rise to at least 0.08 at higher energies. Interference fringes were never observed from rubidium films, suggesting that the trend to higher absorbance continues with increasing molecular weight.

---

[9] J. C. Sutherland *et al.*, *Optical Properties of Sodium in the Vacuum Ultraviolet*, ORNL-TM-1776 (1967).

[10] J. C. Sutherland and E. T. Arakawa, *J. Opt. Soc. Am.* **58**, 1080 (1968).

[11] H. E. Ives and H. B. Briggs, *J. Opt. Soc. Am.* **27**, 181 (1937) and references cited therein.

[12] H. E. Ives and H. B. Briggs, *J. Opt. Soc. Am.* **26**, 238 (1936) and references cited therein.

[13] N. V. Smith, *Phys. Rev.* **21**, 96 (1968).

[14] B. Hietel, thesis, der Bergakademie Clausthal, 1965.

[15] M. H. El Naby, thesis, der Bergakademie Clausthal, 1962.

[16] W. R. Hunter, *J. Phys. Radium* **25**, 154 (1964).

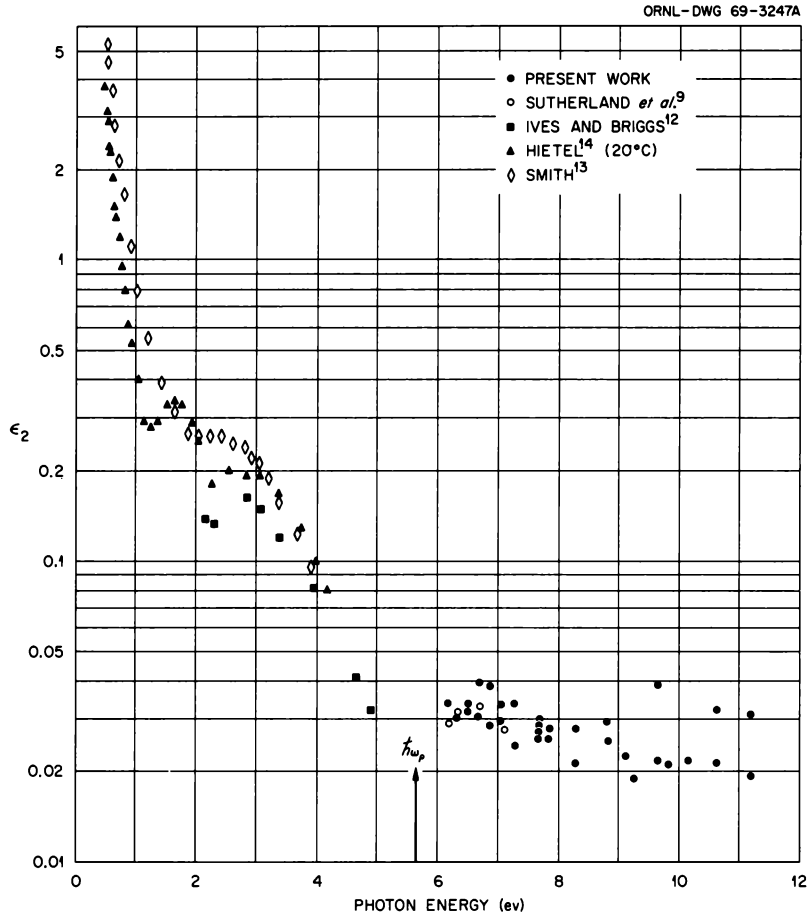

Fig. 15.2. ϵ_2 for Na vs Photon Energy. An arrow marks the plasma resonance energy.

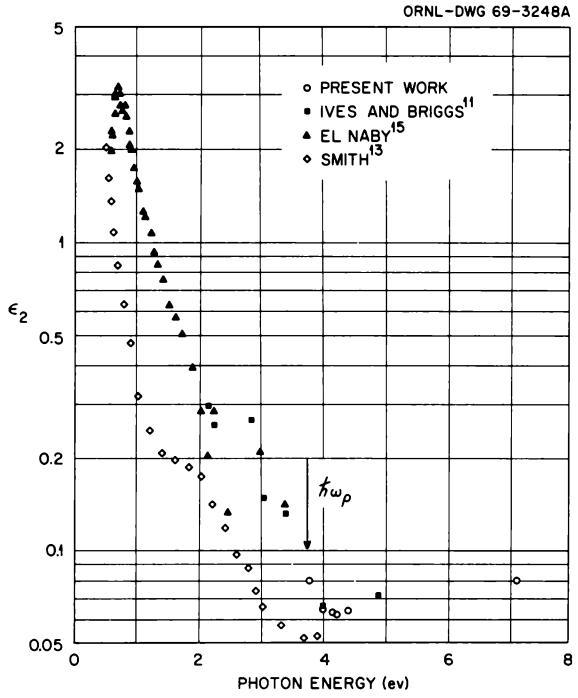

Fig. 15.3. ϵ_2 for K vs Photon Energy. An arrow marks the plasma energy. The transmission data are from measurements made on a potassium film deposited on a quartz substrate.

OPTICAL PROPERTIES OF SOME ORGANIC LIQUIDS

There are few data in the literature of the optical properties of liquid insulators in the vacuum ultraviolet, owing to experimental difficulties. However, the absorption processes in such liquids, particularly organic liquids, are of great biological interest. A method[17] has been developed which enables the optical constants of liquids to be obtained from reflectance measurements. Liquid is placed in a sealed cell, one side of which consists of a transparent semicylinder. Electromagnetic radiation enters the semicylinder normal to its curved surface and is reflected at the plane semicylinder-liquid interface. Semicylinders of MgF_2, CaF_2, and quartz have been used over different wavelength ranges. This method is satisfactory for any liquid in the cell, up to the transmission cutoff of the semicylinder. Depending on the relative refractive indices of the semicylinder and the liquid and on the value of the extinction coefficient of the liquid, n and k, the real and imaginary parts of the refractive index of the liquid are obtained from observations of the critical angle or a least-squares fit of reflectance data as a function of angle of incidence. The values of ϵ_1 and ϵ_2, the real and imaginary parts of the dielectric constant ϵ, are then calculated from $\epsilon_1 = n^2 - k^2$ and $\epsilon_2 = 2nk$.

Collective Oscillations

The optical properties of pure liquid benzene have been obtained from observations of the reflectance as a function of the angle of incidence over the wavelength range 1200 to 3200 A. The values obtained for n and k are shown in Fig. 15.4. The materials used for the semicylinder over different wavelength ranges are also indicated. The calculated values of ϵ_1, ϵ_2, and $-\mathrm{Im}\,(1/\epsilon)$ are shown in Fig. 15.5. The energy loss function describes the probability that high-energy charged particles traversing the material will lose energy, either by exciting single-electron transitions or collective volume plasma oscillations. In distinguishing between these two modes of energy loss, it is noted that single-electron transitions are associated with peaks in ϵ_2, whereas plasma resonances are not associated with structure in ϵ_2.[18] For comparison, one typical set of data,[19] plotted on an arbitrary ordinate scale, is shown in Fig. 15.5 for ϵ_2 of the vapor. In addition, characteristic electron energy loss measurements for benzene vapor,[20] again on an arbitrary ordinate scale, are compared with the loss function $-\mathrm{Im}\,(1/\epsilon)$ calculated for the liquid.

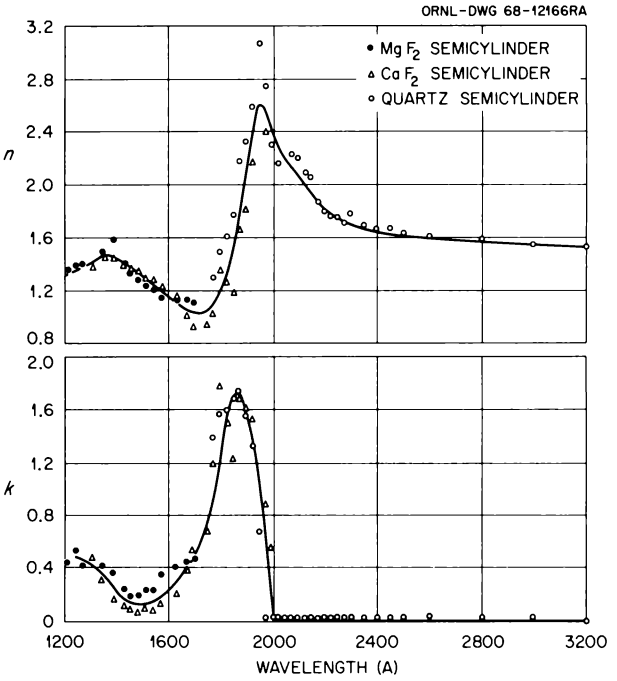

Fig. 15.4. Optical Constants n and k of Pure Liquid Benzene.

In the vapor the maximum radiant absorbance occurs at about 1790 A (6.9 ev; see Fig. 15.5) and has been attributed to the strongly allowed molecular excitation of the π electrons designated[21] by ${}^1A_{1g}^- \rightarrow {}^1E_{1u}^+$ using molecular orbital notation. The characteristic electron energy loss spectrum for the vapor (Fig. 15.5) also shows a loss at 6.9 ev which has been associated with this molecular excitation of the π electrons.[20]

It is seen in Fig. 15.4 that there is a maximum in the radiant absorbance for pure liquid benzene at 1870 A corresponding to the maximum in ϵ_2 at 6.5 ev, shown in Fig. 15.5. We attribute this absorption in the liquid to the same molecular excitation of the π electrons as occurs in the vapor, shifted from 6.9 ev by the perturbation of other molecules in the liquid state. The shoulder in the vicinity of 6.5 ev in the calculated loss

---

[17] L. Robinson Painter *et al.*, *Phys. Rev. Letters* **21**, 282 (1968).

[18] E. T. Arakawa *et al.*, *Health Phys. Div. Ann. Progr. Rept. July 31, 1967*, ORNL-4168, pp. 137–40.

[19] V. J. Hammond and W. C. Price, *Trans. Faraday Soc.* **51**, 605 (1955).

[20] A. Skerbele and E. N. Lassettre, *J. Chem. Phys.* **42**, 395 (1965).

[21] J. B. Birks, L. G. Christophorou, and R. H. Huebner, *Nature* **217**, 809 (1968).

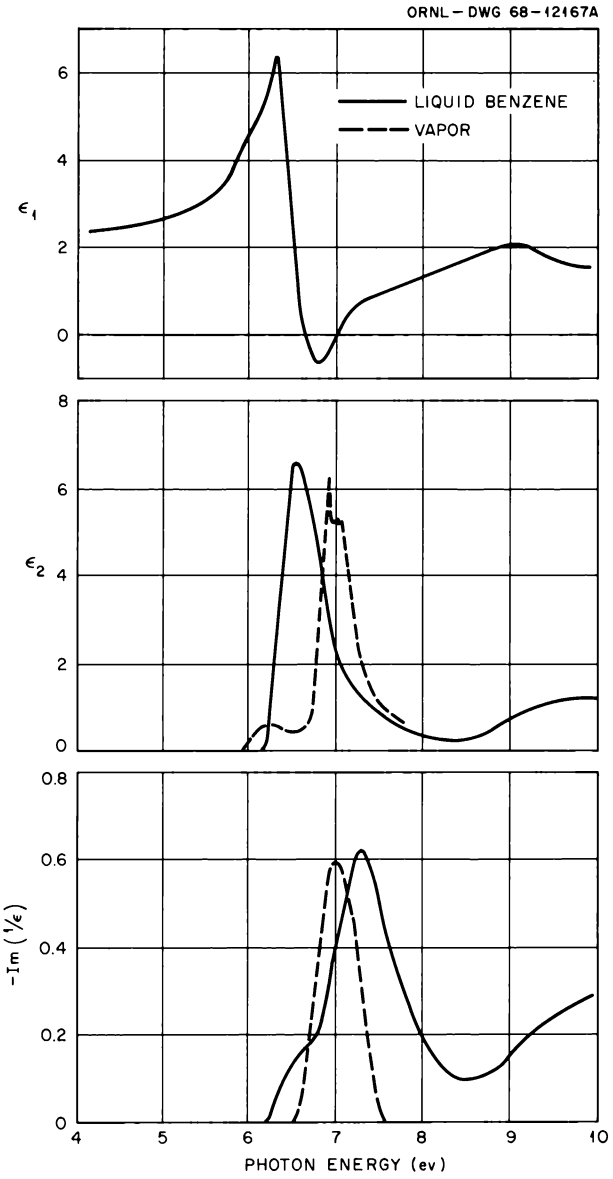

Fig. 15.5. Dielectric Constants ϵ_1 and ϵ_2 and Energy-Loss Function $-\text{Im}\,(1/\epsilon)$ for Pure Liquid Benzene. ϵ_2 for benzene vapor is from ref. 19. For comparison with $-\text{Im}\,(1/\epsilon)$ for the liquid, characteristic electron energy losses for benzene vapor are presented from ref. 20. Both quantities for the vapor are on arbitrary ordinate scales.

function $-\text{Im}\,(1/\epsilon)$ for the liquid corresponds to the structure in ϵ_2 at 6.5 ev and thus is associated with the molecular excitation of the π electrons.

The peak (Fig. 15.5) in $-\text{Im}\,(1/\epsilon)$ at 7.3 ev is thought to be associated with a volume plasma oscillation, since there is no corresponding structure in ϵ_2 and all of the conditions for a plasma resonance are satisfied at 7.3 ev. Presumably this volume plasma oscillation involves the same electrons as are involved in the molecular excitation. This is the first known observation of collective oscillations in a liquid insulator.[22] It is anticipated that liquid benzene would exhibit a strong collective resonance involving both the π and σ electrons at some energy above the 10-ev limit of the present work.

Preliminary measurements of the optical properties of Dow Corning 704 diffusion pump oil (tetramethyltetraphenyltrisiloxane) over the same energy range indicate a strong volume plasma resonance in the vicinity of 7 ev. It is possible that this collective oscillation involves the π electrons in the four phenyl (C_6H_5) groups which are attached on the extremities of the trisiloxane backbone. The optical properties of pump oils are of particular interest, since they are always present to a certain extent as contaminants in vacuum monochromators evacuated by oil diffusion pumps.

Single-Electron Excitations

The investigation of the optical properties of pure liquid hexane is of interest because of its use as a solvent for other organic liquids.

The values obtained for n and k are shown in Fig. 15.6. The values of n and k from 1160 to 1700 A were determined from the measured reflectance as a function of angle of incidence between 50 and 86°. Values of n in the region from 1700 to 3000 A were obtained from the critical-angle analysis of the reflectivity. The extrapolated value of n agrees to within experimental error with those given in the *Smithsonian Physical Tables*[23] in the region between 3900 and 6500 A.

Figure 15.7 shows ϵ_1, ϵ_2, and the loss function $-\text{Im}\,(1/\epsilon)$. The apparent shoulder in the region of 8.2 ev and the peak at 9.7 ev are associated with single-electron transitions at these energies. The structure in $-\text{Im}\,(1/\epsilon)$ appears to be associated with the structure in ϵ_2 and is thus associated with the same single-electron transitions.

The optical constants of pure liquid methyl and ethyl alcohols have also been measured over the same energy range. Further analysis of hexane and the investigation of other organic liquids are being continued to facilitate the study of the electronic properties of liquids.

---

[22] M. W. Williams *et al., Phys. Rev. Letters* **22**, 1088 (1969).

[23] *Smithsonian Physical Tables*, prepared by F. E. Fowle, p. 371, The Smithsonian Institution, Washington, D.C., 1934.

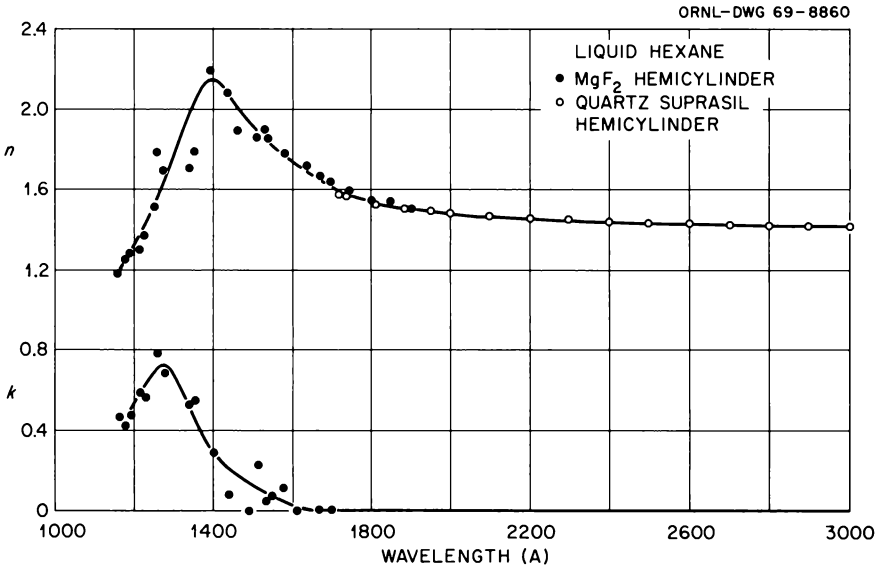

Fig. 15.6. Optical Constants n and k of Pure Liquid Hexane.

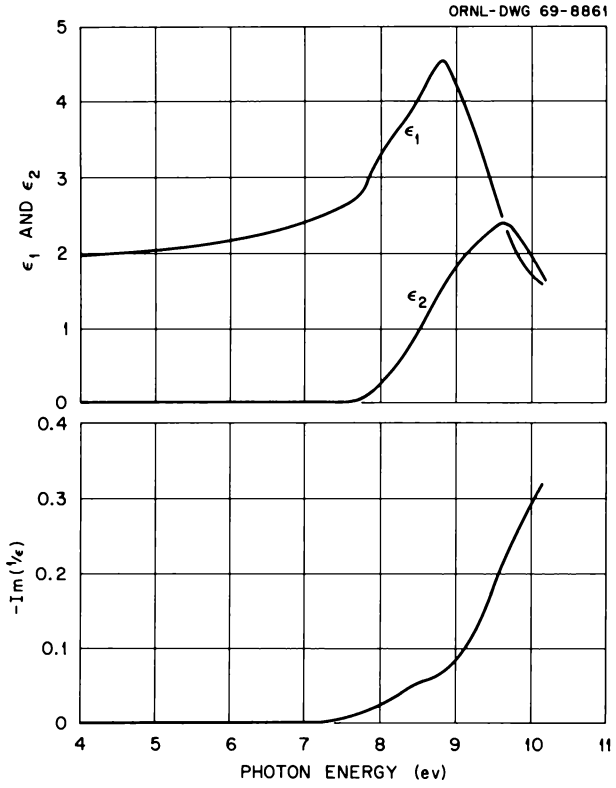

Fig. 15.7. Dielectric Constants ϵ_1 and ϵ_2 and Energy-Loss Function $-\mathrm{Im}\,(1/\epsilon)$ for Pure Liquid Hexane.

PHOTOEMISSION AND WORK FUNCTION MEASUREMENTS FOR FRESH AND CONTAMINATED METALLIC FILMS

Mg-MgO

Photoelectric emission measurements have been made in the low 10^{-8}-torr range on thin magnesium films formed by in situ vacuum evaporation. Magnesium was initially chosen because of its nearly-free-electron character, which would simplify interpretation of any structure that might appear in the photoelectron energy distributions. The very rapid contamination of the fresh magnesium surface made it necessary to study the effects of contamination on the photoelectron energy distributions.

Although the interaction chamber was left unchanged from previous studies,[24] the instrumentation was changed to permit direct plotting of the photoelectron energy densities vs retarding voltage, thus eliminating the need for computerized reduction of the data.

The general results of the photoelectron energy distribution measurements are summarized in Figs. 15.8 and 15.9. The distributions have been plotted against

[24] E. T. Arakawa *et al.*, *Health Phys. Div. Ann. Progr. Rept. July 31, 1968*, ORNL-4316, pp. 179–84.

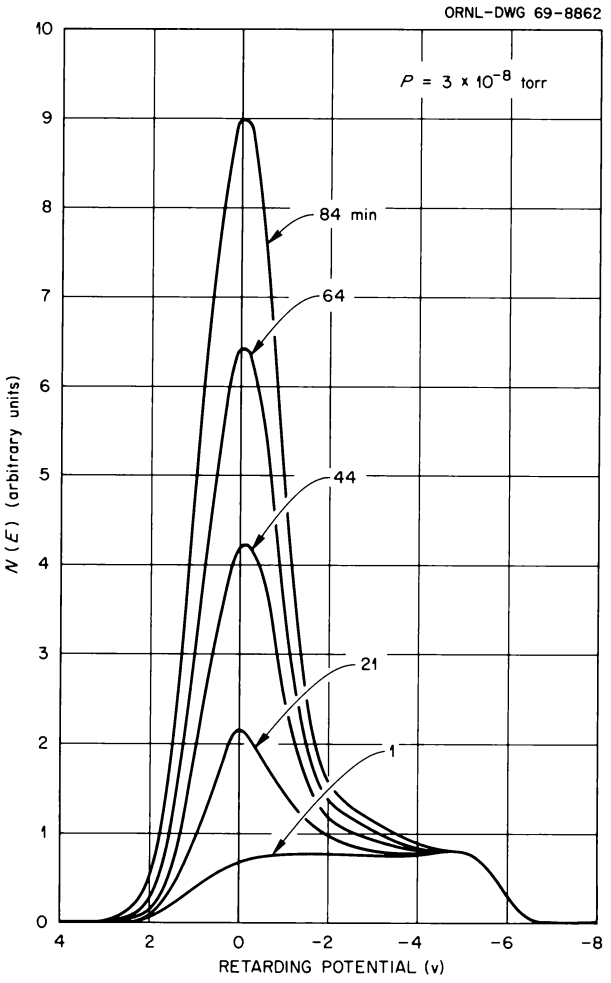

Fig. 15.8. Photoelectron Energy Distributions as a Function of Time for Magnesium ($h\nu$ = 10.2 ev).

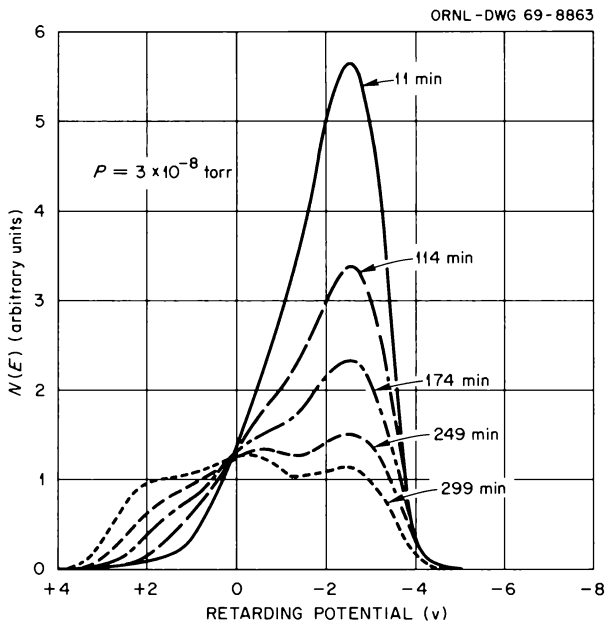

Fig. 15.9. Photoelectron Energy Distributions as a Function of Time for Magnesium ($h\nu$ = 7.64 ev).

the retarding potential since there are uncertainties about the work functions of the retarding grid and the sample. These work functions must be known to locate the distributions correctly on an energy scale. A certain amount of broadening of the distributions is introduced by the nonideal geometry of the sample and the retarding grid and by the instrumentation. In addition, any nonuniformity of the work function over the surface of the sample or the collector will lead to broadening. For a metal the total width of the distribution, including inelastic scattering of electrons on emission, should ideally be

$$\Delta = h\nu - \phi , \qquad (1)$$

where $h\nu$ is the photon energy and ϕ is the photoelectric work function of the surface. Any deviations from this width may be attributed to the broadening effects mentioned.

Figure 15.8 shows the rapid growth of a low-energy peak in the photoelectron energy distribution for 10.2-ev photons. Since the high-energy end of the distribution does not change, the increasing low-energy peak is presumed to originate from surface emission rather than electron energy loss processes. Figure 15.9 shows the time behavior of the photoelectron energy distribution for 7.65-ev photons. Compared with the 10.2-ev curves, the changes in the photoelectron energy distributions are smaller for an equivalent time period. The behavior of the photoelectron energy distributions can be interpreted in terms of the growth of an insulating surface layer on the magnesium which has a band gap between 7.65 and 10.2 ev. Thus the 10.2-ev photons would cause photoelectron emission from the surface layer, but the 7.65-ev photons would be unable to excite electrons across the band gap. In addition, the insulating surface layer would tend to cause reflection of the electrons excited in the metal by the 7.65-ev photons, thus causing the decrease in the high-energy portion of the distribution.

The change of the low-energy edge of the distributions in Fig. 15.9 can be explained by the behavior of the photoelectric work function of the film. Figure 15.10 shows the change in the photoelectric work

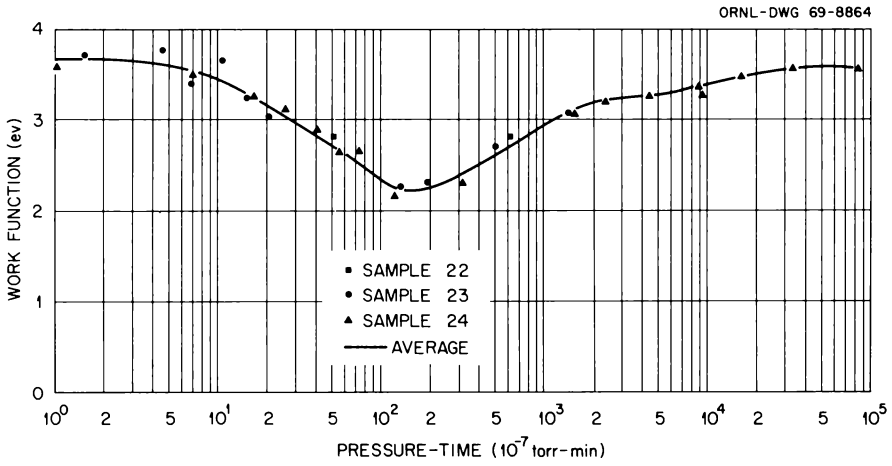

Fig. 15.10. Photoelectric Work Function of Evaporated Magnesium Film vs Time Pressure. Average data for three films.

function as a function of time-pressure. These measurements were made by observing the long-wavelength limit of the photoemission as a function of time. As the work function gets lower (Fig. 15.10), the width of the distribution (Fig. 15.9) increases in accordance with Eq. (1). The shift in the work function and the shift in the photoelectron energy distributions of Fig. 15.9 are about 1.5 ev for times of about 300 min.

In order to determine if residual gas was responsible for the changing surface conditions, separate runs were made in an atmosphere consisting of the normal background constituents plus a small amount (partial pressure 2×10^{-8} torr) of N_2, H_2O, and O_2. The total yield at 10.2 ev, which was taken as a measure of the surface contamination, is plotted in Fig. 15.11. It is clear that that of the gases tested, oxygen causes the largest increase in yield over time. This suggests that the formation of magnesium oxide on the surface is a principal contamination mechanism. The photoelectron energy distributions are consistent with this view since MgO has a band gap of about 8 ev.[25]

Currently, an effort is being made to reduce the rate of surface contamination by including a liquid-nitrogen cold trap surrounding the sample. When the contamination problem is overcome, measurements will be extended to higher energies, and electron energy loss processes will be studied.

Al-Al_2O_3

Measurements of the reflectance and photoelectron energy distribution as a function of time after film deposition have also been made for aluminum films using five different incident photon energies. For the first 24 hr after film deposition in situ the pressure was maintained at 3×10^{-8} torr and for the following 24 hr at 10^{-5} torr. Finally the films were exposed to the

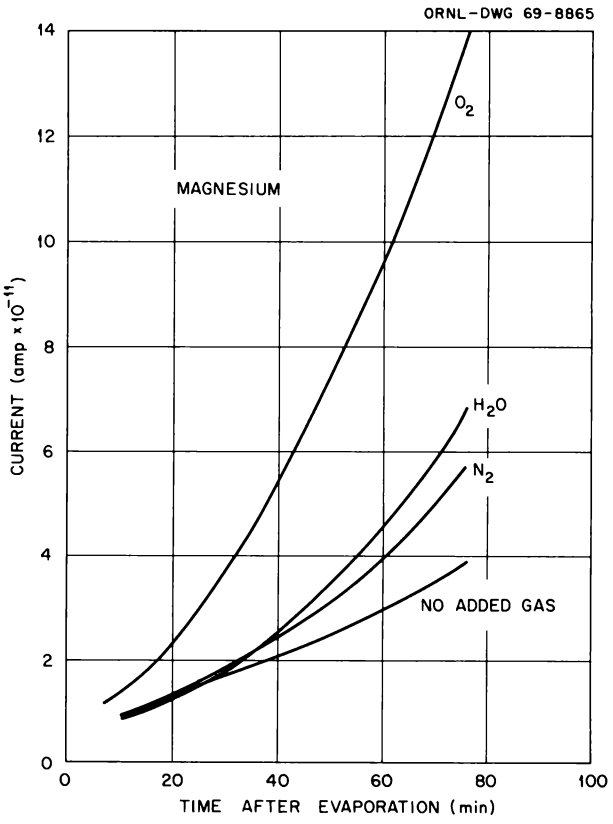

Fig. 15.11. Total Yield for $h\nu$ = 10.2 ev as a Function of Time for Various Gases Admitted to the Vacuum System. The partial pressure of each gas was 2×10^{-8} torr.

[25] M. W. Williams and E. T. Arakawa, *J. Appl. Phys.* 38, 1272 (1967).

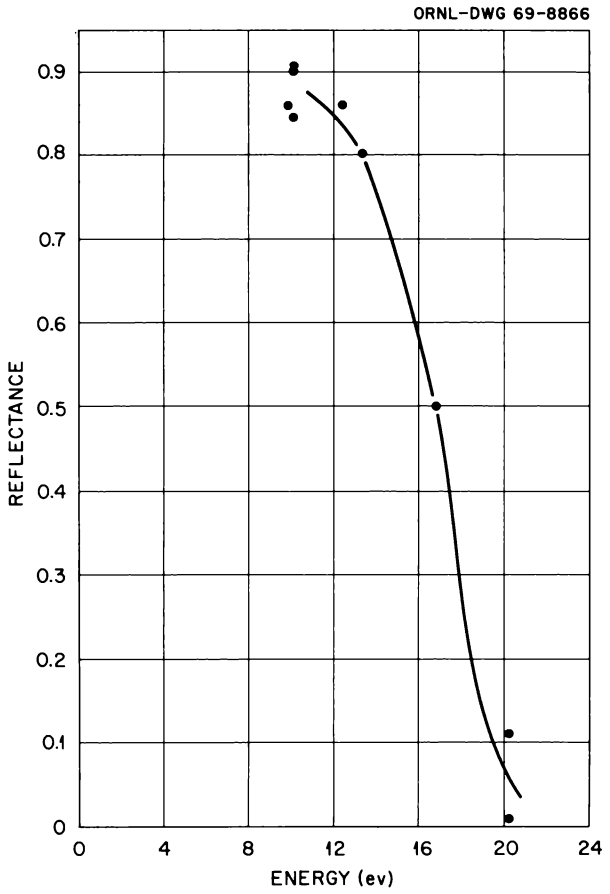

Fig. 15.12. Reflectance at the Instant of Aluminum Film Deposition vs Incident Photon Energy.

atmosphere for several days, during which time the photoelectric yields and reflectances were essentially constant for a given incident photon energy.

Figure 15.12 shows reflectance at the instant of completion of film deposition obtained by extrapolating reflectance vs time after deposition curves for each incident photon energy. Reflectance values above 15 ev, the volume plasma energy of aluminum, may be modified by interference effects, but below 15 ev the reflectance at the instant of deposition gives an indication of the quality of the film – the higher the reflectance the better the quality of the film. In this investigation only films of high quality were used. Below 15 ev the reflectances are either comparable with, or higher than, those in the literature.[26,27] The

[26]R. P. Madden, L. R. Canfield, and G. Hass, *J. Opt. Soc. Am.* 53, 620 (1963).

[27]R. C. Vehse, E. T. Arakawa, and J. L. Stanford, *J. Opt. Soc. Am.* 57, 551 (1967).

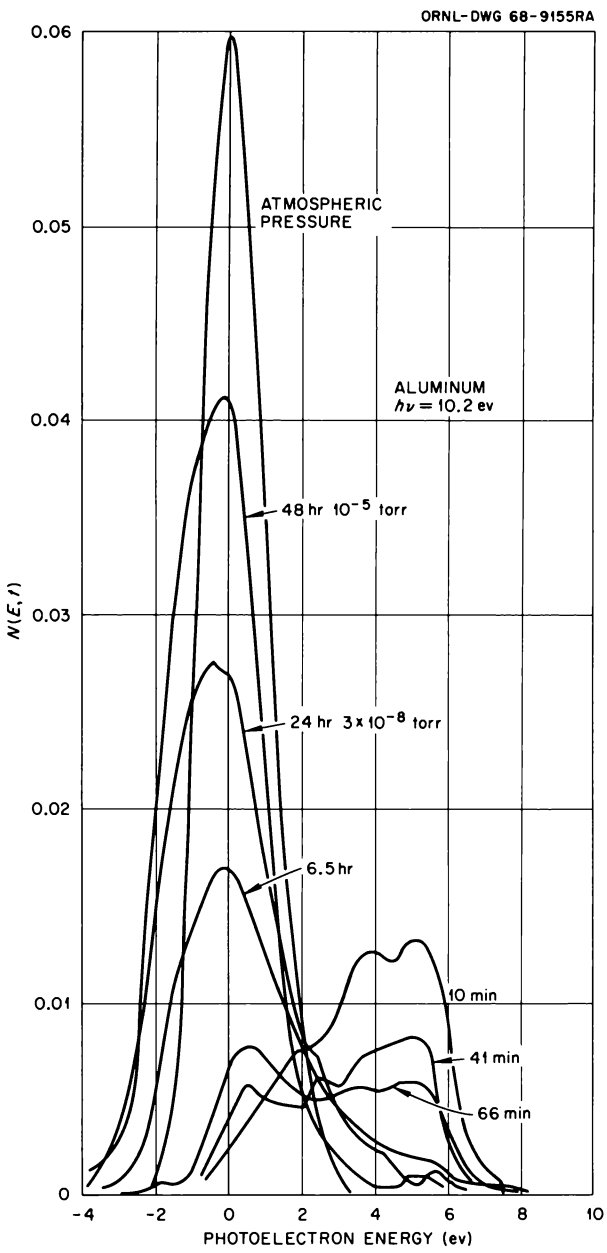

Fig. 15.13. Photoelectron Energy Distribution Curves of Aluminum at an Incident Photon Energy of 10.2 ev as a Function of Sample Age.

scatter in the reflectance values in the neighborhood of 10 ev may be associated with photon excitation of surface plasmons. This process has a strong dependence on the surface roughness of the films.

Figure 15.13 shows the photoelectron energy distribution curves for an incident photon energy of 10.2 ev. At 10 min after film deposition the energy distribution

shows the form expected for the density of electronic states of aluminum.[28] Thus we infer that the electrons originate in the aluminum and suffer little or no loss by scattering on being emitted. After the film has been maintained at 3×10^{-8} torr for just over 1 hr, the number of electrons originating in the aluminum and emerging without loss of energy has decreased, and a new contribution has appeared at a lower energy. This consists of electrons originating in the aluminum and scattered to lower energies on emerging across the surface and/or electrons originating in the surface layer. Subsequent observations, shown in Fig. 15.13, indicate that this contribution must originate principally in the surface layer, as the yield becomes too large for all the electrons to have originated in the aluminum. The threshold for photoelectron emission from the surface layer is found from Fig. 15.14 to be about 8.6 ev. This is consistent with the surface layer being Al_2O_3.[29] For amorphous Al_2O_3 the absorption edge is at 6.8 ev and for crystalline Al_2O_3 at 8.55 ev. This would indicate an electron affinity, measured from the onset of appreciable absorption, to be from 0 to 1.8 ev.

The data for approximately 10 min after film deposition are summarized in Fig. 15.14, where the curves are plotted so that the energy scale is relative to the Fermi level and represents the energy state from which the electron is emitted, that is, $E^* = E - h\nu + \phi$, where E is the energy of the emitted electron. The work function, ϕ, of aluminum has been taken as 4.2 ev. Figure 15.14 illustrates several points. It shows the consistency of the position of the lower peak in the photoelectron energy distribution and of the threshold for photoelectric emission from the oxide layer. Below 15 ev, the plasma energy of aluminum, the absorption of the incident photons in the aluminum is relatively high, and there is a contribution to the energy distribution which can be attributed to electrons originating in the aluminum and emerging across the surface without loss of energy. Above 15 ev the absorption in the aluminum becomes very small, and the number of electrons originating in the aluminum and emerging across the surface becomes negligible. For incident photon energies of 12.5 and 13.4 ev, the structure at $E^* = -7.7$ ev is interpreted as due to electrons originating in the aluminum and losing 7.2 ev in the excitation of surface plasmons as they escape

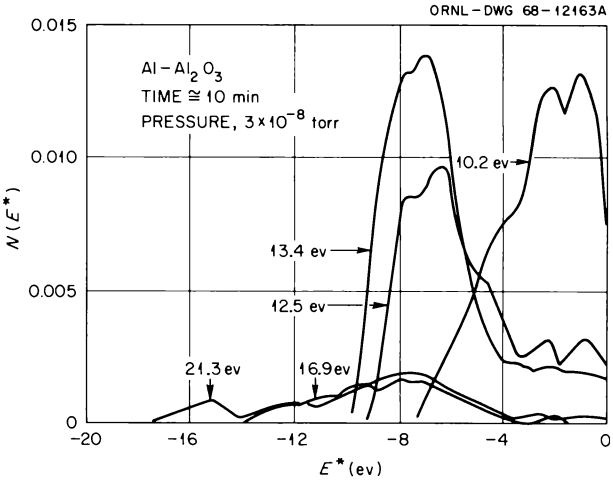

Fig. 15.14. Normalized Photoelectron Energy Distributions in Aluminum for Photon Energies from 10.2 to 21.3 ev.

across the surface. Since above 15 ev, electrons originating in the aluminum are not seen in the photoelectron energy distribution, no structure is seen corresponding to photoelectron excitation of volume plasmons in the aluminum, as has been seen in some other metals.[30]

ULTRAHIGH VACUUM ELLIPSOMETRY

A new sample chamber has been constructed and installed which provides a much greater degree of control during the evaporation and deposition of the specimen under study. The new chamber is equipped with a separate evaporator and movable baffle which can be used to optically shield the substrate surface. The evaporator is fitted with windows which permit the source to be viewed both directly and by reflection. After considerable difficulty, fused quartz entrance and exit windows were obtained which proved to be free of detectable strain birefringence.

The optimum angle of incidence was determined by carrying out a series of calculations of the extinction azimuths for the polarizing and analyzing prisms for ranges of n and k of interest, where n and k are the real and imaginary parts of the complex index of refraction respectively. The results of a typical calculation are shown in Fig. 15.15. All azimuths are measured counterclockwise from the plane of incidence looking

[28] F. Wooten, T. Huen, and R. N. Stuart, *Optical Properties and Electronic Structure of Metals and Alloys*, ed. by F. Abelès, p. 333, North-Holland, Amsterdam, 1966.

[29] E. T. Arakawa and M. W. Williams, *Phys. Chem. Solids* 29, 735 (1968).

[30] R. C. Vehse, J. L. Stanford, and E. T. Arakawa, *Phys. Rev. Letters* 19, 1041 (1967).

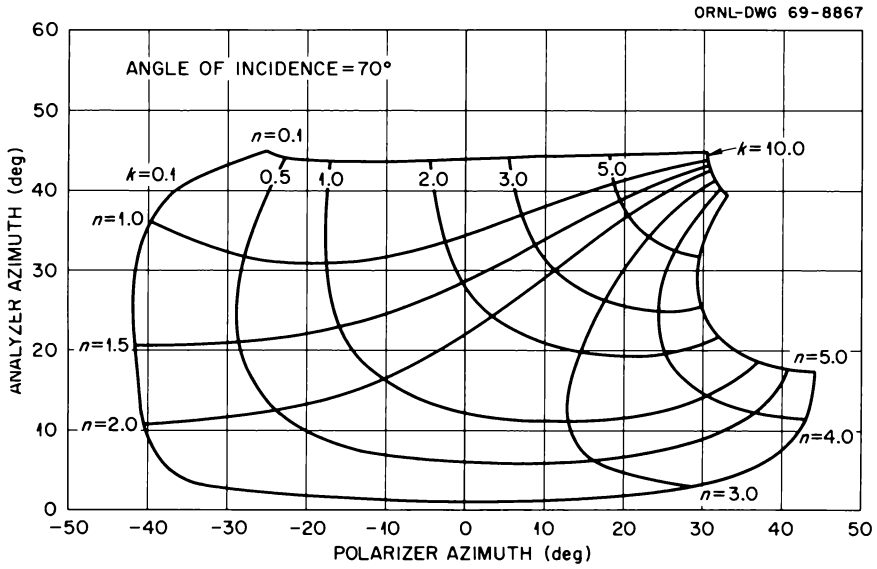

Fig. 15.15. Extinction Azimuths as a Function of the Optical Constants.

in the negative propagation direction. As can be seen from the figure an angle of incidence of 70° affords good sensitivity for values of n and k less than about 3. The optical constants of most materials will fall in this region. It has recently been shown[31] that a wave plate, in addition to introducing a phase retardation along the fast and slow axes, transmits light along these axes in a nonuniform fashion. Corrections for this nonuniformity have been added to the computer program for the reduction of ellipsometric data. An additional correction has been added to take account of small and inadvertent misalignment of the substrate surface.

A major problem has been experienced in obtaining a prism pair which exhibits a sufficiently high extinction ratio in the near-uv spectral region to obtain meaningful data. The problem apparently results from the mismatch of the index of refraction at the junction between the uv-transmitting cement and the calcite surfaces. The cement normally used, Canada balsam, provides an excellent match for the "o" and "e" rays in calcite, but it is opaque below 3300 A.

SURFACE PLASMON EMISSION

In order for surface plasmons created in a thin metallic foil to radiate, their phase velocity must be greater than the velocity of light in vacuum, or $\omega/k > c$. This can only occur if surface irregularities are present on the surface of the foil to decrease the momentum of the surface plasmons. The optical emission spectrum from aluminum films bombarded at nonnormal incidence by 80-kev electrons has been investigated experimentally. A trace of the spectrum recorded at an electron incidence angle of 60° and an observation angle of 30° is shown in Fig. 15.16. The angles are measured with respect to the foil normal with the two directions being 90° apart.

The prominent peak at about 800 A is due to volume plasmon radiation. The smaller peak near 1600 A is due to second-order diffraction of the volume peak. Because second-order diffraction appears in the region where the surface plasmon radiation is expected, it is clear that the response of the grating with regard to second-order diffraction will have to be known accurately. An additional problem is the decreasing response of the open-window photomultiplier as one goes to longer wavelengths. Any radiation peak present in the region 1200 to 2000 A may thus be difficult to detect. It is seen from Fig. 15.16 that there is a peak at 1150 A, where radiative surface plasmons are expected, but the exact location of this peak is not certain due to the corrections mentioned above. The investigation of this radiation is continuing, and future results are expected to include angular dependence, electron energy dependence, and possibly the surface condition dependence of this radiation for aluminum and other metals.

[31] R. J. Archer and C. V. Shank, *J. Opt. Soc. Am.* 57, 191 (1967).

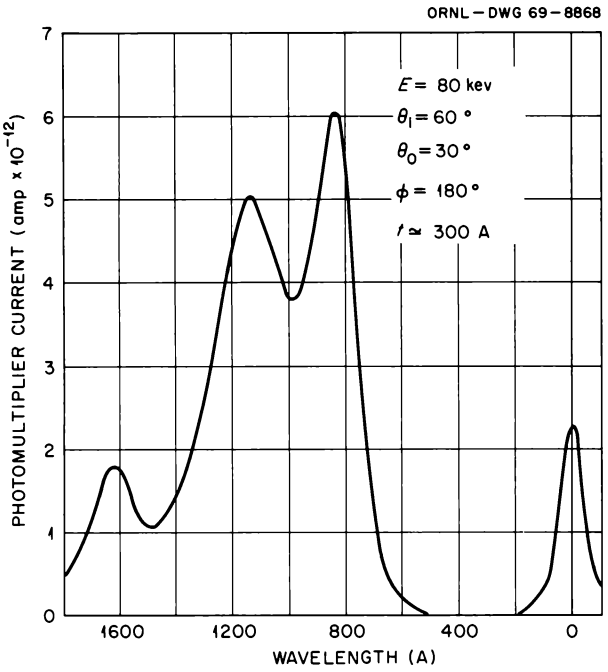

Fig. 15.16. Emission Spectrum from Aluminum Film 300 A in Thickness Bombarded by 1.0 μa of 80-kev Electrons.

SURFACE PLASMON RESONANCE EFFECT IN GRATING DIFFRACTION

Measurements of anomalies in the intensity of *p*-polarized light from concave diffraction gratings have been extended to include (1) silver layers on the grating surface, (2) varying thicknesses of dielectric materials on different grating substrates, and (3) the investigation of the ultraviolet and vacuum ultraviolet regions with aluminum-coated gratings.

Results for the anomalous peaks obtained from vacuum evaporating aluminum and gold onto the surface of the grating have been reported previously.[32] An additional layer of silver (~400 A thick) was vacuum evaporated over the aluminum and gold layers, and data are shown in Fig. 15.17 for *p*-polarized light in the wavelength region 4000 to 7500 A for the first-order on-blaze spectrum. The *s* component, as for aluminum and gold coatings, varies smoothly with wavelength for all angles θ between the source and detector. The photon energy at which the peaks occur

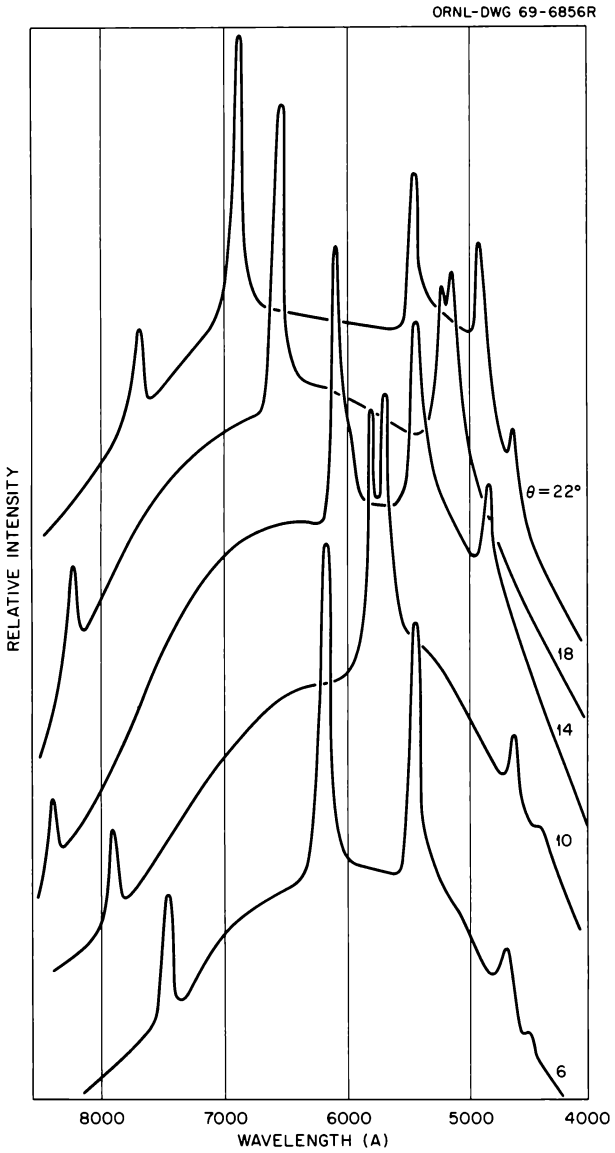

Fig. 15.17. Tungsten Emission Spectra Showing Anomalies in the *p*-Polarized Component from a Silver-Coated Diffraction Grating. The half-angle between source and detector is denoted by θ.

is plotted as a function of θ in Fig. 15.18. Peaks for the aluminum coating are included for comparison. According to the surface plasmon resonance interaction theory, the propagation vector of the surface plasmon is given by

$$K_n = \frac{\omega}{c}\sin\alpha + \frac{2\pi n}{\delta},$$

where ω is the incident photon frequency, n is a

[32] E. T. Arakawa *et al.*, *Health Phys. Div. Ann. Progr. Rept. July 31, 1968*, ORNL-4316, pp. 170–72, 189.

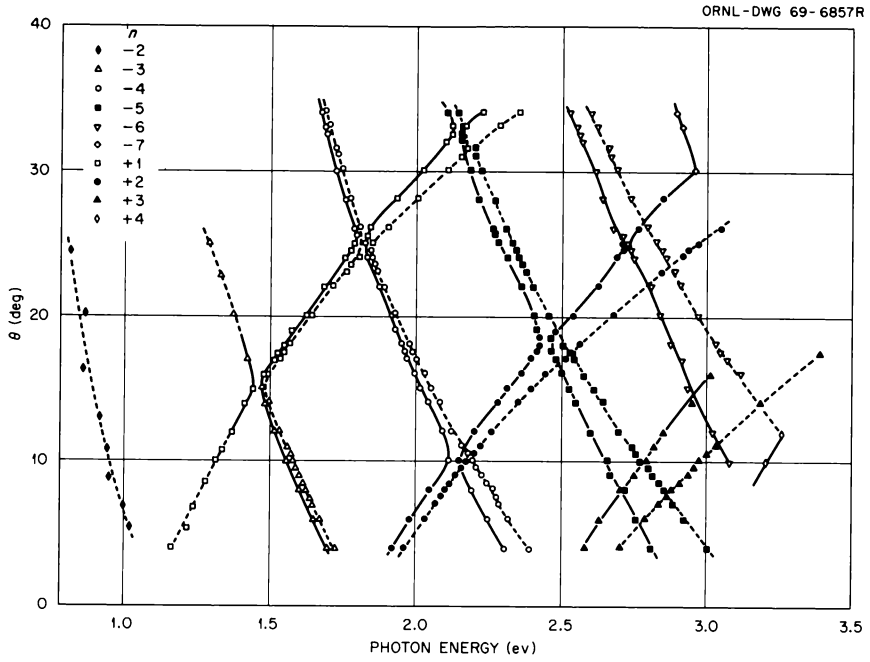

Fig. 15.18. Photon Energies of Anomalous Peaks vs θ for Silver (——) and Aluminum (– – –) Coated Gratings.

positive or negative integer, δ is the grating spacing, and α is the angle of incidence to the grating surface. The condition for an intermediate-state resonance is that the energy of the virtual surface plasmon should be equal to the energy of the incident photon, that is, $\omega = \Omega$. The Feynman diagram for this process is shown in Fig. 15.19*a*. The angle of incidence α for first-order diffraction is given as a function of the half angle θ between the source and detector by the grating equation

$$\alpha = \theta + \sin^{-1}\left(\frac{\pi c}{\delta\omega\cos\theta}\right). \tag{2}$$

Using this in the previous equation one obtains the surface plasmon dispersion relation

$$K_n = \frac{\pi}{\delta}(2n+1) + \frac{\omega}{c}\sin\theta\sqrt{1-\left(\frac{\pi c}{\delta\omega\cos\theta}\right)^2}. \tag{3}$$

In this equation the grating spacing δ and the angle θ are known, and ω can be calculated from the measured wavelength of an anomalous peak. From these parameters the second term in Eq. (3) is obtained. The first term in Eq. (3) is found by substituting the proper value of the integer n. This is done by assuming a value for n, solving for $|K_n|$, and finding the best fit of $|K_n|$ to the dispersion curve, which, for example, in the low-frequency region we expect to be very close to the light line, $\omega = cK$ (Fig. 15.19*b*). It is found that each proper n value corresponds to a given branch of the experimental data, as seen from Fig. 15.18, the positive values being for branches sloping to the right and negative values for those sloping to the left, the higher n values being found for higher-energy photons. The dispersion curve obtained in this way for silver is shown in Fig. 15.19*b*. The curves obtained earlier for aluminum and gold are included for comparison. The dotted lines are the classical dispersion curves obtained from[33]

$$K = \frac{\Omega}{c}\left[\frac{\epsilon_1(\Omega)}{1+\epsilon_1(\Omega)}\right]^{1/2} \tag{4}$$

using ϵ_1, the real part of the dielectric constants of silver, aluminum, and gold. The agreement is seen to be excellent for all values of the photon energy, except for slight deviations in aluminum at higher energies.

Small gaps can be seen in the dispersion plot at multiples of π/δ. This may be explained quantum-mechanically on the basis of the second-order self-energy of the surface plasmon. Qualitatively we may

[33] E. A. Stern, as quoted in R. A. Ferrell, *Phys. Rev.* **111**, 1214 (1958); see also R. H. Ritchie and H. B. Eldridge, *Phys. Rev.* **126**, 1935 (1962).

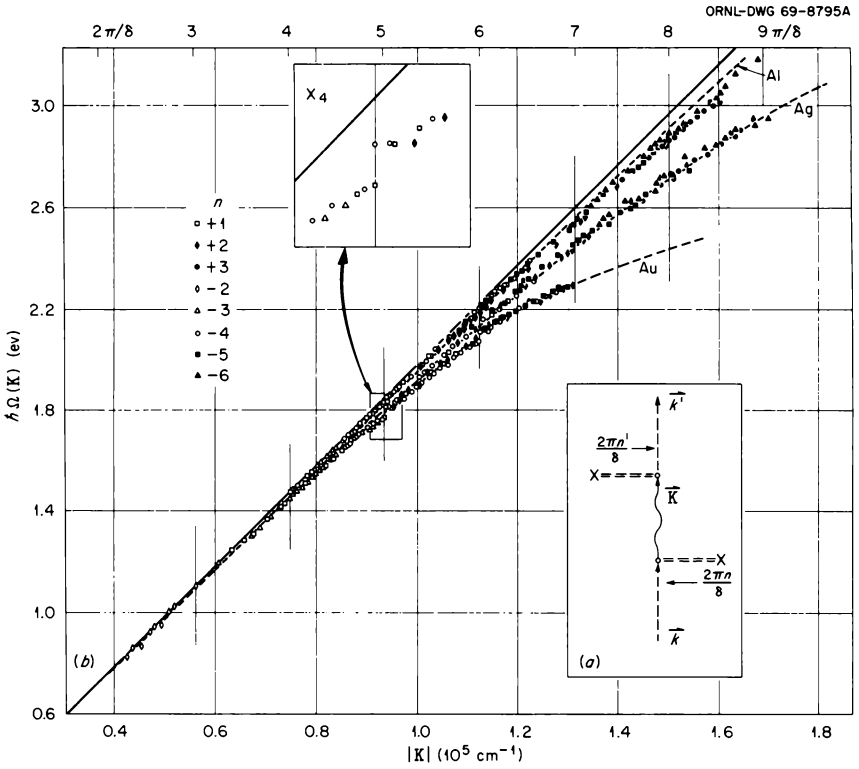

Fig. 15.19. Feynman Diagram for Photon–Surface-Plasmon–Photon Interaction (*a*) and Surface Plasmon Dispersion Curves for Al, Ag, and Au (*b*).

regard them as the interaction of surface plasmons having the same momentum but propagating in opposite directions and forming standing waves in the periodic electronic density of the grating surface. This is analogous to the well-known formation of Brillouin zone gaps in crystalline solids. Note that the gaps in the dispersion curve correspond to the gaps in Fig. 15.18, where a branch having a positive value of n makes its closest approach to one having a negative n value.

The deviations from the theoretical dispersion curve noted for aluminum are due, to a great extent, to the oxide layer that forms on aluminum but not on the other two metals. Other deviations are due to minute quantities of pump oil that adhere to the surface. The natural oxide layer may be from 20 to 40 A or more in thickness and depends on the smoothness of the surface and the purity of the metal.[34,35] Aluminum oxide layers thicker than this can be produced on an aluminum substrate by an anodization process. Here the grating is immersed into a 3% ammonium tartrate solution, and with the grating forming the positive electrode and a sheet of pure aluminum the negative one, one obtains oxide thicknesses that are proportional to the applied voltage. Layer thicknesses up to 810 A were obtained in this way, and the spectra obtained at $\theta = 25.7°$ for varying oxide thicknesses are shown in Fig. 15.20. The shift to longer wavelengths becomes more pronounced as the oxide layer thickness is increased. The wave vectors for the above data were calculated from Eq. (4) and plotted on the dispersion curve in Fig. 15.21. The solid lines are theoretical values obtained from the classical (retarded) surface-plasmon dispersion relation for a finite layer of dielectric on a semi-infinite conducting slab,

$$\epsilon = -\eta \frac{K_3}{K_2} \frac{\eta K_1 \tanh K_2 \tau + K_2}{\eta K_1 + K_2 \tanh K_2 \tau}, \qquad (5a)$$

[34] P. H. Berning, G. Hass, and R. P. Madden, *J. Opt. Soc. Am.* **50**, 586 (1960). These authors measure a maximum Al_2O_3 thickness of 22 A on a very smooth substrate after one month's exposure to air.

[35] Larger thicknesses (~40 A) have been reported for coarser surfaces by other authors: W. Walkenhorst, *Z. Tech. Physik* **22**, 14 (1941); G. Hass, *Z. Anorg. Allgem. Chem.* **254**, 96 (1947).

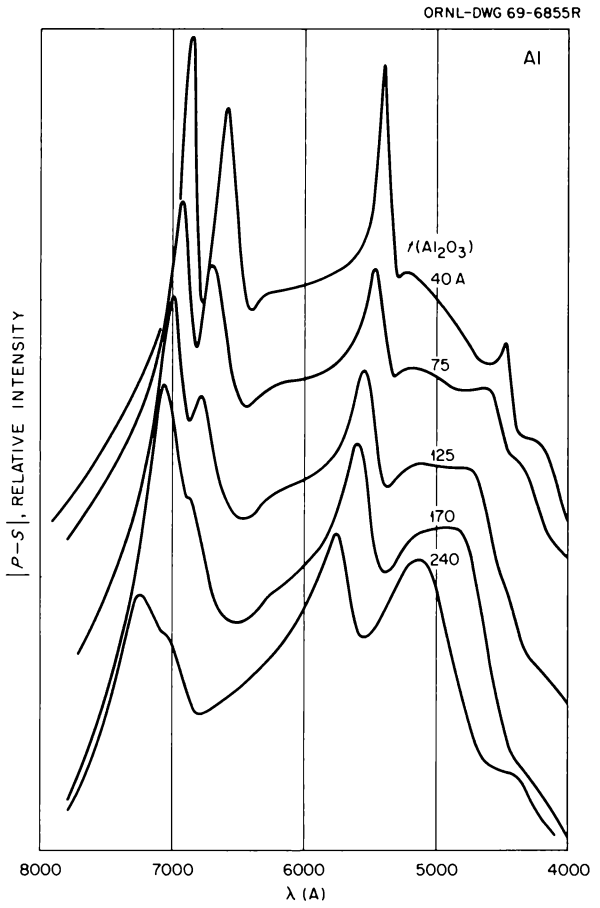

Fig. 15.20. Anomalous Peaks for Aluminized Grating Covered with Varying Thicknesses of Al_2O_3, $\theta = 25.7°$.

where

$$K_1 = \sqrt{K^2 - \omega^2/c^2},$$
$$K_2 = \sqrt{K^2 - \eta\omega^2/c^2},$$
$$K_3 = \sqrt{K^2 - \epsilon\omega^2/c^2},$$

and $\epsilon = \epsilon_1 + i\epsilon_2$ = dielectric constant of the conductor, $\eta = \eta_1 + i\eta_2$ = dielectric constant of the dielectric layer, τ = dielectric layer thickness, and $\omega = \Omega$ = surface plasmon frequency = incident light frequency. The real parts, ϵ_1 and η_1, of the dielectric constants are usually much greater than the imaginary parts, ϵ_2 and η_2. Since η_1 unlike ϵ_1 is positive, it is possible that $\eta_1\,\omega^2/c^2 > K^2$ near the light line. For this case the substitution $K_2 \rightarrow iK_2'$, where

$$K_2' = \sqrt{\eta\frac{\omega^2}{c^2} - K^2},$$

transforms Eq. (5*a*) into

$$\epsilon = -\eta\frac{K_3}{K_2'}\frac{\eta K_1 \tan K_2'\tau + K_2'}{\eta K_1 - K_2' \tan K_2'\tau}. \qquad (5b)$$

Conceptually, this means that there is no additional absorption introduced by this transformation since the imaginary number i does not appear explicitly in Eq. (5*b*), but the exponential decay of the surface wave (surface plasmon field) away from the metal surface is

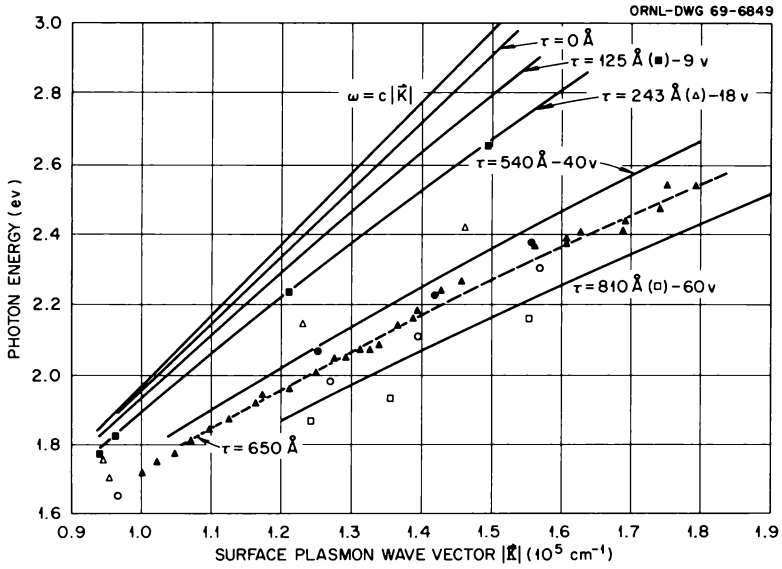

Fig. 15.21. Surface Plasmon Dispersion Curves for Spectra Shown in Fig. 15.20. Solid lines are theoretical curves; symbols ○, ×, ● are experimental values from left, central, and right portions of grating respectively.

replaced by an oscillatory decay. Also, if $\eta_1 \omega^2/c^2 > K^2$ the phase velocity of the surface wave is greater than the speed of light, $c/\sqrt{\eta_1}$, in the dielectric which corresponds to a radiating wave. However, this is true only within the dielectric; beyond the dielectric-vacuum interface, the wave amplitude again decays exponentially. Thus we may consider the surface wave here as being confined between the metal and vacuum. For the case where $K^2 > \omega^2/c^2$ there is also an exponential decay of the wave amplitude in the metal and in the vacuum, but the phase velocity is always less than light in the dielectric.

The disagreement between the experimental points and theoretical curves in Fig. 15.21 could also be due to an uncertainty in the thickness-voltage anodization curve when applied to grating surfaces since this curve was originally derived for a flat surface. In order to check this discrepancy, the anodization process was carried out on the central portion of the same grating at 40 v. This should have given a thickness of 540 A, but the experimental points from this surface agreed most closely with the theoretical curve for 650 A. The results of a third anodization, also at 40 v, on the other edge of the grating are included in Fig. 15.21. Note the difference in experimental values between the three anodizations, all done at the same voltage. One important factor in the spread of values is that the peaks are broader and not as well defined as those for the unanodized case, indicating that anodization increases the damping of the surface plasmon resonance peaks.

Better results were obtained with a second Bausch and Lomb concave reflection grating having the same line spacing and blaze angle but coated with 350 A of MgF_2. A typical spectrum of the $|p-s|$ difference signal extended into the near ultraviolet is shown in Fig. 15.22. Note that the anomalous peaks get closer together, appearing to approach a continuum, as expected, and also less intense and broader. Figure 15.23 shows the dispersion curve for the MgF_2-coated grating and the grating coated with a natural layer of Al_2O_3. The dotted lines are from Eq. (5), with the appropriate parameters for each case. Note that the agreement between theory and experiment here is excellent.

Time studies of the polarization ratio (R_p/R_s) were made in the vacuum ultraviolet after vacuum evaporating layers of aluminum, silver, and gold on the grating. The results are given in Fig. 15.24. Note that the peak appearing at 1580 A for a layer of aluminum (115 A) decreases only slightly after remaining in vacuum (10^{-6} torr) for several days, but after exposure to air for a few hours its intensity decreases and the peak shifts to longer wavelengths (1700 A at maximum). This peak

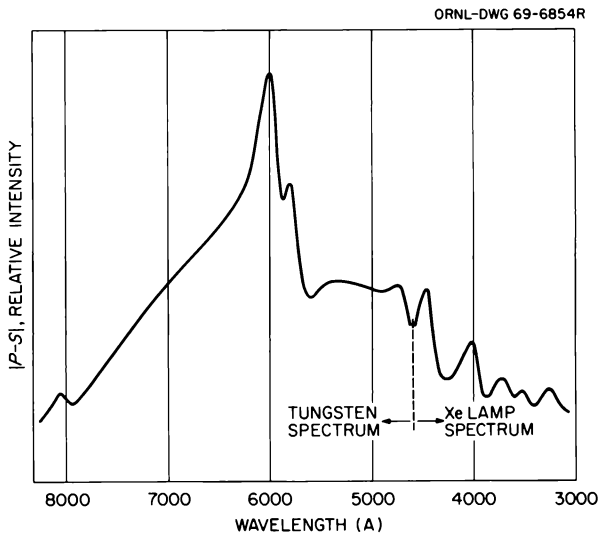

Fig. 15.22. Anomalous Peaks for Aluminized Grating Coated with MgF_2.

can be shifted back to 1580 A by recoating with a fresh layer of aluminum and the shift to longer wavelengths observed by reexposing to air. This peak has been identified with the surface plasma resonance in aluminum modified by the presence of the Al_2O_3 coating. The 1580-A peak occurs at a longer wavelength than the surface plasma peak in aluminum (1170 A) due to the small oxide layer that forms at 10^{-6} torr. Using the dispersion relation, Eq. (5), extended into the vacuum ultraviolet energy region, we obtain the set of curves (Fig. 15.25) for different thicknesses of Al_2O_3 on the aluminum substrate. Since our analysis of the observed peaks is based on the idea that momentum transfers occur at the grating surface, we expect peaks to occur at those energies that have the greatest "density of states." That is, for $|\bar{K}|$ far removed from the light line, even though the contribution to the intensity from each state may be small, the total transition probability is large if many states having the same or similar energy are involved. From Fig. 15.25 we see that the greatest density of states occurs in a region slightly below where these curves have their maxima; so the observed peaks should occur at the corresponding energies. The curve having its maximum density of states at 7.85 ev (the 1580-A peak observed at 10^{-6} torr) is for an oxide thickness of about 20 A, and the peak at 1700 A resulting from exposure to air for 24 hr corresponds to an oxide thickness of 45 to 50 A. While these values seem somewhat high for a perfectly smooth surface, they may be reasonable for the grating surface and evaporation conditions used here.

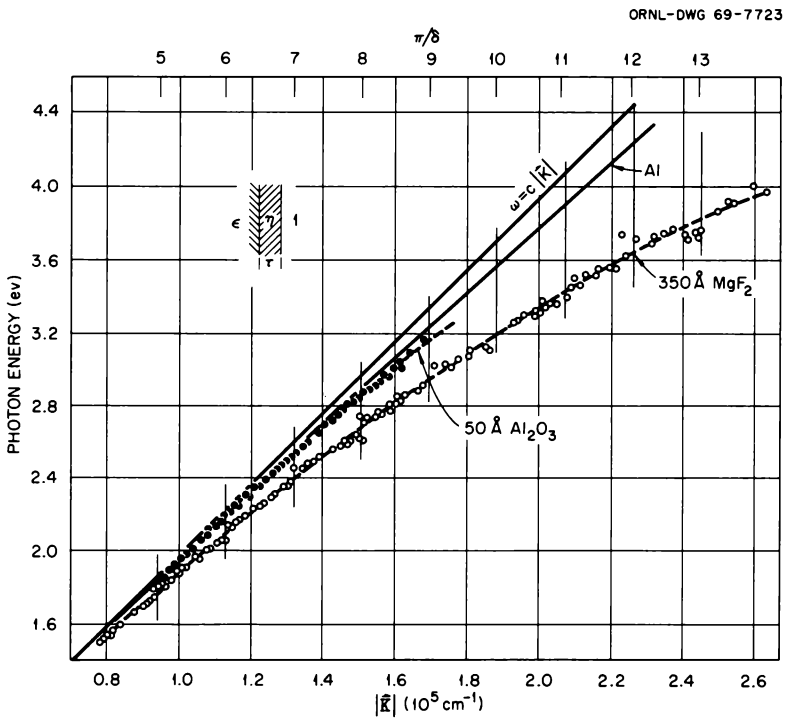

Fig. 15.23. Surface Plasmon Dispersion Curves for Al, Al_2O_3 on Al, and MgF_2 on Al.

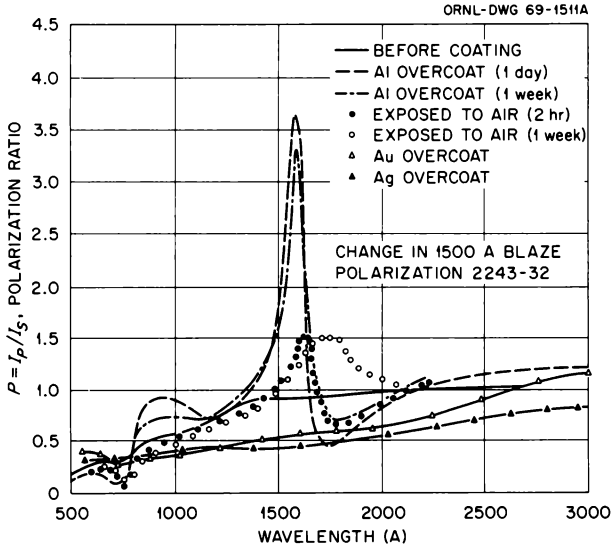

Fig. 15.24. Change in Polarization of Light from Diffraction Grating as a Function of Time after Aluminum Evaporation and for Silver and Gold Overcoatings.

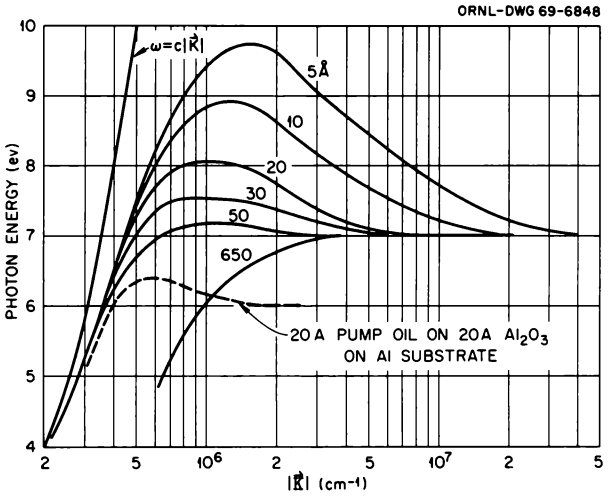

Fig. 15.25. Theoretical Surface Plasmon Dispersion Curves for Various Thicknesses of Al_2O_3 on Aluminum and for a Layer of 20 A of Pump Oil.

The first grating was also analyzed in the vacuum ultraviolet region for a 650-A Al_2O_3 coating. A peak was observed at 1750 A, which is in good agreement with the value of 1770 A obtained from the dispersion curve for this thickness. This grating was then overcoated with 150 A of aluminum which was allowed to oxidize naturally. The dispersion relation for a vacuum-oxide-metal-oxide-metal multilayer as we have here was

derived from the boundary conditions and is given below:

$$\exp(-2K_2 d) = [(A+H)\cosh K_1\tau_1 \sinh K_1\tau_2 + (D+E)\sinh K_1\tau_1 \sinh K_1\tau_2 + (B+G)\cosh K_1\tau_1 \cosh K_1\tau_2 + (C+F)\sinh K_1\tau_1 \cosh K_1\tau_2 + (B+G)\cosh(K_1\tau_1 + K_1\tau_2) + (C+F)\sinh(K_1\tau_1 + K_1\tau_2)] \div [(A+H)\cosh K_1\tau_1 \sinh K_1\tau_2 + (D+E)\sinh K_1\tau_1 \sinh K_1\tau_2 - (B+G)\sinh K_1\tau_1 \sinh K_1\tau_2 - (C+F)\cosh K_1\tau_1 \sinh K_1\tau_2], \quad (6a)$$

where

τ_1 = thickness of oxide layer next to substrate,

τ_2 = thickness of natural oxide layer,

d = thickness of aluminum overcoating layer,

η = dielectric constant of Al_2O_3,

ϵ = dielectric constant of aluminum,

$A = \eta\epsilon^3 K_0 K_1^3$, $B = \eta^2\epsilon^2 K_0 K_1^2 K_2$,

$C = \eta^3\epsilon K_0 K_1 K_2^2$, $D = \eta^4 K_0 K_2^3$,

$E = \epsilon^3 K_1^4$, $F = \eta\epsilon^2 K_1^3 K_2$,

$G = \eta^2\epsilon K_1^2 K_2^2$, $H = \eta^3 K_1 K_2^3$,

$K_0 = \sqrt{K^2 - \omega^2/e^2}$,

$K_1 = \sqrt{K^2 - \eta\omega^2/e^2}$,

$K_2 = \sqrt{K^2 - \epsilon\omega^2/e^2}$.

For values near the light line, $K_1 \to iK_1'$, where $K_1' = \sqrt{\eta\omega^2/e^2 - K^2}$, and Eq. (6*a*) transforms with

$$\exp(-2K_2 d) = [(A-H)\cos K_1'\tau_1 \sin K_1'\tau_2 - (D+E)\sin K_1'\tau_1 \sin K_1'\tau_2 - (B+G)\cos K_1'\tau_1 \cos K_1'\tau_2 - (C-F)\sin K_1'\tau_1 \cos K_1'\tau_2 - (B+G)\cos(K_1'\tau_1 + K_1'\tau_2) - (C-F)\sin(K_1'\tau_1 + K_1'\tau_2)] \div [(A-H)\cos K_1'\tau_1 \sin K_1'\tau_2 - (D+E)\sin K_1'\tau_1 \sin K_1'\tau_2 - (B+G)\sin K_1'\tau_1 \sin K_1'\tau_2 + (C-F)\cos K_1'\tau_1 \sin K_1'\tau_2]. \quad (6b)$$

The experimental dispersion curve was evaluated from Eq. (2) and is plotted in Fig. 15.26. The lower dashed line and the dotted line are Eq. (6) assuming a natural oxide layer of 40 A. The lower (tangential) mode is the only one observed in this case. Again we see excellent agreement between theory and experiment. The upper dashed line in Fig. 15.26 is the dispersion curve for a 40-A oxide layer on a semi-infinite aluminum slab.

Shifts of the anomalous peaks to longer wavelengths have been observed for other gratings that already had a natural oxide layer but were operated continuously in the monochromator for weeks or months. These shifts have been attributed to layers of diffusion pump oil that adhere to the surface of the grating. For an aluminum substrate, the dispersion relation is for a vacuum–pump-oil–oxide–metal multilayer and is given below:

$$\tanh K_1 a = \frac{-(A+H) - (D+E)\tanh K_2 d}{(C+F) + (B+G)\tanh K_2 d}, \quad (7a)$$

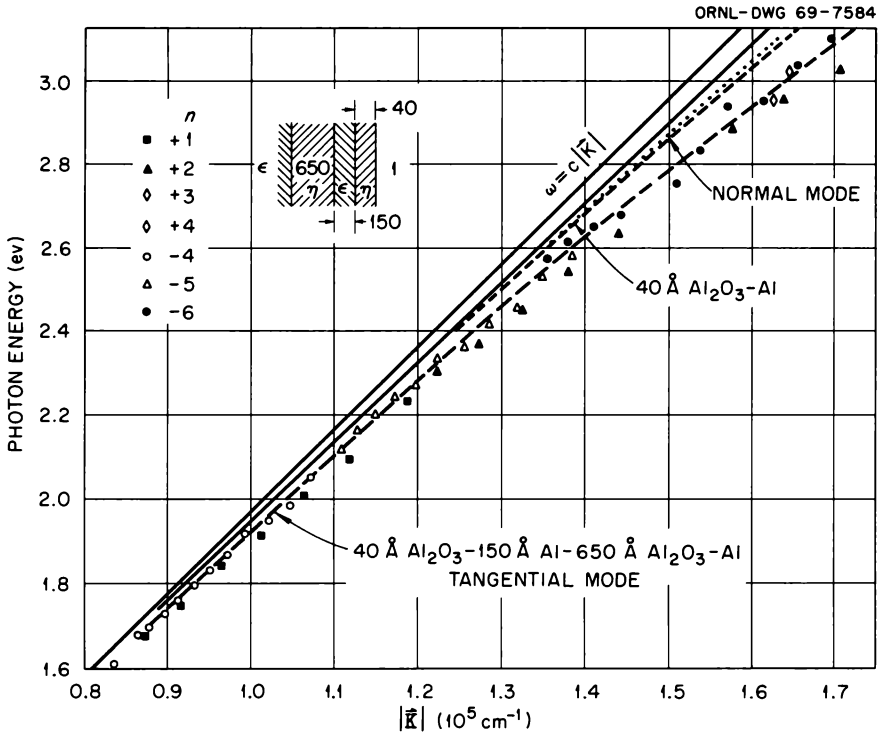

Fig. 15.26. Surface Plasmon Dispersion Curves for Multilayer Films on Aluminum Substrate.

where

a = pump oil thickness,

d = Al_2O_3 thickness,

$A = \eta\nu\epsilon K_0 K_1 K_2$,

$B = \nu^2 \epsilon K_0 K_2^2$,

$C = \eta\epsilon K_1^2 K_2$,

$D = \nu\epsilon K_1 K_2^2$,

$E = \eta^2 \nu K_0 K_1 K_3$,

$F = \nu^2 \eta K_0 K_2 K_3$,

$G = \eta^2 K_1^2 K_3$,

$H = \nu\eta K_1 K_2 K_3$,

$\eta = \eta_1 + i\eta_2$ = dielectric constant of Al_2O_3,

$\nu = \nu_1 + i\nu_2$ = dielectric constant of pump oil (DC-704),

$K_0 = \sqrt{K^2 - \omega^2/c^2}$,

$K_1 = \sqrt{K^2 - \nu\omega^2/e^2}$,

$K_2 = \sqrt{K^2 - \eta\omega^2/e^2}$,

$K_3 = \sqrt{K^2 - \epsilon\omega^2/e^2}$.

This equation also transforms like Eqs. (5) and (6) for values near the light line, but here either one or both of the values K_1 and K_2 can be imaginary, so that we obtain

$$\tan K_1' a = \frac{(A + H) - (D - E)\tan K_2' d}{(C - F) + (B + G)\tan K_2' d}, \qquad K_1' \to iK_1, K_2' \to iK_2; \quad (7b)$$

$$\tan K_1' a = \frac{-(A + H) - (D + E)\tanh K_2 d}{(-C + F) + (B - G)\tanh K_2 d}, \qquad K_1' \to iK_1; \quad (7c)$$

$$\tanh K_1' a = \frac{-(A + H) + (D - E)\tan K_2' d}{(C + F) + (-B + G)\tan K_2' d}, \qquad K_2' \to iK_2; \quad (7d)$$

where

$K_1' = \sqrt{\nu\omega^2/e^2 - K^2}$,

$K_2' = \sqrt{\eta\omega^2/e^2 - K^2}$.

Equation (7) is shown plotted as the dotted line in Fig. 15.25 for an assumed 20-A oxide layer and a 20-A pump-oil layer on an aluminum substrate. The photon energy for this situation is 6.40 ev, which is 0.6 ev less than that for an infinite oxide layer. The wavelength corresponding to 6.40 ev is 1938 A, in good agreement with the 1900-A peak observed for a grating that had been operating continuously for 27 days in the monochromator.[32]

16. Atomic and Molecular Radiation Physics

L. G. Christophorou

V. E. Anderson[1]
J. B. Birks[2]
R. P. Blaunstein[2]
D. Q. Brown[2]
Ada Carter
J. G. Carter
E. L. Chaney[3]
A. A. Christodoulides[4]
P. M. Collins[5]
J. T. Cox
C. E. Easterly[6]
J. A. Harter
A. G. Kenerly[7]
C. E. Klots
D. L. McCorkle[2]
Betty L. McGill
DeVaughn Pittman
O. E. Wagner[8]

SCATTERING OF SLOW ELECTRONS BY POLAR MOLECULES

Measurements have been made of the drift velocity of electrons through polar gases at different temperatures. An analysis of these data allowed a determination of the velocity dependence of the momentum transfer cross section σ_m for an assumed form. For $\sigma_m = A_\alpha/v^\alpha$ we obtained both A_α and the power α of the electron velocity v (see Table 16.1). From the data presented in the table it is seen that for strongly polar molecules, α is around its Born-approximation value of 2.

Other assumed forms of σ_m [e.g., $(A^2/v) + (B^2/v^2)$] enabled separation of the contribution of the various terms in the scattering potential to the measured scattering cross sections. The results obtained are under theoretical scrutiny.

Table 16.1. Values of A_α and α for Polar Molecules for $\sigma_m = A_\alpha/v^\alpha$

Molecule	Electric Dipole Moment (debye units)	A_α	α
Butyl alcohol	1.63	3.91	1.976
1-Propanol	1.66	1.036	1.887
Ethyl alcohol	1.7	48.84	2.127
Methyl alcohol	1.7	38	2.113
Water	1.85	158	2.163
Propionaldehyde	2.74	1204	2.282
Cyclopentanone	3.3	110	2.124
Acrylonitrile	3.89	7.71	1.946
Butyronitrile	4.06	345	2.172

ENERGY LOST BY SLOW ELECTRONS IN COLLISIONS WITH MOLECULES

A comprehensive study of published data on electron transport through a large number of molecular gases has been made and has allowed a determination of the mean energy lost by slow electrons ($\lesssim$3 ev) in collisions with molecules. Figure 16.1 shows the result of this study. The electron energy has been assumed to be characteristic of a Druyvesteyn function. The general features of the large fractional energy losses have been explained[9] in terms of either direct molecular excitation or indirect via the decay of low-energy compound negative-ion states. The latter are effective ways of slowing down in matter of subexcitation electrons.

---

[1] On loan from Computing Technology Center, Union Carbide Corporation, Nuclear Division.

[2] Consultant.

[3] Oak Ridge Graduate Fellow.

[4] Graduate student, University of Tennessee.

[5] Radiological Health Physics Fellow.

[6] USAEC Health Physics Fellow.

[7] On loan from Instrumentation and Controls Division.

[8] Postdoctoral Fellow.

[9] L. G. Christophorou and J. G. Carter, *Chem. Phys. Letters* 2, 607 (1968).

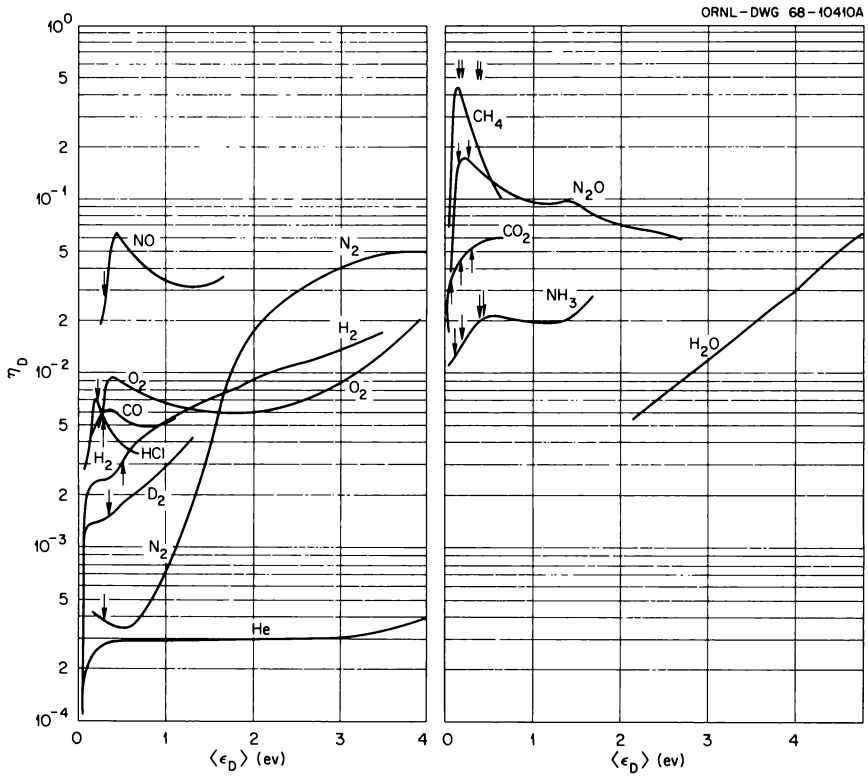

Fig. 16.1. Mean Fractional Energy Loss η_D as a Function of Mean Electron Energy $\langle \epsilon_e \rangle$.

ELECTRON ATTACHMENT AND "CARRIER GAS" ENERGY DISTRIBUTION FUNCTIONS[10]

Experimental data have been obtained which provide a basis for comparison of the electron energy distribution functions for the gases C_2H_4, N_2, and Ar, used in electron attachment studies. In Fig. 16.2 the attachment rates for *p*-benzoquinone, measured independently in each of the carrier gases C_2H_4, N_2, and Ar, are plotted as a function of the mean electron energy $\langle \epsilon_e \rangle$ for the respective carrier gas. The mean electron energies for argon have been calculated from the revised distribution functions of Ritchie and Whitesides.[11] Those for N_2 have been calculated from two sources: Carleton and Megill[12] and Engelhardt *et al.*[13] The mean electron energies for C_2H_4 have been calculated from D/μ data[14] by assuming a Maxwellian and a Druyvesteyn form of the electron energy distribution function. It is seen from Fig. 16.2 that the measured attachment rates in the three gases are in excellent agreement when plotted vs $\langle \epsilon_e \rangle$ obtained from ref. 11 for argon, from ref. 13 for N_2, and from D/μ data[14] using a Maxwellian form for the distribution function for C_2H_4. These three carrier gases with the respective distribution functions just mentioned are then recommended as standard carrier gases for electron attachment work. The attachment rates, plotted as a function of $\langle \epsilon_e \rangle$, obtained from Carleton and Megill[12] are seen (Fig. 16.2) to be in less satisfactory agreement with the argon data, for which the distribution functions are well accepted.

In addition, we have used cross-section data on the formation of O^- from N_2O in connection with the distribution functions of Ritchie and Whitesides[11] for argon and Engelhardt[13] and Carleton and Megill[12] for

[10] L. G. Christophorou, E. L. Chaney, and A. A. Christodoulides, *Chem. Phys. Letters* (in press).

[11] R. H. Ritchie and G. E. Whitesides, ORNL-3081 (1961); revised distributions by G. E. Whitesides and D. R. Nelson (private communication).

[12] N. P. Carleton and L. R. Megill, *Phys. Rev.* 126, 2089 (1962); L. R. Megill (private communication).

[13] A. G. Engelhardt, A. V. Phelps, and C. G. Rick, *Phys. Rev.* 135, A1566 (1964); A. V. Phelps (private communication).

[14] E. B. Wagner, F. J. Davis, and G. S. Hurst, *J. Chem. Phys.* 47, 3138 (1967).

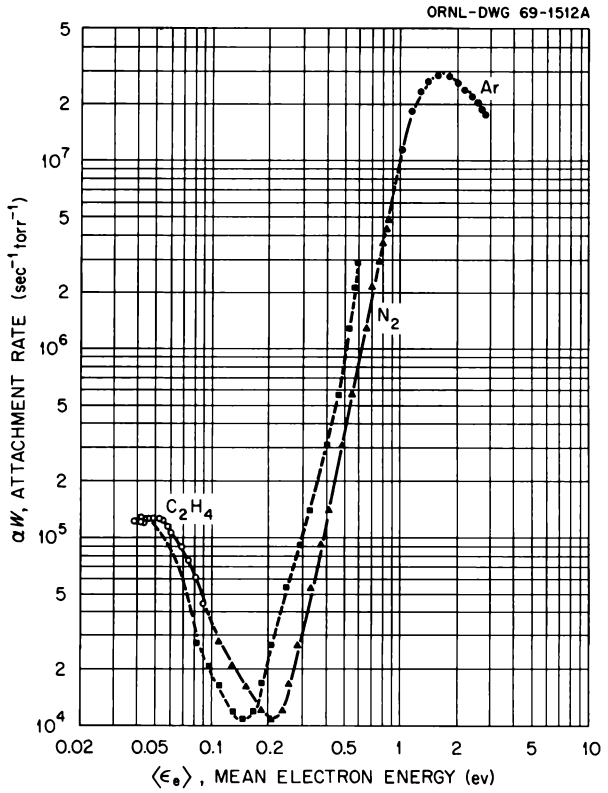

Fig. 16.2. Attachment Rate αw as a Function of Mean Electron Energy $\langle \epsilon_e \rangle$ for *p*-Benzoquinone: Comparison of Carrier Gases. ■, Carleton and Megill;[12] ▲, Engelhardt *et al.*[13]

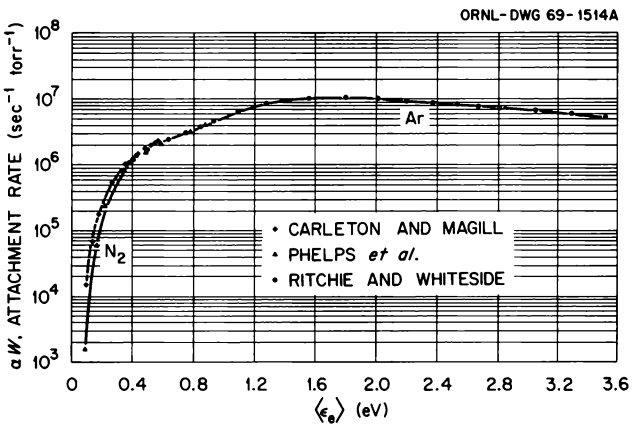

Fig. 16.3. Variation of the Attachment Rate for the Formation of O^- from N_2O with $\langle \epsilon_e \rangle$.

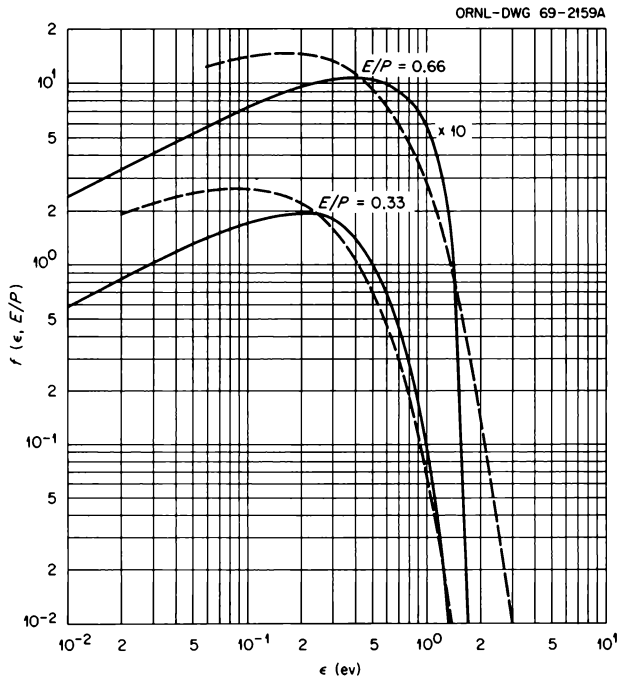

Fig. 16.4. Comparison of Distribution Functions in N_2: Carleton and Megill[12] (– – –); Engelhardt *et al.*[13] (——).

N_2 and calculated[15] the corresponding attachment rates as a function of the mean electron energy $\langle \epsilon_e \rangle$. Figure 16.3 shows these results. The attachment rates are plotted as a function of $\langle \epsilon_e \rangle$ for the respective carrier gases. It is seen again that there exists excellent agreement between the argon distributions of ref. 11 and the N_2 distributions of ref. 13.

The comparisons discussed above (Figs. 16.2 and 16.3) are valid insofar as the distribution functions have the same shape in the region of energy overlap. At low *E/P* values the distribution functions in N_2 approach a Maxwellian shape, while at higher *E/P* values the distribution functions of ref. 13 approach a shape characteristic of those in argon.

The attachment rates in N_2, plotted as a function of $\langle \epsilon_e \rangle$ obtained from Carleton and Megill,[12] do not mesh in a continuous fashion (Figs. 16.2 and 16.3) with the experimental or calculated attachment rates in argon. This result may be due to the difference in shape (Fig. 16.4) of the Carleton and Megill distribution functions.

[15] E. L. Chaney and L. G. Christophorou, *J. Chem. Phys.* (in press).

ELECTRON ATTACHMENT TO N_2O

Electron attachment to N_2O has been studied with the swarm method in mixtures with argon and nitrogen, and the measured absolute attachment rates have been combined with beam data on the production of O^- from N_2O. The cross section for the production of O^- from N_2O at 373°K has a peak value of 8.3×10^{-18}

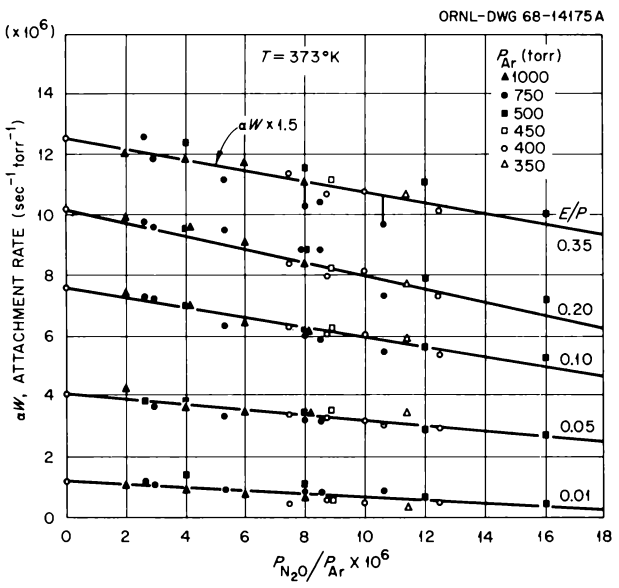

Fig. 16.5. Electron Attachment Rate of N_2O vs P_{N_2O}/P_{Ar}.

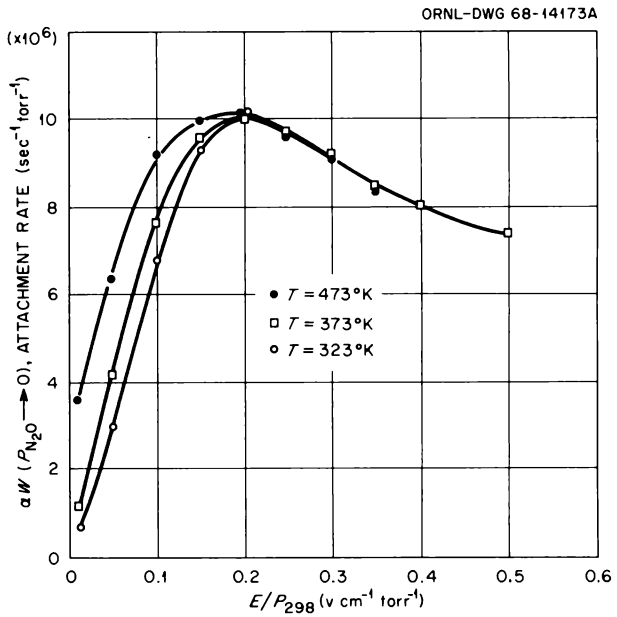

Fig. 16.6. Electron Attachment Rates of N_2O in Ar vs E/P_{298} at Various Temperatures.

cm^2 at 2.3 ev. In the energy region between ~0.2 and ~1.5 ev the cross section for the production of O^- from N_2O increases with increasing temperature ($323 \leqslant T \leqslant 473°K$), suggesting dissociative attachment from higher variational levels of N_2O. The results on mixtures with N_2 evidence the formation of N_2O^- as a primary product of electron attachment, although this ion has not been observed in mass spectrometric studies. The apparent three-body attachment rate coefficient increases with increasing electron energy, suggesting an activation energy for the formation of N_2O^-.

N_2O-Ar Mixtures

Figure 16.5 shows αw vs P_{N_2O}/P_{Ar}. The values, $(\alpha w)_0$, of αw for $P_{N_2O}/P_{Ar} \to 0$ obtained from Fig. 16.5 are plotted in Fig. 16.6 as a function of E/P for three different temperatures: 323, 373, and 473°K. It is seen that at lower energies the attachment rates increase with increasing temperature, but they are not significantly affected at the high-energy side of the dissociative attachment resonance. The results shown in Fig. 16.6 are compared with the total ionization electron beam data of Rapp and Briglia[16] as shown in Fig. 16.7. We used Rapp and Briglia's cross sections for O^-/N_2O in connection with the electron energy distribution functions for argon. The calculated attachment rates in the manner described above as a function of $\langle \epsilon_e \rangle$ are in excellent agreement with our directly measured absolute rates of electron attachment for 373°K. The agreement for the other two temperatures can be seen from the data shown in Fig. 16.7. The shapes of the O^-/N_2O curves as given by Schulz[17] and Rapp and Briglia[16] differ appreciably. We have applied the swarm-beam technique using our values for $(\alpha w)_0$ vs E/P, the argon energy distribution functions, and the O^-/N_2O ion-current curves of Schulz[17] and Rapp and Briglia,[16] and we obtained absolute electron attachment cross sections as a function of electron energy. The results are shown in Fig. 16.8 for 373°K. There is good agreement between the present data and the results of Rapp and Briglia at this temperature. It is very interesting to note that when using our attachment rates for 323°K, both the energy scales of Schulz[17] and Rapp and Briglia[16] are off by +0.22 and +0.14 ev respectively. This can very well account for the apparent appearance[17] of O^- by ~0.21 ev below the energetically allowed threshold. Further, the cross sections obtained by Rapp and Briglia[16] are slightly higher than those determined in the present work. Schulz's shape of the O^-/N_2O current seems to be more appropriate to a higher temperature than that of Rapp and Briglia.

[16] D. Rapp and D. D. Briglia, *J. Chem. Phys.* 43, 1480 (1965).
[17] G. J. Schulz, *J. Chem. Phys.* 34, 1778 (1961).

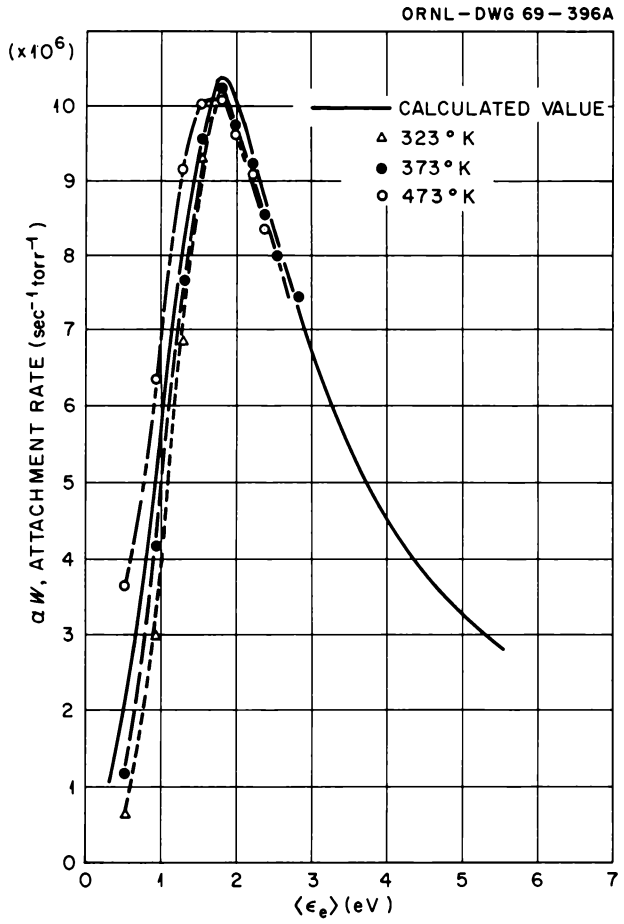

Fig. 16.7. Experimental and Calculated Attachment Rates of N_2O in Ar vs $\langle \epsilon_e \rangle$.

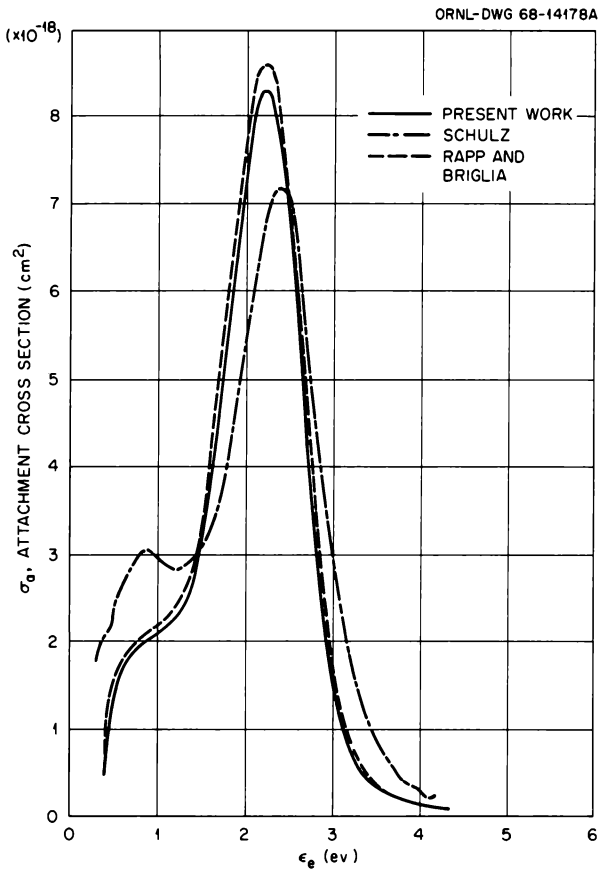

Fig. 16.8. Electron Attachment Cross Section of N_2O vs $\langle \epsilon_e \rangle$ at 373°K.

N_2O-N_2 Mixtures

We have studied N_2O in mixtures with N_2 at room temperature and at total pressures ranging from 300 to 900 torr and for N_2O pressures ranging from 0.1 to 0.9 torr. The measured attachment rates were found to increase with N_2 pressure.

Experimental evidence supports the conclusion that the attachment rates in the N_2O-N_2 mixtures for $P_{N_2} \rightarrow 0$ are characteristic of the process

$$e + N_2O \xrightarrow{k_1} O^- + N_2 \,. \qquad (1)$$

The fact that the αw in N_2O-N_2 mixtures are higher for $P_{N_2} > 0$ than those associated with process (1) can be attributed to the process

$$e + N_2O + N_2 \xrightarrow{k_3} N_2O^- + N_2 + \text{energy}. \qquad (2)$$

We may then write for the rate dn_e/dt of disappearance of electrons from the electron swarm

$$\frac{dn_e}{dt} = -\nu_a n_e = -k_1 P_{N_2O} n_e - k_3 P_{N_2O} P_{N_2} n_e \,, \qquad (3)$$

where ν_a is the attachment frequency and n_e is the electron density. From Eq. (3) we have

$$\alpha w \,(\text{sec}^{-1}\ \text{torr}^{-1}) = (\alpha w)_0 + k_3 P_{N_2} \,, \qquad (4)$$

which is consistent with the observed increase of αw with increasing N_2 pressure. Figure 16.9 shows the dependence of k_3 ($\text{cm}^6\ \text{sec}^{-1}$) on the mean electron energy. A thermal value for k_3 equal to $3 \pm 0.5 \times 10^{-33}$ ($\text{cm}^6\ \text{sec}^{-1}$) has been obtained by extrapolation. It is interesting to see the large increase in k_3 with electron energy. This suggests that although N_2O^- may be a primary electron attachment product at thermal

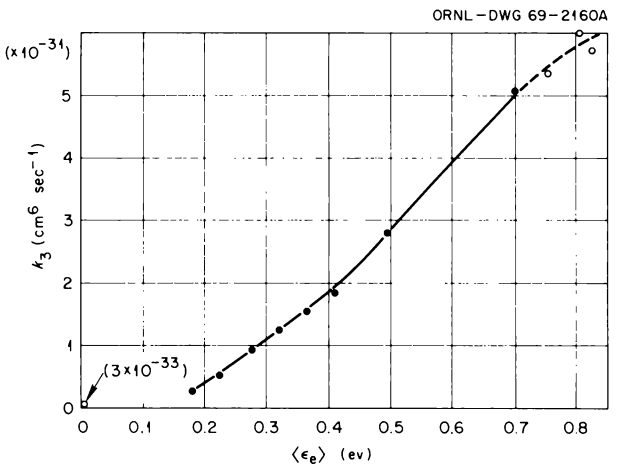

Fig. 16.9. Three-Body Electron Attachment Rate Coefficient for N_2O-N_2 Mixtures vs $\langle \epsilon_e \rangle$.

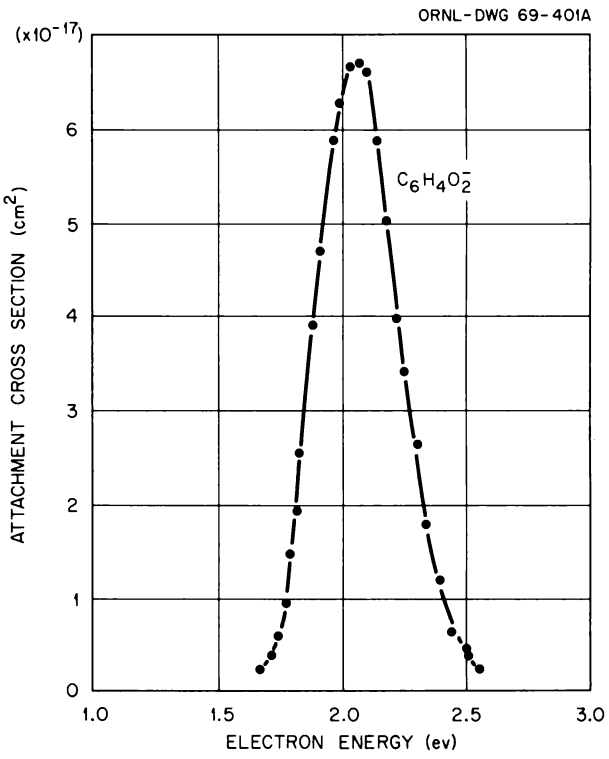

Fig. 16.10. Electron Attachment Cross Section for *p*-Benzoquinone.

energies, it seems to have a greater probability of formation at higher energies. This certainly is consistent with the argument that the formation of N_2O^- requires some activation energy,[18] which on the basis of the data in Fig. 16.9 is in the vicinity of 1 ev.

LONG-LIVED, POLYATOMIC, NEGATIVE IONS FORMED BY ELECTRON CAPTURE IN THE FIELD OF THE GROUND AND EXCITED STATES OF THE PARENT MOLECULE

Contrary to the case of aromatic hydrocarbons and other polyatomic molecules, two separate, nondissociative, electron attachment processes have been observed for *p*-benzoquinone, an oxygen-containing aromatic hydrocarbon molecule. The first peaked at thermal energies, and the second, which was much stronger, peaked at 2.1 ev (see Fig. 16.2). The second resonance had a peak cross section of 6.7×10^{-17} cm^2 (see Fig. 16.10) and has been attributed to electron attachment in the field of the lowest excited $n \rightarrow \pi^*$ transition. The parent ion lifetime was found equal to ~38 μsec at 2.1 ev. This is believed to be the first example of a long-lived, polyatomic parent negative ion formed by electron capture in the field of an excited state. Further, the measured cross sections and lifetimes have been compared theoretically with the internal molecular degrees of freedom. This allowed a direct determination of the electron affinity of the molecule in its excited state, which was found equal to ~0.5 ev. Oxygen-containing compounds are obviously of importance in biology, and a study of other oxygen-containing hydrocarbons is in progress.

ELECTRON ATTACHMENT TO AZULENE AND OTHER ORGANIC MOLECULES

Electron attachment to azulene has been studied with the electron beam and the electron swarm methods. In the latter experiments azulene was mixed in small proportions with the carrier gases C_2H_4, N_2, and Ar. A sharp electron capture resonance has been observed at zero energy; the resonance was identical in shape and position to the SF_6^- resonance, but less intense. The lifetime of the unstable azulene negative ion at zero energy was found equal to 7 μsec. In addition, beam data have shown that long-lived metastable azulene negative ions form at energies corresponding to excited electronic states of the molecule. In swarm studies, in addition to the attachment rates at thermal and near thermal electron energies, large electron attachment rates have been measured at mean electron energies up to ~3 ev, a finding which is consistent with our beam

[18] E. E. Ferguson, F. C. Fehsenfeld, and A. L. Schmeltekopf, *J. Chem. Phys.* 47, 3085 (1967).

work. From the measured rates and lifetime at thermal energies, the electron affinity of the parent molecule was found equal to 0.58 ev.

The energy dependence of the fragment ions (H^-, O^-, CH_3^-, C_2HO^-, and $C_2H_3O^-$) formed in acetaldehyde has been studied. No long-lived temporary parent negative ion has been detected for this molecule.

Other oxygen-containing compounds, such as *p*-naphthoquinone, and organic molecules are being studied.

GEMINATE SCAVENGING PROBABILITIES

The irradiation of matter at high densities produces, for the most part, only transient charge separation. Positive hole-electron recombination occurs rapidly. Nevertheless an appropriate solute can intercept members of this geminate pair if present in sufficiently high concentration. The probability of this "scavenging" is a complicated function of concentration, of the dielectric and transport properties of the medium, and of the initial charge-separation distance. It has been worked out for selected media and is illustrated by the solid line in Fig. 16.11 for irradiated cyclohexane. The dashed line represents the first-order solution, previously thought to be sufficient. Shown also are experimentally observed scavenging probabilities, taken from the literature. Their adherence at low concentrations to the theoretical curve can be used to deduce values of the parameter k/D, where k is the rate constant for the scavenging mechanism,

$$M + e \xrightarrow{k} M^- ,$$

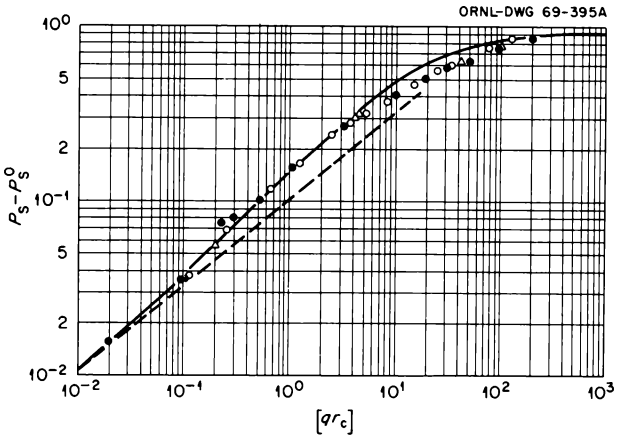

Fig. 16.11. Geminate Scavenging Probabilities as a Function of Scavenger Concentration. Experimental points: closed circles, CH_3Br; open circles, C_2H_5Br; triangles, CH_3Cl; solid line, present theory.

and D is the diffusion coefficient of the transient electron. The magnitudes found for the following solutes are (in liters mole^{-1} cm^{-2}): CH_3Br, 1.3×10^{14}; C_2H_5Br, 5.2×10^{13}; and CH_3Cl, 3.2×10^{13}. Such values are plausible but suggest a rather high diffusion coefficient for the electron.

EFFICIENCIES OF PHOTOSENSITIZED IONIZATION

When a molecule absorbs a photon of energy greater than the ionization potential, ionization may ensue. The efficiency for this process is invariably less than unity and is a sensitive function of wavelength and of the molecular species involved. These photoionization efficiencies, η_0, have been measured at selected wavelengths for a number of molecules.[19]

Similarly when these same wavelengths are used to excite electronic transitions in a suitably chosen atomic system, argon, for example, the excited atom may transfer its energy to a molecular contaminant of low ionization potential and hence give rise to ionization. This indirect mechanism is thought to underlie the phenomena of enhanced ionization in irradiated rare gases, the so-called Jesse effect. Let τ be the effective lifetime of the excited atomic system and k_s the rate constant for the sensitization mechanism:

$$A^* + M \xrightarrow{k_s} M^* + A .$$

The quantum efficiency for the sensitization process should then take the form:

$$\eta_i = \eta_i^0 \left[\frac{k_s[M]}{k_s[M] + \tau^{-1}} \right] . \qquad (5)$$

Here η_i^0 represents the ultimate efficiency with which the excited intermediate M^* leads to ionization. Measurements of η_i have been made for systems containing excited argon atoms and various molecular additives. Figure 16.12 presents a plot of η_0/η_i vs the reciprocal of C_2H_4 concentration; the argon was excited at its 1067-A resonance line. The data assume a form suggested by an inversion of Eq. (1). The effective lifetimes τ are a complicated function of the argon pressure and give rise to the variation in slopes of the indicated straight lines. This curious dependence can be understood in terms of radiation imprisonment. Most remarkable is the common intercept, corresponding to η_0/η_i^0. Invariably a value rather different than unity is

[19] C. E. Klots, *Chem. Phys. Letters* 2, 645 (1968).

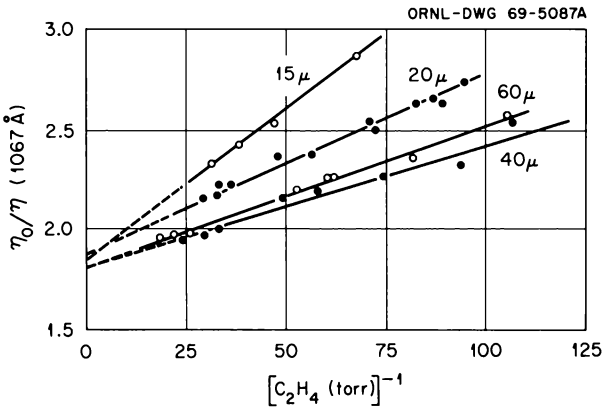

Fig. 16.12. Stern-Volmer Plot of Sensitized Ionization Efficiencies in Argon-Ethylene.

indicated. This result is unexpected, contrary to the assumption made in a great deal of earlier work, and at present is quite inexplicable.

STUDIES OF MOLECULAR COMPLEXES AND MOLECULAR INTERACTIONS

A double ultraviolet monochromator has been used in connection with an ultraviolet light source to study photophysical processes in organic liquids. The binding energies B for a number of organic excimers (excited dimers) have been determined from observations of the dependence of the luminescence spectra on temperature. The measured binding energies were found to be strong functions of sample purity, and their values for a number of benzene derivatives were found to be significantly higher than previously reported values by others. For example, our values for benzene, toluene, and ethyl benzene are, respectively, 0.39, 0.37, and 0.49 ev, while the literature values are, respectively, 0.22, 0.29, and 0.16 ev. Recent studies by Lipsky and co-workers[20] are in agreement with our findings. Detailed analyses of spectra are currently in progress. Further, the effects of oxygen on the molecular and excimer luminescence spectra and intensities have been investigated. Observations of low-temperature phosphorescence have also been made.

LIFETIMES OF EXCITED FLUORESCING SPECIES IN LIQUID BENZENE, TOLUENE, AND MESITYLENE

Measurements have been made of the lifetimes of excited fluorescing species formed in liquid benzene,

[20] S. Lipsky, private communication (1969).

Table 16.2. Lifetimes of Liquid Benzene, Toluene, and Mesitylene Excited by a Pulsed-Electron Beam

Method of Deoxygenation[a]	τ (nsec)	$\bar{\tau}$[b] (nsec)
	Benzene (99.99%)	
A(0)[c]	11.6; 12.1	12.1
	12.5; 10.9; 13.6	
A(15)	15.6; 16.3	15.9
A(30)	22.4	22.4
A(60)	24.8; 25.9	26.3
	26.5; 27.1; 28.9	
	24.9	
B(3)[d]	22.9; 23.4	23.1
B(5)	25.5	25.5
C(30)[c]	31.8; 30.7	31.2
C(45)	31; 30.2;	30.2
	29.3; 30.2	
C(60)	28.8; 29.0;	29.5
	28.9; 31.4	
C(90)	31.8	31.8
C(125)	29.8	29.8
C(125)	29.6	29.6
	29.9	29.9
		Av 30.3
	Toluene	
Sample No. 1 (99.99%)		
A(0)[c]	8.3; 8.8; 9.8	8.9
C(60)	37.8; 42.7	41.2
	43.1	
Sample No. 2 (99.99%)		
C(60)[c]	35.4	
		36.3
C(90)	36.5; 37.1	
Sample No. 3 (99.7%)		
C(0)[c]	8.8; 9.8	9.3
C(18)	28.7	28.7
C(30)	28.2	28.3
C(60)	28.4; 29.2	28.8
C(120)	28.3; 29.9	29.1
		Av 28.7
	Mesitylene	
Sample No. 1 (99.9+%)		
A(0)[c]	10.8; 10.0; 11.4	10.7
A(15)	17.3; 22.8	20.1
A(45)	36.5	36.5
A(60)	42.5	42.5
A(90)	44.1; 41.5	44.2
	44.5; 46.5	
Sample No. 2 (99.8%)		
C(90)[c]	30.3	30.3
Sample No. 3		
C(30)[c]	36.5	
		36.6
C(60)	36.8	

[a] Method A, nitrogen gas bubbling through the liquid in a nitrogen atmosphere; B, freeze-pump-thaw technique; C, high-purity helium gas passed through a porous filter into the liquid under study and the helium flow arranged such that only small-size bubbles are formed; the liquid was contained in a vacuum-tight box under a nitrogen atmosphere.

[b] Arithmetic mean.

[c] Bubbling time (min).

[d] Number of cycles.

toluene, and mesitylene at 25°C under pulsed-electron irradiation. Various samples and deoxygenation procedures have been tried, and the results are summarized in Table 16.2. They clearly show that oxygen content and sample purity are the critical factors in lifetime measurements rather than the accuracy of the method itself. The results summarized in Table 16.2 also show that other previously published data on the lifetimes of organic molecules in the liquid state or in solution may be lower than their actual values.

DEGRADATION SPECTRA CALCULATIONS

It has been recognized for some time that the degradation or slowing-down spectrum associated with radiation in matter represents the definitive link between microscopic cross-section data and the array of possible energy-absorption mechanisms. Calculations and measurements of such spectra have hitherto been confined to rather specialized media and have left unresolved a number of questions of a more general nature. The utility of the continuous approximation, the nature of energy partition among shells, and the extent of the subexcitation electron effect, for example, all remain questionable. In order to focus directly upon these problems, exact Monte Carlo calculations have been made of the degradation spectra associated with fast electrons slowing down in model systems.

Illustrative of the results obtained are those presented in Fig. 16.13. Simple hydrogen-like cross sections were used, with the atomic number Z being varied. The results pertain to an electron density of 2.70×10^{19}/cc. In each case the lower curve is that obtained in the continuous approximation model. The latter is seen to depart slightly from the more exact result at low energies, yet always to be a good approximation. Indeed even this small departure can be understood in terms of "transient effects" associated with the birth of secondary electrons.

Similar calculations on atoms containing several electron shells, each with a characteristic Z, have been performed. Most remarkably, additivity laws emerge whereby the spectrum associated with a given atom can be obtained from a superposition of curves for each electron shell.

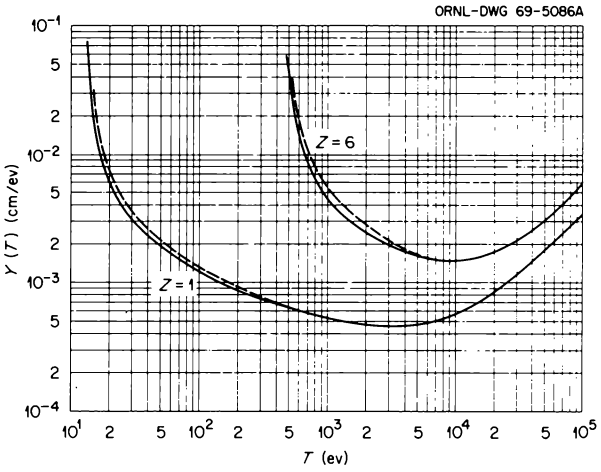

Fig. 16.13 Slowing-Down Spectra for 100-kev Electrons in Model Systems. Dashed line, exact results; full line, continuous model.

TOTAL IONIZATION PRODUCED IN GASES BY THE COMPLETE ABSORPTION OF ALPHA AND BETA PARTICLES

The average energy required to produce an ion pair in a gaseous medium irradiated by energetic radiation is known as W and is expressed in ev per ion pair. The available published information on the total ionization produced in 45 molecular gases and 5 noble-gas atoms by the complete absorption of high-energy α-(W_α) and β-(W_β) particles has been summarized, evaluated, and discussed. For molecules, W_α and W_β were found to vary with the ionization potential I of the species involved, and the relations (1) $W_\alpha = 9.8 \pm 1.67I$ and (2) $W_\beta = 5.9 \pm 1.82I$ were found to describe reasonably well the variation of W and I. The difference in the slope and the intercept between (1) and (2) was attributed to the effect of elastic collisions. For the noble gases, $W_\alpha \simeq W_\beta$ and the W vs I relation is not linear and does not pass through the origin. An analysis of the data for the noble gases suggested that a considerable amount (~30%) of the ionization may originate via the process $R^* + R \rightarrow R_2^* \rightarrow R_2^+ + e$, where R is a noble-gas atom and R_2^* is a short-lived excited transient dimeric species which may well be a noble-gas excited dimer (excimer).

17. Electron and Ion Collision Physics

R. N. Compton

V. E. Anderson[1]
Ada Carter
C. D. Cooper[2]
F. J. Davis
W. R. Garrett
J. T. Grissom[3]
J. A. Harter
G. S. Hurst[2]
W. T. Naff[4]
S. J. Nalley[3]
D. R. Nelson
P. W. Reinhardt
H. C. Schweinler
J. A. Stockdale

ELECTRON IMPACT EXCITATION OF ATOMS

In 1958 Schulz[5] introduced the trapped-electron method, in which low-energy electrons resulting from inelastic scattering of a high-energy electron beam are trapped in a shallow electrostatic well (~0.1–0.2 ev) introduced into the scattering chamber. The well depth W is a sum of two contributions,

$$W = W_0 + \alpha V_c , \qquad (1)$$

where W_0 is any contact or surface potentials present, V_c is the collector potential, and α is a proportionality constant. The parameter α is determined by observing the shift in the He^- (19.31-ev) resonance as a function of V_c, and W_0 is determined in two independent procedures, both of which are accurate to 0.01 ev. The well depth can now be determined to within 0.02 ev.

The trapped-electron technique has been used to study threshold excitation spectra of helium and argon. Figures 17.1 and 17.2 show trapped-electron and "SF_6 scavenger" spectra of the first few electronic states of argon. Cross sections for the production of slow electrons above the ionization potential have been recorded and, hopefully, will aid in our understanding of the threshold laws for ionization.

The most interesting threshold excitation spectra of the rare gases are found in the region of the two-electron excitation states. Here simultaneous excitation of two electrons may cause the incident electron to lose sufficient energy to be captured by the well, that is, e +

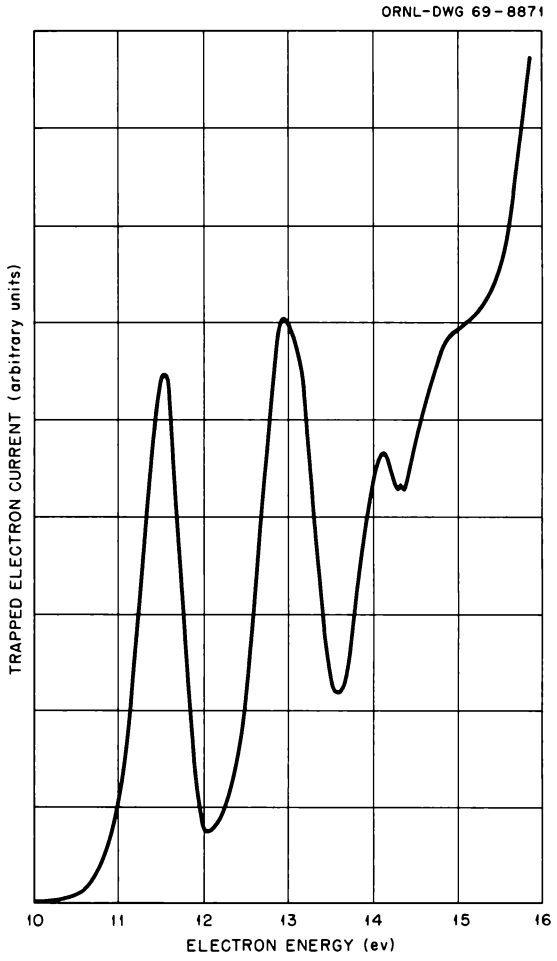

Fig. 17.1. Trapped Electron Spectrum of Argon.

[1] On loan from Computing Technology Center (ORGDP).
[2] Consultant.
[3] Radiological Health Physics Fellow.
[4] Oak Ridge Graduate Fellow.
[5] G. J. Schulz, *Phys. Rev.* 112, 150 (1958).

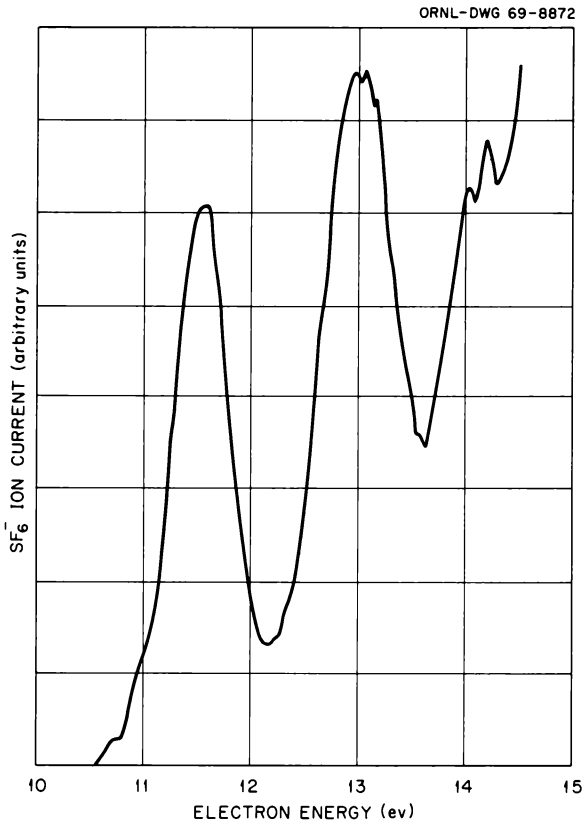

Fig. 17.2. SF_6 Scavenger Spectrum of Argon.

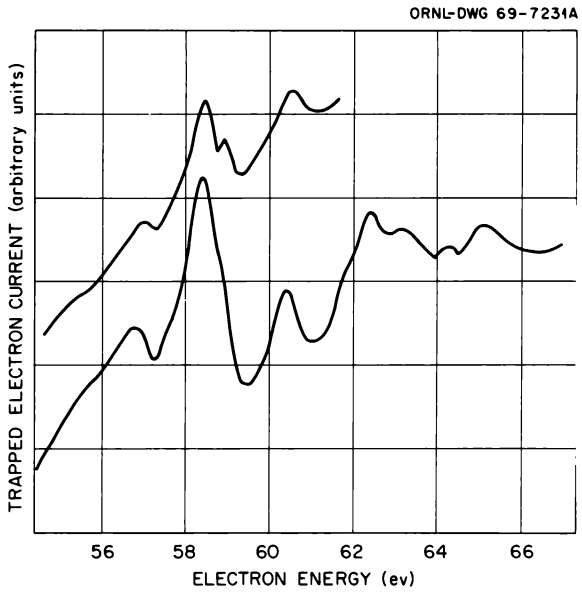

Fig. 17.3. Threshold Excitation Spectra of Helium.

He ($1s^2$) → He** ($2s,np$) + e (slow). Figure 17.3 shows the threshold excitation spectra of He in the energy range from 56 to 66 ev for well depths of 0.02 and 0.2 ev. Peaks are observed at 58.38, 58.79, 60.41, 61.93, 62.43, 63.24, 64.33, and 65.14 ev. The electron energy scale is calibrated by observing the 19.31 He^- resonance and the 19.81 ^3S He level. The dip in the spectra at 57.2 ev may be due to the known He^- (57.1-ev) transmission resonance. Recordings of the positive-ion cross section in the region of 56 to 59 ev show two very clear dispersion-type resonances at 57.2 ± 0.1 and ~58.3 ± 0.1 ev which occur at the energy position of the two known negative-ion resonances in helium.[6]

ELECTRON IMPACT EXCITATION OF MOLECULES

Threshold electron impact excitation of ammonia has been studied using both "trapped-electron" and SF_6 "scavenger" techniques.[7] Results from the two excitation studies show four well-defined peaks in the energy range from 6 to 12 ev. The scavenger technique exhibits a small peak below the first singlet state which is analogous to that previously found for H_2O and is tentatively attributed to a triplet state. Many other intense peaks were observed in the region between 12 and 19 ev, and the data indicate that dissociation as well as ionization products are occurring in this energy range. A broad peak centered at ~16.8 ev corresponds to the strong absorption observed in the vacuum ultraviolet spectrum.

Threshold electron impact excitation spectra were determined for XeF_4 and XeF_6 by means of the SF_6 electron scavenger technique.[8] Figure 17.4 shows the threshold spectrum for XeF_6. No evidence was found for a low-lying electronic triplet state in the region 1 to 3 ev. Molecular beam experiments also indicate that there are no such triplet states. The observed peaks in the XeF_6 and XeF_4 data do not correspond very well to the available ultraviolet absorption data on these molecules. The first state observed (lowest in energy), however, does agree with those reported by optical absorption. The ultraviolet spectra are broad and poorly resolved, and in the case of XeF_6 the peaks are superimposed on an intense, continuously increasing absorption. This makes the comparison difficult. Further, the probability of electric quadrupole and singlet-triplet transitions is much greater for low-energy electron impact than for photon irradiation.

[6] C. E. Kuyatt, J. A. Simpson, and S. R. Mielczarek, *Phys. Rev.* 138, 385 (1965).

[7] R. N. Compton, J. A. Stockdale, and P. W. Reinhardt, *Phys. Rev.* 180, 111 (1969).

[8] G. M. Begun and R. N. Compton, *J. Chem. Phys.* (in press).

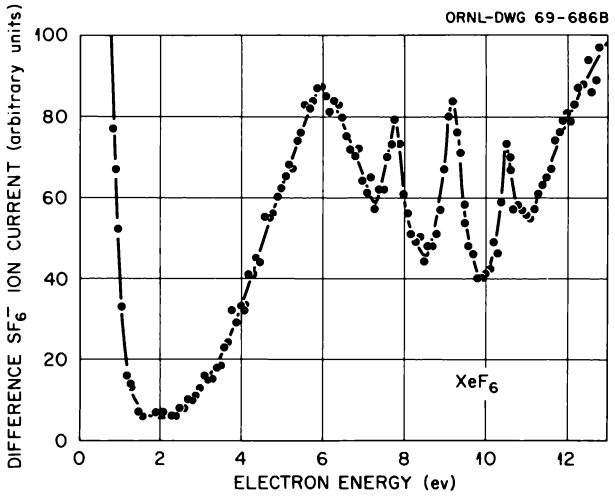

Fig. 17.4. Threshold Electron Impact Excitation Spectrum of Xenon Hexafluoride.

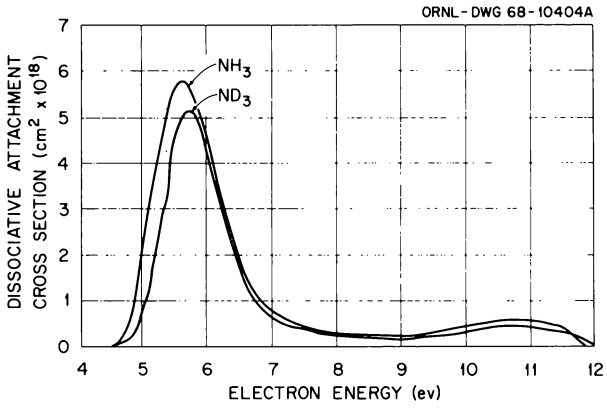

Fig. 17.5. Dissociative Electron Attachment Cross Sections for Ammonia and Ammonia-d_3.

STUDIES OF DISSOCIATIVE ELECTRON ATTACHMENT

Figure 17.5 shows dissociative electron attachment cross sections for electron collisions with ammonia and ammonia-d_3.[7] The effect of isotopic substitution on the negative-ion cross sections for ammonia ($\sigma_{NH_3}/\sigma_{ND_3} \cong 1.1$) is in the same direction but somewhat smaller than that previously found for water vapor ($\sigma_{H_2O}/\sigma_{D_2O} = 1.3$). This small isotope effect can be accounted for in a quite straightforward manner by assuming that electron capture is possible due to the breakdown of the separation of nuclear and electronic motion in the Schrödinger equation without invoking autodetachment from the dissociating negative-ion system.

Electron attachment to a series of benzene derivatives (C_6H_5X) and fluorinated benzene derivatives (C_6F_5X) produced a number of interesting observations which are summarized below. Benzaldehyde (C_6H_5-CHO) forms a temporary negative-ion resonance at ~0.7 ev with a lifetime of $\sim 10^{-10}$ to 10^{-13} sec, whereas C_6F_5-CHO attaches thermal electrons into a negative-ion state which autodetaches with a mean lifetime of roughly 40 μsec. Pentafluorobenzonitrile (C_6F_5CN) attaches thermal electrons with a lifetime also of ~40 μsec. Pentafluoroaniline ($C_6F_5NH_2$) and pentafluorophenol (C_6F_5OH) lose one fluorine and form a negative ion upon electron impact; the peak electron energies for the processes are ~0.4 and ~0 ev respectively. Pentafluorochlorobenzene (C_6F_5Cl) and pentafluorobromobenzene (C_6F_5Br) form parent ions at thermal energies with lifetimes of ~12 and 30 μsec respectively. Breakup

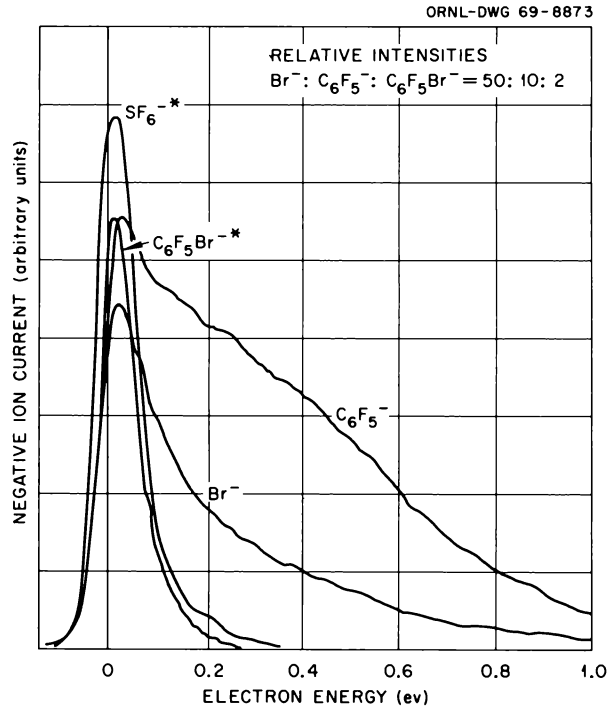

Fig. 17.6. Negative Ion Yields from Pentafluorobromobenzene (C_6F_5Br).

into a halogen negative ion and $C_6F_5^-$ occurs over a broader range of electron energies extending from 0 to ~1 ev. The breakup curves are satisfactorily interpreted in terms of competitive dissociation using quasi-equilibrium theory. Figure 17.6 shows the negative-ion breakdown curves for C_6F_5Br. In summary, fluorination of the benzene derivatives increases the electron

affinity of the molecule to the point where long-lived negative ions can be formed with the added possibility that dissociation and autodetachment are in competition with the attached electron.

TEMPORARY ATTACHMENT OF ELECTRONS TO AZULENE-h_8 AND AZULENE-d_8

The autodetachment lifetimes of a number of metastable negative ions have recently been determined by Compton *et al.*[9] The lifetime measurements are determined by sampling the number of negative ions and neutrals resulting from autodetachment for various ion residence times in the flight tube of a time-of-flight mass spectrometer. After drifting a time t, some of the metastable ions decay by autodetachment, and the remaining molecular negative ions, $N^-(t)$, and neutrals, $N^0(t)$, are separated in time by a potential barrier and then detected. The time during which autodetachment occurs is varied by changing the ion-acceleration voltage. Thus the lifetime can be found for each time of flight and the average, τ_{av}, taken, or from the slope of a plot of $-\ln[1 - N^0(t)/N_0]$ vs the measured time of flight, τ_{slope}.

At low sample gas pressures ($<10^{-5}$ torr) the molecular negative ions of azulene-h_8 or azulene-d_8 occurred only for electrons incident with energies less than 0.1 ev. The width and slope of the $C_{10}H_8^{-*}$ or $C_{10}D_8^{-*}$ ion current as a function of energy are identical to those of the SF_6^- ion current, indicating that attachment occurs for electron energies $\leqslant 0.05$ ev.

Negative-ion lifetime measurements of azulene-h_8 and azulene-d_8 yielded the following results. For $C_{10}H_8^{-*}$, $\tau_{av} = 8.24 \pm 1.1$ μsec and $\tau_{slope} = 8.57$ μsec, and for $C_{10}D_8$, $\tau_{av} = 8.18 \pm 0.68$ μsec and $\tau_{slope} = 8.13$ μsec. Thus within experimental error the negative-ion lifetimes of $C_{10}H_8^{-*}$ and $C_{10}D_8^{-*}$ formed by thermal-electron attachment are the same.

The existence of long-lived negative ions has been satisfactorily accounted for by assuming that the excess energy is distributed among all of the various vibrational modes of the molecule.[9] Microscopic reversibility predicts that the rate of attachment, k_a, is connected to the rate of autodetachment, k_d, by $k_a = (\rho^0/\rho^-)k_d$, where ρ^0 and ρ^- are the density of states of the free electron and neutral molecule and the negative ion respectively. Since ρ^- is inversely proportional to the product of the vibrational frequencies, it is expected that the ratio of k_a/k_d for azulene-h_8 would be greater than for azulene-d_8. Wentworth[10] finds no significant difference in the attachment rate for $C_{10}H_8$ and $C_{10}D_8$. Thus the lifetime data presented here suggest that C-H or C-D vibrations are not effective in trapping the electron and that C-C skeletal vibrations and possible ring distortion act to trap the electron.

NEGATIVE-ION FORMATION IN SELECTED HEXAFLUORIDE MOLECULES

Slow electrons are known to attach to sulfur hexafluoride with a cross section approaching the theoretical maximum for s-wave capture. A mass spectrometer search for negative ions of hexafluoride molecules formed from atoms directly below sulfur in the same column in the periodic chart yielded little, if any, ion current; collisions of low-energy electrons with selenium and tellurium hexafluoride produced no detectable SeF_6^- or SeF_5^- and TeF_6^- or TeF_5^-.

Molybdenum hexafluoride (MoF_6) was found to attach electrons dissociatively and nondissociatively as shown in Fig. 17.7. Electron attachment appears to proceed through two resonances separated by ~0.5 ev. Dissociation of the peak at ~0.8 ev into F^- occurs infrequently, and MoF_4^- occurs only for energies above ~4 ev.

Uranium hexafluoride (UF_6) attaches electrons dissociatively at ~2 ev, leading to $UF_5^- + F$, and direct attachment to form a long-lived UF_6^- does not occur. However, UF_6^- is formed by charge-exchange reactions from UF_5^- or SF_6^-. Figure 17.8 shows a plot of the ion current yields of UF_6^-, UF_5^-, and SF_6^- resulting from a mixture of UF_6 and SF_6. The UF_6^- ion current at ~0 ev is due to charge exchange with SF_6^- and increases linearly with increasing concentration of SF_6. The UF_6^- ion current at ~2 ev occurs as a result of charge exchange of UF_5^- with UF_6. Charge-exchange rates for these reactions were determined by observing the increase in secondary ion currents as a function of reaction time in the ion source (see Table 17.4).

Collisions of slow electrons with xenon hexafluoride result in extensive dissociation into a number of negative-ion products. A scan of the negative-ion mass spectrum of XeF_6 revealed the following ions: XeF^-, XeF_2^-, XeF_3^-, XeF_4^-, F_2^-, and F^-, with F_2^- being the most abundant.

[9] R. N. Compton *et al.*, *J. Chem. Phys.* **45**, 4634 (1966); R. N. Compton and L. Bouby, *Compt. Rend.* **264**, 1153 (1967); W. T. Naff, C. D. Cooper, and R. N. Compton, *J. Chem. Phys.* **49**, 2784 (1968).

[10] W. E. Wentworth (private communication).

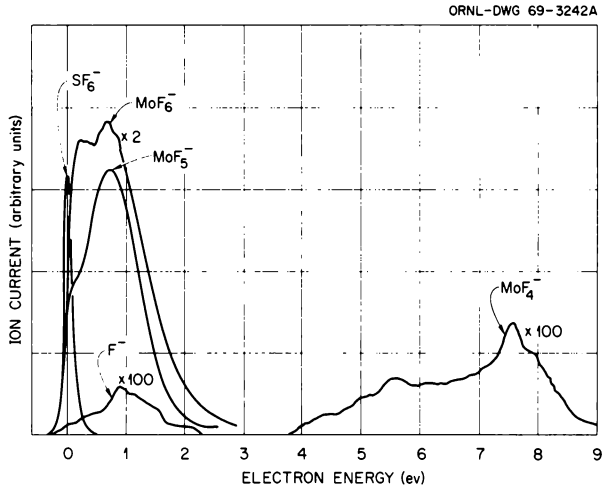

Fig. 17.7. Negative Ion Yields from Molybdenum Hexafluoride as a Function of Electron Energy.

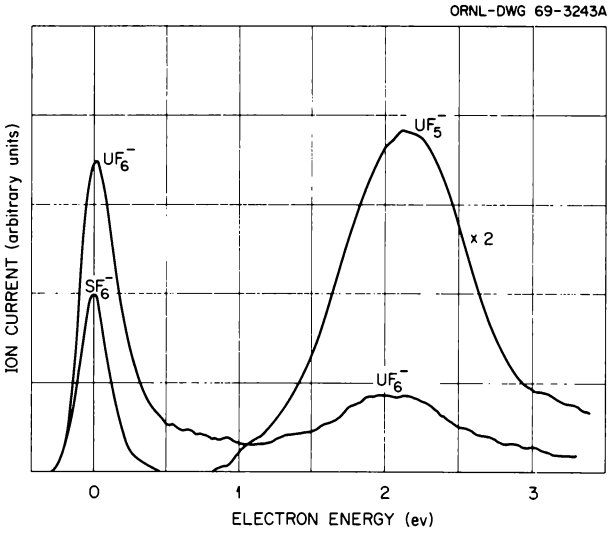

Fig. 17.8. Negative Ion Yields from a Mixture of UF_6 and SF_6 (~2:1) as a Function of Electron Energy.

ATTACHMENT RATES OF THERMAL ELECTRONS BY SF_6 IN DIFFERENT CARRIER GASES

Studies of thermal-electron attachment have led to rather diverse rates being reported for the same molecule by different investigators. The absolute thermal-electron attachment rates reported for SF_6 vary by a factor of 10^5, as shown in Table 17.1. Thus, a study of

Table 17.1. Summary of Previously Reported Electron Attachment Rates for SF_6

Attachment Rate (sec^{-1} $torr^{-1}$)	Temperature (°K)	Carrier Gas	Method
10×10^9	300	Helium	Microwave[a]
8.7×10^9	300	Helium	Microwave[b]
7.8×10^9	300	10% CH_4 + 90% Ar	Pulse sampling[c]
5.9×10^9	300	CH_4	Swarm (DDD)[d]
1.25×10^9	300	C_2H_4	Swarm[e]
9.7×10^4	380	C_7H_{14}	Competition experiment[f]
9.3×10^3	300	Xenon	Microwave[g]

[a]B. H. Mahan and C. E. Young, *J. Chem. Phys.* **44**, 2192 (1966).

[b]C. E. Young, UCRL-17171 (September 1966).

[c]E. Chen, R. D. George, and W. E. Wentworth, *J. Chem. Phys.* **49**, 1973 (1968).

[d]D. R. Nelson and F. J. Davis, *Bull. Am. Phys. Soc.* **14**, 258 (1969).

[e]R. N. Compton *et al.*, *J. Chem. Phys.* **45**, 4634 (1966).

[f]G. R. Freeman, *Radiation Res. Rev.* **1**, 1 (1968). [It is not clear how this attachment rate value was calculated from the data of Holtslander and Freeman, *J. Chem. Phys.* **71**, 2562 (1967).]

[g]J. B. Hasted and S. Beg, *Brit. J. Appl. Phys.* **16**, 74 (1965).

thermal electron attachment by SF_6 in different carrier gases under identical experimental conditions was undertaken to show whether different carrier gases are in part responsible for the discrepancies in reported attachment rates.

Beam experiments have shown that a resonance two-body-capture process produces SF_6^- in an unstable excited state,

$$e + SF_6 \underset{k_2}{\overset{k_1}{\rightleftharpoons}} SF_6^{-*}, \tag{2}$$

which autodetaches with a lifetime k_a^{-1} of approximately 25 μsec.[11] Such a long lifetime raises the possibility that a third body M (carrier gas) colliding with $SF_6^{-1}*$ can promote either electron detachment from or stabilization of the ion through the processes

$$SF_6^{-*} + M \overset{k_2}{\rightarrow} SF_6 + M + e$$
$$\rightarrow k_3\ SF_6^- + M. \tag{3}$$

If the lifetime of the SF_6^{-*} ion against autoionization is long compared with the time between collisions with M (which is most certainly true for SF_6), then the

[11]R. N. Compton *et al.*, *J. Chem. Phys.* **45**, 4634 (1966).

Table 17.2. Summary of Thermal Energy Attachment Rates for SF_6 in Different Carrier Gases from the Present Investigation

αw (sec^{-1} $torr^{-1}$)	Carrier Gas	Number of SF_6^- Carrier-Gas Mixtures	Range of SF_6 Concentrations (ppm)
$6.90 \pm 0.10 \times 10^9$	He	3	2.1–5.0
6.4	1% CH_4 + 99% Ar	1	2.9
6.5	11% CH_4 + 89% Ar	1	6.3
7.1	H_2	1	23.9
6.7	N_2	1	2.5–2.7
7.0	CO	2	5.2–6.1
3.74 ± 0.03	CO_2	3	1.1–2.5
5.86 ± 0.07	CH_4	6	11.7–24.2
6.8	CF_4	1	17.7
6.8	C_2H_2	1	16.7
2.46 ± 0.07	C_2H_4	3	6.4–24.4
6.0	C_2F_6	1	18.7
5.8	*cis*-C_4H_8	1	11.3
6.5	C_4H_{10}	1	17.0

measured rate of loss of electrons is given by

$$-\frac{d[e]}{dt} = \frac{k_1 k_3}{k_2 + k_3} [SF_6][e] = (\alpha w)[SF_6][e] , \quad (4)$$

where the brackets indicate concentration. Thus the measured attachment rate, αw, is pseudo-first-order in that no concentration dependence on the carrier gas is observed, but there is a dependence of αw on the nature of M according to the relative rates k_2 and k_3 of detachment and stabilization processes. Mahan and Walker[12] have used the above general stabilization-detachment model to explain their attachment rates for nitrogen dioxide.

There are several alternative mechanisms which would also yield two-body attachment dependence upon the nature of the third body: third body M could (1) promote dissociation of SF_6^{-*} (e.g., into SF_5^- and F); (2) undergo an ion-molecule reaction leading to some stable product negative ion (in either case the permanent removal of the electron from the swarm depends upon the third body); or (3) temporarily form negative ions, trapping electrons into a state whose lifetime τ is inversely proportional to the density of M.[13,14] Thus, temporary attachment by M would effectively prevent the electrons from interacting with SF_6 for some fraction of the time, which would yield a measured attachment rate correspondingly lower than the true rate.

A modified time-of-flight electron swarm method was used to obtain the present results.[15,16] The attachment rate is determined from a drift-dwell-drift (DDD) technique in which the electron swarm is drifted from the photocathode to the center of the reaction chamber where it is left for accurately measured periods of dwell time under zero ($<3 \times 10^{-5}$ v/cm)[15] electric field conditions before being drifted to the electron multiplier detector at the anode. The relative electron density (N/N_0) per photolight flash is then obtained as a function of the dwell time T. The slope of the semilog plot of N/N_0 vs T gives the value of αwP, where αw is the attachment rate and P is the partial pressure of the attaching gas. Mixtures of SF_6 with the carrier gases were made under the same conditions in 3-liter steel cylinders. Several mixtures of SF_6 with the same carrier gas were made at the same and different concentrations in order to (1) check the experimental reproducibility and (2) examine any concentration effects. In these cases the experimental reproducibility as indicated by the standard deviation of the average ranged from 1 to 3%. Where only one mixture was made the deviation is estimated to be ±5%. No attaching gas concentration effects were observed for those gases investigated (see Table 17.2). The attachment rates were also independent of the carrier gas pressure.

[12] B. H. Mahan and I. C. Walker, *J. Chem. Phys.* **47**, 3780 (1967).

[13] G. S. Hurst and J. E. Parks, *J. Chem. Phys.* **45**, 282 (1966).

[14] L. Frommhold, *Phys. Rev.* **172**, 118 (1968).

[15] D. R. Nelson and F. J. Davis, *J. Chem. Phys.* (in press).

[16] D. R. Nelson and F. J. Davis, ORNL-TM-2222 (1968).

The mean thermal-electron attachment rates found in this study for SF_6 in 14 different carrier gas mixtures are given in Table 17.2. The experimental standard deviation of the average is given for those carrier gases where three or more measurements were made. With the exception of carbon dioxide (CO_2) and ethylene (C_2H_4), the SF_6 attachment rate in the other carrier gases only varies from a low of 5.8×10^9 to a high of 7.1×10^9 sec^{-1} $torr^{-1}$. However, the attachment rates of 2.46×10^9 and 3.73×10^9 for C_2H_4 and CO_2, respectively, are significantly different from the above values. The details of the "ion-molecule (carrier gas) interaction" which might explain these results for the various carrier gases are not known. Even though the differences among the attachment rates for those carrier gases other than CO_2 and C_2H_4 are small and probably not very significant, the overall pattern of these attachment rates may be helpful in eventually evaluating specific interaction models.

Studies of thermal-electron attachment to other molecules are being made. Preliminary measurements of attachment in C_7F_{14} show a factor of 2 reduction in the attachment rate, using helium and C_2H_4 as carrier gases, similar to the factor of 2.8 found for SF_6. Bouby *et al.*[17] have reported different two-body attachment rates for molecules in CO_2, C_2H_4, and N_2 as the carrier gases, but offered no interpretation of the differences.

The results reported here for SF_6^-, in addition to those cited from Mahan and Walker[12] and Bouby *et al.*,[17] indicate that the nature of carrier gases affects two-body attachment rates for thermal electrons as a rule rather than as an exception. Similar results should be expected for both (1) higher-energy nondissociative attachment and (2) dissociative attachments where lifetimes against dissociation are sufficiently long compared with the mean time between collisions.

UPPER ESTIMATES OF THERMAL-ELECTRON ATTACHMENT RATES BY SOME HALOCARBONS AND TeF_6

There have been surprisingly large discrepancies among the reported capture rates (αw) of many thermal-electron-attaching molecules just as has been discussed for SF_6. Where the attachment rates are not too high, an exploratory study of thermal-electron attachment to some halocarbons has been made in the pure gases. An upper limit (no diffusion loss correction) of the thermal attachment rates found is given in Table 17.3. Lee[18] has measured α for the first four molecules listed in the table using N_2 as the carrier, and Blaunstein and Christophorou[19] used the measurements of α by Lee to estimate thermal capture rates (αw) for these molecules. Their estimate for CF_4 of 2.5×10^{-4} sec^{-1} $torr^{-1}$ is in good agreement with that found here. However, their estimates for CHF_3, $CHClF_2$, and $CClF_3$ are three orders of magnitude higher than the upper estimates found here. In view of the real but small carrier gas effect found for SF_6, it seems unlikely that there is a three-order-of-magnitude increase in αw using nitrogen as a carrier.

Table 17.3. Summary of Upper Limit Thermal-Electron Attachment Rates in Pure Gases

Molecule	Thermal Attachment Rate (sec^{-1} $torr^{-1}$)	Experimental Pressure (torrs)
CF_4	$<1 \times 10^4$	2
CHF_3	$<2 \times 10^3$	2
$CHClF_2$	$<4.5 \times 10^3$	2
$CClF_3$	$<1 \times 10^4$	2
$C_2H_2F_2$	$<7.1 \times 10^3$	2
$C_2H_4F_2$	$<4.5 \times 10^4$	1
C_2ClF_5	$<2 \times 10^5$	1
C_2F_6	$<5 \times 10^3$	2
C_3F_8	$<4 \times 10^4$	2
TeF_6	$<1.3 \times 10^6$	½

The study of thermal-electron attachment to hexafluoride molecules is continuing. An upper estimate of the thermal attachment rate by TeF_6 is 1.3×10^6. This rate is, surprisingly, over three orders of magnitude smaller than that for SF_6. Further studies with TeF_6 and SeF_6 (S, Se, and Te all belong to the same chemical group, VI, of the periodic table) are in progress to elucidate the molecular properties behind such widely varying thermal attachment rates of these hexafluorides.

[17] L. M. Bouby, F. Fiquet-Fayard, and H. Abgrall, *Compt. Rend.* **261**, 4059 (1965).

[18] T. G. Lee, *J. Phys. Chem.* **67**, 360 (1963).

[19] R. P. Blaunstein and L. G. Christophorou, *J. Chem. Phys.* **49**, 1526 (1968).

LOW-ENERGY NEGATIVE-ION–MOLECULE REACTIONS

Measurements of the cross sections for the ion-molecule reactions

$$H^- + H_2O \rightarrow OH^- + H_2 \,, \tag{5}$$

$$D^- + D_2O \rightarrow OD^- + D_2 \,, \tag{6}$$

and

$$O^- + NO_2 \rightarrow NO_2^- + O \tag{7}$$

are shown in Figs. 17.9 and 17.10. These results, among the first obtained[20] for the important low-energy region between thermal energies and a few electron volts, were made by the pulsed mass spectrometer technique described previously.[21] The primary H^-, D^-, and O^- ions were obtained by dissociative electron attachment in a variety of gases, and the use of a modulated retarding-potential-difference procedure applied to the electron beam permitted ion energy resolutions of ~0.1 ev in many cases.

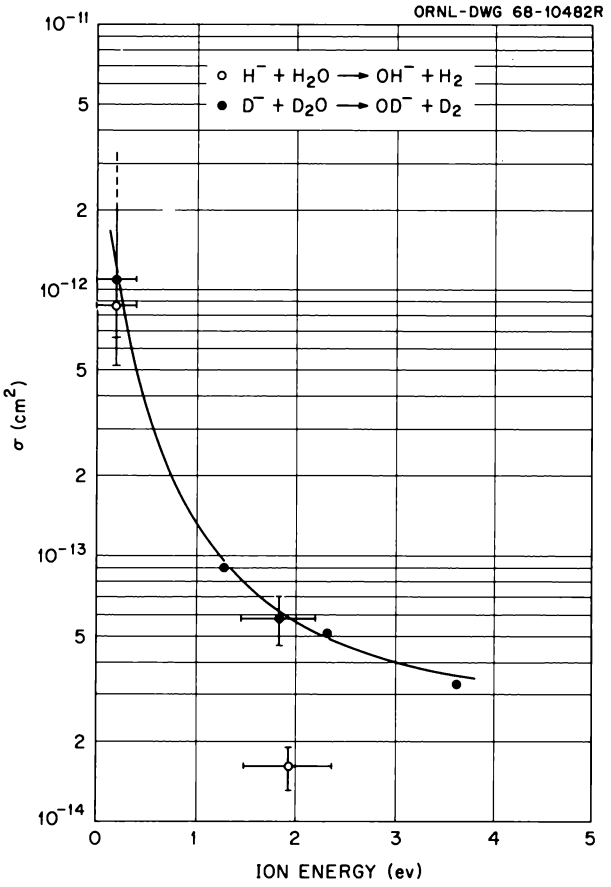

Fig. 17.9. Cross Section vs Ion Energy for the Reactions $H^- + H_2O \rightarrow OH^- + H_2$ and $D^- + D_2O \rightarrow OD^- + D_2$.

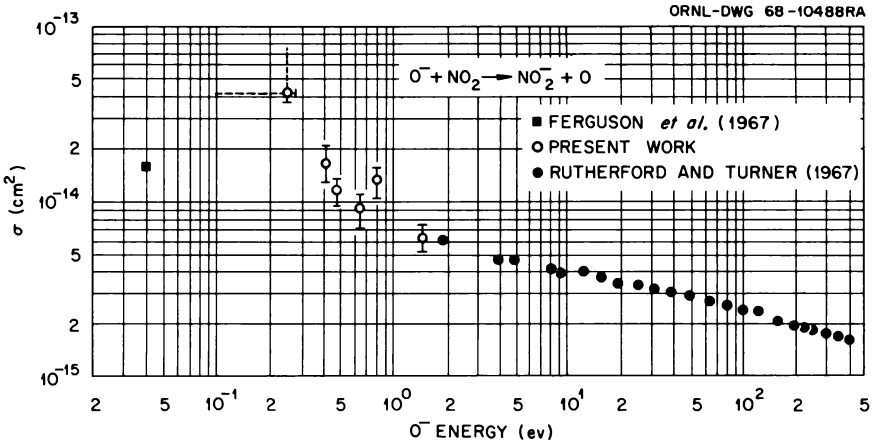

Fig. 17.10. Cross Section vs Ion Energy for the Reaction $O^- + NO_2 \rightarrow NO_2^- + O$.

[20] J. A. D. Stockdale, R. N. Compton, and P. W. Reinhardt, ORNL-TM-2546 (1969), summarizes work in this field.

[21] J. A. D. Stockdale, R. N. Compton, and P. W. Reinhardt, *Phys. Rev. Letters* 21, 664 (1968).

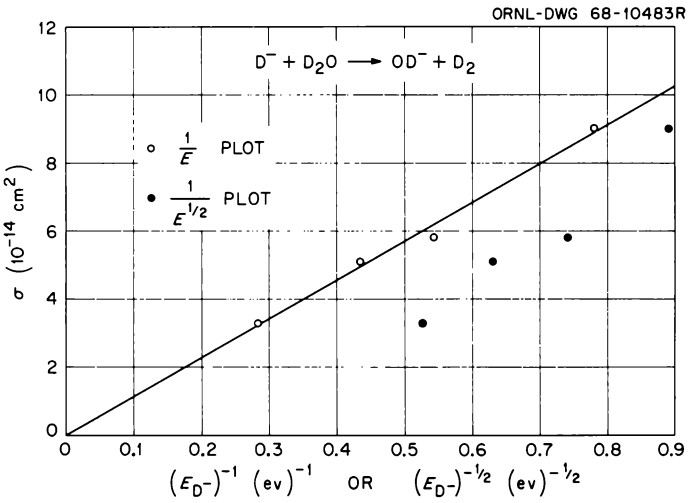

Fig. 17.11. Cross Section vs $1/E$ and $(1/E)^{1/2}$ for the Reaction $D^- + D_2O \rightarrow OD^- + D_2$.

The present results for reaction (7) join smoothly onto the retarded beam measurements of Rutherford and Turner[22] but appear to deviate away from the thermal energy flowing-afterglow measurement of Ferguson *et al.*[23] Both these results and those of Fig. 17.9 suggest that at low primary ion energies ($\lesssim$2 ev) in cases where the target molecule possesses a permanent electric dipole moment, the form of the cross section may deviate from the $1/v$ dependence predicted by the classical orbiting theory of Langevin[24] toward a steeper dependence, perhaps tending toward $1/v^2$. Figures 17.11 and 17.12 illustrate this. (Here v is the collision velocity in the center-of-mass system, at infinite separation.) Such a trend is in qualitative agreement with the recent calculations of Dugan and Magee,[25] which include the effects of a permanent dipole moment as well as the induced moment considered in the Langevin calculation.

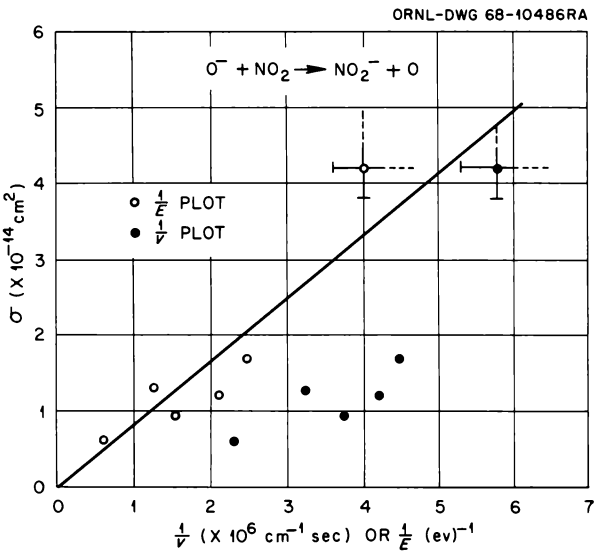

Fig. 17.12. Cross Section vs $1/E$ and $1/v$ for the Reaction $O^- + NO_2 \rightarrow NO_2^- + O$.

Reaction rates for a number of other negative-ion–molecule processes have been obtained. These are included in Table 17.4.

[22] J. A. Rutherford and B. R. Turner, *J. Geophys. Res.* **72**, 3795 (1967).

[23] E. E. Ferguson, F. C. Fehsenfeld, and A. L. Schmeltekopf (1967), private communication reported by F. A. Wolf and B. R. Turner, *J. Chem. Phys.* **48**, 4226 (1968).

[24] P. Langevin, *Ann. Chim. Phys.* **5**, 245 (1905); G. Gionmousis and D. P. Stevenson, *J. Chem. Phys.* **29**, 294 (1958).

[25] J. V. Dugan, Jr., and J. L. Magee, *J. Chem. Phys.* **47**, 3103 (1967).

Table 17.4. Negative-Ion–Molecule Reaction Rates and Cross Sections

Reaction	Resonance[a]	Primary Ion Energy,[b] E (ev)	Rate Constant, k (molecule^{-1} cm^3 sec^{-1})	Cross Section, σ (cm^2)
$H^- + H_2O \rightarrow OH^- + H_2$	H^-/H_2O at 6.4 ev	1.9 ± 0.4	$3.1 \pm 0.6 \times 10^{-8}$	$1.6 \pm 0.3 \times 10^{-14}$
	H^-/H_2 at 14 ev	~0	$5.4 \pm 1.6 \times 10^{-7}$	
$D^- + D_2O \rightarrow OD^- + D_2$	D^-/D_2O at 8.5 ev	3.6 ± 0.6	$6.1 \pm 1.2 \times 10^{-8}$	$3.3 \pm 0.7 \times 10^{-14}$
	D^-/D_2O at 6.5 ev	2.3 ± 0.2		$5.1 \pm 1.0 \times 10^{-14}$
	D^-/D_2O at 6.5 ev	1.8 ± 0.4	$7.7 \pm 1.5 \times 10^{-8}$	$5.8 \pm 1.2 \times 10^{-14}$
	D^-/D_2O at 6.5 ev	1.3 ± 0.2		$9.0 \pm 1.8 \times 10^{-14}$
	D^-/D_2 at 14 ev	~0	$4.7 \pm 1.5 \times 10^{-7}$	
$O^- + NO_2 \rightarrow NO_2^- + O$	O^-/O_2 at 6.7 ev	1.6 ± 0.3	$2.7 \pm 0.3 \times 10^{-9}$	$6.3 \pm 1.2 \times 10^{-15}$
	O^-/NO at 9.3 ev	0.8 ± 0.2	$3.9 \pm 0.4 \times 10^{-9}$	$1.3 \pm 0.2 \times 10^{-14}$
	O^-/N_2O at 2.6 ev	0.65 ± 0.05	$2.5 \pm 0.3 \times 10^{-9}$	$9.3 \pm 1.7 \times 10^{-15}$
	O^-/N_2O at 2.6 ev	0.48 ± 0.1	$2.8 \pm 0.3 \times 10^{-9}$	$1.15 \pm 0.2 \times 10^{-14}$
	O^-/N_2O at 2.6 ev	0.41 ± 0.1	$3.8 \pm 0.7 \times 10^{-9}$	$1.7 \pm 0.4 \times 10^{-14}$
	O^-/NO_2 at 8.8 ev	7.45 ± 0.1[c]	$4.4 \pm 0.4 \times 10^{-10}$	
	O^-/NO_2 at 8.8 ev	6.82 ± 0.1[c]	$1.0 \pm 0.2 \times 10^{-9}$	
	O^-/NO_2 at 3.8 ev	2.27 ± 0.1[c]	$1.8 \pm 0.2 \times 10^{-9}$	
	O^-/NO_2 at 3.8 ev	1.9 ± 0.1[c]	$2.4 \pm 0.3 \times 10^{-9}$	
	O^-/NO_2 at 3.8 ev	1.3 ± 0.1[c]	$2.4 \pm 0.3 \times 10^{-9}$	
	O^-/NO_2 at 1.9 ev	0.4 ± 0.1[c]	$6.6 \pm 0.8 \times 10^{-9}$	
	O^-/NO_2 at 1.9 ev	0.0 ± 0.1[c,d]	$8.0 \pm 1.0 \times 10^{-9}$	$\leqslant 4.2 \times 10^{-14}$
	O^-/NO_2 at 1.9 ev	-0.25 ± 0.1[c]	$4.2 \pm 0.4 \times 10^{-9}$	
$O^- + N_2O \rightarrow NO^- + NO$	O^-/N_2O at 2.6 ev	$0.65 \pm {}^{0.0}_{0.1}$	$4.0 \pm 0.4 \times 10^{-11}$	$1.5 \pm 0.3 \times 10^{-16}$
$SO^- + SO_2 \rightarrow SO_2^- + SO$	SO^-/SO_2[e] at 4.8 ev		$3.7 \pm 1.8 \times 10^{-9}$	
$HCOO^- + SF_6 \rightarrow SF_5^{-*} + (HCOOF)$[f]	$HCOO^-/HCOOH$ at 1.7 ev	~0	$\geqslant 6.0 \times 10^{-8}$[g]	
$SF_6^- + HCl \rightarrow F_2Cl^- + (SF_4H)$	*h*	Thermal	$8.6 \pm 2.7 \times 10^{-8}$	
$SF_6^- + UF_6 \rightarrow UF_6^- + SF_6$	*h*	Thermal	$1.4 + 0.3 \times 10^{-9}$	
$UF_5^- + UF_6 \rightarrow UF_6^- + UF_5$	UF_5^-/UF_6 at 2.2 ev		$1.5 + 0.3 \times 10^{-9}$	

[a] Dissociative attachment resonance supplying primary ion.
[b] Primary ion energy (ev) in the laboratory system.
[c] Electron energy relative to main, 1.9-ev, O^-/NO_2 peak.
[d] Primary ion energy here was measured to be $\leqslant 0.25$ ev. This yields $\sigma \geqslant 4.2 \times 10^{-14}$ cm^2.
[e] It is possible that there was some contribution from primary O^- ions to this reaction.
[f] Asterisk denotes SF_5^- excited.
[g] Calculated with the assumption that the SF_6 pressure was $\leqslant 10^{-5}$ torr.
[h] SF_6^- from capture of zero-energy electrons.

18. Graduate Education and Vocational Training

K. Z. Morgan

M. F. Fair

J. C. Ashley
R. D. Birkhoff
L. G. Christophorou
L. C. Emerson
W. R. Garrett
C. E. Klots
R. H. Ritchie
H. C. Schweinler
J. E. Turner
H. A. Wright

The field training program at ORNL during the summer months is open to all AEC Fellowship students who have completed their first academic school year under the fellowship program. In the past most of the Fellows have come from Vanderbilt University and The University of Tennessee; in recent years more students have come from other schools. The field training consists of two major phases, namely, applied health physics and research health physics. The university program cannot, in itself, produce the desired product. The summer training program is absolutely essential in the education of a health physicist.

Five Fellows participated in the summer training program at ORNL during July and August 1968 – one from Vanderbilt, two from the University of Rochester, one from the University of Illinois, and one from the University of California.

The summer training began with a three-day orientation program which was followed by five weeks with the applied health physics groups and five weeks with the research health physics groups. One week was spent at the Special Training Division (ORAU) doing health physics experiments. Numerous seminars were held throughout the summer highlighting recent advances in health physics and closely allied fields. Many of the seminar speakers were from laboratories and universities from around the world.

In the applied health physics training, the student gains practical experience in all phases of radiation protection under the supervision of a senior health physicist. The student learns of all the protection services that are provided for the Physics Division, Reactor Chemistry Division, Metals and Ceramics Division, Solid State Division, Chemical Technology Division, Tracer Facilities, High-Level Radiochemical Development Laboratory, Fission Products Pilot Plant, Waste Disposal Group, and the Ecology Research Group. In addition, he learns of personnel monitoring, instrument calibration, counting facilities, bioassay techniques, and whole-body counting.

In health physics research the students are first given a brief summary of all the research projects in progress in the Division. They then choose the group in which they remain for a five-week period. They become part of the team and are truly engaged in doing health physics research under senior scientist supervision. The fields of investigation include: interaction of radiation with gases, solids, and liquids; theoretical radiation physics; health physics research reactor; dosimetry; radioactive waste disposal; and radiation ecology.

The summer program gives the student sufficient experience in applied health physics to enable him to take a position in this field, where with only a little additional experience he will soon qualify for a position of responsibility in radiation protection. Also, he learns of the tremendous breadth in research health physics and is made aware of the diverse problems available for thesis work should he decide to continue his education for the M.S. or Ph.D. degree under the AEC Fellowship.

Fifteen students were enrolled in the course in General Health Physics (Physics 4710-20-30) taught by a member of the Division at The University of Tennessee. This was a three-quarter course which met 3 hr/week. A course in Applied Radiation Physics (Physics 234) at Vanderbilt University was taken by three AEC Fellows and eight physics majors. This was a one-semester course which met 4 hr/week.

Universities and colleges at which ORNL health physics research and educational activities were discussed are listed below:

Berea College
Columbia University
Florida State University
Geneva College
Knoxville College
Lincoln Memorial University
Louisiana State University
Loyola University (Chicago)
Mellon Institute
New York University
Ohio State University
Rensselaer Polytechnic Institute
Texas A and M
University of California
University of Kentucky
University of Missouri
University of Wisconsin
Vanderbilt University
Wayland College
Yale University

There were a number of Oak Ridge Graduate Fellows, AEC Fellows, and USPHS students in the Division working on theses as partial requirements for advanced degrees. Their thesis titles and universities are listed below:

1. M.-E. M. Abu-Zeid, "Emission and Decay of Organic Liquids Under Electron Impact" (UT)
2. A. J. Braundmeier, Jr., "Plasmon Radiation from Electron Bombarded Aluminum Foils" (UT)
3. E. L. Chaney, "Electron Attachment to Polyatomic Molecules" (UT)
4. A. A. Christodoulides, "Scattering of Thermal Electrons by Polar Molecules" (UT)
5. P. M. Collins, "Investigation of Negative Ions with Electron Beams" (UT)
6. J. J. Cowan, "Surface Plasmon Resonance Effects in Grating Diffraction" (UT)
7. C. E. Easterly, "Study of Aromatic Hydrocarbons in Relation to Carcinogenesis" (UT)
8. F. W. Garber, "Low-Energy Electron Beam Studies in Thin Metal Films" (UT)
9. T. F. Gesell, "Photoelectric Properties of Magnesium in the Vacuum Ultraviolet" (UT)
10. J. T. Grissom, "Threshold Electron Impact Excitation and Negative Ion Formation" (UT)
11. J. H. Grossen, "A Monte Carlo Calculation of High-Energy Nucleon Penetration Through Matter" (UT)
12. W. T. Naff, "Transient Negative Ion State in Alicyclic and Aromatic Fluorocarbon Molecules" (U. of Georgia – M.S.)
13. W. T. Naff, "Slow Electron Collisions with Molecules" (U. of Georgia – Ph.D.)
14. S. J. Nalley, "Charge Exchange Between Fast Atoms and Molecules" (UT)
15. Linda R. Painter, "Electronic Properties of Liquid Water in the Vacuum Ultraviolet Region" (UT)
16. J. A. D. Stockdale, "Studies of Negative Ion-Molecule Reactions in the Energy Region from Zero to Three Electron Volts" (UT)
17. R. B. Vora, "Stopping Power of Matter at Extreme Relativistic Energies" (UT)
18. U. S. Whang, "Optical Properties of Cesium in the Vacuum Ultraviolet" (UT)

The Division provided assistance to the staff at the University of Tennessee in updating and revising its graduate curriculum in health physics. This included courses in General Health Physics, Radiation Chemical Physics, Radiation Biology, Physics of Polyatomic Molecules, Interaction of Electrons with Gases, Interaction of Electrons with Solids, and Interaction of Radiation with Matter. This curriculum has attracted Fellows who desire education to the Master's level and also those who wish to pursue the Ph.D. degree. A great deal of help was provided to the University of Tennessee in establishing a co-op type program with ORNL leading to the B.S. degree in Health Physics. This type of assistance and consultation is available to any school desiring to set up a Health Physics Program or institute courses in this field. For example, queries have been received from Georgia Institute of Technology, Southern Technical Institute, Texas Woman's University, University of Mississippi, University of Wyoming, Auburn University, Oklahoma State University, and Loyola University with regard to setting up courses in Health Physics. Assistance was given to the University of Tennessee and Vanderbilt University in the preparation of qualifying examinations in Health Physics. Visits to ORNL with lectures and tours were provided for classes in Health Physics from the University of Arkansas and the University of North Carolina.

One member of the Education Group of the Health Physics Division helped in the screening of applicants for the 1969–1970 USAEC Fellowship Program. This work was done at the Oak Ridge Associated Universities (ORAU). Assistance was also given to ORAU in the presentation of a ten-week course in Health Physics

and several courses for medical personnel entitled "Medical Radioisotopes."

Eight student trainees from ORAU were assigned to the Division for the summer, and six faculty members spent the summer in the Division as Research Participants sponsored by ORAU. One student from Southern University, New Orleans, spent the summer in the Division under the Summer Science and Engineering Program for students from predominantly Negro colleges. Ten undergraduate research participants in ecology worked in the Division during the summer.

The demands for education in health physics have continued to rise. Although emphasis will be on education to the Ph.D. level to provide personnel for positions of leadership in industrial, academic, and medical institutions, education will continue to be offered during the summer at the Master's level to provide vocational training which includes a knowledge of health physics principles and procedures. The needs of the reactor industry must be met.

RADIATION PHYSICS SEMINARS

In an effort to more thoroughly acquaint staff members with the physical and biological principles underlying the field of radiation protection and to provide a convenient environment for discourse between various disciplines within the Radiation Physics Section, a series of seminars has been initiated on the topic "Physical Basis for Radiation Protection." These seminars are more in the nature of discussions and have dealt with a broad variety of topics common to the fields of physics, chemistry, and biology. For the most part the seminars have been conducted by staff members who were either well versed or were particularly interested in a specific topic. Outside speakers have included M. L. Randolph, ORNL Biology Division, who discussed several topics in radiation biology and R. Katz, the University of Nebraska, who discussed some of his recent work on the interaction of charged particles with matter.

19. Physics of Tissue Damage

E. T. Arakawa
R. D. Birkhoff

L. C. Emerson
F. W. Garber[1]
R. N. Hamm
H. C. Schweinler
W. J. McConnell
L. R. Painter[2]
M. S. Reidinger[2]

DISPERSION ANALYSIS OF LIQUID WATER IN THE VACUUM ULTRAVIOLET

In a condensed phase the effective electric field at a given molecule is no longer the external field impressed on the sample but is modified by the polarization of neighboring molecules. We have carried out an analysis, in which such an internal field is incorporated, of the optical response of liquid water in the vacuum ultraviolet.[3] If it is assumed that each molecule is effectively in a spherical cavity in a polarizable medium, then one obtains the following expression:

$$\frac{\epsilon - 1}{\epsilon + 2} = \frac{1}{3} \sum_l \frac{f_{l0} \omega_p^2}{\omega_{l0}^2 - \omega^2 - i\gamma_l \omega} , \tag{1}$$

where ϵ is the complex dielectric constant, ω_p the plasma energy, f_{l0} the oscillator strengths, γ_l the damping constants, and ω_{l0} the resonant frequencies. Taking the imaginary part of each side, we have

$$\mathrm{Im}\left(\frac{\epsilon - 1}{\epsilon + 2}\right) = \frac{\omega_p^2}{3} \sum_l \frac{f_{l0} \gamma_l \omega}{(\omega_{l0}^2 - \omega^2)^2 + \gamma_l^2 \omega^2} . \tag{2}$$

We have applied this analysis to the dielectric constants of water in the vacuum ultraviolet, which we have previously obtained.[4] Figure 19.1 shows the agreement between the experimental data and calculated values based on Eq. (2). The fit is quite good except for the lower energies. From this analysis we have obtained the energies, line widths, and oscillator strengths of the two peaks as shown in the figure.

TRANSITION RADIATION FROM LIQUID WATER

The recent experimental determination of the optical properties of liquid water in the vacuum ultraviolet spectral region by Painter *et al.*[5] has raised the interesting possibility of observing transition radiation from water. The question of the fluorescence of water has long been a matter for much speculation. Earlier, Ritchie and Eldridge[6] showed that the number distribution for the transition radiation emitted at angle θ when electrons of velocity v are incident upon the surface of any target characterized by a complex dielectric constant, $\tilde{\epsilon} = \epsilon_1 + i\epsilon_2$, and of finite thickness is given by

$$\frac{d^2N}{d\Omega\, d\omega} = \frac{\alpha\beta^2}{\pi^2 \omega} \mu^2 (1 - \mu^2) \left| \frac{\gamma}{\Delta} \right|^2 , \tag{3}$$

[1] Oak Ridge Graduate Fellow.

[2] Consultant.

[3] R. N. Hamm *et al.*, *Bull. Am. Phys. Soc.* 13, 1412 (1968).

[4] L. R. Painter, R. D. Birkhoff, and E. T. Arakawa, *J. Chem. Phys.* (in press); L. R. Painter *et al.*, *Phys. Rev. Letters* 21, 282 (1968); L. R. Painter, R. D. Birkhoff, and E. T. Arakawa, *Electronic Properties of Liquid Water in the Vacuum Ultraviolet Region*, ORNL-TM-2261 (1968).

[5] L. R. Painter *et al.*, *Phys. Rev. Letters* 21, 282 (1968).

[6] R. H. Ritchie and H. B. Eldridge, *Phys. Rev.* 126, 1935 (1962).

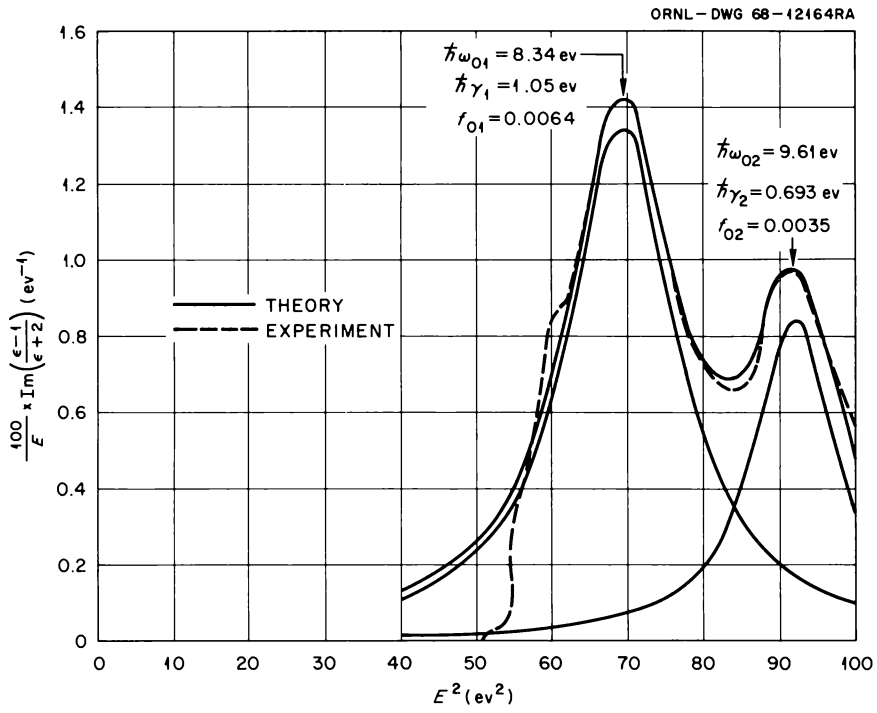

Fig. 19.1. Comparison of Theoretical and Experimental Dielectric Response of Liquid Water as a Function of E^2.

where

$$\gamma = \left(\frac{\beta\sigma+\epsilon}{1-\beta^2\mu^2} - \frac{1}{1-\beta\sigma}\right)(\mu\epsilon+\sigma)e^{-it\sigma} + \left(\frac{\beta\sigma-\epsilon}{1-\beta^2\mu^2} + \frac{1}{1+\beta\sigma}\right)(\mu\epsilon-\sigma)e^{it\sigma} - 2\sigma\left(\frac{\epsilon}{1-\beta\mu} - \frac{1+\beta\epsilon\mu}{1-\beta^2\sigma^2}\right)e^{-it/\beta},$$

$$\sigma = \sqrt{\epsilon - 1 + \mu^2},$$

$$\Delta = (\mu\epsilon-\sigma)^2 e^{it\sigma} - (\mu\epsilon+\sigma)^2 e^{-it\sigma},$$

$$t = a\omega/c,$$

$$\alpha = e^2/\hbar c,$$

$$\mu = \cos\theta,$$

$$\beta = v/c.$$

By letting a, the thickness of the target, approach infinity, one may show that the general expression for the transition radiation number distribution is given by

$$\frac{d^2N}{d\Omega\, d\omega} = \frac{\alpha\beta^2}{\pi^2\omega}\frac{\mu^2(1-\mu^2)}{(1-\beta^2\mu^2)^2} \times \left|\frac{(1-\beta^2\mu^2)-(1-\beta\sigma)(\beta\sigma+\epsilon)}{(\sigma+\mu\epsilon)(1-\beta\sigma)}\right|^2. \quad (4)$$

This expression has been programmed and used to calculate the spectral distribution of transition radiation as a function of angle with respect to the incident beam direction as well as its dependence on electron energy. The energy distribution is obtained from the number distribution from the relation

$$\frac{dE}{d\Omega\, d\lambda} = \frac{4\pi^2\hbar c}{\lambda^3}\frac{dN}{d\Omega\, d\omega} \quad (5)$$

and is shown in Fig. 19.2 for several angles. The peak in the distributions at 1530 A is associated with the possible exciton level reported at 8.3 ev.[5] The turnover in each of the curves at 1250 A results from only a single experimental point and thus may not be significant. The energy dependence of the transition radiation at the wavelength of the characteristic peak is shown in Fig. 19.3. The effect of electron slowing down in water has not been taken into account. One would expect,

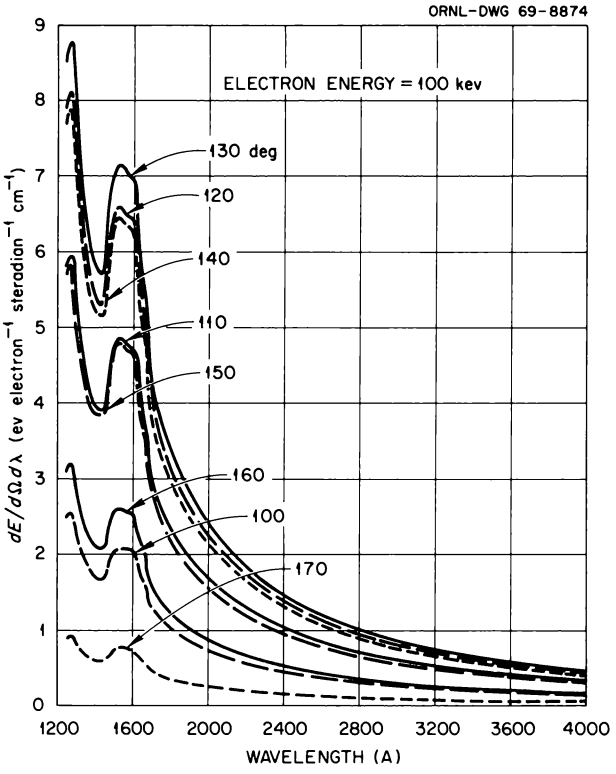

Fig. 19.2. Angular Distribution of Transition Radiation from Liquid Water.

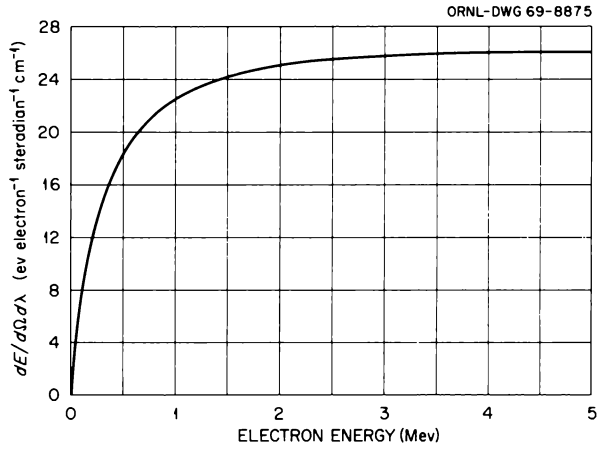

Fig. 19.3. Energy Distribution of Transition Radiation from Liquid Water at 1527 A.

however, that the photons that escape from the surface would have been generated in the topmost surface layers, where the approximation of constant velocity would hold.

These calculations indicate that transition radiation from electron-bombarded liquid water is sufficiently intense to be observable experimentally. An irradiation cell was constructed to investigate this possibility. The bottom of the cell consisted of a water reservoir which was capable of being cooled by conduction to a temperature just above the freezing point. The sample to be irradiated was condensed from the vapor above the reservoir on a copper plate cooled by a small thermoelectric unit. The plate was mounted vertically at the intersection of the electron beam axis and the axis of the entrance arm of the spectrometer. The angle of intersection was 130°, which corresponds to the expected peak in the angular distribution of the transition radiation. The electron beam entered the sample chamber through a 0.040-in.-diam hole which was sealed by means of a 1600-A-thick aluminum foil. The exit window of the cell was a 1-mm-thick polished disk of calcium fluoride. The cell was provided with a thermocouple for temperature monitoring purposes as well as a glass view port to permit visual observation of the water sample.

The cell was installed within the angular distribution chamber[7] on the 100-kev electron accelerator. The initial data obtained with the new cell indicated an extremely intense emission centered at 2800 A but with skirts extending far to both sides into the short- and long-wavelength regions. The expected transition radiation from the water sample was not observed because of the intensity of this extraneous light. It has been determined that the emission resulted from scattered-electron-induced fluorescence of the calcium fluoride window. Efforts are now being made to shield the window magnetically in order to reduce or eliminate the source of the high background light.

LOW-ENERGY ELECTRON TRANSMISSION IN SOLIDS

The work initiated previously on the interaction of low-energy electrons with metals[8] was continued with the following results. The attenuation lengths of low-energy electrons in aluminum were measured at 128 A for 50-ev electrons, decreasing to 49 A for 300-ev electrons. These lengths are substantially smaller than

[7] *Health Phys. Div. Ann. Progr. Rept. July 31, 1962,* ORNL-3347, p. 82.

[8] F. W. Garber *et al., Low-Energy Electron Beam Studies in Thin Metal Films,* ORNL-TM-2406 (1969).

those measured within a few electron volts of the top of the conduction band by other experimenters. The latter are quite long because of the difficulty an electron near the conduction band has in colliding with another electron in such a way that both electrons still lie above the top of the Fermi sea. That is, the exclusion principle severely restricts the collision probability, with the result that long mean free paths are noted at very low energies and shorter mean free paths at the energies we employed in this experiment. At somewhat higher electron energies the stopping power of aluminum could be determined. Data were corrected for the increased path length in our thin films by using a modified version of the Yang theory. Typical values were 3 ev/A at about 300 ev, ranging to about 4.4 ev/A at 950 ev. These values are in general accord with the calculations of Ritchie[9] on electron interactions in the conduction band and L shell but lie somewhat above the theory at the higher energy and somewhat below the theory at the lower energy. The so-called "charge equilibrium distance" was determined in aluminum as a function of electron energy. This distance is the depth an electron beam penetrates an aluminum sample at which the net electronic charge delivered to the traversed region is zero; that is, as many electrons are scattered into this layer as are scattered out. These data were found to be in good agreement with data of Kanter and Sternglass,[10] Holliday and Sternglass,[11] and Young.[12] Our data extended down to 300 ev and formed a smooth curve with higher-energy data. The general shape of the electron transmission curves as a function of energy was compared with the Monte Carlo theory of Ritchie[9] and found to be in semiquantitative agreement. The principal discrepancy lies below 50 ev, where experiments show electrons are able to traverse relatively large thicknesses of aluminum, whereas the theory does not. Further experimental work of this type seems impractical until better theoretical values for the fundamental cross sections are derived and an experimental method is devised wherein mean free paths may be studied under single-collision conditions.

ELECTRON SLOWING-DOWN STUDIES

The electron slowing-down theory given by Spencer and Fano[13] is numerically calculable with the aid of a computer. However, if one wishes to examine the effect of an additional source of electrons (e.g., Auger electrons) on the flux spectrum or to calculate radiation yields, an analytical expression for the flux is more convenient. We have derived such an expression for aluminum using an empirical stopping power:

$$\frac{dT}{dx} = 2.7 \times 10^{10} T^{-0.7}\,, \quad 100\ \text{ev} < T < 300\ \text{kev}\,, \quad (6)$$

where dT/dx is in ev/cm and T is in ev. With this stopping power and the Thomson electron-electron scattering cross section,[14] the flux $y(T)$ in cm/ev at energy T in ev is given by

$$y(T) = \frac{T^{0.7}}{2.7 \times 10^{10}} + \frac{\pi N_e e^4 T^{0.7}}{(2.7 \times 10^{10})^2} \times \left[\frac{T_0^{0.7}}{0.7T} + \frac{2}{0.3T_0^{0.3}} - \frac{2^{0.7}}{0.7T^{0.3}} - \frac{2}{0.3(2T)^{0.3}} \right], \quad 100\ \text{ev} < T < T_0/2\ \text{kev}\,, \quad (7)$$

where N_e is the electron density, e is the electronic charge, and T_0 is the initial electron energy in ev (assumed to be $\leqslant$300 kev). This equation predicts a $T^{-0.3}$ dependence of flux on electron energy at low energies rather than a T^{-1} dependence found experimentally. The reasons for this discrepancy are possibly the neglect of other sources of electrons, such as from Auger effect, and the reabsorption of photons from bremsstrahlung and decay of excited atoms to their ground states.

The electron flux from ^{64}Cu beta rays slowing down in lead was measured. The purpose was to determine the influence of the reabsorption of bremsstrahlung in generating secondary electrons. The flux at low energies was found to be about a factor of 3 higher in lead than for ^{64}Cu beta rays slowing down in aluminum. However, a comparison between gold and aluminum irradiated by ^{198}Au beta rays does not show this difference. The reasons for this are not understood although the lead data are somewhat suspect because of the roughness of the emitting surface.

In order to measure the electron flux generated by alpha particles, a ^{241}AmAl alloy was made. Reactor irradiation of this alloy would result in a ^{242}Cm alpha source in aluminum. Surface contamination problems resulting from the high specific activity of the source

---

[9] R. H. Ritchie, in F. W. Garber *et al.*, *Low-Energy Electron Beam Studies in Thin Metal Films*, ORNL-TM-2406 (1969).

[10] H. Kanter and E. J. Sternglass, *Phys. Rev.* **126**, 620 (1962).

[11] J. E. Holliday and E. J. Sternglass, *J. Appl. Phys.* **30**, 1428 (1959).

[12] J. R. Young, *J. Appl. Phys.* **27**, 1 (1956).

[13] L. V. Spencer and U. Fano, *Phys. Rev.* **93**, 1172 (1954).

[14] J. J. Thomson, *Phil. Mag.* **6**, 23, 449 (1912).

prevented its use in our facility in Building 4500S. Lack of funds prevented us from moving the spectrometer into an area with proper containment.

We have made calculations which indicate that we can measure the slowing-down spectra of ^{71}Ge and ^{31}Si beta rays in germanium and silicon, respectively, by irradiating these materials in a nuclear reactor. These measurements have a practical use in understanding radiation processes in solid-state electronics and as such are of concern to those interested in "hardening" military electronics. Similar calculations indicate that there is enough phosphorus in bone to measure the slowing-down spectrum of ^{32}P beta rays in bone. Sources of the semiconductors are under construction.

An attempt has been initiated to develop a slowing-down theory using the Born approximation cross sections of Ritchie[15] in contrast to the Spencer-Fano[13] theory, which utilizes free-electron cross sections only. The problem is being coded, and no results are available as yet.

---

[15] R. H. Ritchie, in W. J. McConnell *et al.*, *Radiation Res.* 33, 216 (1968).

Part IV. Radiation Dosimetry Research

J. A. Auxier

20. Dosimetry for Human Exposures and Radiobiology

J. A. Auxier

J. S. Cheka
W. F. Fox
F. F. Haywood
H. H. Hubbell, Jr.
J. E. Jackson
T. D. Jones
W. H. Shinpaugh
W. S. Snyder
D. R. Stone
E. B. Wagner

JAPANESE DOSIMETRY PROGRAM

Shielding Studies

There has been an increased amount of concern since 1967 about certain situations in which the 9 Parameter Formulae (9PF)[1] method of evaluating doses of radiation to Japanese survivors had been applied. This concern came after an inspection of the histories of survivors who received more than 800 rads of ionizing radiation. It seemed that a significant portion of these survivors were inside typical Japanese houses (houses built from standard Japanese building materials) in close proximity to several other typical Japanese houses. This provided a complicated shielding situation, considerably more complicated, in fact, than all but a very small fraction of the cases from Operations Hardtack and BREN, the experiments which provided the data for the derivation of the 9PF. Applications of the 9PF to these cases amounted to an extrapolation outside their known regions of validity.

The 9PF results for some of these intricately shielded stations were compared with the data from CEX-62.11[1] and with the attenuation factors from T57D (method of radiation evaluation) results, with the comparison summarized in Table 20.1.

In addition to the comparisons shown in the table, minimum gamma transmission factors were computed according to the 9PF and found to be 0.65 for Nagasaki and 0.78 for Hiroshima; from all these simple comparisons it is felt that no errors of any significance are encountered for cases of survivors inside typical Japanese houses.

During a liaison trip (November 29 to January 28), many shielding histories of survivors receiving from 500 to 800 rads were also studied. A very small fraction of these cases were for survivors exposed inside a typical Japanese house which had, in turn, received shielding from other Japanese houses. A significant fraction of the cases were in typical Japanese houses of very simple construction with no external shielding from surrounding houses (cases for which the 9PF are extremely accurate), so that these cases appear to be the result of statistical fluctuation; the fraction of the survivors in this category to the total number of survivors makes this seem reasonable.

There were two gravestones in Nagasaki and one in Hiroshima which provided some of the data that were

[1] J. S. Cheka *et al., Distribution of Weapons Radiation in Japanese Residential Structures,* CEX-62.11 (August 1965).

Table 20.1.

Number	M.F. Number (Hiroshima)	Attenuation Factors: T65D, 9PF Predictions		Attenuation Factors: CEX-62.11, Approximations		Attenuation Factors: T57D Predictions		Station in CEX-62.11 and Comments About T65D vs CEX-62.11 Comparison	
		T_n[a]	T_γ[b]	T_n	T_γ	T_n	T_γ		
1	234-333	0.193	0.810	0.21	0.78	0.26	0.64	(Reactor-8-A-E)[c]	(^{60}Co-16-A-E). close
2	225-124	0.252	0.845	0.21	0.78	0.25	0.51	(Reactor-8-A-E)	(^{60}Co-16-A-E).close
3	237-404	0.259	0.862	0.21	0.81	0.25	0.47	(Reactor-8-A-B)	(^{60}Co-16-A-B).close
4	234-774	0.205	0.810	0.34	0.76	0.39	0.56	(Reactor-5-C-E)	(^{60}Co-16-A-E).[d]
5	234-477	0.231	0.791	0.20	0.73	0.25	0.54	(Reactor-8-A-H)	(^{60}Co-16-A-H).close
6	215-763	0.231	0.804	0.34	0.75	0.41	0.60	(Reactor-5-C-E)	(^{60}Co-16-A-E).close
7	207-013	0.231	0.804	0.34	0.75	0.50	0.74	(Reactor-5-C-E)	(^{60}Co-16-A-E).close
8	234-436	0.223	0.826	0.29	1.00	0.34	0.68	(Reactor-6-B-A)	(^{60}Co-15′-B-A).close

[a]Neutron transmission factor.
[b]Gamma-ray transmission factor.
[c]Source of radiation – neighboring house configuration – house size – location in house.
[d]CEX-62.11 should slightly overestimate neutron dose. The net effect on gammas is difficult to predict because of n,γ interactions.

used by Lord Penney in his recent report[2] on the yields of the Hiroshima and Nagasaki weapons. The orientation of the stones relative to a line to the hypocenter (projection of the epicenter on the ground) and the coordinates of the stone's location were extremely critical in the calculations of the yields for the two weapons. In order to extract the maximum amount of information from these data, it was desirable to try to locate the stones and to verify or correct the orientation and coordinate values. The stones were located and identified to the satisfaction of Lord Penney and did not significantly change his earlier results.

T65D dose estimates are presently in use at ABCC, and serious attempts are being made to formulate mathematical models so that relationships may be obtained between observed effects and quality and quantity of radiation exposure. Several attempts have been made to compute RBE's (relative biological effectiveness) of neutrons for prompt effects, epilation, and leukemia, but none have provided satisfactory results. Some attempts assumed linearity of RBE (for neutrons) over a wide range of exposure levels. Initially these attempts yielded negative RBE's, and the trouble was that the sample included survivors receiving near zero amounts of exposure as well as those receiving extremely high levels of exposure (claims of up to 20 times mean lethal dose). The reason that these RBE's became negative was that enough of the extremely high exposure cases were included that the number of leukemia cases observed was actually fewer than those which should have been due to the gamma portion of the exposure alone, so that a negative effect had to be attributed to neutrons in order to have a solution to the constants in the model. Additional attempts to compute RBE were made by excluding survivors receiving less than 50 rads and those receiving more than 300 rads. For this sample, an RBE of 5 for neutrons seemed to correlate the number of leukemia cases to dose better than other integral values of RBE.

Neutron and Gamma-Ray Leakage from the Hiroshima and Nagasaki Weapons

A ^{252}Cf source was used to determine the neutron and gamma-ray leakage from weapons similar to those exploded over Hiroshima and Nagasaki. This experiment was designed to provide data to supplement those obtained by previous investigations.[3-8] The experiment

[2]Lord Penney, D. E. J. Samuels, and G. C. Scorgie, *The Explosive Yields at Hiroshima and Nagasaki*, United Kingdom Atomic Energy Authority (February 1968).

[3]P. S. Harris *et al.*, *Project 39.7, Operation Teapot*, ITR-1167 (April 1955) (classified).

[4]G. S. Hurst and R. H. Ritchie, *Project 39.5, Operation Plumbbob*, WT-1504 (September 1958) (classified).

[5]R. H. Ritchie and G. S. Hurst, *Health Phys.* 1, 390–404 (1959).

[6]J. A. Auxier, J. S. Cheka, and F. W. Sanders, *Projects 39.1 and 39.2, Operation Hardtack, Phase II*, WT-1725 (March 1961) (classified).

[7]F. W. Sanders *et al.*, *Operations Plan and Hazard Report – Operation BREN*, CEX-62.02 (April 1962).

[8]J. H. Thorngate, D. R. Johnson, and P. T. Perdue, *Neutron and Gamma-Ray Leakage from the Ichiban Critical Assembly*, CEX-64.7 (June 1966).

was conducted at the Burlington AEC Plant because facilities were available there for the storage, handling, and modifications of the weapons. Modifications were necessary because a means had to be provided for the introduction of the ^{252}Cf source into the center of the weapons. Angular and spatial measurements of neutron dose, gamma-ray dose, and neutron fluence were made. Several weeks prior to the Burlington experiment, measurements were made of the bare ^{252}Cf source to determine the source strength, neutron spectrum, and neutron and gamma ratios at various distances and angles.[9] The measurements were made with active- and passive-type dosimetry instrumentation similar to that used for Operations BREN, HENRE, etc.[3-8] The passive-type dosimeters were metaphosphate glass, sulfur, threshold detectors employing solid-state detectors, and fissile radiators. The active-type dosimeters used were fast-neutron proportional counters, a modified long counter, and neutron-insensitive Geiger counters.

The Hiroshima weapon will be referred to as "Small Boy" and the Nagasaki weapon as "Fat Man" to simplify identification. During weapons modifications, a reference point had been marked on the top outer housing of each weapon which was directly above the location of the ^{252}Cf source. Using these reference points and some measuring tools such as plumb bobs, steel tapes, chalk lines, etc., measurement location points were located and marked on the floor using a reference coordinate system as shown in Fig. 20.1. The longitudinal axis, labeled *XL* in Fig. 20.1, passing through the core center and the front and back of the weapon is used as the reference for angles at which measurements were made. The front of the longitudinal axis was defined as the 0° angle. A line *XH* through the core center and perpendicular to the longitudinal axis constitutes the lateral axis. An imaginary plane (shown by the dashed lines in Fig. 20.1) is passed through the longitudinal and lateral axes, and the weapon position is adjusted so that this plane is parallel to the floor and at a height of 1 m above the floor. All measurements were made in this plane at various angles and distances as shown in Figs. 20.2 and 20.3.

Two sets of data, experiment No. 1 and experiment No. 2, were run with Fat Man. Experiment No. 1 was conducted with one type of *X* unit to see if there was an appreciable difference in shielding characteristics. It can be seen, by comparing Figs. 20.4 and 20.5, that *X* unit No. 2 causes a decrease in gamma response at an angle of approximately 18°, indicating that it is a better gamma shield than *X* unit No. 1. The data for the Fat

[9] D. R. Stone *et al.*, "Calculated and Experimentally Determined Neutron Dose Conversion Factor for Californium," *Health Phys.*, in press.

ORNL-DWG 69-8876

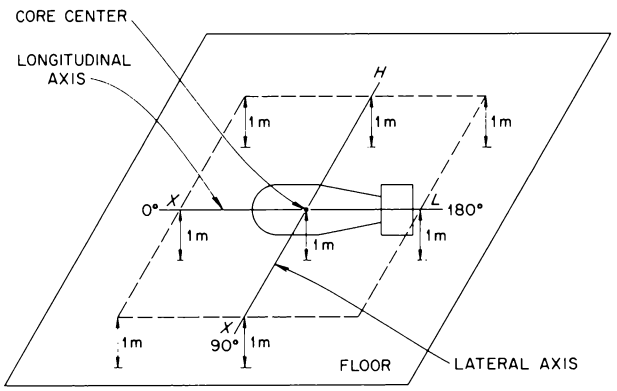

Fig. 20.1. Reference System of Coordinates Used in Measuring the Spatial Distribution of Radiations from the Small Boy.

ORNL-DWG 69-8877

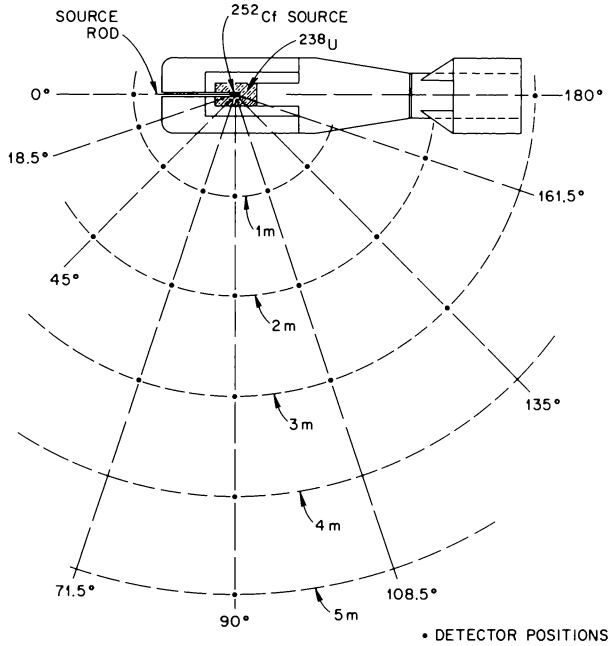

Fig. 20.2. Location of Detectors Used in the Measurement of Radiations from the Small Boy Viewed Looking Down on a Horizontal Plane 1 m from the Floor.

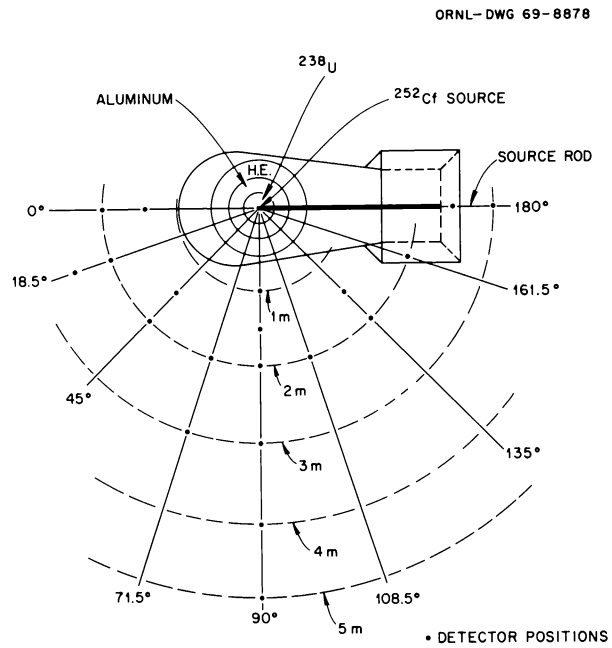

Fig. 20.3. Location of Detectors Used in the Measurement of Radiations from the Fat Man Viewed Looking Down on a Horizontal Plane 1 m from the Floor.

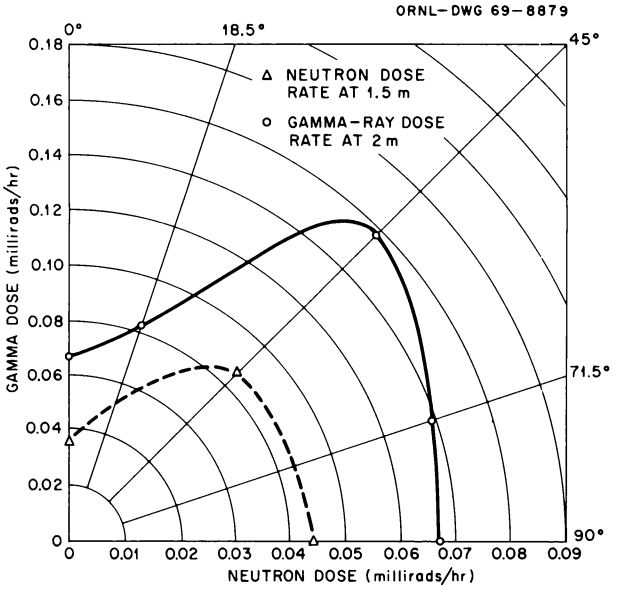

Fig. 20.4. Neutron and Gamma-Ray Dose Rate as a Function of Angle from Fat Man Experiment 1.

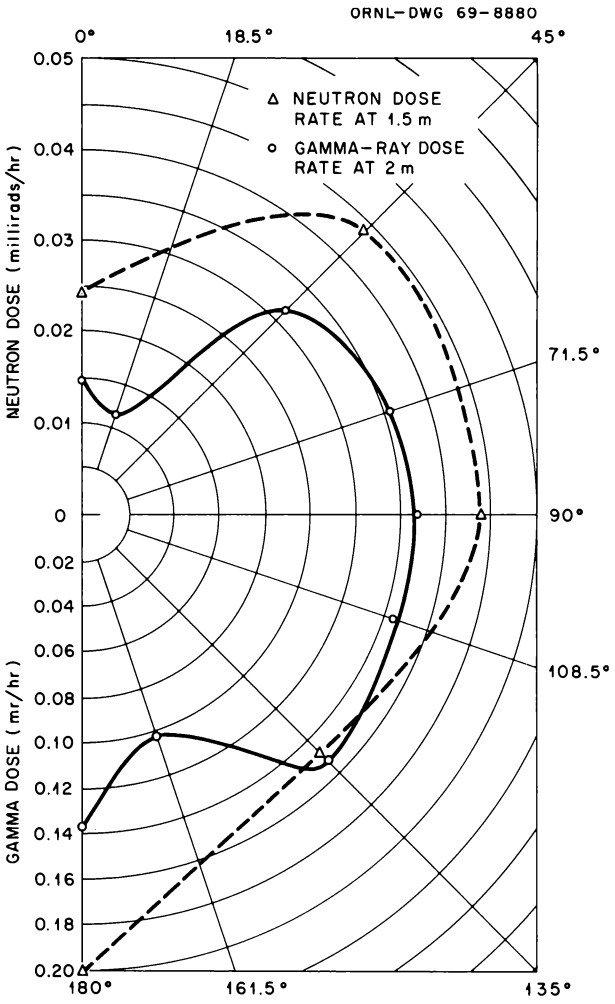

Fig. 20.5. Neutron and Gamma-Ray Dose Rate as a Function of Angle from Fat Man Experiment 2.

Man experiments are shown graphically by Figs. 20.4 through 20.7. The neutron dose at 1.5 m was quite low due to the excellent shielding afforded by the large amount of hydrogenous material contained in the Fat Man. When the angular response patterns of the fast-neutron fluence (Fig. 20.6) are compared with the fast-neutron dose rate angular response pattern (Fig. 20.5), it can be seen that at an angle of 180° the fast-neutron dose rate is somewhat greater than one would expect. This could be due to a streaming effect out of the source insertion hole and the fact that the fast-neutron detector is much smaller than the long counter.

The Small Boy data are summarized in Figs. 20.8 and 20.9. The graphs of Small Boy show no unusual perturbations, and the neutron dose shown by the polar

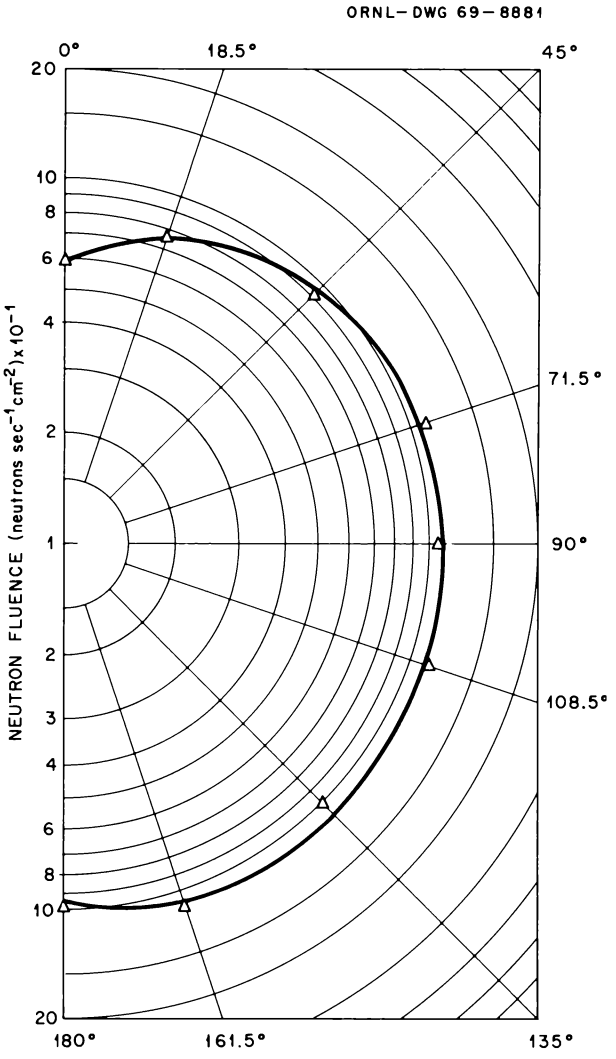

Fig. 20.6. Fat Man Experiment 2 Neutron Fluence at 2 m (Determined by the Long Counter) as a Function of Angle.

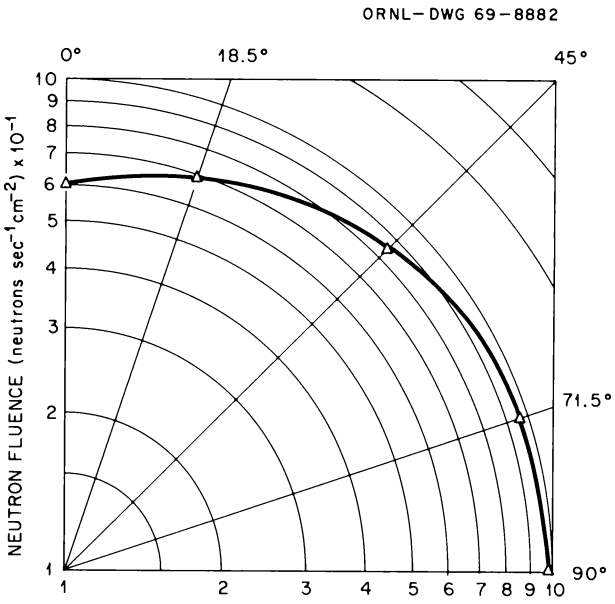

Fig. 20.7. Fat Man Experiment 1 Neutron Fluence at 2 m (Determined by the Long Counter) as a Function of Angle.

plot (Fig. 20.8) as obtained with the Radsan agrees quite well with the neutron fluence shown by the polar plot (Fig. 20.9) as obtained with the long counter. In addition, one can readily see the effect of the shielding geometry of the weapon, since the neutron radiation from the sides of the weapon (90 to 135°) is more than four times the neutron fluence in front (0 to 18°).

Radiation leakage data (neutron fluence, neutron dose rate, and gamma-ray dose rate) as a function of distance were also determined for each weapon. The data confirmed that the source contained inside either weapon is not a point source and therefore does not conform to an inverse square relationship.

By comparing the data obtained at 90° for the two weapons, it can be seen that the total neutron fluence for Small Boy is approximately 375 times that of Fat Man, and the fast-neutron fluence for Small Boy is a factor of 170 greater than that of Fat Man. The gamma-ray dose rate from Small Boy, compared to Fat Man, is only a factor of 5 greater. These leakage factors can be explained by the fact that the bulk of Fat Man's shielding is a hydrogenous material, while that of the Small Boy is composed chiefly of steel.

CALCULATION OF DEPTH DOSE AND LET

The Monte Carlo LET code[10,11] from many previous calculations was used to study dose and LET distributions in the phantoms shown in Fig. 20.10 (this phantom was used to study the dose and LET of neutrons from a broad parallel beam incident on the side of the phantom) and Fig. 20.11 (this phantom was used to study the dose and LET from neutrons incident

[10] J. A. Auxier, W. S. Snyder, and T. D. Jones, "Neutron Interactions and Penetration in Tissue," pp. 275–316 in *Radiation Dosimetry*, vol. I, 2d ed., ed. by F. H. Attix and W. C. Roesch, Academic, New York, 1968.

[11] W. S. Snyder, "The LET Distribution of Dose in Some Tissue Cylinders," in *Biological Effects of Neutron and Proton Irradiations*, vol. I, IAEA, Vienna, 1964.

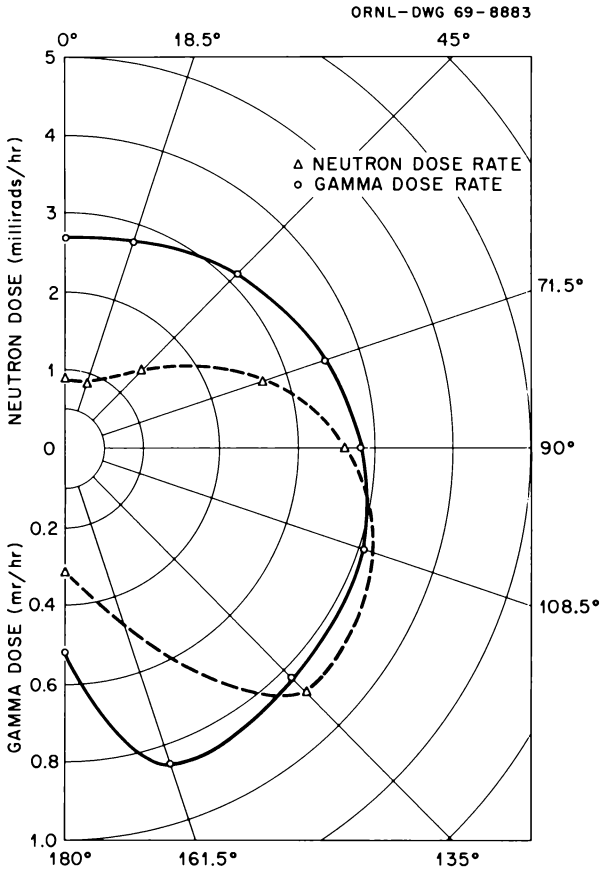

Fig. 20.8. Small Boy Neutron and Gamma-Ray Dose Rate at 2 m as a Function of Angle.

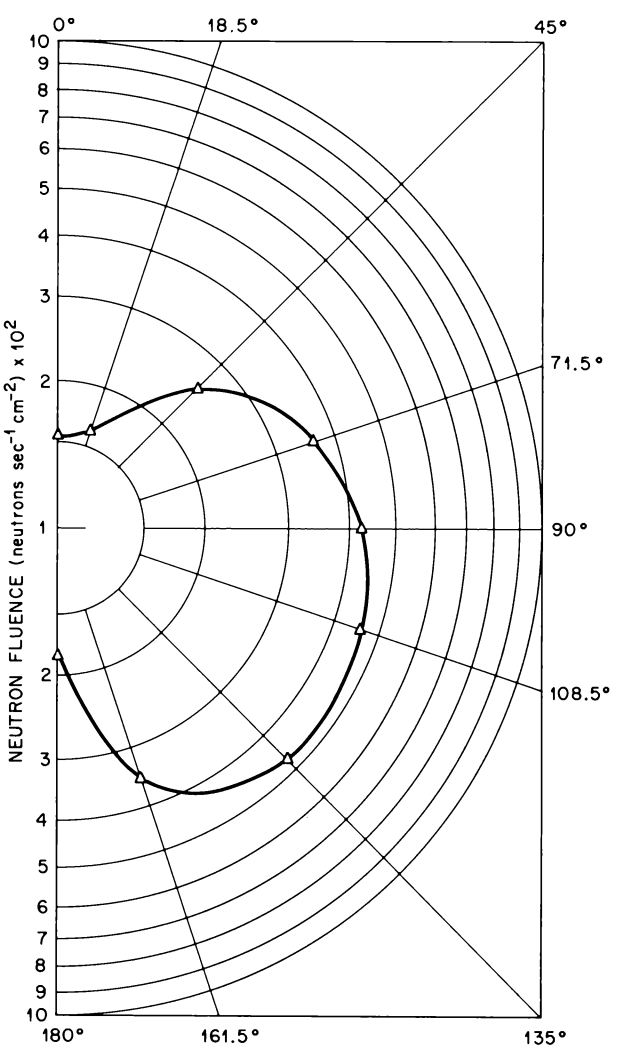

Fig. 20.9. Small Boy Neutron Fluence at 2 m (Determined by the Long Counter) as a Function of Angle.

on a 5-cm-diam circular area on the side of the phantom). Dose due to recoil ions and neutron-produced gamma rays were computed for neutron energies of 1, 2.5, 5, 7 and 14 Mev and 0.025 ev separately and were compared with broad-beam results (some of the comparisons are shown in Figs. 20.12–20.14). The doses at the front of the phantom, in the center of the restricted beam, were found to approximate those of a broad beam for 14 Mev and to converge to a value of about 75% of those for broad beams of lower energies. At depths in the phantom the dose from recoil ions decreases with variable relaxation lengths, so that at the back of the phantom a factor of ~3 was observed for the decrease in dose from 14, 7, and 5 Mev; a factor of ~15 for 1 Mev; and ~2 orders of magnitude for thermal neutrons. The doses inside the area of the beam (if a cylinder of 0.5 cm radius is used in addition to the 2.5-, 3.5-, 6-, and 8-cm cylinders) show no difference at a given depth except for 1-Mev and 0.025-ev neutrons. These two cases differ in the front 6 and 10 cm of depth, respectively, but converge at greater depths. The difference is thought to be due to neutrons escaping from the front of the phantom. Dose from recoil ions averaged over an annular region 1 cm thick, immediately outside the area of the incident beam, was found to be lower by an order of magnitude (for all energies except thermal, where a factor of 4 was observed) as compared with dose at corresponding depths within the beam.

LET spectra were computed in various volume elements according to the stopping-power data shown in Fig. 20.15.[10,11] The LET intervals were chosen as

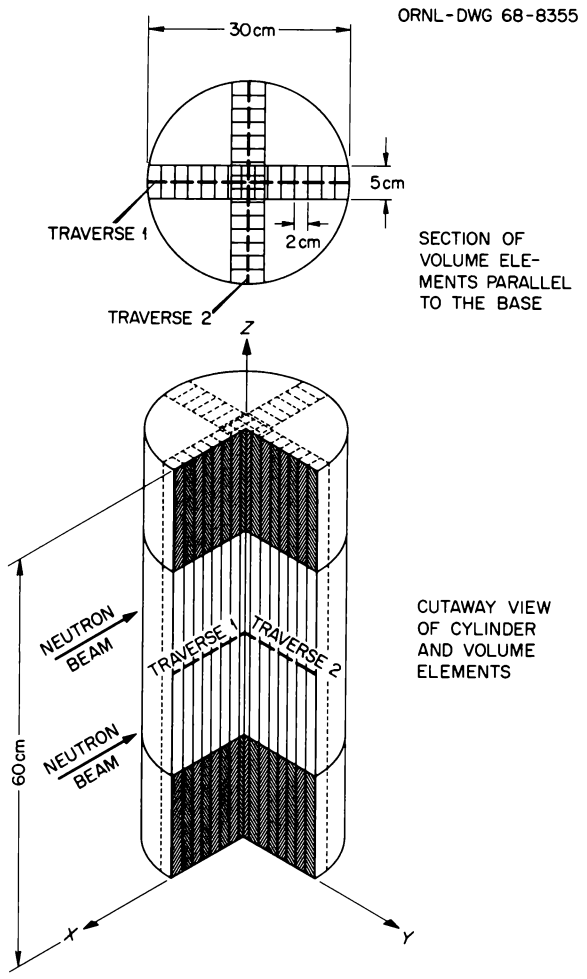

Fig. 20.10. Cylindrical Phantom and Volume Elements for Averaging of Dose and Dose Equivalent.

shown in Table 20.2, which also gives various LET spectra (in numerical form) for the 0.025-ev case.

Figures 20.16 and 20.17 show fraction of dose as a function of LET. These data have been averaged over the previously mentioned LET intervals and have been smoothed somewhat to illustrate better the changing effect of LET on dose.

The LET curves in Figs. 20.16 and 20.17 are the result of total LET in tissue, and their shape is determined by:

1. Low LET (<5 kev/μ): due mainly to gamma rays, the dominant being the 2.2-Mev gamma ray from the $^1H(n,\gamma)^2H$ reaction.
2. Intermediate LET (>5 kev/μ and <100 kev/μ): due mainly to the protons from hydrogen recoil. The spike at a value of slightly less than 100 kev/μ is due to the Bragg peak on the proton curve as seen in Fig. 20.15. The broader peak at slightly lower energy is due to protons with energies both below and above the Bragg peak.
3. High LET (>100 kev/μ): due mainly to heavy ions (O, C, N, and secondary ions of B and Be).

LET Distributions for 2.5-Mev Neutrons

For volume elements 16, 23, and 30, which are all in the path of the unattenuated particles, there is a gradual softening or degrading of the LET spectrum as the penetration distance is increased. The spikes are nearly constant with respect to their respective broad peaks. For volume elements 46, 53, and 60, which are just outside the path of unattenuated neutrons, the trends set in 16, 23, and 30 are still present; however, it is noticeable from all of the curves that as penetration depth is increased and/or as distance from the path of the unattenuated particles is increased, there is a gradual degrading of the LET spectrum so that there is a dose "pile-up" at lower values of LET. It seems that the ratio of the spike to that of the curve is nearly constant with depth but increases with distance from the unattenuated path so that the ratio of the two is unity at distances of more than 1 cm from the path of the unattenuated particles. Curves for volume elements 30 and 60 appear quite similar except at extremely low values of LET, where the two differ markedly. Curves for elements 23 and 46 are nearly identical, as are 53 and 62. Each of these two cases illustrates essentially the same LET spectrum for volume elements at significantly different locations in the phantom. This is due to a compensating effect of two different factors: (1) depth from the front of the phantom and (2) distance from the path of the unattenuated particles or the angle of scatter necessary to reach the volume element.

LET Distributions for 14-Mev Neutrons

For the 14-Mev case the LET spectrum seemed to be invariant with penetration depth because of the greater mean free path of 14-Mev neutrons as compared with 2.5-Mev neutrons; however, the effect of scatter angle differed more than in the 2.5-Mev case. Most noticeable was the variation in the magnitude of the height of the spike relative to the broad peak of the curve. In the case of volume elements 16, 23, and 30, the spike appears conspicuously absent (actually just hidden by heavy-ion contribution); however, for volume elements outside the path of the unattenuated particles, it appeared and

Table 20.2. LET as a Function of Detector Position for 0.025-ev Incident Neutrons (Circular Beam, 5 cm Diameter)

Volume Element No.	LET (kev/μ)												
	0–3.5(n,γ)	0–3.5	3.5–7.0	7.0–15.0	15.0–25.0	25.0–35.0	35.0–50.0	50.0–62.5	62.5–75.0	75.0–87.5	87.5–100.	100.–200.	200.–950.
16	.145–9*	.107–13	.319–13	.141–12	.322–12	.491–12	.134–10	.116–10	.736–11	.529–11	.804–11	.529–12	
23	.137–11	.421–17	.125–16	.556–16	.126–15	.193–15	.527–14	.457–14	.289–14	.208–14	.316–14	.208–15	
30	.893–12												
46	.645–10	.269–14	.803–14	.356–13	.808–13	.123–12	.337–11	.293–11	.185–11	.133–11	.202–11	.133–12	
53	.254–11	.401–17	.120–16	.530–16	.120–15	.184–15	.502–14	.436–14	.276–14	.198–14	.301–14	.198–15	
60	.308–12												
62	.279–10	.501–15	.149–14	.662–14	.150–13	.229–13	.627–12	.544–12	.344–12	.247–12	.376–12	.247–13	
68	.273–11	.337–17	.100–16	.445–16	.101–15	.154–15	.422–14	.366–14	.232–14	.166–14	.253–14	.166–15	
74	.430–12	.859–19	.256–18	.114–17	.258–17	.394–17	.108–15	.934–16	.590–16	.424–16	.645–16	.424–17	
93	.189–11	.368–17	.110–16	.487–16	.111–15	.169–15	.461–14	.400–14	.253–14	.182–14	.276–14	.182–15	
98	.827–12	.214–18	.638–18	.283–17	.643–17	.981–17	.268–15	.233–15	.147–15	.106–15	.161–15	.106–16	
103	.278–12												

*Rads Neutron^{-1} cm^2

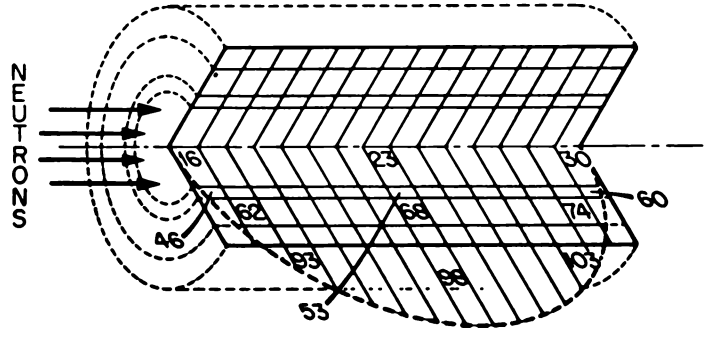

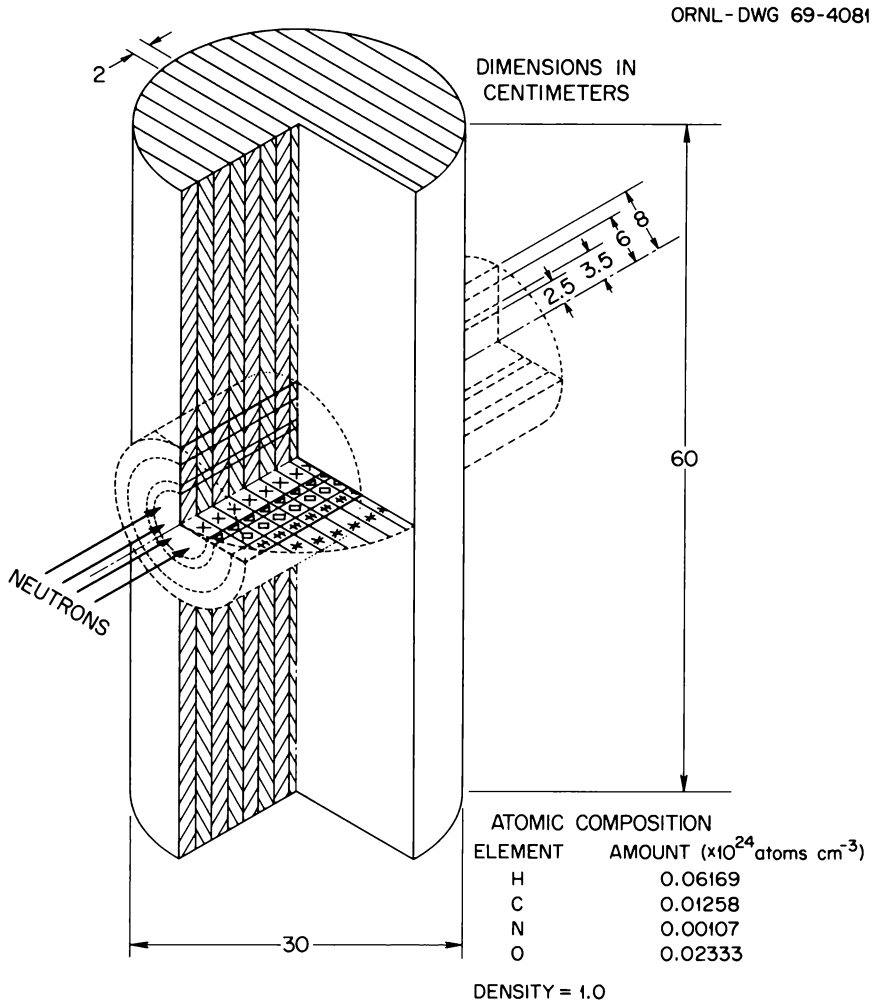

Fig. 20.11. Phantom for Study of *D* and *DE* Due to a Collimated Beam of Neutrons.

grew larger as angle of scatter increased. It is interesting to note that over these two cases of 2.5 and 14 Mev, the ratio of the height of the spike to the height of the broad peak varies from near zero to unity.

DOSIMETRY FOR ^{252}Cf SOURCES

By use of the theoretical spectrum published by Hyde *et al.*,[12] a conversion factor which relates neutron fluence from ^{252}Cf to dose to a small mass of tissue was calculated. Two independent dosimetry systems were used to determine the conversion factor experimentally. The values obtained by measurements agreed to within 3 and 4%, respectively, with the calculated value. A neutron to gamma dose ratio of 1.59 was found and was within 5% of the values obtained from each system.

The dose per unit neutron fluence was calculated from the general expression for the "first collision" dose and the energy spectrum of a ^{252}Cf source using the relation:

$$\text{Dose (rads neutron}^{-1}\text{ cm}^2) = \left(\sum_{j=1}^{n} P_j \frac{[E_j + E_{j+1}]}{2}\right) \times \left(\sum_i \frac{4M_i A_{ioi} \cos^2\theta}{(M_i+1)^2}\right) 1.6 \times 10^{-8} ,$$

[12] E. K. Hyde, *A Review of Nuclear Fission Part I. Fission Phenomena at Low Energy*, UCRL-9036 (1960).

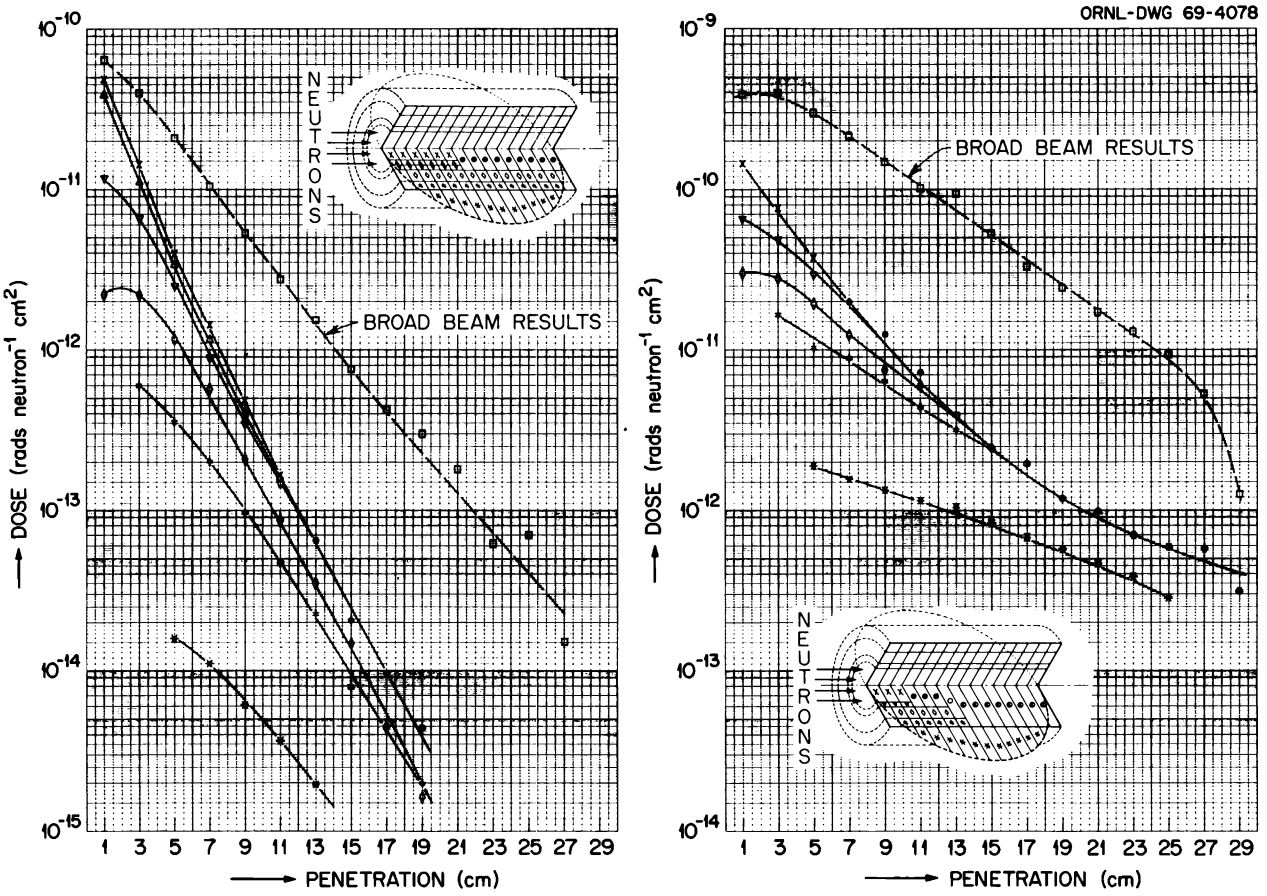

Fig. 20.12. Dose from Recoil Ions and Neutron-Produced Gamma Rays for Collimated Beam and Broad Beam of 0.025-ev Neutrons.

where P_j is the probability that a neutron from ^{252}Cf has energy between E_j and E_{j+1}. The other symbols used are the same as those used in *NBS Handbook 63*. The fluence and dose histograms are shown in Fig. 20.18.

An active dosimetry system consisting of the Radsan pulse-height integrator using a cyclopropane-filled, polyethylene-lined proportional counter for the detector and the Phil was used to measure the dose from the californium. Also, a passive system consisting of the threshold detector employing solid-state nuclear track detectors and Toshiba RPL glass was used to measure the dose.

DOSE DISTRIBUTIONS IN CYCLINDERS EXPOSED DURING OPERATION HENRE

Experimental measurements of the dose at the center of cylinders of various sizes and compositions were made for exposures to neutrons produced by the HENRE accelerator. To gain insight into the energy and angular distribution of the neutrons and how this distribution affects the dose and LET patterns, a calculational experiment was undertaken for an H_2O-filled cylinder 40 cm in diameter and 46 cm in height. In order to observe what factors were important, the Monte Carlo LET[10,11] code was run assuming (1) 10% of the neutrons reaching the cylindrical phantom were unmoderated 14-Mev neutrons; (2) 60% of the neutrons were incident on the forward half (isotropically distributed with respect to angle) of the cylinder with the energy distribution predicted by Trubey[13] for $4\pi R^2$ flux vs energy at 605 m from a point isotropic fission source in an infinite air medium as shown in Fig. 20.19; and (3) 30% of the neutrons were incident on the back

[13] E. A. Straker, *Calculations of the Transport of Neutrons from Fission and 14-Mev Point Sources in an Infinite Medium of Air*, ORNL-TM-1547 (August 1966).

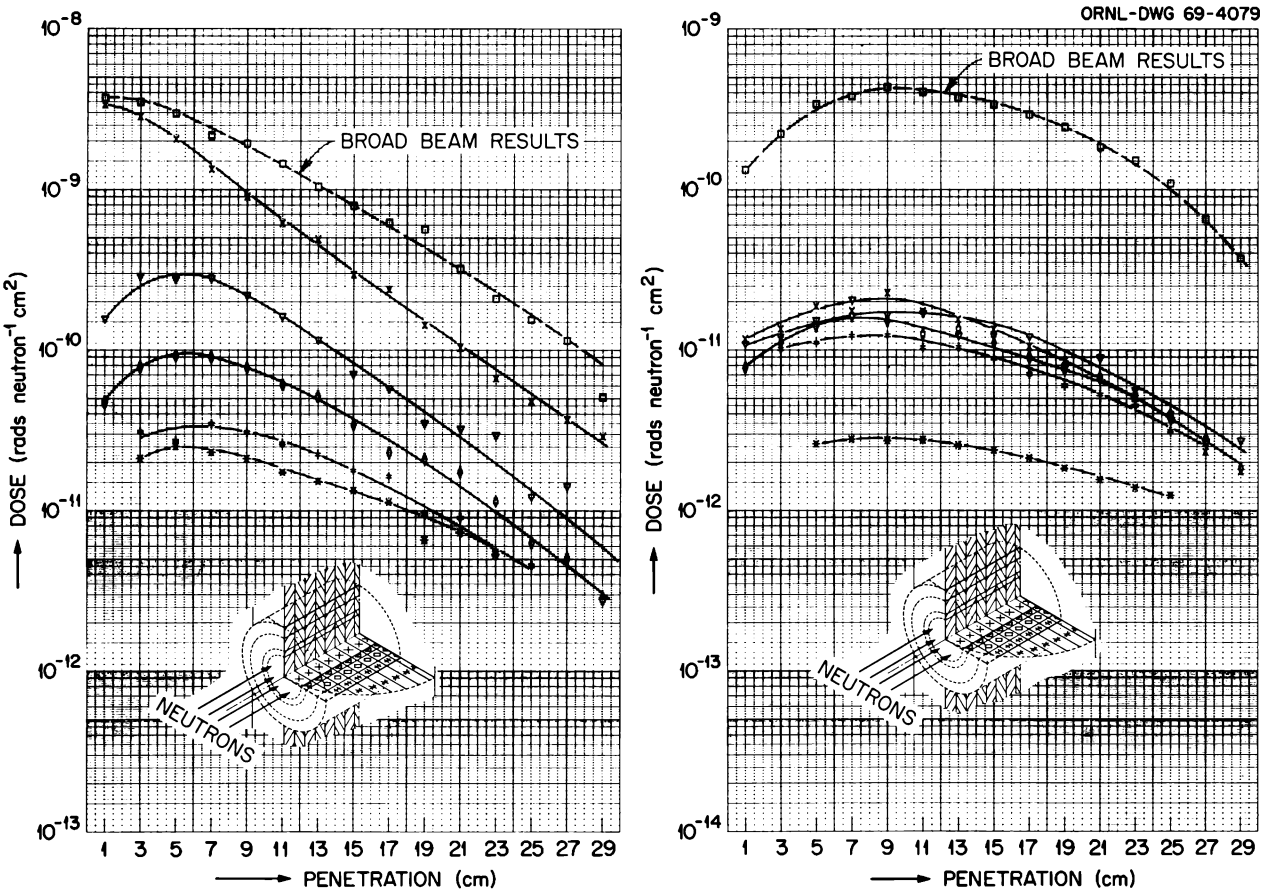

Fig. 20.13. Dose from Recoil Ions and Neutron-Produced Gamma Rays for Collimated Beam and Broad Beam of 2.5-Mev Neutrons.

half (isotropically distributed with respect to angle), also distributed according to the Trubey energy spectrum. The dose as a function of distance from the front surface along the diameter is shown in Fig. 20.20.

The experimental results for dose are lower than the value at the center of the cylinder by about 50%; however, the cylinder used in the actual experiment had a cylindrical cavity in the center (radius of about 0.1 diameter of the large phantom). Because dose decreases as distance from the surfaces increases, it was necessary to refine the calculations further to see if it was essential to make a void in the theoretical model to correspond to the hole in the experimental model.

The next step was undertaken using Straker's[14] results from the discrete-ordinates method of solving the transport problem by utilizing the two-dimensional anisotropic scattering code (DOT).[15] Straker's results were all in tabular form and gave both energy and angular distributions for neutrons at a source height of 344 m and a horizontal distance of 879 m with initial neutron energy at the source of 15 Mev. Straker's results were to provide the energy, angle of entry, and position of entry into the phantom for each successive neutron started by the Monte Carlo LET code. After the task of programming Straker's results was finished and debugging was complete, the subroutine was called several times to test its validity and applicability. The energy distribution from the subroutine is shown in Fig. 20.21 for a $4\pi R^2$ geometry at the phantom and compares well (considering the small number of times

[14] E. A. Straker and R. J. Rodgers, "Neutron Transport in the Atmosphere," presented at the American Nuclear Society Winter Meeting, Chicago, Ill., Nov. 5–9, 1967, and published in the transactions.

[15] F. R. Mynatt, *A User's Manual for DOT, a Two-Dimensional Discrete Ordinates Transport Code with Anisotropic Scattering*, K-1694 (to be published).

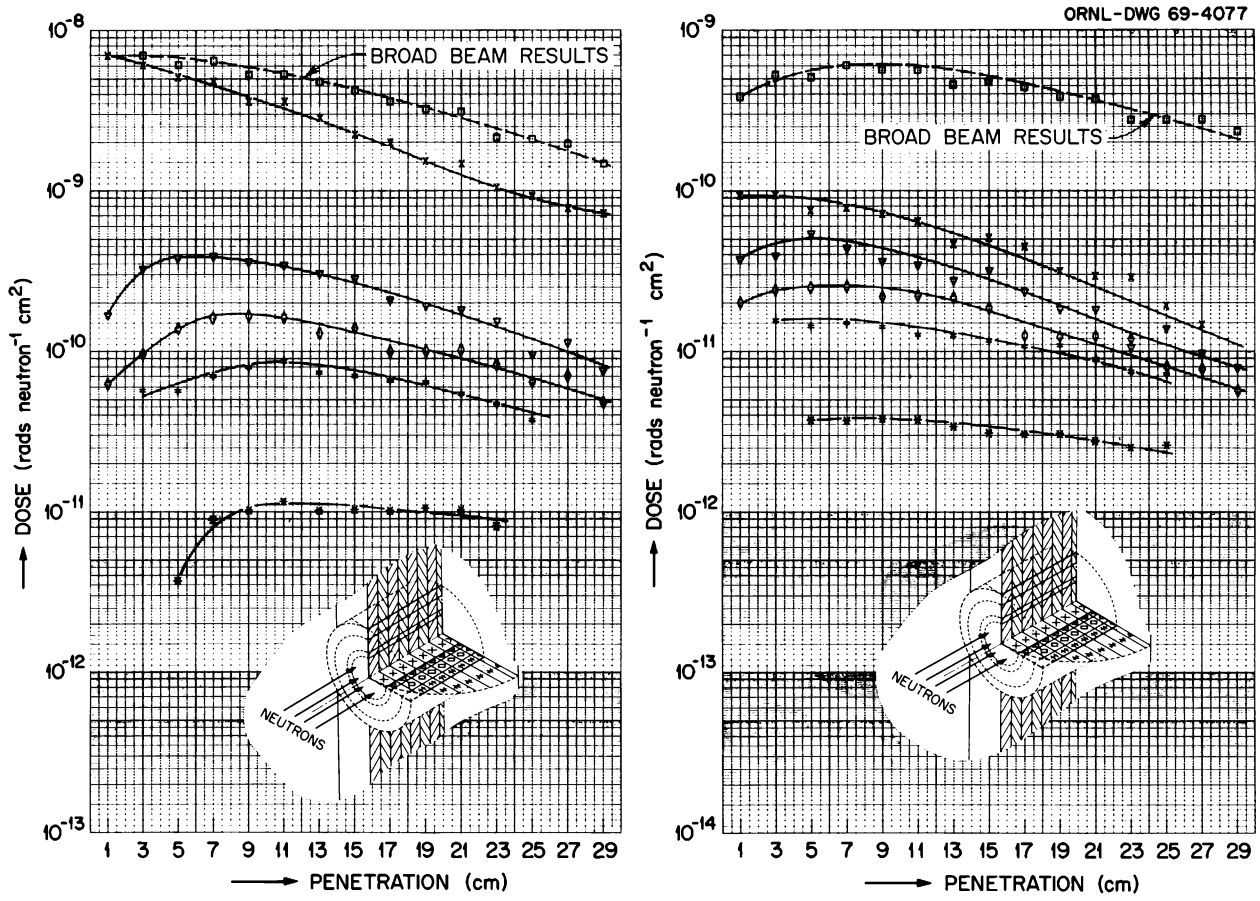

Fig. 20.14. Dose from Recoil Ions and Neutron-Produced Gamma Rays for Collimated Beam and Broad Beam of 14-Mev Neutrons.

the subroutine was called) with Straker's original data and the results of measurements taken in the field during Operation HENRE. The results of dose vs depth are shown in Fig. 20.20; they are lower than experimental ones by about 50%, and at the present time the LET code is being revised to produce a void in the center of the cylinder so that results may be compared directly.

^{24}Na DETERMINATION IN SWINE IRRADIATED WITH 14-Mev NEUTRONS

In cooperation with the UT-AEC Agricultural Research Laboratory, a series of swine irradiations were made at the Nevada Test Site using 14-Mev neutrons from the HENRE[16,17] neutron generator. Of specific interest, in addition to clinical signs and survival as a function of dose, was the determination of the quotient, dose per unit of ^{24}Na activation normalized to the concentration of elemental sodium in blood serum; and the absorbed dose at the center line of the animal both in the chest and abdomen sections.

In the experiment, a total of 28 swine weighing about 200 lb each were exposed to target neutron dose levels of 200, 400, and 600 rads.

Preliminary indications are that for a 200-lb pig, the average dose per unit of ^{24}Na activation in blood is

$$1.81 \pm 0.30 \times 10^{-4} \frac{\text{rads}}{\mu\text{c } ^{24}\text{Na/mg Na}} .$$

Because of geometry conditions, which were not well suited for this experiment, the animals were exposed (bilaterally) at two fixed distances, 6 ft and 7.5 ft, from

[16] T. G. Provenzano *et al.*, *Feasibility Study: Intense 14-Mev Neutron Source for Operation HENRE*, CEX-65.01 (May 1966).

[17] F. F. Haywood, T. G. Provenzano, and J. A. Auxier, *Operations Plan – Operation HENRE*, CEX-65.03 (September 1965).

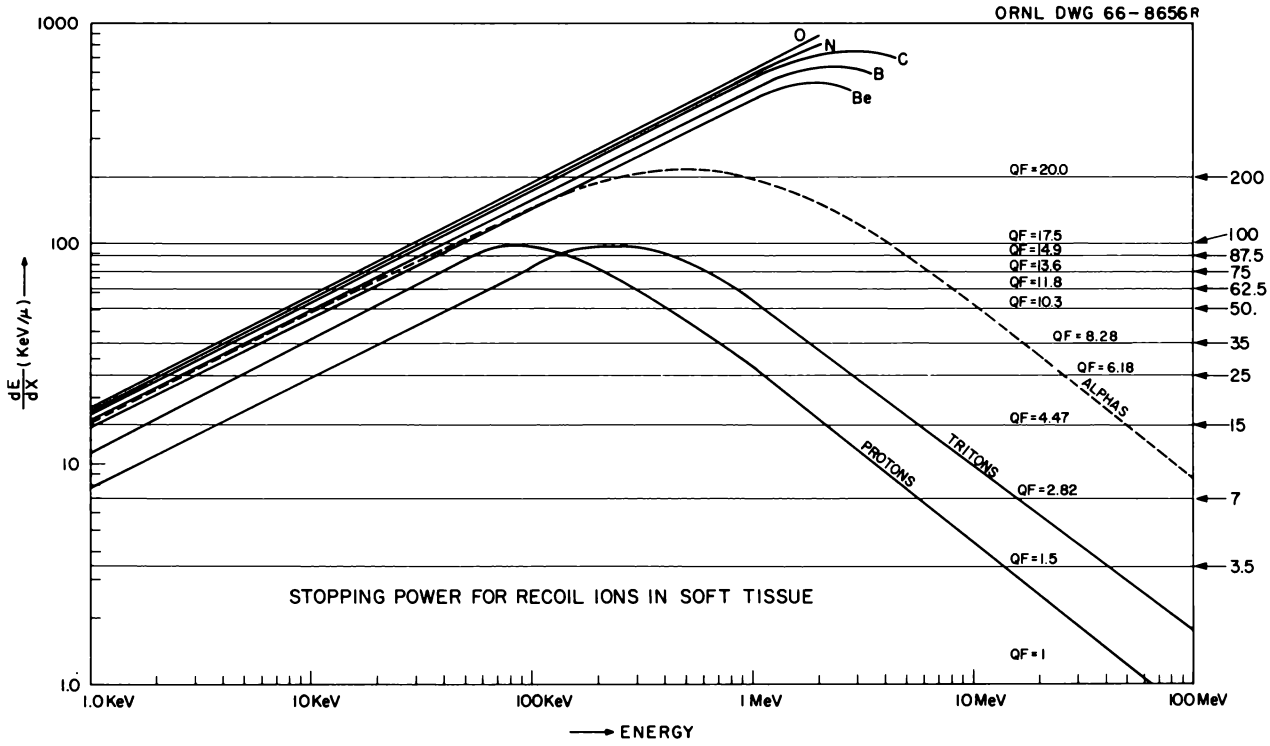

Fig. 20.15. Stopping Power for Recoil Ions in Soft Tissue.

the center of the target. Unembalmed cadavers were exposed (unilaterally, one at each location) in order to determine neutron and gamma dose at the midline of the animal. For the 6-ft cage position, preliminary neutron doses in the chest and abdomen cavities were 0.51 and 0.73 times the incident dose, and for gamma rays in the same location, the dose was 0.63 and 0.88 times the incident dose. Measurements of dose in the chest and abdomen cavities relative to the incident dose at the 7.5-ft position were 0.36 and 0.66 for neutrons and 0.59 and 0.78 for gamma rays.

THERMAL-NEUTRON DISTRIBUTIONS FROM A POINT SOURCE OF 14-Mev NEUTRONS

In making calculations of fast-neutron fluence as a function of distance from a point source, it is desirable to know the distribution of thermal neutrons, in the same geometry conditions, which serves as an end point index for the neutrons put into a program. During the last phase of Operation HENRE at the Nevada Test Site, measurements of thermal-neutron fluence were made at ground level for distances to 3500 ft with the 14-Mev neutron source positioned 54 ft above ground. This distribution, shown in Fig. 20.22, bears out earlier findings which indicate that the neutron spectrum is not in equilibrium at 3500 ft. In addition to the distribution at ground level, the thermal-neutron fluence as a function of height up to 145 ft was determined for the source at 54 ft above ground and for the detector station 1150 ft horizontal distance from the source. This distribution was found to be approximately flat between 25 ft and 100 ft. However, below 25 ft the fluence increases by 40% at ground level and above 100 ft decreases by 38% at 145 ft. These data are shown in Fig. 20.23.

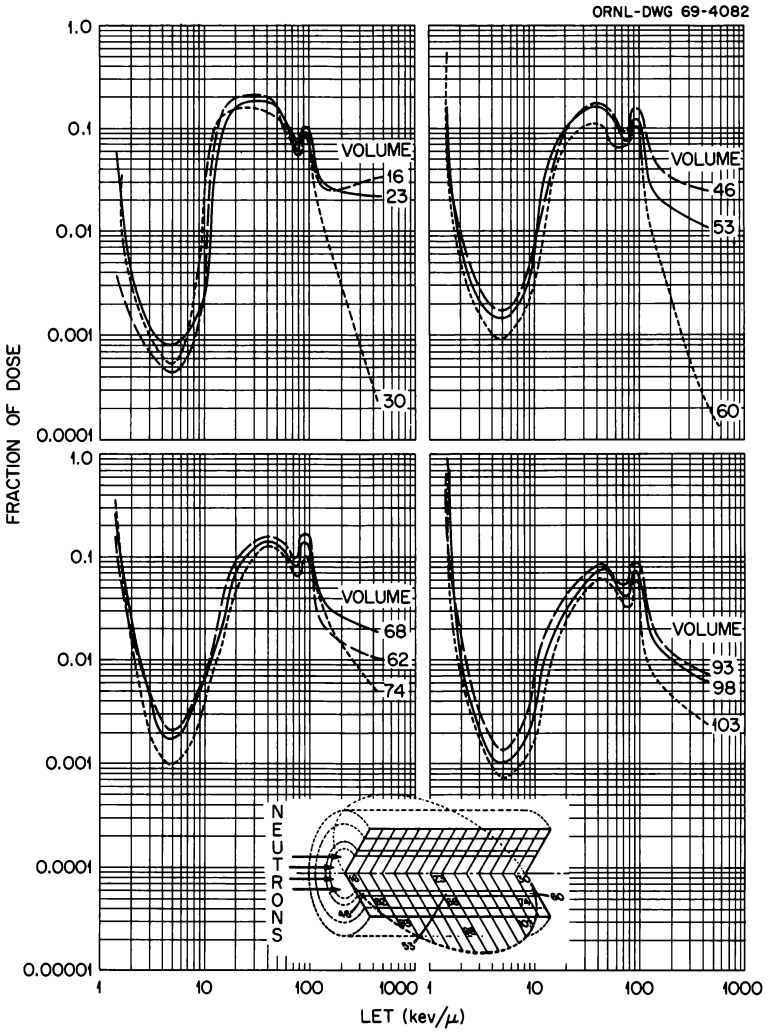

Fig. 20.16. Fraction of Dose as a Function of LET for 2.5-Mev Incident Neutrons.

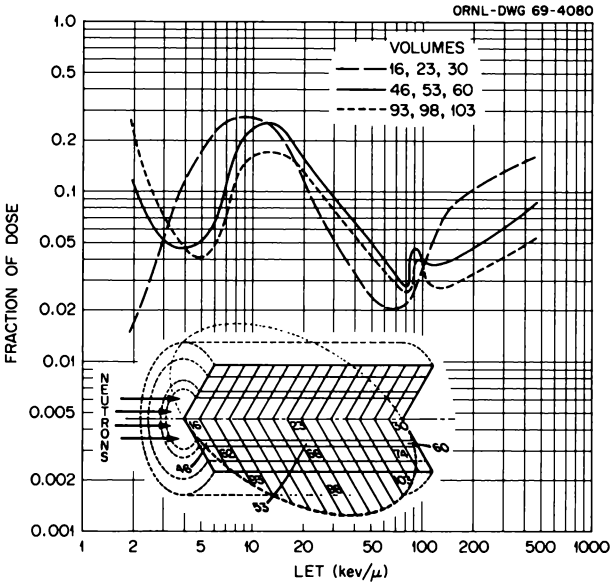

Fig. 20.17. Fraction of Dose as a Function of LET for 14-Mev Incident Neutrons.

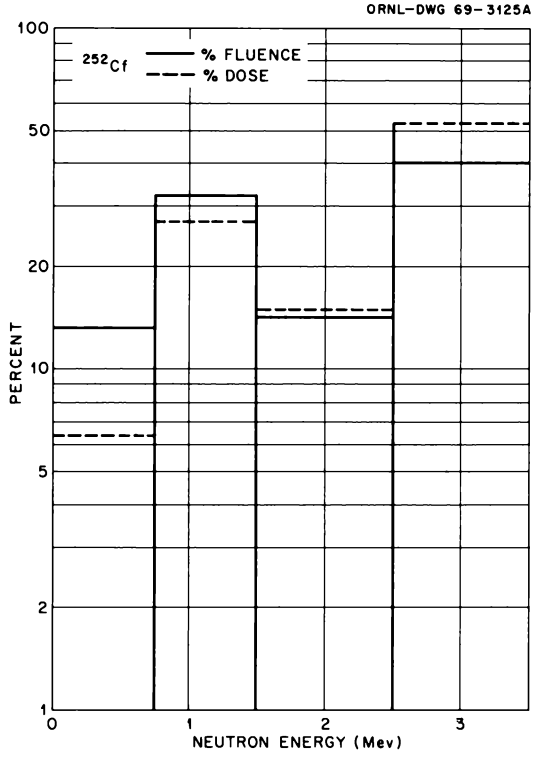

Fig. 20.18. Histogram Showing Percent of Total Fluence and Percent of Total Dose as a Function of Neutron Energy from a ^{252}Cf Source in Air as Measured with TDU's.

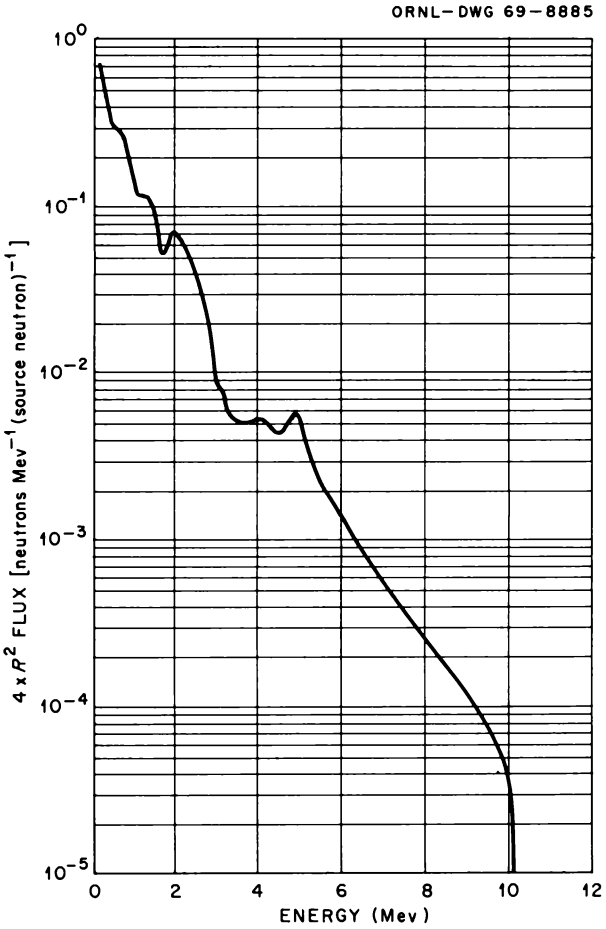

Fig. 20.19. Trubey Energy Spectrum from Moments Calculation of $4\pi R^2$ Flux vs Energy at 605 m from a Point Isotropic Fission Source in an Infinite Air Medium of Density 1.29 mg/cc.

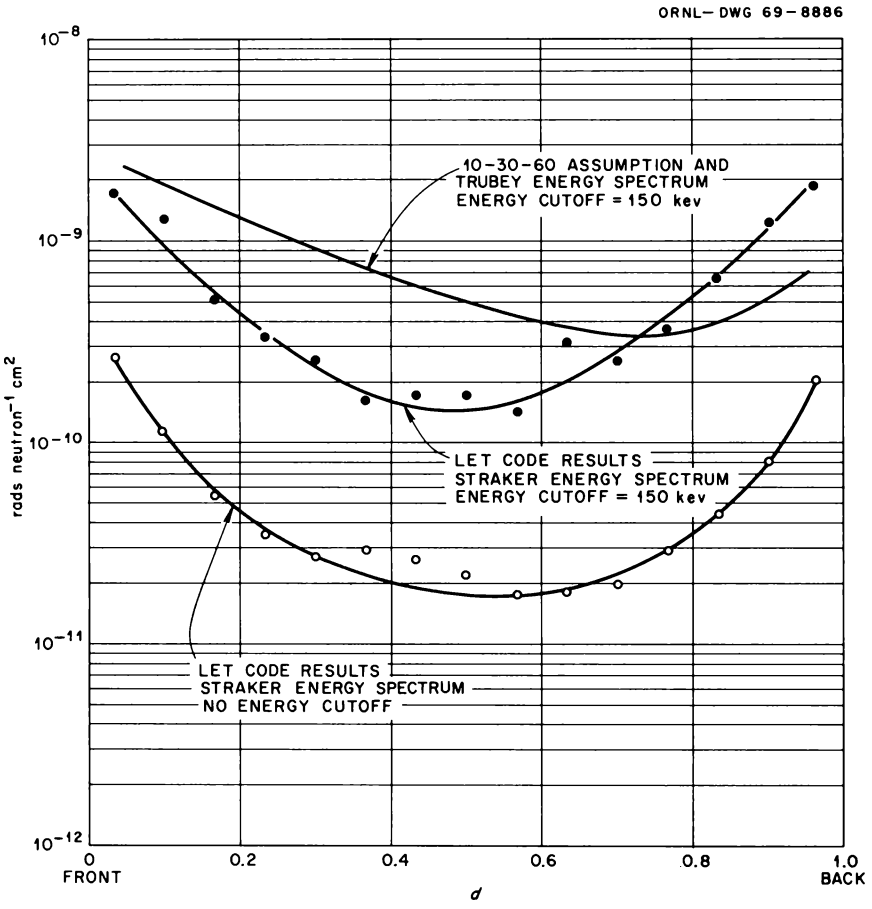

Fig. 20.20. Dose from Recoil Ions in a Cylindrical Phantom Filled with H_2O (Height = 46 cm; Radius = 40 cm).

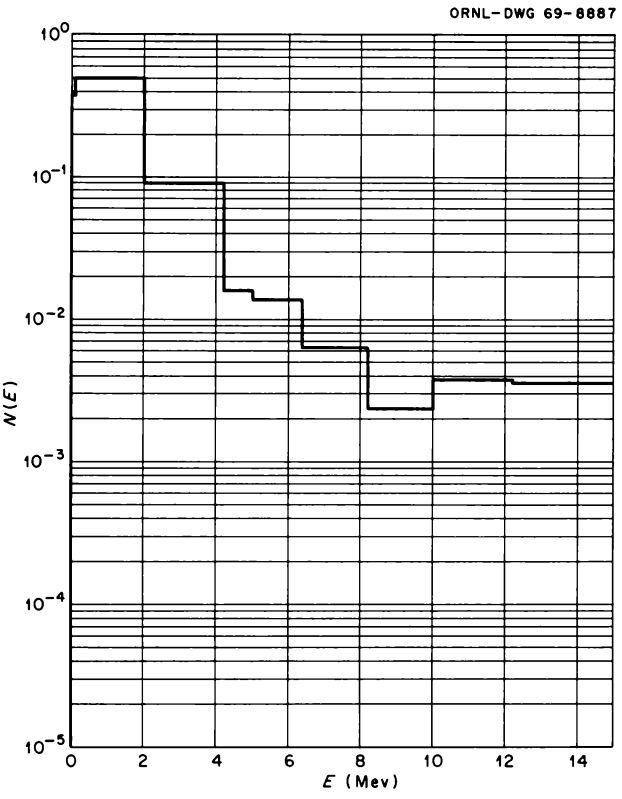

Fig. 20.21. Probability Density Function of Neutron Energy from a 15-Mev Neutron Source Based on a Monte Carlo Description of Straker's Calculational Data (Energy Cutoff at 150 kev; Source Height = 344 m; Horizontal Distance = 879 m).

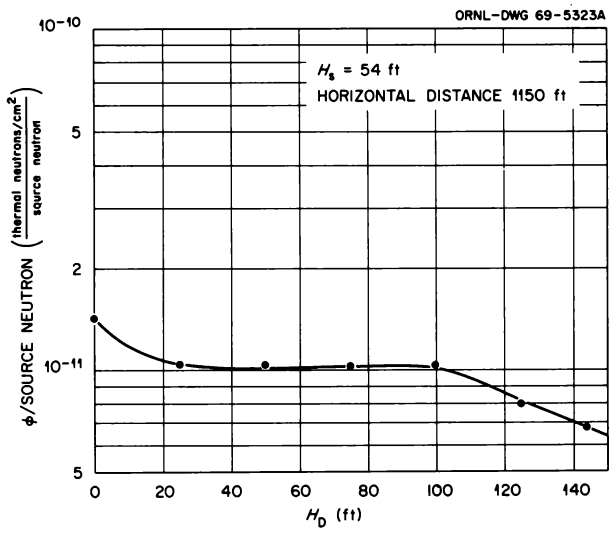

Fig. 20.23. Thermal-Neutron Distribution as a Function of Height Above the Air-Ground Interface at 1150 ft Horizontal Distance from a Point 14-Mev Neutron Source Operating 54 ft Above Ground.

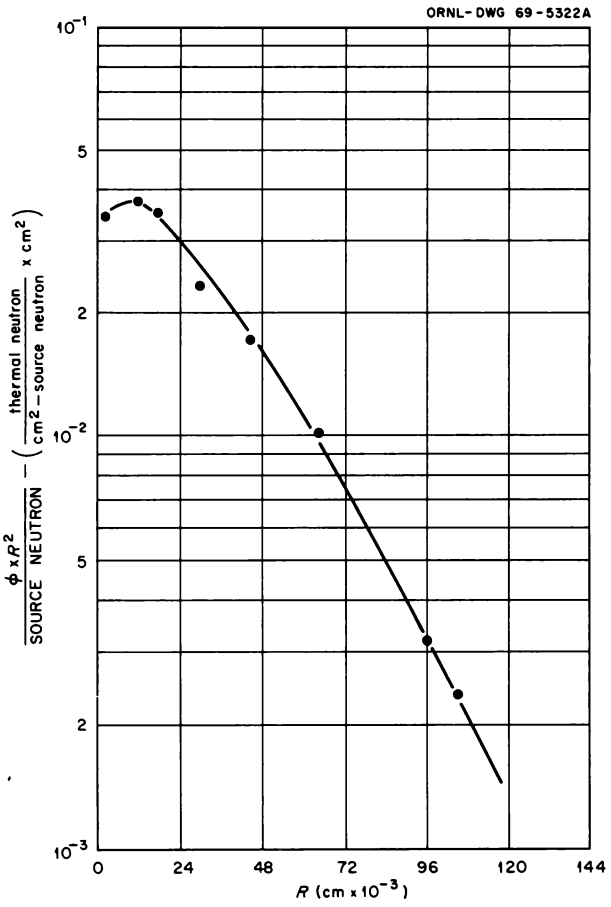

Fig. 20.22. Thermal-Neutron Distribution Along the Air-Ground Interface for Distances to 3500 ft from a Point 14-Mev Neutron Source Operating 54 ft Above Ground.

21. Spectrometry Research and Development

J. H. Thorngate
M. D. Brown[1] P. T. Perdue
T. Saigusa[2]

ENERGY AND ANGULAR DISTRIBUTIONS OF RADIATIONS FROM THE ACCELERATOR USED DURING OPERATION HENRE

Preliminary results of the energy and angular distributions of neutrons and gamma rays measured during Operation HENRE have been presented in previous annual reports.[3,4] The final results are now available and have been reported in detail, so only a brief summary will be presented here for Project 1.1.[5]

The most important conclusion reached was that an equilibrium condition in the neutron spectrum was not reached even at ranges as great as 1500 m from the source. That is, the mean energy of the fast-neutron spectrum decreases monotonically for ranges between 350 and 1500 m. To include distances this great, the conclusion must be based upon the calculations.[6] Such a procedure is justified by good agreement between the measurements and calculations, as shown in Figs. 21.1 and 21.2, which were recorded at ranges of 215 and 766 m respectively. The experimental points fall within three standard deviations of the calculations, with most of the difference due to the approximations necessary to get the measurements into the same units as the calculations. Between 350 and 1500 m the mean energy can be expressed by a power function of the range, $\bar{E}_n = 35.04R^{-0.375}$, with a correlation coefficient of −0.992. Because all of the data measured depend upon what happens to the neutrons from the source, most of the effects discussed below result from the variation of the neutron spectrum.

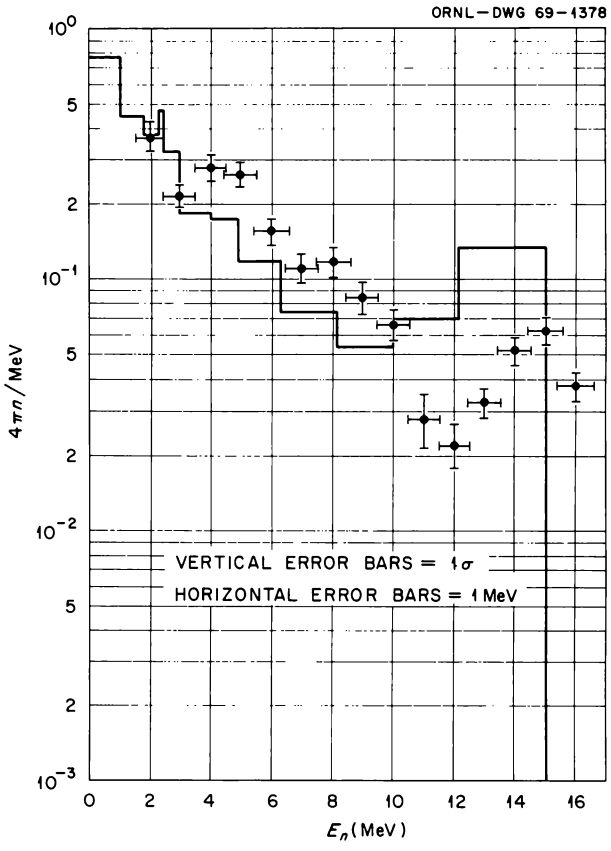

Fig. 21.1. Neutron Spectrum in Air at a Range of 215 m. Source height 500 ft, lateral distance 500 ft. Data normalized to 4π neutrons per Mev per source neutron. Compared with calculations at the same range (source height of 1125 ft).

[1] Part time.

[2] Alien guest.

[3] J. A. Auxier *et al., Health Phys. Div. Ann. Progr. Rept. July 31, 1967,* ORNL-4168, p. 190.

[4] J. A. Auxier *et al., Health Phys. Div. Ann. Progr. Rept. July 31, 1968,* ORNL-4316, p. 234.

[5] J. H. Thorngate, D. R. Johnson, and P. T. Perdue, *Energy and Angular Distribution of Neutrons and Gamma-Rays – Operation HENRE,* CEX-65.11, in press.

[6] E. A. Straker, private communication.

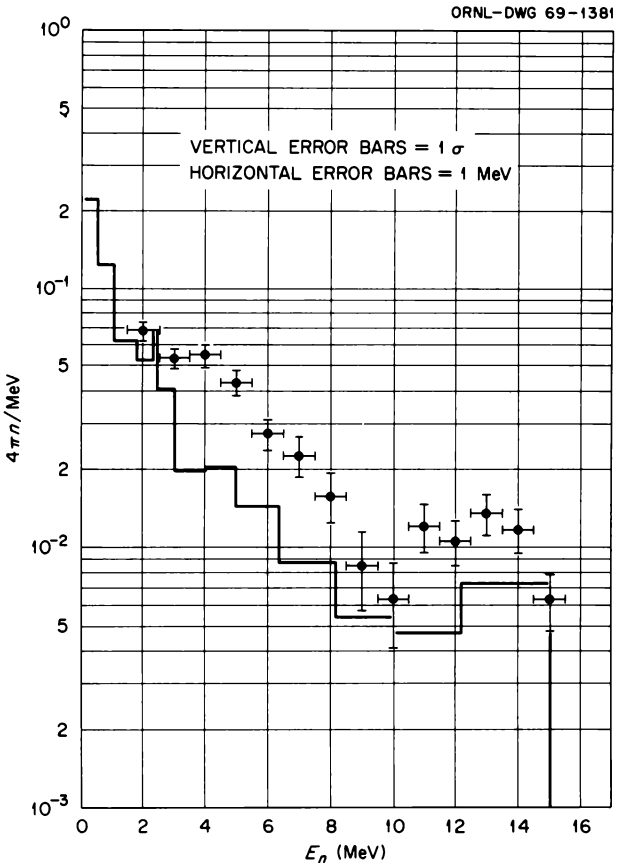

Fig. 21.2. Neutron Spectrum in Air at a Range of 766 m. Source height 1125 ft, lateral distance 2250 ft. Data normalized to 4π neutrons per Mev per source neutron. Compared with calculations for the same conditions.

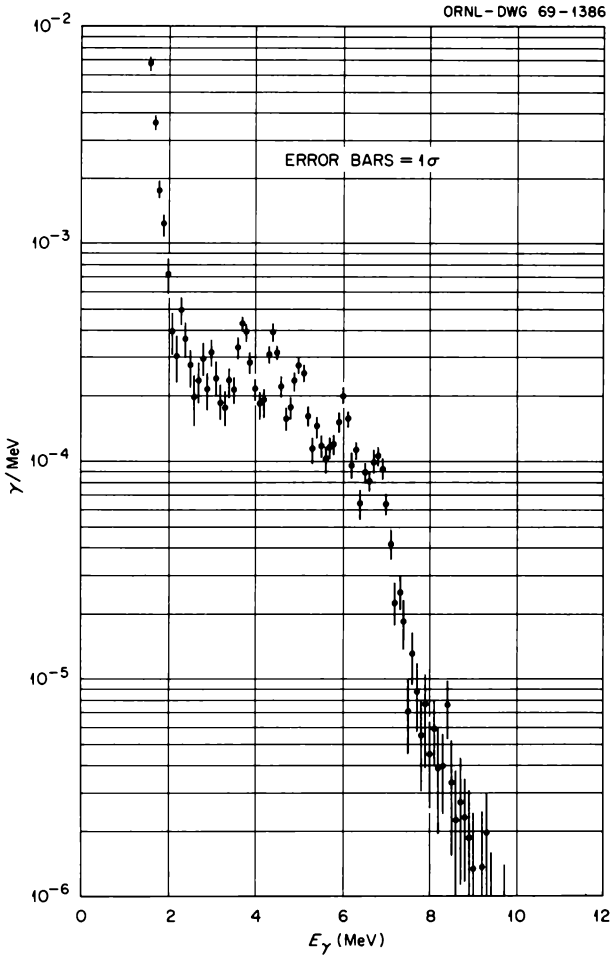

Fig. 21.3. Gamma-Ray Spectrum for a 0° Polar Angle, 30° Collimator Acceptance Angle, Source Height of 500 ft, and a Slant Range of 527 yd (482 m). Data normalized to 4π gamma rays per Mev per source neutron.

Results for the gamma-ray spectrum measurements are summarized by Figs. 21.3–21.5. Figure 21.3 shows the amount of detail recorded in a typical measurement, in this case for the spectrometer aimed directly at the source at a range of 482 m. In Fig. 21.4 the same data have been integrated so that the energy intervals compare with those of the calculations, and the two are compared. Once again some of the difference is due to the approximations required to express the measurements and calculations in the same units. Figure 21.5 shows the gamma spectra as a function of incident angle, measured with a collimator that had a conical opening with a 30° total angle. The range was 571 m. These data were integrated to reduce statistical fluctuations in the 45 and 90° data, with the energy intervals chosen to be consistent with other data presented.

Conclusions reached from the measurement of the gamma-ray spectrum are that (1) little of the observed gamma field is produced by the $^{14}N(n,\gamma)^{15}N$ reaction, (2) more gamma rays were measured in the 3-to-5-Mev region than found in the calculations, and (3) fewer gamma rays were observed above 8 Mev than predicted by the calculations. The latter two could be correlated if the difference between measurement and calculation is assumed to be a result of the omission from the calculation of some possible reactions that produce 3- to 5-Mev gamma rays. The omitted reactions would use some of the neutrons that might otherwise yield gamma rays in the energy region above 8 Mev. Gamma rays from the $^{14}N(n,\gamma)^{15}N$ reaction are produced more efficiently by low-energy neutrons, and the measurements show that for ranges near 500 m, there are few low-energy neutrons. Calculations of the mean energy of the gamma spectrum as a function of range show it is quite stable until the range nears 1500 m, where the

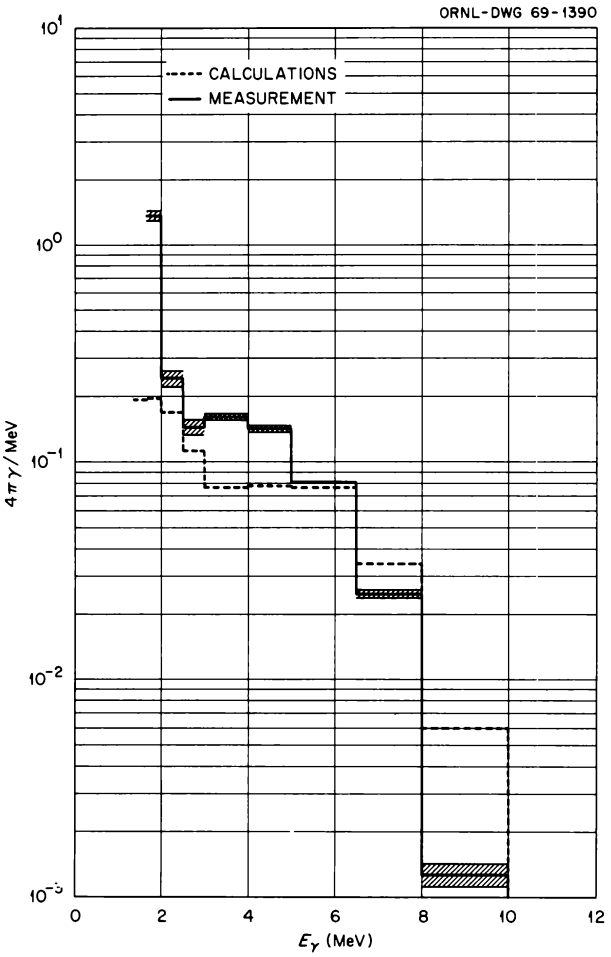

Fig. 21.4. Comparison of Measured 0°, 500 ft Gamma Spectrum with Calculations.

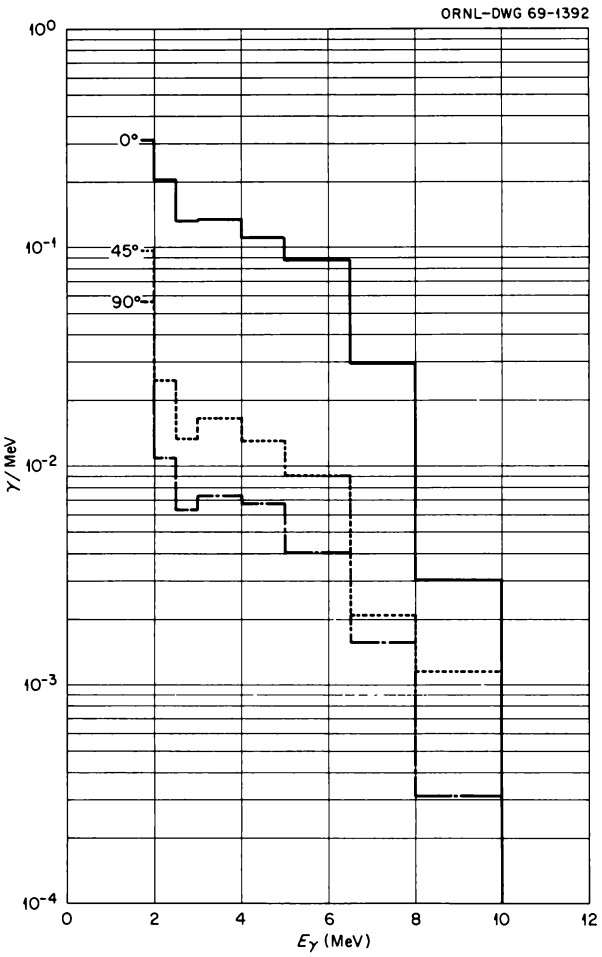

Fig. 21.5. Gamma-Ray Spectra as a Function of Polar Angle for a Source Height of 1125 ft. Data integrated over the energy intervals used for the calculations.

neutron spectrum contains a greater percentage of low-energy neutrons, so that more of the $^{14}N(n,\gamma)^{15}N$ reactions will occur. The neutron spectrum produced by a reactor, such as during Operation BREN, would result in the $^{14}N(n,\gamma)^{15}N$ reaction being the predominant source of gamma rays and should result in a higher mean energy than the HENRE spectrum. In either case the air is the primary source of gamma rays, with the earth being the source of the remainder.

The effects of the changing neutron spectrum are shown by comparing neutron dose as a function of polar angle measured at a range of 766 m for two different air densities (Figs. 21.6 and 21.7). If the neutron spectrum was in equilibrium, changes of the air density would produce little effect in the ratio of dose to total neutrons. For a neutron spectrum with a decreasing mean energy, the dose per neutron decreases with increasing air density, and the distribution becomes less peaked at 0° polar angle.

Related changes are observed in the gamma-ray dose as a function of polar angle. These are shown for a range of 766 m in Figs. 21.8 and 21.9. Most of the gamma rays measured are produced by neutron interactions with the air, so a greater air density produces more of the total reactions between the source and the detector. Thus, distribution is more peaked toward 0° polar angle for a higher air density. These measurements were related to the total gamma-ray dose at the detector site rather than the total fluence; therefore changes in range at a given air density can overcome the effects of changes in air density. That is, the gamma measurements, as made, were more sensitive to geometric effects than to changes in the gamma-ray spectrum.

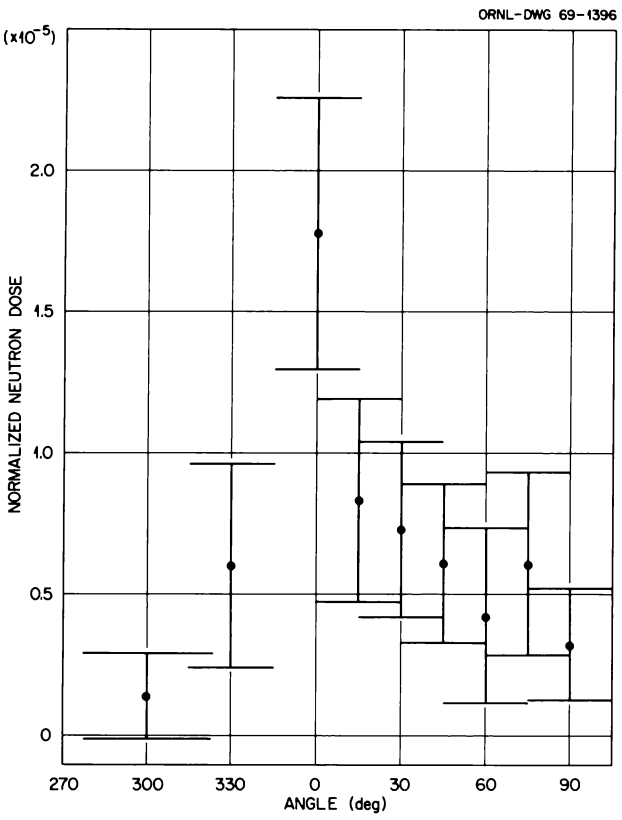

Fig. 21.6. Neutron Dose as a Function of Polar Angle for an Acceptance Angle of 30°, a Source Height of 1125 ft, and a Slant Range of 838 yd. Data normalized to the number of neutrons at the detector site during each measurement. Value at 300° polar angle obtained with a 45° acceptance angle. Data from winter runs. Vertical bar indicates one standard deviation; horizontal bar indicates the size of the collimator opening.

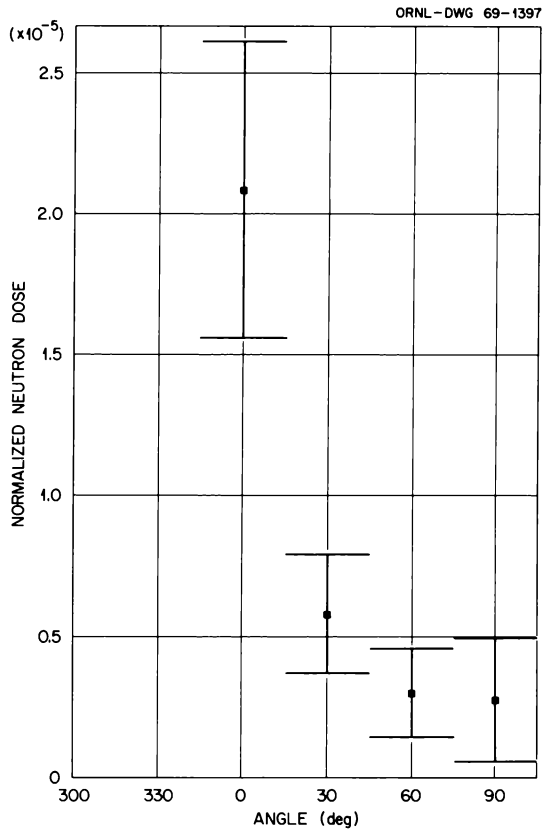

Fig. 21.7. Neutron Dose as a Function of Polar Angle for an Acceptance Angle of 30°, a Source Height of 1125 ft, and a Slant Range of 838 yd. Data normalized to the number of neutrons at the detector site during each measurement. Data from summer runs. Vertical bar indicates one standard deviation; horizontal bar indicates the size of the collimator opening.

Another observation made during the measurement of the gamma dose as a function of polar angle is of some importance. During operations BREN and HENRE, the gamma dose for a polar angle just below the air-ground interface was found to be higher than for a comparable polar angle above the interface, which was contrary to the results obtained during the weapons tests in Nevada.[7,8] The variation was the result of the variation in the source of the gamma rays. From a weapon an appreciable part of the total field originates in the fission products in the fireball; for HENRE and BREN, neutron interactions with the air and ground were the principal source of gamma rays. The increase in dose below the interface, when the collimator was in the tower-detector plane, may be explained by the increased importance of the gamma rays produced in the ground and by the change in geometry caused by the diffuse source. These effects were less for angles in a plane perpendicular to the source-detector line.

HIGH-PURITY ORGANIC SCINTILLATORS

All organic scintillators have trace impurities accumulated in the manufacturing or refining process that inhibit the scintillation process. Zone refining was employed to remove impurities from scintillation-grade

[7] J. H. Thorngate *et al., Energy and Angular Distribution of Neutrons and Gamma Rays – Operation BREN,* CEX-62.12 (February 1967).

[8] R. H. Ritchie and G. S. Hurst, *Health Phys.* 1, 390–404 (1959).

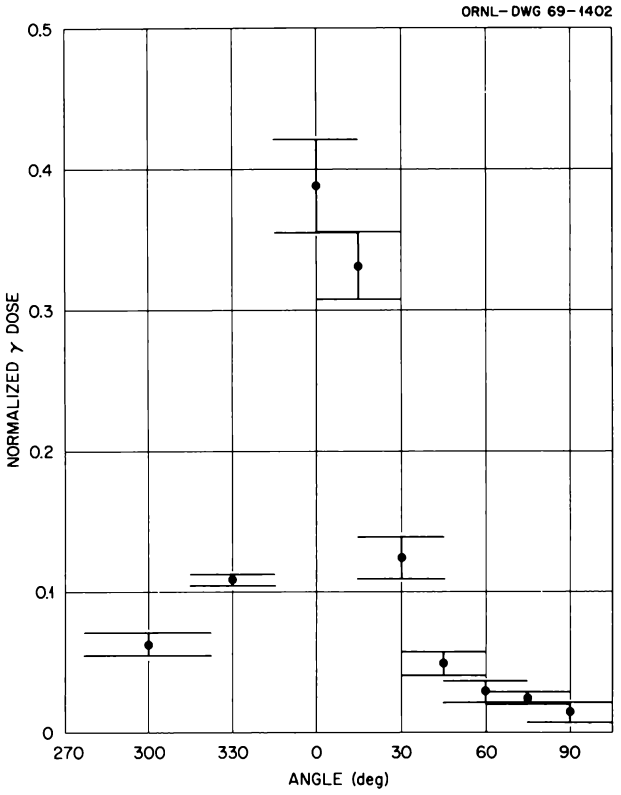

Fig. 21.8. Gamma-Ray Dose as a Function of Polar Angle for an Acceptance Angle of 30°, a Source Height of 1125 ft, and a Slant Range of 838 yd. Data normalized to the total gamma-ray dose at the detector site during each measurement. Value at 300° polar angle obtained with a 45° acceptance angle. Data from winter runs. Vertical bar indicates one standard deviation; horizontal bar indicates the size of the collimator opening.

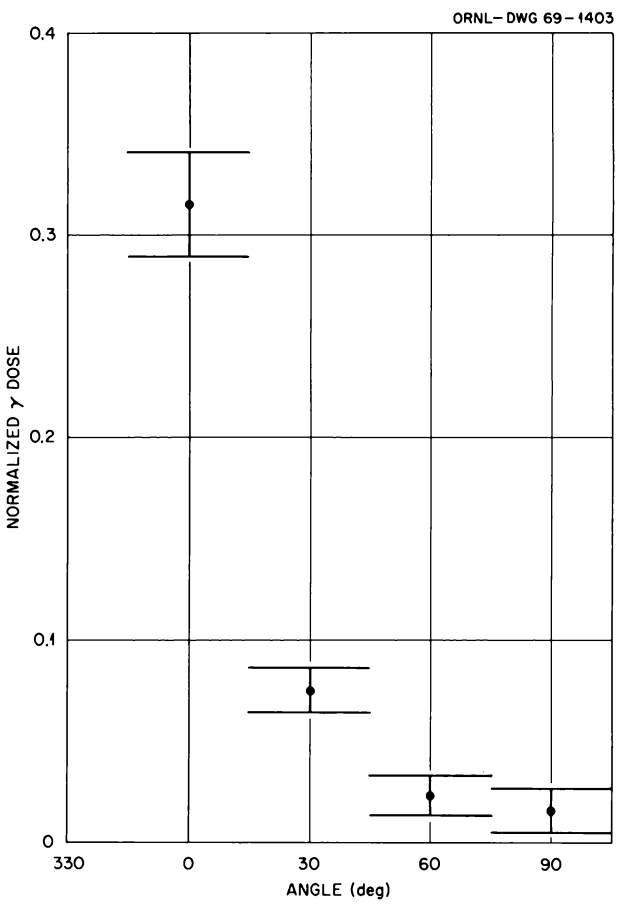

Fig. 21.9. Gamma-Ray Dose as a Function of Polar Angle for an Acceptance Angle of 30°, a Source Height of 1125 ft, and a Slant Range of 838 yd. Data normalized to the total gamma-ray dose at the detector site during each measurement. Data from summer runs. Vertical bar indicates one standard deviation; horizontal bar indicates the size of the collimator opening.

Table 21.1. Pulse Heights for Various Organic Scintillators Compared with the Compton Peak in NaI(Tl) for ^{137}Cs Gamma Source (Collimated)

Scintillator	Zone Passes	Number of Points Averaged	Percent of NaI(Tl) Compton Peak
NaI(Tl)		2	
Pilot "B"[a]		5	33
NE-213[b]		2	35
Anthracene	0	10	61
Anthrancene	1	5	74
Anthrancene	7	5	85
Paraquaterphenyl	0	5	32
Paraquaterphenyl	1	5	33
Paraquaterphenyl	33	6	92
trans-Stilbene	0	8	22
trans-Stilbene	5	10	23
trans-Stilbene	9	8	27

[a]Pilot Chemical Co.

[b]Nuclear Enterprises, Ltd.

stilbene, anthracene, and paraquaterphenyl.[9,10] Table 21.1 shows the relative pulse-height improvements obtained to date in these materials.

The results obtained for shape discrimination measurements of these three scintillators are shown in Table 21.2. Although the pulse shape characteristics of a scintillator depend primarily on the material and the method of measurement, the full width at half maximum is somewhat affected by the purity of the material. Since this function is important for neutron detection, even small improvements are of value.

[9]J. H. Thorngate *et al., Health Phys. Div. Ann. Progr. Rept. July 31, 1968,* ORNL-4316, p. 264.

[10]P. T. Perdue and M. D. Brown, *Nucl. Instr. Methods* 71, 113–16 (1969).

Table 21.2. Difference in Crossover Times (Δt) for Pulses Produced by Neutron and Gamma Irradiations of Organic Scintillators

Scintillator	Zone Passes	Peak-to-Peak Time Separation, Δt (nsec)	Neutron Peak FWHM (nsec)	Δt/FWHM
NE-213		22.0	9.46	2.21
Paraquaterphenyl	0	18.9	7.2–8.4	2.62
Paraquaterphenyl	1	21.2	7.4–7.9	2.86
Paraquaterphenyl	33	20.0	8.7	2.18
trans-Stilbene	0	22.8	10.0	2.28
trans-Stilbene	5	24.2	10.9–11.9	2.22
trans-Stilbene	9	24.7	9.96	2.48
Anthracene	0	14.6	7.2–10.3	2.02
Anthracene	1	14.9	6.6–8.1	2.26
Anthracene	19	15.3	6.2–8.2	2.48

Work is continuing to produce single crystals of the materials already purified and to prepare and purify higher polyphenyls. The parapolyphenyls with further condensation than paraquaterphenyl are of particular interest because:[11]

1. The relative pulse height is known to increase with increasing length of the paraphenyl chain, in decreasing amounts above paraoctaphenyl.
2. All of the known parapolyphenyls are clear materials and all scintillate.
3. Strength of materials increases with increasing chain length (i.e., they become more like plastics).
4. The scintillation decay time becomes shorter as the parapolyphenyl chain length increases, an important consideration in pulse shape discrimination.
5. Chemical activity decreases with increasing condensation. This characteristic is important when the bare materials are employed.
6. The separation of the fluorescence and absorption bands increases.
7. The macroscopic cross section for neutrons increases.

Since there are few solvents, it is expected that zone refining will be increasingly employed as a purification technique of the polyphenyls.

INVESTIGATIONS OF AVAILABLE X-RAY CROSS SECTIONS

The dosimetric and spectrometric studies of the x rays from extraneous sources such as vacuum high-voltage equipment have required accurate values of x-ray cross sections. Consequently, low-energy x-ray absorption coefficients have been reviewed in detail. Several recent measurements and compilations are found to have accuracies approaching 1%. This is in sharp contrast to the state of the art a decade ago, when the available information was good to about 10%.

Some examples of x-ray absorption coefficients are presented in Table 21.3 for carbon and oxygen in the energy range from 0.277 to 40.0 kev. Only recent measurements are presented, since it is only recently that the various researchers agree to within 1% in their measurements and calculations of the absorption coefficients. The wavelengths and energies of the characteristic radiations and absorption edges are taken from Bearden.[12]

Care must be exercised in reading the tables within 1 kev of an absorption edge. It is in this region where many monatomic solids, homonuclear diatomic molecular gases, and other polyatomic systems have considerable fine structure.[13] The commonly used "mixture rule," which equates the absorption by a compound to a weighted sum of atomic constituents, fails close to an absorption edge in gases. More restraint should be exercised in using this rule at low energies and close to absorption edges.

[11] P. Kovacic and R. M. Lange, *J. Org. Chem.* 29, 2416 (1964).

[12] J. A. Bearden, *Rev. Mod. Phys.* 39, 78 (1967).

[13] R. D. Deslattes, *Acta Cryst.* A25, 89 (1969).

Table 21.3. X-Ray Absorption Coefficients for Carbon and Oxygen

Element	Line	Wavelength (A)	E (kev)	Henke[a]	North[b]	McCrary[c]	Bearden[d]	Ogier[e]	Bearden[f]	Batterman[g]	McMaster[h]	McGinnies[i]
						Carbon						
^{6}C	K_α	44.7	0.277	2280				2280				
^{6}C	K abs edge	43.68	0.28384									
^{7}N	K_α	31.60	0.3924	25400								
^{8}O	K_α	23.62	0.5249	12200								
^{9}F	K_α	18.32	0.6768	6400								
^{27}Co	$L_{\alpha_{1,2}}$	15.972	0.7762	4470								
^{28}Ni	$L_{\alpha_{1,2}}$	14.561	0.8515				3190					
^{29}Cu	$L_{\alpha_{1,2}}$	13.336	0.9297	2740			2543	2580				
		12.40	1.000								2110	
^{30}Zn	$L_{\alpha_{1,2}}$	12.254	1.0117				2026					
^{12}Mg	$K_{\alpha_{1,2}}$	9.8900	1.25360	1167			1093	1235				
^{13}Al	K_{α_1}	8.33934	1.48670	720			667	725				
		8.265	1.500								668.5	
^{13}Al	K_β	7.960	1.55745				572					
		6.199	2.000								290	
^{42}Mo	L_{α_1}	5.40655	2.29316				171					
^{47}Ag	L_{α_1}	4.15443	2.98431				85.3		89.4			
		4.134	3.000								87.4	89.0
^{50}Sn	L_{α_1}	3.59994	3.44398				60.7		60.9			
		3.100	4.000								36.7	37.5
^{22}Ti	K_{α_1}	2.74851	4.51084				25.0		25.0			
		2.480	5.000								18.6	18.6
^{24}Cr	K_{α_1}	2.28970	5.41472				15.2		15.2			
		2.066	6.000								10.6	10.0
^{26}Fe	K_{α_1}	1.936042	6.40384				8.78		8.79			
		1.550	8.000								4.43	4.3
^{29}Cu	K_{α_1}	1.540562	8.04778				4.33		4.33	4.30		
^{32}Ge	K_{α_1}	1.254054	9.88642		2.277							
		1.2398	10.000								2.29	0.222
^{34}Se	K_{α_1}	1.10477	11.2224		1.589							
^{38}Sr	K_{α_1}	0.87526	14.1650		0.847							
		0.86254	15.000								0.770	0.755
^{42}Mo	K_{α_1}	0.709300	17.47934		0.529							
		0.619905	20.000								0.421	0.424
		0.4959	25.00		0.2968							
		0.41327	30.000								0.248	0.253
		0.4127	30.04			0.2466						
		0.30995	40.00								0.204	0.205
		0.3096	40.04			0.2032						

Table 21.3 (continued)

Element	Line	Wavelength (A)	E (kev)	Henke[a]	North[b]	McCrary[c]	Bearden[d]	Ogier[e]	Bearden[f]	Batterman[g]	McMaster[h]	McGinnies[i]
						Oxygen						
^{6}C	$K\alpha$	44.7	0.277	6250				6150				
^{7}N	$K\alpha$	31.60	0.3924	2550								
^{8}O	$K\alpha$	23.62	0.5249	1440								
^{8}O	K abs edge	23.32	0.5317									
^{9}F	$K\alpha$	18.32	0.6768	12620								
^{27}Co	$L\alpha_{1,2}$	15.972	0.7762	8850								
^{29}Cu	$L\alpha_{1,2}$	13.336	0.9297	5560			5459	5340				
		12.40	1.000								4570	
^{30}Zn	$L\alpha_{1,2}$	12.254	1.0117				4330					
^{12}Mg	$K\alpha_{1,2}$	9.8900	1.25360	2540			2511	2480				
^{13}Al	$K\alpha_{1}$	8.33934	1.48670	1604			1611	1540				
		8.265	1.500								1570	
^{13}Al	$K\beta$	7.960	1.55745				1378					
		6.199	2.000								708	
^{42}Mo	$L\alpha_{1}$	5.40655	2.29316				418					
^{47}Ag	$L\alpha_{1}$	4.15443	2.98431				220		223			
		4.134	3.000								219.5	221
^{50}Sn	$L\alpha_{1}$	3.59994	3.44398				156		156			
		3.100	4.000								93.1	100
^{22}Ti	$K\alpha_{1}$	2.74851	4.51084				69.3		69.1			
		2.480	5.000								47.3	50.5
^{24}Cr	$K\alpha_{1}$	2.28970	5.41472				41.0		41.1			
		2.066	6.000								27.1	29.0
^{26}Fe	$K\alpha_{1}$	1.936042	6.40384				25.3		25.3			
		1.550	8.000								11.2	11.8
^{29}Cu	$K\alpha_{1}$	1.540562	8.04778				11.8		11.8			
^{32}Ge	$K\alpha_{1}$	1.254054	9.88642		5.851							
		1.2398	10.000								5.65	5.78
^{34}Se	$K\alpha_{1}$	1.10477	11.2224		4.019							
^{38}Sr	$K\alpha_{1}$	0.87526	14.1650		2.030							
		0.86254	15.000								1.72	1.75
^{42}Mo	$K\alpha_{1}$	0.709300	17.47934		1.137							
		0.619905	20.000								0.818	0.823
		0.41327	30.000								0.362	0.369
		0.30995	40.000								0.255	0.251

[a] B. L. Henke *et al.*, *Norelco Reporter* 14(3,4), 112–31 (1967).
[b] P. R. North, *Norelco Reporter* 14(1), 10–11 (1967).
[c] J. H. McCrary *et al.*, *Phys. Rev.* 153, 307 (1967).
[d] A. J. Bearden, *J. Appl. Phys.* 37, 1681 (1966).
[e] W. T. Ogier, G. J. Lucas, and R. J. Park, *Appl. Phys. Letters* 5, 146 (1964).
[f] A. J. Bearden, *Bull. Am. Phys. Soc.* II, 4, 66 (1959).
[g] B. W. Batterman, *Rev. Sci. Instr.* 29, 1132 (1958).
[h] W. H. McMaster *et al.*, *Population of X-Ray Cross Sections*, UCRL-50174, sect. 2 (1967).
[i] R. T. McGinnies, "X-Ray Attenuation Coefficients from 10 kev to 100 Mev," suppl. to *Natl. Bur. Std. (U.S.), Circ.* 583 (October 1959).

TEMPERATURE CONTROLLER

An electronic device was designed, built, and tested that provides a wide range of linear heating rates for use with the TSEE experiments discussed in the next section. It provides linear heating rates continuously variable from a maximum of 12°C/sec to a minimum of 0.5°C/sec. Maximum temperatures may be adjusted up to 800°C. A block diagram of the circuit employed is given in Fig. 21.10. Basically the circuit compares the voltage produced by a thermocouple at the heating element with a linear ramp and adjusts the heater current so the two are the same. Heater currents up to 10 amp and potentials to 30 v can be supplied by the circuit. The maximum heating rate is limited by the amount of power available coupled with the limitations of the heater used. Figure 21.11 shows the performance obtained. Heater temperature is shown as a function of time with the setting of the rate adjust control as a parameter.

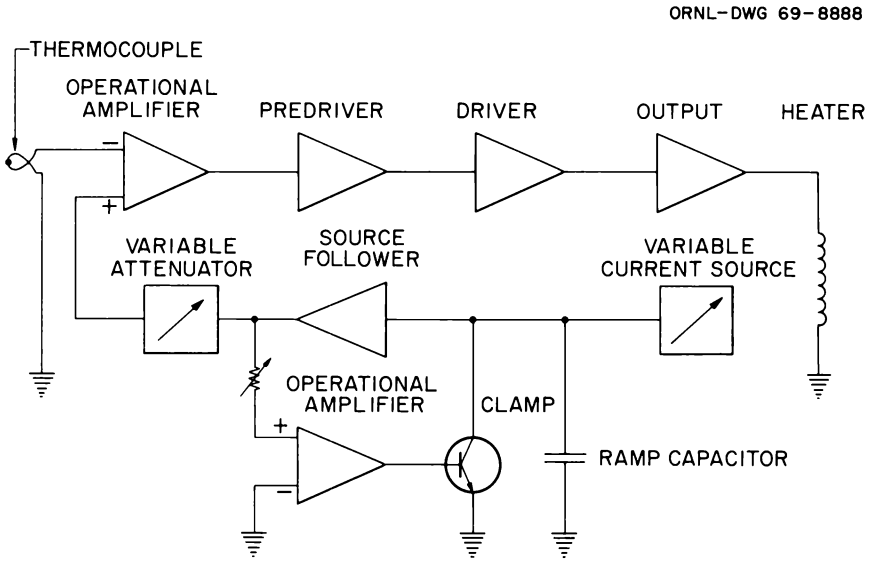

Fig. 21.10. Temperature Controller Block Diagram.

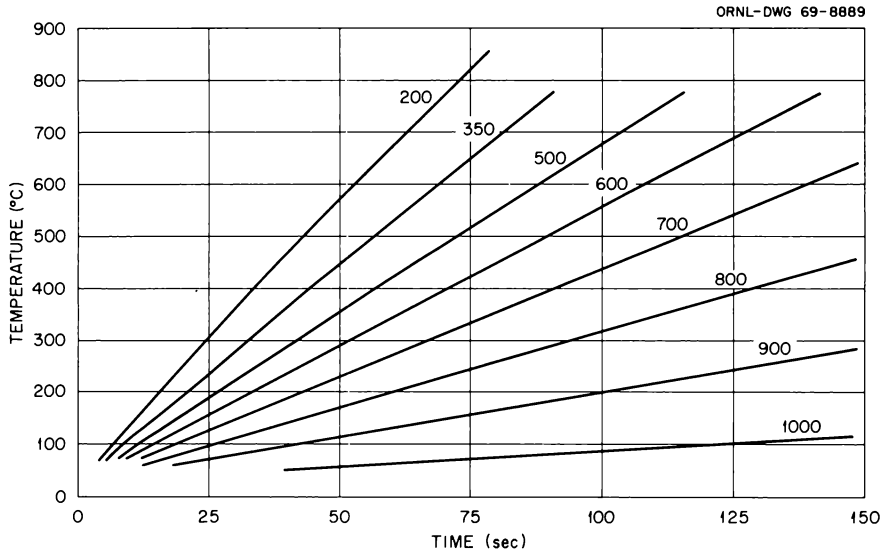

Fig. 21.11. Temperature as a Function of Time as Produced by the Linear Temperature Controller.

22. Applied Research

Klaus Becker

R. H. Boyett
Nongnooch Chantanakom[1]
J. S. Cheka
K. W. Crase[1]
D. R. Johnson
M. Oberhofer[2]
E. M. Robinson
J. F. Wilson[1]

TSEE DOSIMETRY

TSEE Instrumentation

Several types of conventional gas-flow G-M counters which had been converted into exoelectron detectors by installing a heater ceased to function properly at temperatures above ~300 to 350°C. In order to investigate TSEE from deep trapping levels corresponding to peak temperatures between this temperature and an upper limit given by the increasing thermionic glow emission of electrons, which begins to occur around 700°C, a high-temperature TSEE reader has been designed.[3] Its basic design feature is a spatial separation of the heater part and the counting volume (Fig. 22.1) with a water-flow cooling loop between. In order to compare TSEE "glow curves" and to obtain information on the heating-rate dependence of the TSEE peak locations, a device which permits linear heating at rates between 0.5 and ~10°C/sec (as described in chapter 21) has been used for regulating the power input of the heater. A schematic diagram of the reader setup is given in Fig. 22.2. The temperature of the emitting surface agrees within ±5°C with the reading of the thermocouple.

Besides gas-flow G-M counters, whose basic disadvantage is a dead-time loss if the count rate exceeds certain

[1] Graduate student, University of Tennessee.

[2] Alien guest.

[3] M. Oberhofer and E. M. Robinson, "A High Temperature TSEE G-M Gasflow Counter," *Kerntechnik*, submitted for publication.

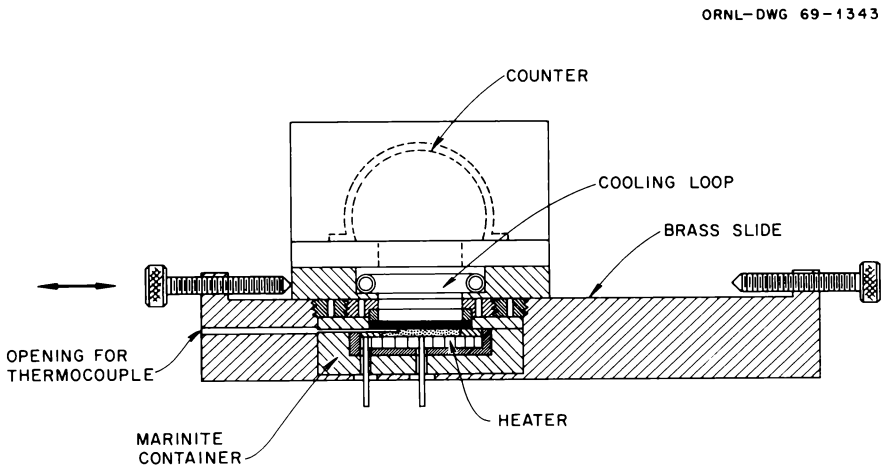

Fig. 22.1. High-Temperature TSEE Detector Unit.

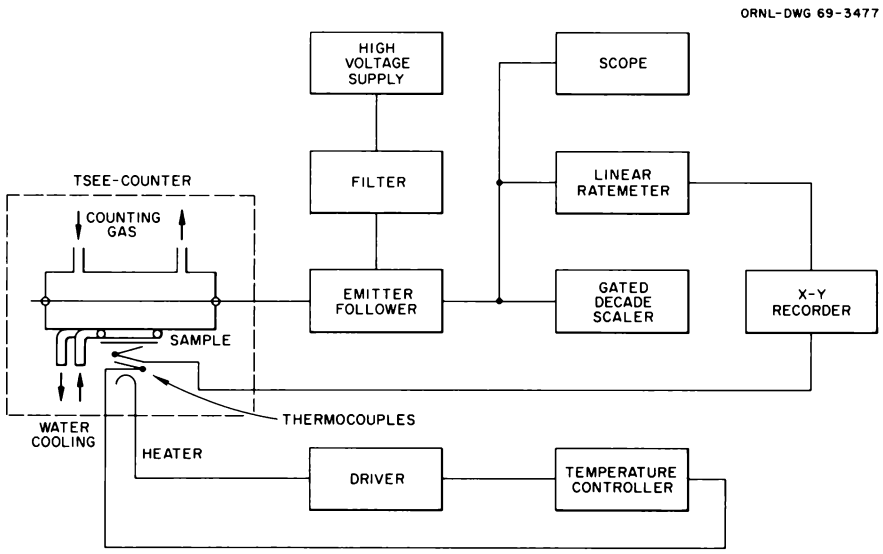

Fig. 22.2. Block Diagram of TSEE Reader.

limits, ionization-chamber types of TSEE detectors have been developed and tested. In order to study the energy distribution of the exoelectrons, a device based on acceleration of exoelectrons in vacuum, after their penetration of a biasing screen, and detection in an electron multiplier has been built. Instrumentation still under development includes a device for measurements with high spatial resolution based on TSEE release by a laser beam.

LET Dependence of TSEE Response

It was first observed in the alkaline earth sulfates, using the old instrumentation, that the TSEE peak ratio was quite different after exposure to gamma and alpha radiation.[4] A typical example, $CaSO_4$, is given in Fig. 22.3. Using the new linear-heating high-temperature reader, a similar LET dependence of the peak ratios has also been observed in materials such as LiF (Fig. 22.4) and BeO. The high LET to low LET response ratio of detectors can be varied by annealing up to a given temperature only. These effects are at present being studied in more detail.

Several possible practical applications of the LET dependence of TSEE are evident, in particular: (1) the possibility of obtaining, in addition to the dose, information on the effective LET of the radiation from a dosimeter and (2) the possibility of discriminating against gamma radiation in fast-neutron dosimeters which are based on the detection of recoil protons from hydrogenous materials.

TSEE detectors are of interest for both applications because they permit the sensitive registration of even very low-energy particles having a range of a few angstroms only. Fast-neutron dosimetry, for example, can be done by placing a polyethylene foil over the detector surface. If such a detector is exposed to a mixed fast-neutron and gamma radiation field, the sum

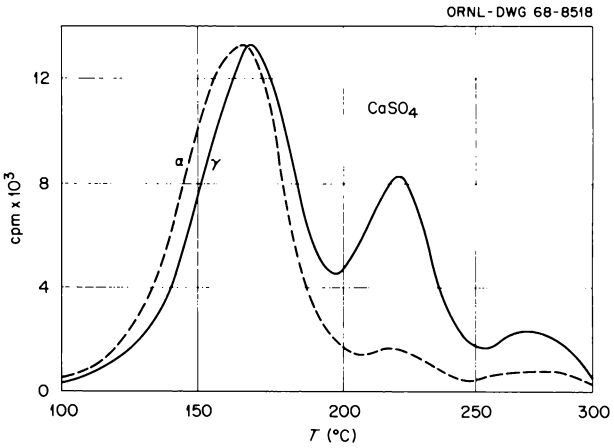

Fig. 22.3. TSEE Curve During Nonlinear Heating of $CaSO_4$ (Baker, Prefired 1 hr at 950°C) After Exposure to ^{239}Pu Alpha and ^{60}Co Gamma Radiation.

[4] K. Becker and N. Chantanakom, *Nucl. Instr. Methods* 66, 353 (1968).

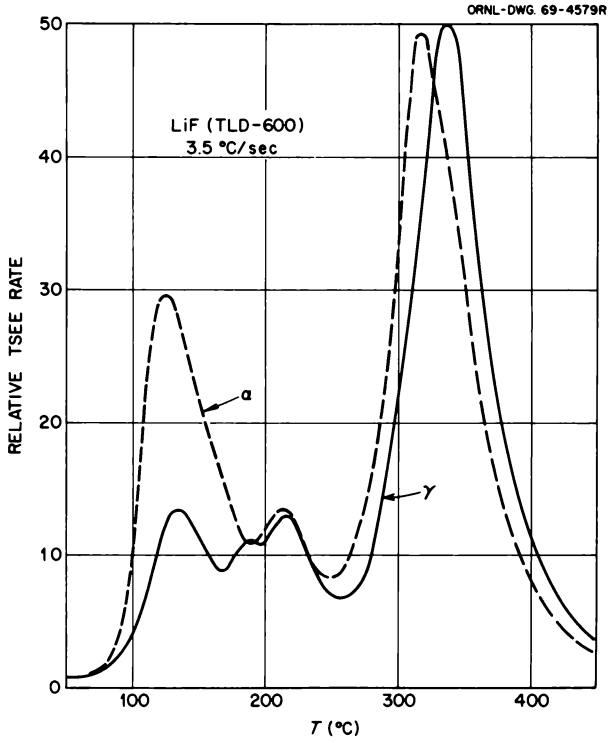

Fig. 22.4. TSEE Curve of a TL-Grade LiF After Exposure to Alpha and Gamma Radiation, Linear Heating.

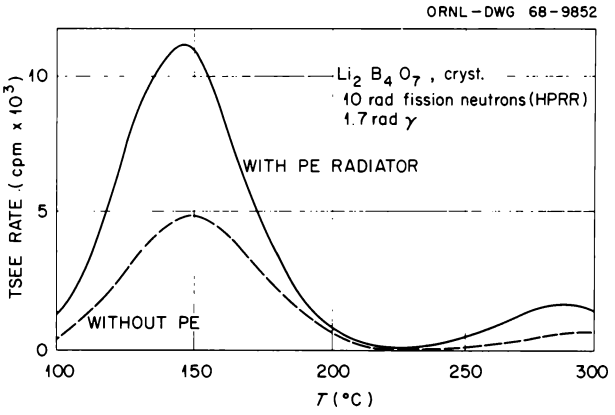

Fig. 22.5. TSEE Curves of Crystalline $Li_2B_4O_7$ After Exposure to a Mixed Reactor Radiation Field with a 1-mm Polyethylene Foil and a Graphite Disk Covering the Detector Surface.

of the gamma and recoil proton effect is recorded, and the neutron component can be obtained by subtracting the gamma radiation effect (Fig. 22.5). Studies on the sensitivity and energy response of such and similar systems are in progress.

Thermal Stability (Fading) of TSEE

For many practical applications the storage capability of TSEE detectors has to exceed certain minimal requirements. Obviously, the thermal fading of the radiation effect will depend on the trap depth; electrons from deeper traps require higher temperatures to be released. There has also been some evidence that parameters other than temperature may influence the fading characteristics. Three materials have been studied mainly: LiF, because of its simple structure and because its properties have been studied intensely in connection with TLD; BeO, because of its high TSEE sensitivity, convenient peak locations, and its thermal and chemical resistance; and $CaSO_4$, because it is a nontoxic, sensitive, and relatively well-studied TSEE material.[5]

In LiF (Fig. 22.6), the fading characteristics for the low-temperature (~150°C) peak are identical after alpha and gamma exposure. No difference in the fading kinetics was observed when the detectors were stored in vacuum (45 μ Hg), normal laboratory air, dry air (0% relative humidity), and humid air (100% relative humidity). Also in BeO, which shows a much higher thermal stability (no observable fading in dry air up to 60°C), no LET dependence of the fading in the low-temperature (~250°C) TSEE peak has been observed (Fig. 22.7). The high-temperature peaks in this material are even more fading resistant and can be used for high-temperature dosimetry up to 400°C (in volcanic minerals or ancient pottery, TSEE from deep trapping levels may be used as a dating method similar to thermoluminescence dating). A surprisingly high fading rate of BeO stored at 180°C in vacuum may be explained by desorption of oxygen from the surface. With the air replaced by water vapor, the fading rate became even more rapid. This, however, appears to be due to a chemical reaction of water vapor with BeO at the high temperature. The nonlinear fading shown in the semilogarithmic plot is evidence that several trapping levels are superimposed in the peak. Indeed, a shift in the TSEE peak to higher temperatures has been observed during fading in BeO. The peak, initially around 285°C, shifted to ~320°C after 67 hr at 180°C in dry air. In H_2O vapor, however, no such shift occurred, indicating the dominance of a different fading mechanism.

[5] K. Becker and N. Chantanakom, "On the Thermal Fading Characteristics of Some TSEE Dosimetry Materials," *Atompraxis*, submitted for publication.

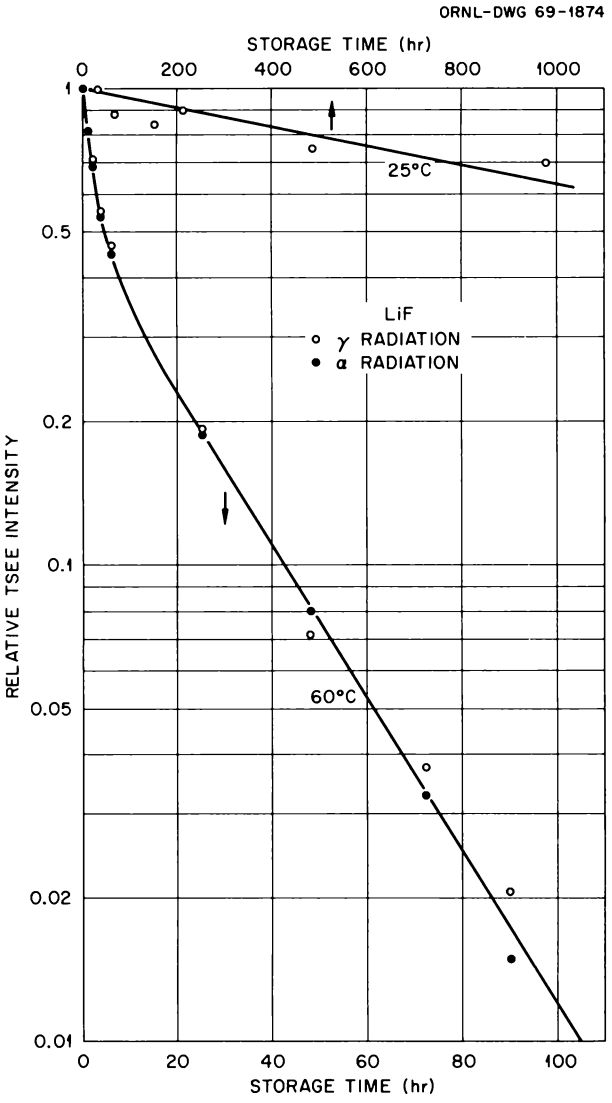

Fig. 22.6. Fading of the ~150°C TSEE Peak in LiF (Baker) After Alpha and Gamma Irradiation at Different Storage Temperatures in Unmodified Laboratory Atmosphere.

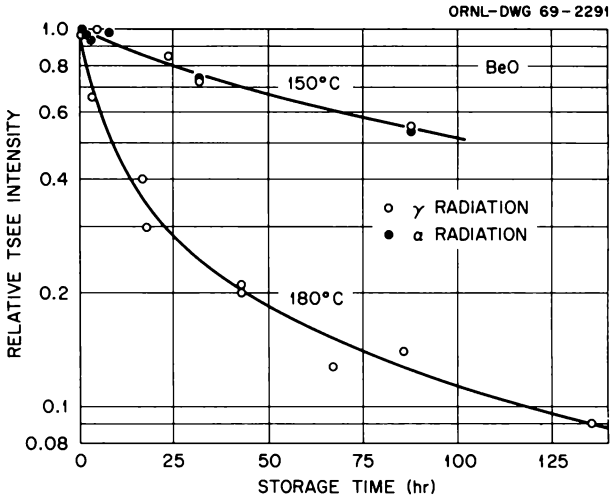

Fig. 22.7. Fading of the ~250°C TSEE Peak in BeO (Brush) in Samples Stored in Laboratory Air at 150 and 180°C.

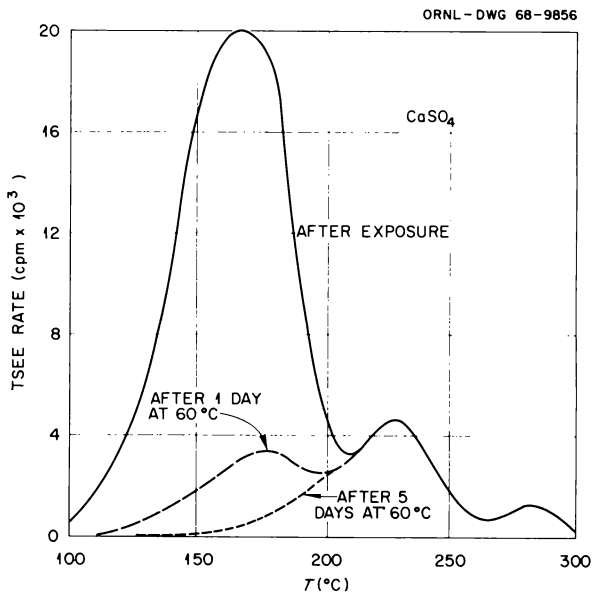

Fig. 22.8. Changes in the TSEE Curve of $CaSO_4$ Occurring During Storage at 60°C, Nonlinear Heating.

As expected, also in $CaSO_4$ (Fig. 22.8), the low-temperature peaks disappear much more rapidly than the high-temperature peaks during the annealing of the shallow traps. No temporary increase in the high-temperature peaks during the annealing due to retrapping processes has been observed. The lack of a retrapping provides some evidence that a direct-ejection mechanism for the exoelectrons from the trap may dominate in the emission mechanism.

As expected from the different peak ratios, there is an LET effect on the fading kinetics in $CaSO_4$ (Fig. 22.9). The fading rate of the lowest $CaSO_4$ peak is faster, despite its somewhat higher peak temperature, than that of the ~150°C LiF peak, indicating an influence of the air humidity, perhaps caused by the addition of crystal water (a change in the crystal lattice can be expected to destroy the TSEE "information storage"). In general, environmental effects on the fading rate of

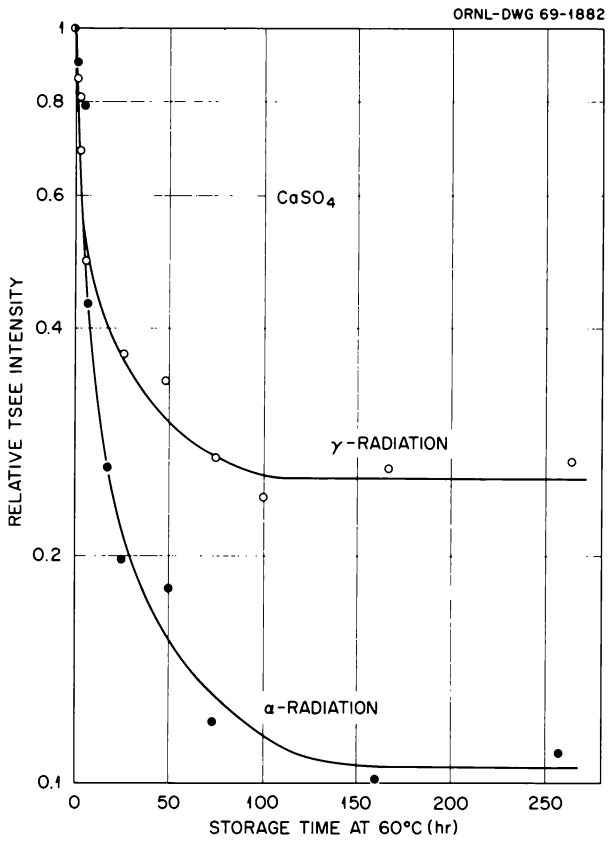

Fig. 22.9. TSEE Fading in $CaSO_4$ at 60°C After Exposure to Alpha and Gamma Radiation, Normal Laboratory Atmosphere.

unprotected TSEE dosimeters can be expected whenever the extremely thin (<10 to 100 A) crystal layer, from which the electron emission occurs, is subject to a physical or chemical change such as adsorption of oxygen, lattice transformation because of the addition of crystal water, or (in particular at higher temperatures) chemical reactions with atmospheric constituents.

Pretreatment on TSEE

The TSEE characteristics (peak shape and location, sensitivity, etc.) in a given material depend strongly, and in a complex way, on several parameters, such as its thermal and irradiation history and its impurity content. Investigations of these parameters resulted in the accumulation of a large number of data, but so far not in a consistent theory of the processes involved.

Preheating of the TSEE material at high temperatures (700 to 1000°C) resulted in an initial increase of sensitivity in several materials (LiF, BeO, and $CaSO_4$), reflecting the increase in the surface disorder concentration, which later (at extended heating times or higher temperatures) is usually replaced by a decrease in sensitivity, frequently associated with changes in the TSEE glow curve. A typical example, a special type of unfired BeO, is given in Fig. 22.10 (high-temperature treatment also reduces the toxicity of BeO).

Preirradiation to high dose levels may also increase the sensitivity. With charged particles, new traps are created. With photon radiation, other processes dominate. In BeO, for example, preirradiation with ~1 megarad of gamma radiation and annealing at 400°C resulted in an increase of the sensitivity of the ~250°C TSEE peak by a factor of more than 4 (Fig. 22.11), probably due to a lack of competition with the deeper trapping levels which remain completely filled.

An interesting new effect has been observed in BeO, in particular after high-temperature pretreatment: If an unirradiated sample is repeatedly heated, a "self-stimulation" peak around 330°C appears which reaches a constant maximum after several heating cycles (Fig. 22.12). No conclusive explanation of this effect is available yet.

Relation Between TSEE and Thermoluminescence (TL)

The physical mechanisms of TSEE and TL are known to be related, and a better understanding of the mechanisms of both processes can be expected from comparisons. A program was therefore initiated to

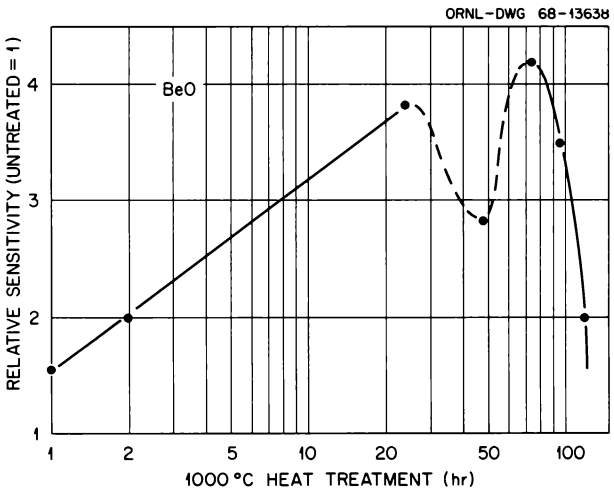

Fig. 22.10. TSEE Sensitivity of the Low-Temperature (~250°C) Peak in a Sintered BeO (Brush) as a Function of Storage Time at 1000°C.

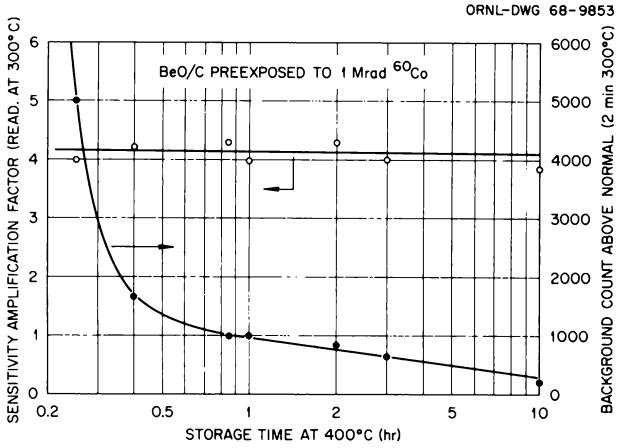

Fig. 22.11. Enhancement of Sensitivity in the Low-Temperature BeO Peak (Left Scale) and Increase in Background per Heating Cycle in BeO (Brush) Detectors (Right Scale) After Preirradiation to 1 megarad of Gamma Radiation, as a Function of Storage Time at 400°C.

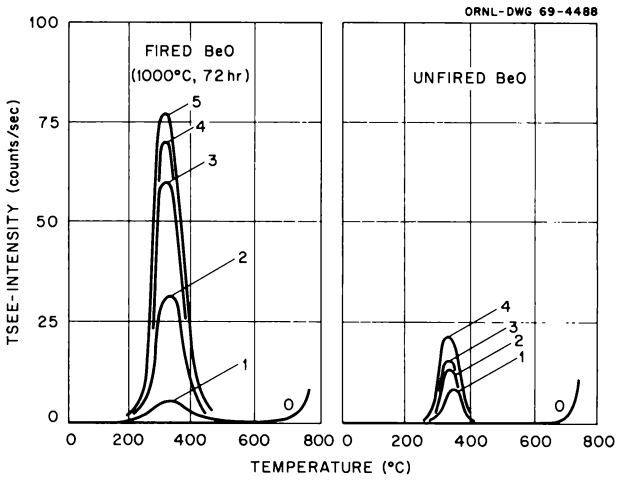

Fig. 22.12. TSEE of an Unfired BeO and of the Same Material After Preheating (72 hr at 1000°C) During Repeated Reading Cycles Without Radiation Exposure.

compare TSEE, TLD, and impurity ("activator") content in a number of materials of possible dosimetric interest, in particular LiF and BeO from different sources. In addition, those results make it easier to choose optimized material for practical TSEE dosimeters.

Earlier results, that location and height of the 150°C TSEE peak in LiF depends on the type of LiF used and is independent of its TL sensitivity,[6,7] have been confirmed by more detailed studies using the improved TSEE reader. Different analytical-grade (Merck, Baker), technical (American Potash), and TLD-grade (Radiation Detection Corp., Harshaw TLD-100, TLD-600, and TLD-700, Dohna-Lum) lithium fluorides all exhibited TSEE peaks at ~150 and at ~350°C, with the absolute sensitivities as well as the peak ratios and locations being somewhat different (Fig. 22.13). In some materials the peak ratio depends on LET (Fig. 22.4).

In order to compare the peak locations in TSEE and TL glow curves of the same materials, a correction for the Randall-Wilkins shift is required. As can be seen in Fig. 22.14, a TSEE peak in LiF which is at 120°C for a heating rate of 1°C/sec would, for example, be located at 166°C for a heating rate of 17°C/sec, which is the heating rate used in the TL measurements.

In the highly sensitive TLD-grade LiF samples, no pronounced peaks corresponding to the TSEE peaks have been observed. In the unactivated samples, however, a TL peak corresponding to the low-temperature TSEE peak appears at high dose levels (Fig. 22.15). Of course, no TL peaks can be observed above ~400°C because of the rapidly increasing infrared emission.

In BeO the situation appears to be more complex. Depending on what type of BeO is used, the sensitivity and location of the peaks can be quite different (Fig. 22.16). The most sensitive materials for TSEE dosimetry are two sintered materials (Coors Porcelain and Brush Thermaload). A correlation between TSEE and TL peak locations (Fig. 22.17), sensitivities, and impurity content is difficult but is being investigated further. Under study also are other TLD and analytical-grade calcium fluorides and sulfates.

Miscellaneous TSEE Studies

It has been observed in experiments using irradiated BeO detectors that their submersion in water or organic solvents such as acetone or alcohol does not affect the "information storage" if they are dried prior to reading. This opens the possibilities of activity and dose measurements in solutions, for instance, of low-energy beta or alpha emitters. It is also possible to irradiate the (previously annealed) detector in suspension or as a dry powder and prepare the detectors prior to the reading.

[6] K. Becker, "Some Studies on Radiation Dosimetry by Thermally Stimulated Exoelectron Emission (TSEE)," pp. 200–19 in *Proceedings of the Second International Conference on Luminescence Dosimetry*, CONF-680920, USAEC-DTI (November 1968).

[7] K. Becker, *Health Phys.* 16, 527 (1969).

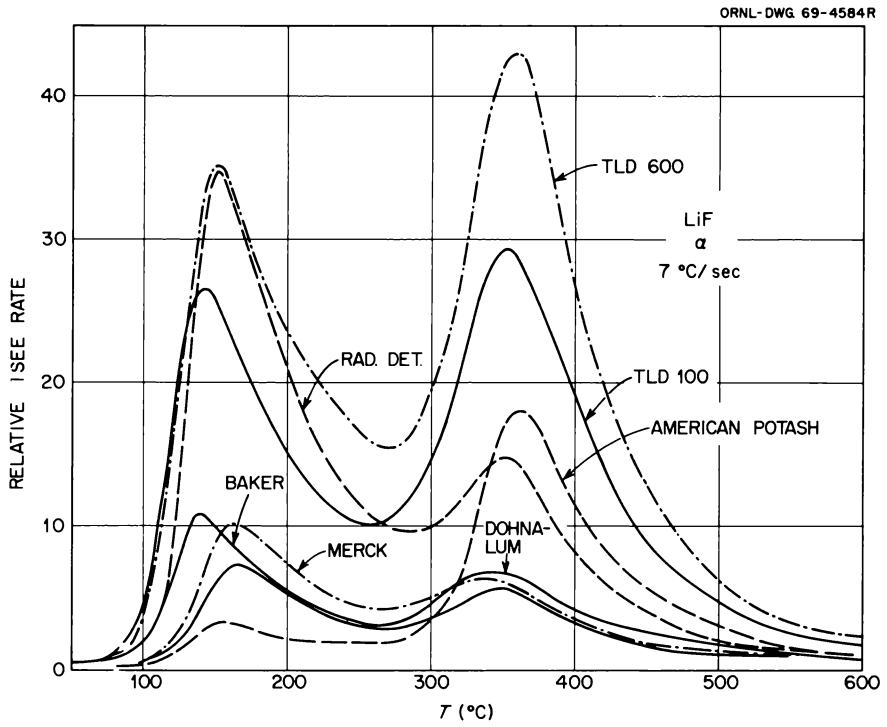

Fig. 22.13. TSEE Curves of LiF from Different Sources After Exposure to a Constant Alpha Radiation Dose.

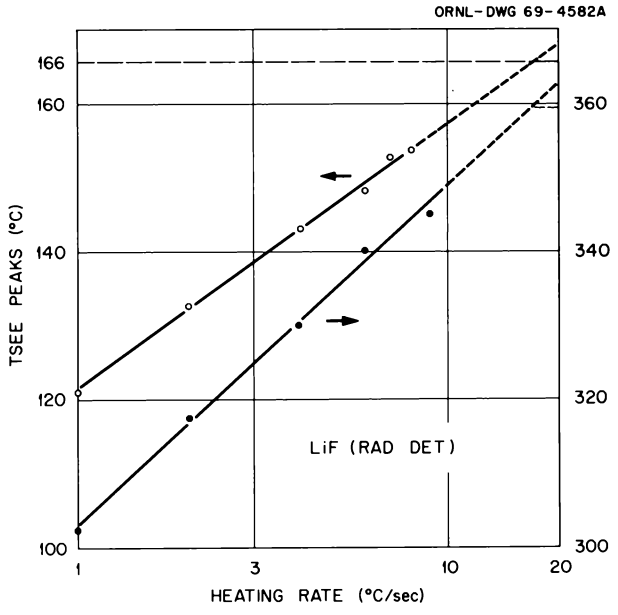

Fig. 22.14. Heating-Rate Dependence of the Low-Temperature (Left Scale) and the High-Temperature (Right Scale) Peak Locations in LiF.

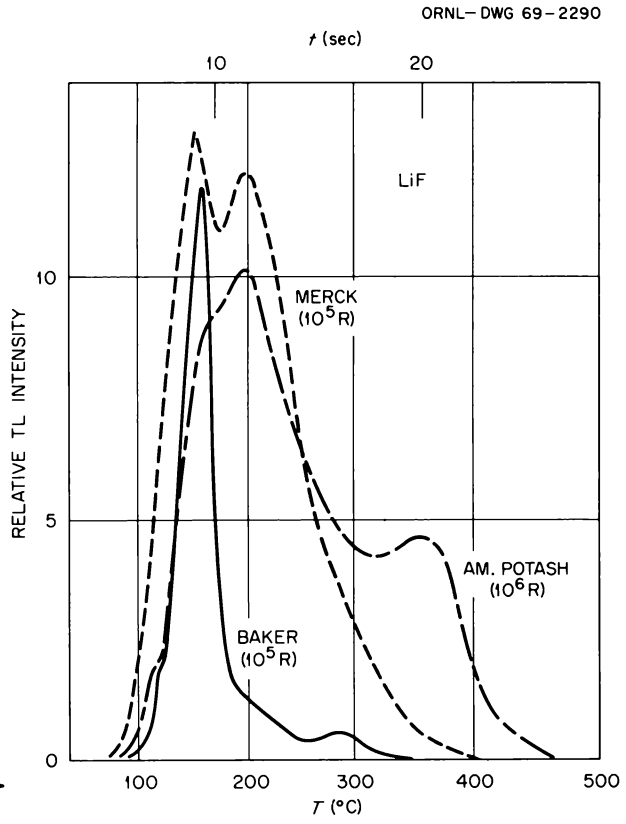

Fig. 22.15. Thermoluminescence (TL) Glow Curves of Different Analytical-Grade (Unactivated) Lithium Fluorides After Exposure to Gamma Radiation.

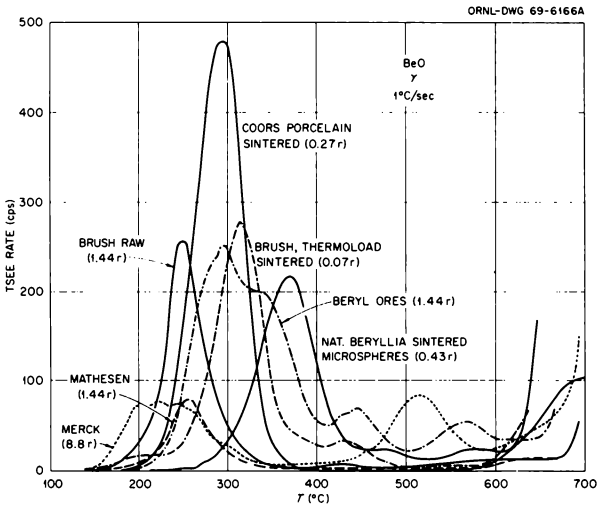

Fig. 22.16. TSEE Curves of Unsintered and Sintered BeO from Different Sources and with Different Impurity Content.

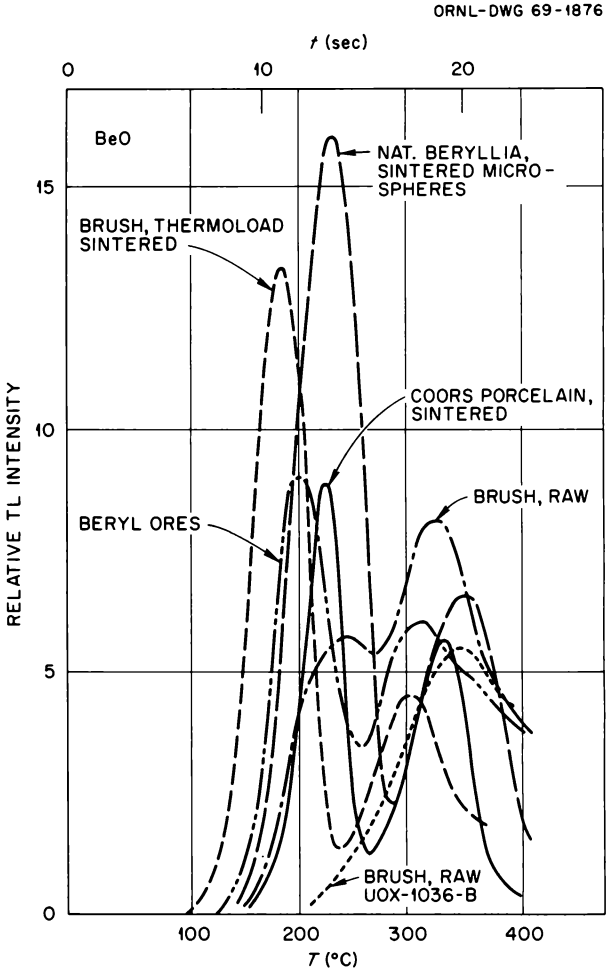

Fig. 22.17. TL Glow-Curves of Different Gamma-Irradiated BeO Samples.

By using this technique, it is possible to prepare very small detectors for radiobiological experiments or use suspensions of the detector in liquids or gels.

Other types of detectors have also been investigated. For example, hot-pressed tablets consisting of mixtures of the detector and graphite with a small addition of a heat-resistant binder exhibited a high sensitivity. If a metal oxide exhibits strong TSEE, as is the case with BeO, the metal can be covered with a sensitive layer simply by heating the metal in air.

In studies concerning the energy dependence of detectors consisting of a BeO/C mixture plated on graphite disks, a slight anomaly has been observed (Fig. 22.18). A systematic investigation of the effect of the environment, in particular the atomic number of the gas or solid between photon source and detector surface, on its sensitivity and energy response is in progress. Also in progress are a number of other studies involving TSEE in more exotic compounds and their possible applications in health physics research and technology, and studies on promising ceramic BeO disks on which conductive metal layers have been vacuum deposited.

RADIOPHOTOLUMINESCENCE AND THERMOLUMINESCENCE

A disadvantage of the newly developed energy-independent dosimeter glass which is based on silver-activated lithium borate instead of metaphosphate[8,9] is its reduced weathering stability. In a laboratory atmosphere with a relative humidity of 50 to 70% at 20 to 25°C, no change has been observed, but if it is kept at higher humidities for extended periods or submersed in water, its surface begins to dissolve. It was, however, found that an addition of 7.5% of BeO to the glass not only decreased its solubility in water by a factor of 13 but also increased its sensitivity by ~30% without adversely affecting its excellent fading stability (Fig. 22.19) or the small energy dependence of its response.[10]

[8] K. Becker and J. S. Cheka, *Health Phys.* 16, 125 (1969).

[9] J. S. Cheka and K. Becker, *Nucl. Appl.* 6, 163 (1969).

[10] K. Becker and J. S. Cheka, "Low-*Z* Radiophotoluminescent Glasses Based on Lithium Borate," pp. 148–60 in *Proceedings of the Second International Conference on Luminescence Dosimetry*, CONF-680920, USAEC-DTI (November 1968).

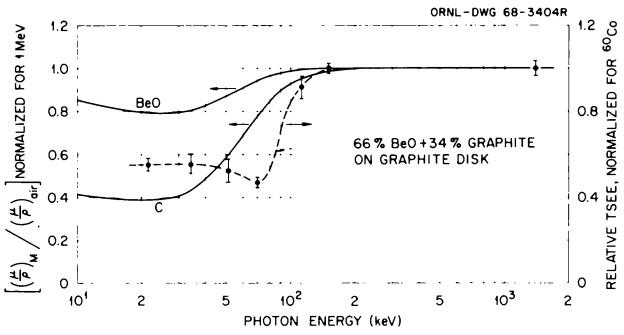

Fig. 22.18. Calculated (Left Scale) and Measured (Right Scale) Energy Dependence of a TSEE Detector Consisting of a BeO/C Mixture Plated on Graphite Disks.

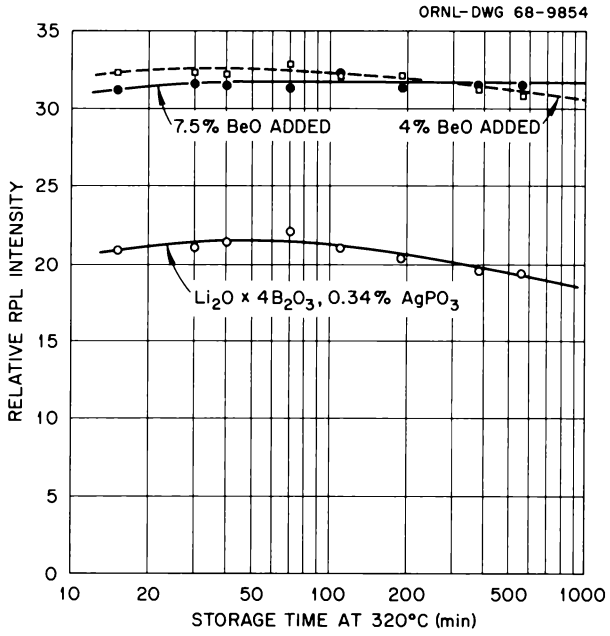

Fig. 22.19. Relative Radiophotoluminescence Intensity in Gamma-Irradiated Glasses as a Function of Storage Time at 320°C Without and With the Addition of Different Amounts of BeO.

The stabilizing effect of BeO on the Li_2O-B_2O_3 system led to investigations of $Li_2B_4O_7$:Mn, which is, chiefly because of its excellent energy response and low price, at present the most interesting thermoluminescent material but which has the serious disadvantage of being hygroscopic. Calculations of the energy response demonstrated that systems consisting of BeO, Li_2O, and B_2O_3 and containing different amounts of $MnCl_2$ could be adjusted to the energy response of air, muscle, or standard tissue within a few percent between at least 10 kev and several Mev of photon energy (Fig. 22.20).

Experiments with a number of powdered glasses which had been prepared according to these calculations revealed a single symmetrical peak at ~180°C (heating rate 17°C/sec) and a sensitivity which was, in the TLD reader used in these experiments, somewhat below that of the crystalline $Li_2B_4O_7$:Mn. The response turned out to be linear for both the peak height

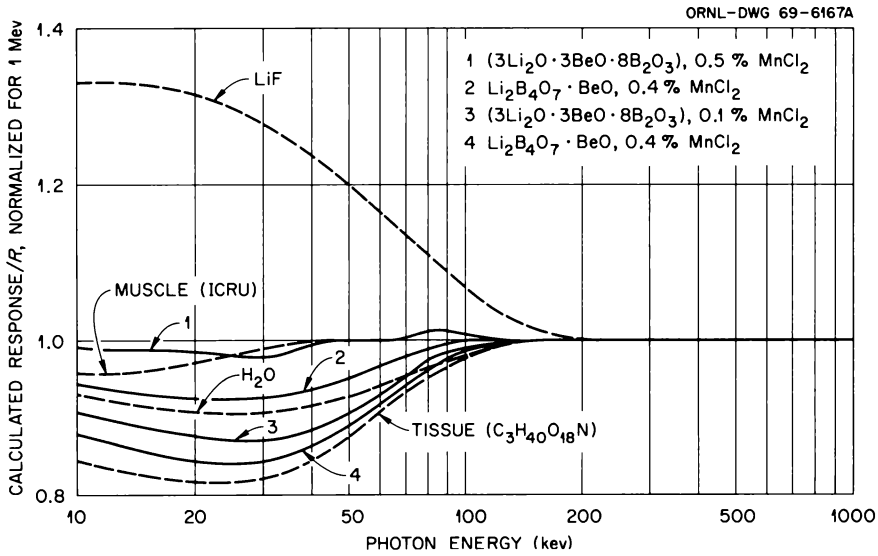

Fig. 22.20. Calculated Energy Dependence of Different New BeO-Containing, Mn-Activated Lithium Borate Glass TL Dosimeter Materials Compared with Air, Muscle, and Standard Tissue.

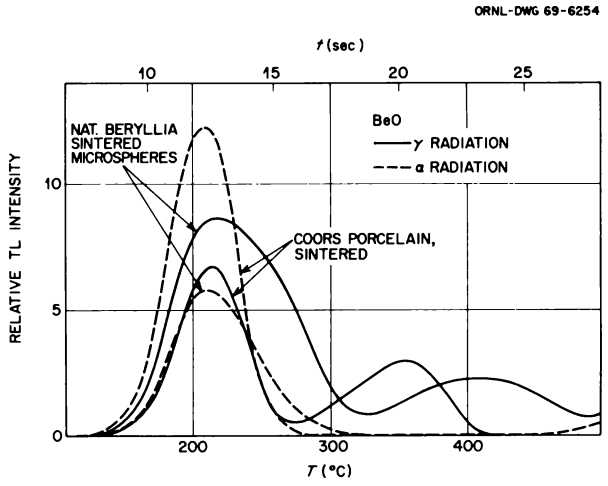

Fig. 22.21. TL Glow-Curves of Two Sintered BeO Samples After Exposure to Alpha and Gamma Radiation.

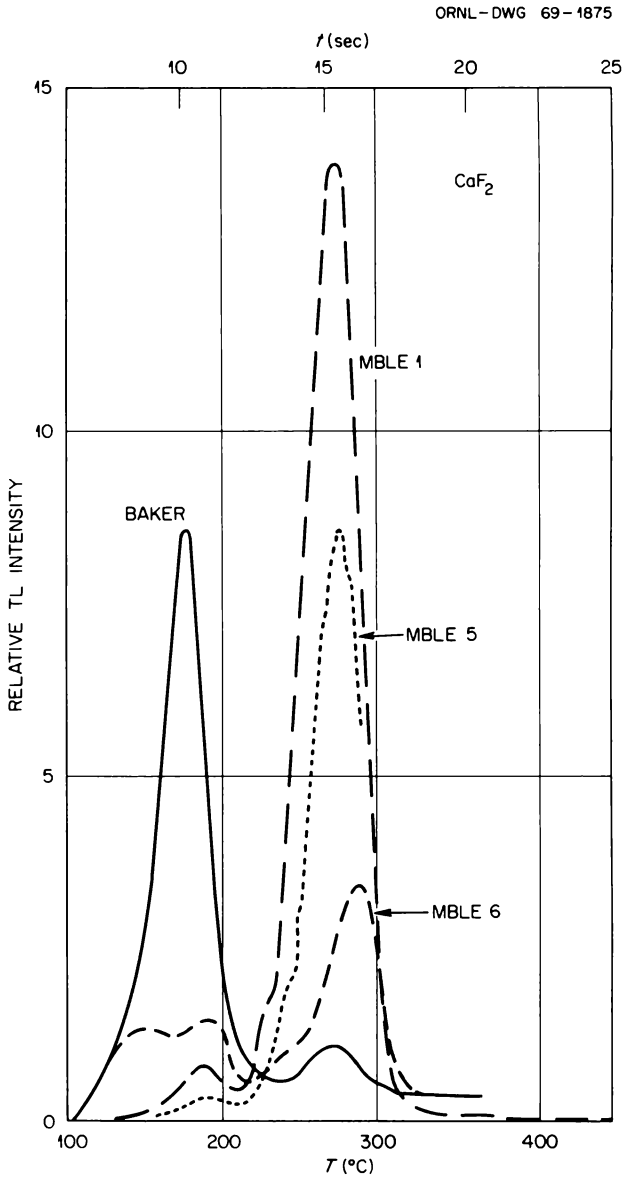

Fig. 22.22. TL Glow-Curves of Different TL-Grade and One Analytical-Grade Calcium Fluorides.

and the peak area up to much higher dose levels (~10^5 rads of ^{60}Co gamma radiation) than in LiF:Mg,Ti and $Li_2B_4O_7$:Mn, which both exhibit a pronounced supralinearity at rather low doses. Saturation occurs in the lower megarad range. The effect of several parameters, such as glass composition, further additives, preparation techniques, and preirradiation, on the phosphor's sensitivity and other dosimetric characteristics, its fading at different temperatures and humidities, etc., is being investigated.

Studies on the LET dependence of the TL glow curves revealed a pronounced difference between alpha- and gamma-irradiated samples in many materials, including LiF and BeO. In some beryllium oxides the second high-temperature peak is not observed at all after exposure to alpha radiation (Fig. 22.21). Other TLD experiments involved activated and analytical-grade calcium fluorides (Fig. 22.22) and a number of other compounds.

NUCLEAR TRACK REGISTRATION IN POLYMERS

Damage Mechanism

The increased etchability of the damaged channel along a charged-particle track in a polymer is probably due to the interaction of low-energy (less than a few hundred ev) delta rays with the macromolecules. It has, for example, been calculated that doses exceeding several megarads occur in a region of less than 100 A diameter along the trajectory of an alpha particle of several Mev. Only little is known about the mechanism of the chemical radiation damage in the most sensitive detector materials such as cellulose nitrate and cellulose acetate. Therefore, experiments have been carried out to provide some additional experimental data on this subject and to study the effect of several parameters, which are known to affect the radiochemistry, on the sensitivity and/or etching kinetics of sensitive track

detectors. They are described in detail in another report.[11]

Breaking of chemical bonds results primarily in the formation of free radicals. Only few data are available on the radical formation rate in solid polymers. To measure the G value of this important initial step in the radiolytical damage chain, which may account for approximately half of the total damage, a radical-scavenger technique has been used. This method permits, unlike electron spin resonance techniques, a quantitative determination of G values independent of ambient temperature. A stable radical, diphenylpicrylhydrazyl (DPPH), has been added in small quantities to polymer solutions prior to preparation of thin films. The reduction in optical density in the 525-nm absorption band after irradiation is measured and indicates the amount of DPPH which disappeared because of its combination with radicals (Fig. 22.23).

[11] R. H. Boyett, D. R. Johnson, and K. Becker, "Some Studies on the Chemical Damage Mechanism Along Charged Particle Tracks in Polymers," *Radiation Res.*, submitted for publication, and presented by K. Becker at the International Topical Conference on Nuclear Track Registration in Insulating Solids, Clermont-Ferrand, France, May 6 to 9, 1969, and to be published in the proceedings.

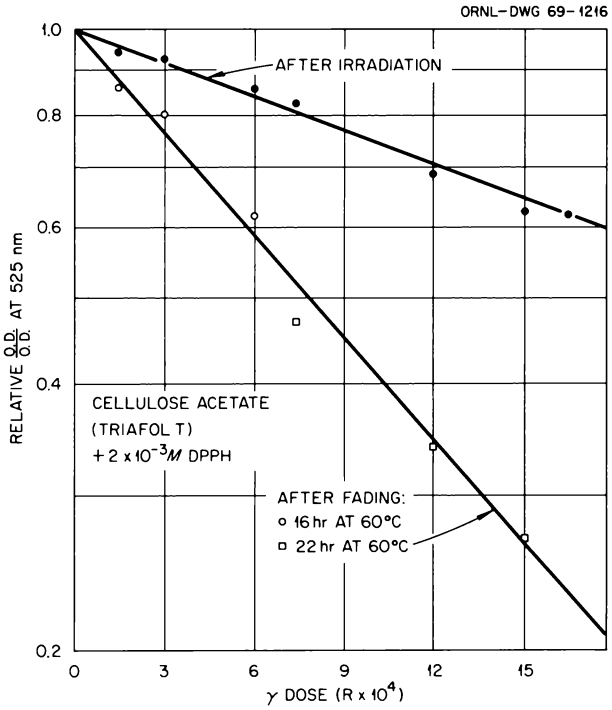

Fig. 22.23. Post- to Preirradiation Optical Density at 525 nm as a Function of the Gamma Radiation Dose in Cellulose Acetate Containing DPPH as a Radical Scavenger.

Due to the low concentration of the DPPH, not all of the radicals formed are close enough to DPPH molecules to be scavenged immediately. This process can be accelerated by storing the exposed foils at an elevated temperature prior to the optical density measurement. Sixteen hours of storage at 60°C results in a stable reading.

From the semilogarithmic plot (Fig. 22.23), G values can easily be determined in a way similar to the interpretation of exponential survival curves in radiobiological studies. The residual "surviving" DPPH is proportional to the ratio of the optical density after exposure to the optical density prior to exposure, and the removal coefficient is given by Eq. (1). From K the G value is obtained by Eq. (2). Using this method, the G value for the disappearance of DPPH has been determined in cellulose triacetate, for high-LET recoil nuclei produced by fission neutrons, to be 5.6, and for low-LET ^{60}Co gamma radiation, $G = 17$.

$$\frac{D}{D_0} = e^{-Kd}, \tag{1}$$

where

D = postexposure optical density,
D_0 = preexposure optical density,
K = removal coefficient (rad^{-1}),
d = dose (rads).

$$G = \frac{A \times K \times 1.6 \times 10^{-12} \text{ erg/ev} \times 100 \text{ ev}}{100 \text{ ergs/g-rad}}, \tag{2}$$

where G = radicals scavenged per 100 ev and A = molecules DPPH per gram polymer.

In cooperation with the Reactor Chemistry Division, further experiments on the identification and quantitative measurement (G-value determination) of low-molecular-weight radiolytic end products of the radiation damage have been carried out as a function of different parameters. The results are described in another report.[12] The thermal stability of latent recoil particle tracks in fast-neutron-exposed cellulose nitrate turned out to be surprisingly high. After one day at 100°C, still 80% of the initially visible tracks remained (Fig. 22.24). This result indicates a higher stability of "volume tracks" than of "surface tracks."

[12] D. R. Sears and D. O. Bopp, *Radiation Chemical Studies of Plastic for Charged Particle Track Registration*, ORNL-4351 (1969).

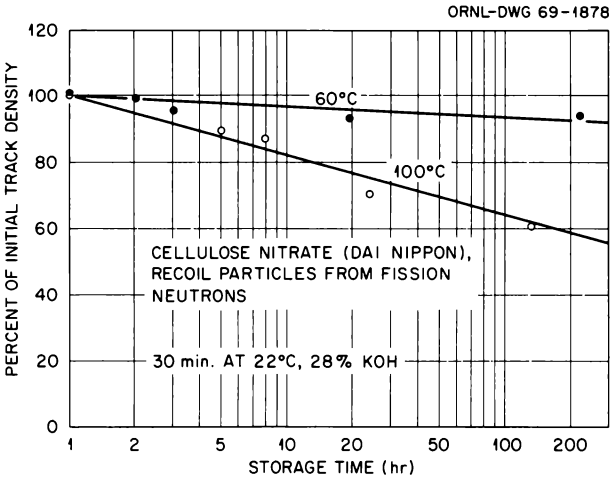

Fig. 22.24. Fading of "Latent" Recoil Particle Tracks in a Cellulose Nitrate Foil Exposed to Fission Neutrons as a Function of Storage Time at Different Elevated Temperatures in Air.

In order to study the newly discovered[13] oxygen humidity effect on the foil sensitivity and etching kinetics in more detail, an exposure chamber was built (Fig. 22.25) which permitted the exposure of samples to different radiation sources at any pressure and in any gas mixture with well-defined relative humidity in the $\sim 10^{-5}$- to 10^{3}-torr pressure range. The remotely controlled foil cassette also houses a silicon diode alpha spectrometer which permits the measurement of the actual alpha-particle flux and energy spectrum at the sample location. Two alpha sources have been used: a thick ^{238}U foil representing a broad energy and LET spectrum between 0 and 4.2 Mev and a thin ^{241}Am source emitting essentially monoenergetic alpha particles of about 5.5 Mev. Both spectra have been found to degrade by increasing the oxygen partial pressure by 8.81 and 11.41 kev/percent O_2 respectively.

Variation of the argon partial pressure between 10^{-4} and 100% did not affect the foil sensitivity. There was, however, a remarkable difference in both etching speed and the maximum visible track number, which is a measure of the registration threshold (sensitivity) of the foils, for cellulose acetate foils exposed to ^{241}Am alpha particles in oxygen and in argon (Fig. 22.26). If the narrow alpha energy distribution of the ^{241}Am spectrum is replaced by the broad ^{238}U spectrum, tracks become visible after much shorter etching times. This difference can be explained by the different LET distribution as a function of depth in the polymer.

The oxygen enhancement ratio (OER) of the track registration efficiency has been measured in cellulose triacetate (Triafol T) and cellulose nitrate (Fig. 22.27). The resulting curve is not dissimilar to the OER of the x-ray damage in mouse ascites tumor cells. This is somewhat surprising because it is known that the OER in biological materials approaches unity for an LET

[13] K. Becker, *Radiation Res.* **36**, 107 (1968).

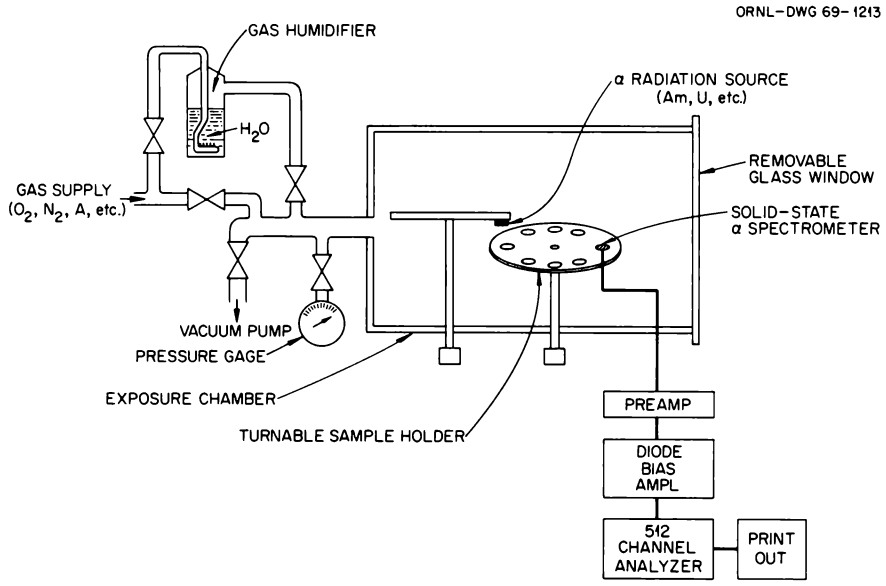

Fig. 22.25. Schematical Diagram of Exposure Chamber for Studies of the Environmental Effect on Foil Sensitivities.

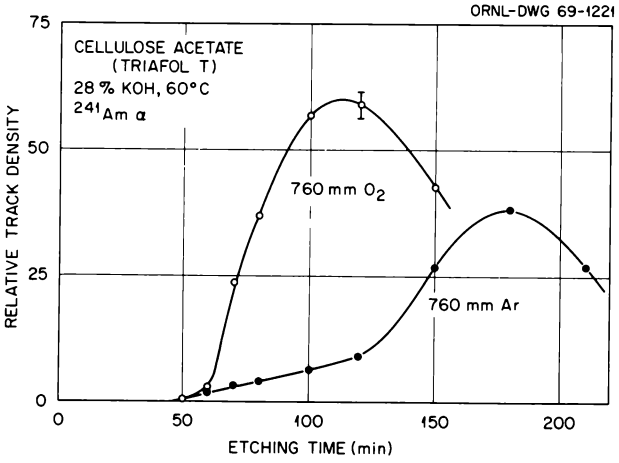

Fig. 22.26. Oxygen Effect on Etching Kinetics and Maximum Visible Number of ^{241}Am Alpha Particle Tracks in Cellulose Triacetate (Triafol T).

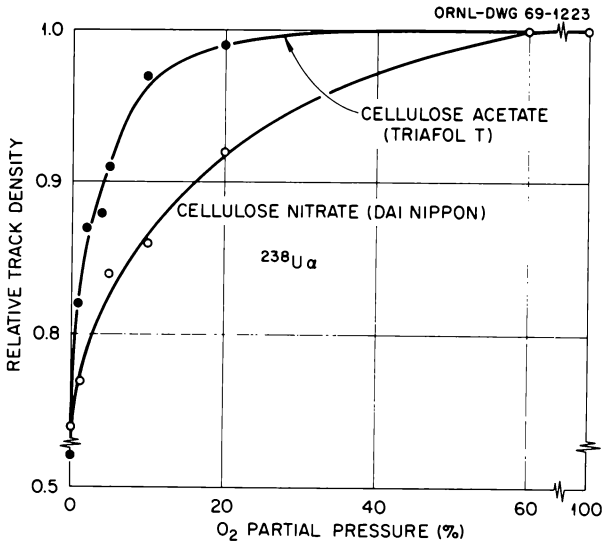

Fig. 22.27. Relative ^{238}U Alpha-Particle Track Registration Efficiency, Normalized for 100% O_2, as a Function of Oxygen Partial Pressure.

above 200 kev/μ. An explanation may be that the biological samples, unlike the plastics in these experiments, contain water and that the radiolysis of water along high-LET particle tracks creates enough oxygen and other radical scavengers to mask the "normal" oxygen effect. Indeed, a much less pronounced oxygen enhancement was found in an experiment under humid conditions, a result which strongly supports this assumption.

Preirradiation of polymer foils with ultraviolet or low-LET ionizing radiation did not increase their track registration sensitivity. In cellulose nitrate, some increase of the etching speed, but no enhancement of the alpha registration efficiency, occurs during uv postirradiation of the foils.

It can be concluded that pre- or posttreatment with a number of physical or chemical agents, which are known to cause chemical damage in the macromolecule, also affects the etching kinetics and, to a lesser extent, the threshold sensitivity of foils. For example, "hardening" of freshly prepared cellulose nitrate films by extended storage, in particular at increased temperatures, decreases the etching speed, whereas "softening" with damaging agents like H_2O, H_2O_2, NO, and uv increases it. These effects should be considered whenever reproducible quantitative track measurements are attempted.

Automatic Track Counting

A major problem in work with tracks of relatively low-LET particles is their automatic counting. Visual microscopic counting is too inaccurate, tedious, and, in the case of low track densities, too insensitive for routine applications. Numerous methods have been described to avoid visual counting of fission fragments, etc.[14] Unfortunately, none permitted the automatic counting of alpha and other low-LET particle tracks. Two new principles for automatic alpha and recoil particle track counting have therefore been studied.[15]

A slightly modified Cintel flying-spot particle resolver has been tested for different track densities using fission fragment tracks in microscopic slides and alpha-particle tracks from a thick ^{238}U foil in cellulose triacetate (Triafol T) (Fig. 22.28). If the etch pits have a diameter of less than ~4 to 5 μ, an increasing number are "overlooked" by the counter, whereas if the average diameter exceeds 9 μ, multiple counting of tracks occurs. However, it is not difficult to adjust etching conditions in such a way that most alpha-particle etch pits are in the 4-to-9-μ range. The counting efficiency depends somewhat on the track density too. This problem can be solved, at least partially, by proper

[14] K. Becker, *Biophysik* 5, 207 (1968).

[15] K. Becker, R. H. Boyett, and D. R. Johnson, "Some Applications of the Track Etching Process in Radiation Protection," *Proceedings of the International Topical Conference on Nuclear Track Registration in Insulating Solids*, Clermont-Ferrand, France, May 6 to 9, 1969, to be published.

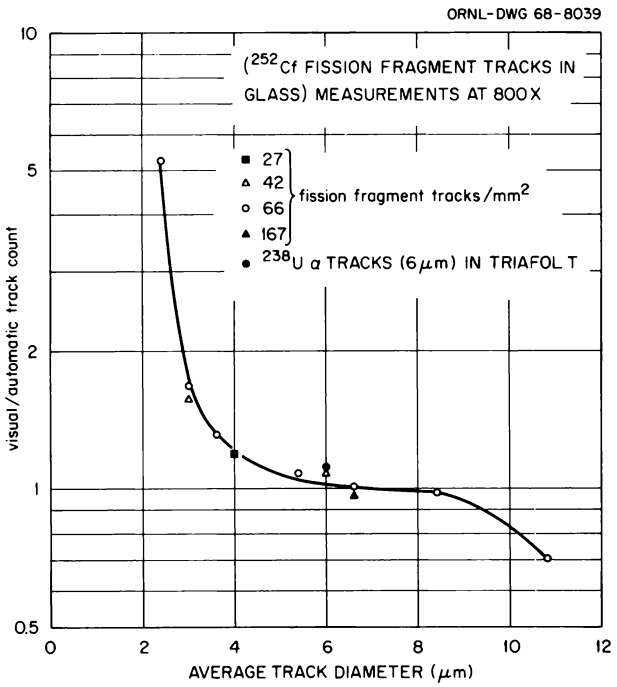

Fig. 22.28. Ratio of Visual to Automatic Track Count as a Function of Average Etch Pit Diameter for Different Fission Fragment Track Densities in Silicate Glass (Microscopic Slides) and ^{238}U Alpha-Particle Tracks in Triafol T.

adjustment of an attached "intercept analyzer." This discriminator also permits a distinction between the fission fragment and the alpha etch pit size distribution.

Advantages of the system are that thick samples can easily be counted, a crude size analysis can be performed, and the counting procedure can be supervised at the TV screen. Disadvantages are a high sensitivity to dirt and surface scratches as well as limitations in track size and density.

Therefore, with the discovery of the "jumping spark" counting method for automatic fission fragment counting by Cross,[16] we initiated studies of this simpler system and extended its applicability to alpha-particle tracks. This method for counting perforations created by proper etching of fission fragment tracks in thin polycarbonate foils is based on the sequential evaporation of aluminum from aluminized Mylar after the application of ~500 v of sparking potential. The etched films, containing holes, are placed between two plane electrodes (the lower of thick metal and the upper of aluminized Mylar). The holes or etched tracks provide an easy passageway for electrical current after the application of ~500 v potential, and sparks occur as the aluminum is evaporated from an area whose diameter is 10 to 20 times the diameter of the etched holes. This area is large enough that a second spark cannot start at the same point. The sparks, therefore, occur sequentially and can easily be counted with a scaler. The original design was modified by clamping the foil in a nylon retainer ring in which it remains for both etching and sparking (Fig. 22.29). This greatly simplifies the handling of the fragile foil. The performance of the counter was first tested with fission fragment tracks in a 6-μ Makrofol foil. If the spark count is plotted as a function of etching time, a "plateau" is obtained after ~90 min at 60°C in 28% KOH which remains constant up to at least 150 min. If the track count is measured as a function of the sparking voltage, a plateau around 500 v is obtained. At higher voltages the count increases, partly because multisparking occurs through larger holes, but mainly because insufficiently etched holes become "spark punched." Therefore foils are sparked for the first time at a higher voltage, for example at 700 v, and consecutive sparkings of this foil are performed at 450 to 500 v. Frequently repeated sparking of the same foil gives a surprisingly constant count (standard deviation $<\pm 3\%$).

For alpha-particle registration, thin (~10 to 20 μ) cellulose nitrate foils have been prepared by slow evaporation of an ethyl acetate solution in flat-bottomed dishes and drying of the resulting foils overnight at 80°C. Optimized counting is obtained in such a foil, also clamped in rings, after 45 to 200 min of etching at 35°C in 28% KOH (Fig. 22.30). After initial difficulties, very uniform foils with a better than ±10% reproducibility have been prepared. The foil thickness and etching time for optimized spark registration efficiency depend on the alpha-particle energy distribution. For example, ~4-Mev alpha particles can be detected in a 16-μ foil after 3 hr of etching in 28% KOH at 35°C with ~50% efficiency. The background to alpha-particle count ratio is, unlike in fission fragment counting, quite dependent on the etching time. The linear range of the spark-counting technique can be extended to above ~5000 tracks/cm by increasing the thickness of the aluminum layer to be evaporated.

[16] W. G. Cross, "Rapid Reading Techniques for Nuclear Particle Damage Tracks in Insulating Foils," *Proceedings of the International Topical Conference on Nuclear Track Registration in Insulating Solids*, Clermont-Ferrand, France, May 6 to 9, 1969, to be published.

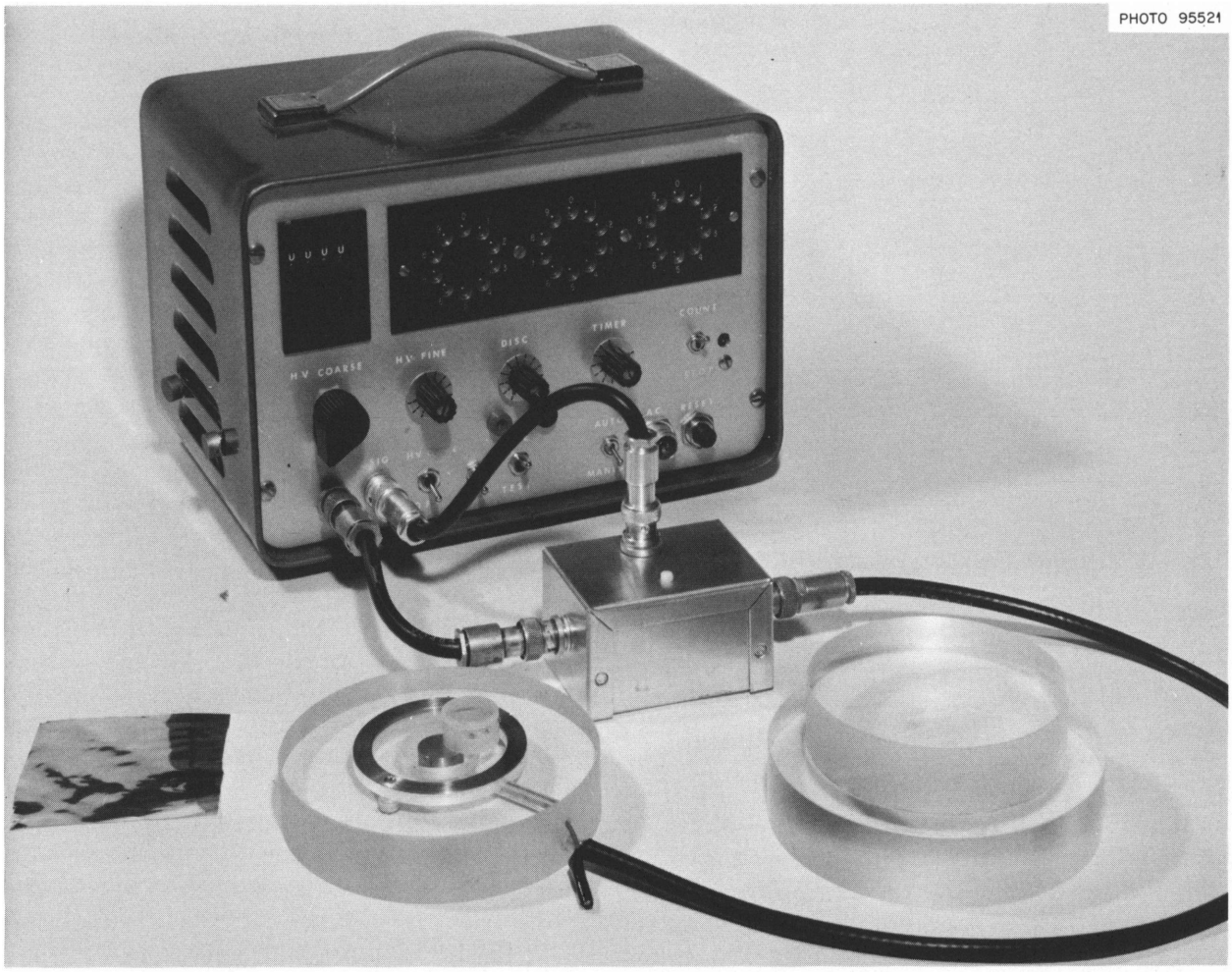

Fig. 22.29. Automatic Flying-Spark Alpha-Particle Track Counter with Portable High-Voltage Supply and Scaler.

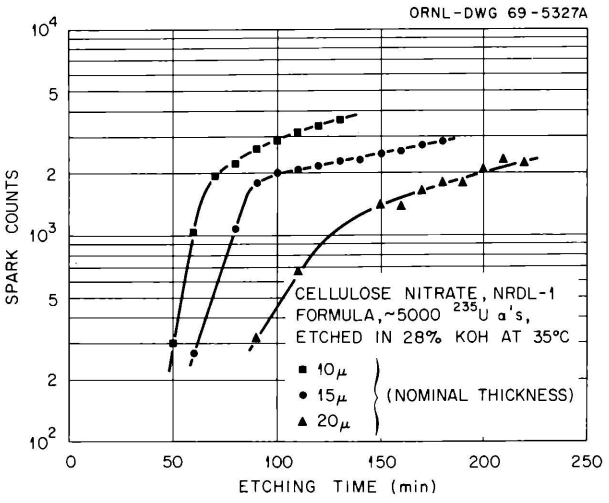

Fig. 22.30. Spark Count as a Function of Etching Time for Alpha-Exposed Cellulose Nitrate Foils of Different Thicknesses.

Direct Fast-Neutron Interaction with Polymers

Encouraged by previously reported results[17] on the direct fast-neutron effect (recoil particle registration) in sensitive polymer foils, sensitivity determinations for Triafol T, Triafol B, Makrofol N, Makrofol G, and Makrofol E, using fission neutrons from the HPRR, 3- and 14-Mev neutrons from an accelerator, and neutrons from Am/Be and Am/B sources have been repeated. All results agreed within less than a factor of 2 with those reported previously. In Triafol T, for example, between 1.6 and 2.5 $\times$ 10^{-5} track/neutron are found in the 3-to-14-Mev neutron energy range after optimized etching for 2 hr at 60°C in 28% KOH. The required etching times did not depend noticeably on the neutron

[17] K. Becker, *Health Phys.* **16**, 113 (1969).

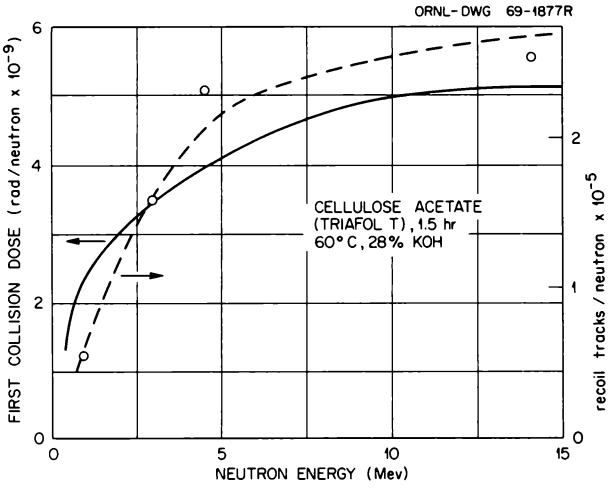

Fig. 22.31. Energy Dependence of the First Collision Neutron Dose as Recommended by ICRP Compared with the Recoil-Track Density in Neutron-Irradiated Triafol T.

energy. The etch pit size distribution is rather symmetrical and peaks around 2.2 μ diameter in a Triafol T foil exposed to 14-Mev neutrons and etched for 2 hr. In Fig. 22.31 the response as a function of neutron energy of Triafol T and the energy dependence of the maximum permissible first collision dose are compared, indicating reasonably good agreement in the 1-to-14-Mev neutron energy range. Recent experiments using monoenergetic neutrons resulted in good agreement also for 1.2- and 0.5-Mev neutrons. Cellulose nitrate made by Dai Nippon exhibits a particularly high sensitivity of $\sim 1 \times 10^{-5}$ track/neutron for fission neutrons and 6×10^{-5} track/neutron for 14-Mev neutrons. This would correspond to a detection limit of 4×10^{6} fission neutrons with ±10% accuracy in a 2.5-cm^2 sample, or an integrated flux of less than 10^5 neutrons/cm^2 for 14-Mev neutrons.

The sensitivity depends somewhat on the direction of neutron incidence. In cellulose nitrate a 37% drop in sensitivity was found when the foils were irradiated parallel to a fission neutron beam compared with foils perpendicular to the beam. No fading has been observed at room temperature, less than 10% within one week at 60°C, and 40% within five days at 100°C. The sensitivity depends, among other factors, on the environment. A 50% sensitivity increase was, for example, observed if cellulose nitrate foils were exposed in air instead of in a thin paper envelope. If exposed in a helium atmosphere to fission neutrons, the alpha recoils increased the number of visible tracks per neutron by a factor of 12.

Radon Daughter Product Personnel Dosimetry

After initial experiments[17] in 1967 had demonstrated the feasibility of alpha-particle track detectors for the measurement of radon and its daughter products in air (a Triafol T foil gave a sensitivity of ~0.3 track/mm^2 per pc-hr/ml), it became evident that the varying radon to daughter product ratio in uranium mines makes a selective measurement of the daughters which are attached to aerosol particles desirable. Furthermore, the development of the alpha-track spark counter greatly enhanced the sensitivity by permitting the automatic counting of large areas in a very short time. Two dosimeter types, both using frame-mounted cellulose nitrate foils, have been tested (Fig. 22.32). One system is a passive device without moving parts, containing two detector foils. One is exposed to both radon and radon daughter products, while the other is exposed to radon in filtered air only. The difference indicates the daughter product cencentrations. The sensitivity covers a range of at least 0.1 to 10 working-level months.

In an active system (Fig. 22.33), air is forced through a filter by a small propeller, which is operated with a constant-speed motor powered by a rechargeable battery (15 hr running time per charge). Aerosols and attached daughter products are continuously collected at the filter surface during the working period of the miner. Alpha particles emitted are registered by the cellulose nitrate foil. Both filter and detector foils are replaced after an adequate period, such as a week, and the exposed foil is etched and counted. The very high initial sensitivity of this system had to be reduced in order to meet the range requirements (integral exposures of less than one working-level hour increased the background count by a factor of 4). Humidity and dust, according to preliminary tests, had no adverse effects on the dosimeters. The weight of the unit is less than 60 g, and it can easily be attached to the miner's safety helmet. The battery can be recharged between shifts in a charging rack.

Special Applications of Spark Counting

There are several other interesting applications of the etching and spark-counting technique. It can be used in alpha autoradiography of biological samples, for instance, for the determination of the quantity and distribution of radium or plutonium in bone.

In the conventional technique of alpha autoradiography, plutonium- or uranium-containing bone samples have to be exposed for up to several years in contact with nuclear track emulsions. However, when the

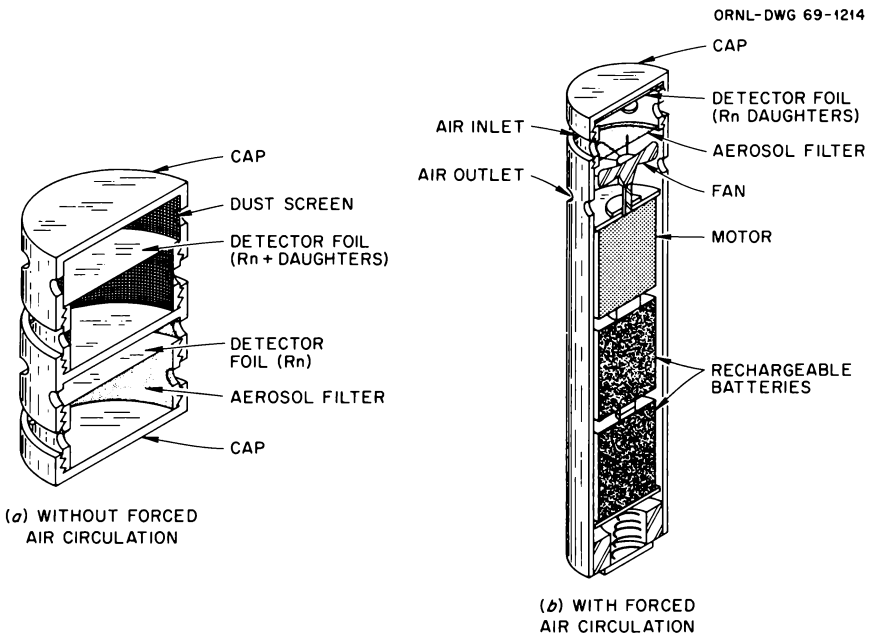

Fig. 22.32. Schematic Sketch of Passive and Active (Forced Air Circulation) Radon Daughter Product Personnel Dosimeters for Uranium Miners.

samples are covered with a Makrofol foil and exposed for a few minutes in the thermal column of a reactor to a known thermal-neutron flux, the etched and sparked foil gave a picture of the plutonium distribution within a few hours (Fig. 22.34). The total spark count can be used for a quantitative determination of the fissionable material in the sample. Many replicas can be made which can be used directly as slides or as photographic "negatives" for enlargements. Depending on the track density, contrast, and resolution desired, the resistor, sparking voltage, and aluminum thickness may be varied, resulting in different hole sizes in the aluminum. For low concentrations of fissionable materials, the samples have to be mounted on plastic instead of glass slides because the natural uranium content of the glass results in a high "background" spark density.

This method can be used for imaging distributions of materials which undergo other nuclear reactions, for example, lithium and boron, if an alpha-sensitive detector foil is used. There are also interesting applications in thermal- and fast-neutron radiography, for which combinations of detector and (n,α) or fissionable converter foils can be used.

Spark counting can also be used for the fast, accurate determination of small amounts of fissionable materials in liquids and gases. Two examples illustrate this application:

1. A small, known amount (several drops) of a water sample or a body fluid (urine, blood) is evaporated on a nylon-frame-mounted detector foil. The foil is exposed to a known neutron flux in a reactor, etched, and spark counted. A large number of samples can thus be analyzed in a short time.
2. A filter through which a known volume of air has passed can, in contact with a foil, undergo the same procedure for the determination of small amounts of U, Th, or Pu. This method permits ultrasensitive measurements. The U/Th ratio can be determined by separate exposure of samples to thermal and fast neutrons.

MISCELLANEOUS TRACK STUDIES

An energy fluence of 10^4 to 10^8 ergs/cm^2 of alpha particles, deuterons, or protons produces a significant track density in polycarbonate (Lexan) foils due to recoil reactions.[18] This does not, however, limit the application of fission fragment detectors in accident dosimetry if visual counting is done for the evaluation. When Lexan which has previously been exposed to an alpha-particle fluence as high as 10^{12} cm^{-2} (corres-

[18] D. R. Stone, *Health Phys.* 16, 772 (1969).

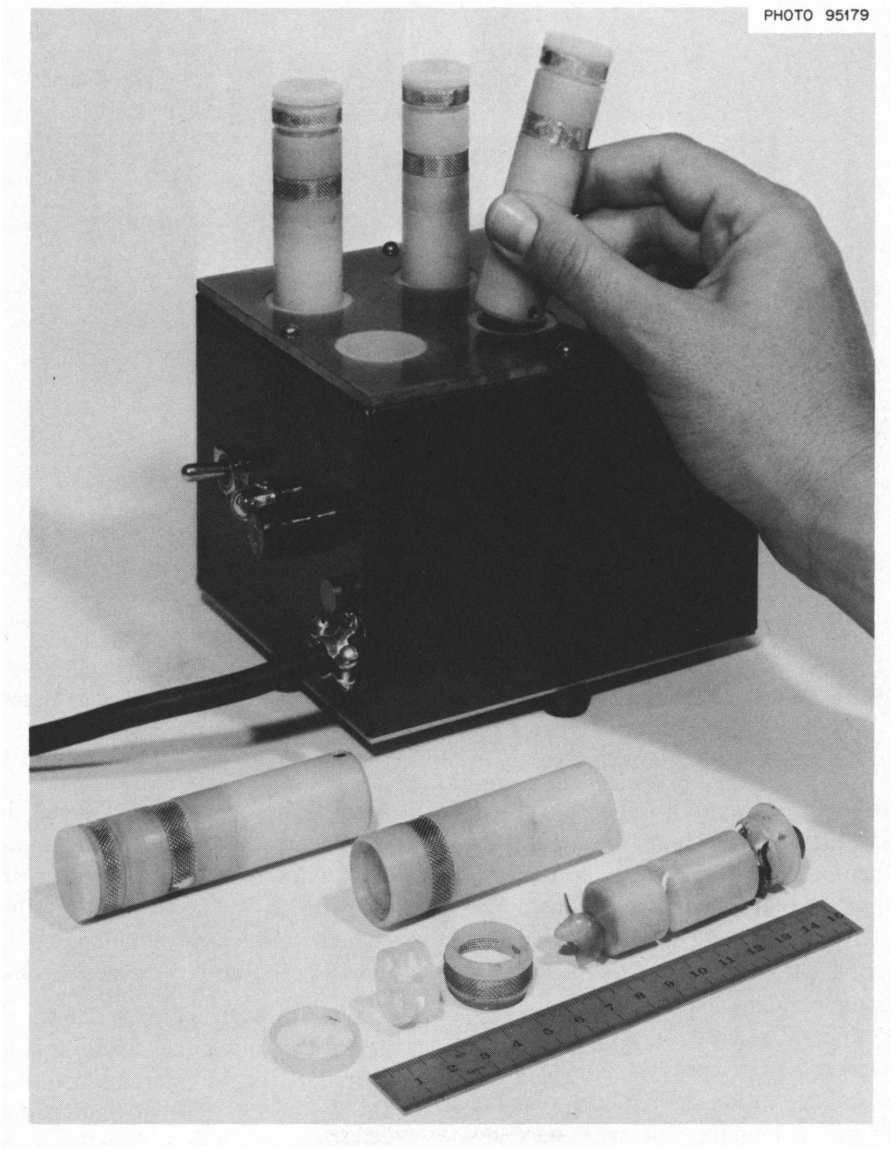

Fig. 22.33. Prototype of Personnel Dosimeters for Uranium Miners, Closed and Disassembled; Charging Unit in Background.

ponding to an exposure received during 2.5 years in contact with a 22-$\mu g/cm^2$ ^{239}Pu radiator) is exposed to fission fragments, the fission fragments are registered in the Lexan with an efficiency to within 1% of the efficiency of registration with no previous alpha exposure. Bombardment by a significant energy fluence of charged particles or of photons alters, however, the etchability of the surface (the etching rate is increased by such an exposure). The foil should therefore be etched for shorter periods and inspected between etchings when determining the number of fission fragment tracks in foils which have also been irradiated with charged particles or photons in order to prevent overetching resulting in obscured visibility of the fission fragment tracks (Fig. 22.35).

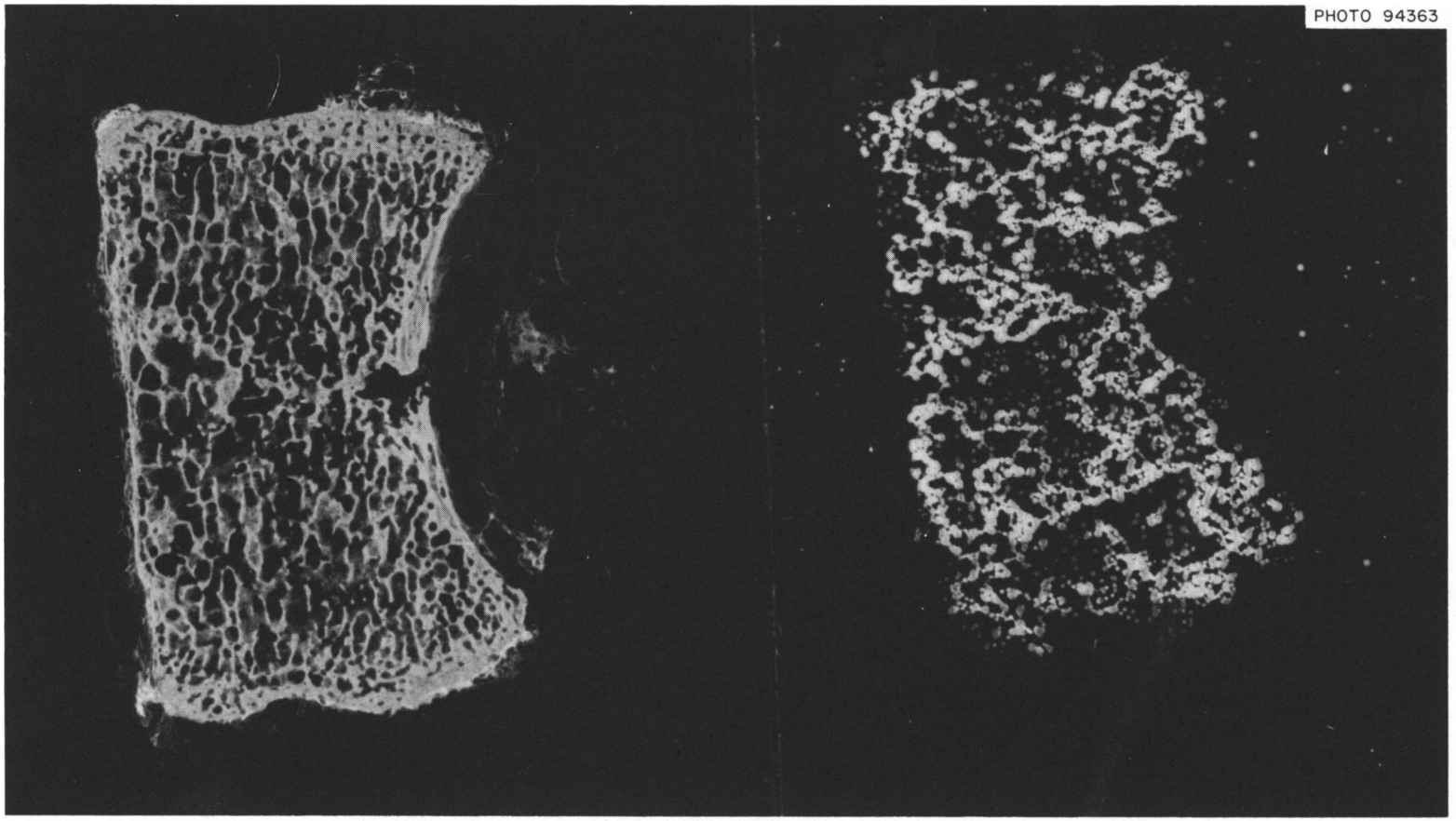

Fig. 22.34. Beagle Bone Sample (Left) and Its Neutron-Induced Autoradiograph (Right) Showing Amount and Distribution of ^{239}Pu in It.

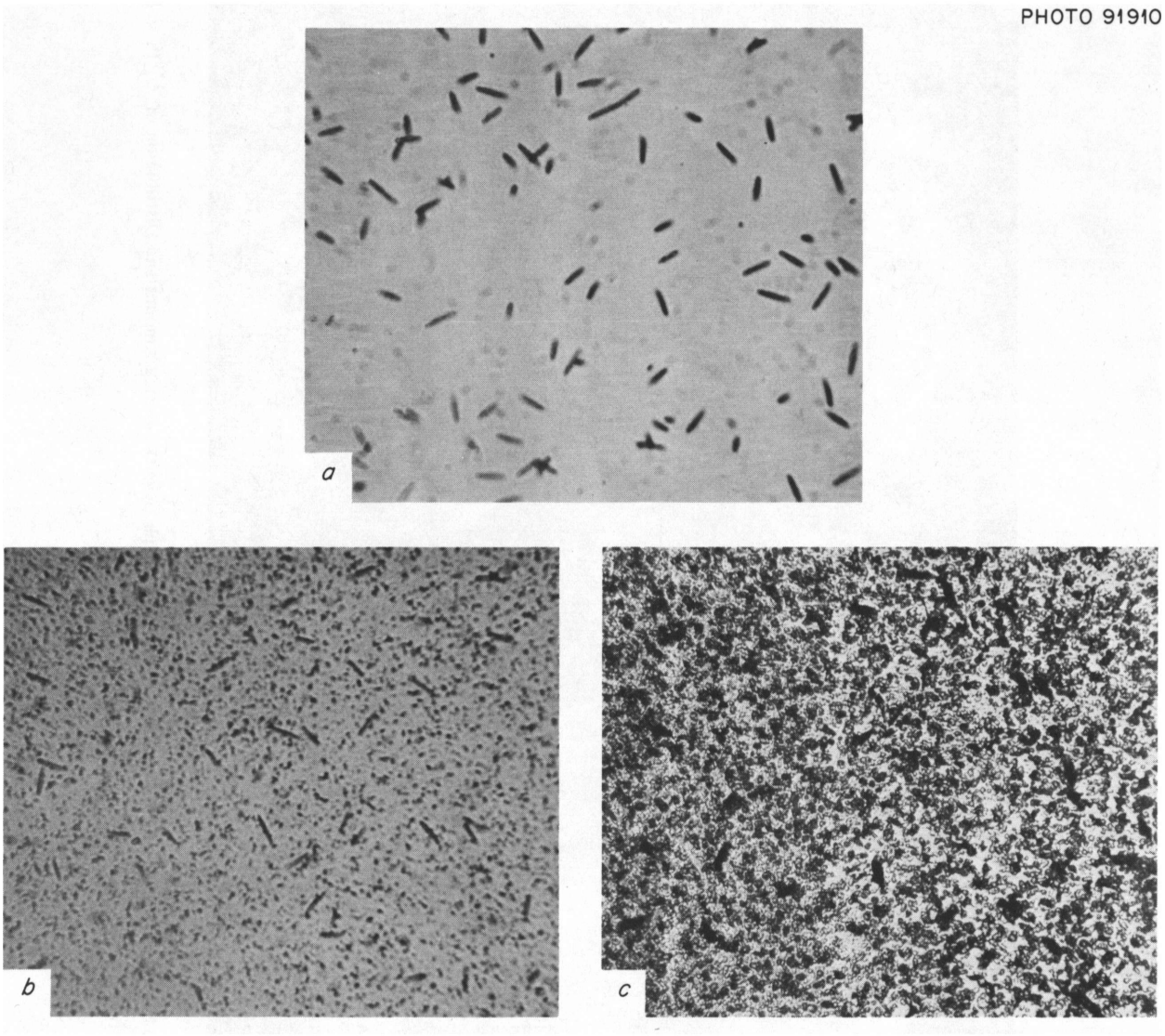

Fig. 22.35. Microphotograph (400 X) of Fission Fragment Tracks in Lexan After Etching in 28% KOH at 60°C. (a) After 60 min in a foil not exposed to alpha particles; (b) after 30 min in a foil exposed to a high alpha-particle flux; (c) after 60 min in the same foil. Reduced 20%.

23. HPRR and Accelerator Operations

F. F. Haywood D. R. Ward[1]
R. A. Francis[2]
L. W. Gilley
J. W. Poston[3]

HPRR OPERATIONS

The Health Physics Research Reactor (HPRR) has been used this year for a wide variety of radiobiological experiments. DOSAR participation included irradiations, dosimetry, and consultation for the following typical studies:

1. Investigation of the effects of fission neutrons on the immune response in mice.
2. Observation of the increase in percent volume opacity in the lenses in mice eyes. In this case, the study was centered on effects vs dose rate and total dose and compared with similar effects using 250-kvp x radiation.
3. Numerous experiments involving fission neutrons to study effects in grain seed and seedlings. Typical in these studies was the determination of the oxygen enhancement ratio in barley for fission neutrons, effects as a function of moisture content, storage after irradiation (cold storage as well as at room temperature), pretreatment with gamma rays, and irradiation in vacuum and postirradiation treatment with moisture and/or O_2. Seeds in this series were irradiated for the University of Tennessee–Atomic Energy Commission Agricultural Research Laboratory and for a staff member at the ASTRA Reactor at Seibersdorf, Austria.
4. Determination of depth dose in small animals.
5. Study of the increased incidence of tumors in the mammary glands of Sprague-Dawley rats.
6. Determination of RBE for fission neutrons for several non-cell-dividing effects in cereal plants.
7. Determination of effects of fission neutrons on 16- to 20-hr-old mice embryos; these irradiations were done for the Federal Aviation Agency.

Considerable work was done to improve the accuracy in predicting fission yield in bursts. Results of this effort indicate that the ability to repeat previous bursts lies in close control over variables such as core temperatures, position of core with respect to surrounding moderating material, and accuracy of readout dial indicators. It appears that there is a "family of curves" of yield vs reactivity. In general, burst yields are found to lie on a curve for a particular experimental setup (i.e., core height above floor). It was suspected that the orientation (circular) of the safety block with respect to its fully inserted position in the core might be responsible for some variations in burst yield. During the recent core inspection, nothing was found to substantiate this reasoning as the safety block was found to come to a repeatable position each time it was brought into the insert position. A small misalignment in the safety block pickup mechanism was observed but appears not to be responsible for variations in burst yield, because the misalignment was noticed to be identical for any rotational position of the safety block. This alignment problem was corrected with shims.

Small cracks noticed in some of the fuel disks several years ago were examined carefully during this core inspection. No changes were observed in these disks.

A low-yield 14-Mev neutron generator was installed in the HPRR building to be used to trigger reactor bursts. It has been shown to be effective in this role. When required, this generator is capable of producing a short pulse of neutrons to permit precise timing for reactor bursts and collection of data after each burst.

---

[1] On loan from Neutron Physics Division.

[2] On loan from Instrumentation and Controls Division.

[3] On leave of absence.

During the period July 8–19, 1968, the fifth in a series of intercomparisons of nuclear accident dosimetry systems was conducted at the DOSAR facility. Studies of this type are conducted annually and are generally comprised of participants from several countries.

In addition to the intercomparison study, there was a third week of activities devoted to lectures and discussions on current research in the etch pit method of track detection as it is related to neutron dosimetry.

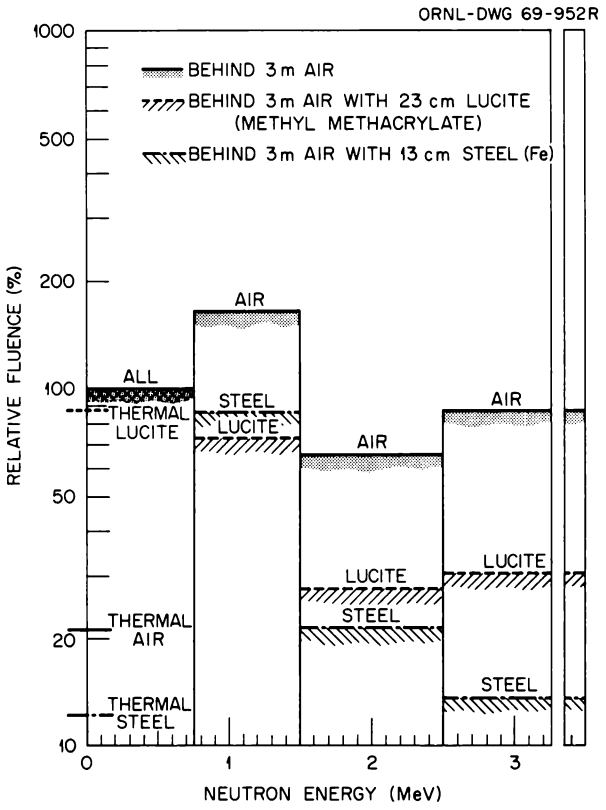

Fig. 23.1. Health Physics Research Reactor (HPRR) Neutron Fluence Spectra.

For this intercomparison, there were three HPRR pulses: one unmoderated, one for which the reactor was shielded with 13 cm of steel, and one for which a 23-cm Lucite shield was used. A neutron histogram spectrum for these three radiation fields is shown in Fig. 23.1. In addition, a rotating phantom in lateral motion away from the reactor provided an experiment for determining the orientation of the phantom with respect to a line between it and the reactor. Results of this intercomparison are given in Tables 23.1–23.4. A typical view of the experimental area is given in Fig. 23.2.

One of the more important aspects of this intercomparison involved the use of a phantom filled with a saline solution (~1.56 mg Na/ml). Several of the participating laboratories have as an integral part of their personnel dosimetry techniques a means of determining the orientation of a person with respect to the direction of the incident radiation. In time of an emergency, information of this type might prove beneficial to the patient through specific treatment. Therefore, in addition to determining the dose due to neutron and gamma-ray exposure, the participants were requested to estimate the orientation of the phantom. Motion of the phantom, both rotational and lateral, was recorded on video tape to document the exact position at the time of the pulse. Ironically, the phantom was facing an approximate forward direction for both pulses 2 and 3. It was stationary and facing the reactor for pulse 1. Almost all reports on orientation were correct.

The sixth intercomparison was held in July 1969. Participation in this program was limited largely to those companies holding AEC special nuclear material licenses. It is felt that there is a significant potential for nuclear accidents among those groups and that their dosimetrists should have the same opportunity to test their systems and techniques as provided to the major laboratories throughout the country. Data from these tests were not available at the time of preparation of this report.

Table 23.1. Fifth Intercomparison of Nuclear Accident Dosimetry Systems

Pulse 1 – unmoderated
Yield = 6.34×10^{16} fissions

Study Group	Dose (RAD)		n/γ	Neutron Fluence × 10^{-10}							Distance (m)	Type Detector System	
	Neutron	Gamma*		Thermal	Pu >8 kev	Np >750 kev	U >1.5 Mev	S >2.5 Mev	Cu	In		Gamma	Neutron
France	264	55	4.80	0.69	13.	6.86	4.41	2.3				RPL	ACT
Japan		19		0.21	11.7			0.89			4.0	Film	ACT
		22										RPL	
		24										TDU	
LASL	250	44	5.68	0.63				1.8	3.5	4.8		Film	ACT
	290	44	6.59									Film	MOD
LRL	267	55	4.85	0.53	11.7	6.8	3.4	1.8	2.9	5.4	3.0	TLD	TDU
	268	55	4.82									TLD	MOD
ORGDP	261	36	7.25	0.54				2.0		4.23	3.0	RPL	ACT
	238	36	6.61		9.3	7.1	3.4				3.0	RPL	TDU
ORNL	246	36	6.83	0.46	9.7	7.4	3.6	2.0			3.0	RPL	TDU
	254	36	7.05	0.50	10.6	6.8	3.6	2.0			3.0	RPL	TDU-A
United Kingdom	272	46.5	5.85	0.35	10.7	7.63	3.80	2.26			3.0	TLD	TDU-A
	282	53.5	5.27	0.80							3.0	Film	ACT
Y-12	265	39	6.79	0.54	13.	6.92	3.52	2.07			3.0	RPL	TDU
	265	39	6.79									RPL	TDU
(HPRR-Staff)	251	36	6.97									G-M	Prop.

*Gamma reported as exposure in R; conversion factor 0.87 (rad/R) used in this table.

Table 23.2. Fifth Intercomparison of Nuclear Accident Dosimetry Systems

Pulse 2 – Hydrogenous Shield
Yield = 5.38×10^{16} fissions

Study Group	Dose (rad)		n/γ	Neutron Fluence × 10^{-10}							Distance	Type Detector System	
	Neutron	Gamma*		Thermal	Pu >8 kev	Np >750 kev	U >1.5 Mev	S >2.5 Mev	Cu	In	(m)	Gamma	Neutron
France	14	31	0.45	0.35	1.15†	0.32	0.2	0.11			3.0	RPL	ACT
Japan		17		0.24	0.84		0.21	0.11			3.0	Film	ACT
		24									3.0	RPL	
		12									3.0	TLD	
LASL	17	29	0.58	0.32				0.09	0.56	0.34	3.0	Film	ACT
	10	29	0.34								3.0	Film	MOD
LRL	14.6	29	0.50	0.26	0.61	0.37	0.16	0.08	0.46	0.22	3.0	TLD	TDU
	22	29	0.76								3.0	TLD	MOD
ORGDP	12.8	23	0.56	0.35				0.07		0.19	3.0	RPL	ACT
	12.3	23	0.53		0.53	0.32	0.15	0.09			3.0	RPL	TDU
ORNL	13.5	23	0.59	0.31	0.65	0.38	0.17	0.09			3.0	RPL	TDU
		23		0.25		0.42	0.22	0.11			3.0	RPL	TDU-A
United Kingdom	11.2	26	0.43	0.30	0.55	0.28	0.18	0.12			3.0	TLD	TDU-A
	10.9	24.5	0.44	0.59							3.0	Film	ACT
Y-12	12	22	0.54	0.40	0.50	0.36	0.12	0.10			3.0	RPL	TDU
	11	22	0.50								3.0	RPL	TDU
(HPRR-Staff)	11.4	17.6	0.65								3.0	G-M	Prop.

*Gamma reported as exposure in R; conversion factor 0.87 (rad/R) used in this table.

†E >0.4 ev.

Table 23.3. Fifth Intercomparison of Nuclear Accident Dosimetry Systems

Pulse 3 – Steel Shield
Yield = 7.11×10^{16} fissions

Study Group	Dose (rad)		n/γ	Neutron Fluence × 10^{-10}							Distance	Type Detector Systems	
	Neutron	Gamma*		Thermal	Pu > 8 kev	Np > 750 kev	U > 1.5 Mev	S > 2.5 Mev	Cu	In	(m)	Gamma	Neutron
France	52	14.8	3.51	0.36	4.2[†]	1.10	0.73	0.39			3.0	RPL	ACT
Japan		6.4		0.18	2.7			0.12			4.0	Film	ACT
		9.7										RPL	
		5.6										TLD	
LASL	94	17.4	5.40	0.40				0.30	2.2	1.9	3.0	Film	ACT
	59										4.0		MOD
LRL	113	17.4	6.49	0.30	5.8	2.6	0.82	0.30	1.7	1.4	3.0	TLD	TDU
	61	17.4	3.50								4.0	TLD	MOD
ORGDP	90	10.4	8.65							1.14		RPL	ACT
	105	10.4	10.10	0.38	5.1	2.8	0.81	0.34			3.0	RPL	TDU
ORNL	110	11.3	9.73	0.34	5.2	2.9	0.85	0.33			3.0	RPL	TDU
	118	11.3	10.44	0.30	6.1	2.5	0.8	0.30			3.0	RPL	TDU-A
ORNL	57										4.0		TDU
United Kingdom	51.5	9.0	5.72	0.17	2.71	1.31	0.46	0.19			4.0	TLD	TDU-A
	50.1	12.3	4.07	0.28							4.0	Film	ACT
Y-12	101	11.3	8.94	0.2	5.9	2.6	0.70	0.32			3.0	RPL	TDU
	90	11.3	7.96								3.0		TDU
(HPRR-Staff)	104	10	10.40									G-M	Prop.

Pulse 4 – Unmoderated
Yield = 7.48×10^{16}

France	311	64	4.86	0.8	15.3[†]	8.08	5.2	2.73			3.0	RPL	ACT
United Kingdom	329	54.5	6.04	0.65								TLD	TDU-A
	338	66	5.12	1.09								Film	ACT
(HPRR-Staff)	295	42	7.02									G-M	Prop.

*Gamma reported as exposure in R; conversion factor 0.87 (rad/R) used in this table.

[†]E > 0.4 ev.

Table 23.4. Fifth Intercomparison of Nuclear Accident Dosimetry Systems Results of Monitoring for Phantom Exposure

Pulses 1–3

Study Group	Pulse No.	ORNL Phantom						United Kingdom Phantom					
		Distance (m)	Orientation	Neutron Dose (rad)	Gamma Dose (rad)	^{24}Na μCi/mg	Neutron Dosimeter Type	Distance (m)	Neutron Dose (rad)	Gamma Dose (rad)	^{24}Na μCi/mg	Neutron Dosimeter Type
France				No data submitted						No data submitted		
Japan	1	4.0		190 Surface 130 First collision	41.8 (average of 3)		TDU-B TDU-B					
	2	5.3		18 Surface 10 First collision	8.2 (average of 3)		TDU-B TDU-B	3.0	18 Surface 11 First collision	25.2 (average of 3)		TDU-B TDU-B
	3	4.9		20 Surface 12 First collision	13.6 (average of 3)		TDU-B TDU-B	4.0	44 Surface 25 First collision	14.8 (average of 3)		TDU-B TDU-B
LASL	1	4.0		180 180	57	4.0×10^{-4}	ACT-1 ACT-2					
	2	5.3	Forward & left	30	14	8.7×10^{-5}	ACT-1	3.0	17	37.4	5.0×10^{-5}	ACT-1
				29			ACT-2		26			ACT-2
	3	4.9	45° Left or right quad.	34 31		7.2×10^{-5}	ACT-1 ACT-2	4.0	64 64	26.1	1.86×10^{-4}	ACT-1 ACT-2
LRL	1	4.0		140 142	106 front 23 rear	4.1×10^{-4}	Na ACT ACT					
	2	5.3	Forward	48 30	15.7 front 6.8 rear	8.7×10^{-5}	Na ACT ACT	3.0	11 15	36.5	4.8×10^{-5}	Na ACT ACT
	3	4.9	Forward	15 16	20 front 11.3 rear	8.8×10^{-5}	Na ACT ACT	4.0	98 59	17.4	1.96×10^{-4}	Na ACT ACT
ORGDP	1	4.0		177	47 front	4.0×10^{-4}	Na ACT					
	2	5.3	Forward	22	7 front 5.2 rear	8.0×10^{-5}		3.0	15.4	25.2	5.6×10^{-5}	
	3	4.9	Forward	28	10.4 front 5.5 rear	9.0×10^{-5}		4.0	65	12.2	2.08×10^{-4}	
ORNL-1	1	4.0		155	52		ACT					
	2	5.3	Forward	17	11.3		ACT					
	3	4.9		20 front 8 rear	17.4 front 8.7 rear		ACT ACT					
ORNL-2	1	4.0		165		4.2×10^{-4}	Na ACT					
	2	5.3	Forward-left	22	12.2 front 4.4 rear	7.7×10^{-5}	Na ACT					
	3	4.9	Forward	27	17.4 front 8.7 rear	9.5×10^{-5}	Na ACT					
United Kingdom	1	4.0										
	2	5.3	Forward	32.0	12.2		ACT	3.0	16.3	31		ACT
	3	4.9	Forward	21.2	18		ACT	4.0	78.5	20 film 18 TLD		ACT
	4							3.0	449	98 film 126 TLD		ACT
SRL	1	4.0		145 First collision 132 5 cm depth	60	4.9×10^{-4}	ACT ACT					
	2	5.3	Forward-left	35 First collision 25 5 cm depth	12.1	9.8×10^{-5}	ACT ACT					
	3											
Y-12	1	4.0		164	51	3.7×10^{-4}	ACT					
	2	5.3		29		7×10^{-5}	ACT	3.0	20		5.2×10^{-5}	ACT
	3	4.9		31		8.4×10^{-5}	ACT	4.0	67		1.81×10^{-4}	ACT

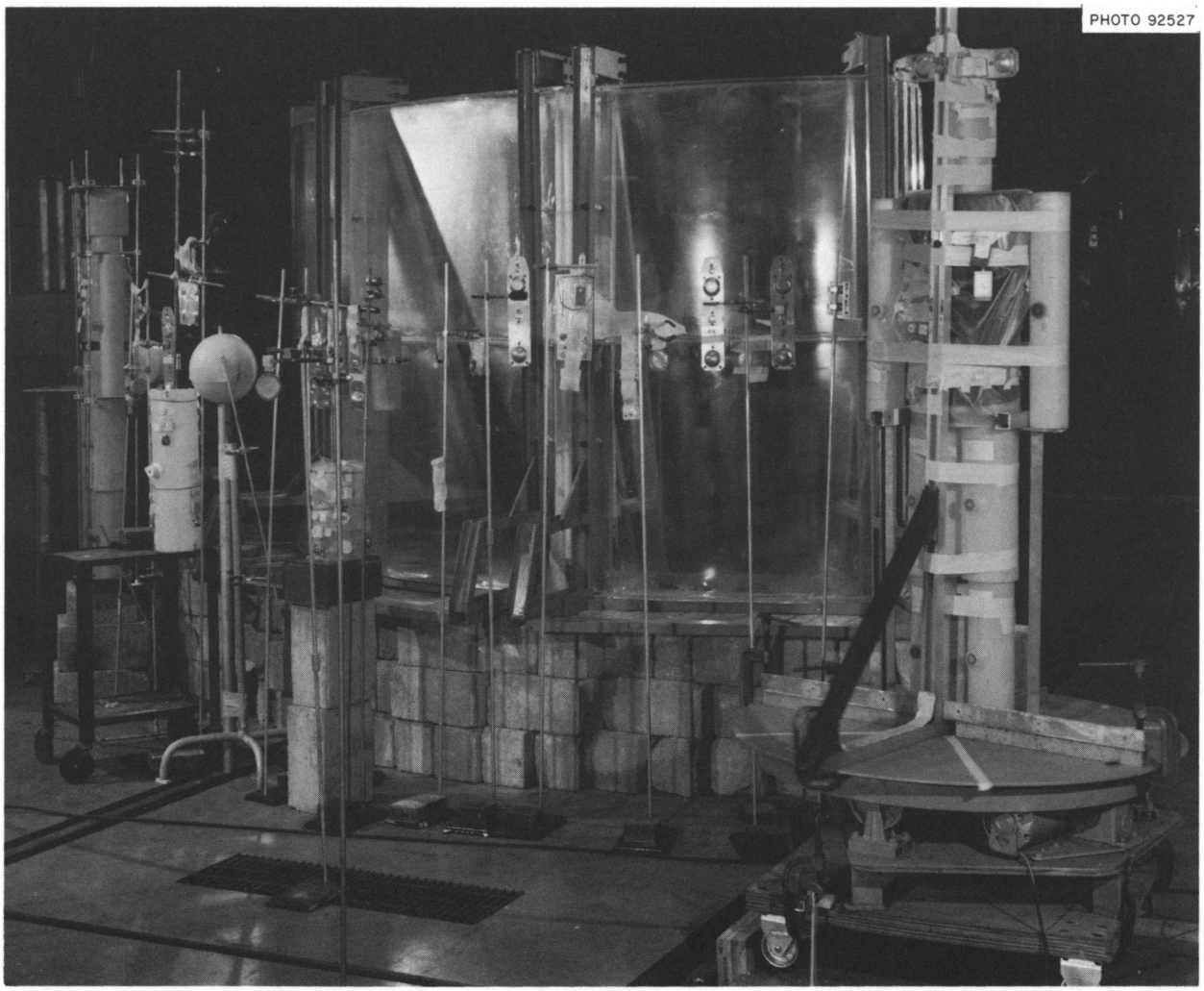

Fig. 23.2. View of Experimental Area for Pulse No. 2 Using a Lucite Shield.

ACCELERATOR OPERATIONS

Two positive-ion accelerators are readily available for use by the Radiation Dosimetry Research Section: the DOSAR Low-Energy Accelerator (DLEA) and the Physics Division 3-Mv Van de Graaff. Both were used heavily.

At the DLEA, irradiations of plastic foils with 3- and 15-Mev neutrons were made. The positive-ion facilities were put into operation and first used to check the proton optics of a magnetically analyzing intermediate-energy neutron spectrometer. A careful calibration of the beam-analyzing magnet was performed using the resonance in the $^{11}B(p,\gamma)^{12}C$ reaction. Initial work on the stopping power of hydrocarbon gases for low-energy heavy ions has begun.

Operations at the 3-Mv Van de Graaff centered around the testing and calibration of the intermediate-energy neutron spectrometer using neutrons produced by the $^{7}Li(p,n)^{7}Be$ reaction. Monoenergetic neutrons from the $^{3}H(p,n)^{3}He$ reaction were used to test the sensitivity of polycarbonate plastic foils and TSEE materials to direct irradiations by neutrons. A number of energies of monoenergetic neutrons from the $^{7}Li(p,n)^{7}Be$, $^{3}H(p,n)^{3}He$, $^{2}H(d,n)^{3}He$, and $^{3}H(d,n)^{4}He$ reactions were made available to a visiting scientist for the testing of a newly developed dosimeter system. Three other neutron spectrometer systems under development by the section also underwent testing and evaluation using a wide range of monoenergetic neutrons.

Part V. Internal Dosimetry

W. S. Snyder

24. Internal Dose Estimation

A GENERALIZED COMPARTMENT MODEL WITH AN APPLICATION TO DOSE FROM ^{55}Fe AND ^{59}Fe

W. S. Snyder S. R. Bernard

Introduction

In this paper we develop a technique for computing residence times (microcurie-days) of a radionuclide whose behavior in the body is described by a compartment model somewhat more general than the usual system in that exchange rates between compartments are not assumed to be constant in time. The model was suggested by that developed by Pollycove[1] for metabolism of iron, and the technique will be illustrated below by calculating dose commitment to man from administration of radioactive iron. The technique is particularly simple when only an estimate of dose commitment is wanted. It does not seem to offer any special advantages if the course of dose rate in time is to be estimated or if the residence time of the radionuclide in the body is an appreciable fraction of the life-span.

The Model

The metabolism of iron is not representable in terms of a simple compartment model with constant exchange rates. Once iron is taken up by a red blood cell, it remains in the cell during the life of the cell, subject only to elimination by radioactive decay. During this period of the life of the cell, the iron present in the cell is not subject to exchange with other compartments or pools of iron in the body. Since the red blood cells have a mean life of 120 days (standard deviation = 12 days),[1] there is a considerable period of delay before the iron in these cells is again available for exchange with other pools of iron in the body.

A model constructed by Pollycove is shown in Fig. 24.1. Pollycove also supplies some data on the amount present in many of these pools, as well as some of the rates. These data are summarized in Table 24.1. It will be noticed that these data suffice to determine the exchange rates λ_{ij} = fraction of pool i entering pool j per day in most cases. However, pool 6 is an exception in that data are not available to determine the rate $\lambda_{5,6}$.

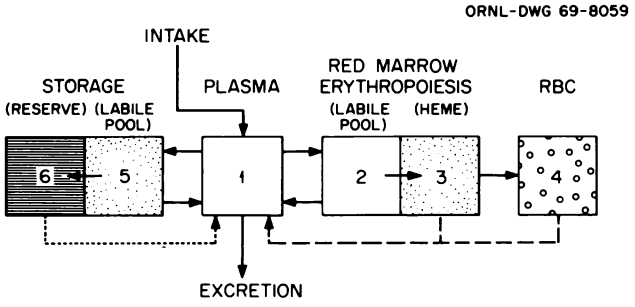

Fig. 24.1. Pollycove's Compartment Model for Iron Kinetics in Man.

[1] M. Pollycove, "Iron Kinetics," p. 148 of *Iron Metabolism* (ed. by F. Gross), Springer-Verlag, Berlin, 1964.

Table 24.1. Iron Pool Sizes and Flow of Iron into and out of Plasma Pool

Source: M. Pollycove, "Iron Kinetics," p. 148 of *Iron Metabolism* (ed. by F. Gross), Springer-Verlag, Berlin, 1964.

Pool[a]	Amount (mg)	Rate of Exchange from Plasma (mg/day)	Into Plasma
1	4		
2	85	32	11
3	30		
4	2700		21
5,6	1000	1	1
ECF		1	1
	Excretion	1	
	Intake		1
Total		35	35

[a]See Fig. 24.1.

Also, as mentioned above, pool 4 entails a delay time of about 120 days before the material is available to recycle back to the plasma. Also, there does not seem to be an estimate of the amount of iron in the extracellular fluid. In this paper we assume it to be part of the 1000 mg in the storage compartment, and for intake and outgo for this compartment, we assume 2 mg/day.

General Model

In Fig. 24.2 we indicate an abstract model which includes the essential feature of a delay time in one or several of the compartments as a special case. The model consists of any number N of "loops"; a loop is defined to consist of one or more compartments whose interconnection is such that a radionuclide entering any one of them from plasma will pass from one to another of the compartments of the loop and return to plasma without entering other compartments of the model or reentering another compartment of the loop. Thus in Fig. 24.2, the nuclide may enter loop 1 from the plasma either by way of compartment C_1 or C_3, and it may follow any of the pathways $C_1 \rightarrow C_2 \rightarrow C_3 \rightarrow C_4 \rightarrow P$; $C_1 \rightarrow C_3 \rightarrow C_4 \rightarrow P$; $C_1 \rightarrow C_3 \rightarrow P$. The nuclide may be excreted from any of these compartments without impairment of the method of calculation presented below. Another way of describing a loop is to consider it as consisting of pathways of the nuclide through the loop which begin and terminate in plasma or excretion, but which do not reenter any compartment already traversed during this passage from P to P. The complete model consists of plasma and any number of loops, indicated by 1, 2, ..., K in Fig. 24.2. Pollycove's model is easily seen to consist of two loops, one including red marrow and RBC, the other including labile and reserve in the storage compartment.

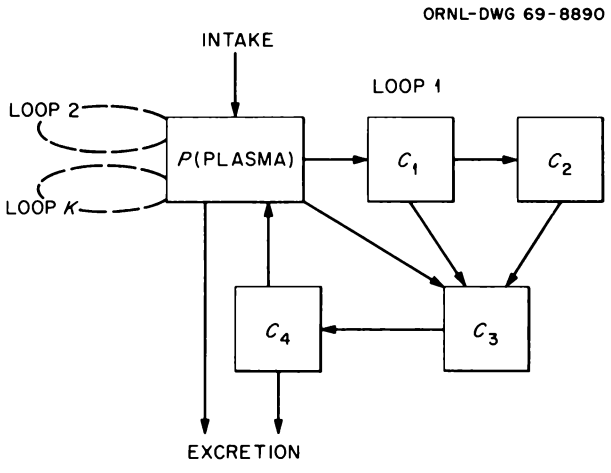

Fig. 24.2. Generalized Compartment Model for Tracer Kinetics.

Returning now to Fig. 24.2, suppose a unit amount of nuclide is introduced into P. We may think of each of these atoms as being tagged, say, with the number 1, signifying that this is the first entry of that atom into P. When any of these atoms return to P bearing the tag 1, we may suppose the tag is replaced by 2, and so on for each subsequent return. Suppose further that the residence time in any particular compartment while the atom bears the tag 1 can be computed, as well as the quantity returning to P. Denote these quantities by R_i (residence time in compartment i in microcurie-days of atoms tagged 1) and A_{iP} (activity returning to P from compartment i, microcuries). Of course, $A_{iP} = 0$ if there is no direct pathway from i to P. For the present method to apply, it is essential that the quantities R_i and A_{iP} be computable. In general, this will be a simple problem if the time course of material along a pathway is known. Since R_i and A_{iP} are computed only for one passage of the material (i.e., while the atoms are tagged with 1), no recycling of material back to a compartment is involved.

Clearly, $S_1 = \sum_i A_{iP}$, where the summation extends over all compartments, represents the total activity returning to P bearing the tag 1. The fact that this activity does not return at one and the same time is immaterial if only the total residence time is wanted, but it would be otherwise if the time course of dose was required.

Assuming the model remains unchanged, the activity S_1 will begin a new course through the system, and we

may conceptually imagine each atom now tagged with 2. Clearly, this second passage will produce $S_1 R_i$ microcurie-days of residence in compartment i, and an amount $S_1 A_{Pi}$ μc returns to P from compartment i. Thus atoms bearing the tag 2 which return to P will total $S_1^2 = \Sigma S_1 A_{iP}$, where the summation extends over all compartments. By continuation of this argument, one obtains a total residence time in compartment i of

$$R_i + S_1 R_i + S_1^2 R_i + S_1^3 R_i + \ldots = R_i/(1 - S_1). \qquad (1)$$

Formula (1) assumes that the process continues indefinitely, which would appear to be unrealistic. However, if the time course of the radionuclide in the body is short enough that essentially all the activity either decays in the body or is excreted from the body within the life-span of the individual, then the error in taking the infinite sum (1) will be negligible. Since it is not assumed that the material all recycles back to P simultaneously, it would appear complicated to describe the time course of the nuclide in each compartment. However, to obtain total dose (dose commitment), one need not follow the course in time but only obtain the total microcurie-days of residence in each compartment.

We illustrate the above method by applying it to the model of Pollycove but with a slight modification. The data supplied by Pollycove do not suffice to separate the reserve compartment and the labile pool. He implies that the labile pool is small in comparison with the reserve, and hence two compartments will be considered as one compartment, which we designate as 6 and continue to call the reserve. Also, we let 2 mg/day leave and enter this storage compartment. With this simplification the data of Pollycove suffice to determine the exchange rates $\lambda_{16}, \lambda_{61}, \lambda_{12}, \lambda_{21}, \lambda_{23}, \lambda_{31}$ since compartments 1, 2, 3, and 6 are assumed to transfer material at constant rates of exchange. However, the RBC (i.e., compartment 4) is assumed to hold each atom entering it for a period of 120 days and then discharge it to P unless radioactive decay has intervened. The data of Pollycove on pool size and exchange rates in Table 24.1 are consistent with the following values of the exchange rates: $\lambda_{12} = 8$ days^{-1}, $\lambda_{21} = 11/85$ days^{-1}, $\lambda_{23} = 21/85$ days^{-1}, $\lambda_{34} = 7/10$ days^{-1}, $\lambda_{16} = 1/2$ days^{-1}, $\lambda_{61} = 1/500$ days^{-1}. Since Pollycove indicates about 21 mg/day of stable iron enters the RBC compartment and that it has a pool size of 2700 mg, it follows that mean residence time is 2700/21 days $\cong$ 128 days, which is close to the postulated 120 days. Thus the model seems reasonably in accord with the assumed pool sizes and metabolic behavior of stable iron.

For a radioactive isotope of iron, it follows that

$$R_1 = \int_0^\infty 1 e^{-(\lambda_{16}+\lambda_{12}+\lambda_r+\lambda_e)t}\, dt$$

$$= \frac{1}{\lambda_{16} + \lambda_{12} + \lambda_r + \lambda_e} = \frac{1}{8.75 + \lambda_r} \text{ days}^{-1},$$

where λ_r is the radioactive decay constant of a radioactive isotope of iron and where λ_e is the rate of excretion from P (i.e., $\lambda_e = 1/4$ days^{-1}). The activity entering 6 and 2 from P is given by

$$A_{16} = 2/(8.75 + \lambda_r)\ \mu\text{c}$$

and

$$A_{12} = 8/(8.75 + \lambda_r)\ \mu\text{c}$$

respectively. Similarly,

$$R_6 = \frac{0.5}{8.75 + \lambda_r} \times \frac{1}{\lambda_{61} + \lambda_r}$$

$$= \frac{0.5}{(8.75 + \lambda_r)(0.002 + \lambda_r)}\ \mu\text{c-days},$$

and

$$A_{61} = \frac{0.5 \times 0.002}{(8.75 + \lambda_r)(0.002 + \lambda_r)}$$

$$= \frac{0.001}{(8.75 + \lambda_r)(0.002 + \lambda_r)}\ \mu\text{c};$$

$$R_2 = \frac{A_{12}}{\lambda_{23} + \lambda_{21} + \lambda_r}$$

$$= \frac{8}{(8.75 + \lambda_r)(32/85 + \lambda_r)}\ \mu\text{c-days},$$

$$A_{23} = (21/85) R_2 = \frac{168/85}{(8.72 + \lambda_r)(32/85 + \lambda_r)}\ \mu\text{c},$$

$$A_{21} = (11/85) R_2 = \frac{88/85}{(8.75 + \lambda_r)(32/85 + \lambda_r)}\ \mu\text{c};$$

$$R_3 = \frac{A_{23}}{\lambda_{34} + \lambda_r}$$

$$= \frac{168/85}{(8.75 + \lambda_r)(32/85 + \lambda_r)(7/10 + \lambda_r)}\ \mu\text{c-days},$$

$$A_{34} = (7/10)\,R_3 = \frac{1176/850}{(8.75+\lambda_r)(32/85+\lambda_r)(7/10+\lambda_r)}\ \mu c;$$

$$R_4 = A_{34} \times \left(\frac{1-e^{-\lambda_r 128}}{\lambda_r}\right)\ \mu c\text{-days},$$

$$A_{41} = \frac{A_{34}\,e^{-\lambda_r 128}}{\lambda_r}\ \mu c.$$

Thus the total activity entering P after the first passage of the radionuclide through the system is

$$S_1 = A_{61} + A_{21} + A_{41}\ \mu c.$$

It follows from (1) that the total residence time in any compartment i is given by

$$R_i^T = \frac{R_i}{1-S_1}\ \mu c\text{-days}.$$

Substituting numerical values of λ_r for ^{59}Fe (λ_r = 0.693/45.6 days) and ^{55}Fe (λ_r = 0.693/949.5 days), we obtain the estimates of microcurie-days as shown in Table 24.2.

Dose Commitment for ^{55}Fe and ^{59}Fe

In order to estimate dose to the organs and tissues from an intake to blood of 1 μc of ^{55}Fe and ^{59}Fe, the decay scheme, the absorbed energy, and the microcurie-days of residence in the organ are needed. Decay scheme data are obtained from the computer code written by Dillman.[2] The absorbed fractions of the photon energy (AF) for a uniformly distributed radionuclide in the total body are obtained from the Monte Carlo code of Fisher and Snyder.[3] If the distributions of storage iron in liver, spleen, and muscle were known adequately, the distribution of dose to these organs might be estimated. Also, if we had the AF's for dose to red marrow, then a dose estimate could be made for this "organ." Here, we only can estimate dose to the total body from ^{55}Fe and ^{59}Fe and the dose to the red blood cells from ^{55}Fe, because we do not have AF's for the red marrow "organ" nor adequate data on the iron contents in liver and spleen.

In the estimation of total body dose for ^{55}Fe, we employ the energy of the x rays and microcurie-days residence in all compartments of the body. The low-energy Auger electrons originating within a RBC will largely be absorbed within the cell. (Their range is estimated by Wrenn[4] to be $\sim 1/3$ μ.) The Auger electrons originating outside a RBC, that is, resulting from microcurie-days of residence in storage, plasma, and marrow compartments, are included in the dose estimated for the total body. But for ^{59}Fe, we assume the electrons (of average energy 0.12 Mev, Table 24.3) originating in red cell iron uniformly irradiate the whole body together with the gamma rays. The Auger electrons have 4.38×10^{-3} Mev per decay in the total body. In Table 24.4 there appears the absorbed energy of the x rays of ^{55}Fe of 0.00155 Mev per decay and of gamma rays of ^{59}Fe of 0.371 Mev per decay. Thus, for total body dose D_{TB} due to ^{55}Fe,

[2] L. T. Dillman, "Radionuclide Decay Schemes and Nuclear Parameters for Use in Radiation-Dose Estimation," MIRD Pamphlet No. 4, suppl. No. 2, *J. Nucl. Med.* (March 1969).

[3] H. L. Fisher, Jr., and W. S. Snyder, "Distribution of Dose in the Body from a Source of Gamma Rays Distributed Uniformly in an Organ," *Health Phys. Div. Ann. Progr. Rept. July 31, 1967*, ORNL-4168, p. 245.

[4] M. E. Wrenn, "The Dosimetry of ^{55}Fe," p. 843 in *Proceedings of the First International Congress of Radiation Protection*, W. S. Snyder *et al.*, eds., Pergamon Press, Oxford, 1968.

Table 24.2. Microcurie-Days Residence for ^{55}Fe and ^{59}Fe in Various Iron Compartments

Radionuclide	T_r (days)	R_1^T	R_2^T	R_3^T	R_4^T	R_6^T	Total Body[a]
^{59}Fe	45.6	0.187	3.82	1.32	52.1	5.43	62.9
^{55}Fe	949.5	1.15	24.3	8.57	733.0	210.0	977.0

[a] This is $\sum_{i=1}^{6} R_i^T - R_5^T$.

Table 24.3. Decay Scheme Data of ^{55}Fe and ^{59}Fe

A. 59 Iron 26 Beta-Minus Decay

Half-life = 1.080×10^3 hr = 45.00 days

1. Beta Rays

	End-Point Energy (Mev)	Percent per Decay	Average Energy (Mev)	Forbiddenness
Beta 1	1.300×10^{-1}	1.10	3.548×10^{-2}	Allowed
Beta 2	2.730×10^{-1}	4.50×10^{1}	8.083×10^{-2}	Allowed
Beta 3	4.750×10^{-1}	5.30×10^{1}	1.527×10^{-1}	Allowed
Beta 4	1.573	3.00×10^{-1}	6.397×10^{-1}	Second
All betas		9.94×10^{1}	1.203×10^{-1}	

2. Gamma Rays and Associated X Rays, Internal-Conversion Electrons, and Auger Electrons

	Percent per Decay	Energy (Mev)	Internal Conversion Coefficient Parameters (T Indicates Theoretical Value)
Gamma 1	7.88×10^{-1}	1.430×10^{-1}	$AK(T) = 1.41 \times 10^{-2}$; $AL(T) = 1.15 \times 10^{-3}$; M1 multipole
ICE K shell	1.11×10^{-2}	1.353×10^{-1}	
Gamma 2	2.78	1.925×10^{-1}	$AK(T) = 6.63 \times 10^{-3}$; $AL(T) = 5.33 \times 10^{-4}$; M1 multipole
ICE K shell	1.84×10^{-2}	1.848×10^{-1}	
Gamma 3	6.96×10^{-1}	3.400×10^{-1}	$AK(T) = 4.85 \times 10^{-3}$; $AL(T) = 4.25 \times 10^{-4}$; E2 multipole
Gamma 4	5.60×10^{1}	1.095	$AK(T) = 1.33 \times 10^{-4}$; $AL(T) = 1.06 \times 10^{-5}$; M1 multipole
Gamma 5	4.30×10^{1}	1.292	$AK = 1.00 \times 10^{-4}$; $AL(T) = 9.05 \times 10^{-6}$; E2 multipole
KLL Auger	2.33×10^{-2}	6.101×10^{-3}	
LMM Auger	7.00×10^{-2}	6.850×10^{-4}	
MXY Auger	1.49×10^{-1}	5.950×10^{-5}	

B. 55 Iron 26 Electron Capture Decay

Half-life = 2.60 years = 2.279×10^4 hr = 9496×10^2 days

This table of the electron capture transitions is included for reference purposes. Except for x rays and Auger electrons, which are included in the following table, the energy is lost in the form of neutrinos and does not contribute to the dose.

1. Electron Capture

	Transition Energy (Mev)	Percent per Decay	Forbiddenness
EC 1	2.310×10^{-1}	1.00×10^{2}	Allowed

2. X Rays and Auger Electrons

	Percent per Decay	Energy (Mev)
KA1 x rays	1.55×10^{1}	5.899×10^{-3}
KA2 x rays	7.87	5.888×10^{-3}
KB1 x rays	2.57	6.490×10^{-3}
KB2 x rays	6.21×10^{-2}	6.539×10^{-3}
KLL Auger	5.15×10^{1}	5.219×10^{-3}
KLX Auger	1.22×10^{1}	5.830×10^{-3}
LMM Auger	1.48×10^{2}	5.629×10^{-4}
MXY Auger	3.12×10^{2}	4.860×10^{-5}

Source: L. T. Dillman, "Radionuclide Decay Schemes and Nuclear Parameters for Use in Radiation-Dose Estimation," MIRD Pamphlet No. 4, suppl. No. 2, *J. Nucl. Med.* (March 1969).

Table 24.4. Effective Energy ϵ (in Mev) for the X- and Gamma-Ray Components of ^{55}Fe and ^{59}Fe in the Total Body

Radionuclide	Radiation	Percent per Decay	Energy (Mev)	AF[a]	ϵ (Mev/decay)[b]
^{55}Fe	$K\alpha_1$ x ray	1.55×10^{1}	0.00590	1	0.000915
	$K\alpha_2$ x ray	7.87×10^{0}	0.00589	1	0.000464
	$K\beta_1$ x ray	2.57×10^{0}	0.00649	1	0.000167
	$K\beta_2$ x ray	6.21×10^{-2}	0.00654	1	0.00000406
	Total				0.00155
^{59}Fe	γ_1	7.88×10^{-1}	0.143	0.35	0.000394
	γ_2	2.78×10^{0}	0.193	0.34	0.00182
	γ_3	6.96×10^{-1}	0.340	0.34	0.000805
	γ_4	5.60×10^{1}	1.095	0.32	0.196
	γ_5	4.30×10^{1}	1.292	0.31	0.172
	Total				0.371

[a]Absorbed fraction; interpolated and extrapolated values from Fig. 25.9 of ORNL-4168.
[b]Column 3 X column 4 X column 5/100.

$$D_{TB} = \frac{(51.1)(1.55 \times 10^{-3})(62.9)}{7 \times 10^{4}}$$

$$+ \frac{(51.1)(4.38 \times 10^{-3})(10.80)}{7 \times 10^{4}}$$

$$= 7.12 \times 10^{-5} + 3.45 \times 10^{-5} \text{ rad} = 1.06 \times 10^{-4} \text{ rad},$$

while for ^{59}Fe

$$D_{TB} = \frac{(51.1)(0.371 + 0.1203 + 4.9 \times 10^{-5})(977)}{7 \times 10^{4}}$$

$$= 0.350 \text{ rad}.$$

In the above, 51.1 is the (g-rads/μc-day)/(absorbed Mev/decay), 7×10^{4} is the grams of total body weight, 1.55×10^{-3} and 0.371 are the absorbed photon energy (Mev) per decay for ^{55}Fe and ^{59}Fe (Table 24.4), respectively, 4.38×10^{-3} is the absorbed Auger electron energy, and 0.1203 and 4.9×10^{-5} are the absorbed beta and internally converted electron energy, respectively, of ^{59}Fe (Table 24.3); 62.9 and 977 are the total body microcurie-days residence of ^{55}Fe and ^{59}Fe, respectively, while 10.8 is the microcurie-days residence of ^{55}Fe in plasma, storage, and red marrow.

The dose received by the red blood cell, D_{RBC}, from ^{55}Fe is estimated assuming complete internal absorption of the low-energy Auger electrons, D_β, and external irradiation in the total body by the x rays. For ^{59}Fe we assume the red blood cells are irradiated to the same extent as the total body. Thus, for ^{55}Fe

$$D_{RBC} = D_\beta + D_{TB}$$

$$= \frac{51.1\,(4.38 \times 10^{-3})(52.1)}{(5.4 \times 10^{9})(5.5 \times 10^{3})(0.47)(8.6 \times 10^{-11})}$$

$$+ 7.12 \times 10^{-5} = 0.00978 \text{ rad}.$$

In the above, 4.38×10^{-3} is the absorbed Mev of the Auger electrons, 52.1 is the microcurie-days residence in the red cells, 5.4×10^{9} is the number of red cells per cubic centimeter of whole blood in man,[5] 5.5×10^{3} is the cubic centimeters of whole blood, 0.47 is the hematocrit, and 8.6×10^{-11} is the mass in grams of the red blood cell[4] assuming a density of 1 g/cc.

In this red cell dose estimate it must be remembered that the microcurie-days residence is taken over the life-span of adult man and not over the 120-day lifetime of the red cells. Thus it is the dose to all the cells produced during a 70-year period (50 years occupational exposure). More refined calculations will consider the 120-day lifetime of the red cell.

[5]*Radiological Health Handbook,* revised ed., p. 194, U.S. Department of Health, Education, and Welfare, Public Health Service, Washington, September 1960.

APPLICATION OF A MAMMILLARY COMPARTMENT MODEL TO THE ESTIMATION OF MICROCURIE-DAYS RESIDENCE OF ^{232}Th PARENT AND ^{228}Ra DAUGHTER IN MAN

S. R. Bernard C. F. Holoway

The purpose of this report is to present estimates of microcurie-days residence of ^{232}Th parent and ^{228}Ra daughter in organs and tissues of man based upon a mammillary compartment-model representation of the distribution and excretion of thorium and radium in man. For both of these elements, we have assumed a four-compartment model, as shown in Fig. 24.3. In the model, q_i denotes the amount of element (microcuries) present in compartment i. Blood is represented by compartment number 1; bone by compartments 2 and 3, 2 being the region for long-term bone retention and 3 for short-term bone retention; soft tissues by compartment 4; and total excretion by compartment 0. The fractional rate transfer constant for passage of material from compartment j to i is denoted by λ_{ij} $(i \neq j)$. In our application to radium and thorium, we assume the fractional rates of release from compartment 3 to 1 (λ_{13}) is the same as from 4 to 1 (λ_{14}) that is, $\lambda_{13} \sim \lambda_{14}$. We assume this for two reasons: (1) it does not seem unreasonable that there are regions in bone, perhaps bone surface or exchangeable calcium regions or trabecular bone, in which the turnover is as rapid as in soft tissues, and (2) this allows us to use only three exponential terms for each compartment. This four-compartment model then reduces to a three-equivalent-compartment system, two of the compartments combining into a single compartment. This will be seen later by summing the equations for the contents of compartments 3 and 4.

When no intake to or production in the body of the kth daughter occurs, the amounts q_i^k of the kth radionuclide, $k = 0, 1, \ldots n$, present at time t in the jth compartment, $j = 1, \ldots, 4$, are solutions of the system

$$\begin{pmatrix} \dot{q}_1^k(t) \\ \dot{q}_2^k(t) \\ \dot{q}_3^k(t) \\ \dot{q}_4^k(t) \end{pmatrix} = - \begin{pmatrix} \lambda_{11}^k + \lambda_r^k & -\lambda_{12}^k & -\lambda_{13}^k & -\lambda_{13}^k \\ -\lambda_{21}^k & \lambda_{12}^k + \lambda_r^k & 0 & 0 \\ -\lambda_{31}^k & 0 & \lambda_{13}^k + \lambda_r^k & 0 \\ -\lambda_{41}^k & 0 & 0 & \lambda_{13}^k + \lambda_r^k \end{pmatrix} \begin{pmatrix} q_1^k(t) \\ q_2^k(t) \\ q_3^k(t) \\ q_4^k(t) \end{pmatrix} \qquad (1)$$

with λ_{11} defined as $\lambda_{11} = \lambda_{01} + \lambda_{21} + \lambda_{31} + \lambda_{41}$. Total excretion is given by

$$\dot{q}_0^k(t) = \lambda_{01}\, q_1^k(t)\,. \qquad (2)$$

In the above equations, $\dot{q}_j^k(t)$ denotes the time derivative, and λ_r^k is the radiological decay constant of the kth radionuclide. If the radionuclide is entering the body or is being produced in the body by radioactive decay of its parent, an intake vector must be added. If

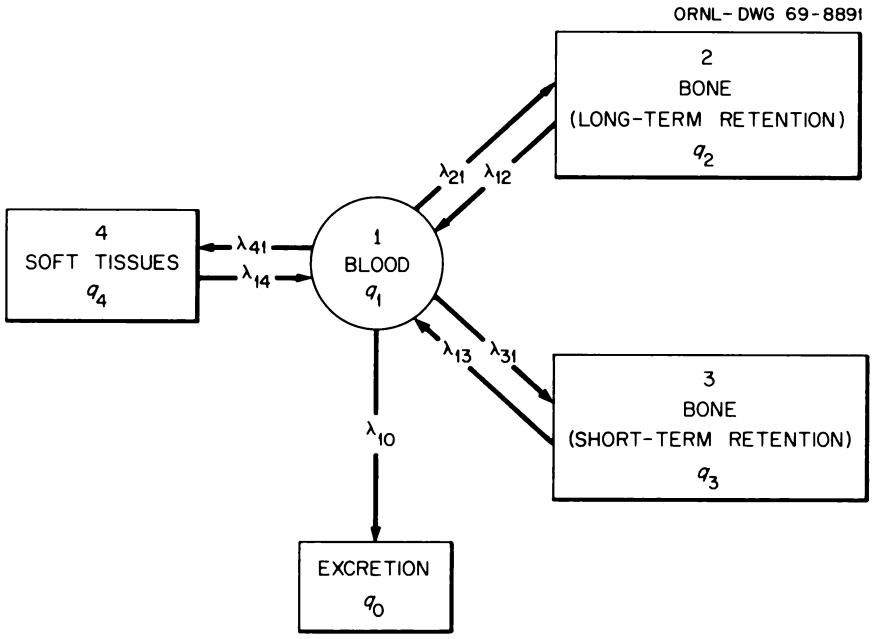

Fig. 24.3. A Mammillary Model for Distribution and Excretion of Radium and Thorium in Dogs and Man.

we let the square matrix in (1) be denoted by A^k and the column vectors on the left and right of (1) be denoted by $\dot{q}^k(t)$ and $q^k(t)$, then, in matrix notation,

$$\dot{q}^k(t) = -A^k\, q^k(t)\,. \tag{3}$$

When we interpret data which are corrected for radiological decay, we may set $\lambda_r^k = 0$. When the last two equations in (1) are summed, the system may be represented by equations involving a 3 X 3 matrix, and thus there will be only three eigenvalues at most.[1] This reduced form is

$$\begin{pmatrix} \dot{Q}_1^k(t) \\ \dot{Q}_2^k(t) \\ \dot{Q}_3^k(t) \end{pmatrix} = - \begin{pmatrix} \lambda_{11}^k + \lambda_r^k & -\lambda_{12}^k & -\lambda_{13}^k \\ -\lambda_{21}^k & \lambda_{12}^k + \lambda_r^k & 0 \\ -\lambda_{31}^k - \lambda_{41}^k & 0 & \lambda_{13}^k + \lambda_r^k \end{pmatrix} \begin{pmatrix} Q_1^k(t) \\ Q_2^k(t) \\ Q_3^k(t) \end{pmatrix}. \tag{4}$$

where $Q_1^k(t) \equiv q_1^k(t)$, $Q_2^k(t) \equiv q_2^k(t)$, and $Q_3^k(t) \equiv q_3^k(t) + q_4^k(t)$. In what follows, the notation $Q_i^k(t)$ will not be used.

For application of the mammillary model to estimate microcurie-days in the organs and tissues of man, it is necessary to have numerical values of the rate transfer coefficients, λ_{ij}^k, appearing in the A^k matrix of Eq. (4). In general, the matrix will have distinct eigenvalues, and then each organ burden as well as the total body burden, $q_1^k(t) + q_2^k(t) + q_3^k(t)$, will be a linear combination of three exponential terms. Conversely, if the total body retention is known, perhaps from experimental data, and if it is a sum of three exponentials, the numerical values of the λ_{ij}^k can be obtained as solutions of certain algebraic equations. That is, assume

$$R(t) = \sum_{i=1}^{3} b_i e^{-\mu_i t},\ t \geqslant 0,\ \sum_{i=1}^{3} b_i = 1, \tag{5}$$

represents the total body burden of the parent following a unit intake to blood. We assume this is identical with the solution arising by integration of Eq. (4), and we prove that the exchange constants with blood satisfy the equations

$$g(\lambda_{1j}^k) = \sum_{i=1}^{3} \frac{b_i \mu_i}{(\lambda_{1j}^k - \mu_i)} = 0\ (j = 2, 3), \tag{6}$$

and

$$\sum_{j=2}^{3} \frac{\lambda_{1j}^k}{\lambda_{1j}^k - \mu_i}\, \lambda_{j1}^k = \lambda_{11}^k - \mu_i\ (i = 1, 2), \tag{7}$$

where

$$\lambda_{11}^k = \left(\sum_{i=1}^{3} b_i \mu_i^2 \right) \Big/ \left(\sum_{i=1}^{3} b_i \mu_i \right).$$

Actually, the procedure sketched below is valid for a mammillary system consisting of any number of compartments. Equation (6) is derived from straightforward integration of the differential equation corresponding to peripheral compartment j of Eq. (4), $j = 2, 3$. Thus for the jth peripheral compartment,

$$\frac{dq_j^k(t)}{dt} = \lambda_{j1}^k\, q_1^k(t) - \lambda_{1j}^k\, q_j^k(t)\,. \tag{8}$$

By integration of Eq. (8) one obtains

$$q_j^k(t) = \lambda_{j1}^k \int_0^t q_1^k(\tau)\, e^{-\lambda_{1j}^k (t-\tau)}\, d\tau\ (j = 2, 3), \tag{9}$$

where $q_j^k(0) = 0$ has been used as the initial condition. Now $q_1^k(t) = \dot{q}_0^k(t)/\lambda_{01}$, from Eq. (2). However, $\dot{q}_0^k(t)$ is the excretion rate, and hence $\dot{q}_0^k(t)$ equals $-\dot{R}(t)$. Hence λ_{01}^k, which is the rate of excretion from blood, satisfies the equation $\lambda_{01}^k = \dot{q}_0^k(0) = -\dot{R}(0)$. Thus

$$q_1^k(t) = -R(t)/[-\dot{R}(0)]\,. \tag{10}$$

Substituting for $\dot{R}(t)$ and $\dot{R}(0)$ from Eq. (5) into Eq. (10), one obtains

$$q_1^k(t) = \sum_{i=1}^{3} \mu_i b_i e^{-\mu_i t} \Big/ \sum_{i=1}^{3} \mu_i b_i\,. \tag{11}$$

Substituting for $q_1^k(t)$ in Eq. (9) and performing the indicated integration, one obtains

$$q_j^k(t) = \frac{\lambda_{ij}^k \sum_{i=1}^{3} \mu_i b_i (e^{-\mu_i t} - e^{-\lambda_{1j}^k t})}{\sum_{i=1}^{3} \mu_i b_k}, \quad j = 2, 3.$$

In this equation there are four exponential terms, but since a 3 X 3 matrix for our mammillary model only

[1] C. W. Sheppard and A. S. Householder, "The Mathematical Basis of the Interpretation of Tracer Experiments in Closed Steady-State Systems," *J. Appl. Phys.* **22**, 510 (1951).

has three exponentials and these have the μ_i (eigenvalues) as exponents, then, since $e^{-\lambda_{1j}^k(t)} \neq 0$ for all t, its coefficient, which equals

$$\left(\lambda_{j1}^k \Big/ \sum_{i=1}^{3} b_i\mu_i\right) g\left(\lambda_{1j}^k\right),$$

must equal zero. This proves Eq. (6).

Equation (7) is derived from the differential equation for blood, compartment 1, of Eqs. (4) and (8) by use of the general solution

$$q_j^k(t) = \sum_{i=1}^{3} C_{ji}^k e^{-\mu_i t} \quad (j = 1, 2, 3) \quad , \tag{12}$$

where C_{ji} is the real-valued coefficient of the jth exponential. For unit intake to blood,

$$\sum_{i=1}^{3} C_{ji} = 1 \ (j = 1),$$
$$= 0 \ (j = 2, 3).$$

Substituting Eq. (12) into Eq. (8) and remembering that the exponentials are linearly independent, one obtains, by use of Eq. (10),

$$C_{ji} = \frac{\lambda_{j1}^k C_{1i}}{\lambda_{1j}^k - \mu_i} = \frac{\lambda_{j1}^k (b_i\mu_i)/[-\dot{R}(0)]}{\lambda_{1j}^k - \mu_i} \ . \tag{13}$$

Inserting this equation into the differential equation for blood in Eqs. (4), together with Eq. (12) for $j = 1$, and again invoking linear independence of the three exponentials, the linear equations (7) are derived.

A computer code, MAMX, was written by C. W. Nestor and K. Chandler (Mathematics Division) to solve Eqs. (6), (7), and (13) for the numerical values of λ_{ij}^k and C_{ji} given the b_i and μ_i values in Eq. (5). In the case where $\lambda_{13} = \lambda_{14}$, MAMX gives the sum $\lambda_{31} + \lambda_{41}$. To estimate λ_{31} and λ_{41} separately, one needs measurements of the amounts in each of compartments 3 and 4.

Numerical values are presented in Table 24.5 of the λ_{ij}^k of the A^k matrix corresponding to the mammillary model representing thorium and radium metabolism in man and dog. Table 24.6 contains constants for the exponential sum used in MAMX to approximate total body retention for each of the above elements and species and thus obtain the data in Table 24.5. Thus,

Table 24.5. Numerical Values of the Fractional Rate Transfer Constants in the A Matrix Estimated with the MAMX Code and the Data in Table 24.6

Species	Tissue	Thorium				Radium			
Man	Blood	+0.460	−0.306	−0.221	−0.221	+0.0345	−0.0000880	−0.00328	−0.00328
	Bone, long term	−0.687	+0.306	0.0	0.0	−0.000528	+0.0000880	0.0	0.0
	Bone, short term	−0.250	0.0	+0.221	0.0	−0.000855	0.0	+0.00328	0.0
	Soft tissues	−0.109	0.0	0.0	+0.221	−0.000421	0.0	0.0	+0.00328
Dog	Blood	+0.691	−0.000372	−0.00289	−0.00289	+0.647	−0.000181	−0.0658	−0.0658
	Bone, long term	−0.108	+0.000372	0.0	0.0	−0.0462	+0.000181	0.0	0.0
	Bone, short term	−0.320	0.0	+0.00289	0.0	−0.150	0.0	+0.0658	0.0
	Soft tissues	−0.172	0.0	0.0	+0.00289	−0.300	0.0	0.0	+0.0658

Table 24.6. Parameter Values for the Exponential Sum Approximating the Total Body Retention[a] in Dogs and Man

Species	Thorium						Radium					
	b_1	b_2	b_3	μ_1	μ_2	μ_3	b_1	b_2	b_3	μ_1	μ_2	μ_3
Man	0.07	0.23	0.7	0.462	0.0005	0.00000950	0.94	0.044	0.016	0.0347	0.00315	0.0000866
Dog	0.13	0.18	0.69	0.693	0.001	0.00014	0.21	0.56	0.23	0.693	0.01925	0.00014

[a] $R(t) = \sum_{i=1}^{3} b_i e^{-\mu_i t}$.

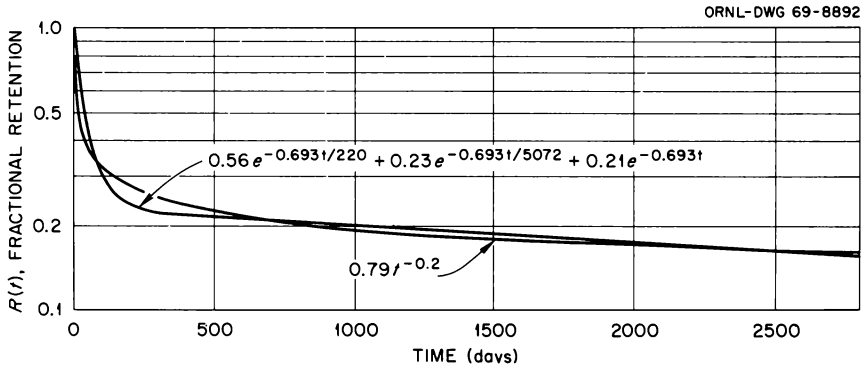

Fig. 24.4. ^{226}Ra Retention in Dogs – Comparison of the Power Function with an Exponential Sum Approximation.

these representations of total body retention in man and dog are based on experimental data for whole-body retention, obtained as detailed below. A graph of the power function[2] and an approximation as a sum of three exponentials corresponding to retention of ^{226}Ra in the dog's body are displayed in Fig. 24.4. As can be seen, the approximation is better at longer times. In Fig. 24.5, the Norris (power) function[3] and a three-exponential approximation for ^{226}Ra retention in man over a 50-year period of time are displayed. Closer agreement between these curves would occur if a larger number of exponential terms, perhaps as high as 100, the maximum number MAMX can handle, were taken. However, we would then have the problem of identifying 99 compartments, and we defer this problem until more sophisticated experimental measurements become available against which these very large compartment models can be tested. Figure 24.6 contains the power function representation of Maletskos *et al.*[4] and the three-exponential approximation for thorium retention in man.

Listed in Table 24.7 are the solutions (12) in matrix form for retention in man and in dog; that is, the matrices of constants C_{ji}^{k} are given as well as the exponentials to which they apply. Here we assumed $\sim 3/5$ of $(\lambda_{31} + \lambda_{41})$ for thorium and $2/3$ for radium enter compartment 3. In Figs. 24.7 and 24.8 we present graphs of the retention equations and the experimental

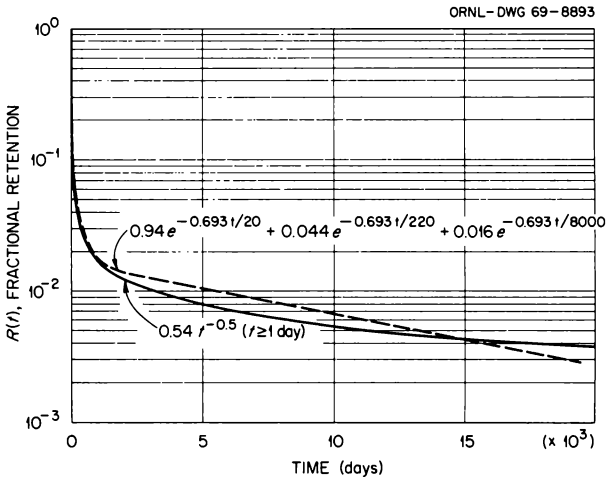

Fig. 24.5. A Plot of the Norris Power Function, $0.54t^{-0.5}$, Together with a Three-Exponential Sum Approximating Total Body Retention of ^{226}Ra in Man.

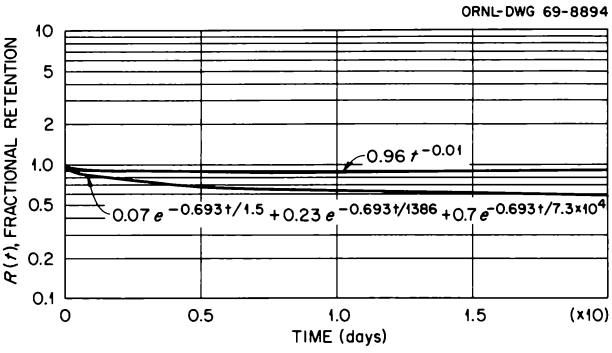

Fig. 24.6. A Plot of Maletskos *et al.*'s Power Function, $0.96t^{-0.01}$, Together with a Sum of Three Exponential Terms for Approximating Total Body Retention of Thorium in Man.

[2] M. A. Van Dilla *et al.*, "Radium (^{226}Ra) and Radon (^{222}Em) Metabolism in Dogs," *Radiation Res.* 8, 417 (1958).

[3] W. P. Norris, T. W. Speckman, and P. F. Gustafson, "Studies of Radium in Man," *Am. J. Roentgenol.* 73, 785 (1955).

[4] C. J. Maletskos *et al.*, "Metabolic Data on Injected and Ingested ^{234}Th in Human Beings," *Proc. 12th Annual Bio-Assay and Analytical Chemistry Meeting*, CONF-661016 (TID-4500), p. 191.

Table 24.7. Equations for Retention of a Single Intravenous Injection of Thorium and Radium in Compartments of the Mammillary Model for Man and Dog

Species	Tissue	Thorium				Radium			
Man	Blood	0	+0.000205	+0.00354	+0.996	$e^{-0.00221t}$	0	+0.0000424	+0.00424	+0.996	$e^{-0.00328t}$
	Bone, long term	0	+0.663	−0.518	−0.148	$e^{-0.00000950t}$	0	+0.0159	−0.000731	−0.0152	$e^{-0.0000866t}$
	Bone, short term	0	+0.0233	+0.518	−0.542	$e^{-0.0005t}$	0	+0.0000108	+0.0271	−0.0271	$e^{-0.00315t}$
	Soft tissues	0	+0.0102	+0.226	−0.237	$e^{-0.462t}$	0	+0.00000558	+0.01336	−0.0134	$e^{-0.0347t}$
Dog	Blood	0	+0.00107	+0.00199	+0.997	$e^{-0.00289t}$	0	+0.000334	+0.0686	+0.931	$e^{-0.0608t}$
	Bone, long term	0	+0.498	−0.342	−0.156	$e^{-0.00014t}$	0	+0.000827	+0.220	−0.221	$e^{-0.000128t}$
	Bone, short term	0	+0.124	+0.338	−0.462	$e^{-0.001t}$	0	+0.00165	+0.440	−0.442	$e^{-0.014t}$
	Soft tissues	0	+0.0669	+0.182	−0.249	$e^{-0.693t}$	0	+0.291	−0.229	−0.0621	$e^{-0.693t}$

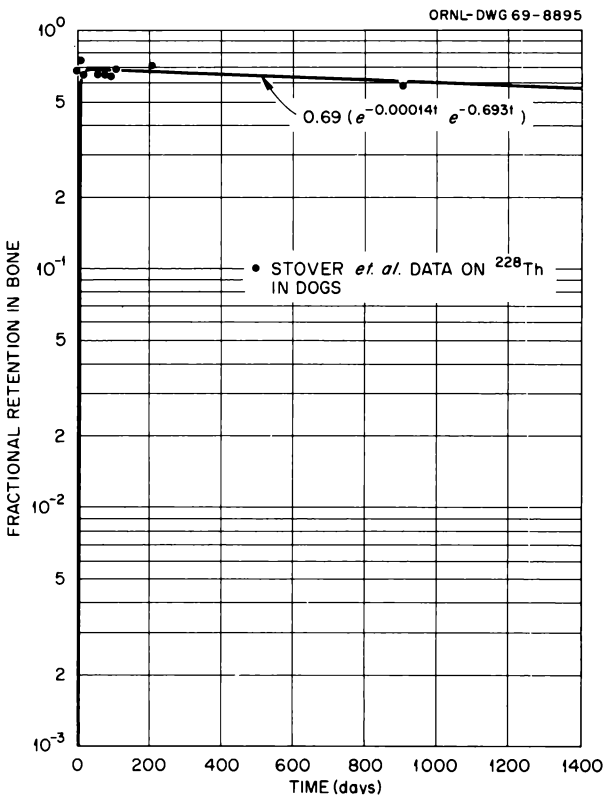

Fig. 24.7. Comparison of ^{228}Th Retention in Bone of Dogs with Estimate from a Lumped Four-Compartment Mammillary Model of Distribution of Thorium in the Dog Body.

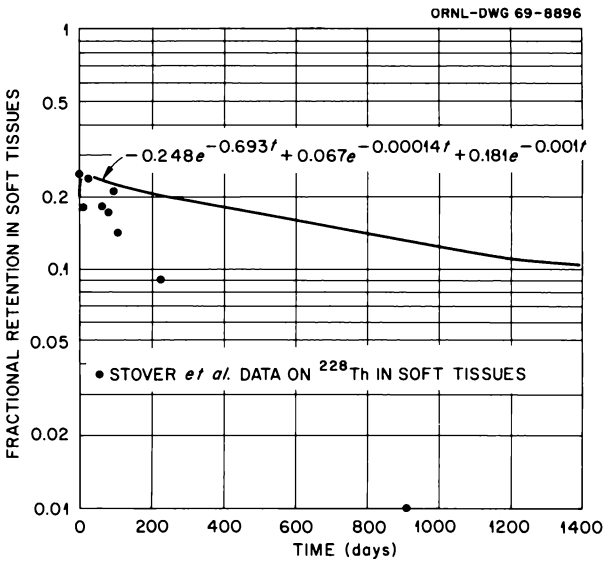

Fig. 24.8. Comparison of ^{228}Th Retention in Soft Tissues of Dogs with Estimate from a Four-Compartment Mammillary Model of Distribution of Thorium in Dog Body.

measurements of Stover *et al.*[5] for thorium in bone and soft tissues of dogs which received a single intravenous injection of ^{228}Th citrate. As can be seen, the level in soft tissues is overestimated. This might be due to the fact that the retention function for thorium in dogs was estimated from excretion data, and it may have overestimated the total body retention because of small daily losses of excreta. It does suggest, however, that we should employ Stover *et al.*'s retention function based on tissue measurements in conjunction with MAMX.

With the above values for the rate transfer coefficients of the mammillary matrix, we can now apply the model to the ^{228}Th parent–^{224}Ra daughter decay chain in dogs and the ^{232}Th-^{228}Ra chain in man. The transfer constants for these chains in these two species and for two assumptions concerning the behavior of radium produced by decay of thorium are shown in Table 24.8. Case I assumes no recycling of radium to blood; that is, the radium produced in a compartment gets there by decay of thorium in that compartment.

Here the matrices are 8 X 8, and the equations are of the form

$$\begin{pmatrix} \dot{q}_j^0(t) \\ \dot{q}_j^1(t) \end{pmatrix} = - \begin{pmatrix} A^0 & 0 \\ B & A^1 \end{pmatrix} \begin{pmatrix} q_j^0(t) \\ q_j^1(t) \end{pmatrix} ,$$

where the A^0 and A^1 are each 4 X 4 matrices corresponding to the mammillary model for thorium and radium respectively. Also for case I,

$$B = \lambda_r^1 I$$

is a 4 X 4 matrix, λ_r^1 is the (scalar) radiological decay constant and I is the 4 X 4 identity matrix. Thus for the matrix of the ^{228}Th-^{224}Ra chain in dogs, the 0.191 day^{-1} radiological decay constant of ^{224}Ra occurs in positions (5, 1), (6, 2), (7, 3), and (8, 4) of the A^1 matrix, meaning that ^{224}Ra in blood, long-term bone, short-term bone, and soft tissues arrives there from decay of ^{228}Th in blood, long-term bone, short-term bone, and soft tissues respectively.

In case II, representing 100% recycling to blood of ^{224}Ra produced in the various compartments, the radioactive decay constant, 0.191, appears in positions

[5] B. J. Stover *et al.*, "The ^{228}Th Decay Series in Adult Beagles: ^{224}Ra, ^{212}Pb and ^{212}Bi in Blood and Excreta," *Radiation Res.* 26, 226 (1965).

Table 24.8. Matrices of Rate Transfer Constants for ^{228}Th-^{224}Ra Chain in Dogs and ^{232}Th-^{228}Ra Chain in Man for Different Cases of Recycling of Radium Daughter to Blood

	Radionuclide	Compartment								
Dog, 0% recycling	^{228}Th	Blood	+0.692	−0.000372	−0.00289	−0.00289	0.0	0.0	0.0	0.0
		Bone, long term	−0.108	+0.00137	0.0	0.0	0.0	0.0	0.0	0.0
		Bone, short term	−0.320	0.0	+0.00389	0.0	0.0	0.0	0.0	0.0
		Soft tissues	−0.172	0.0	0.0	+0.00389	0.0	0.0	0.0	0.0
	^{224}Ra	Blood	−0.191	0.0	0.0	0.0	+0.838	−0.000181	−0.0658	−0.0658
		Bone, long term	0.0	−0.191	0.0	0.0	−0.0462	+0.191	0.0	0.0
		Bone, short term	0.0	0.0	−0.191	0.0	−0.150	0.0	+0.257	0.0
		Soft tissues	0.0	0.0	0.0	−0.191	−0.300	0.0	0.0	+0.257
Dog, 100% recycling	^{228}Th	Blood	+0.692	−0.000371	−0.00289	−0.00289	0.0	0.0	0.0	0.0
		Bone, long term	−0.108	+0.00137	0.0	0.0	0.0	0.0	0.0	0.0
		Bone, short term	−0.320	0.0	+0.00389	0.0	0.0	0.0	0.0	0.0
		Soft tissues	−0.172	0.0	0.0	+0.00389	0.0	0.0	0.0	0.0
	^{224}Ra	Blood	−0.191	−0.191	−0.191	−0.191	+0.838	−0.000181	−0.0698	−0.0658
		Bone, long term	0.0	0.0	0.0	0.0	−0.046	+0.191	0.0	0.0
		Bone, short term	0.0	0.0	0.0	0.0	−0.150	0.0	+0.257	0.0
		Soft tissues	0.0	0.0	0.0	0.0	−0.300	0.0	0.0	+0.257
Man, 0% recycling	^{232}Th	Blood	+0.460	−0.0000306	−0.00221	−0.00221	0.0	0.0	0.0	0.0
		Bone, long term	−0.0687	+0.0000306	0.0	0.0	0.0	0.0	0.0	0.0
		Bone, short term	−0.250	0.0	+0.00221	0.0	0.0	0.0	0.0	0.0
		Soft tissues	−0.109	0.0	0.0	+0.00221	0.0	0.0	0.0	0.0
	^{228}Ra	Blood	−0.00033	0.0	0.0	0.0	+0.0349	−0.000088	−0.00328	−0.00328
		Bone, long term	0.0	−0.00033	0.0	0.0	−0.000528	+0.000418	0.0	0.0
		Bone, short term	0.0	0.0	−0.00033	0.0	−0.000855	0.0	+0.00361	0.0
		Soft tissues	0.0	0.0	0.0	−0.00033	−0.000421	0.0	0.0	+0.00361
Man, 100% recycling	^{232}Th	Blood	+0.460	−0.0000306	−0.00221	−0.00221	0.0	0.0	0.0	0.0
		Bone, long term	−0.0687	+0.0000306	0.0	0.0	0.0	0.0	0.0	0.0
		Bone, short term	−0.250	0.0	+0.00221	0.0	0.0	0.0	0.0	0.0
		Soft tissues	−0.109	0.0	0.0	+0.00221	0.0	0.0	0.0	0.0
	^{228}Ra	Blood	−0.00033	−0.00033	−0.00033	−0.00033	+0.0349	−0.000088	−0.00328	−0.00328
		Bone, long term	0.0	0.0	0.0	0.0	−0.000528	+0.000418	0.0	0.0
		Bone, short term	0.0	0.0	0.0	0.0	−0.000855	0.0	+0.00361	0.0
		Soft tissues	0.0	0.0	0.0	0.0	−0.000421	0.0	0.0	0.00361

Table 24.9*a*. Equations for Retention of ^{232}Th Parent–^{228}Ra Daughter in Man Given a Single Intravenous Intake of ^{232}Th

Radionuclide	Percent Recycling	Compartment									
^{232}Th	0	Blood	0.0	0.0	0.0	0.0	0.00354	0.000205	0.0	0.996	$e^{-0.00221t}$
		Bone, long term	0.0	0.0	0.0	0.0	−0.518	0.666	0.0	−0.148	$e^{-0.00361t}$
		Bone, short term	0.0	0.0	0.0	0.0	0.518	0.0233	0.0	−0.541	$e^{-0.00348t}$
		Soft tissues	0.0	0.0	0.0	0.0	0.226	0.0102	0.0	−0.237	$e^{-0.000417t}$
^{228}Ra		Blood	0.0	0.0	−0.00895	−0.00677	0.0132	0.00171	0.00157	−0.000774	$e^{-0.0005t}$
		Bone, long term	0.0	0.0	0.00155	−0.0255	0.0200	0.540	−0.000024	0.000107	$e^{-0.00000949t}$
		Bone, short term	0.0	−0.00214	−0.0575	−0.00181	0.0586	0.00254	−0.0000429	0.000391	$e^{-0.035t}$
		Soft tissues	0.0	0.00214	−0.0283	−0.000891	0.0258	0.00113	−0.0000211	0.000171	$e^{-0.462t}$
^{232}Th	100	Blood	0.0	0.0	0.0	0.00354	0.000205	0.0	0.0	0.996	$e^{-0.00221t}$
		Bone, long term	0.0	0.0	0.0	−0.518	0.666	0.0	0.0	−0.148	$e^{-0.00361t}$
		Bone, short term	0.0	0.0	0.0	0.518	0.0233	0.0	0.0	−0.541	$e^{-0.000417t}$
		Soft tissues	0.0	0.0	0.0	0.226	0.0107	0.0	0.0	−0.237	$e^{-0.0005t}$
^{228}Ra		Blood	0.0	0.0	0.0000146	0.00226	0.00688	−0.00039	−0.00872	−0.0000541	$e^{-0.00000949t}$
		Bone, long term	0.0	0.0	0.00549	−0.0146	0.00890	0.0000672	0.000133	0.0000000619	$e^{-0.0348t}$
		Bone, short term	0.0	0.0	0.0000039	0.000621	0.00163	−0.0025	0.000238	0.000000101	$e^{-0.035t}$
		Soft tissues	0.0	0.0	0.00000192	0.000305	0.000804	−0.00123	0.000117	0.0000000497	$e^{-0.462t}$

Table 24.9*b*. Equations for Retention of ^{228}Th Parent–^{224}Ra Daughter in Dogs Given a Single Intravenous Intake of ^{228}Th

Radionuclide	Percent Recycling	Compartment								
^{228}Th	0	Blood	0.0	0.00107	0.00199	0.0	0.0	0.0	0.997	0.0	$e^{-0.00389t}$
		Bone, long term	0.0	0.498	−0.342	0.0	0.0	0.0	−0.156	0.0	$e^{-0.00114t}$
		Bone, short term	0.0	0.124	0.338	0.0	0.0	0.0	−0.462	0.0	$e^{-0.002t}$
		Soft tissues	0.0	0.0669	0.182	0.0	0.0	0.0	−0.249	0.0	$e^{-0.191t}$
^{224}Ra		Blood	0.0	0.0135	0.0361	−0.000334	−0.0635	0.0	0.999	−0.984	$e^{-0.210t}$
		Bone, long term	0.0	0.504	−0.337	−0.359	0.159	0.0	−0.0326	0.0656	$e^{-0.257t}$
		Bone, short term	0.0	0.1007	0.275	−0.000763	−0.202	−0.267	−0.141	0.235	$e^{-0.694t}$
		Soft tissues	0.0	0.0658	0.179	−0.00153	−0.404	0.267	−0.577	0.470	$e^{-0.885t}$
^{228}Th	100	Blood	0.0	0.0	0.00107	0.00199	0.0	0.0	0.997	0.0	$e^{-0.389t}$
		Bone, long term	0.0	0.0	0.498	−0.342	0.0	0.0	−0.156	0.0	$e^{-0.257t}$
		Bone, short term	0.0	0.0	0.124	0.338	0.0	0.0	−0.462	0.0	$e^{-0.00114t}$
		Soft tissues	0.0	0.0	0.0669	0.182	0.0	0.0	−0.249	0.0	$e^{-0.002t}$
^{224}Ra		Blood	0.0	0.0	0.183	0.0477	−0.000182	−0.052	0.118	−0.296	$e^{-0.191t}$
		Bone, long term	0.0	0.0	0.0445	0.0117	−0.195	0.130	−0.0108	0.0197	$e^{-0.210t}$
		Bone, short term	0.0	0.0	0.107	0.0281	−0.000415	−0.166	−0.0403	0.0708	$e^{-0.694t}$
		Soft tissues	0.0	0.0	0.215	0.0562	−0.00083	−0.331	−0.0807	0.142	$e^{-0.884t}$

(5, 1), (5, 2), (5, 3), and (5, 4) of the A^1 matrix, meaning that ^{224}Ra comes into blood as a result of its production from radioactive decay of ^{228}Th in blood, long-term bone, short-term bone, and soft tissues. The solutions of the corresponding differential equations for the levels of radium and thorium in the tissues were provided by a computer code written by J. A. Carpenter, Mathematics Division. This code diagonalizes non-Hermitian matrices having real or complex elements and, in addition, computes the microcurie-days residence. Appearing in Table 24.9*a* in the form of matrices are the solutions of the differential equations corresponding to cases I and II for man. As can be noted, the solutions are sums of exponentials, and the coefficients of the longest-term exponential are positive. Also, the coefficients of the exponentials for retention of the thorium parent in blood are all positive.

In order to test this model, we have computed the levels of ^{228}Th and ^{224}Ra present in the dog's body at any time t from the retention equations in Table 24.9*b*. From these equations we obtain total-body retention in dogs and can calculate the fraction of ^{224}Ra undergoing translocation in the body,

$$F_T(t) = \frac{1 - (^{224}\mathrm{Ra}/^{228}\mathrm{Th})_{\mathrm{body}}}{0.3}, \qquad (14)$$

which is due to Stover *et al.*[5] We compare this with the estimates from the data by Stover *et al.* In Eq. (14) the ratio $(^{224}\mathrm{Ra}/^{228}\mathrm{Th})_{\mathrm{body}}$ denotes the quotient of the amounts of ^{224}Ra in the dog body and the amounts of ^{228}Th in the dog body, estimated from excretion data following a single intravenous injection into the dog. The numerator and denominator are, approximately, the fractions of radium atoms excreted. The constant 0.3 is the value estimated by Stover *et al.*, assuming the power function $0.79t^{-0.2}$ ($t \geq 1$ day) for retention of radium in the dog body. We have substituted the equations for total body retention into Eq. (14) and obtain for $t \geq 30$ days for no recycling of ^{224}Ra

$$F_T(t) = \frac{1}{0.3}\,\frac{0.006 + 0.027e^{-0.00086t}}{0.69 + 0.18e^{-0.00086t}} \qquad (15)$$

and for 100% recycling of ^{224}Ra

$$F_T(t) = \frac{1}{0.3}\,\frac{0.14 + 0.036e^{-0.00096t}}{0.69 + 0.18e^{-0.00096t}}. \qquad (16)$$

Equations (15) and (16) are plotted in Fig. 24.9 together with $F_T(t)$ as estimated by Stover *et al.* from the experimental measurements. As can be seen in the case of no recycling, Eq. (15) underestimates the experimentally determined $F_T(t)$ curve, while Eq. (16) overestimates it.

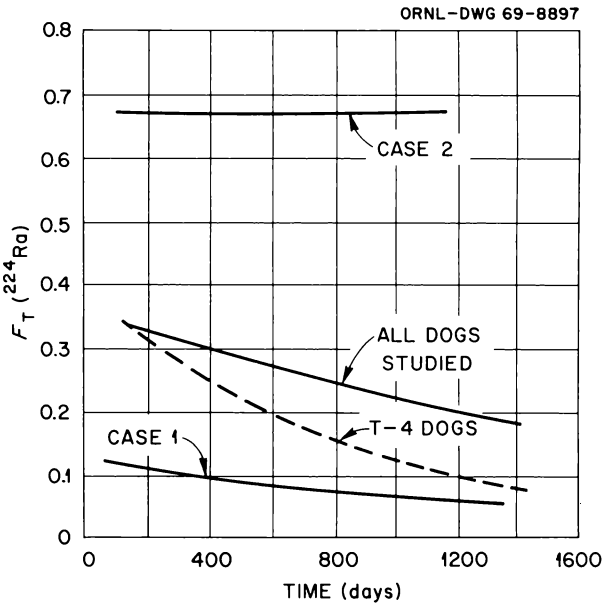

Fig. 24.9. Stover *et al.*, Estimate of Fraction of ^{224}Ra Formed in the Dog Which Translocates. Upper curve derived from all the data excretion data, lower curve from 4-level data only, at 20 to 30 days, $F_T(^{224}\mathrm{Ra}) = 0.79$.

Estimates of the residence in man of each radionuclide in each compartment for the ^{232}Th-^{228}Ra chain at 50 years for the two different cases appear in Table 24.10. For ^{232}Th microcurie-days are the same for both cases, as would be expected; for ^{228}Ra the microcurie-days are highest in long-term bone in both

Table 24.10. Microcurie-Days at 50 Years for ^{232}Th-^{228}Ra Chain in Man for Cases of No Recycling to Blood of ^{228}Ra Daughter and of 100% Recycling

Radionuclide	Compartment	Microcurie-Days at 50 Years	
		0% Recycling	100% Recycling
^{232}Th	Blood	1.267×10^{1}	1.267×10^{1}
	Bone, long term	1.014×10^{4}	1.014×10^{4}
	Bone, short term	1.425×10^{3}	1.425×10^{3}
	Soft tissues	6.229×10^{2}	6.229×10^{2}
^{228}Ra	Blood	3.643×10^{1}	1.196×10^{2}
	Bone, long term	6.963×10^{3}	1.332×10^{2}
	Bone, short term	1.382×10^{2}	2.792×10^{1}
	Soft tissues	6.086×10^{1}	1.375×10^{1}

cases and 60 times higher in the case of no recycling. Blood microcurie-days is next, higher than soft tissues in the case of 100% recycling, as might be expected, and lower than soft tissues in the case of no recycling.

These studies for man indicate a more conservative estimate of microcurie-days using the assumption of no recycling of radium. The similar analysis for dog indicates that the assumption of no recycling of radium, at least in the early periods after injection, is a more conservative estimate than that of 100% recycling of the radium daughter. Additional studies need to be made assuming various compartments recycle various fractions of the radium daughter.

FLUCTUATIONS OF DAILY EXCRETION OF PLUTONIUM AND THEIR INTERPRETATION FOR ESTIMATION OF THE BODY BURDEN

W. S. Snyder J. R. Muir
Mary R. Ford G. G. Warner

The minimum detectable amount (MDA) of ^{239}Pu may be discussed from several points of view, all of which have some relevance to the problem of protection or monitoring of plutonium workers. We wish to consider here the question of how one can distinguish a high level in urine due to a new intake from a high level that is merely a result of the day-to-day fluctuations of urinary excretion. That such daily fluctuations exist is well documented, for example, in the classical studies of Langham.[1] The distribution of these excretion values has been studied by three of the present authors.[2] Beach and Dolphin[3] also have studied the distribution of excretion values for a group of occupationally exposed subjects with rather similar results. That is to say, high excretion values – and low excretion values too – seem to occur with a certain frequency which we consider here as occurring by chance, but with a distribution which is approximately known. The problem then is the following: How can one distinguish a high urine level which is only a sporadic high value, one due to a "chance fluctuation," from a high value due to a new intake of plutonium? Of course, one answer is easy: Collect additional samples and thus determine whether the excretion now fluctuates about the old level or at a higher level. No doubt, that is the "conservative" answer, but it does involve collecting and analyzing quite a few samples.

To state the problem clearly, we are not presupposing an "incident" or unusual occurrence in the work record of the employee. If there is such an incident and attendant suspicion of intake of plutonium, then one must collect sufficient samples to assess properly the probable amount of this supposed intake. Rather, we consider here the employee with potential exposure to plutonium who is being routinely sampled but without any immediate and special reason for suspecting a recent intake. An occasional sample will be high just because fluctuations do occur. Is there any plausible basis for deciding whether one should collect more samples in attempting to decide whether a new intake has occurred? Of course, our consideration of this problem is only preliminary.

The problem may be formulated as follows: Suppose an employee has a chronic body burden of 1 unit, so that his excretion may be considered as somewhat comparable with that of the terminal patients studied by Langham when their data are normalized to unit intake to blood. Let $y(t)$ be the excretion predicted t days post intake according to Langham's formula or any similar formula; the actual excretion values $U(t)$ will fluctuate about the predicted values, and only if they are exceptionally high – say, by some factor S – would one consider that a new intake had occurred. Finally, let I be a supposed new intake which occurs on some day j prior to t. Then the total urine output on day t should satisfy

$$I\,U(t-j) + U(t) \geqslant S\,y(t) \qquad (1)$$

if the new intake will be noticed. The two terms of the left member represent the excretion due to the recent intake on day $t - j$ and that due to the chronic burden, respectively, and the inequality is interpreted to mean that only in case the excretion is significantly high will a new intake be investigated. Here we explore in a preliminary way the practical implications of the use of such a level of significance with this interpretation.

In Fig. 24.10 the distribution of fluctuations about the excretion model $y(t)$ is shown for one case, namely, where

---

[1] W. H. Langham *et al., Distribution and Excretion of Plutonium Administered Intravenously to Man,* LA-1151 (Sept. 20, 1950).

[2] W. S. Snyder, Mary R. Ford, and Gordon Warner, "A Study of Individual Variation of Excretion of Plutonium by Man and of Its Significance in Estimating the Systemic Burden," *Diagnosis and Treatment of Deposited Radionuclides* (Excerpta Medica Foundation, Amsterdam, 1968), Monographs on Nuclear Medicine and Biology No. 2.

[3] S. A. Beach and G. W. Dolphin, *Assessment of Radioactivity in Man,* vol. II, p. 603, IAEA, Vienna, 1964.

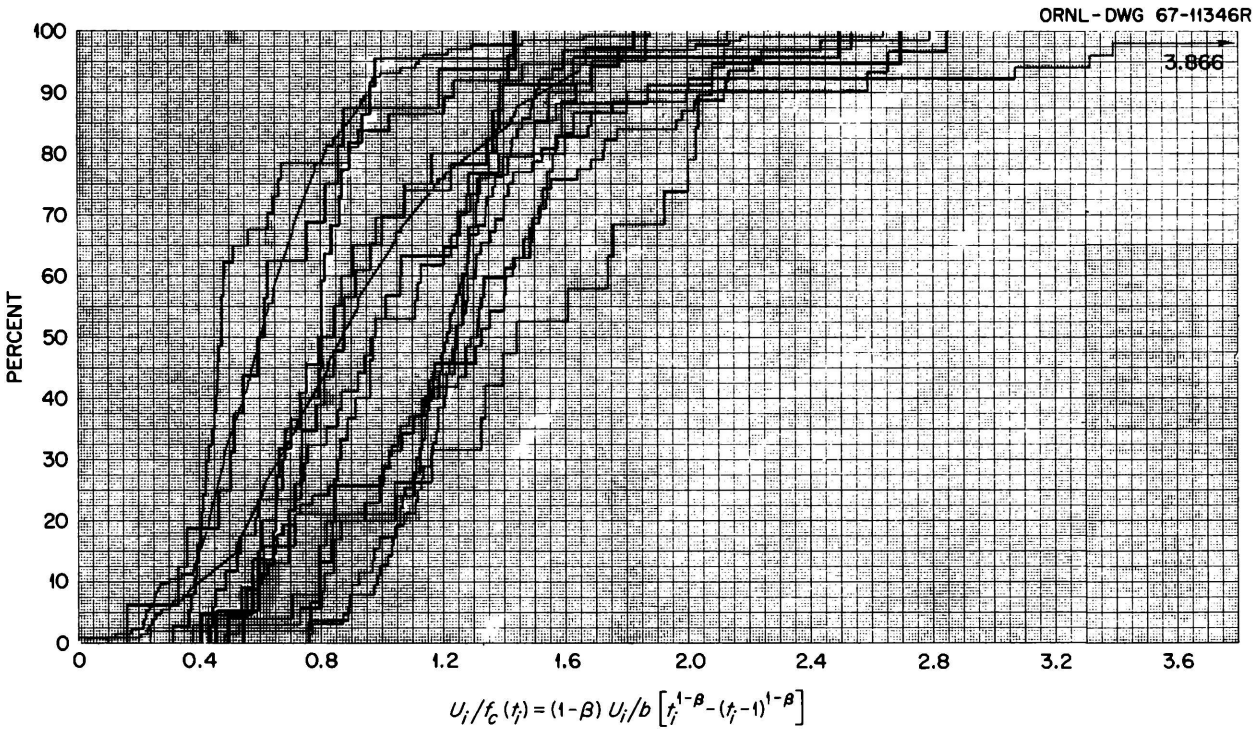

Fig. 24.10. Fluctuations of Daily Urinary Excretion Data of All Patients (Langham-1950) About the Typical Formula of Best Fit – "Area Fit" Formula Obtained by Minimizing the Sum of Absolute Deviations.

$$y(t) = \int_{t-1}^{t} b\tau^{-\alpha}\, d\tau$$

$$= \frac{b}{1-\alpha}\left[t^{1-\alpha} - \left(t-1\right)^{1-\alpha}\right]. \quad (2)$$

As reported in ref. 2, this formula has been fitted to the excretion data of all the hospital patients studied by Langham[1] to minimize the sum of absolute deviations, thus obtaining the values $b = 0.0014$ and $\alpha = 0.61$. One could use a number of other formulas in place of this one, but the results do not seem to be much different. The cumulative distribution of the ratios $U(t)/y(t)$ has been plotted in Fig. 24.10 for each of the hospital patients, though the smallest region including all these curves is shown. It is seen, for example, that the ratio $U(t)/y(t)$ may exceed 2.5, but not for more than 10% of the sample values of any one patient, and likewise it might be expected to exceed 2.03 for 20% of the samples in some cases. The significance factor S will be chosen from this graph; that is, a value of $S = 2.5$ represents a significance level such that no hospital patient had more than 10% of the sample values higher than 2.5 $y(t)$. We term this a 90% significance level. Likewise, the values $S = 1.9$, 1.7, and 1.3 are significance levels of 80, 70, and 50% respectively.

Here we consider the probability of the additional excretion due to an intake I being "significantly" high in the sense that inequality (1) is satisfied, and we examine this as a function of the sampling time. Thus, supposing $j = t - 1$ (i.e., that the hypothetical intake for a certain patient occurred one day before the beginning of the sampling day), the additional excretion to be expected, IU_1, is taken from the excretion data of that hospital patient. The supposed day of intake in relation to the sampling day is varied. Thus in (1) we choose $t = 31, 32, \ldots, 40$ and always take $j = t - 1$. Doing this for all the patients, one has a total of, at most, 120 possible cases. In Fig. 24.11 we show the results for $I = 1$ when sampling occurs j days post intake for $j = 1, 2, 3, 4, 5, 6, 7, 8, 9, 10, 13, 18, 26$ days prior to the close of the sampling period. Three curves are shown for t in the ranges 31–60, 61–100, and 101–140 days respectively. In all cases the additional excretion was significantly high, that is, by a factor of 2.5 more

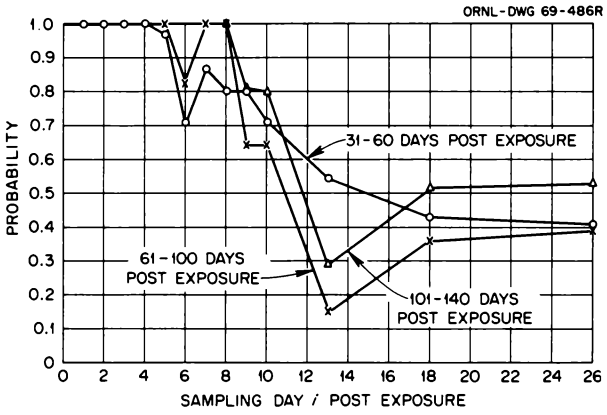

Fig. 24.11. Probability of Observing a New Intake, I = 1; Significance Level – 90% for Different Ranges of Chronic Exposure.

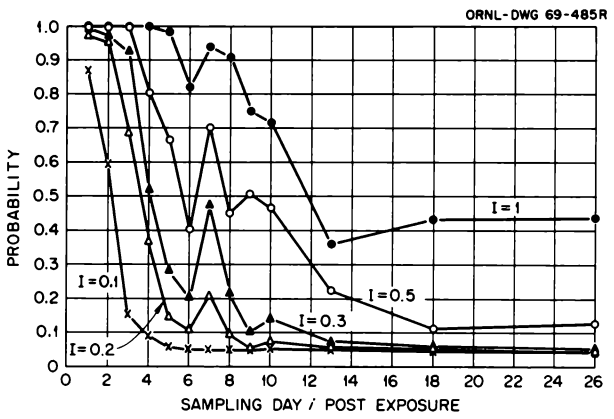

Fig. 24.12. Probability of Observing a New Intake, I; Significance Level – 90%.

than expected by the formula if sampling occurred within a few days of the intake. However, the probability of being above the significance level decreases rapidly as sampling is postponed. Because these curves did not differ significantly, the results were pooled for t ranging from 31 to 140 days or to the death of the patient.

In Fig. 24.12 we show how the probability of detection varies as I is decreased. It will be noted that the curves rapidly approach zero as I is decreased. Thus we must conclude that one cannot distinguish additional excretion from normal fluctuations at the 90% level of significance (S = 2.5) except for a few days post exposure even when the intake amounts to the body burden of the employee. At lower levels of intake the probability is generally small that the "intake" would be noticed.

In Fig. 24.13 the corresponding results are shown for the 80% level of significance, that is, S = 1.9. Although the probability of being considered significant is near 1 for a somewhat longer period than is true at the 90% level, nevertheless the curves quickly decrease. Thus the former pessimistic conclusion is confirmed. One cannot distinguish intakes which amount to 10 to 100% of the body burden unless sampling occurs soon after the intake. Figures 24.14 and 24.15 contain the corresponding results for significance levels of 70 and 50%, respectively, and, while the results are somewhat better, they do not support the view that sampling once a month is sufficiently frequent for a routine monitoring program. If one lowers the level of significance, one will be investigating many high values which are mere fluctuations, and if one uses a high level of significance, one cannot distinguish intakes of the order of the employee's present body burden.

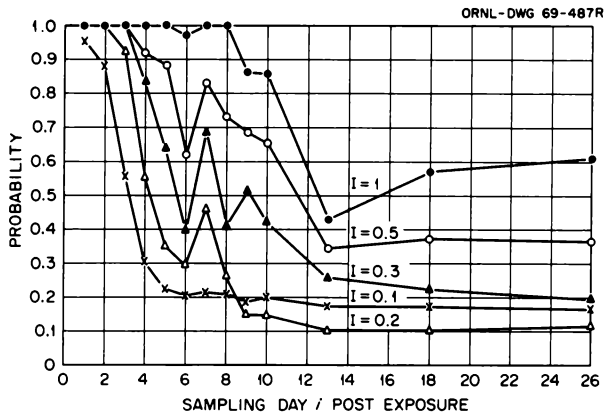

Fig. 24.13. Probability of Observing a New Intake, I; Significance Level – 80%.

Of course, one may raise numerous objections to the procedure studied here. The hospital patients were terminal patients, and the administered plutonium was complexed with citrate, and so their excretion patterns may not be those of employees. Certainly one would like to have other data, but other than the data on employees whose intake is largely indeterminate, this is all we have. Moreover, the distribution of fluctuations as analyzed by Beach and Dolphin does not differ markedly from that used here. This study assumes that the fluctuations of excretion due to the recent intake and for the excretion due to the chronic burden are uncorrelated. It is possible that they are correlated, and we plan to explore the implications of this in another

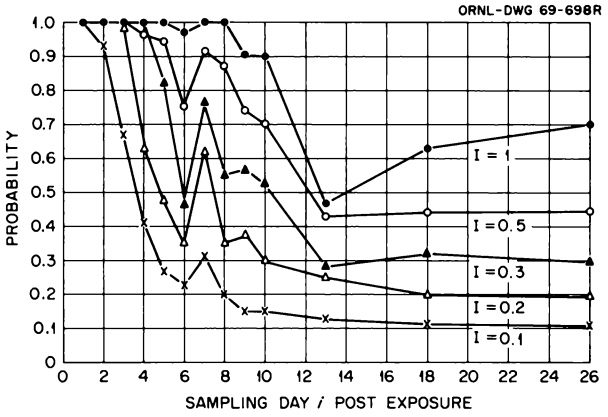

Fig. 24.14. Probability of Observing a New Intake, I; Significance Level – 70%.

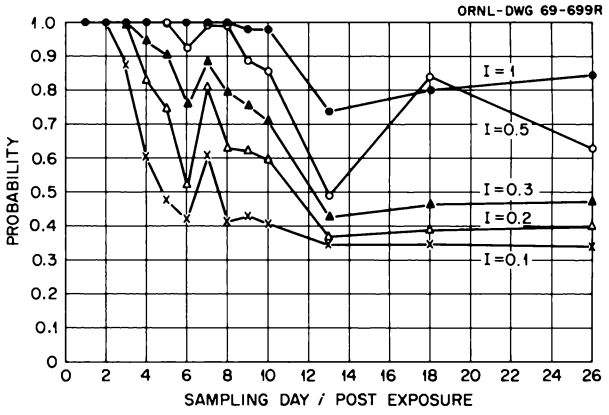

Fig. 24.15. Probability of Observing a New Intake, I; Significance Level – 50%.

study. We can only conclude that a sampling frequency of once a month does not suffice to detect new intakes of, say, 50% or less of the body burden with a high probability. It seems necessary to follow each high value by one or more resamplings with the expectation that many of them will be rejected finally as merely spurious "high" fluctuations of the daily excretion.

Beach *et al.*[4] have suggested that a program of pooled samples affords a better basis for a monitoring program. Therefore we are undertaking a study of the effects of such pooling. In Fig. 24.16 are shown the cumulative curves corresponding to pooled samples extending over five days. As will be noted, these cumulative distributions are somewhat more narrowly grouped about 1 than in Fig. 24.10 and thus should afford a somewhat better basis for a monitoring program. We plan to explore the implications of this procedure in another study.

We are exploring other uses of these data, particularly when more than one sample is obtained. For example, we were asked to study a case arising from a contaminated wound. After a period of treatment with DTPA, the excretion pattern fitted well within the pattern of fluctuations found here. Thus if plutonium were leaching from the wound, the amounts were too small to produce an excess of high values. We cannot prove with finality that transport of material was not occurring;

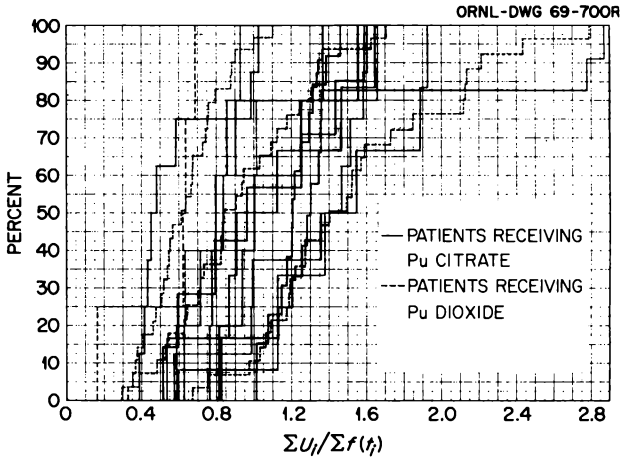

Fig. 24.16. Fluctuations of Pooled Daily Urinary Excretion Data (Five Days) of All Patients (Langham-1950) About the "Typical" Formula of Best Fit – "Area Fit" Formula Obtained by Minimizing the Sum of Absolute Deviations.

however, one can say that the data are compatible with the hypothesis of no significant transport. Further details of this analysis are reported in our annual progress report for 1968.[5]

[4] S. A. Beach *et al.*, *Health Phys.* 12(12), 1671 (1966).

[5] W. S. Snyder, Mary R. Ford, and G. G. Warner, *Health Phys. Div. Ann. Progr. Rept. July 31, 1968*, ORNL-4316, p. 271.

25. Stable Element Metabolism

ELEMENTAL COMPOSITION OF TOTAL BODY AND CERTAIN TISSUES

Isabel H. Tipton

To determine the dose of ionizing radiation to the human being, the concentration and distribution of elements in the human body must be known. Since very few systematic studies have been designed to provide this information directly, it must be inferred from whatever sources are available.

The concentrations of oxygen, carbon, and hydrogen in the total body are rarely, if ever, determined directly. In fact, entire cadavers are difficult to analyze for any component, and the usual procedure is to dissect the cadaver into separate organs and tissues[1-4] which are then analyzed for the gross components, water, ash, fat, protein, and sometimes carbohydrate. The amount of each component in the total body is then calculated as the sum of the amounts in the separate tissues and organs. The amounts of oxygen, carbon, and hydrogen in the parts and in the total body are calculated from commonly accepted values for the concentration of these elements in the gross components (Table 25.1). The ash is usually analyzed for mineral constituents.

The total body content of certain elements, e.g., sodium, potassium, and chlorine, may be estimated by techniques of isotopic dilution and by whole-body counting. In addition to furnishing information on living human beings, these techniques provide a check on values resulting from adding together the amounts determined by direct analysis of the tissues and organs of cadavers. They do not, however, provide information about the amounts in the various organs and tissues. These must be determined by direct analysis.

The elements which make up 99.7% of the total body are indicated in Table 25.2, which shows the concentration of these elements in the total body, the total adipose tissue, the striated muscle, the total skeleton, and the bone.

The concentrations of oxygen, carbon, hydrogen, and nitrogen were calculated as described above from the

[1] E. M. Widdowson, R. A. McCance, and C. M. Spray, "The Chemical Composition of the Human Body," *Clin. Sci.* **10**, 113 (1951).

[2] R. M. Forbes, A. R. Cooper, and H. H. Mitchell, "The Composition of the Adult Human Body as Determined by Chemical Analysis," *J. Biol. Chem.* **203**, 359 (1953).

[3] R. M. Forbes, H. H. Mitchell, and A. R. Cooper, "Further Studies on the Gross Composition and Mineral Elements of the Human Body," *J. Biol. Chem.* **223**, 969 (1956).

[4] G. B. Forbes and A. M. Lewis, "Total Sodium, Potassium and Chloride in Adult Man," *J. Clin. Invest.* **35**, 396 (1956).

Table 25.1. Elemental Composition of Body Components

Used in calculation of concentrations of these elements in tissue

Component	Carbon		Hydrogen		Nitrogen		Oxygen	
	Percent	Reference	Percent	Reference	Percent	Reference	Percent	Reference
Water			11				89	
Fat	77	1, p. 87	12	1, p. 87			11	1, p. 87
Protein	52	2, p. 27	7	2, p. 27	16	2, p. 27	23	2, p. 27
Carbohydrate	42	1, p. 47	6	1, p. 47			52	1, p. 47
Bone ash	2	3, p. 385					42	3, p. 385

[1] P. B. Hawk, B. L. Oser, and W. H. Summerson, *Practical Physiological Chemistry*, 12th ed., The Blakiston Company, 1947.

[2] J. S. Fruton and S. Simmons, *General Biochemistry*, 2d ed., Wiley, New York, 1959.

[3] F. Bronner, *Mineral Metabolism*, vol. II, part A, Comar and Bronner, eds., Academic, New York, 1964.

Table 25.2. Concentration of Major Elements in Human Tissues

Component	Concentration (wt %)				
	Whole Body	Adipose Tissue	Muscle	Bone	Skeleton
Oxygen	61	23	75	43	49
Carbon	23	64	11	16	23
Hydrogen	10	12	10	4.1	7.1
Nitrogen	2.6	0.80	2.6	4.3	3.9
Calcium	1.4	0.0022	0.0031	21	10
Phosphorus	1.0	0.016	0.18	10	7.0
Sulfur	0.20	0.073	0.23	0.31	0.17
Potassium	0.20	0.032	0.30		0.15
Sodium	0.14	0.050	0.075	0.62	0.32
Chlorine	0.12	0.12	0.078		0.14
Magnesium	0.027	0.002	0.019	0.22	0.12
Total	99.687	99.92	99.48	99.55	100.9

water, ash, fat, protein, and carbohydrate content of the various tissues, using values for these components which, after a thorough search of published information, were chosen as appropriate for a 70-kg "Standard Man." The concentrations of the other elements are based on direct analyses of the separate tissues and summation to give total body.

The term "adipose tissue" is used to denote the actual tissue, which includes some connective tissue, blood vessels, etc., in addition to "fat," which is defined as the ether-soluble component of any tissue. These two terms, "adipose tissue" and "fat," are frequently used interchangeably, which makes for considerable confusion. Adipose tissue does, in general, contain about 80% fat, but it contains other components as well (about 15% water and 5% protein). Fat, on the other hand, is a component of all tissues, essential fat being a necessary component of all cells. Nonessential fat is the fat contained in the adipose tissue. The subcutaneous adipose, the separable adipose surrounding organs like the kidney and the gastrointestinal tract, the nonseparable adipose which interlards tissues like muscle, and the yellow bone marrow – these make up the sum total of adipose tissue and contain 90% of the total body fat, but they are not the "body fat."

The same kind of confusion exists between the words "skeleton" and "bone" – the two terms are often used interchangeably. The skeleton contains bone, of course, but in addition it contains red and yellow bone marrow, skeletal cartilage, and some blood. It is difficult sometimes to decide whether an author means "bone" or "skeleton"; so values in the table are based insofar as possible on unambiguous reports.

Forbes *et al.*[2,3] have reported analyses of the entire skeleton for gross components, and the values in Table 25.2 for O, C, H, and N under "skeleton" are based on these analyses. On the basis of the commonly accepted gross composition of bone mineral, the ash contains 42% oxygen and 2% carbon. This has been taken into account in calculating the total in skeleton and bone.

The values included in the table under "bone" are, for the most part, based on analyses of carefully prepared samples of cortical bone which included no marrow or other types of tissues.[5-8] Assuming that the actual bone portion of trabecular bone has the same composition by weight as cortical bone, values for total bone have been extrapolated from those for cortical bone.

Values for concentration of elements in bone or in skeleton are usually reported on the basis of "dry fat-free bone." To make these values useful in calculating radiation dose, it is necessary to express them on the basis of wet living tissue. This can be done with certainty only if the water and fat contents of the particular bones analyzed are also reported. Likewise, values reported on the basis of ash are not unequivocally useful unless the ash content is given. When conversion information is not provided for a specific set of data, it is necessary to use commonly accepted values for ash, fat, and water content, and this introduces uncertainties into the calculated values.

---

[5] J. W. Agna, H. C. Knowles, Jr., and G. Alverson, "The Mineral Content of Normal Human Bone," *J. Clin. Invest.* 37, 1357 (1958).

[6] E. D. Pellegrino and S. J. Farber, *J. Lab. Clin. Med.* 56, 520 (1960).

[7] H. Q. Woodard, "The Elementary Composition of Human Cortical Bone," *Health Phys.* 8, 513 (1962).

[8] H. Q. Woodard, "Composition of Cortical Bone," *Clin. Orthopaed.* 37, 187 (1964).

The values in Table 25.2 are the best estimates on the basis of the information available in July 1969.

There is no element for which the quantity present in every organ and tissue is known. Even for the major elements – O, C, H, and N – information is lacking for about 3% of the human body. The values for sulfur in the table are based for the most part on analyses of samples from one individual (not necessarily the same individual for all tissues). The value for sulfur in adipose tissue, for instance, is based on analyses of one sample of yellow marrow, the only information available for any kind of adipose tissue. The value for muscle is based on unreferenced information from *Documenta Geigy*.

Whereas good values for sulfur are few, values for iodine are practically nonexistent. A value for total body iodine can be inferred from isotopic dilution studies, which are well documented, and it is possible to make an estimate of the iodine in the thyroid, but no good data exist for the concentration of this element in any other tissues.

Normal levels in most human tissues are lacking, questionable, or meager for Ac, Sb, As, At, Be, Bi, Br, Cs, Co, F, Fr, Ga, Ge, Au, Hf, In, I, Ir, La, Li, Hg, Nb, Os, Pd, Pt, Po, Re, Rb, Rn, Ru, Sc, Se, Si, Pa, Ta, Te, Tl, Ti, W, Y, Zr, and all the rare earths. Although the biological significance, if any, of most of these elements has not been determined, all are potentially harmful if the radioactive form is ingested, and thus none can be considered entirely unimportant.

WEIGHT OF TOTAL GASTROINTESTINAL (GI) TRACT AND ITS SUBFRACTIONS

Isabel H. Tipton Mary Jane Cook

The values given by various textbooks on human anatomy and by other sources of anatomical information for the weight of the GI tract and the various portions vary widely. Therefore, to have some direct evidence on which to choose a value appropriate for "Standard Man," a study was carried out with the help of the New York Medical Examiner's office. Dr. Michael Lyons, at that time connected with that office, collected, cleaned, dissected, and weighed the various portions of the GI tract – esophagus, stomach, duodenum, jejunum, ileum, ascending colon, transverse colon, descending colon, and sigmoid colon plus rectum – from 61 individuals, 49 men and 12 women.

Tables 25.3–25.5 show the mean and standard deviation as well as the median and 10th and 90th percentiles (80% range) of the age, height, body weight, and GI tract weight for the entire group, for the 49 males, and for the 12 females respectively. The values for total GI tract, intestine, small intestine, large intestine, upper large intestine, and lower large intestine were determined by adding the component parts for each individual, and the sums were treated statistically in the same way as each part. All values for the GI tract were rounded to two significant figures.

On the basis of this supporting evidence, the values of 1200 g for the entire GI tract and 1000 g for the intestine appear to be appropriate for "Standard Man."

Table 25.3. GI Tract Study for 61 Individuals, 49 Males and 12 Females

	Mean	Standard Deviation	Median	Low	High	80% Range	
						10th Percentile	90th Percentile
Age, years	43	12	42	22	68	28	60
Body weight, kg	71	7	72	59	86	61	81
Height, cm	168	6	169	157	183	160	175
GI tract weight, g							
Esophagus	36	6	35	23	50	28	42
Stomach	150	42	140	110	450	120	160
Intestine	1000	150	1000	670	1500	830	1200
Small intestine	640	81	640	460	840	540	740
Duodenum	57	9	58	35	75	45	65
Jejunum	280	41	280	200	380	210	320
Ileum	310	33	300	220	380	280	350
Large intestine	370	70	360	200	650	290	450
Upper large intestine	210	36	200	100	350	170	240
Ascending colon	91	15	85	65	150	75	100
Transverse colon	120	22	120	40	190	95	140
Lower large intestine	160	34	150	100	300	120	200
Descending colon	88	19	85	50	190	65	100
Sigmoid colon and rectum	74	16	70	50	110	55	100
Total GI tract	1200	190	1200	800	2000	980	1400

Table 25.4. GI Tract Study for 49 Male Individuals

	Mean	Standard Deviation	Median	Low	High	80% Range	
						10th Percentile	90th Percentile
Age, years	43	12	41	22	68	28	60
Body weight, kg	73	7	74	59	86	61	81
Height, cm	169	6	169	157	183	160	177
GI tract weight, g							
Esophagus	37	6	36	23	50	29	42
Stomach	150	46	140	110	450	120	170
Intestine	1000	150	1000	670	1500	840	1200
Small intestine	650	78	650	460	830	550	740
Duodenum	56	9	55	35	70	45	65
Jejunum	280	39	290	200	380	220	320
Ileum	310	33	300	220	380	290	350
Large intestine	370	73	370	200	650	290	450
Upper large intestine	210	38	210	100	350	170	240
Ascending colon	91	15	90	65	150	75	100
Transverse colon	120	24	120	40	190	95	140
Lower large intestine	160	36	160	100	300	120	200
Descending colon	88	21	85	50	190	65	100
Sigmoid colon and rectum	75	17	75	50	110	55	100
Total GI tract	1200	190	1200	800	2000	990	1400

Table 25.5. GI Tract Study for 12 Female Individuals

	Mean	Standard Deviation	Median	Low	High	80% Range	
						10th Percentile	90th Percentile
Age, years	43	9	45	28	55	28	54
Body weight, kg	65	6	64	59	82	59	68
Height, cm	166	3	165	159	170	160	169
GI tract weight, g							
Esophagus	34	7	34	25	50	26	40
Stomach	140	18	140	110	170	120	160
Intestine	950	130	930	740	1200	750	1100
Small intestine	600	76	590	470	750	480	690
Duodenum	57	10	60	45	75	45	68
Jejunum	250	39	230	200	330	210	300
Ileum	290	29	290	220	350	230	320
Large intestine	360	50	350	270	460	280	410
Upper large intestine	200	27	190	150	260	160	220
Ascending colon	89	14	85	75	120	75	100
Transverse colon	110	14	110	75	130	75	120
Lower large intestine	160	24	150	120	200	130	180
Descending colon	88	13	90	65	110	75	110
Sigmoid colon and rectum	69	11	65	55	95	65	85
Total GI tract	1100	150	1100	880	1400	890	1300

PATTERNS OF ELEMENTAL EXCRETION IN LONG-TERM BALANCE STUDIES. II

Isabel H. Tipton Peggy L. Stewart

In the program for analysis of total self-chosen diets and total excretion for trace elements, the material from an additional man (see annual report 1968) for 50 weeks has been analyzed for 25 elements. Statistical treatment has been completed for a 140-day period, January 5, 1964, to May 23, 1964. A summary of the average daily elemental intake, excretion, and balance is given in Table 25.6.

Subject E was 56 years old and 174 cm tall and weighed about 85 kg. The water content of his dietary intake (Table 25.7) was the same as that of subject C, though the individual items of diet were quite different in all three subjects in the present study. The main difference in pattern for subject E was in fecal excretion. Whereas for subject C the total number of fecal samples was less than half and for subject D about half of the total number of days during the period under consideration, for subject E there was a fecal sample for every day, and the mass of these fecal samples averaged about twice that of the other two subjects. For certain elements (Al, Ba, Fe, Mo, Ni, Sr, and Zn) the ratio of the amount excreted in urine to the total amount excreted, F_u (last column in Table 25.6) is lower for subject E, who excreted feces every day, than for subject C, whose excretion interval was more like three days. This suggests that the absorption of these elements continues for the entire time ingested material remains in the gut.

For equilibrium conditions, and assuming no entry into the body by any other route than ingestion, F_u is equivalent to the fraction of an element ingested which is excreted in the urine. It is not equivalent to f_1, the total fraction that is absorbed from the gut, because some portions of absorbed elements are, to varying degrees, depending on the element, reexcreted into the gut and thus excreted in the feces. If it is assumed that approximately the same proportion of an absorbed element is reexcreted into the gut no matter how long the ingested material remains in the gut, then the ratio urine/total excreta for elements in equilibrium is proportional to f_1. In other words, the data for the three individuals studied so far suggest that the value of f_1 might not be constant for certain elements but could be affected by the length of time ingested material remains in the gut.

When the excretion patterns of subjects C and E are compared month by month, the differences still appear. The only element for which the difference is significant at the 95% level is zinc.

In addition to being an essential element subject to controls in biological systems, zinc is the element for which the analytical method in the present study is most precise. Therefore the variation in the daily values for zinc is not so great as for other elements, which makes it possible to make finer distinctions for this element.

Table 25.6. Mean Daily Intake by Ingestion and Fecal and Urinary Excretion

Subjects C and D: September 5, 1966–August 17, 1967 (347 days)
Subject E: January 5, 1964–May 23, 1964 (140 days)

All values except ratio in milligrams per day

Element	Subject	Diet, Mean (±S.E.)	Feces, Mean (±S.E.)	Urine, Mean (±S.E.)	Excreta, Sum of Feces Plus Urine (±S.E.)	Balance (±95% Confidence Interval), Difference, Diet Minus Excreta (±2S.E.)	Urine/Excreta, F_u
Aluminum	C	17(2)	17(3)	0.87(0.07)	18(3)	−1.0(6.0)	0.048
	D	17(2)	15(2)	0.72(0.04)	16(2)	1.0(5.0)	0.045
	E	31(7)	23(2)	0.45(0.08)	23(2)	8.0(15)	0.020
Barium	C	0.65(0.03)	0.69(0.08)	0.037(0.012)	0.73(0.08)	−0.08(0.18)	0.051
	D	0.92(0.07)	0.88(0.18)	0.017(0.003)	0.90(0.18)	0.02(0.20)	0.019
	E	1.3(0.3)	1.1(0.5)	0.025(0.010)	1.1(0.5)	0.2(1.2)	0.023
Boron	C	1.2(0.1)	0.25(0.32)	1.2(0.1)	1.4(0.4)	−0.20(0.68)	0.86
	D	2.8(0.3)	0.36(0.05)	0.95(0.08)	1.3(0.1)	1.5(0.35)	0.73
	E	11(1)	0.31(0.01)	4.7(2.0)	5.0(2.0)	6.3(4.4)	0.94
Calcium	C	940(36)	820(90)	150(4)	970(90)	−30(200)	0.15
	D	2300(62)	1200(81)	140(4)	1300(85)	1000(200)	0.11
	E	1500(52)	880(49)	230(10)	1200(50)	300(140)	0.19
Cadmium	C[a]	0.10(0.01)	0.030(0.008)	0.083(0.005)	0.11(0.01)	−0.010(0.014)	0.75
	D[a]	0.22(0.01)	0.047(0.007)	0.092(0.004)	0.14(0.01)	0.080(0.014)	0.66
	E	0.18(0.02)	0.049(0.005)	0.11(0.02)	0.16(0.02)	0.02(0.06)	0.69
Chromium	C	0.20(0.03)	0.078(0.013)	0.11(0.01)	0.19(0.02)	0.01(0.06)	0.58
	D	0.29(0.06)	0.092(0.014)	0.12(0.01)	0.21(0.02)	0.08(0.14)	0.57
	E	0.20(0.04)	0.063(0.005)	0.16(0.04)	0.22(0.04)	−0.02(0.12)	0.73

Table 25.6. (continued)

Element	Subject	Diet, Mean (±S.E.)	Feces, Mean (±S.E.)	Urine, Mean (±S.E.)	Excreta, Sum of Feces Plus Urine (±S.E.)	Balance (±95% Confidence Interval), Difference, Diet Minus Excreta (±2S.E.)	Urine/Excreta, F_u
Cobalt	C	0.31(0.04)	0.034(0.006)	0.24(0.02)	0.27(0.02)	0.04(0.09)	0.89
	D	0.47(0.03)	0.059(0.008)	0.23(0.02)	0.29(0.02)	0.18(0.08)	0.79
	E	0.29(0.05)	0.088(0.010)	0.16(0.02)	0.25(0.02)	0.04(0.14)	0.64
Copper	C	0.95(0.05)	1.3(0.2)	0.022(0.003)	1.3(0.2)	−0.30(0.34)	0.017
	D	1.7(0.1)	1.3(0.1)	0.042(0.013)	1.3(0.1)	0.40(0.28)	0.032
	E	6.2(0.4)	4.2(0.2)	0.029(0.010)	4.2(0.2)	2.0(0.9)	0.0069
Iron	C	15(1)	13(2)	0.92(0.16)	14(2)	1.0(3.6)	0.066
	D	28(5)	12(1)	0.83(0.13)	13(1)	15(11)	0.064
	E	22(2)	20(1)	0.52(0.01)	21(1)	2.0(4.5)	0.025
Magnesium	C	180(5)	170(19)	98(5)	270(20)	−90(40)	0.36
	D	360(9)	200(13)	92(4)	290(14)	70(32)	0.32
	E	310(11)	270(13)	84(3)	350(13)	−40(35)	0.24
Manganese	C	3.3(0.2)	2.5(0.6)	0.043(0.008)	2.5(0.6)	0.8(1.2)	0.017
	D	5.5(0.2)	3.0(0.4)	0.053(0.016)	3.0(0.4)	2.5(1.0)	0.018
	E	9.3(0.6)	2.9(0.2)	0.009(0.002)	2.9(0.2)	6.1(1.2)	0.0031
Molybdenum	C	0.21(0.02)	0.088(0.017)	0.11(0.01)	0.20(0.02)	0.01(0.06)	0.55
	D	0.46(0.08)	0.099(0.015)	0.13(0.01)	0.23(0.02)	0.23(0.17)	0.57
	E	0.11(0.01)	0.071(0.003)	0.026(0.006)	0.097(0.007)	0.013(0.025)	0.27
Nickel	C	0.39(0.04)	0.22(0.03)	0.11(0.03)	0.33(0.04)	0.06(0.09)	0.33
	D	0.81(0.11)	0.35(0.05)	0.11(0.02)	0.46(0.07)	0.35(0.24)	0.24
	E	0.28(0.03)	0.29(0.02)	0.049(0.016)	0.34(0.05)	0.06(0.12)	0.14
Phosphorus	C	1600(46)	430(46)	1200(32)	1600(78)	0(150)	0.75
	D	3300(110)	600(39)	1100(21)	1700(60)	1600(240)	0.65
	E	1700(53)	770(44)	940(28)	1700(52)	0(150)	0.55
Potassium	C	1700(38)	250(28)	2500(64)	2700(70)	−1000(160)	0.93
	D	3800(72)	310(21)	2900(52)	3200(56)	600(180)	0.91
	E	3300(90)	500(21)	2500(63)	3000(66)	300(220)	0.83
Sodium	C[b]	3500(89)	34(5)	4600(110)	4600(110)	−900(280)	1.0
	D	4600(140)	41(4)	4500(98)	4500(98)	100(340)	1.0
	E	4500(150)	230(20)	4300(150)	4500(150)	0(420)	0.96
Strontium	C	1.9(0.1)	1.7(0.2)	0.12(0.01)	1.8(0.2)	0.10(0.50)	0.067
	D	2.1(0.1)	2.1(0.2)	0.10(0.01)	2.2(0.2)	−0.10(0.48)	0.045
	E	2.3(0.1)	3.8(0.2)	0.098(0.008)	3.9(0.2)	−1.6(0.5)	0.025
Tin	C	5.8(0.7)	3.6(0.7)	0.085(0.011)	3.7(0.7)	2.1(1.8)	0.023
	D	8.8(1.1)	3.6(0.5)	0.058(0.006)	3.7(0.5)	5.1(2.4)	0.016
	E	6.7(1.3)	1.3(0.2)	0.019(0.004)	1.3(0.2)	5.4(2.6)	0.015
Titanium	C	0.75(0.08)	0.46(0.09)	0.49(0.07)	0.95(0.11)	−0.20(0.28)	0.52
	D	2.0(0.4)	0.82(0.20)	0.47(0.06)	1.3(0.2)	0.70(0.72)	0.36
	E	0.18(0.02)	0.39(0.03)	0.16(0.02)	0.55(0.04)	−0.37(0.09)	0.29
Vanadium	C	0.061(0.005)	0.12(0.03)	0.018(0.002)	0.14(0.03)	0.079(0.034)	0.13
	D	0.17(0.01)	0.15(0.02)	0.023(0.002)	0.18(0.02)	−0.010(0.038)	0.13
	E	0.069(0.006)	0.037(0.005)	0.012(0.002)	0.049(0.005)	0.020(0.016)	0.24
Zinc	C	11(0.3)	14(1.7)	1.3(0.1)	15(1.7)	−4.0(3.4)	0.087
	D	18(0.5)	16(1.4)	1.2(0.1)	17(1.4)	1.0(3.0)	0.071
	E	14(0.6)	15(0.7)	0.55(0.02)	16(0.7)	−2.0(2.0)	0.034
Zirconium	C	0.43(0.03)	0.12(0.02)	0.084(0.014)	0.20(0.03)	0.23(0.08)	0.42
	D	0.55(0.08)	0.059(0.008)	0.18(0.06)	0.24(0.06)	0.31(0.20)	0.75
	E	0.088(0.012)	0.066(0.008)	0.17(0.05)	0.24(0.05)	−0.15(0.12)	0.71

[a]Cadmium data for 63 days only.
[b]Subject C failed to add salt to his duplicate meal.

Table 25.7. Gross Daily Intake and Excretion

Subjects C and D: September 5, 1966–August 17, 1967
Subject E: January 5, 1964–May 23, 1964

	Mean ± Standard Deviation (g)		
	Subject C	Subject D	Subject E
Total daily intake by ingestion	3100 ± 520	3000 ± 600	3000 ± 390
Water content	2500 ± 660	2200 ± 560	2500 ± 560
Total daily fecal excretion	100 ± 130	120 ± 120	220 ± 67
Total daily urinary excretion	1300 ± 530	1100 ± 270	1100 ± 160

TRACE ELEMENT RECOVERY

Cyrus Feldman F. S. Jones

Since previous work had shown that most of the phosphate can be removed from a bone-ash solution by electrodialysis, attention was turned to checking the recovery of trace elements present in the bone-ash solution. In this type of operation, trace elements can be lost by (1) migration to the anode compartment of elements which form anions, (2) adsorption or precipitation on walls or membrane, and (3) deposition on cathode. The recovery of a number of elements from the electrodialysis process was checked by radioactive tracer methods, and the results are given in Table 25.8.

Table 25.8. Recovery of Trace Elements After Removal of Phosphate from Bone-Ash Solutions by Electrodialysis

Element	Percent Recovery
Europium	99.0
Zinc	98.0
Manganese	97.5
Copper	94.3
Cobalt	93.0
Bismuth	83.1
Iron	75.7
Beryllium	45.7
Gallium	32.0
Ruthenium	20.8
Indium	18.2
Antimony	17.6
Chromium	14.5
Tantalum	7.5
Tin	7.9
Molybdenum	7.2

It was considered important to test elements which were known to have a tendency to be amphoteric or to form complexes; most of the elements in the latter part of the table are in this category. Thus, although the list of elements giving good recovery could undoubtedly be lengthened, enough elements were found to give incomplete recovery to indicate that this method of phosphate removal could not form part of a procedure designed to collect all trace elements.

Experiments were performed to test the effectiveness of hydrated zirconium oxide for the above purpose. This reagent is said to remove phosphate from acid solutions (pH 1–2) and to have little affinity for other elements or groups. Our tests showed that different batches varied in their effectiveness for removing phosphate and that recoveries of the first trace elements tested were not high enough (Sn = 28%, Cr = 69%, Sb = 29%).

The main purpose of this investigation is to prevent the precipitation of calcium phosphate during the Mitchell-Scott trace element collection procedure. Since attempts to accomplish this by first removing phosphate led to unacceptable losses of some trace elements, it was decided to try the opposite approach, that is, preliminary removal of the calcium by oxalate precipitation, followed by application of the Mitchell-Scott procedure to both the calcium and the phosphate fractions. Trace element recovery tests show the following overall recoveries: Co, 92%; Fe, 94%; Cr, 32%. Tests with other trace elements will be made.

In order to determine the fat and nitrogen content of bone, it is advisable to pulverize the sample. A ball-mill shaker device was unsuccessful, but an 18,000-rpm motor driving a steel burr gave excellent results.

Theses, Papers, Publications, and Lectures

Theses

M-E. M. Abu-Zeid, L. G. Christophorou, and J. G. Carter
Emission and Decay of Organic Liquids Under Electron Impact, ORNL-TM-2219 (February 1969).

R. P. Blaunstein and L. G. Christophorou
Electron Attachment to Organic Molecules, ORNL-TM-2216 (February 1969).

A. J. Braundmeier, Jr.
Plasmon Radiation from Electron Bombarded Aluminum Foils, ORNL-TM-2612 (in preparation).

E. L. Chaney
Electron Attachment to Polyatomic Molecules, ORNL-TM-2613 (in preparation).

N. Chantanakom
"On the Effect of LET and Environment of the Thermally Stimulated Exoelectron Emission and Its Fading Rate," Master's thesis, University of Tennessee, June 1969.

A. A. Christodoulides and L. G. Christophorou
Scattering of Thermal Electrons by Polar Molecules, ORNL-TM-2257 (August 1968).

P. M. Collins
Investigation of Negative Ions with Electron Beams, ORNL-TM-2614 (in preparation).

J. J. Cowan
Surface Plasmon Resonance Effects in Grating Diffraction, ORNL-TM-2615 (in preparation).

C. E. Easterly
Study of Aromatic Hydrocarbons in Relation to Carcinogenesis, ORNL-TM-2616 (in preparation).

F. W. Garber, R. D. Birkhoff, R. H. Ritchie, and J. A. Harter
Low-Energy Electron Beam Studies in Thin Metal Films, ORNL-TM-2406 (February 1969).

T. F. Gesell
Photoelectric Properties of Magnesium in the Vacuum Ultraviolet, ORNL-TM-2617 (in preparation).

J. T. Grissom
Threshold Electron Impact Excitation and Negative Ion Formation, ORNL-TM-2618 (in preparation).

J. H. Grossen
A Monte Carlo Calculation of High-Energy Nucleon Penetration Through Matter, ORNL-TM-2619 (in preparation).

R. N. Hamm, R. H. Ritchie, and J. C. Ashley
Electron Mean Free Paths in a Free Electron Gas, ORNL-TM-2072 (July 1968).

J. M. Kelly
Production and Compartmental Transfers in Two Grassland Communities, M.S. thesis, University of Tennessee, Knoxville, 134 pp. Part A of ORNL-4316 (June 1969).

S. Kolehmainen and D. J. Nelson
*The Balances of ^{137}Cs, Stable Cesium, and Potassium, and the Feeding Rates of Bluegill (*Lepomis macrochirus *Raf.) in White Oak Lake,* ORNL-4445 (in press).

W. T. Naff, R. N. Compton, C. D. Cooper, and P. W. Reinhardt
Transient Negative Ion States in Selected Alicyclic and Aromatic Fluorocarbon Molecules, ORNL-TM-2260 (November 1968).

S. J. Nalley
Charge Exchange Between Fast Atoms and Molecules, ORNL-TM-2620 (in preparation).

D. R. Nelson and F. J. Davis
Determination of Diffusion Coefficients of Thermal Electrons with a Time-of-Flight Swarm Experiment, ORNL-TM-2222 (November 1968).

P. A. Opstrup
Systems Analysis of Two Old-Field Ecosystems, M.S. thesis, University of Tennessee, Knoxville, 164 pp. Part B of ORNL-4316 (June 1969).

Linda R. Painter, R. D. Birkhoff, and E. T. Arakawa
Electronic Properties of Liquid Water in the Vacuum Ultraviolet Region, ORNL-TM-2261 (September 1968).

H. L. Ragsdale, J. P. Witherspoon, and D. J. Nelson
The Effects of Biotic Complexity and Fast Neutron Radiation on Cesium-137 and Cobalt-60 Kinetics in Aquatic Microcosms, ORNL-4318 (December 1968).

Gary R. Sandberg, J. S. Olson, and E. E. C. Clebsch
Internal Distribution and Loss from Roots by Leaching of Cesium-137 Inoculated into Liriodendron tulipifera *L. Seedlings Grown in Sand Culture,* ORNL-TM-2660 (in press).

J. A. Stockdale, R. N. Compton, and P. W. Reinhardt
Studies of Negative Ion–Molecule Reactions in the Energy Region from Zero to Three Electron Volts, ORNL-TM-2546 (May 1969).

R. C. Vehse and E. T. Arakawa
Optical and Photoemissive Properties of Evaporated Films of Palladium, Nickel, and Copper in the Vacuum Ultraviolet Spectral Region, ORNL-TM-2240 (September 1968).

R. B. Vora
Stopping Power of Matter at Extreme Relativistic Energies, ORNL-TM-2621 (in preparation).

U. S. Whang
Optical Properties of Cesium in the Vacuum Ultraviolet, ORNL-TM-2622 (in preparation).

Papers

S. I. Auerbach

Radioecological Studies, Vulnerability of Food Crop and Livestock Production to Fallout Radiation Symposium, Colorado State University, June 18, 1969, Ft. Collins, Colorado.

J. A. Auxier

Multilaboratory Intercomparisons and Standardization of Nuclear Accident Dosimetry Systems, Panel on "Nuclear Accident Dosimetry Systems," February 17 Through 21, 1969, Vienna, Austria.

Dosimetry for Human Exposures: Research at the Oak Ridge National Laboratory, Waldemar Noll Memorial Symposium, March 29, 1969, Berea, Kentucky.

C. E. Baker and P. B. Dunaway

Investigation of the Concept of Using Radionuclides for Metabolic Measurements, American Society of Mammalogists, June 15–21, 1969, New York, New York.

K. Becker

Some Studies on Radiation Dosimetry by Thermally Stimulated Exoelectron Emission (TSEE), Second International Conference on Luminescence Dosimetry, September 23 Through 26, 1968, Gatlinburg, Tennessee.

A New Class of Small Energy-Independent High-Sensitivity Dosimeters Based on TSEE, American Association of Physicists in Medicine, December 5 Through 7, 1968, Chicago, Illinois.

Radiophotoluminescence Dosimetry, Symposium on Solid-State Dosimetry, Radiation Research Society, May 21 Through 23, 1969, Cincinnati, Ohio.

Thermally Stimulated Exoelectron Emission (TSEE) Dosimetry, Symposium on Solid-State Dosimetry, Radiation Research Society, May 21 Through 23, 1969, Cincinnati, Ohio.

K. Becker, R. H. Boyett, and D. R. Johnson

Some Applications of the Track Etching Process in Radiation Protection, International Topical Conference on Nuclear Track Registration in Insulating Solids, May 6 Through 9, 1969, Clermont-Ferrand, France.

K. Becker and J. S. Cheka

LET Effects on the Radiophotoluminescence in Silver-Activated Dosimeter Glasses, Second International Conference on Luminescence Dosimetry, September 23 Through 26, 1968, Gatlinburg, Tennessee.

Low-Z Radiophotoluminescent Glasses Based on Lithium Borate, Second International Conference on Luminescence Dosimetry, September 23 Through 26, 1968, Gatlinburg, Tennessee.

K. Becker, M. Oberhofer, and J. S. Cheka

TSEE, TL, and Impurities, Health Physics Society, June 8 Through 12, 1969, Pittsburgh, Pennsylvania.

S. R. Bernard

A Model for Estimation of Mean Activity Present in Segments of the GI Tract at Any Time Postinjection, Health Physics Society, June 8–12, 1969, Pittsburgh, Pennsylvania.

R. D. Birkhoff

The Electron Flux Spectra and Radiation Yields in Solids Irradiated by Nuclear Radiation, IEEE Conference on Nuclear and Space Radiation Effects, July 7–11, 1969, University Park, Pennsylvania.

The Electron Flux Spectra and Radiation Yields in Solids Irradiated by Nuclear Radiation, American Physical Society, April 28–May 1, 1969, Washington, D.C.

R. P. Blaunstein

Nondissociative Electron Attachment to Aromatic Hydrocarbons, 21st Annual Gaseous Electronics Conference, October 16–18, 1968, Boulder, Colorado.

W. J. Boegly, Jr.

Utility Tunnels and Their Potential Use as Emergency Shelters, September 19, 1968, Mountain View Hotel, Gatlinburg, Tennessee.

R. L. Bradshaw and W. C. McClain
Roof Bolt Test and Application in Supporting a Two-Foot-Thick Roof Bed, Third Symposium on Salt, April 21–25, 1969, Cleveland, Ohio.

J. G. Carter, O. E. Wagner, and L. G. Christophorou
Emission and Decay of Organic Liquids Under Intense Electron Bombardment, Health Physics Society, June 9–11, 1969, Pittsburgh, Pennsylvania.

E. L. Chaney and L. G. Christophorou
Electron Attachment to N_2O, Sixth International Conference on the Physics of Electronic and Atomic Collisions, July 26–August 2, 1969, Cambridge, Massachusetts.

L. G. Christophorou
Atomic and Molecular Physics at the Oak Ridge National Laboratory, Nuclear Research Center "Democritus," March 14, 1969, Athens, Greece.

Electron Capture Processes in Gases, Miller Conference on Ionic and Electronic Processes, April 14–18, 1969, Portmeirion, North Wales.

Total Ionization Produced in Gases by the Complete Absorption of α and β Particles, 21st Annual Gaseous Electronics Conference, October 16–18, 1968, Boulder, Colorado.

Electron Attachment Processes, Westinghouse Electric Corporation, Seminar, June 12, 1969, Pittsburgh, Pennsylvania.

L. G. Christophorou and J. G. Carter
Long-Lived Polyatomic Negative Ions Formed by Electron Capture in the Field of the Ground and Excited States of the Parent Molecule, Atomic and Molecular Physics Congress, March 31–April 3, 1969, Manchester, England.

L. G. Christophorou, D. Pittman, and A. A. Christodoulides
Transport of Thermal Electrons Through Polar Gases, 21st Annual Gaseous Electronics Conference, October 16–18, 1968, Boulder, Colorado

R. J. Cloutier,[1] Sarah A. Smith,[1] W. S. Snyder, and G. G. Warner[2]
Dose to the Fetus from Gamma Emitters Present in the Bladder, Health Physics Society, June 8–12, 1969, Pittsburgh, Pennsylvania.

R. N. Compton and R. H. Huebner
Electron Impact Excitation and Negative Ion Formation in Azulene, American Physical Society, Southeastern Section, October 9–11, 1968, Athens, Georgia.

R. N. Compton, J. A. Stockdale, and P. W. Reinhardt
Electron Impact Excitation and Negative Ion Formation in NH_3 and ND_3, 21st Annual Gaseous Electronics Conference, October 16–18, 1968, Boulder, Colorado.

R. N. Compton, J. A. Stockdale, and H. C. Schweinler
Negative Ion Formation in Selected Hexafluoride Molecules, Sixth International Conference on the Physics of Electronic and Atomic Collisions, July 26–August 2, 1969, Cambridge, Massachusetts.

D. C. Cooper, W. T. Naff, and R. N. Compton
Transient Negative Ion States in Selected Alicyclic and Aromatic Fluorocarbons, 21st Annual Gaseous Electronics Conference, October 16–18, 1968, Boulder, Colorado.

J. J. Cowan, R. H. Ritchie, and E. T. Arakawa
Surface Plasmon Resonance Effect in Grating Diffraction, American Physical Society, November 25–27, 1968, Miami Beach, Florida.

---

[1] Oak Ridge Associated Universities.

[2] Mathematics Division, ORNL.

K. E. Cowser, W. S. Snyder, and E. G. Struxness
Application of ICRP Recommendations Relevant to Internal Dose, Symposium on Public Health Aspects of Peaceful Uses of Nuclear Explosives, April 7–11, 1969, Las Vegas, Nevada.

K. W. Crase
Dosimetric Research Involving Thermally Stimulated Exoelectron Emission, Waldemar Noll Memorial Symposium, March 29, 1969, Berea, Kentucky.

Julian Crowell and R. H. Ritchie
Surface Plasmon Effect in the Optical Reflectivity of a Nonuniform Bounded Electron Gas, American Physical Society, Southeastern Section, October 9–11, 1968, Athens, Georgia.

J. W. Curlin
Nutrient Cycling as a Factor in Site Productivity and Forest Fertilization, North American Forest Soils Conference, August 1968, Raleigh, North Carolina.

Water Flux in Forested Watersheds: Properties of Hydrologic Phenomena, Working Meeting on Temperate Forest Productivity Analysis of Ecosystems: Temperate Woodland, July 29–31, 1968, Gatlinburg, Tennessee.

J. W. Curlin, R. E. Farmer, Jr., and E. A. Snow
Bio-economic Interpretation of a N-P-K Response Surface from Pole-Sized Loblolly Pine, Soil Science Society of America, November 10–15, 1968, New Orleans, Louisiana.

R. C. Dahlman
Root Production and Turnover of Carbon in the Root-Soil Matrix of a Grassland Ecosystem, Methods of Productivity Studies in Root Systems and Rhizosphere Organisms, August 28–September 12, 1968, Leningrad, U.S.S.R.

R. C. Dahlman, S. I. Auerbach, and P. B. Dunaway
Behavior of ^{137}Cs Tagged Particles in a Fescue Meadow, IAEA Seminar on Agricultural and Public Health Aspects of Environmental Contamination by Radioactive Materials, March 24–28, 1969, Vienna, Austria.

R. C. Dahlman and Clair L. Kucera
Carbon-14 Cycling in the Root and Soil Components of a Prairie Ecosystem, Second National Symposium on Radioecology, May 15–17, 1967, Ann Arbor, Michigan.

Wallace de Laguna
Control of Environmental Pollution from Generation of Nuclear Power, Annual Meeting of Institute of Electrical and Electronics Engineers, April 16–18, 1969, Washington, D.C.

Disposal of Medium Level Radioactive Waste by Hydraulic Fracturing, 1969 Annual Meeting of the American Institute of Mining, Metallurgical, and Petroleum Engineers, February 17–18, 1969, Washington, D.C.

Radioactive Waste Disposal by Hydraulic Fracturing, Meeting of the National Water Well Association, September 23–25, 1968, Washington, D.C.

P. B. Dunaway
Maintenance of Wild Vertebrates in Captivity, American Association for Laboratory Animal Science, May 27, 1969, Oak Ridge, Tennessee.

P. B. Dunaway with G. E. Cosgrove and J. D. Story
Malignant Tumors Associated with Subcutaneously Implanted ^{60}Co Wires in Peromyscus maniculatus, Wildlife Disease Association, June 17–19, 1969, Ames, Iowa.

P. B. Dunaway, J. T. Kitchings III, and J. D. Story
Prediction of Radiosensitivity in Mammals, Radiation Research Society, May 18–22, 1969, Cincinnati, Ohio.

F. M. Empson, R. L. Bradshaw, W. C. McClain, and B. L. Houser
Results of the Operation of Project Salt Vault: A Demonstration of Disposal of High-Level Radioactive Solids in Salt, Third Symposium on Salt, April 21–25, 1969, Cleveland, Ohio.

B. R. Fish

Insuring Environmental Quality Through Site, Design, and Operation Review, Geoscience-Electronics Symposium of the Institute of Electrical and Electronics Engineers, April 16–18, 1969, Washington, D.C.

The Exploding Wire Aerosol Generator, AEC Conference on Aerosol Physics, May 30, 1969, USAEC-NYOO Health and Safety Laboratory, New York, N.Y.

W. R. Garrett

Nonadiabatic Atomic Distortion in Low-Energy Electron and Positron Scattering, 21st Annual Gaseous Electronics Conference, October 16–18, 1968, Boulder, Colorado.

Variational Methods for Long-Range Scattering Interactions, Sixth International Conference on the Physics of Electronic and Atomic Collisions, July 26–August 2, 1969, Cambridge, Massachusetts.

D. F. Grigal and H. F. Arneman

Numerical Classification of Some Forested Minnesota Soils, American Society of Agronomy Annual Meeting, November 10–15, 1968, New Orleans, Louisiana.

R. N. Hamm, Linda R. Painter, R. D. Birkhoff, and H. C. Schweinler

Electronic Structure of Liquids from Optical Measurements – I. Dispersion of Water in the Vacuum Ultraviolet, American Physical Society, November 25–27, 1968, Miami Beach, Florida.

F. F. Haywood and J. A. Auxier

Current Radiobiological Dosimetry at the DOSAR Facility, DASA Medical Coordination Conference, Air Force Weapons Laboratory, May 27 Through 29, 1969, Kirtland AFB, New Mexico.

Dosimetry Standardization and Interlaboratory Comparison, DASA Medical Coordination Conference, Air Force Weapons Laboratory, May 27 Through 29, 1969, Kirtland AFB, New Mexico.

Occupational X Radiation Hazards from Vacuum Electrical Components, Health Physics Society, June 8 Through 12, 1969, Pittsburgh, Pennsylvania (paper presented by J. A. Auxier).

H. H. Hubbell, Jr., and J. A. Auxier

Review of Neutron Depth-Dose Theory and Experiments, Health Physics Society, June 8 Through 12, 1969, Pittsburgh, Pennsylvania.

D. G. Jacobs, Y. E. Kim, Judith A. Varga, and Susan M. Burke

Factors Affecting the Behavior of Calcium and Strontium in Mineral Exchange Systems, Health Physics Society Annual Meeting, June 8–12, 1969, Pittsburgh, Pennsylvania.

Global Cycling of Tritium Released from an Expanding Nuclear Power Economy, Symposium on Control of Tritium Hazards, October 5, 1968, Gaithersburg, Maryland.

D. R. Johnson, K. Becker, and R. H. Boyett

On the Mechanism of Radiation Damage Along Charged Particle Tracks in Organic Polymers, Symposium on Solid-State Dosimetry, Radiation Research Society, May 21 Through 23, 1969, Cincinnati, Ohio (paper presented by K. Becker).

D. R. Johnson, R. H. Boyett, and K. Becker

Some Studies on the Chemical Damage Mechanism Along Charged Particle Tracks in Polymers, International Topical Conference on Nuclear Track Registration in Insulating Solids, May 6 Through 9, 1969, Clermont-Ferrand, France (paper presented by K. Becker).

Sensitive Automatic Alpha Particle Track Counting in Polymers and Its Applications in Dosimetry, Health Physics Society, June 8 Through 12, 1969, Pittsburgh, Pennsylvania.

T. D. Jones, W. S. Snyder, and J. A. Auxier

Dose and LET Distributions in a Man Equivalent Cylinder Due to a Collimated Beam of Monoenergetic Neutrons, Health Physics Society, June 8 Through 12, 1969, Pittsburgh, Pennsylvania.

S. V. Kaye

Estimating Radiation Doses to Members of the Public from Environmental Contamination, and Identifying the Artificial Nuclides, Pathways, and Population Groups, Eighteenth Meeting of the Plowshare Advisory Committee, November 21–22, 1968, Oak Ridge, Tennessee.

Introductory Remarks for Symposium on Radiation Effects in Man's Environment, Annual Meeting of the Health Physics Society, June 9–12, 1969, Pittsburgh, Pennsylvania.

Dose Estimation for Gasbuggy, Meeting of Gasbuggy Participants with Division of Peaceful Nuclear Explosives, October 10, 1968, AEC Headquarters, Germantown, Maryland.

S. V. Kaye and P. S. Rohwer

Methods of Estimating Population Exposures from Plowshare Applications, Symposium on Public Health Aspects of Peaceful Uses of Nuclear Explosives, April 7–11, 1969, Las Vegas, Nevada.

S. V. Kaye with P. S. Rohwer

Predicting Radiation Dose Equivalents for Populations. II. Results Obtained with the Dose Models, AIBS Symposium, "Sea Level Canal, Bioenvironmental Studies," September 3–6, 1968, Columbus, Ohio.

S. V. Kaye, P. S. Rohwer, K. E. Cowser, and W. S. Snyder

Predicting Radiation Dose Equivalents for Populations. I. Dose Models and Methods of Application, AIBS Symposium, "Sea Level Canal, Bioenvironmental Studies," September 3–6, 1968, Columbus, Ohio.

C. E. Klots

Transition Yields in Irradiated Gases, International Conference on Radiation Chemistry, August 12–15, 1968, Argonne, Illinois.

Ionization Mechanisms in Molecules, American Chemical Society, Southeastern Regional Meeting, December 11–14, 1968, Tallahassee, Florida.

Fundamental Processes in Gas-Phase Radiolysis, Gordon Conference on Radiation Chemistry, July 14–18, 1969, New Hampton, New Hampshire.

T. F. Lomenick

Effects of Gamma Radiation, Elevated Temperatures, and Pressure on the Structural Stability of Limestone, 1968 Annual Meeting of the Geological Society of America, November 10–15, 1968, Mexico City, Mexico.

C. R. Malone and D. J. Nelson

*Feeding Rates of Freshwater Snails (*Goniobasis clavaeformis*) Determined with ^{60}Cobalt,* presented before the 1968 annual meeting of the AIBS, August 1968, Columbus, Ohio.

W. C. McClain

The Mechanics of Hydraulic Fractures in Shales, Third Symposium on Salt, April 21–24, 1969, Cleveland, Ohio.

W. C. McClain and R. L. Bradshaw

The Disposal of Solidified Radioactive Wastes in Salt Mines, Annual Meeting of the American Institute of Mining, Metallurgical, and Petroleum Engineers, February 17–20, 1969, Washington, D.C.

W. J. McConnell and R. D. Birkhoff

Measurement of the Low-Energy Portion of a Beta-Ray Spectrum, American Physical Society, Southeastern Section, October 9–11, 1968, Athens, Georgia.

W. T. Naff, C. D. Cooper, and R. N. Compton

Electron Attachment in Cyclic Fluorocarbons: Production of HF_2^- and Lifetime Measurements of Transient Negative Ion States, American Physical Society, Southeastern Section, October 9–11, 1968, Athens, Georgia.

D. J. Nelson

Measurement and Sampling of Outputs from Watersheds, Working Meeting on Temperate Forest Productivity Analysis of Ecosystems: Temperate Woodland, July 29–31, 1968, Gatlinburg, Tennessee.

D. R. Nelson and F. J. Davis
Measurements of Thermal Electron Attachment Rates in SF_6, C_6F_6, C_6F_{11}, CF_3, and TeF_6 by a Time-of-Flight Swarm Method, 21st Annual Gaseous Electronics Conference, October 16–18, 1968, Boulder, Colorado.

Thermal Electron Attachment Rates of SF_6 for Different Carrier Gas Dilutants, Sixth International Conference on the Physics of Electronic and Atomic Collisions, July 26–August 2, 1969, Cambridge, Massachusetts.

M. Oberhofer, J. F. Wilson, and K. Becker
The Effect of High Temperature Treatment on TSEE in BeO, Health Physics Society, June 8 Through 12, 1969, Pittsburgh, Pennsylvania.

R. V. O'Neill
What Are the Minimal Mathematics Requirements Necessary to Produce Quality Research in Ecology, AIBS Conference, September 1968, Columbus, Ohio.

Radiocesium Turnover and Energy Flow in a Forest Centipede Population, AIBS Conference, September 1968, Columbus, Ohio.

P. T. Perdue, J. H. Thorngate, and M. D. Brown
The Use of Zone Refining to Purify Organic Scintillators Used for Neutron Detection, Health Physics Society, June 8 Through 12, 1969, Pittsburgh, Pennsylvania.

D. E. Reichle
Soil Fauna in Decomposition Processes, International Biological Program Meeting on Temperate Forest Productivity, July 29–31, 1968, Gatlinburg, Tennessee.

T. Saigusa
Calculation of Spectra of Recoil Heavy Particles, Health Physics Society, June 8 Through 12, 1969, Pittsburgh, Pennsylvania.

H. C. Schweinler
$C_{6v} = C_2 \times C_{3v}$ and $D_6 = C_2 \times D_3$, American Physical Society, November 25–27, 1968, Miami Beach, Florida.

H. C. Schweinler and J. W. McKeever
Potential Energy and Vibrational Wave Functions for HBr^{81}, American Physical Society, February 3–6, 1969, New York, New York.

Shuang-Yuan Shieh
Phase Aspect of the Plasma Resonance Absorption in Thin Metal Films, American Physical Society, November 25–27, 1968, Miami Beach, Florida.

S. Y. Shieh and R. H. Ritchie
Crucial Tests for Surface Plasmon Theory of Smith-Purcell Effect, American Physical Society, November 25–27, 1968, Miami Beach, Florida.

A. F. Shinn
Radiation Effects on Social Structure and Survival of Honeybee Populations, Symposium on Radiation Effects in Man's Environment, Health Physics Society, 14th Annual Meeting, June 8–12, 1969, Pittsburgh, Pennsylvania.

U.S. Food Supply, Reserves, and Distribution, Civil Defense Research Project, Annual Information Meeting, ORNL, April 9, 1969, Oak Ridge, Tennessee.

W. S. Snyder, Mary R. Ford, J. R. Muir, and G. G. Warner[2]
Fluctuations of Daily Excretion of Plutonium and Their Interpretation for Estimation of the Body Burden, Health Physics Society Midyear Symposium on Operational Monitoring – A Continuing Challenge; January 28–31, 1969; Los Angeles, California.

W. S. Snyder and G. G. Warner[2]
Dose to Body Organs from a Source of Photons in One of Them: Validity of the Reciprocity Theorem, First European Congress on Radioprotection, October 9–11, 1968, Menton, France.

J. A. Stockdale, R. N. Compton, and P. W. Reinhardt

Measurements of Some Negative Ion–Molecule Reaction Cross Sections in the Region from 0 to 2 eV, 21st Annual Gaseous Electronics Conference, October 16–18, 1968, Boulder, Colorado.

Detection of Autoionization Electrons from the Dissociative State of CO_2^- near 4 eV by a Scavenger Technique, American Physical Society, February 3–6, 1969, New York, New York.

Tsuneo Tamura

Soil Processes Related to Environmental Pollution, September 19, 1968, Mountain View Hotel, Gatlinburg, Tennessee.

F. G. Taylor

Effects of Beta Radiation on Pine and Oak Trees, Association of Southeastern Biologists, April 18, 1969, Memphis, Tennessee.

W. A. Thomas

Calcium Turnover by Dogwood Trees, Soil Science Society of America, November 9–14, 1968, New Orleans, Louisiana.

J. H. Thorngate

Neutron and Gamma-Ray Spectrometry in Radiobiological Research, DASA Medical Coordination Conference, Air Force Weapons Laboratory, May 27 Through 29, 1969, Kirtland AFB, New Mexico.

J. H. Thorngate and D. R. Johnson

Neutron Spectra in Air at Large Distances from a Source of 14 Mev Neutrons, Health Physics Society, June 8 Through 12, 1969, Pittsburgh, Pennsylvania.

Isabel H. Tipton

Analysis of Biological Materials, St. Louis Section of Society for Applied Spectroscopy and St. Louis Society of Analysts, November 25, 1968, St. Louis, Missouri.

Long-Term Studies of Elemental Intake and Excretion of Three Adult Male Subjects, Mid-America Symposium on Spectroscopy, May 15, 1969.

Analytical Methods for the Determination of Trace Elements – Standard Man Studies, University of Missouri Third Annual Conference on Trace Substances in Environmental Health, June 25, 1969, Columbia, Missouri.

J. E. Turner

Calculations of the Penetration of Charged Particles Through Matter at Very High Energies, American Physical Society, April 28–May 1, 1969, Washington, D.C.

R. I. Van Hook and D. A. Crossley, Jr.

Uses of Radiochromium in Insect Ecology, National Meeting of Entomological Society of America, December 2–5, 1968, Dallas, Texas.

O. E. Wagner

Electron Affinities of Radicals Obtained by the Salt-Filled Matrix Method, American Physical Society, November 25–27, 1968, Miami Beach, Florida.

M. W. Williams, R. A. MacRae, and E. T. Arakawa

Electronic Structure of Liquids from Optical Measurements – II. Studies on Benzene, American Physical Society, November 25–27, 1968, Miami Beach, Florida.

J. P. Witherspoon

Retention of a Fallout Simulant by Pine and Oak Trees, Association of Southeastern Biologists, April 18, 1969, Memphis, Tennessee.

Effects of Fast Neutrons on Plants and Plant Communities, Health Physics Society, June 9, 1969, Pittsburgh, Pennsylvania.

Martin Witkamp

External Factors Influencing Mineralization and Immobilization of Some Radionuclides from Tree Litter, IAEA Symposium on the Use of Isotopes and Radiation in Soil Organic-Matter Studies, July 15–19, 1968, Vienna, Austria.

Systems Analysis and Analog Computer Simulation of Transfer of Isotopic Minerals in Microbial Food Chains, Symposium on Microbial Ecology: Methodology and Momentum, 69th Annual Meeting, American Society for Microbiology, May 4–9, 1969, Miami Beach, Florida.

Publications

M-E. M. Abu-Zeid, L. G. Christophorou, J. G. Carter, R. D. Birkhoff, and J. A. Harter

"Emission and Decay of Excited Organic Molecules Under Electron Impact," *IEEE Trans. Nucl. Sci.* **NS-15**(3), 117–21 (1968).

E. T. Arakawa and M. W. Williams

"Optical Properties of Aluminum Oxide in the Vacuum Ultraviolet," *J. Phys. Chem. Solids* **29**, 735–44 (1968).

J. C. Ashley and R. H. Ritchie

"Quantum Treatment of Multiple Real Transitions," *Phys. Rev.* **174**, 1572–77 (1968).

"Double-Plasmon Excitation in a Free Electron Gas," submitted for publication in the *Physical Review.*

S. I. Auerbach

Progress Report in Postattack Ecology, ORNL-TM-2466 (March 1969).

S. I. Auerbach with W. F. Blair, D. M. Gates, F. R. Inger, and B. H. Ketchum

The Importance of Ecology and the Study of Ecosystems, Joint House-Senate Colloquium to Discuss a National Policy for the Environment, 1968.

J. A. Auxier

Report of Trip Abroad by J. A. Auxier During Period February 10 Through 24, 1969, internal memorandum (Mar. 20, 1969).

"Kerma Versus First Collision Dose: The Other Side of the Controversy," *Health Phys.* **17**. 342 (1969).

"Multilaboratory Intercomparisons and Standardization of Nuclear Accident Dosimetry Systems," to be published in *Proceedings of Panel on "Nuclear Accident Dosimetry Systems," February 17 Through 21, 1969, Vienna, Austria.*

J. A. Auxier, K. Becker, and E. M. Robinson, eds.

Proceedings of the Second International Conference on Luminescence Dosimetry, September 23 Through 26, 1968, Gatlinburg, Tennessee, CONF-680920 (November 1968), 1021 pp.

J. A. Auxier and M. D. Brown

"Neutron Cross-Sections and Reaction Products for H, C, N, and O for the Energy Range from Thermal to 15 MeV," *Proceedings of the First International Congress of Radiation Protection, September 5 Through 10, 1966, Rome, Italy,* vol. 2, pp. 853–59, Pergamon, New York, 1968.

C. E. Baker and P. B. Dunaway

"Retention of ^{134}Cs as an Index to Metabolism in the Cotton Rat (*Sigmodon hispidus*)," *Health Phys.* **16**, 227–30 (1969).

G. M. Begun and R. N. Compton

"Threshold Electron Impact Excitation and Negative Ion Formation in XeF_6 and XeF_4," submitted for publication in the *Journal of Chemical Physics.*

K. Becker

Report on Trip to Interlaken, Switzerland, and Braunschweig, Germany, by K. Becker During Period May 25 to June 5, 1968, internal memorandum (July 30, 1968).

Report on Trip to Copenhagen by K. Becker August 29 to September 10, 1968, internal memorandum (Oct. 15, 1968).

Report on Trip to Canada by K. Becker October 28 and 29, 1968, internal memorandum (Nov. 14, 1968).

"Range and Depth Dose Distribution of Low Energy Charged Particles in Dosimeter Glasses," *Proceedings of the First International Congress of Radiation Protection, September 5 Through 10, 1966, Rome, Italy,* vol. 1, pp. 135–40, Pergamon, New York, 1968.

"Some Studies on Radiation Dosimetry by Thermally Stimulated Exoelectron Emission (TSEE)," *Proceedings of the Second International Conference on Luminescence Dosimetry, September 23 Through 26, 1968, Gatlinburg, Tennessee,* CONF-680920, pp. 200–19 (November 1968).

"Neutronen-Personendosimetrie durch Kernspurregistrierung in Festkorpern," *Atompraxis* **14**, 331–36 (1968).

"The Effect of Oxygen and Humidity on Charged Particle Registration in Organic Foils," *Radiation Res.* **36**, 107–18 (1968).

"Nuclear Track Registration in Solids by Etching," *Biophysik* **5**, 207–22 (1968).

"Personnel Dosimetry in Large-Scale Nuclear Emergencies," *Radiological Protection of the Public in a Nuclear Mass Disaster,* pp. 175–86, Fachverband fur Strahlenschutz, Interlaken, 1968.

"Alpha Particle Registration in Plastics and Its Applications for Radon and Neutron Personnel Dosimetry," *Health Phys.* **16**, 113–23 (1969).

"Thermally Stimulated Exoelectron Emission (TSEE) as a Method for Sensitive Dose Measurements Using Unactivated Lithium Fluoride." *Health Phys.* **16**, 527–32 (1969).

"Radiological Protection of the Public in Large-Scale Nuclear Emergencies," *Health Phys.* **16**, 788–89 (1969).

"Radiophotoluminescence Dosimetry Bibliography II," to be published in *Health Physics.*

K. Becker and J. A. Auxier

"Progress in Luminescence Dosimetry," *Science* **164**, 974–78 (May 23, 1969).

K. Becker, R. H. Boyett, and D. R. Johnson

"Some Applications of the Track Etching Process in Radiation Protection," to be published in *Proceedings of the International Topical Conference on Nuclear Track Registration in Insulating Solids, May 6 Through 9, 1969, Clermont-Ferrand, France.*

K. Becker and N. Chantanakom

"On the LET Dependence of Thermally Stimulated Exoelectron Emission," *Nucl. Instr. Methods* **66**, 353–54 (1968).

"On the Thermal Fading Characteristics of Some TSEE Dosimetry Materials," to be published in *Atompraxis.*

K. Becker and J. S. Cheka

"LET Effects on the Radiophotoluminescence in Silver-Activated Dosimeter Glasses," *Proceedings of the Second International Conference on Luminescence Dosimetry, September 23 Through 26, 1968, Gatlinburg, Tennessee,* CONF-680920, pp. 501–17 (November 1968).

"Low-*Z* Radiophotoluminescent Glasses Based on Lithium Borate," *Proceedings of the Second International Conference on Luminescence Dosimetry, September 23 Through 26, 1968, Gatlinburg, Tennessee,* CONF-680920, pp. 148–60 (November 1968).

"Silver-Activated Lithium Borate Glasses as Radiophotoluminescence Dosimeters with Low Energy Dependence," *Health Phys.* **16**, 125–33 (1969).

K. Becker and E. M. Robinson

"Integrating Dosimetry by Thermally Stimulated Exoelectron (After-) Emission," *Health Phys.* **15**, 463–66 (1968).

R. D. Birkhoff, J. E. Turner, V. E. Anderson, J. M. Feola, and R. N. Hamm
"The Determination of LET Spectra from Energy Proportional Pulse-Height Measurements – I. Track-Length Distributions in Cavities," to be published in *Health Physics.*

R. E. Blanco and K. E. Cowser
Waste Treatment and Disposal Semiannual Progress Report, July–December 1967, ORNL-TM-2294 (January 1969).

R. P. Blaunstein and L. G. Christophorou
"Electron Attachment to Halogenated Aliphatic Hydrocarbons," *J. Chem. Phys.* **49**, 1526–31 (1968).

B. G. Blaylock
"The Effects of Ionizing Radiation on Interspecific Competition," *Symposium on Radioecology,* ed. by D. J. Nelson and F. C. Evans, USAEC-CONF-670503, 774 pp.

"The Fecundity of a *Gambusia affinis affinis* Population Exposed to Chronic Environmental Radiation," *Radiation Res.* **37**, 108–17 (1969).

B. G. Blaylock with P. G. Koehler
"Terminal Chromosome Rearrangements in *Chironomus riparius*," *Am. Naturalist* (in press).

B. G. Blaylock and T. J. Mitchell
"The Effect of Temperature on the Dose Response of *Gambusia affinis affinis* from Two Natural Populations," *Radiation Res.* (in press).

W. J. Boegley, Jr., F. M. Empson, W. C. McClain, and F. L. Parker
"Disposal of High Activity Power Reactor Wastes in Salt Mines: Mine Renovations Required for Project Salt Vault," *Nucl. Eng. Design* **8**, 360–66 (1968).

W. J. Boegley, Jr., and W. L. Griffith
"Utility Tunnels for Urban Areas," *Proceedings of the Eighth Annual Environmental and Water Resources Engineering Conference, Vanderbilt University, June 5–6, 1969* (in press).

"Utility Tunnels Enhance Urban Renewal Areas," *Am. City* (February 1969).

W. J. Boegly, Jr., W. L. Griffith, and K. P. Nelson
Conceptual Design of a Dual-Use Utility Tunnel Blast Shelter for White Plains, New York, ORNL-4362 (March 1969).

W. J. Boegly, Jr., D. G. Jacobs, T. F. Lomenick, and O. M. Sealand
Deep Well Injection of Brine Effluents from Inland Desalting Plants, ORNL-TM-2453 (January 1969).

W. J. Boegly, Jr., F. L. Parker, and E. G. Struxness
"Disposal of Radioactive Wastes in Geologic Formations," pp. 701–11 in *Proceedings of the First International Congress of Radiation Protection, Held at Rome, Italy, September 5–10, 1966,* Pergamon, Oxford and New York, 1968.

L. Bouby, R. N. Compton, and A. Souleyrol
"Formation d'ions negatifs dans l'alcool allylique et l'acroleine," *Compt. Rend. Acad. Sci. Paris* **266**, 1250 (1968).

R. H. Boyett, D. R. Johnson, and K. Becker
"Some Studies on the Chemical Damage Mechanism Along Charged Particle Tracks in Polymers," to be published in *Radiation Research.*

R. L. Bradshaw, F. M. Empson, W. C. McClain, and B. L. Houser
"Results of a Demonstration and Other Studies of the Disposal of High Level Solidified Wastes in a Salt Mine," *Health Phys.* (in press).

R. L. Bradshaw and W. C. McClain
"Roof Bolt Test and Application in Supporting a Two-Foot-Thick Roof Bed," *Proceedings Third Symposium on Salt, April 1969, Cleveland, Ohio* (in press).

R. L. Bradshaw and Florentino Sanchez
"Migration of Brine Cavities in Rock Salt," *J. Geophys. Res.* (in press).

E. L. Chaney and L. G. Christophorou
"Electron Attachment to N_2O," to be published in the *Journal of Chemical Physics.*

E. L. Chaney, L. G. Christophorou, P. M. Collins, and J. G. Carter
"Electron Attachment in the Field of Ground and Excited Electronic States of the Azulene Molecules," submitted for publication in the *Journal of Chemical Physics.*

J. S. Cheka
"Long Term Stability of Radiophotoluminescence in Metaphosphate Glass," *Health Phys.* **15**, 363–68 (1968).

Distribution of Radiation from a 14 MeV Neutron Source in and near Structures, to be published as CEX-65.13.

J. S. Cheka and K. Becker
"High Dose-Level Glass Dosimeters with Low Dependence on Energy," to be published in *Nuclear Applications.*

L. G. Christophorou
Report of Foreign Travel to Greece, England, France, Italy, and North Wales March 10 Through April 19, 1969, internal memorandum.

L. G. Christophorou, M-E. M. Abu-Zeid, and J. G. Carter
"Emission and Decay of Liquid Benzene and Naphthalene Derivatives Excited by Electron Impact," *J. Chem. Phys.* **49**, 3775–82 (1968).

L. G. Christophorou and R. P. Blaunstein
"Nondissociative Electron Attachment to Aromatic Hydrocarbons," *Radiation Res.* **37**, 229–45 (1969).

L. G. Christophorou and J. G. Carter
"Energy Lost by Slow Electrons in Collisions with Molecules," *Chem. Phys. Letters* **2**, 607–9 (1968).

L. G. Christophorou, J. G. Carter, and A. A. Christodoulides
"Long-Lived Parent Negative Ions in *p*-Benzoquinone Formed by Electron Capture in the Field of the Ground and Excited States," *Chem. Phys. Letters* **3**, 237–40 (1969).

L. G. Christophorou, E. L. Chaney, and A. A. Christodoulides
"Electron Attachment and 'Carrier Gas' Energy Distribution Functions," to be published in *Chemical Physics Letters.*

L. G. Christophorou and A. A. Christodoulides
"Scattering of Thermal Electrons by Polar Molecules," *J. Phys. B* **2**, 71–85 (1969).

R. N. Compton and R. H. Huebner
"Collisions of Low-Energy Electrons with Molecules: Excitation and Negative Ion Formation," to be published in *Advances in Radiation Chemistry* (ed. by J. L. Magee).

"Temporary Attachment of Electrons to Azulene-h_8 and Azulene-d_8," submitted for publication in the *Journal of Chemical Physics.*

R. N. Compton, J. A. Stockdale, and P. W. Reinhardt
"Electron Impact Excitation and Negative Ion Formation in NH_3 and ND_3," *Phys. Rev.* **180**, 111–20 (1969).

James J. Cowan and E. T. Arakawa
"Dispersion of Surface Plasmons in Dielectric Metal Coatings on Concave Diffraction Gratings," submitted for publication in the *Physical Review.*

J. J. Cowan, E. T. Arakawa, and L. R. Painter
"Time Studies of the Polarization Due to Gratings," *Appl. Optics* (in press).

K. E. Cowser, W. S. Snyder, and E. G. Struxness
"Application of ICRP Recommendations Relevant to Internal Dose," *Proceedings of the Symposium on Public Health Aspects of Peaceful Uses of Nuclear Explosives, April 7–11, 1969, Las Vegas, Nevada* (in press).

Julian Crowell and R. H. Ritchie
"Radiative Decay of Coulomb Stimulated Plasmons in Spheres," *Phys. Rev.* **172**, 436–40 (1968).

J. W. Curlin
"Models of the Hydrologic Cycle," *Analysis of an Ecosystem: The Temperate Deciduous Forest* (in press).

"Nutrient Cycling as a Factor in Site Productivity and Forest Fertilization," *Proceedings North American Forest Soils Conference* (in press).

J. W. Curlin with H. C. Jones III
"The Role of Fertilizers in Improving the Hardwoods of the Tennessee Valley," *Forest Fertilization, Theory and Practice,* Tennessee Valley Authority, Muscle Shoals, Ala., 1969.

J. W. Curlin with W. M. Snyder
Walker Branch Watershed Project: Hydrologic Analysis and Data Processing, ORNL-4392 (1969).

R. C. Dahlman
"Root Production and Turnover of Carbon in the Root-Soil Matrix of a Grassland Ecosystem," pp. 11–12 in *Methods of Productivity Studies in Root Systems and Rhizosphere Organisms,* ed. by M. S. Ghilarov.

R. C. Dahlman and S. I. Auerbach
Preliminary Estimation of Erosion and Radiocesium Redistribution in a Fescue Meadow, ORNL-TM-2343 (November 1968).

R. C. Dahlman and P. B. Dunaway
"Behavior of ^{137}Cs Tagged Particles in a Fescue Meadow," *IAEA Seminar on Agricultural and Public Health Aspects of Environmental Contamination by Radioactive Materials, Vienna* (in press).

R. C. Dahlman and Clair L. Kucera
"Tagging Native Grassland Vegetation with Carbon-14," *Ecology* **49**(6), 1199–1203 (1969).

Carbon-14 Cycling in the Root and Soil Components of a Prairie Ecosystem, pp. 652–60 in *Proceedings Second National Symposium on Radioecology,* ed. by D. J. Nelson and F. E. Evans, CONF-670503 (1969).

R. C. Dahlman, J. S. Olson, and Kenneth Doxtader
"The Nitrogen Economy of Grassland and Dune Soils," pp. 54–82 in *Proceedings of Biology and Ecology of Nitrogen Conference,* 1969.

Patricia Dalton and J. E. Turner
"New Evaluation of Mean Excitation Energies for Use in Radiation Dosimetry," *Health Phys.* **15**, 257–62 (1968).

F. J. Davis and D. R. Nelson
"Pseudo-First-Order Attachment Rates of Thermal Electrons by SF_6 in Different Carrier Gases," *Chem. Phys. Letters* (in press).

Wallace de Laguna
"Importance of Deep Permeable Disposal Formations in Location of a Large Nuclear-Fuel Reprocessing Plant," pp. 21–31 in *Subsurface Disposal in Geologic Basins – a Study of Reservoir Strata – Memoir No. 10,* The American Association of Petroleum Geologists, 1968.

"Isotopes in Hydrology, Proceedings of a Symposium" (book review), *Health Phys.* **15**(5), 472–73 (November 1968).

"Tritium and Other Environmental Isotopes in the Hydrological Cycle" (book review), *Nucl. Appl.* **4**, 448–49 (June 1968).

Wallace de Laguna, Tsuneo Tamura, H. O. Weeren, E. G. Struxness, W. C. McClain, and R. C. Sexton
Engineering Development of Hydraulic Fracturing as a Method for Permanent Disposal of Radioactive Wastes, ORNL-4259 (August 1968).

L. T. Dillman
"Radionuclide Decay Schemes and Nuclear Parameters for Use in Radiation-Dose Estimation," MIRD Pamphlet No. 4, suppl. No. 2, *J. Nucl. Med.* (March 1969).

"Average Particle Energy in Beta Decay," submitted to *Health Physics.*

P. B. Dunaway
" 'Perfect' Polydactylism in Hind Feet of a Gray Squirrel," *Am. Midland Naturalist* **81**, 244–47 (1969).

P. B. Dunaway, L. L. Lewis, J. D. Story, J. A. Payne, and J. M. Inglis
"Radiation Effects in the Soricidae, Cricetidae, and Muridae," pp. 173–84 in *Proceedings Second National Symposium on Radioecology,* ed. by D. J. Nelson and F. C. Evans, CONF-670503 (1969).

P. B. Dunaway with G. E. Cosgrove and J. D. Story
"Malignant Tumors Associated with Subcutaneously Implanted ^{60}Co Wires in *Peromyscus maniculatus,*" *Bull. Wildlife Disease Assoc.* (in press).

P. D. Dunaway with T. P. O'Farrell
"Effect of Acute Ionizing Radiation on Incorporation of ^{131}TUDR by Cotton Rats, *Sigmodon hispidus,*" *Radiation Res.* **38**, 109–24 (1969).

P. B. Dunaway with K. B. Jacobson and J. B. Murphy
"Phylogenetic Relationships in a Group of Rodents on the Basis of Isoenzymes of Lactate Dehydrogenase," *Comp. Biochem. Physiol.* **28**, 1135–44 (1969).

J. W. Elwood and T. F. Waters
"Effects of Floods on Food Consumption and Production Rates of a Stream Brook Trout Population," *Trans. Am. Fisheries Soc.* **98**, 253–62 (1969).

L. C. Emerson
"Summary of Second International Conference on Vacuum Ultraviolet Radiation Physics – Interaction with Solids," *Phys. Today* **21**(12), 95–99 (1968).

F. M. Empson
"An Introduction to Radioactivity for Engineers" (book review), *Ind. Eng. Chem.* **61**(41), 7–8 (1969).

F. M. Empson, R. L. Bradshaw, W. C. McClain, and B. L. Houser
"Results of the Operation of Project Salt Vault: A Demonstration of Disposal of High Level Radioactive Solids in Salt," *Proceedings Third Symposium on Salt, April 21–25, 1969, Cleveland, Ohio* (in press).

B. R. Fish
"Radiation in Perspective – the Role of Nuclear Energy in the Control of Air Pollution," *Nucl. Safety* **10**(2), 119 (1969).

H. L. Fisher, Jr., and W. S. Snyder
"Distribution of Dose in the Body from a Source of Gamma Rays Distributed Uniformly in an Organ," p. 1473 in *Proc. First Intern. Congress on Radiation Protection,* ed. by W. S. Snyder *et al.,* vol. 2, Pergamon, Oxford, 1968.

W. R. Garrett
"Non-Adiabatic Target Distortion in Low-Energy Electron and Positron Scattering," *Phys. Rev.* **178**, 210–17 (1969).

W. R. Garrett and L. D. Mullins
"*l*-Averaged Exchange Term in the Hartree-Fock Equations," *J. Chem. Phys.* **48**, 4140–43 (1968).

W. R. Garrett, J. E. Turner, and V. E. Anderson
Analysis of Ground-State Energy Eigenfunctions for Finite Dipole, ORNL-4431 (in preparation).

"A Spherical Coordinate Analysis of Ground-State Energy Eigenfunctions for an Electron in the Field of a Finite Dipole," submitted for publication in the *Physical Review.*

M. Gerrard
"Tagging of Small Animals with Radioisotopes for Tracking Purposes," *Isotopes Radiation Technol.* **6**, 200–204 (1969).

T. F. Gesell, E. T. Arakawa, and T. A. Callcott
"Exo-Electron Emission During Oxygen and Water Chemisorption on Fresh Magnesium Surfaces," submitted for publication in *Physical Review Letters.*

M. Goolsby
"How Does Nuclear Radiation Affect Honey Bees?" *Am. Bee J.* **108**, 352–53 (1969).

A. J. P. Gore
"The Supply of Six Elements by Rain to an Upland Peat Area," *J. Ecol.* (1969).

"Interaction Between Modeling and Experiment in an Eriophorum/Calluna Ecosystem," pp. 36–39 in *Proceedings Working Meeting on Analysis of Ecosystems Tundra Zone, Ustaoset, Norway,* 1968.

D. F. Grigal and H. F. Arneman
"Numerical Classification of Some Forested Minnesota Soils," *Soil Sci. Soc. Am., Proc.* **33**, 433–38 (1969).

J. T. Grissom and R. N. Compton
"Electron Impact Excitation and Ionization of Helium near 60 eV," submitted for publication in *Physical Review Letters.*

J. D. Hayes, E. T. Arakawa, and M. W. Williams
"Optical Properties of Vacuum Evaporated Selenium and Tellurium," *J. Appl. Phys.* **39**, 5527–32 (1968).

V. G. Horton, E. T. Arakawa, R. N. Hamm, and M. W. Williams
"A Triple-Reflection Polarization for Use in the Vacuum Ultraviolet," to be published in *Applied Optics.*

H. H. Hubbell, Jr., E. T. Arakawa, Shogo Nagaoka, Shoichi Ueda, and Sunao Tanaka
The Epicenters of the Atomic Bombs. I. An Estimate Based on Thermal Ray Shadows – Nagasaki, ABCC TR 5-66 (1968).

H. H. Hubbell, T. D. Jones, and J. S. Cheka
The Epicenters of the Atomic Bombs in Japan. II. Reevaluation of All Available Data and Our Recommended Values, to be published as an ABCC Technical Report.

R. H. Huebner, R. N. Compton, and H. C. Schweinler
"Temporary Negative Ion Resonance of Pyridine," *Chem. Phys. Letters* **2**, 407–8 (1968).

G. S. Hurst and J. E. Turner
Elementary Radiation Physics, Wiley, New York, 1969.

D. G. Jacobs
Sources of Tritium and Its Behavior upon Release to the Environment, AEC Critical Review Series, USAEC Division of Technical Information Extension, Oak Ridge, Tennessee, December 1968.

D. G. Jacobs, P. S. Rohwer, and K. E. Cowser
Third Quarterly Progress Report on the Theoretical Evaluation of Consumer Products from Project Gasbuggy, ORNL-TM-2657 (July 1969).

D. G. Jacobs, E. G. Struxness, and M. J. Kelly
First Quarterly Progress Report on the Theoretical Safety Evaluation of Consumer Products from Project Gasbuggy, ORNL-TM-2427 (February 1969).

D. R. Johnson, R. H. Boyett, and K. Becker
"Some Studies on the Chemical Damage Mechanism Along Charged Particle Tracks in Polymers," to be published in *Proceedings of the International Topical Conference on Nuclear Track Registration in Insulating Solids, May 6 Through 9, 1969, Clermont-Ferrand, France.*

D. R. Johnson, J. H. Thorngate, and P. T. Perdue
"A Sensitive Spectrometer for Fast Neutrons Using ^{6}LiI(Eu)," to be published in *Nuclear Instruments and Methods.*

T. D. Jones
Report of Trip to Japan by T. D. Jones During Period November 29, 1968, to January 28, 1969, internal memorandum (Apr. 8, 1969).

T. D. Jones, J. A. Auxier, J. W. Poston, and D. R. Johnson
"Dose Distribution Functions for Neutrons and Gamma Rays in Anthropomorphous and Radiological Phantoms," pp. 1461–67 in *Proceedings of the First International Congress of Radiation Protection, September 5 Through 10, 1966, Rome, Italy,* vol. 2, Pergamon, 1968.

S. V. Kaye
"Distribution and Retention of Orally Administered Radiotungsten in the Rat," *Health Phys.* **15**, 399–417 (1968).

S. V. Kaye and S. J. Ball
"Systems Analysis of a Coupled Compartment Model for Radionuclide Transfer in a Tropical Environment," *Symposium on Radioecology,* CONF-670503 (1969).

S. V. Kaye and P. S. Rohwer
"Methods of Estimating Population Exposures from Plowshare Applications," *Proceedings of Symposium on Public Health Aspects of Peaceful Uses of Nuclear Explosives* (in press).

S. V. Kaye, P. S. Rohwer, K. E. Cowser, and W. S. Snyder
"Predicting Radiation Dose Equivalents for Populations: I. Dose Models and Methods of Application," *BioScience* **19**, 238–41 (1969).

T. M. Kegley, Jr., and F. M. Empson
Examination of Modified Pillar and Simulated Waste Container Test Heaters, ORNL-TM-2422 (January 1969).

J. M. Kelly, P. A. Opstrup, J. S. Olson, S. I. Auerbach, and G. M. Van Dyne
Models of Seasonal Primary Productivity in Eastern Tennessee Festuca *and* Andropogon *Ecosystems,* ORNL-4310.

M. J. Kelly, P. S. Rohwer, D. G. Jacobs, and C. R. Bowman
Second Quarterly Progress Report on the Theoretical Evaluation of Consumer Products from Project Gasbuggy, ORNL-TM-2513 (March 1969).

G. D. Kerr and J. S. Cheka
"A Lithium-7 Phosphate Glass Detector for Exposure Measurements in Mixed Neutron Gamma-Ray Radiation Fields," *Health Phys.* **16**, 231 (1969).

G. D. Kerr and D. R. Johnson
Radiation Survey and Dosimeter Intercomparison Study at the Health Physics Research Reactor, ORNL-TM-2334 (November 1968).

J. T. Kitchings III, P. B. Dunaway, and J. D. Story
"Uptake and Excretion of ^{134}Cs from Fallout Simulant and Vegetation by Cotton Rats," *Health Phys.* (in press).

J. T. Kitchings III, P. B. Dunaway, J. D. Story, and L. E. Tucker
"Use of Radioiron (^{59}Fe) as an Index to Hemopoietic Damage Caused by Ionizing Radiation," *J. Tenn. Acad. Sci.* **43**, 85–87 (1968).

C. E. Klots

"Energy Deposition Mechanisms," chap. 1, pp. 1–57 in *Fundamental Processes of Radiation Chemistry* (ed. by Pierre Ausloos), Wiley, New York, 1968.

"The Interpretation of Geminate Scavenging Yields," submitted for publication in the *Journal of Physical Chemistry.*

"Transition Yields in Irradiated Gases," in *Proceedings International Conference on Radiation Chemistry* (in press).

"Yield of Resonance States in Irradiated Argon," *Chem. Phys. Letters* **2**, 645–46 (1968).

S. Kolehmainen with E. Häsänen and J. K. Miettinen

"Biological Half-Times of ^{137}Cs and ^{22}Na in Different Fish Species and Their Temperature Dependence," pp. 401–6 in *Proceedings First International Congress on Radiological Protection,* ed. by W. S. Snyder, vol. 1, 1968.

S. Kolehmainen, E. Häsänen, and J. K. Miettinen

"^{137}Cs in Plants, Plankton and Fish of the Finnish Lakes and Factors Affecting Its Accumulation," pp. 407–15 in *Proceedings First International Congress of Radiological Protection,* ed. by W. S. Snyder, vol. 1, 1968.

S. Kolehmainen, H. Romantschuk, S. Takatalo, and J. K. Miettinen

"Pollution Experiments with Cs-137 in Lakes of Two Limnòlogically Different Types," *Congres International sur la Radioprotection du Milieu devant le Developpement des Utilisations Pacifiques de l'Energie Nucleaire,* 1968.

S. Kolehmainen, S. Takatalo, and J. K. Miettinen

"A Tracer Experiment with I-131 in an Oligotrophic Lake," *Symposium on Radioecology,* ed. by D. J. Nelson and F. C. Evans, CONF-670503 (1969).

T. F. Lomenick and R. L. Bradshaw

"Model Pillar Tests for Evaluating the Structural Stability of Openings in Rock Salt Utilized for the Disposal of Radioactive Wastes," *Nucl. Eng. Design* **9**, 269–78 (1969).

"Deformation of Rock Salt in Openings Mined for the Disposal of Radioactive Wastes," *Rock Mech. Eng. Geol.* (in press).

C. R. Malone

"Effects of Diazinon Contamination on an Old-Field Ecosystem," *Am. Midland Naturalist* (in press).

C. R. Malone and D. J. Nelson

"Feeding Rates of Freshwater Snails (*Goniobasis clavaeformis*) Determined with ^{60}Cobalt," *Ecology* (in press).

C. R. Malone and M. B. Swartout

"Size, Mass, and Caloric Content of Particulate Organic Matter in Old-Field and Forest Soils," *Ecology* (in press).

W. C. McClain

"Disposal of Radioactive Wastes by Hydraulic Fracturing: Part V. Site Evaluations," *Nucl. Eng. Design* **9**, 315–26 (1969).

"Rock Mechanics in the Disposal of Radioactive Wastes by Hydraulic Fracturing," *Felsmech. Ingenieurgeol.* **6**, 139–61 (1968).

"The Mechanics of Hydraulic Fractures in Shales," *Proceedings of Third Symposium on Salt, April 21–24, 1969, Cleveland, Ohio* (in press).

W. C. McClain and R. L. Bradshaw

"The Disposal of Solidified Radioactive Wastes in Salt Mines," *Mines Mag.* (in press).

W. J. McConnell and R. D. Birkhoff

"Response of an Electron Spectrometer at Low Energies," *Nucl. Instr. Methods* **69**, 209–12 (1969).

R. H. Monheimer

"Interaction Between *Clostridium botulinum* Type E Toxin in White Mice," *Nature* **222**, 788–89 (1969).

K. Z. Morgan
"Protection Against Ionizing Radiation," *Salt* **4**, 8–23 (Autumn 1967).

"Common Sources of Human Exposure to Ionizing Radiation in the United States," *Am. Engr.*, pp. 38–42 (July 1968).

"Risks from Diagnostic X-Rays," *Yale Sci. Mag.* **43**, 2–5, 25 (February 1969).

"You of the Medical Profession Could and Should Take a Far Greater Role in Reducing Unnecessary Patient X-Ray Exposure," *Consultant*, to be published.

K. Z. Morgan and J. E. Turner
"Health Physics," to be published in *American Institute of Physics Handbook.*

O. H. Myers and W. C. McClain
The ORNL Seismograph: Installation and Operation from September 1, 1967, to February 29, 1968, ORNL-CF-68-8-26 (Oct. 31, 1968).

O. H. Myers
The ORNL Seismograph Station ORT: Operation from March 1, 1968, to August 31, 1968 (in press).

W. T. Naff, C. D. Cooper, and R. N. Compton
"Transient Negative Ion States in Alicyclic and Aromatic Fluorocarbon Molecules," *J. Chem. Phys.* **49**, 2784–88 (1968).

D. J. Nelson
"Ecological Behavior of Radionuclides in the Clinch and Tennessee Rivers," pp. 169–87, *Reservoir Fishery Resources Symposium, 1968.*

"Cesium, Cesium-137, and Potassium Concentrations in White Crappie and Other Clinch River Fish," *Symposium on Radioecology*, ed. by D. J. Nelson and F. C. Evans, CONF-670503 (1969).

"Radioecology of Aquatic Organisms" (book review), *Quart. Rev. Biol.* **43**(2), 214 (1968).

"Measurement and Sampling of Outputs from Watersheds," *Analysis of an Ecosystem: The Temperate Deciduous Forest*, ed. by D. E. Reichle (in press).

D. J. Nelson, N. R. Kevern, J. L. Wilhm, and N. A. Griffith
"Estimates of Periphyton Mass and Stream Bottom Area Using Phosphorus-32," *Water Res.* (in press).

D. R. Nelson and F. J. Davis
"Determination of Diffusion Coefficients of Thermal Electrons with a Time-of-Flight Swarm Experiment," to be published in the *Journal of Chemical Physics.*

Jacob Neufeld
"Comments on Quality Factor," *Health Phys.* (in press).

"Radiation Quantities and Their Significance in Health Physics," submitted for publication in *Health Physics.*

"Revised Formulation of the Kinetic Plasma Theory," submitted for publication in the *International Journal of Electronics.*

"Revised Formulation of the Macroscopic Maxwell Theory – I. Fundamentals of the Proposed Formulation," submitted for publication in *Nuovo Cimento.*

"Revised Formulation of the Macroscopic Maxwell Theory – II. Propagation of an Electromagnetic Disturbance in Dispersive Media," submitted for publication in *Nuovo Cimento.*

"Wave Propagation and Group Velocity in Absorbing Media," *Phys. Letters* **29A**(2), 68–69 (1969).

Jacob Neufeld, V. E. Anderson, Harvel Wright, W. S. Snyder, and J. E. Turner
"Effects of Phantom Geometry on Dose Distribution," pp. 1469–72 in *Proceedings First International Congress on Radiation Protection,* Pergamon, New York, 1968.

J. Neufeld, W. S. Snyder, J. E. Turner, Harvel Wright, B. M. Wheatley, and Harold Wyckoff
"Radiation Dose from Neutrons and Protons in the Energy Range from 400 MeV to 2 GeV," *Health Phys.* (in press).

M. Oberhofer and E. M. Robinson
"A High Temperature TSEE G-M Gasflow Counter," to be published in *Kerntechnik.*

J. S. Olson
"Primary Production and Radionuclide Cycling," pp. 60–62 in *Proceedings Working Meeting on Analysis of Ecosystems Tundra Zone, Ustaoset, Norway,* 1968.

"Distribution and Radiocesium Transfers of Roots in Tagged Mesophytic Appalachian Forest in Tennessee," *International Biological Program Symposium on Methods of Productivity Studies in Root Systems and Rhizosphere Organism, 1968.*

J. S. Olson with V. Obenhaus and L. Walford
"Technology and Man's Relation to His Natural Environment," *Human Values and Advancing Technology,* ed. by C. P. Hall, 1967.

J. S. Olson with J. D. Ovington
"Biomass and Chemical Content of El Verde Lower Montane Rain Forest Plants," *A Tropical Rainforest,* ed. by H. T. Odum, USAEC-TID-24270, submitted for publication.

R. V. O'Neill
"Indirect Estimation of Energy Fluxes in Animal Food Webs," *J. Theoret. Biol.* **22**, 284–90 (1968).

"Minimal Mathematical Requirements for Quality Research in Ecology," submitted to *BioScience.*

"Systems Approaches to the Study of Forest Floor Arthropods," to be published in *Ecological Systems Research,* ed. by B. C. Patten.

"A Stochastic Model of Energy Flow in Predator Compartments of an Ecosystem," submitted to *Proceedings International Symposium on Statistical Ecology.*

"Behavior of *Narceus americanus* (Diplopoda) on Slopes and Its Ecological Significance," *Am. Midland Naturalist* **77**, 535–39 (1967).

"Niche Segregation in Seven Species of Diplopods," *Ecology* **48**, 983 (1967).

"Population Energetics of a Millipede, *Narceus americanus* (Beauvois)," *Ecology* **49**, 803–9 (1968).

"Adaptive Responses to Desiccation in the Millipede, *Narceus americanus,*" *Am. Midland Naturalist* **81**, 578–83 (1969).

"Comparative Desiccation Tolerance in Seven Species of Millipedes," to be published in *American Midland Naturalist.*

R. V. O'Neill and C. E. Styron
"Application of Compartment Modeling Techniques to Collembola Population Studies," to be published in *American Midland Naturalist.*

L. Robinson Painter, R. D. Birkhoff, and E. T. Arakawa
"Optical Measurements of Liquid Water in the Vacuum Ultraviolet," *J. Chem. Phys.* (in press).

L. Robinson Painter, R. N. Hamm, E. T. Arakawa, and R. D. Birkhoff
"Electronic Properties of Liquid Water in the Vacuum Ultraviolet," *Phys. Rev. Letters* **21**, 282–84 (1968).

B. C. Patten
"Mathematical Models of Plankton Production," *Int. Rev. Gesamten. Hydrobiol.* **54**(3), 357–408 (1968).

B. C. Patten with Joel S. O'Conner
"Mathematical Models of Plankton Productivity," pp. 207–8 in *Reservoir Fishery Resources Symposium, 1968.*

B. C. Patten and G. M. Van Dyne
"Factorial Productivity Experiments in a Shallow Estuary: Energetics of Individual Plankton Species in Mixed Populations," *Limnol. Oceanogr.* **13**(2), 309–14 (1968).

P. T. Perdue and M. D. Brown
"Effects of Zone Refining on the Pulse Height and Pulse Shape of Anthracene, Trans-Stilbene, and *p*-Quaterphenyl Crystal Scintillators," *Nucl. Instr. Methods* **71**, 113–16 (1969).

J. R. Reed
"Uptake and Excretion of ^{60}Co by Black Bullheads (*Ictalurus melas*)," *Health Phys.* (submitted).

"Uptake and Elimination of Radiotungsten in Black Bullheads (*Ictalurus melas*)," *Health Phys.* (submitted).

J. R. Reed with B. A. Martinedes
"Uptake and Retention of Tungsten-181 by Crayfish," *Health Phys.* (submitted).

J. R. Reed and D. J. Nelson
"Radiostrontium Uptake in Blood and Flesh in Bluegills (*Lepomis macrochirus*)," pp. 226–33 in *Symposium on Radioecology,* ed. by D. J. Nelson and F. C. Evans, CONF-670503 (1969).

D. E. Reichle
"Relation of Body Size to Food Intake, Oxygen Consumption and Trace Element Metabolism in Forest Floor Arthropods," *Ecology* **49**, 538–42 (1968).

Analysis of an Ecosystem: The Temperate Deciduous Forest (ed.), Springer-Verlag, Heidelberg (in press).

"Lethal Effects of Gamma Radiation on Eggs and Larvae of the Bagworm, *Thyridopteryx ephemeraeformis,*" *Ann. Entomol. Soc. Am.* (in press).

D. E. Reichle and D. A. Crossley, Jr.
"Trophic Level Concentrations of Cesium-137, Sodium and Potassium in Forest Arthropods," *Symposium on Radioecology,* ed. by D. J. Nelson and F. C. Evans, CONF-670503 (1969).

D. E. Reichle with D. A. Crossley, Jr.
"Analysis of Transient Behavior of Radioisotopes in Insect Food Chains," *BioScience* **19**, 341–43 (1969).

D. E. Reichle, P. B. Dunaway, and D. J. Nelson
"Turnover and Concentration of Radionuclides in Food Chains," *Nucl. Safety* (in press).

D. E. Reichle with C. A. Edwards and D. A. Crossley, Jr.
"Experimental Manipulation of Soil Invertebrate Populations for Trophic Studies," *Ecology* (in press).

"The Role of Soil Invertebrates in Turnover of Organic Matter and Nutrients," *Analysis of an Ecosystem: The Temperate Deciduous Forest,* ed. by D. E. Reichle, Springer-Verlag, Heidelberg (in press).

D. E. Reichle, M. H. Shanks, and D. A. Crossley, Jr.
"Calcium, Potassium and Sodium Content of Forest Arthropods," *Ann. Entomol. Soc. Am.* **62**, 57–62 (1969).

R. H. Ritchie
"Radiative Decay of Tangential Surface Plasmons," *Phys. Letters* **27A**, 660–62 (1968).

R. H. Ritchie, E. T. Arakawa, J. J. Cowan, and R. N. Hamm
"Surface Plasmon Resonance Effect in Diffraction Gratings," *Phys. Rev. Letters* **21**, 1530–33 (1968).

R. H. Ritchie, F. W. Garber, M. Y. Nakai, and R. D. Birkhoff
"Low-Energy Electron Mean Free Paths in Solids," *Advances in Radiation Biology,* vol. 3 (in press).

R. H. Ritchie and R. E. Wilems
"Photon-Plasmon Interaction in a Non-Uniform Electron Gas," *Phys. Rev.* **178**, 372–81 (1969).

P. S. Rohwer and S. V. Kaye
"Predicting Radiation Dose Equivalents for Populations: II. Results Obtained with the Dose Models," *BioScience* **19**, 326–30 (1969).

T. Saigusa
"Calculation of Spectra of Recoil Heavy Particles," to be published in *Health Physics.*

W. F. Schaffer, Jr., W. J. Boegly, Jr., R. L. Bradshaw, and F. L. Parker
"Project Salt Vault: Design of Equipment," *Nucl. Eng. Design* **8**, 327–36 (1968).

Henry A. Schroeder and Isabel H. Tipton
"The Human Body Burden of Lead," *Arch. Environ. Health* **17**, 965 (1968).

A. F. Shinn
"Vulnerability of Grain Stocks and Food Supplies," *Annual Progress Report, Civil Defense Research Project, March 1967–March 1968,* ORNL-4284, part I, pp. 352–70 (November 1968).

B. M. Smith,[1] Jack Wagman,[1] and B. R. Fish
"Interaction of Airborne Particles with Gases," *Environ. Sci. Technol.* **3**, 558 (June 1969).

W. S. Snyder
"Health Physics Aspects of Supersonic Transport," *Proc. First Intern. Congress of Radiation Protection,* ed. by W. S. Snyder *et al.,* vol. 2, p. 863, Pergamon, Oxford, 1968.

W. S. Snyder, Mary R. Ford, G. G. Warner,[2] and H. L. Fisher, Jr.[3]
"Estimates of Absorbed Fractions for Monoenergetic Photon Sources Uniformly Distributed in Various Organs of a Heterogeneous Phantom," MIRD Pamphlet No. 5, suppl. No. 3, *J. Nucl. Med.* (in press).

W. S. Snyder, H. A. Wright, J. E. Turner, and J. Neufeld
"Calculations of Depth-Dose Curves for High-Energy Neutrons and Protons and Their Interpretation for Radiation Protection," *Nucl. Appl.* **6**, 336–43 (1969).

J. A. Stockdale, R. N. Compton, G. S. Hurst, and P. W. Reinhardt
"Collisions of Monoenergetic Electrons with NO_2: Possible Lower Limits to the Electron Affinities of O_2 and NO," *J. Chem. Phys.* **50**, 2176–80 (1969).

J. A. Stockdale, R. N. Compton, and P. W. Reinhardt
"Measurement of the Cross Sections for the Reactions $H^- + H_2O \rightarrow OH^- + H_2$ and $D^- + D_2O \rightarrow OD^- + D_2$ at Incident Ion Energies near 2 Electron Volts," *Phys. Rev. Letters* **21**, 664–67 (1968).

J. A. D. Stockdale, R. N. Compton, and P. W. Reinhardt
"Studies of Negative Ion–Molecule Reactions in the Energy Region from Zero to Three Electron Volts," *Phys. Rev.* (in press).

D. R. Stone
"Identification of Fission Fragment Tracks in Lexan After Preirradiation to High Doses of Alpha Particles," *Health Phys.* **16**, 772 (1969).

D. R. Stone, E. B. Wagner, T. D. Jones, and W. H. Shinpaugh
"Calculated and Experimentally Determined Neutron Dose Conversion Factor for Californium," to be published in *Health Physics.*

C. E. Styron
"Ecology of Two Populations of an Aquatic Isopod, *Lirceus fontinalis* Raf.," *Ecology* **49**, 629–36 (1968).

Operation and Maintenance of the Madison Research, Inc., Thermoluminescent Dosimetry System, ORNL-CF-68-11-56 (1968).

"Ecology of Two Populations of an Aquatic Isopod (*Lirceus fontinalis* Raf.) with Emphasis on Ionizing Radiation Effects," pp. 53–60 in *Symposium on Radioecology, Ann Arbor, Michigan,* CONF-670503 (1969).

"Taxonomy of Two Populations of an Aquatic Isopod, *Lirceus fontinalis* Raf.," *Am. Midland Naturalist* **80**, (1969).

Operation and Maintenance of the Beckman OMEGA Data Reduction System, ORNL-CF-69-6-9 (1969).

---

[1] National Air Pollution Control Administration, Cincinnati, Ohio 45227.

[2] Mathematics Division, ORNL.

[3] U.S. Public Health Service, Rockville, Md.

C. E. Styron and G. J. Dodson
"Effects of Beta and Gamma Radiation on *Sinella curviseta* (Collembola)," *Progress Report in Postattack Ecology,* ORNL-TM-2466 (1969).

C. E. Styron with W. D. Burbanck, O. G. Goodchild, Elizabeth S. Dennis, and Madeline P. Burbanck
"Chromatographic Studies of Three Species of *Cyathura* (Isopoda, Anthuridae) and *Lirceus fontinalis* (Isopoda, Asellota)," *Verhandl. Intern. Verein Limmol.* **17** (1969).

J. C. Sutherland and E. T. Arakawa
"Optical Properties of Potassium for Photons of Energy 3.96 to 9.69 eV," *J. Opt. Soc. Am.* **58**, 1080–83 (1968).

J. C. Sutherland, R. N. Hamm, and E. T. Arakawa
"Extinction Coefficient and Imaginary Part of the Dielectric Constant for Sodium and Potassium Above the Plasma Energy," submitted for publication in the *Journal of the Optical Society of America.*

Tsuneo Tamura
"Movement of Cesium-137 by Runoff, Erosion, and Infiltration from a Soil Under Different Cover Conditions," pp. 149–67 in *Proceedings of the Symposium Held at Fort Monroe, Virginia, November 6–9, 1967, Under Auspices of Advisory Committee on Civil Defense, Advisory Committee on Emergency Planning, Office of Civil Defense, and Office of Emergency Planning, Postattack Recovery from Nuclear War* (October 1968).

F. G. Taylor
"Oak Ridge, Tennessee, Flora 2: Spring Flowering Dates," *Univ. Tenn. Arboretum Soc. Bull.* **4**(1), 13 (1969).

W. A. Thomas
"Cycling of ^{45}Ca by Dogwood Trees," *Symposium on Radioecology,* ed. by D. J. Nelson and F. C. Evans, CONF-670503 (1969).

"Accumulation and Cycling of Calcium by Dogwood Trees," *Ecol. Monogr.* (in press).

"Decomposition of Loblolly Pine Needles With and Without Addition of Dogwood Leaves," *Ecology* **49**, 568–71 (1968).

"Energy Turnover by Dogwood Trees," *Ecology* (submitted).

"Decomposition of Irradiated Persimmon Leaves," *Radiation Botany* (submitted).

"From Sea to Shining Sea, a Report on the American Environment – Our Natural Heritage (by President's Council on Recreation and Natural Beauty, 1968)" (book review), *J. Am. Med. Assoc.* (in press).

"Weight and Calcium Losses from Decomposing Tree Leaves on Land and in a Stream," *J. Appl. Ecol.* (submitted).

"Retention of ^{45}Ca by Dogwood Trees," *Plant Physiol.* (submitted).

"Accumulation of ^{144}Ce by Hickory and ^{60}Co by Black Gum Seedlings," *J. Exptl. Botany* (submitted).

"The Conquest of Nature. Technology and Its Consequences (by R. J. Forbes)" (book review), *Ecology* (submitted).

W. A. Thomas and D. G. Jacobs
"Curium Behavior in Plants and Soil," *Soil Sci.* (in press).

J. H. Thorngate
"An Experimental Measurement of the High Energy Gamma Rays Produced by the Slowing Down of 14 Mev Neutrons in Air," to be published in *Health Physics.*

J. H. Thorngate and J. A. Auxier
"Fast Neutron Spectrometry for Radioprotection," *Colloque d'Electronique Nucleaire et Radioprotection,* Tome 1, University of Toulouse, 1968.

J. H. Thorngate, D. R. Johnson, and P. T. Perdue
Energy and Angular Distribution of Neutrons and Gamma Rays – Operation HENRE, to be published as CEX-65.11.

Isabel H. Tipton
"Long-Term Studies of Elemental Intake and Excretion of Three Adult Male Subjects," *Proceedings Mid-America Symposium on Spectroscopy* (in press).

"Analytical Methods for the Determination of Trace Elements – Standard Man Studies," *Proceedings Third Annual Conference on Trace Substances in Environmental Health* (in press).

Isabel H. Tipton, Judy C. Johns, and Monica Boyd
"The Variation with Age of Elemental Concentration in Human Tissue," *Proc. First Intern. Congress of Radiation Protection,* ed. by W. S. Snyder *et al.*, vol. 1, p. 759, Pergamon, Oxford, 1968.

Isabel H. Tipton, Peggy L. Stewart, and Judith Dickson
"Patterns of Elemental Excretion in Long-Term Balance Studies," *Health Phys.* **16,** 455 (1969).

L. H. Toburen and M. Y. Nakai
"Double Electron Capture Cross Sections for Incident Protons in the Energy Range 75 to 250 keV," *Phys. Rev.* **177,** 191–96 (1969).

L. H. Toburen, M. Y. Nakai, and R. A. Langley
"Measurement of High-Energy Charge-Transfer Cross Sections for Incident Protons and Atomic Hydrogen in Various Gases," *Phys. Rev.* **171,** 114–22 (1968).

J. E. Turner
Calculations of the Penetration of Charged Particles Through Matter at Very High Energies, to be published as a National Academy of Sciences–National Research Council Report.

"Health Physics: Principles of Radiation Protection (by D. J. Rees, MIT Press, Cambridge, 1967)" (book review), *Nucl. Safety* **9,** 519 (1968).

"Radiation Dosimetry, vol. I, Fundamentals (ed. by F. H. Attix and W. C. Roesch), Academic, New York" (book review), *Nucl. Sci. Eng.* **34,** 199 (1968).

"Where Does Physics Stop and Biology Begin" [book review of *Medical and Biological Physics* (by H. C. Webster and D. E. Robertson, University of Queensland Press, St. Lucia, Queensland, Australia, 1967) and *Radiation Biology* (by Alison P. Casarett, Prentice-Hall, New Jersey, 1968)], to be published in *Physics Today.*

J. E. Turner, V. E. Anderson, R. D. Birkhoff, and D. R. Johnson
"The Determination of LET Spectra from Energy Proportional Pulse-Height Measurements. II. A Monte Carlo Unfolding Procedure," to be published in *Health Physics.*

J. E. Turner, V. E. Anderson, and Kenneth Fox
"Ground-State Energy Eigenvalues and Eigenfunctions for an Electron in an Electric Dipole Field," *Phys. Rev.* **174,** 81–89 (1968).

Ground-State Energy Eigenvalues and Eigenfunctions for an Electron in an Electric-Dipole Field, ORNL-4297 (December 1968).

J. E. Turner, V. E. Anderson, H. A. Wright, W. S. Snyder, and J. Neufeld
"Radiation Dose from High-Energy Nucleons in Targets Containing Soft Tissue and Bone," *Radiation Res.* **35,** 596–611 (1968).

J. E. Turner and Hal Hollister
"RBE, LET, z, v; Some Further Thoughts," *Health Phys.* (in press).

J. E. Turner, V. N. Neelavathi, R. B. Vora, T. S. Subramanian, and M. A. Prasad
"Contributions of Spin, Anomalous Magnetic Moment, and Form Factors to the Stopping Power of Matter for Protons and Muons at Extreme Relativistic Energies," *Phys. Rev.* (in press).

J. E. Turner, Patricia Dalton Roecklein, and R. B. Vora
"Mean Excitation Energies for Chemical Elements," submitted for publication in *Health Physics.*

James E. Turner and Robert W. Wood
"Atomic, Molecular, and Nuclear Disciplines Combine in Health Physics," *Phys. Today* **21**(11), 107 (1968).

J. E. Turner, H. A. Wright, and J. H. Grossen
"A New Model for Calculation of High-Energy Nucleon Penetration Through Matter," to be published in *Health Physics.*

R. I. Van Hook and D. A. Crossley, Jr.
"Assimilation and Biological Turnover of Cesium-134, Iodine-131, and Chromium-51 in Brown Crickets, *Acheta domesticus* (L.)," *Health Phys.* **16**, 463–67 (1969).

R. C. Vehse and E. T. Arakawa
"Optical and Photoemissive Properties of Nickel in the Vacuum Ultraviolet Spectral Region," *Phys. Rev.* **180**, 695–700 (Apr. 15, 1969).

R. B. Vora, M. A. Prasad, and J. E. Turner
"Effect of Delta-Ray Buildup in High-Energy Dose Calculations," *Health Phys.* **15**, 139–43 (1968).

O. E. Wagner
"On the Temperature Dependence of Ovshinky Type Devices," submitted for publication in the *Journal of Applied Physics.*

O. E. Wagner, L. G. Christophorou, and J. G. Carter
"Lifetimes of Liquid Benzene, Toluene, and Mesitylene Excited by a Pulsed-Electron Beam," submitted for publication in *Chemical Physics Letters.*

M. A. Warren, Wallace de Laguna, and N. J. Lusczynski
"Studies of Sites for Nuclear Energy Facilities – Brookhaven National Laboratory," *Hydrology of Brookhaven National Laboratory and Vicinity, Suffolk County, New York,* Geological Survey Bulletin 1156-C, U.S. Government Printing Office, Washington, D.C., 1968.

J. L. Wilhm
"Some Aspects of Community Structure and Function of Benthic Macroinvertebrates in a Constant Spring," *Am. Midland Naturalist* (submitted).

"Transfer of Radionuclides from Detritus to Benthic Macroinvertebrates in Laboratory Microecosystems," *Health Phys.* (submitted).

M. W. Williams, R. A. MacRae, R. N. Hamm, and E. T. Arakawa
"Collective Oscillations in Pure Liquid Benzene," *Phys. Rev. Letters* **22**, 1088–92 (1969).

R. B. Williams
"A Table of Mean Effective Temperatures for the Metabolism of Biological Systems Subjected to Sinusoidal Cycles in Temperature," *J. Theoret. Biol.* **24** (in press).

R. B. Williams, J. S. Olson, and S. I. Auerbach
Mathematical Models of Natural Systems: Analysis of Stability and Change in Ecosystems 2, Second Interim Report on an Ecological Study for the Ford Foundation (1968).

J. P. Witherspoon
"Radiosensitivity of Forest Tree Species to Acute Fast Neutron Radiation," *Proceedings of the Second National Symposium on Radioecology,* CONF-670503 (1969).

Ecological Recovery, Civil Defense, Little Harbor Report, TID-24690, pp. 27–32 (1969).

J. P. Witherspoon and F. G. Taylor
"Radiation-Induced Anatomical Modifications in Forest Trees," *J. Tenn. Acad. Sci.* **44** (in press).

"Retention of a Fallout Simulant Containing ^{134}Cs by Pine and Oak Trees," *Health Phys.* (in press).

"Effects of External Beta Radiation on Higher Plants," *Progress Report in Postattack Ecology,* ORNL-TM-2466, pp. 2–17 (1969).

M. Witkamp

"External Factors Influencing Mineralization and Immobilization of Some Radionuclides from Tree Litter," *Isotopes and Radiation in Soil Organic-Matter Studies,* IAEA, Vienna, pp. 231–40, 1968.

"Accumulation of ^{137}Cs by *Trichoderma viride* Relative to ^{137}Cs in Soil Organic Matter and Soil Solution," *Soil Sci.* **106**, 309–11 (1968).

"Mineral Retention by Epiphyllic Organisms," *The Tropical Rainforest,* ed. by E. P. Odum (in press).

"Environmental Effects of Microbial Turnover of Some Mineral Elements: I. Abiotic Factors," *Soil Biol. Biochem.* **1** (in press) (1969).

"Environmental Effects of Microbial Turnover of Some Mineral Elements: II. Biotic Factors," *Soil Biol. Biochem.* **1** (in press) (1969).

"Daily Cycles in Soil Respiration," *Ecology* (in press).

"Aspects of Soil Microflora in Gamma Irradiated Rain Forest," *The Tropical Rainforest,* ed. by H. T. Odum (in press).

M. Witkamp and B. Barzansky

"Microbial Immobilization of ^{137}Cs in Forest Litter," *Oikos* **19**, 392–95 (1968).

M. Witkamp and M. L. Frank

"Evolution of CO_2 from Litter, Humus, and Subsoil of a Pine Stand," *Pedobiologia* (in press).

"Cesium-137 Kinetics in Terrestrial Microcosms," *Symposium on Radioecology,* ed. by D. J. Nelson and F. C. Evans, CONF-670503 (1969).

"Effects of Temperature, Rainfall, and Fauna on Transfer of ^{137}Cs, K, Mg, and Mass in Consumer-Decomposer Microcosms," *Ecology* (submitted).

"Loss of Weight and Minerals from Tree Litter in Three Subsystems of a Watershed," *Environ. Sci. Technol.* (submitted).

H. A. Wright, V. E. Anderson, J. E. Turner, Jacob Neufeld, and W. S. Snyder

"Calculation of Radiation Dose Due to Protons and Neutrons with Energies from 0.5 to 2.0 GeV," *Health Phys.* **16**, 13–31 (1969).

Harvel Wright, E. E. Branstetter, Jacob Neufeld, J. E. Turner, and W. S. Snyder

"Calculation of Radiation Dose Due to High-Energy Protons," pp. 1487–92 in *Proc. of First International Congress on Radiation Protection,* Pergamon, New York, 1968.

Harvel Wright and W. S. Snyder

"On the Differentiability of Arbitrary Real-Valued Set Functions – I," to be published in the *Transactions of the American Mathematical Society.*

H. A. Wright and J. E. Turner

"Free-Nucleon Target Model Applied to Penetration and Dose Calculations for 200 and 400 MeV Protons and Neutrons," submitted for publication in *Health Physics.*

Edward Yeargers

"Ultraviolet Light Effects on Proteins," pp. 37–46 in *The Biologic Effects of Ultraviolet Radiation,* ed. by Frederick Urbach, Pergamon, London, 1969.

Lectures

S. I. Auerbach

Radioecological Research Relevant to Radioactive Waste Releases, Visit of the National Academy of Sciences Committee on Radioactive Waste Disposal, Oak Ridge National Laboratory, October 18, 1968, Oak Ridge, Tennessee.

Ecology, Representative Faculty Members of East Central College Consortium, Oak Ridge National Laboratory, November 8, 1969, Oak Ridge, Tennessee.

Radioisotopes and the Dynamics of Forest Ecosystems, Seminar in Environmental Biology, Smithsonian Institution, March 6, 1969, Washington, D.C.

Radionuclides in the Study of Forest Ecosystem Dynamics, Radiation Biology Seminar, Colorado State University, June 17, 1969, Ft. Collins, Colorado.

J. A. Auxier

Dosimetry for Human Exposures: Field Experiments and Laboratory Intercomparisons, Blue Grass Chapter, Health Physics Society, September 7, 1968, Prestonsburg, Kentucky.

Standardization and Intercomparison of Dosimetry Systems, Florida Chapter, Health Physics Society, January 17, 1969, St. Petersburg, Florida.

Dosimetry for Nuclear Accidents, Florida Chapter, Health Physics Society, January 17, 1969, St. Petersburg, Florida.

K. Becker

Recent Work on Solid-State Dosimetry at ORNL, Department of Medical Physics, Royal Graduate Medical School, August 30, 1968, London, England; Niels-Bohr Institute, Copenhagen University, September 5, 1968, Copenhagen, Denmark; Julich Nuclear Research Center, September 9, 1968, Julich, Germany.

Modern Techniques of Solid-State Dosimetry, Ten-Week Course in Health Physics, October 10, 1968, Oak Ridge, Tennessee.

Recent Research in Solid-State Dosimetry at ORNL, Atomic Energy of Canada, Ltd., October 28, 1968, Chalk River, Canada; Defence Research Board of Canada, October 29, 1968, Ottawa, Canada.

Research on Glass and Exoelectron Dosimetry, USAF School of Aerospace Medicine, Brooks AFB, February 20, 1969, San Antonio, Texas.

Thermally Stimulated Exoelectron Emission (TSEE) Dosimetry, Department of Physics and Astronomy, Western Kentucky University, March 21, 1969, Bowling Green, Kentucky.

TSEE Dosimetry Research at ORNL, Physikalisch-Technische Bundesanstalt, April 28, 1969, Braunschweig, Germany.

Solid-State Dosimetry Research at ORNL, Hahn-Meitner-Institute for Nuclear Research, April 30, 1969, Berlin, Germany; Nuclear Physics Centre, University of Toulouse, May 10, 1969, Toulouse, France.

Nuclear Track Registration in Solids, Euratom Central Laboratory for Nuclear Measurements, May 13, 1969, Geel, Belgium.

S. R. Bernard

Information Center for Internal Exposure, COSATI Committee, May 9, 1969, ORNL, Oak Ridge, Tennessee.

R. D. Birkhoff

The Electron Flux Spectra and Radiation Yields in Solids Irradiated by Nuclear Radiation, University of Kentucky, April 25, 1969, Lexington, Kentucky.

W. P. Bonner

Aspects of Pollution in the Gainesville Water Supply, Civil Engineering Department, Vanderbilt University, February 25, 1969, Nashville, Tennessee.

Land-Water Interactions, Students of the Radiological Health Program, University of Arkansas, March 28, 1969, Oak Ridge National Laboratory, Oak Ridge, Tennessee

R. L. Bradshaw and F. M. Empson (technical advisors on motion picture)

Project Salt Vault, produced by ORNL, 1968.

R. N. Compton

The Radiation Physics of Slow Electron Collisions with Molecules, Rensselaer Polytechnic Institute, April 7, 1969, Troy, New York.

Mary Jane Cook

Radiation Biology, UT Physics Class (4730), May 13, 15, and 20, 1969, Knoxville, Tennessee.

K. E. Cowser

Radioactive Waste Management, Sanitary Engineering Students, Tennessee Technological University, May 16, 1969, Oak Ridge, Tennessee.

Clinch River Study, National Academy of Sciences, Committee on Radioactive Waste Disposal, October 17–18, 1968, Oak Ridge, Tennessee.

Research and Development Studies in Radioactive Waste Management, Briefing for Personnel of the National Center for Air Pollution Control, May 2, 1968, Oak Ridge, Tennessee.

Radioactive Waste Management, U.S. Army Nuclear Science Training Session, July 24, 1968, Oak Ridge, Tennessee.

Radioactive Waste Disposal, American Association for the Advancement of Science, Committee on Environmental Alterations, February 8, 1969, New York, New York.

Introduction to Radioactive Waste Disposal, Students of the Radiological Health Program, University of Arkansas, March 28, 1969, Oak Ridge National Laboratory, Oak Ridge, Tennessee.

Wallace de Laguna

Radioactive Waste Disposal by Hydrofracturing, Students of the Radiological Health Programs, University of Arkansas, March 28, 1969, Oak Ridge National Laboratory, Oak Ridge, Tennessee.

P. B. Dunaway

Interaction of Ionizing Radiation and Parasitism, Biology Department, University of Georgia, April 8, 1969, Athens, Georgia.

Comparative Hematology of Mammals, Biology Division, Battelle Northwest Laboratory, September 3, 1969, Richland, Washington.

F. M. Empson

Radioactive Waste Disposal in Salt Deposits, University of Arkansas, Students of the Radiological Health Program, March 28, 1969, Oak Ridge National Laboratory, Oak Ridge, Tennessee.

B. R. Fish

The Citizen's Role in Air Pollution Control, Knoxville Women's Club, November 25, 1968; Bearden Rotary Club, January 3, 1969; Ossoli Circle, March 17, 1969, Knoxville, Tennessee; Roane County Air and Water Pollution Committee, April 7, 1969, Harriman, Tennessee; Chilhowee Club, May 6, 1969, Maryville, Tennessee.

Source and Environmental Sampling of Airborne Radioactivity, UT Physics Department, April 10, 1969, Knoxville, Tennessee.

Forestry's Role in the Control of Air Pollution, National Council of Forestry Association Executives, June 30, 1969, Gatlinburg, Tennessee.

Measurement and Meaning of Radioactive Surface Contamination, Bluegrass Chapter of Health Physics Society, September 7, 1968, Prestonsburg, Kentucky.

Health Physics Fellowship Program, Tennessee Technological University, November 25, 1968, Cookeville, Tennessee.

W. R. Garrett

Variational Method for Long-Range Scattering Interaction, Louisiana State University, April 25, 1969, Baton Rouge, Louisiana.

D. G. Jacobs

Waste Disposal and Environmental Movement of Radionuclides, Sanitary Engineering Students, Tennessee Technological University, May 16, 1969, Oak Ridge, Tennessee.

Radioactive Waste Disposal, Students in Health Physics Course, University of Tennessee, April 15, 17, 22, 24, 29, and May 1, 6, and 8, 1969, Knoxville, Tennessee.

Environmental Safety Evaluation Studies, Students of the Radiological Health Program, University of Arkansas, March 28, 1969, Oak Ridge National Laboratory, Oak Ridge, Tennessee.

Waste Disposal and Mineral Exchange of Radionuclides, Health Physics and Radiation Protection Course sponsored by Oak Ridge Associated Universities, June 3, 1969, Oak Ridge, Tennessee.

Hazards Evaluation, Civil Engineering Department, Vanderbilt University, March 11, 1969, Nashville, Tennessee.

S. Kolehmainen

Kinetics of ^{137}Cs in Bluegill, Atomic Energy of Canada Ltd., Chalk River Laboratories, March 26, 1969, Chalk River, Ontario, Canada.

T. F. Lomenick

Earthquakes, West Knoxville, Tennessee, Optimist Club, March 20, 1969, Knoxville, Tennessee.

Site Selection and Geohydrologic Explorations, TVA meeting on Burial Ground Planning Operations and Maintenance, April 8, 1969, Oak Ridge National Laboratory, Oak Ridge, Tennessee.

W. C. McClain

Rock Mechanics Aspects of Hydraulic Fracturing and Determination of Fracture Orientation, National Academy of Sciences, Committee on Radioactive Waste Disposal, October 17–18, 1968, Oak Ridge, Tennessee.

The Disposal of Solidified Radioactive Wastes in Salt Mines, Army Chemical Corps, Edgewood Arsenal, December 17, 1968, Baltimore, Maryland.

Disposal of High Level Radioactive Wastes in Specially Designed Salt Mine, Civil Engineering Department, University of Kentucky, January 24, 1969, Lexington, Kentucky.

K. Z. Morgan

The Need for Standardization Procedures in the Application of Ionizing Radiation to Medical and Dental Patients, National Center for Radiological Health, November 15, 1968, Rockville, Maryland.

The Proper Working Level of Radon and Its Daughter Products in the Uranium Mines of the United States, Hearing on Radiation Standards for Mines, November 20, 1968, Washington, D.C.

Comments on Congressional Bills for Radiation Hazard Control, S.2067, H.R. 10790, and S.2075, Prepared as a comparative evaluation for the use of members of the Health Physics Society and others who are interested in radiation hazard control, January 19, 1968.

Supplemental Statement on the Proper Working Level of Radon and Its Daughter Products in the Uranium Mines of the USA, Supplement to testimony presented November 20, 1968, Washington, D.C.

Future Opportunities in Health Physics, Health Physics Society Midyear Topical Symposium, January 29–31, 1969, Los Angeles, California.

Internal Dose Lectures, University of Tennessee, March 27, 1969; April 1, 1969; April 3, 1969; April 8, 1969.

Maximizing the Ratio of Benefits to Risks from Medical X-Rays, Memphis and Shelby County Medical and Dental Societies, April 1, 1969, Memphis, Tennessee.

Health Physics, Military Reserve Officers Seminar, July 24, 1968, Oak Ridge, Tennessee (ORAU); Navy Seminar, Sponsored by ORAU, August 22, 1968, Special Training Building, Oak Ridge, Tennessee.

Ionizing Radiation: Benefits Versus Risks, Tennessee Valley Industrial Health Conference, September 19, 1968, Gatlinburg, Tennessee.

Assumptions Made by the Internal Dose Committee of the International Commission on Radiological Protection, Sixth Annual Meeting of the Gesellschaft fur Nuclearmedizin, September 26–28, 1968, Wiesbaden, Germany.

Redirecting Health Physics Studies to Areas of Greatest Interest, First European Congress of the International Radiation Protection Association, October 9–11, 1968, Menton, France.

Making the Benefits from Dental X-Rays Far in Excess of the Risks, American Academy of Oral Roentgenology, October 26, 1968, Miami Beach, Florida.

Ionizing Radiation: Benefits Versus Risks, American Nuclear Society (Ohio Section), November 7, 1968, Cleveland, Ohio.

Benefits vs Risk of Medical X-Rays, ORAU Tenth Week of ORAU's Health Physics Course, November 11, 1968, Oak Ridge, Tennessee.

Internal Dose Lectures, Vanderbilt University, Nashville, Tennessee, April 28, 1969; April 29, 1969; May 5, 1969; May 6, 1969.

Lecture to X-Ray Technologists on Radiation Protection, University of Tennessee Hospital, May 8, 1969, Knoxville, Tennessee.

Medical X-Ray Exposures, New England Chapter of Health Physics Society, May 28, 1969, Boston, Massachusetts.

Health Physics Research at Oak Ridge National Laboratory, ORNL Management Advisory Council, June 11, 1969, Oak Ridge, Tennessee

Reducing the Unneccessary Diagnostic Exposure, Joint Meeting of Hazards of Radiation, June 28, 1969, Milwaukee, Wisconsin.

Education, Training, and Certification Requirements of the X-Ray Technologist, American Society of Radiological Technologists, July 2, 1969, Atlanta, Georgia.

D. J. Nelson

Biological Aspects of Thermal Pollution, ORAU Exhibits Division, January 6, 1969, Oak Ridge, Tennessee.

Clams as Biological Monitors, Regional Science Experience Center, March 13, 1969, Oak Ridge, Tennessee.

Trace Elements in Clam Shells, Departments of Geology, Botany, and Zoology, The University of Tennessee, May 19, 1969, Knoxville, Tennessee.

P. S. Rohwer

Estimating Expected Radiation Doses to Populations in Plowshare, UT-AEC Farm, October 30, 1968, Oak Ridge, Tennessee.

H. C. Schweinler

Dimensional Analysis, Geneva College, February 7, 1969, Beaver Falls, Pennsylvania.

A. F. Shinn

Radiation and Bees, U.S. Army Nuclear Science Training Session, July 23, 1968, Oak Ridge, Tennessee.

Radioactivity and Its Effect on Bees and Honey, Tennessee State Beekeepers Association, October 11, 1968, Nashville, Tennessee.

Bees and Radiation, Florida State Beekeepers Association, November 1, 1968, Redington Beach, Florida.

Civil Defense Measures for Agriculture and Population, Social Issues Seminar, St. John's Lutheran Church, June 27, 1969, Knoxville, Tennessee.

W. S. Snyder

Health Physics Organizations and Journals, ORAU Ten-Week Course in Health Physics, September 25, 1969, Oak Ridge, Tennessee.

The Use of Monte Carlo Methods for Obtaining Dose Distributions in the Human Body from Sources of Neutrons or Photons, University of Alabama, November 20, 1968, University, Alabama; University of Alabama, November 21, 1968, Birmingham; Auburn University, November 22, 1968, Auburn.

Tsuneo Tamura

Agronomic Crop Culture for the Middle East, Mid-East Senior Advisory Panel Meeting, June 16–17, 1969, Oak Ridge National Laboratory, Oak Ridge, Tennessee.

Isabel H. Tipton

Standard Man, Knoxville Science Club, April 11, 1969, Knoxville, Tennessee.

J. P. Witherspoon

Ecology at ORNL, U.S. Naval Reserve Seminar, August 29, 1968, Oak Ridge, Tennessee.

Radiosensitivity of Higher Plants, UT-AEC Agricultural Research Laboratory Seminar, March 26, 1969, Oak Ridge, Tennessee.

Beta Radiation and Higher Plants, Civil Defense Seminar, UT-AEC, June 4, 1969, Oak Ridge, Tennessee.

H. A. Wright

Differentiability of Set Functions, University of Missouri, December 13, 1968, Rolla, Missouri.

HEALTH PHYSICS DIVISION

SEPTEMBER 1, 1969

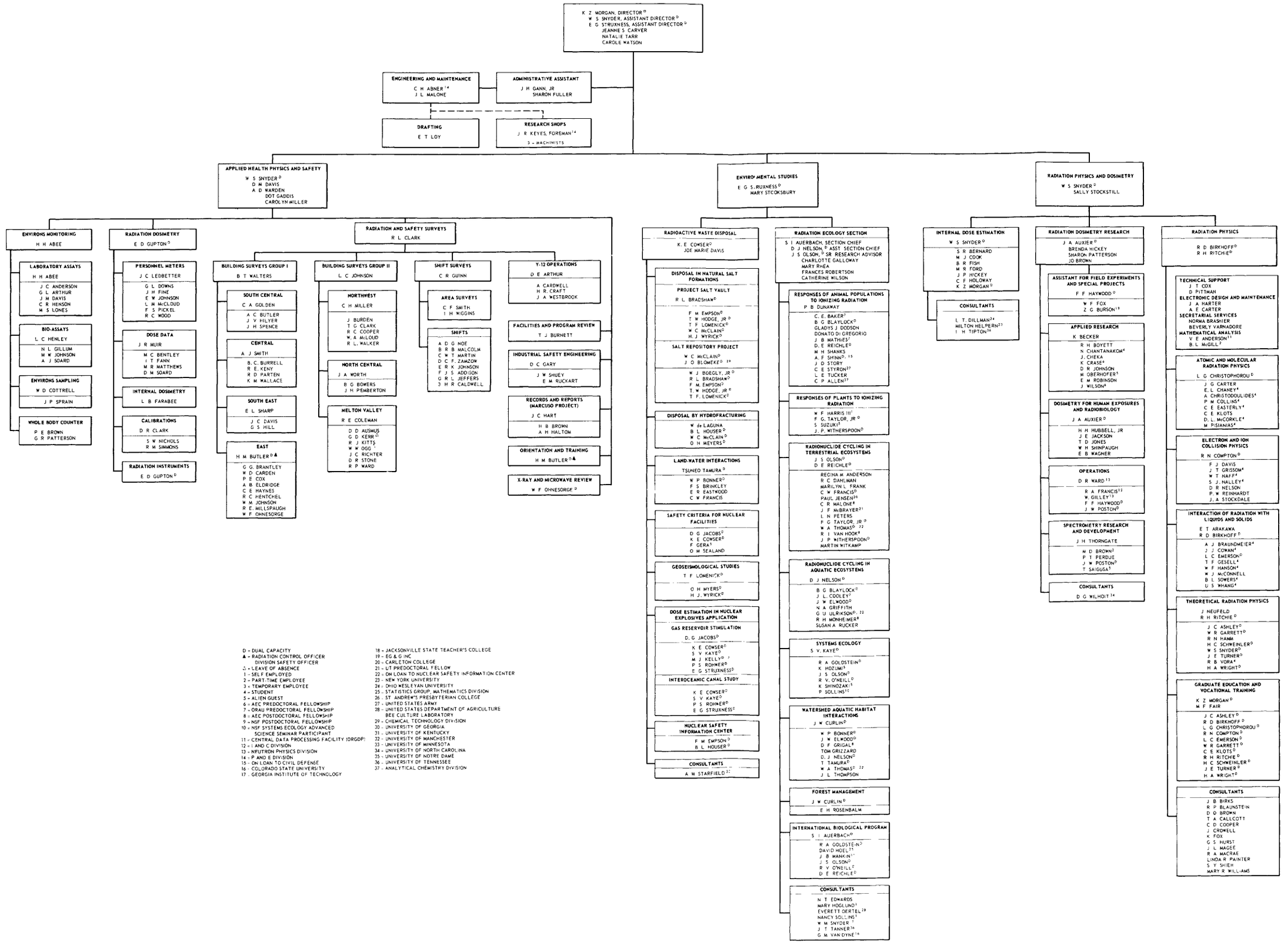

D = DUAL CAPACITY
▲ = RADIATION CONTROL OFFICER
DIVISION SAFETY OFFICER
Δ = LEAVE OF ABSENCE
1 = SELF EMPLOYED
2 = PART-TIME EMPLOYEE
3 = TEMPORARY EMPLOYEE
4 = STUDENT
5 = ALIEN GUEST
6 = AEC PREDOCTORAL FELLOWSHIP
7 = ORAU PREDOCTORAL FELLOWSHIP
8 = AEC POSTDOCTORAL FELLOWSHIP
9 = NSF POSTDOCTORAL FELLOWSHIP
10 = NSF SYSTEMS ECOLOGY ADVANCED SCIENCE SEMINAR PARTICIPANT
11 = CENTRAL DATA PROCESSING FACILITY (ORGDP)
12 = I AND C DIVISION
13 = NEUTRON PHYSICS DIVISION
14 = P AND E DIVISION
15 = ON LOAN TO CIVIL DEFENSE
16 = COLORADO STATE UNIVERSITY
17 = GEORGIA INSTITUTE OF TECHNOLOGY
18 = JACKSONVILLE STATE TEACHER'S COLLEGE
19 = EG & G INC
20 = CARLETON COLLEGE
21 = UT PREDOCTORAL FELLOW
22 = ON LOAN TO NUCLEAR SAFETY INFORMATION CENTER
23 = NEW YORK UNIVERSITY
24 = OHIO WESLEYAN UNIVERSITY
25 = STATISTICS GROUP, MATHEMATICS DIVISION
26 = ST. ANDREW'S PRESBYTERIAN COLLEGE
27 = UNITED STATES ARMY
28 = UNITED STATES DEPARTMENT OF AGRICULTURE BEE CULTURE LABORATORY
29 = CHEMICAL TECHNOLOGY DIVISION
30 = UNIVERSITY OF GEORGIA
31 = UNIVERSITY OF KENTUCKY
32 = UNIVERSITY OF MANCHESTER
33 = UNIVERSITY OF MINNESOTA
34 = UNIVERSITY OF NORTH CAROLINA
35 = UNIVERSITY OF NOTRE DAME
36 = UNIVERSITY OF TENNESSEE
37 = ANALYTICAL CHEMISTRY DIVISION

ORNL-4446
UC-41 – Health and Safety

INTERNAL DISTRIBUTION

1. Biology Library
2–4. Central Research Library
5. Laboratory Shift Supervisor
6–7. ORNL, Y-12 Technical Library Document Reference Section
8–61. Laboratory Records Department
62. Laboratory Records, ORNL RC
63. H. H. Abee
64. H. I. Adler
65. E. T. Arakawa
66. D. E. Arthur
67. J. C. Ashley
68. S. I. Auerbach
69–75. J. A. Auxier
76. S. E. Beall
77. K. Becker
78. S. R. Bernard
79. R. D. Birkhoff
80. W. P. Bonner
81. R. H. Boyett
82. R. L. Bradshaw
83. P. E. Brown
84. F. R. Bruce
85. T. H. J. Burnett
86. J. G. Carter
87. H. P. Carter
88. J. S. Cheka
89. L. G. Christophorou
90. R. L. Clark
91. T. G. Clark
92. W. E. Cohn
93. W. C. Colwell
94. R. N. Compton
95. M. J. Cook
96. K. E. Cowser
97. J. T. Cox
98. F. L. Culler
99. J. W. Curlin
100. Roger Dahlman
101. D. M. Davis
102. F. J. Davis
103. Wallace deLaguna
104. P. B. Dunaway
105. L. C. Emerson
106. F. M. Empson
107. M. F. Fair
108. L. B. Farabee
109. B. R. Fish
110. M. R. Ford
111. C. E. Francis
112. J. A. Gabbard
113. W. R. Garrett
114. D. C. Gary
115. J. H. Gillette
116. C. R. Guinn
117. E. D. Gupton
118. R. N. Hamm
119. C. S. Harrill
120. J. C. Hart
121. J. A. Harter
122. F. F. Haywood
123. R. F. Hibbs
124. L. B. Holland
125. C. F. Holoway
126. H. H. Hubbell
127. D. G. Jacobs
128. D. R. Johnson
129. L. C. Johnson
130. T. D. Jones
131. W. H. Jordan
132. M. A. Kastenbaum
133. M. T. Kelley
134. R. F. Kimball
135. C. E. Klots
136. T. A. Lincoln
137. J. L. Liverman
138. R. S. Livingston
139. T. F. Lomenick
140. H. G. MacPherson
141. F. C. Maienschein
142. W. C. McClain
143. W. J. McConnell
144. A. J. Miller
145. K. Z. Morgan
146. D. J. Nelson
147. D. R. Nelson

148. Jacob Neufeld
149. J. S. Olson
150. R. V. O'Neill
151–152. R. B. Parker
153. G. R. Patterson
154. R. W. Peelle
155. J. W. Poston
156. H. P. Raaen
157. M. L. Randolph
158. D. E. Reichle
159. P. W. Reinhardt
160. R. H. Ritchie
161. E. M. Robinson
162. P. S. Rohwer
163. H. C. Schweinler
164. H. E. Seagren
165. M. J. Skinner
166. W. S. Snyder
167. J. A. Stockdale
168. E. G. Struxness
169. D. A. Sundberg
170. T. Tamura
171. E. H. Taylor
172. J. H. Thorngate
173. J. E. Turner
174. E. B. Wagner
175. B. T. Walters
176. D. R. Ward
177. A. D. Warden
178. A. M. Weinberg
179. J. P. Witherspoon
180. Martin Witkamp
181. H. A. Wright
182. Gale Young
183. MIT Practice School
184. J. E. Cantlon (consultant)
185. J. C. Frye (consultant)
186. E. Gerjuoy (consultant)
187. J. B. Hursh (consultant)
188. H. O. Wyckoff (consultant)
189. J. B. Birks (consultant)
190. R. P. Blaunstein (consultant)
191. W. Brandt (consultant)
192. M. D. Brown (consultant)
193. E. Burke (consultant)
194. J. F. Burns (consultant)
195. Thomas Callcott (consultant)
196. L. W. Cochran (consultant)
197. C. D. Cooper (consultant)
198. J. Crowell (consultant)
199. B. J. Eastlund (consultant)
200. Charles Eisenhauer (consultant)
201. Ugo Fano (consultant)
202. K. Fox (consultant)
203. John Garth (consultant)
204. W. T. Ham, Jr. (consultant)
205. G. S. Hurst (consultant)
206. M. Inokuti (consultant)
207. R. J. Lovell (consultant)
208. R. A. MacRae (consultant)
209. Linda R. Painter (consultant)
210. J. E. Parks (consultant)
211. S. Y. Shieh (consultant)
212. T. D. Strickler (consultant)
213. G. E. Thoma (consultant)
214. I. H. Tipton (consultant)
215. J. R. Totter (consultant)
216. G. M. Van Dyne (consultant)
217. Neil Wald (consultant)
218. D. G. Willhoit (consultant)
219. M. R. Williams (consultant)
220. J. T. Tanner (consultant)

EXTERNAL DISTRIBUTION

221–445. Given external distribution
446. Laboratory and University Division, AEC, ORO
447–728. Given distribution as shown in TID-4500 under Health and Safety category (25 copies – CFSTI)